"CURRENT PROBLEMS IN NUCLEAR PHYSICS AND ATOMIC ENERGY", Kyiv, 2012

NPAE 2012

September 3-7, 2012
Kyiv, Ukraine

The 4-th International Conference

Current Problems in Nuclear Physics and Atomic Energy

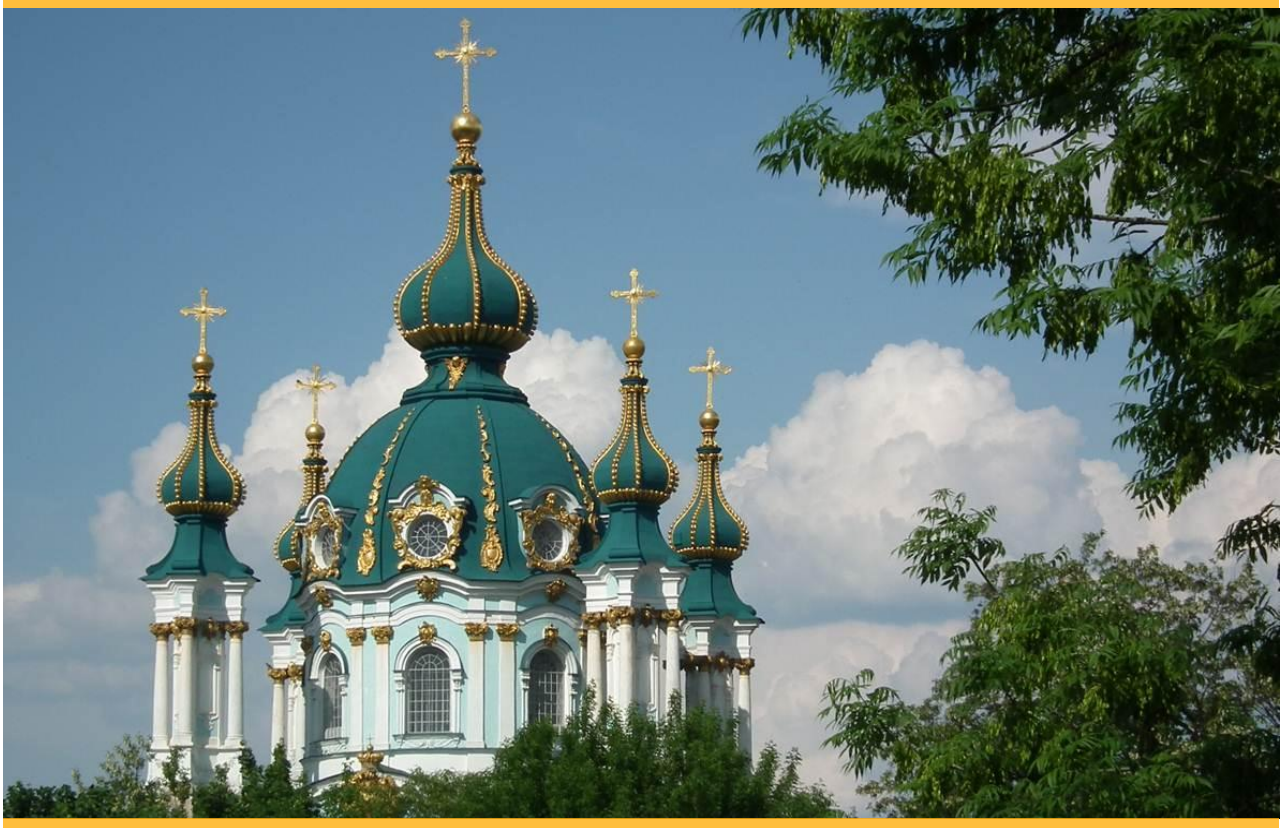

Proceedings, part 1

Proceedings


КИЇВСЬКИЙ НАЦІОНАЛЬНИЙ УНІВЕРСИТЕТ імені ТАРАСА ШЕВЧЕНКА
ІНСТИТУТ ПІСЛЯДИПЛОМНОЇ ОСВІТИ

National Academy of Sciences of Ukraine
Institute for Nuclear Research

The 4-th International Conference

Current Problems in Nuclear Physics and Atomic Energy (NPAE-Kyiv2012)

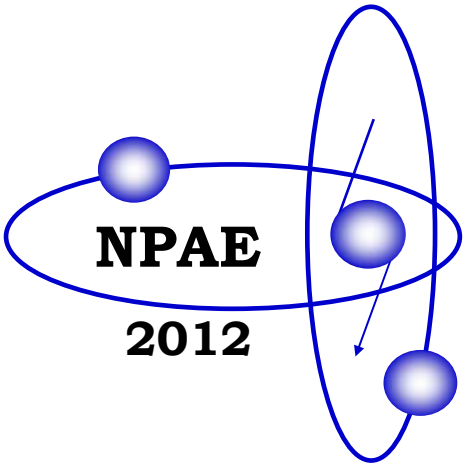

Proceedings

September 3 - 7, 2012
Kyiv, Ukraine

Part I

Kyiv 2013

International Advisory Committee

A. Barabash	ITEP, Russia	I. M. Neklyudov	KIPT, Ukraine
R. Bernabei	RU, Italy	V. E. Oberacker	VU, USA
S. Gales	GANIL, France	Yu. Ts. Oganessian	JINR, Russia
K.A. Gridnev	SPU, Russia	V. Pronyaev	IPPE, Russia
S. Hofmann	GSI, Germany	P. Ring	TUM, Germany
A. Iwamoto	JU, Japan	S. Shlomo	TAMU, USA
A. A. Korsheninnikov	KIAE, Russia	A. Sobiczewski	SINS, Poland
M. Lattuada	LNS, Italy	V. G. Zelevinsky	MSU, USA
W. Nazarewicz	ORNL, USA		

Organizing Committee

I. M. Vyshnevskyi – Chairman
L. A. Bulavin, V. M. Kolomietz – Vice-Chairs
V. Yu. Denisov – Scientific secretary

Scientific Program Committee:

L. A. Bulavin	NTSU, Kyiv	V. M. Pavlovych	KINR, Kyiv
F. A. Danevich	KINR, Kyiv	V. M. Pugatch	KINR, Kyiv
V. Yu. Denisov	KINR, Kyiv	A. T. Rudchyk	KINR, Kyiv
G. F. Filippov	BITF, Kyiv	N. F. Shulga	KIPT, Kharkiv
O. O. Gritzay	KINR, Kyiv	I. V. Simenog	BITF, Kyiv
V. F. Klepikov	IERT, Kharkiv	V. I. Slisenko	KINR, Kyiv
V. M. Kolomietz	KINR, Kyiv	I. M. Vyshnevskyi	KINR, Kyiv
V. A. Plujko	NTSU, Kyiv	S. N. Yezhov	NTSU, Kyiv

Local Organizing Committee (KINR, Kyiv)

O. O. Beliuskina, V. V. Davydovskyy, O. D. Grygorenko, T. V. Kovalinska, L. M. Lamonova, V. A. Nesterov, N. V. Olesova, V. V. Ostashko, N. A. Pilipenko, Yu. N. Stepanenko, V. P. Verbytskyi, V. V. Uleshchenko

The address of the Organizing Committee

Institute for Nuclear Research, 47, Pr. Nauky, 03680, Kyiv, Ukraine
Tel.: (38044)525-52-38, 525-14-56
Fax: (38044)525-44-63
E-mail: npae-kyiv2012@kinr.kiev.ua
Website: http://www.kinr.kiev.ua/NPAE-Kyiv2012

ISBN 978-966-02-6750-3 (загальний)
ISBN 978-966-02-6751-0 (Частина I)

The 4-th International Conference
Current Problems in Nuclear Physics
and Atomic Energy
(NPAE-Kyiv2012)

September 3 - 7, 2012
Kyiv, Ukraine

Organized by:

National Academy of Sciences of Ukraine
Kyiv Institute for Nuclear Research of NASU
Taras Shevchenko National University of Kyiv

Organizers thank sponsors of conference and authors of reports and all participants for their contribution in success of the conference

Preface

This issue contains the contributed papers of the 4-rd International Conference “Current Problems in Nuclear Physics and Atomic Energy” (NPAE-Kyiv2012), which was held on September 3 - 7, 2012 in Kyiv, Ukraine. The Conference was organized by the National Academy of Sciences of Ukraine, the Institute for Nuclear Research of the National Academy of Sciences of Ukraine, Kyiv in collaboration with Taras Shevchenko National University of Kyiv. This is the continuation of the Conferences held in Kyiv on May 29 - June 3, 2006, June 9 - 15, 2008, and June 7 - 12, 2010.

NPAE-Kyiv2012 Conference covered the following topics:

- Collective processes in atomic nuclei;
- Nuclear reactions;
- Nuclear structure and decay processes;
- Rare nuclear processes;
- Neutron and reactor physics, nuclear data;
- Problems of atomic energy;
- Applied nuclear physics, experimental facilities and detection techniques;
- High-energy physics.

Such wide area of topics, discussed during the Conference, is closely connected with the interests of our country to develop the fundamental research in the field of nuclear physics, which is the base of nuclear energy.

The purpose of these Conferences was to bring together scientists to share their knowledge in the current problems in nuclear physics and atomic energy. 175 scientists participated at the Conference. I would like to note that NPAE-Kyiv2012 Conference attracted the attention of the scientists and the number of experts from all over the world. We were glad to meet scientists from Algeria, Austria, Brazil, Byelorussia, Canada, France, Germany, India, Italy, Japan, Libya, Norway, Poland, Romania, Russia, Slovakia, Slovenia, USA, Uzbekistan and from various scientific institutions of Ukraine.

The program consisted of 5 plenary sessions, where 19 scientific reports were presented, 117 oral and 44 poster presentations. In total 180 scientific reports were presented during the Conference.

Scientific program of the Conference was supplemented by the cultural events. Participants had possibility to learn more on the history and customs of Ukrainian people and enjoyed the beauty of Kyiv. Very broad range of the participants and their informal contacts helped to create new possibilities for the future collaboration concerning different fields of scientific researches.

As suggested by the participants and organizers, the next Conference will be held again in Ukraine, in the year 2014.

Finally, we are thankful to all authors for providing their manuscripts.

Ivan M. Vyshnevskyi

Chairman of the NPAE-Kyiv2012 Conference,
Academician of the National Academy of Sciences
Director of the Institute for Nuclear Research

CONTENTS

Part I

Plenary Sessions

Section 1. Collective Processes in Atomic Nuclei

Section 2. Nuclear Reactions

Section 3. Nuclear Structure and Decay Processes

Part II

Section 4. Rare Nuclear Processes

Section 5. Neutron and Reactor Physics, Nuclear Data

Section 6. Problems of Atomic Energy

Section 7. Applied Nuclear Physics, Experimental Facilities and Detection Techniques

Section 8. High Energy Physics

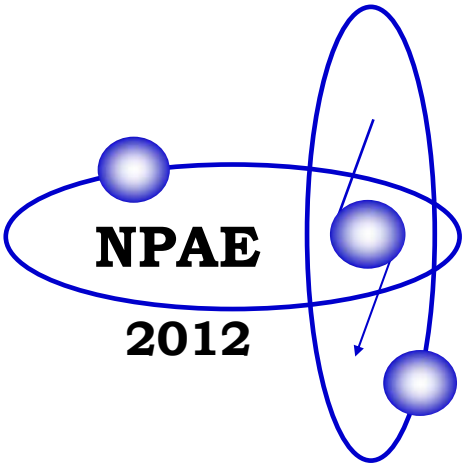

Plenary Sessions

DOUBLE BETA DECAY EXPERIMENTS: BEGINNING OF A NEW ERA

A. S. Barabash

Institute of Theoretical and Experimental Physics, Moscow, Russia

The review of current experiments on search and studying of double beta decay processes is done. Results of the most sensitive experiments are discussed and values of modern limits on effective Majorana neutrino mass ($\langle m_\nu \rangle$) are given. New results on two neutrino double beta decay are presented. The special attention is given to new current experiments with mass of studied isotopes more than 100 kg, EXO-200 and KamLAND-Zen. These experiments open a new era in research of double beta decay. In the second part of the review prospects of search for neutrinoless double beta decay in new experiments with sensitivity to $\langle m_\nu \rangle$ at the level of ~ 0.01-0.1 eV are discussed. Parameters and characteristics of the most perspective projects (CUORE, GERDA, MAJORANA, SuperNEMO, EXO, KamLAND-Zen, SNO +) are given.

1. Introduction

Interest in $0\nu\beta\beta$ decay has seen a significant renewal in recent 10 years after evidence for neutrino oscillations was obtained from the results of atmospheric, solar, reactor, and accelerator neutrino experiments. These results are impressive proof that neutrinos have a nonzero mass. The detection and study of $0\nu\beta\beta$ decay may clarify the following problems of neutrino physics: (i) lepton number non-conservation, (ii) neutrino nature: whether the neutrino is a Dirac or a Majorana particle, (iii) absolute neutrino mass scale (a measurement or a limit on m_1), (iv) the type of neutrino mass hierarchy (normal, inverted, or quasidegenerate), (v) *CP* violation in the lepton sector (measurement of the Majorana *CP*-violating phases).

Progress in the double beta decay is connected with increase in mass of a studied isotope and sharp decrease in a background. During a long time (1948 - 1980) samples with mass of isotope ~ 1 - 25 g were used. So the first observation of a two neutrino double beta decay in direct (counting) experiment was done in 1987 when studying 14 g of enriched ^{82}Se [1]. And only in the 80th - beginning of the 90th the mass of studied isotope increased to hundred grams and even to 1 kg. In the 90th Heidelberg-Moscow [2] and IGEX [3] experiments, containing 11 kg and 6.5 kg of ^{76}Ge, respectively, were started. In zero years the NEMO-3 [4] and CUORICINO [5] installations, containing approximately 10 kg of isotopes (7 kg of ^{100}Mo, 1 kg of ^{82}Se, etc. in NEMO-3 and 40 kg of crystals from a natural oxide of Te, containing 10 kg of ^{130}Te, in CUORICINO) set the fashion.

In 2011 the EXO-200 [6] and KamLAND-Zen [7] installations in which hundreds kilograms of ^{136}Xe are used already were started. Soon it is planned to carry out start of several more installations with mass of studied isotopes ~ 100 kg (SNO + [8] and CUORE [9]). And it means the beginning of a new era in 2β decay experiments when sensitivity to effective Majorana mass of neutrino will reach for the first time values < 0.1 eV.

Structure of the review is the following: in Section 2 current large-scale experiments on $\beta\beta$ decay are considered, in Section 3 the most perspective planned experiments are discussed, the best modern limits on neutrino mass and the forecast for possible progress in the future are given in Section 4 (Conclusion).

2. Current large-scale experiments

In this Section the current large-scale experiments are discussed. NEMO-3 experiment was stopped in January, 2011, but data analysis in this experiment proceeds and consequently it should be carried to the current experiments.

2.1. NEMO-3

This tracking experiment, in contrast to experiments with ^{76}Ge, detects not only the total energy deposition, but other parameters of the process, including the energy of the individual electrons, angle between them, and the coordinates of the event in the source plane. Since June of 2002 and to January of 2011, the NEMO-3 detector has been operated in the Frejus Underground Laboratory (France) located at a depth of 4800 m w.e. The detector has a cylindrical structure and consists of 20 identical sectors (Fig. 1). A thin (30 - 60 mg/cm^2) source containing double beta decaying nuclei and natural material foils have a total area of 20 m^2 and a weight of up to 10 kg was placed in the detector. The energy of the electrons is measured by plastic scintillators (1940 individual counters), while the tracks are reconstructed on the basis of information obtained in the planes of Geiger cells (6180 cells) surrounding the source on both sides. The main characteristics of the detector are the following. The energy resolution of the scintillation counters lies in the interval 14 - 17 % FWHM for electrons of energy 1 MeV. The time resolution is 250 ps for electron energy of 1 MeV and the accuracy in reconstructing the vertex of $2e^-$ events is 1 cm.

Measurements with the NEMO-3 detector revealed that tracking information, combined with time and energy measurements, makes it possible to suppress the background efficiently. Using the NEMO-3 installation 7 isotopes – ^{100}Mo (6.9 kg), ^{82}Se (0.93 kg), ^{116}Cd (405 g), ^{150}Nd (36.6 g), ^{96}Zr (9.4 g), ^{130}Te (454 g) and ^{48}Ca (7 g) are investigated. A full description of the detector and its characteristics can be found in [4].

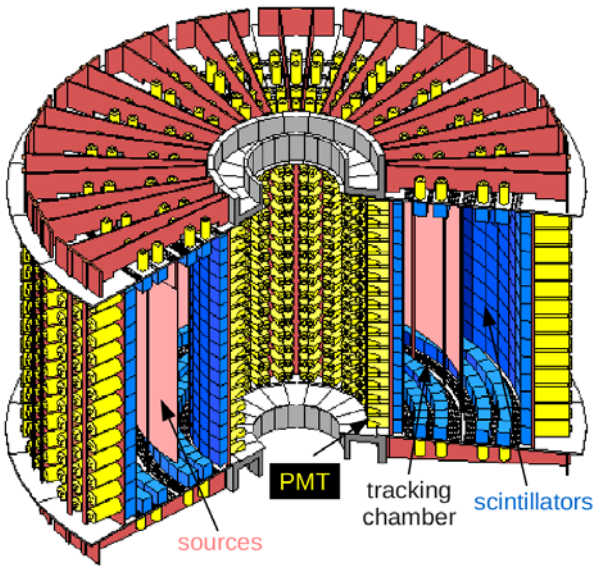

Fig. 1. Scheme of the NEMO-3 detector without shielding [4].

Fig. 2 displays the spectrum of $2\nu\beta\beta$ events for ^{100}Mo that were collected over 3.49 years (low radon Phase II). The angular distribution and single electron spectrum are also shown. The total number of events exceeds 700000 which is much greater than the total statistics of all of the preceding experiments with ^{100}Mo (and even greater than the total statistics of all previous $2\nu\beta\beta$ decay experiments!). It should also be noted that the background is as low as 1.3 % of the total number of $2\nu\beta\beta$ events. Measurements of the $2\nu\beta\beta$ decay half-lives have been performed for seven isotopes available in NEMO-3. The NEMO-3 results of $2\nu\beta\beta$ half-life measurements are given in Table 1. For all the isotopes the energy sum spectrum, single electron energy spectrum and angular distribution were measured. The ^{100}Mo double-beta decay to the 0^+_1 excited state of ^{100}Ru has also been measured by NEMO-3 [13]. For ^{100}Mo, ^{82}Se, ^{96}Zr, ^{150}Nd and ^{130}Te these results are published. For the other isotopes their status is preliminary.

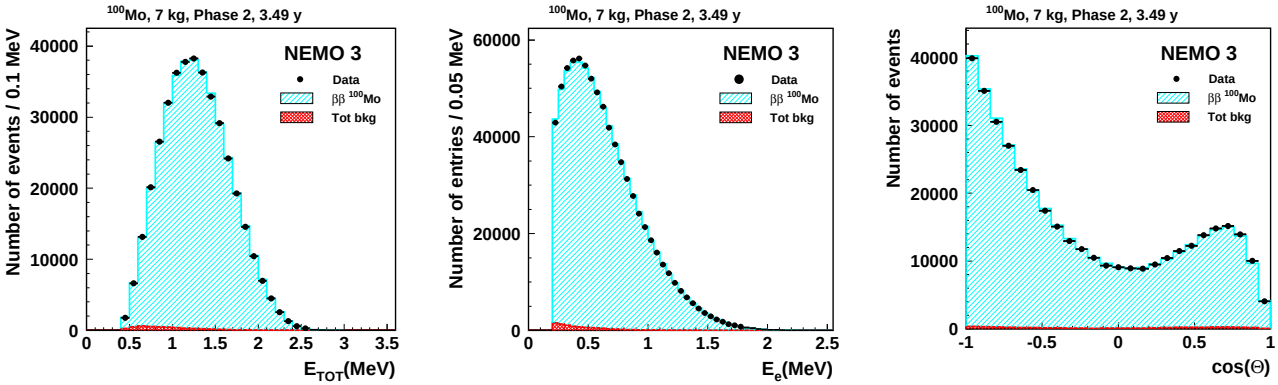

Fig. 2. Total energy, individual energy and angular distributions of the ^{100}Mo 2ν events in the NEMO-3 experiment for the low radon data phase (3.49 years).

Table 1. **Present results from NEMO-3 (only part of full statistic has been analysed)**

Isotope	$T_{1/2}$ (2ν), yr	$T_{1/2}$ (0ν), yr; 90 % C.L.	$T_{1/2}$ ($0\nu\chi^0$), yr; 90 % C.L.
^{100}Mo	$(7.11 \pm 0.02 \pm 0.54)\cdot 10^{18}$ [10]	$> 1.1\cdot 10^{24}$ [11]	$> 2.7\cdot 10^{22}$ [12]
^{100}Mo - ^{100}Ru (0^+_1) [13]	$(5.7^{+1.3}_{-0.9} \pm 0.8)\cdot 10^{20}$	$> 8.9\cdot 10^{22}$	-
^{82}Se	$(9.6 \pm 0.3 \pm 1.0)\cdot 10^{19}$ [10]	$> 3.6\cdot 10^{23}$ [11]	$> 1.5\cdot 10^{22}$ [12]
^{130}Te [14]	$(7.0 \pm 0.9 \pm 1.1)\cdot 10^{20}$	$> 1.3\cdot 10^{23}$	$> 1.6\cdot 10^{22}$
^{116}Cd	$(2.88 \pm 0.04 \pm 0.16)\cdot 10^{19}$	$> 1.3\cdot 10^{23}$	-
^{150}Nd [15]	$(9.2^{+0.25}_{-0.22} \pm 0.62)\cdot 10^{18}$	$> 1.8\cdot 10^{22}$	$> 1.52\cdot 10^{21}$
^{96}Zr [16]	$(2.35 \pm 0.14 \pm 0.19)\cdot 10^{19}$	$> 9.2\cdot 10^{21}$	$> 1.9\cdot 10^{21}$
^{48}Ca	$(4.4^{+0.5}_{-0.4} \pm 0.4)\cdot 10^{19}$	$> 1.3\cdot 10^{22}$	-

No evidence for $0\nu\beta\beta$ decay was found for all seven isotopes. The associated limits are presented in Table 1. Best limits have been obtained for ^{100}Mo ($T_{1/2} > 1.1 \cdot 10^{24}$ yr). Corresponding limits on the neutrino mass is $\langle m_\nu \rangle < 0.29 - 0.7$ eV (using NME values from [17 - 21]). No evidence for $0\nu\chi^0\beta\beta$ decay was found for all seven isotopes too. The limits for ^{100}Mo, ^{82}Se, ^{150}Nd, ^{96}Zr and ^{130}Te are presented in Table 1. In particular, strong limits on "ordinary" Majoron (spectral index 1) decay of ^{100}Mo ($T_{1/2} > 2.7\cdot 10^{22}$ yr) and ^{82}Se ($T_{1/2} > 1.5\cdot 10^{22}$ yr) have been obtained. Corresponding bounds on the Majoron–neutrino coupling constant have been established, $\langle g_{ee} \rangle < (0.25 - 0.67) \cdot 10^{-4}$ and $< (0.6 - 1.9) \cdot 10^{-4}$, respectively (using nuclear matrix elements from [17 - 23]).

Data analysis proceeds and Collaboration hope for receiving final results for all 7 isotopes in the nearest future (2012 - 2013).

2.2. EXO-200 [6, 24]

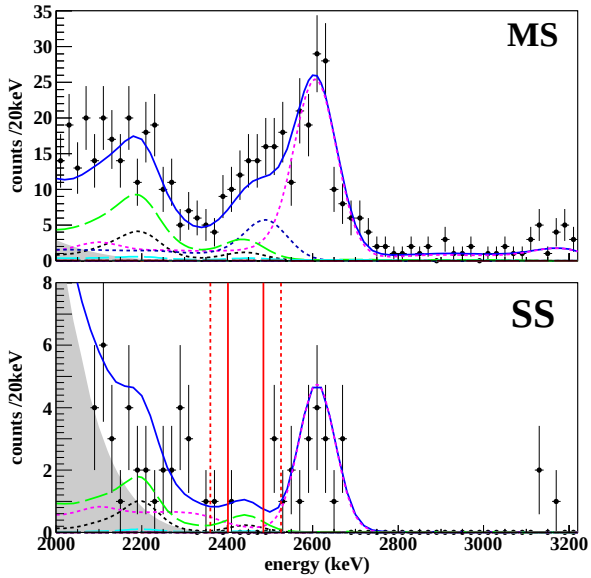

Fig. 3. Energy spectra in the ^{136}Xe $Q_{\beta\beta}$ region for multiple-site (top) and single-site (bottom) events. The 1 (2 σ regions around $Q_{\beta\beta}$ are shown by solid (dashed) vertical lines [24].

EXO-200 (Enriched Xenon Observatory) is operating at the Waste Isolation Pilot Plant (WIPP, 1585 m w.e.) since May 2011. The experiment consists of 175 kg of Xe enriched to 80.6 % in ^{136}Xe housed in a liquid time projection chamber (TPC). The TPC is surrounded by passive and active shields. This detector measures energy through both ionization and scintillation and is capable of effectively rejecting rays through topological cuts. EXO-200 has recently claimed the first observation of 2ν in ^{136}Xe ($Q_{\beta\beta}$ = 2458.7 keV) [6]. Initial results on 0ν decay together with new result for 2ν mode are published in [24].The fiducial volume used in this analysis contains 79.4 kg of ^{136}Xe ($3.52 \cdot 10^{26}$ atoms), corresponding to 98.5 kg of active ^{enr}LXe. Energy resolution is 10.5 % (FWHM) using ionization signal only and 4 % (FWHM) at 2.615 MeV using both ionization and scintillation signals. Background index (BI) in the 0ν region is $1.4 \cdot 10^{-3}$ counts/keV·kg·yr (Fig. 3). Results obtained after 2896.6 h of measurements are the following:

$$T_{1/2}\,(2\nu,\,^{136}\mathrm{Xe}) = [2.23 \pm 0.017\ (\mathrm{stat}) \pm 0.22\ (\mathrm{syst})]\cdot 10^{21}\ \mathrm{yr} \quad (1)$$

$$T_{1/2}\,(0\nu,\,^{136}\mathrm{Xe}) > 1.6\cdot 10^{25}\ \mathrm{yr} \quad (2)$$

Last result provides upper limit $\langle m_\nu \rangle$ < 0.14 - 0.38 eV using NME values from [17 - 19, 21, 23]. Taking into account present background one can predict that EXO-200 sensitivity after 5 years of data taking will be $T_{1/2} \sim (4 - 5) \cdot 10^{25}$ yr ($\langle m_\nu \rangle \sim 0.08 - 0.24$ eV).

The project is also a prototype for a planned 1 tone sized experiment that may include the ability to identify the daughter of ^{136}Ba in real time, effectively eliminating all classes of background except that due to 2ν decay (see Section 3.5).

2.3. KamLAND-Zen [7, 25]

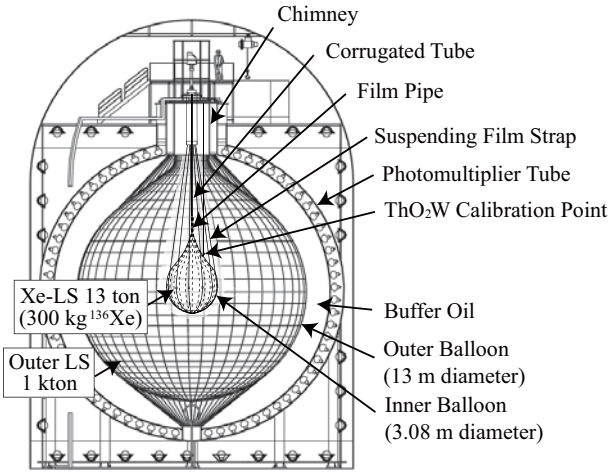

Fig. 4. Schematic diagram of the KamLAND-Zen detector [7].

The detector KamLAND-Zen (Fig. 4) is a modification of the existing KamLAND detector carried out in the summer of 2011. The $\beta\beta$ source/detector is 13 tons of Xe-loaded liquid scintillator (Xe-LS) contained in a 3.08-m-diameter spherical inner balloon (IB). The IB is constructed from 25-μm-thick transparent nylon film and is suspended at the center of the KamLAND detector by 12 film straps of the same material. The IB is surrounded by 1 kton of liquid scintillator (LS) contained in a 13-m-diameter spherical outer balloon (OB) made of 135-μm-thick composite film. The outer LS acts as an active shield for external γ's and as a detector for internal radiation from the Xe-LS or IB. The Xe-LS contains (2.52 ± 0.07) % by weight of enriched xenon gas (full weight of xenon is ~ 330 kg). The isotopic abundances in the enriched xenon were measured by residual gas analyzer to be (90.93 ± 0.05) % ^{136}Xe and (8.89 ± 0.01) % ^{134}Xe. Scintillation light is recorded by 1,325 17-inch and 554 20-inch photomultiplier tubes (PMTs). Details of the KamLAND detector are given in Ref. [26]. The energy resolution at 2.614 MeV is $\sigma = (6.6 \pm 0.3)\ \%/\sqrt{E}$ (MeV). The vertex resolution is $\sigma = 15\ \mathrm{cm}/\sqrt{E}$ (MeV). The energy spectrum of $\beta\beta$ decay candidates is shown in Fig. 5. Unexpectedly detected background (BI ≈ 10^{-4} counts/keV·kg·yr) is ~ two order of magnitude higher than estimated background using previous data of KamLAND detector. Nevertheless quite good results for $\beta\beta$ decay of ^{136}Xe were obtained. The measured $2\nu\beta\beta$ decay half-life of ^{136}Xe [25] is:

$$T_{1/2}\,(2\nu,\,^{136}\mathrm{Xe}) = [2.38 \pm 0.02(\mathrm{stat}) \pm 0.14(\mathrm{syst})]\cdot 10^{21}\ \mathrm{yr} \quad (3)$$

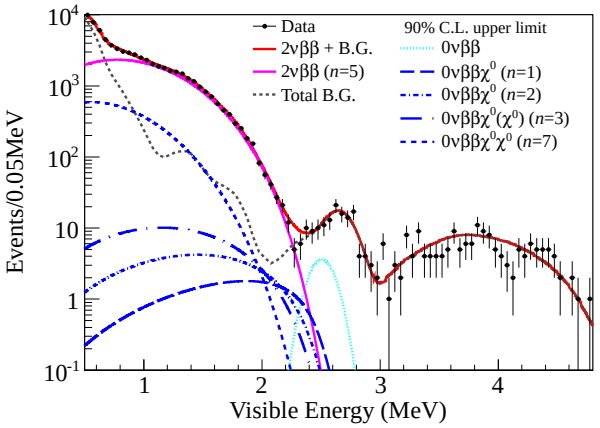

Fig. 5. Energy spectrum of selected $\beta\beta$ decay candidates (data points) together with the best-fit backgrounds (gray dashed lines) and $2\nu\beta\beta$ decay (purple solid line), and the 90 % C.L. upper limit for $0\nu\beta\beta$ decay and Majoron-emitting $0\nu\beta\beta$ decays for each spectral index. The red line depicts the sum of the $2\nu\beta\beta$ decay and background spectra. Figure is taken from [25].

This is consistent with the result obtained by EXO-200 [6, 24]. For $0\nu\beta\beta$ decay, the data give a lower limit of $T_{1/2}(0\nu, {}^{136}\text{Xe}) > 6.2 \cdot 10^{24}$ yr (90 % C.L.) [25], which corresponds to limit, $\langle m_\nu \rangle < 0.22$ - 0.6 eV using NME values from [17-19, 21, 23]. Strong limits on neutrinoless double beta decay with emission of Majoron were obtained too. In particular, a lower limit on the ordinary Majoron (spectral index n = 1) emitting decay half-life of ^{136}Xe was obtained as $T_{1/2}(0\nu\chi^0, {}^{136}\text{Xe}) > 2.6 \cdot 10^{24}$ yr at 90 % C.L. The corresponding upper limit on the effective Majoron-neutrino coupling, using a range of available nuclear matrix calculations, is $\langle g_{ee} \rangle < (0.8 - 1.6) \cdot 10^{-5}$. This is most strong limit on $\langle g_{ee} \rangle$ from $\beta\beta$ decay experiments.

Now the Collaboration undertakes efforts to decrease the background. In principle, the background can be lowered approximately in 100 times. If it will be done, sensitivity of experiment will essentially increase and for 3 years of measurements will be $T_{1/2} \sim 2 \cdot 10^{26}$ yr that corresponds to sensitivity to neutrino mass, $\langle m_\nu \rangle \sim 0.04$ - 0.11 eV. After end of the first phase of the experiment the phase 2 is planned (see the Section 3.6).

2.4. GERDA-I [27]

GERDA is a low-background experiment which searches for the neutrinoless double beta decay of ^{76}Ge, using an array of high-purity germanium (HPGe) detectors isotopically enriched in ^{76}Ge [28]. The detectors are operated naked in ultra radio-pure liquid argon, which acts as the cooling medium and as a passive shielding against the external radiation. This innovative design, complemented by a strict material selection for radio-purity, allows to achieve low background level in the region of the Q-value of ^{76}Ge at 2039 keV. The experiment is located in the underground Laboratori Nazionali del Gran Sasso of the INFN (Italy). The Phase I of GERDA recently started using eight enriched coaxial detectors (totaling approximately 18 kg of ^{76}Ge). The Phase I comes after a one-year-long commissioning, in which natural and enriched HPGe detectors were successfully operated in the GERDA set-up. GERDA-I measurements have been started in November 2011. Results of first measurement are presented in Fig. 6.

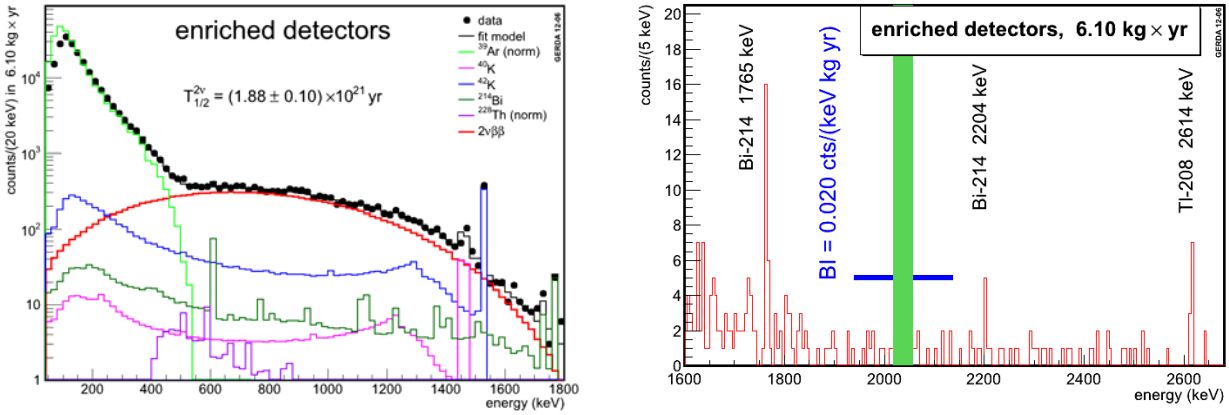

Fig. 6. First results from GERDA-I.

As can be seen the 2ν decay contribution is already clearly visible ($T_{1/2}(2\nu, {}^{76}\text{Ge}) \cong 1.88 \cdot 10^{21}$ yr, preliminary result). Background index in 0ν region is ~ 0.02 c/keV·kg·yr. Blind analysis will be applied to the 0ν region (which is closed now). First result will be reported in the end of 2012. Sensitivity of GERDA-I with present background is $\sim 2 \cdot 10^{25}$ yr for one year of measurement. In 2013 new ~ 20 kg of HPGe crystals will be added and experiment will be transformed to Phase II (GERDA-II). Description of full scale GERDA experiment is done in Section 3.2.

3. Future large-scale experiments

Here seven of the most developed and promising experiments which can be realized within the next few years are discussed (Table 2). The estimation of the sensitivity in the experiments is made using NME from [17 - 23].

3.1. CUORE [8, 29]

This experiment will be run at the Gran Sasso Underground Laboratory (Italy, 3500 m w.e.). The plan is to investigate 760 kg of $^{nat}TeO_2$, with a total of ~ 200 kg of ^{130}Te. One thousand low temperature (~8 mK) detectors, each having a weight of 750 g, will be manufactured and arranged in 19 towers. One tower is approximately equivalent to the CUORICINO detector [5]. Planed energy resolution is 5 kev (FWHM). One of the problems here is to reduce the background level by a factor of about 15 in relation to the background level achieved in the detector CUORICINO. Upon reaching a background level of 0.01 keV^{-1} kg^{-1} y^{-1}, the sensitivity of the experiment to the 0ν decay of ^{130}Te for 5 y of measurements and at 90 % C.L. will become approximately 10^{26} yr ($\langle m_\nu \rangle \sim 0.05$ - 0.13 eV) – see discussion in [35]. The experiment has been approved and funded. A general test of the CUORE detector, comprising a single tower and named CUORE-0, will start to take data in 2012. The full-scale CUORE will start in 2014.

Table 2. **The seven most developed and promising projects. Sensitivity at 90 % CL for three (first step of GERDA and MAJORANA, SNO+, and KamLAND-Zen), five (EXO, SuperNEMO and CUORE) and ten (full-scale GERDA and MAJORANA) years of measurements is presented. *M* - mass of isotopes**

Experiment	Isotope	*M*, kg	Sensitivity $T_{1/2}$ (yr)	Sensitivity $\langle m_\nu \rangle$ (meV)	Status
CUORE [8, 29]	^{130}Te	200	10^{26}	50 - 130	In progress
GERDA [27, 28]	^{76}Ge	40 1000	$2 \cdot 10^{26}$ $6 \cdot 10^{27}$	60 - 200 10 - 40	In progress R&D
MAJORANA [30, 31]	^{76}Ge	20 - 30 1000	10^{26} $6 \cdot 10^{27}$	90 - 300 10 - 40	In progress R&D
SuperNEMO [32,33]	^{82}Se	100 - 200	$(1 - 2) \cdot 10^{26}$	40 - 110	R&D; construction of first module
EXO [6, 34]	^{136}Xe	~ 175 1000	$(4 - 5) \cdot 10^{25}$ $8 \cdot 10^{26}$	80 - 240 20 - 55	Started in 2011 R&D
KamLAND-Zen [7, 25]	^{136}Xe	~ 330 1000	$\sim 2 \cdot 10^{26}$ $\sim 6 \cdot 10^{26}$	40 - 110 23 - 58	Started in 2011 R&D
SNO+ [8]	^{150}Nd	50 500	$\sim 6 \cdot 10^{24}$ $\sim 3 \cdot 10^{25}$	120 - 410 55 - 180	In progress R&D

3.2. GERDA [27, 28]

This is one of two planned experiments with ^{76}Ge (along with the MAJORANA experiment). The experiment is to be located in the Gran Sasso Underground Laboratory (Italy, 3500 m w.e.). The proposal is based on ideas and approaches which were proposed for GENIUS [36] and the GEM [37] experiments. The idea is to place "naked" HPGe detectors in highly purified liquid argon (as passive and active shield). It minimizes the weight of construction material near the detectors and decreases the level of background. The liquid argon dewar is placed into a vessel of very pure water. The water plays a role of passive and active (Cherenkov radiation) shield. The proposal involves three phases. In the first phase, the existing HPGe detectors (~ 18 kg), which previously were used in the Heidelberg-Moscow [2] and IGEX [3] experiments, are utilized (see Section 2.4). In the second phase ~ 40 kg of enriched Ge will be investigated. In the third phase the plan is to use ~ 500 - 1000 kg of ^{76}Ge. The sensitivity of the second phase (for three years of measurement) will be $T_{1/2} \sim 2 \cdot 10^{26}$ yr. This corresponds to sensitivity for $\langle m_\nu \rangle$ at the level of ~ 0.06 - 0.2 eV. The first two phases have been approved and funded. First phase will be finished in the end of 2012. The second phase setup is in an advanced construction stage and data taking is foreseen for 2013. The results of these steps will play an important role in the decision to support the full scale experiment.

3.3. MAJORANA [30, 31]

The MAJORANA facility will consist of ~ 1000 HPGe detectors manufactured from enriched germanium (the enrichment is > 86 %). The total mass of enriched germanium will be 1000 kg. The facility is designed in such a way that it will consist of many individual supercryostats manufactured from low radioactive copper, each containing HPGe detectors. The entire facility will be surrounded by a passive shield and will be located at an underground laboratory in the United States. Only the total energy deposition will be utilized in measuring the $0\nu\beta\beta$ decay of ^{76}Ge to the ground state of the daughter nucleus. The use of HPGe detectors, pulse shape analysis, anticoincidence, and low radioactivity structural materials will make it possible to reduce the background to a value below $2.5 \cdot 10^{-4}$ keV^{-1} kg^{-1} yr^{-1} and to reach a sensitivity of about $6 \cdot 10^{27}$ y within ten years of measurements. The corresponding sensitivity to the effective mass of the Majorana neutrino is about 0.01 to 0.04 eV. The measurement of the $0\nu\beta\beta$ decay of ^{76}Ge to the 0^+ excited state of the daughter nucleus will be performed by recording two cascade photons and two beta electrons. The planned sensitivity for this process is about 10^{27} y. In the first step ~ 20 - 30 kg of ^{76}Ge will be investigated. It is anticipated that the sensitivity to $0\nu\beta\beta$ decay to the ground state of the daughter nuclei for 3 years of measurement will be $T_{1/2} \sim 10^{26}$ yr.

It will reject or to confirm the "positive" result from [38 - 40]. Sensitivity to $\langle m_\nu \rangle$ will be ~ 0.09 - 0.3 eV. During this time different methods and technical questions will be checked and possible background problems will be investigated. The first module of MAJORANA (DEMONSTRATOR) is under constriction now and measurements is planned to begin in 2013.

3.4. SuperNEMO [32, 33]

The NEMO Collaboration has studied and is pursuing an experiment that will observe 100–200 kg of ^{82}Se with the aim of reaching a sensitivity for the 0ν decay mode at the level of $T_{1/2} \sim (1 - 2) \cdot 10^{26}$ y. The corresponding sensitivity to the neutrino mass is 0.04 to 0.11 eV. In order to accomplish this goal, it is proposed to use the experimental procedures nearly identical to that in the NEMO-3 experiment (see Section 2.1). The new detector will have planar geometry and will consist of 20 identical modules (5 - 7 kg of ^{82}Se in each sector). A ^{82}Se source having a thickness of about 40 mg/cm^2 and a very low content of radioactive admixtures is placed at the center of the modules. The detector will again record all features of double beta decay: the electron energy will be recorded by counters based on plastic scintillators ($\Delta E/E \sim 8$ - 10 % (FWHM) at $E = 1$ MeV), while tracks will be reconstructed with the aid of Geiger counters. The same device can be used to investigate ^{150}Nd, ^{100}Mo, ^{116}Cd, and ^{130}Te with a sensitivity to $0\nu\beta\beta$ decay at a level of about (0.5 - 1) $\cdot 10^{26}$ y [32]. The use of an already tested experimental technique is an appealing feature of this experiment. The plan is to arrange the equipment at the new Frejus Underground Laboratory (France; 4800 m w.e.). The construction and commissioning of the Demonstrator (first module) will be completed in 2013 - 2014.

3.5. EXO [6, 34]

In this experiment the plan is to implement Moe's proposal of 1991 [41]. Specifically it is to record both ionization electrons and the Ba^+ ion originating from the double beta decay process $^{136}Xe \rightarrow {}^{136}Ba^{++} + 2e^-$. In [34], it is proposed to operate with 1t of ^{136}Xe. The actual technical implementation of the experiment has not yet been developed. One of the possible schemes is to fill a TPC with liquid enriched xenon. To avoid the background from the 2ν decay of ^{136}Xe, the energy resolution of the detector must not be poorer than 3.8 % (FWHM) at an energy of 2.5 MeV (ionization and scintillation signals will be detected). In the 0ν decay of ^{136}Xe, the TPC will measure the energy of two electrons and the coordinates of the event to within a few millimeters. After that, using a special stick Ba ions will be removed from the liquid and then will be registered in a special cell by resonance excitation. For Ba^{++} to undergo a transition to a state of Ba^+, a special gas is added to xenon. The authors of the project assume that the background will be reduced to one event within five years of measurements. Given a 70 % detection efficiency it will be possible to reach a sensitivity of about $8 \cdot 10^{26}$ yr for the ^{136}Xe half-life and a sensitivity of about 0.02 to 0.06 eV to the neutrino mass. One should note that the principle difficulty in this experiment is associated with detecting the Ba^+ ion with a reasonably high efficiency. This issue calls for thorough experimental tests, and positive results have yet to be obtained. As the first stage of the experiment EXO-200 use 175 kg of ^{136}Xe without Ba ion identification (see Section 2.2).

3.6. KamLAND-Zen-1000

KamLAND-Zen is an upgrade of the KamLAND setup [26]. The idea is to convert it to neutrinoless double beta decay search by dissolving Xe gas in the liquid scintillator. This approach was proposed by R. Raghavan in 1994 [42]. At the first step this mixture (330 kg of Xe in 13 tons of liquid scintillator) will be contained in a small balloon suspended in the centre of the KamLAND sphere. It will guarantee low background level and high sensitivity of the experiment. This experiment (KamLAND-Zen) is in a stage of a data taking and some more years will proceed (see Section 2.3). Experiment KamLAND-Zen-1000 with 1000 kg of the enriched xenon will be the next step. It is planned to upgrade the existing detector. It is supposed that in the new inner balloon more bright liquid scintillator will be used and the number of PMTs will be increased. All this will allow to improve essentially energy resolution of the detector and, thereby, to increase sensitivity of experiment to double beta decay (see Table 2). KamLAND-Zen-1000 will start in ~ 2015.

3.7. SNO+ [8]

SNO+ is an upgrade of the solar neutrino experiment SNO (Canada), aiming at filling the SNO detector with Nd loaded liquid scintillator to investigate the isotope ^{150}Nd. With 0.1 % loading SNO+ will use 0.78 tonnes of neodymium and contain 43.7 kg of ^{150}Nd with no enrichment. SNO+ is in construction phase with natural neodymium. Data taking is foreseen in 2013 - 2014. After 3 yr of data tacking sensitivity will be ~ $6 \cdot 10^{24}$ yr (or 0.12 - 0.41 eV for $\langle m_\nu \rangle$). Finally 500 kg of enriched ^{150}Nd will be used (if enrichment of such quantity of Nd will be possible). Planned sensitivity is ~ $3 \cdot 10^{25}$ yr (or 0.055 - 0.18 eV for $\langle m_\nu \rangle$).

4. Conclusions

Best present limits on $0\nu\beta\beta$ decay and on $\langle m_\nu \rangle$ are presented in Table 3. It is visible that the most strong limits are received in experiments with ^{136}Xe, ^{76}Ge, ^{130}Te and ^{100}Mo. Considering existing uncertainty in values of NME it is

Table 3. **Best current results concerning the search for $0\nu\beta\beta$ decay. All bounds are given with 90 % C.L. The bounds on the effective mass of the Majorana neutrino $\langle m_\nu \rangle$ were obtained using the calculated nuclear matrix elements from [17 - 23]**

Isotope	$E_{\beta\beta}$, keV	$T_{1/2}$, yr		$\langle m_\nu \rangle$, eV
^{48}Ca	4272	$> 5.8 \cdot 10^{22}$	[43]	< 14
^{76}Ge	2039.0	$> 1.9 \cdot 10^{25}$	[2]	**< 0.20 - 0.69**
^{82}Se	2996	$> 3.6 \cdot 10^{23}$	[11]	< 0.77 - 2.4
^{96}Zr	3350	$> 9.2 \cdot 10^{21}$	[16]	< 3.9 - 13.7
^{100}Mo	3034.4	$> 1.1 \cdot 10^{24}$	[11]	**< 0.29 - 0.70**
^{116}Cd	2805	$> 1.7 \cdot 10^{23}$	[44]	< 1.16 - 2.16
^{128}Te	867	$> 1.5 \cdot 10^{24}$ (geochem)	(see [46])	< 1.8 - 4.2
^{130}Te	2527.5	$> 2.8 \cdot 10^{24}$	[5]	**< 0.28 – 0.81**
^{136}Xe	2458.7	$> 1.6 \cdot 10^{25}$	[24]	**< 0.14 - 0.38**
^{150}Nd	3367	$>1.8 \cdot 10^{22}$	[15]	< 2.2 - 7.5

possible to obtain conservative limit $\langle m_\nu \rangle < 0.4$ eV. It is possible to expect that in the next few years sensitivity to $\langle m_\nu \rangle$ will be improved by efforts of experiments of EXO-200, KamLAND-Zen, GERDA-I, MAJORANA-Demonstrator, CUORE-0 several times and will reach values ~ 0.1 - 0.3 eV. Start of full-scale experiments will allow to reach in 2015 - 2020 sensitivity to $\langle m_\nu \rangle$ at the level 0.01-0.1 eV that will allow to begin testing of inverted hierarchy region (~ 50 meV). Using modern experimental approaches it will be extremely difficult to reach sensitivity to $\langle m_\nu \rangle$ on the level of ~ 3 - 5 meV (normal hierarchy region). For this purpose it is required to increase mass of a studied isotope to 10 tons and to provide almost zero level of a background in studied area. Nevertheless it was shown, what even using known today methods such possibility, in principle, exists (see [45]).

REFERENCES

1. *Elliott S.R., Hahn A.A., Moe M.K.* // Phys. Rev. Lett. - 1987. - Vol. 59. - P. 2020 - 2023.
2. *Klapdor-Kleingrothaus H.V. et al.*// Eur. Phys. J. - 2001. - Vol. A 12. - P. 147 - 154.
3. *Aalseth C.E. et al.* // Phys. Rev. - 2002. - Vol. C 65. - P. 09007 (6 p).
4. *Arnold R. et al*. // Nucl. Instr. Meth. - 2005. - Vol. A 356. - P. 79 - 122.
5. *Andreotti E.* // Astropart. Phys. - 2011. - Vol. 34. - P. 822 - 831.
6. *Ackerman N. et al.* // Phys. Rev. Lett. - 2011. Vol. 107. - P. 212501 (5 p).
7. *Gando A. et al.* // Phys. Rev. - 2012. - Vol. C 85. - P. 045504 (6 p).
8. *Hartnell J.* // J. Phys. Conf. Ser. - 2012. - Vol. 375. - P. 042015 (4 p).
9. *Gorla P.* // J. Phys. Conf. Ser. - 2012. - Vol. 375. - P. 042013 (4 p).
10. *Arnold R. et al.* // Phys. Rev. Lett. - 2005. - Vol. 95. - P. 182302 (4 p).
11. *Barabash A.S., Brudanin V.B.* // Phys. At. Nucl. - 2011. - Vol. 74. - P. 312 - 317.
12. *Arnold R. et al.* // Nucl. Phys. - 2006. - Vol. A 765. - P. 483 - 494.
13. *Arnold R. et al*. // Nucl. Phys. - 2007. - Vol. A 781. - P. 209 - 226.
14. *Arnold R. et al.* // Phys. Rev. Lett. - 2011. - Vol. 107. - P. 062504 (4 p).
15. *Argyriades J. et al.* // Phys. Rev. - 2009. - Vol. C 80. - P. 032501R (5 p).
16. *Argyriades J. et al.* // Nucl. Phys. - 2010. - Vol. A 847. - P. 168 - 179.
17. *Kortelainen M., Suhonen J.* // Phys. Rev. - 2007. - Vol. C 76. - P. 024315 (6 p).
18. *Barea J., Iachello F.* // Phys. Rev. - 2009. - Vol. C 79. - P. 044301 (16 p).
19. *Simkovic F. et al.* // Phys. Rev. - 2009. - Vol. C 79. - P. 055501 (10 p).
20. *Rath P.K. et al.* // Phys. Rev. - 2010. - Vol. C 82. - P. 064310 (9 p).
21. *Rodrigues T.R., Martinez-Pinedo G.M.* // Phys. Rev. Lett. - 2010. - Vol. 105. - P. 252503 (4 p).
22. *Kortelainen M., Suhonen J.* // Phys. Rev. - 2007. - Vol. C 75. - P. 051203R (5 p).
23. *Caurier E. et al.* // Phys. Rev. Lett. - 2008. - Vol. 100. - P. 052503 (4 p).
24. *Auger M. et al.* // arXiv:hep-ex/1205.5608.
25. *Gando A. et al.* // arXiv:hep-ex/1205.6372.
26. *Abe S. et al.* // Phys. Rev. - 2010. - Vol. C 81. - P. 025807.
27. *Cattadori C.M.* // J. Phys. Conf. Ser. - 2012. - Vol. 375. - P. 042008 (5 p).
28. *Abt I. et al.* // arXiv:hep-ex/0404039.
29. *Arnaboldi C. et al.* // Nucl. Inst. Meth. - 2004. - Vol. A 518. - P. 775 - 798.
30. *Majorana Collaboration* // arXiv:nucl-ex/0311013.
31. *Wilkerson J.F. et al.* // J. Phys. Conf. Ser. - 2012. - Vol. 375. - P. 042010 (5 p).
32. *Barabash A.S.* // Czech. J. Phys. - 2002. - Vol. 52. - P. 575 - 581.
33. *Barabash A.S.* // J. Phys. Conf. Ser. - 2012. - Vol. 375. - P. 042012 (4 p).
34. *Danilov M. et al.* // Phys. Lett. - 2000. - Vol. B 480. - P. 12 - 18.

35. *Alessandria F. et al.* // arXiv:nucl-ex/1109.0494.
36. *Klapdor-Kleingrothaus H.V., Hellmig J., Hirsch M.* // J. Phys. - 1998. - Vol. G 24. - P. 483 - 516.
37. *Zdesenko Yu.G., Ponkratenko O.A., Tretyak V.I.* // J. Phys. - 2001. - Vol. G 27. - P. 2129 - 2146.
38. *Klapdor-Kleingrothaus H.V. et al.* // Mod. Phys. Lett. - 2001. - Vol. A 16. - P. 2409 - 2420.
39. *Klapdor-Kleingrothaus H.V. et al.* // Phys. Lett. - 2004. - Vol. B 586. - P. 198 - 212.
40. *Klapdor-Kleingrothaus H.V. et al.* // Mod. Phys. Lett. - 2006. - Vol. A 21. - P. 1547 - 1566.
41. *Moe M.* // Phys. Rev. - 1991. - Vol. C 44. - P. R931 - R934.
42. *Raghavan R.S.* // Phys. Rev. Lett. - 1994. - Vol. 72. - P. 1411 - 1414.
43. *Umehara S. et al.* // Phys. Rev. - 2008. - Vol. C 78. - P. 058501 (4 p).
44. *Danevich F.A.* // Phys. Rev. - 2003. - Vol. C 68. - P. 035501 (12 p).
45. *Barabash A.S.* // J. Phys. - 2012. - Vol. 39. - P. 085103 (8 p).
46. *Barabash A.S.* // Phys. Part. Nucl. - 2011. - Vol. 42. - P. 613 - 627.

DAMA/LIBRA RESULTS AND PERSPECTIVES OF THE SECOND STAGE

R. Bernabei[1], P. Belli[1], F. Cappella[2], V. Caracciolo[3], R. Cerulli[3], C. J. Dai[4], A. d'Angelo[2], A. Di Marco[1], H. L. He[4], A. Incicchitti[2], X. H. Ma[4], F. Montecchia[1,5], X. D. Sheng[4], R. G. Wang[4], Z. P. Ye[4,6]

[1] Dipartimento di Fisica, Università di Roma "Tor Vergata"
and Istituto Nazionale di Fisica Nucleare, Sezione di Roma "Tor Vergata", Rome, Italy
[2] Dipartimento di Fisica, Università di Roma "La Sapienza"
and Istituto Nazionale di Fisica Nucleare, Sezione di Roma "La Sapienza", Rome, Italy
[3] Laboratorio Nazionali del Gran Sasso, Istituto Nazionale di Fisica Nucleare, Assergi (AQ), Italy
[4] Institute of High Energy Physics, Chinese Academy of Sciences, Beijing, China
[5] Laboratorio Sperimentale Policentrico di Ingegneria Medica, Università di Roma "Tor Vergata", Rome, Italy
[6] University of Jing Gangshan, Jiangxi, China

The DAMA/LIBRA experiment is mainly dedicated to the investigation on DM particles in the Galactic halo by exploiting the model independent Dark Matter (DM) annual modulation signature. The present DAMA/LIBRA and the former DAMA/NaI (exposed masses: about 250 kg and about 100 kg of highly radiopure NaI(Tl), respectively) experiments have released so far a total exposure of 1.17 ton × yr collected over 13 annual cycles; they provide a model independent evidence of the presence of DM particles in the galactic halo at 8.9 σ C.L.. The data of another annual cycle in the same DAMA/LIBRA running conditions are at hand. After the substitution (at fall 2010) of all the photomultipliers (PMTs) with new ones, having higher quantum efficiency, DAMA/LIBRA has entered the phase 2; that substitution has allowed to lower the software energy threshold of the experiment in the present data taking. Future perspectives are mentioned.

1. Introduction

The DAMA project is an observatory for rare processes located deep underground at the Gran Sasso National Laboratory of the I.N.F.N. It is based on the development and use of low background scintillators. Profiting of the low background features of the realized set-ups, many rare processes are studied [1 - 21].

The main apparatus, DAMA/LIBRA, is investigating the presence of DM particles in the galactic halo by exploiting the model independent DM annual modulation signature.

In fact, as a consequence of its annual revolution around the Sun, which is moving in the Galaxy traveling with respect to the Local Standard of Rest towards the star Vega near the constellation of Hercules, the Earth should be crossed by a larger flux of Dark Matter particles around 2 June (when the Earth orbital velocity is summed to the one of the solar system with respect to the Galaxy) and by a smaller one around 2 December (when the two velocities are subtracted). Thus, this signature has a different origin and peculiarities than the seasons on the Earth and than effects correlated with seasons (consider the expected value of the phase as well as the other requirements listed below). This DM annual modulation signature is very distinctive since the effect induced by DM particles must simultaneously satisfy all the following requirements:

(1) the rate must contain a component modulated according to a cosine function;
(2) with one year period;
(3) with a phase that peaks roughly around 2nd June;
(4) this modulation must be present only in a well-defined low energy range, where DM particles can induce signals;
(5) it must be present only in those events where just a single detector, among all the available ones in the used set-up, actually "fires" (*single-hit* events), since the probability that DM particles experience multiple interactions is negligible;
(6) the modulation amplitude in the region of maximal sensitivity has to be ≤ 7 % in case of usually adopted halo distributions, but it may be significantly larger in case of some particular scenarios such as e.g. those in Refs. [22, 23].

At present status of technology it is the only model independent signature available in direct Dark Matter investigation that can be effectively exploited.

The exploitation of the DM annual modulation signature with highly radiopure widely sensitive NaI(Tl) as target material can permit to answer – by direct detection and in a way largely independent on the nature of the candidate and on the astrophysical, nuclear and particle Physics assumptions – the main question: "Are there Dark Matter (DM) particles in the galactic halo?" The corollary question: "Which are exactly the nature of the DM particle(s) detected by the annual modulation signature and the related astrophysical, nuclear and particle Physics scenarios?" requires subsequent model dependent corollary analyses as those available in literature. One should stress that no approach exists able to investigate the nature of the candidate either in the direct and indirect DM searches which can offer these latter information independently on assumed astrophysical, nuclear and particle Physics scenarios.

In particular, it is worth noting that many possibilities exist about the nature and the interaction types of the DM particles as e.g.: SUSY particles (as neutralino or sneutrino in various scenarios), inelastic Dark Matter in various

scenarios, electron interacting dark matter (including WIMP scenarios), a heavy neutrino of the 4-th family, sterile neutrino, Kaluza-Klein particles, self-interacting dark matter, axion-like (light pseudoscalar and scalar candidate), mirror dark matter in various scenarios, Resonant Dark Matter, DM from exotic 4th generation quarks, Elementary Black holes, Planckian objects, Daemons, Composite DM, Light scalar WIMP through Higgs portal, Complex Scalar Dark Matter, specific two higgs doublet models, exothermic DM, Secluded WIMPs, Asymmetric DM, Isospin-Violating Dark Matter, Singlet DM, Specific GU, SuperWIMPs , WIMPzilla, etc. (see in the literature). Moreover, even a suitable particle not yet foreseen by theories could be the solution or one of the solutions. It is worth noting that often WIMP is adopted as a synonymous of Dark Matter particle, referring usually to a particle with spin-independent elastic scattering on nuclei; on the contrary, WIMP identifies a class of Dark Matter candidates that can have different phenomenologies and interaction types. This is true also when considering a precise candidate as for example the neutralino; in fact the basic supersymmetric theory has a very large number of parameters that are by the fact unknown and, depending on the assumptions, they can present well different features and preferred interaction types. Often constrained SUGRA models (which allow easier calculations for the predictions e.g. at accelerators) are presented as SUSY or as the only way to SUSY, which is not the case. Other open aspects, which have large impact on model dependent investigations and comparisons, are e.g. which is the right description of the dark halo and related parameters, which is the right related atomic/nuclear and particle physics, etc. as well as the fundamental question on how many kinds of Dark Matter particles exist in the Universe[1]. It is also worth noting that the accelerators could prove the existence of some possible Dark Matter candidate particles, but they could never credit by themselves that a certain particle is in the halo as the solution or the only solution for Dark Matter particle(s). Moreover, Dark Matter candidate particles and scenarios (even for neutralino candidate) exist which cannot be investigated at accelerators. Thus, in order to pursue a widely sensitive direct detection of DM particles, model independent approach, ultra-low-background suitable target material, very large exposure and full control of the running conditions are mandatory.

2. Short summary of the results

The DAMA/LIBRA data released so far correspond to six annual cycles for an exposure of 0.87 ton × yr [13, 14]. Considering these data together with those previously collected by DAMA/NaI over 7 annual cycles (0.29 ton × yr), the total exposure collected over 13 annual cycles is 1.17 ton × yr; this is orders of magnitude larger than the exposures typically released in the field.

The DAMA/NaI set up and its performances are described in Refs. [1, 3, 4, 5], while the DAMA/LIBRA set-up and its performances are described in Refs. [12, 14]. The sensitive part of the DAMA/LIBRA set-up is made of 25 highly radiopure NaI(Tl) crystal scintillators placed in a 5-rows by 5-columns matrix; each crystal is coupled to two low background photomultipliers working in coincidence at single photoelectron level. The detectors are placed inside a sealed copper box flushed with HP nitrogen and surrounded by a low background and massive shield made of Cu/Pb/Cd-foils/polyethylene/paraffin; moreover, about 1 m concrete (made from the Gran Sasso rock material) almost fully surrounds (mostly outside the barrack) this passive shield, acting as a further neutron moderator. The installation has a 3-fold levels sealing system that excludes the detectors from environmental air. The whole installation is air-conditioned and the temperature is continuously monitored and recorded. The detectors' responses range from 5.5 to 7.5 photoelectrons/keV. Energy calibrations with X-rays/γ sources are regularly carried out down to few keV in the same conditions as the production runs. A software energy threshold of 2 keV is considered. The experiment takes data up to the MeV scale and thus it is also sensitive to high energy signals. For all the details see Ref. [12].

Several kinds of analyses on the model-independent DM annual modulation signature have been performed (see Refs. [13, 14] and references therein). Here Fig. 1 shows the time behaviour of the experimental residual rates of the *single-hit* events collected by DAMA/NaI and by DAMA/LIBRA in the (2 - 6) keV energy interval [13, 14]. The superimposed curve is the cosinusoidal function: A cos $\omega(t-t_0)$ with a period $T = 2\pi/\omega = 1$ yr, with a phase $t_0 = 152.5$ day (June 2nd), and modulation amplitude, A, obtained by best fit over the 13 annual cycles.

The hypothesis of absence of modulation in the data can be discarded [13, 14] and, when the period and the phase are released in the fit, values well compatible with those expected for a DM particle induced effect are obtained [14]; for example, in the cumulative (2 - 6) keV energy interval: A = (0.0116 ± 0.0013) cpd/kg/keV, T =(0.999 ± 0.002) yr and $t_0 = (146\pm7)$ day.

Summarizing, the analysis of the *single-hit* residual rate favours the presence of a modulated cosine-like behaviour with proper features at 8.9 σ C.L. [14].

The same data of Fig. 1 have also been investigated by a Fourier analysis, obtaining a clear peak corresponding to a period of 1 year [14]; this analysis in other energy regions shows instead only aliasing peaks.

[1] Consider the richness in particles of the luminous Universe which is just 0.007 of the density of the Universe with respect to about 0.22 of the Dark Matter attributed to relic particles by the combination of the results of WMAP, of the SN type IA and clusters observations.

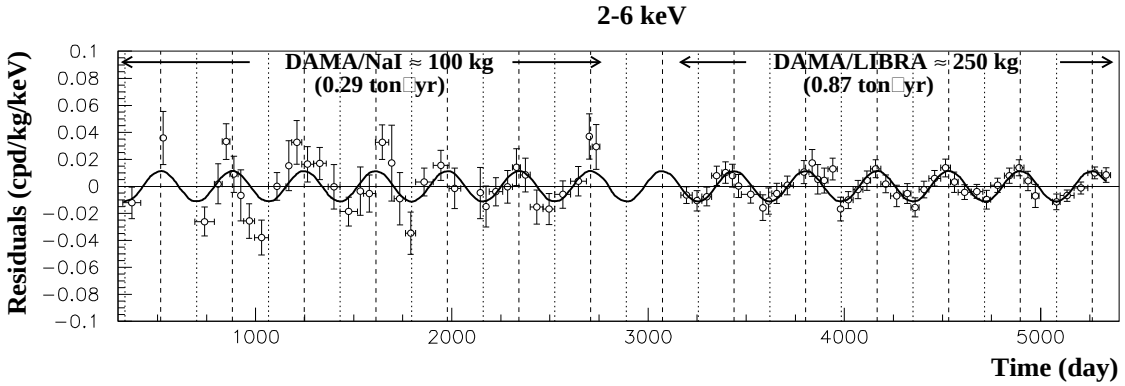

Fig. 1. Experimental model-independent residual rate of the *single-hit* scintillation events, measured by DAMA/NaI over seven and by DAMA/LIBRA over six annual cycles in the (2 - 6) keV energy interval as a function of the time [4, 5, 13, 14]. The zero of the time scale is January 1st of the first year of data taking. The experimental points present the errors as vertical bars and the associated time bin width as horizontal bars. The superimposed curve is A cos $\omega(t-t_0)$ with period $T = 2\pi/\omega = 1$ yr, phase $t_0 = 152.5$ day (June 2nd) and modulation amplitude, A, equal to the central value obtained by best fit over the whole data: cumulative exposure is 1.17 ton × yr. The dashed vertical lines correspond to the maximum expected for the DM signal (June 2nd), while the dotted vertical lines correspond to the minimum. See Refs. [13, 14] and text.

Thus, this allows the study the background behaviour in the same energy interval of the observed positive effect. The result of the analysis is reported in Fig. 2 where it is shown the residual rate of the *single-hit* events measured over the six DAMA/LIBRA annual cycles, as collected in a single annual cycle, together with the residual rates of the *multiple-hits* events, in the same considered energy interval. A clear modulation is present in the *single-hit* events, while the fitted modulation amplitudes for the *multiple-hits* residual rate are well compatible with zero [14].

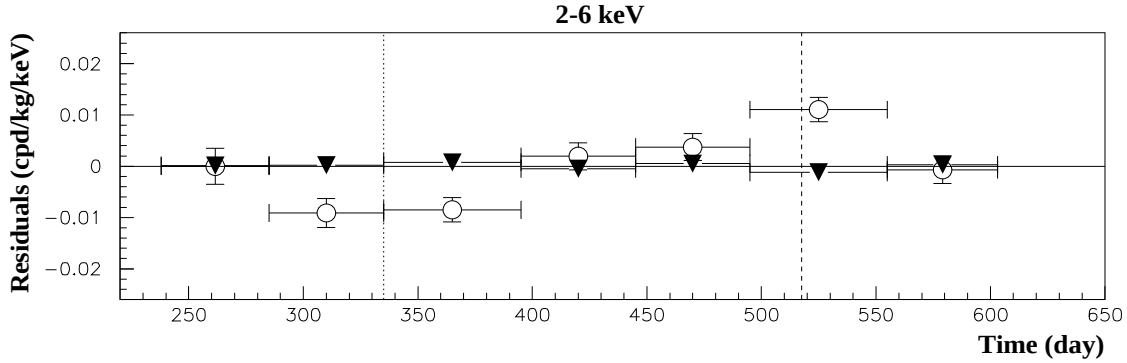

Fig. 2. Experimental residual rates over the six DAMA/LIBRA annual cycles for *single-hit* events (open circles) (class of events to which DM events belong) and for *multiple-hit* events (filled triangles) (class of events to which DM events do not belong). They have been obtained by considering for each class of events the data as collected in a single annual cycle and by using in both cases the same identical hardware and the same identical software procedures. The initial time of the Figure is taken on August 7th. The experimental points present the errors as vertical bars and the associated time bin width as horizontal bars. The errors of the *multiple-hit* residual rates are slightly smaller that the filled triangles symbol. See text and Refs. [13, 14].

Similar results were previously obtained also for the DAMA/NaI case [5]. Thus, again evidence of annual modulation with proper features, as required by the DM annual modulation signature, is present in the *single-hit* residuals (events class to which the DM particle induced events belong), while it is absent in the *multiple-hits* residual rate (event class to which only background events belong). Since the same identical hardware and the same identical software procedures have been used to analyse the two classes of events, the obtained result offers an additional strong support for the presence of a DM particle component in the galactic halo further excluding any side effect either from hardware or from software procedures or from background.

The annual modulation present at low energy has also been analyzed by depicting the differential modulation amplitudes, S_m, as a function of the energy; the S_m is the modulation amplitude of the modulated part of the signal obtained by maximum likelihood method over the data, considering $T = 1$ yr and $t_0 = 152.5$ day. The S_m values are reported as function of the energy in Fig. 3. It can be inferred that a positive signal is present in the (2 - 6) keV energy interval, while S_m values compatible with zero are present just above; in particular, the S_m values in the (6 - 20) keV energy interval have random fluctuations around zero with χ^2 equal to 27.5 for 28 degrees of freedom. It has been also verified that the measured modulation amplitudes are statistically well distributed in all the crystals, in all the annual cycles and energy bins; these and other discussions can be found in Ref. [14].

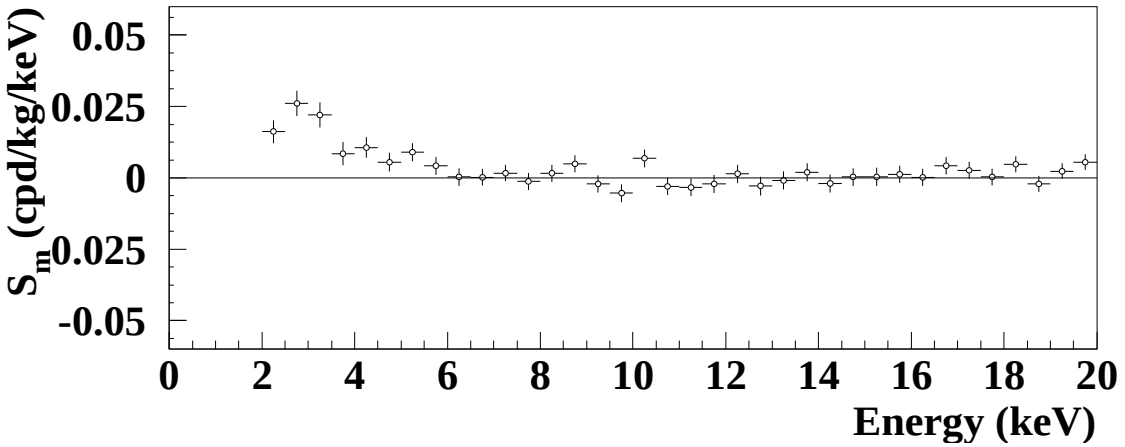

Fig. 3. Energy distribution of the modulation amplitudes S_m for the total cumulative exposure 1.17 ton×yr obtained by maximum likelihood analysis. The energy bin is 0.5 keV. A clear modulation is present in the lowest energy region, while S_m values compatible with zero are present just above. In fact, the S_m values in the (6 - 20) keV energy interval have random fluctuations around zero with χ^2 equal to 27.5 for 28 degrees of freedom. See Refs. [13, 14] and text.

In order to release in the maximum likelihood procedure the assumption of the phase fixed at t_0 = 152.5 day, the signal has been alternatively written as: $S_{0,k} + S_{m,k} \cos \omega(t-t_0) + Z_{m,k} \sin \omega(t-t_0) = S_{0,k} + Y_{m,k} \cos \omega(t-t^*)$, where $S_{0,k}$ and $S_{m,k}$ are the constant part and the modulation amplitude of the signal in k-th energy interval. Obviously, for signals induced by DM particles one would expect: i) $Z_{m,k} \approx 0$ (because of the orthogonality between the cosine and the sine functions); ii) $S_{m,k} \approx Y_{m,k}$; iii) $t^* \approx t_0$ = 152.5 day. In fact, these conditions hold for most of the dark halo models; however, it is worth noting that slight differences in the phase could be expected in case of possible contributions from non-thermalized DM components, such as e.g. the SagDEG stream [6] and the caustics [24]. The 2σ contours in the plane (S_m, Z_m) for the (2 - 6) keV and (6 - 14) keV energy intervals and those in the plane (Y_m , t^*) are reported in Fig. 4 [14]. The best fit values for the (2 - 6) keV energy interval are (1σ errors): S_m = (0.0111 ± 0.0013) cpd/kg/keV; Z_m= –(0.0004 ± 0.0014) cpd/kg/keV; Y_m = (0.0111 ± 0.0013) cpd/kg/keV; t^*= (150.5 ± 7.0) day; while for the (6 - 14) keV energy interval are: S_m= –(0.0001 ± 0.0008) cpd/kg/keV; Z_m = (0.0002 ± 0.0005) cpd/kg/keV; Y_m= –(0.0001 ± 0.0008) cpd/kg/keV and t^* obviously not determined. These results confirm those achieved by other kinds of analyses. In particular, a modulation amplitude is present in the lower energy intervals and the period and the phase agree with those expected for DM induced signals. For more detailed discussions see Ref. [14].

Both the data of DAMA/LIBRA and of DAMA/NaI fulfil all the requirements of the DM annual modulation signature.

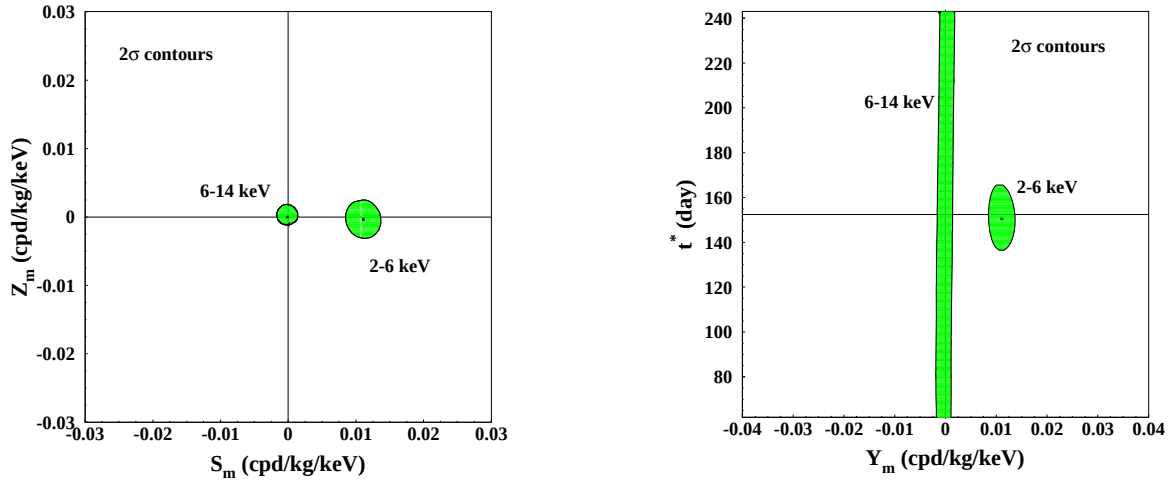

Fig. 4. 2σ contours in the plane (S_m, Z_m) (*left*) and in the plane (Y_m, t^*) (*right*) for the (2 - 6) keV and (6 - 14) keV energy intervals. The contours have been obtained by the maximum likelihood method, considering the cumulative exposure of 1.17 ton × yr. A modulation amplitude is present in the lower energy intervals and the phase agrees with that expected for DM induced signals. See Refs. [13, 14] and text.

Sometimes wrong statements were put forwards as the fact that in nature several phenomena may show some kind of periodicity. The point is whether they might mimic the annual modulation signature in DAMA/LIBRA (and former DAMA/NaI), i.e. whether they might be not only quantitatively able to account for the observed modulation amplitude but also able to contemporaneously satisfy all the requirements of the DM annual modulation signature; the same is also for side reactions.

Careful investigations on absence of any significant systematics or side reaction able to account for the measured modulation amplitude and to simultaneously satisfy all the requirements of the signature have been quantitatively carried out (see e.g. Refs. [4, 5, 12 - 14, 17, 25], and Refs therein). No systematics or side reactions able to mimic the signature (that is, able to account for the measured modulation amplitude and simultaneously satisfy all the requirements of the signature) has been found or suggested by anyone over more than a decade.

The obtained model independent evidence is compatible with a wide set of scenarios regarding the nature of the DM candidate and related astrophysical, nuclear and particle Physics. For examples, some given scenarios and parameters are discussed e.g. in Refs. [2, 4 - 7, 18 - 21] and in Appendix A of Ref. [13]. Further large literature is available on the topics [26]; other possibilities are open. Here we just recall the recent papers [27, 28] where the DAMA/NaI and DAMA/LIBRA results, which fulfill all the many peculiarities of the model independent DM annual modulation signature, are examined under the particular hypothesis of a light-mass DM candidate particle interacting with the detector nuclei by coherent elastic process. In particular, in Ref. [27] allowed regions are given for DM candidates interacting by elastic scattering on nuclei including some of the existing uncertainties; comparison with theoretical expectations for neutralino candidate and with the recent possible positive hint by CoGeNT [29] are also discussed there (Fig. 5), while comparison with possible positive hint by Cresst [30] is discussed in Ref. [28].

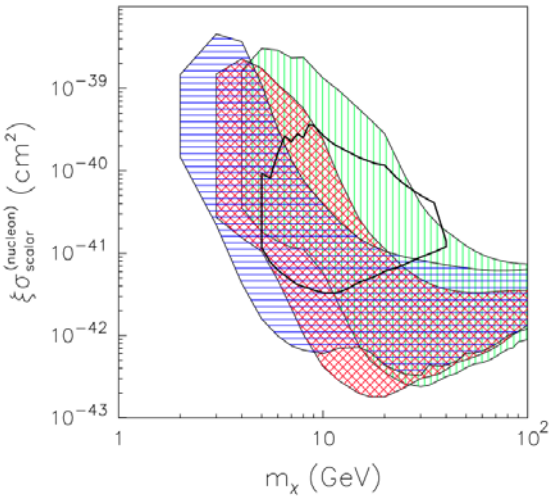

Fig. 5. Regions in the nucleon cross section vs DM particle mass plane allowed by DAMA in three different instances for the Na and I quenching factors: i) without including the channeling effect [(green) vertically-hatched region], ii) by including the channeling effect [(blue) horizontally-hatched region)], and iii) without the channeling effect using the energy-dependent Na and I quenching factors [27] [(red) cross-hatched region]. The velocity distributions and the same uncertainties as in Refs. [4, 5] are considered here. The allowed region obtained for the CoGeNT experiment, including the same astrophysical models as in Refs. [4,5] and assuming for simplicity a fixed value for the Ge quenching factor and a Helm form factor with fixed parameters, is also reported and denoted by a (black) thick solid line. For details see Ref. [27].

No other experiment exists, whose result can be directly compared in a model-independent way with those by DAMA/NaI and DAMA/LIBRA. Some activities (e.g. [31, 32, 33] claim model-dependent exclusion under many largely arbitrary assumptions (see for example discussions in [4, 5, 13, 34, 35]); often some critical points exist in their experimental aspects (e.g. use of marginal exposures, determination of the energy threshold, of the energy resolution and of the energy scale in the few keV energy region of interest, multiple selection procedures, non-uniformity of the detectors response, absence of suitable periodical calibrations in the same running conditions and in the claimed low energy region, stabilities, tails/overlapping of the populations of the subtracted events and of the considered recoil-like ones, well known side processes mimicing recoil-like events, etc.), and the existing experimental and theoretical uncertainties are generally not considered in their presented model dependent result. Moreover, implications of the DAMA results are generally presented in incorrect/partial/unupdated way.

As regards the strongly model dependent indirect searches their results are restricted to some DM candidates and physical scenarios under particular specific assumptions, and require also the modeling of the existing – and largely unknown – competing background for the secondary particles they are looking for. No quantitative comparison can be directly performed between the results obtained in direct and indirect searches because it strongly depends on assumptions and on the considered model framework. In particular, a comparison would always require the calculation and the consideration of all the possible configurations for each given particle model (e.g., for neutralino: in the allowed parameters space), as a biunivocal correspondence between the observables in the two kinds of experiments does not exist. We just mention here that neither negative nor possible positive indications are at present in conflict with the DAMA model independent result.

Finally, for completeness we remind: i) the recent possible positive hints presented by CoGeNT [29] and Cresst [30] exploiting different approaches/different target materials; ii) the uncertainties in the model dependent results and

comparisons; iii) the relevant argument of the methodological robustness [36]. In particular, the general considerations on comparisons reported in Appendix A of Ref. [13] still hold; on the other hand, whatever possible "positive" result has to be interpreted and a large room of compatibility with the DAMA annual modulation evidence is present.

3. Perspectives

A first upgrade of the DAMA/LIBRA set-up was performed in September 2008. One detector was recovered by replacing a broken PMT and a new optimization of some PMTs and HVs was done; the transient digitizers were replaced with new ones, having better performances and a new DAQ with optical read-out was installed.

A further and more important upgrade has been performed in the end of 2010 when all the PMTs have been replaced with new ones having higher quantum efficiency; details on the reached performances are reported in Ref. [37]. This allows a lower software energy threshold and, hence, the improvement of the performance and of the sensitivity for deeper corollary information on the nature of the DM candidate particle(s) and on the various related astrophysical, nuclear and particle Physics scenarios. Since January 2011 the DAMA/LIBRA experiment is again in data taking in the new configuration, named DAMA/LIBRA-phase 2.

The purpose of the last upgrade of the running second generation DAMA/LIBRA set-up is: i) to increase the experimental sensitivity lowering the software energy threshold of the experiment; 2) to improve the investigation on the nature of the Dark Matter particle and related astrophysical, nuclear and particle physics arguments; 3) to investigate other signal features; 4) to improve the sensitivity in the investigation of rare processes other than Dark Matter as done by the former DAMA/NaI apparatus in the past [8] and by itself so far [15, 16]. This requires long and heavy full time dedicated work for reliable collection and analysis of very large exposures, as DAMA collaboration has always done.

REFERENCES

1. *Bernabei R. et al.* // Il Nuovo Cim. - 1999. - Vol. A 112. - P. 545.
2. *Bernabei R. et al.* // Phys. Lett. - 1996. - Vol. B 389. - P. 757; Phys. Lett. - 1998. - Vol. B 424. - P. 195; Phys. Lett. - 1999. - Vol. B 450. - P. 448; Phys. Rev. - 2000. - Vol. D 61. - P. 023512; Phys. Lett. - 2000. - Vol. B 480. - P. 23; Phys. Lett. - 2001. - Vol. B 509. - P. 197; Eur. Phys. J. - 2002. - Vol. C 23. - P. 61; Phys. Rev. - 2002. - Vol. D 66. - P. 043503.
3. *Bernabei R. et al.* // Eur. Phys. J. - 2000. - Vol. C 18. - P. 283.
4. *Bernabei R. el al.* // La Rivista del Nuovo Cimento. - 2003. - Vol. 26. - P. 1.
5. *Bernabei R. et al.* // Int. J. Mod. Phys.- 2004. - Vol. D 13. - P. 2127.
6. *Bernabei R. et al.* // Eur. Phys. J. - 2006. - Vol. C 47. - P. 263.
7. *Bernabei R. et al.* // Eur. Phys. J. - 2008. - Vol. C 53. - P. 205.
8. *Bernabei R. et al.* // Phys. Lett. - 1997. - Vol. B 408. - P. 439; *Belli P. et al.* // Phys. Lett. - 1999. - Vol. B 460. - P. 236; *Bernabei R. et al.* // Phys. Rev. Lett. - 1999. - Vol. 83. - P. 4918; *Belli P. et al.* // Phys. Rev. - 1999. - Vol. C 60. - P. 065501; *Bernabei R. et al.* // Il Nuovo Cimento . - 1999. - Vol. A 112. - P. 1541; Phys. Lett. - 2001. - Vol. B 515. - P. 6; *Cappella F. et al.* // Eur. Phys. J. - 20002. - Vol. C 14. - P. 1; *Bernabei R. et al.* // Eur. Phys. J. - 2005. - Vol. A 23. - P. 7; Eur. Phys. J. - 2005. - Vol. A 24. - P. 51; Astrop. Phys. - 1995. - Vol. 4. - P. 45; The identification of Dark Matter. - Singapore: World Sc. Pub., 1997. - P. 574.
9. *Belli P. et al.* // Astropart. Phys. - 1996. - Vol. 5. - P. 217; Nuovo Cim. - 1996. - Vol. C 19. - P. 537; Phys. Lett. - 1996. - Vol. B 387. - P. 222; Phys. Lett. - 1996. - Vol. B 389. - P. 783 err.; *Bernabei R. et al.* // Phys. Lett. - 1998. - Vol. B 436. - P. 379; *Belli P. et al.* // Phys. Lett. - 1999. - Vol. B 465. - P. 315; Phys. Rev. - 2000. - Vol. D 61. - P. 117301; *Bernabei R. et al.* // New J. of Phys. - 2000. - Vol. 2. - P. 15.1; Phys. Lett. - 2000. - Vol. B 493. - P. 12; Nucl. Instr. & Meth - 2002. - Vol. A 482. - P. 728; Eur. Phys. J. direct. - 2001. - Vol. C 11. - P. 1; Phys. Lett. - 2002. - Vol. B 527. - P. 182; Phys. Lett. - 2002. - Vol. B 546. - P. 23; Beyond the Desert 2003. - Berlin: Springer, 2003. - P. 365; Eur. Phys. J. - 2006. - Vol. A 27. - P. 35.
10. *Bernabei R. et al.* // Astropart. Phys. - 1997. - Vol. 7. - P. 73; Nuovo Cim. - 1997. - Vol. A 110. - P. 189; *Belli P. et al.* // Astropart. Phys. - 1999. - Vol. 10. - P. 115; Nucl. Phys. - 1999. - Vol. B 563. - P. 97; *Bernabei R. et al.* // Nucl. Phys. - 2002. - Vol. A 705. - P. 29; *Belli P. et al.* // Nucl. Instr. & Meth. - 2003. - Vol. A 498. - P. 352; *Cerulli R. et al.* // Nucl. Instr. & Meth - 2004. - Vol. A 525. - P. 535; *Bernabei R. et al.* // Nucl. Instr. & Meth. - 2005. - Vol. A 555. - P. 270; Ukr. J. Phys. - 2006. - Vol. 51. - P. 1037; *Belli P. et al.* // Nucl. Phys. - 2007. - Vol. A 789. - P. 15; Phys. Rev. - 2007. - Vol. C 76. - P. 064603; Phys. Lett. - 2008. - Vol. B 658. - P. 193; Eur. Phys. J. - 2008. - Vol. A 36. - P. 167; Nucl. Phys. - 2009. - Vol. A 826. - P. 256; Nucl. Instr. & Meth. - 2010. - Vol. A 615. - P. 301; Nucl. Instr. & Meth. - 2011. - Vol. A 626 - 627. - P. 31; J. Phys. G: Nucl. Part. Phys. - 2011. - Vol. 38. - P. 015103; Nucl. Inst. and Meth. - 2012. - Vol. A 670. - P. 10.
11. *Belli P. et al.* // Nucl. Instr. & Meth. - 2007. - Vol. A 572. - P. 734; Nucl. Phys. - 2008. - Vol. A 806. - P. 388; Nucl. Phys. - 2009. - Vol. A 824. - P. 101; Proc. of the Int. Conf. "NPAE-2008". - Kyiv, 2009. - P. 473; Eur. Phys. J. - 2009. - Vol. A 42. - P. 171; Nucl. Phys. - 2010. - Vol. A 846. - P. 143; Nucl. Phys. - 2011. - Vol. A 859. - P. 126; Phys. Rev. - 2011. - Vol. C 83. - P. 034603; Eur. Phys. J. - 2011. - Vol. A 47. - P. 91; Phys. Lett. - 2012. - Vol. 711. - P. 41.
12. *Bernabei R. et al.* // Nucl. Instr. & Meth. - 2008. - Vol. A 592. - P. 297.

13. *Bernabei R. et al.* // Eur. Phys. J. - 2008. - Vol. C 56. - P. 333.
14. *Bernabei R. et al.* // Eur. Phys. J. - 2010. - Vol. C 67. - P. 39.
15. *Bernabei R. et al.* // Eur. Phys. J. - 2009. - Vol. C 62. - P. 327.
16. *Bernabei R. et al.* // Eur. Phys. J. - 2012. - Vol. C 72. - P. 1920.
17. *Bernabei R. et al.* // Eur. Phys. J. - 2012. - Vol. C 72. - P. 2064.
18. *Bernabei R. et al.* // Phys. Rev. - 2008. - Vol. D 77. - P. 023506.
19. *Bernabei R. et al.* // Mod. Phys. Lett. - 2008. - Vol. A 23. - P. 2125.
20. *Bernabei R. et al.* // Int. J. Mod. Phys. - 2006. - Vol. A 21. - P. 1445.
21. *Bernabei R. et al.* // Int. J. Mod. Phys. - 2007. - Vol. A 22. - P. 3155.
22. *Smith D., Weiner N.* // Phys. Rev. - 2001. - Vol. D 64. - P. 043502; *Tucker-Smith D., Weiner N.* // Phys. Rev. - 2005. - Vol. D 72. - P. 063509.
23. *Freese K. et al.* // Phys. Rev. - 2005. - Vol. D 71. - P. 043516; Phys. Rev. Lett. - 2004. - Vol. 92. - P. 111301.
24. *Ling F.S., Sikivie P., Wick S.* // Phys. Rev. - 2004. - Vol. D 70. - P. 123503.
25. *Bernabei R. et al.* // AIP Conf. Proceed. - 2010. - Vol. 1223. - P. 50 [arXiv:0912.0660]; J. Phys.: Conf. Ser. - 2010. - Vol. 203. - P. 012040 [arXiv:0912.4200]; http://taup2009.lngs.infn.it/slides/jul3/nozzoli. pdf, talk given by F. Nozzoli; Can. J. Phys. - 2011. - Vol. 89. - P. 11; SIF Atti Conf. - 2011. - Vol. 103. [arXiv:1007.0595]; pre-print ROM2F/2011/12 to appear in Physics Procedia.
26. *Bottino A. et al.* // Phys. Rev. - 2010. - Vol. D 81. - P. 107302; *Fornengo N. et al.* // Phys. Rev. - 2011. - Vol. D 83. - P. 015001; *Fitzpatrick A.L. et al.* // Phys. Rev. - 2010. - Vol. D 81. - P. 115005; *Hooper D. et al.* // Phys. Rev. - 2010. - Vol. D 82. - P. 123509; *Belikov A.V. et al.* // Phys. Lett. - 2011. - Vol. B 705. - P. 82; *Kuflik E. et al.* // Phys. Rev. - 2010. - Vol. D 81. - P. 111701; *Chang S. et al.* // Phys. Rev. - 2009. - Vol. D 79. - P. 043513; *Chang S. et al.* // Phys. Rev. Lett. - 2011. - Vol. 106. - P. 011301; *Foot R.* // Phys. Rev. - 2010. - Vol. D 81. - P. 087302; *Bai Y., Fox P.J.* // JHEP. - 2009. - Vol. 0911. - P. 052; *Alwall J. et al.* // Phys. Rev. - 2010. - Vol. D 81. - P. 114027; *Khlopov M.Yu. et al.* // arXiv:1003.1144; *Andreas S. et al.* // Phys. Rev. - 2010. - Vol. D 82. - P. 043522; *Kopp J. et al.* // JCAP. - 2010. - Vol. 1002. - P. 014; *Barger V. et al.* // Phys. Rev. - 2010. - Vol. D 82. - P. 035019; *Feng J.L. et al.* // Phys. Lett. - 2011. - Vol. B 703. - P. 124.
27. *Belli P. et al.* // Phys. Rev. - 2011. - Vol. D 84. - P. 055014.
28. *Bottino A. et al.* // Phys. Rev. - 2012. - Vol. D 85. - P. 095013.
29. *Aalseth C.E. et al.* // Phys. Rev. Lett. - 2011. - Vol. 106. - P. 131301; *Aalseth C.E. et al.* // Phys. Rev. Lett. - 2011. - Vol. 107. - P. 141301.
30. *Angloher G. et al.* // arXiv:1109.0702.
31. *Ahmed Z. et al.* // Science. - 2010. - Vol. 327. - P. 1619.
32. *Armengaud E. et al.* // Phys. Lett. - 2011. - Vol. B 702. - P. 329.
33. *Aprile E. et al.* // Phys. Rev. Lett. - 2010. - Vol. 105. - P. 131302.
34. *Bernabei R. et al.* "Liquid Noble gases for Dark Matter searches: a synoptic survey", Exorma Ed., Roma, ISBN 978-88-95688-12-1, 2009, pp. 1-53 [arXiv:0806.0011v2].
35. *Collar J.I., McKinsey D.N.* // arXiv:1005.0838; arXiv:1005.3723; *Collar J.I.* // arXiv:1006.2031; arXiv:1010.5187; arXiv:1103.3481; arXiv:1106.0653; arXiv:1106.3559.
36. *Hudson R.* // Found. Phys. - 2009. - Vol. 39. - P. 174.
37. *Bernabei R. et al.* // Journal of Instrumentation. - 2012. - Vol. 7. - P. P03009.

POSSIBILITIES OF STATISTICAL PICK-UP AND KNOCK-OUT IN THE PRE-EQUILIBRIUM (EXCITON MODEL) NUCLEAR REACTIONS FOR THE CLUSTER EMISSION

E. Běták

Institute of Physics, Slovak Academy of Sciences, Bratislava, Slovakia
Faculty of Philosophy and Science, Silesian University, Opava, Czech Republic

Emission of nucleons in low-energy nuclear reactions (say, below the pion threshold) can be well described using statistical model (compound nucleus plus pre-equilibrium emission). On the other hand, that of the complex particles, i.e. light clusters up to α's, is far from satisfactory state. The main reason is – apart of very specific properties of the clusters themselves – that different types of direct reactions, like pick-up, knock-out and others, play an essential role. In the absence of more justified approaches, phenomenological ones are frequently applied, with very little (or no) physics in their background.

We suggest a generalization of the Iwamoto-Harada-Bisplinghoff statistical model which is capable to incorporate the main features of direct reactions leading to the cluster emission, but – obviously, as any other statistical approach – pays for this generality by loosing details of nuclear structure and their manifestation in individual reactions. This approach, originally without spin variables, is easy to be used also in the spin-dependent version of the exciton model. The model is illustrated on several nuclear reactions.

1. Introduction

Attempts to include complex particle (light cluster, i.e. from deuteron to α) emission into pre-equilibrium models appeared already in 1970 [1], but the original (unsuccessful) approach was soon replaced by two different ways, how one can interpret the cluster emission; namely the idea of preformed α particles [2] and of exciton (nucleon) clusterization [3, 4]. Whereas the former one is by the underlying physics restricetd only to strongly bound clusters, i.e. the α particles, the latter one is of general nature. In fact, the preformed α particle model yielded better agreement to the obsrerved α particle energy spectra than the other one, but the consequent development of tle clusaterization model minimized this gap. In addition, the emission of preformed α particle is treated as an emission of just one nucleon of special type, what introduces some inconsistency into the model. Having in mind general applicability for wide range of ejectiles, we feel Iwamoto - Harada model [5, 6] to be a suitable starting point for interpretation of complex particle spectra and other quantities.

2. Calculation of complex particle emission – basic equations

To keep our consideration and especially the equations simple and transparent, we limit our presentation and explicite presentation of formulae here to the case of nucleon-induced reactions only, while other reactions will still be kept in mind. The energy spectrum of the emitted particles (and/or γ quanta) in the spin-independent formulation of the model is

$$\frac{d\sigma}{d\varepsilon_x} = \sigma_R \sum_n \tau_n \lambda_x^c(n, E, \varepsilon_x), \tag{1}$$

where $\lambda_x^c(n,E,\varepsilon_x)$ is the particle (or γ) emission rate from an n-exciton state ($n = p + h$) of excitation energy E to the continuum, the energy of the ejectile of type x is ε_x, and τ_n and σ_R are the time spent in an n-exciton state and the cross section of creation of the composite system, respectively.

In the case of nucleon emission, one has

$$\lambda_x^c(n, E, \varepsilon_x) = \frac{2s_x + 1}{\pi^2 \hbar^3} \mu_x \varepsilon_x \sigma_{INV}(\varepsilon_x) \frac{\omega_R(p-1, h, U)}{\omega_C(p, h, E)} R_x(p), \tag{2}$$

where p_x and s_x are the ejectile reduced mass and spin, respectively, σ_{INV} is the inverse cross section, which is, in fact, replaced by the cross section of the capture of a projectile by the nucleus in its ground state, and U is the energy of residual nucleus, which is produced in an (n - 1)-exciton state. The factor $R_x(p)$ takes into account the proton-neutron composition.In fact, it stands as an effective quantity which arises from replacing the two-component description (i.e. that distinguishing between the neutrons and the protons) by an one-component one [1].

[1] There are several ways of introducing the charge factor. We follow here the charge factor $R_x(p)$ of [3]. Explicitly, the sum of the neutron and the proton charge factors equal 1 at each stage of the reaction. Anyway, none of different suggested forms of charge factors has proper behaviour both at the very early stage of the reaction process and at equilibrium, and similarly these factors cannot withstand the detailed balance principle (see also [4, 5]).

In the most simple case, the cluster emission rate can be written formally in exactly the same way as it was for nucleons, just with replacing the exciton number of the residual nucleus (p - 1, h) by (p - p_x, h) [3][2], where we assume that the cluster is formed by p_x of thetotal of p excited particles (Fig. 1).

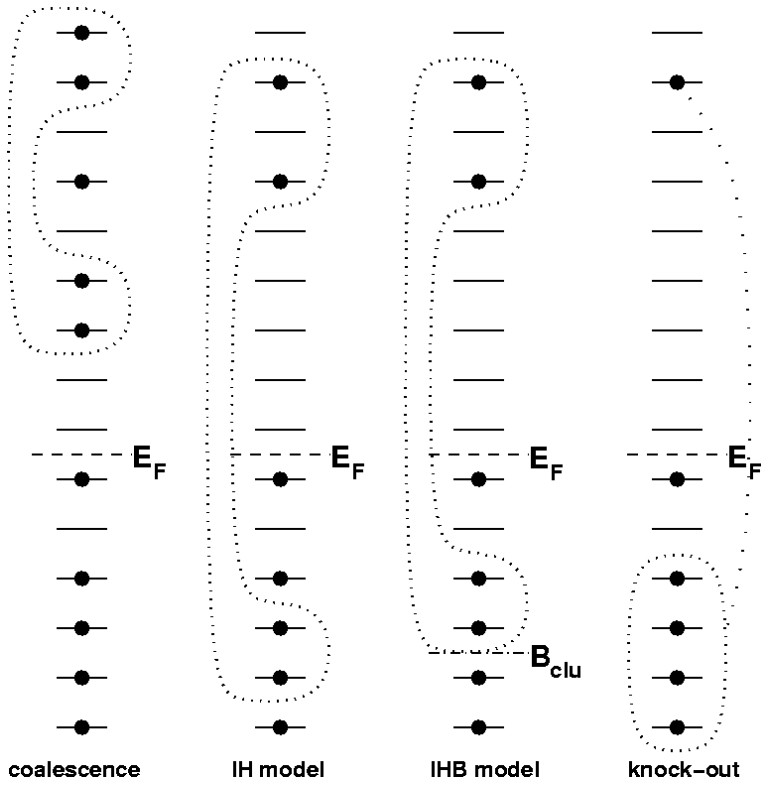

Fig. 1. Schemes of coalescence ("classical coalescence" [3, 6]), Iwamoto - Harada pick-up model [7, 14], Bisplinghoff's improvement [15] for the α particles due to strength of coupling of nucleons within the cluster, and the statistical understanding of the knock-out process [16]. Though all parts depict four nucleons, i.e. the α particle, they are – with the only exception of knock-out – of general validity.

Additionally, the emission rates can be multiplied by γ_x, the formation probability [6] of the coalescence models (or by the α pre-formation factor γ_α, if we assume their existence as special entities (p_α = 1) within the nucleus [2]). The original form of the coalescence model [3] has been soon improved by Ribanský and Obložinský [6] who improved the approach by replacing the artificial $p_x!$ factor by $\gamma_x \omega(p_x, 0, \varepsilon_x + B_x)/g_x$ which has a straightforward physical interpretation: its second part is the number of configurations of the p_x excitons, and γ_x is the formation probability. In practice, however, the single-cluster density g_x is often replaced by the single-particle one[3]. Thus, the emission rate reads [7]

$$\lambda_x^c(n,E,\varepsilon_x) = \frac{2s_x+1}{\pi^2\hbar^3}\mu_x\varepsilon_x\sigma_{INV}(\varepsilon_x)\frac{\omega_R(p-p_x,h,U)}{\omega_C(p,h,E)}\gamma_x\frac{\omega(p_x,0,\varepsilon_x+B_x)}{g_x}R_x(p). \qquad (3)$$

This approach led to both reasonable absolute values and for some clusters even rather good spectra shapes. A commonly used approach is to consider γ_x to be a parameter obtainable from the fit to the data. Typical values are of the order of 10^{-3} for α's and of 10^{-2} for deuterons.

Simple theoretical estimates of the formation probability of the coalescence model yield e.g. $\gamma_x \approx {p_x}^3\left(\frac{p_x}{A}\right)^{p_x-1}$ [8] or $\gamma_x = \left[\frac{4}{3}\left(\frac{P_0}{mc}\right)^3\right]^{p_x-1}$ [9], where P_0 is the radius of the sphere in the momentum space containing the nucleons which are picked up and it is found to be close to the Fermi momentum, or $\gamma_x \approx A^{-m}$ above mass 27, with $m \approx 1$ for deuterons

[2] In fact, this idea appeared already in the paper of Blann and Lanzafame [1]. However, their predicted complex particle spectra were substantially below the experimental data.

[3] See also the discussions of the role of the single-cluster density [6, 7].

and $m \approx 4/3$ for α's, tritons and ^{3}He [10]. However, the presence of formation probabilities and/or other additional functions is not strictly justifiable by detailed balance, and it is therefore rejected by some groups (e.g. [11 - 13]), even though such rejection of this factor means worsening of the agreement between theory and data.

3. Iwamoto-Harada-Bisplinghoff model – Extensions of coalescence concept

3.1. Basic ideas

The coalescence model has been made more sophisticated to allow the cluster to be formed not only of excitons, but also from unexcited nucleons below the Fermi level (see the second column in Fig. 1), i.e. a form of statistical description of pickup. This approach became known as the Iwamoto-Harada model [14][4] even though it has been suggested and applied five years earlier [7]. Mathematically, it means replacing the density product $\omega(p-p_x,h,U)\times\omega(p_x,0,\varepsilon_x+B_x)$ by $\sum_{p^*=1}^{p_x}\int_{\varepsilon_x+B_x}^{E}\omega(p-p^*,h,E-\varepsilon_1)\omega(p^*,0,\varepsilon_1)\omega(0,p_x-p^*,\varepsilon_2)d\varepsilon_1$, where p^* is the number of excitons contributing to forming the cluster, and the remaining $(p_x\text{-}p^*)$ nucleons are picked up from the Fermi sea. Now, the cluster density is $g_x=\gamma_x g[g(\varepsilon_x+B_x+p_xE_F)]^{p_x-1}/[p_x!(p_x-1)!]$ [7], what makes the formulation of the problem – as far as complex particles (clusters) concerns – parameterless (!!).

3.2. Extensions of the Iwamoto - Harada - Bisplinghoff (pickup) model

Bisplinghoff suggested (we use IHB to denote the Iwamoto - Harada model with Bisplinghoff's generalization) that not all nucleons be available for the cluster formation within the model, but only those close to the Fermi energy, and the energy width of the "band of availability" is determined by the binding energy of nucleons inside the cluster [15].
It is natural to generalize the idea to arbitrary combinations of excited and unexcited nucleons, and to all types of clusters. As the binding energy of nucleons in the deuteron is small, the pick-up possibility is hardly likely to be observed in practice. Thus, strongly bound entities, like α's, have large energy space available for their creation (which makes the approach close to the original ideas [7, 14], and loosely coupled objects (e.g. deuterons) practically get close to the standard coalescence model [17, 18].

It is necessary to keep the consistence with the compound nucleus theory when one deals with pre-equilibrium models. One of the principal requirements is the principle of microscopic reversibility applied to the emission rates and to the particle capture, and the other one is the necessity of reaching the compound nucleus theory as the limit (equilibrium) case of the pre-equilibrium emission when one goes to sufficiently long times. Both of them can be dealt relatively easily in the case of nucleon emission [19] and with some additional approximation also for cluster coalescence model in its pure version [21], where the Weisskopf-Ewing formulae within the model by summation over all exciton states can be reached (up to possible charge factor, see [4]). It is much more difficult to reach the proper equilibrium limit for cluster emission with some allowance for pickup and possibly other processes.

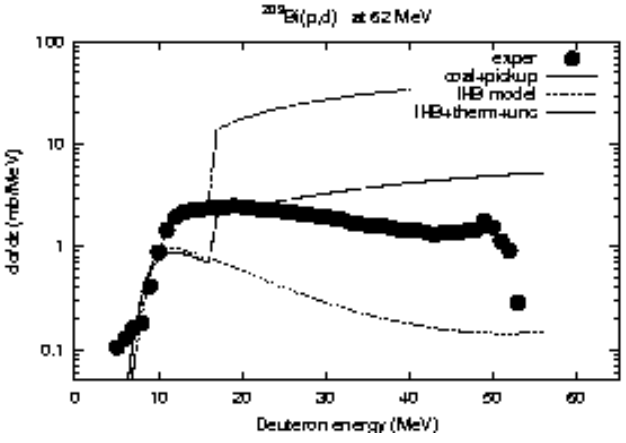

Fig. 2. Angle-integrated deuteron energy spectra from ^{209}Bi + p at 62 MeV. Points are the data, the curves show the spectra calculated within different model assumptions (see the text).

In our model, we assume that the pickup is effective only when the number of excited particles is insufficient to form the cluster of the required type. When the exciton number is large enough, the excitons do not show the need to pu their partner(s) from the Fermi sea. This suggestion does not influence the high-energy part of the spectrum, but is able to yield the proper equilibrium limit.

Two other ideas have been used: We have included some "energy blurring" to simulate the thermal movement of nucleons in excited nucleus, and – in addition – we have incorporated the Heisenberg principle approximately in the very first stage. Therein, the nucleus lives very shortly, and due to the uncertainty relation it is possible with a rather small, but nonzero amplitude, that the exciton can "borrow" enough energy to pick up nucleons from the sea also much deeper than allowed by the cluster binding energy.

Fig. 2 brings the deuteron energy-integrated spectra calculated using the modified PEQAG code [20][5].

[4] We list here only the initial paper by Iwamoto and Harada, and not all relevant subsequent ones.

[5] The calculations presented in this paper are aimed to illustrate the properties of the model and they are done with default parameters (level densities, optical model parameters, intranuclear transition matrix element, ...) and they do not cointain any fitting, which would surely lead to much better agreement to the data.

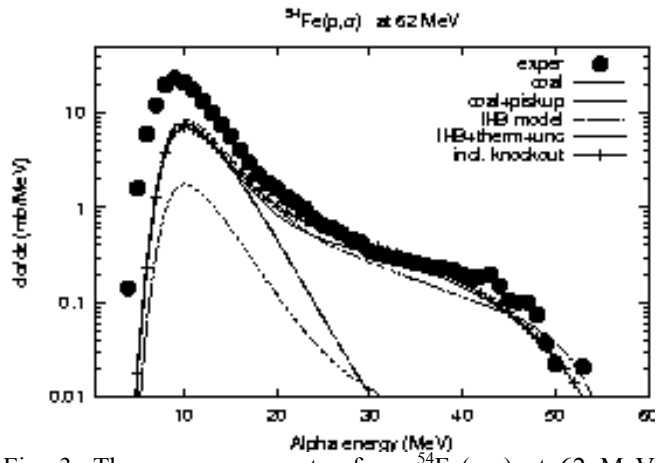

Fig. 3. The α energy spectra from ^{54}Fe(p,α) at 62 MeV showing the influence of different features added to the IHB model. (From [25]).

Thereare no free parameters specific for the cluster emission; the other parameters have been kept at their overall (default) values (see above). If we allow all depth of the nuclear potential to be available for pickup, we get pretty above the experimental data, and the restriction to the deuteron binding energy suggested by the IHB model draws the spectra down. For loosely bound ejectile like the deuteron, this curve is indistinguishable from the pure coalescence calculation (not drawn) in the scale of the Figure. The two added "energy blurrings", i.e. the thermal and the uncertainty ones, bring the resulting spectra close to the experimental points.

The situation with α spectra is somewhat more complicated and it is depicted in Fig. 3. The two "energy blurrings" are separated now, and the pure coalescence is distinctly different from other approaches. In addition, also the spectra containing some admixture of possible knockout mechanism (see below) are drawn with a curve with ticks.

3.3. Knockout admixtures

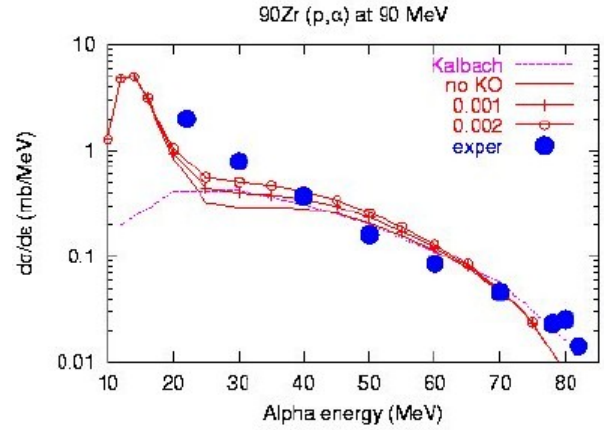

Fig. 4. The α energy spectra from ^{90}Zr(p, α) at 90 MeV without and with the knockout contribution for two different knockout fractions f_{KO} , namely 0.001 and 0.002, compared to the data and also to the calculations of Kalbach [21].

The Iwamoto-Harada model introduced pickup reactions into the statistical formulation of the pre-equilibrium model. However, at least for compact ejectiles, like α particles, a possibility of knockout seems to be reasonable to be added as well.

Expressed in the statistical language of the exciton model, the (N,α) knockout yields the final density $\int_0^E \omega(0,4,U-\varepsilon)\omega(1,0,\varepsilon)d\varepsilon$ [17, 18] (see also Fig. 1, the last column). It is rather complicated to say something *a priori* about the fraction of the knockout reactions f_{KO} in the pre-equilibrium process, and we take it here as a free parameter to be determined from the fit to the data. Fig. 4 presents a comparison at somewhat higher energy and also to the model calculation of Kalbach [21]. Fig. 5, *left* shows the spectral shape and possible values of the knockout contributions with different f_{KO} on three targets, and in the *right* part of the Figure, the ratio of spectra with and without the knockout inclusion are depisted.

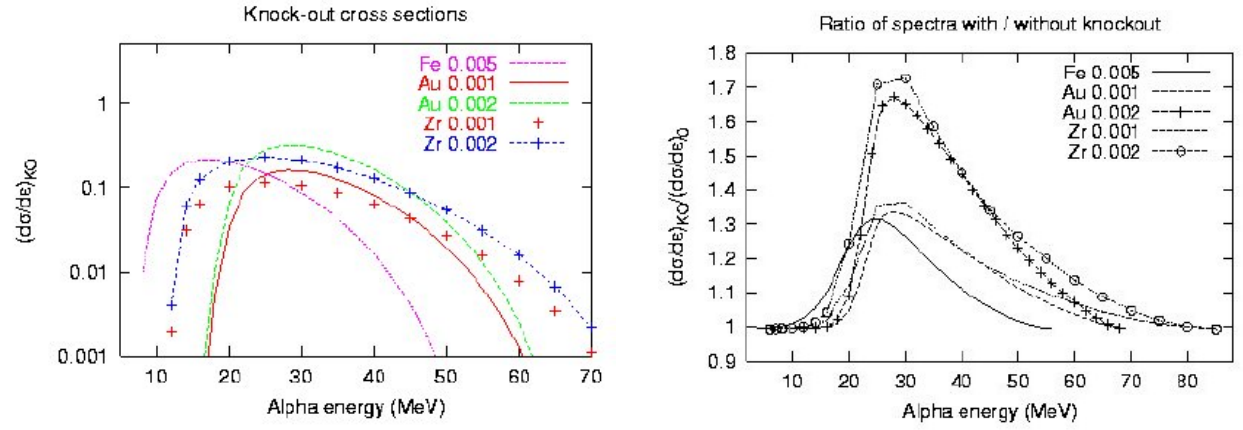

Fig. 5. *Left* - Knockout contributions to the α energy spectra. The curves are denoted by the target (reactions on Zr are with 90 MeV incident protons, others are at 62 MeV) and the knockout fraction f_{KO}. *Right* - Ratio of the calculated spectra of α particles with and without knockout. (From [25].)

The knockout contribution is relatively small, but it significantly improves the fit to the data at outgoing energies around 30 MeV (see Fig. 4). It is rather difficult to fix the knockout fraction precisely, but it is close to $f_{KO} = 0.002$ on heavy nuclei (Au, Bi) and significantly higher (about 0.005) on medium-ones (Fe), even though the absolute values are practically the same.

3.4. Angular momentum in the cluster emission

Current pre-equilibrium models often ignore the influence of angular momentum. This is easily shown to be rather small for the nucleon emission, but is larger for clusters. The effect arises from: *i)* cluster emission is usually enhanced at higher angular momenta, which means increased role of the nuclear surface and consequently effective lowering of the Coulomb barrier, especially in the case of deformed nuclei; *ii)* many of quantities entering the pre-equilibrium reactions are both spin- and energy-dependent, and their simple contraction to one variable necessarily affects the results. The consistent incorporation of the angular momentum is more complicated. Some steps have been undertaken in [22], but the full formulation of the spin-dependent intranuclear transition and emission rates has been enabled by Obložinský with Chadwick [23] and it has been developed for the equilibration process, nucleon and γ emissions. Obviously, if we calculate the time spent in the *n*-exciton state by solving the set of master equations [24], this set becomes much larger (from tens of thousands coupled equations up to millions of them). We do not repeat the spin-coupling formulae here, but refer to the original papers [23] and its realization in the computer code PEGAS [24].

The question arises, how to apply these couplings to the cluster emission? For a first view, similar (but more complicated) set of formulae should be derived here and consequently used in a computer code. However, one can – at least as a good approximation – use the fact that the formation probability γ_x contains all the dynamics of the process, i.e. also the spin couplings. We should emphasize that such happy coincidence of canceling the cluster couplings is possible for the IHB model formulated in the exciton-energy space, and it cannot be straightforwardly applied to the cases, where the final expression for the cluster emission still contains the formation probability or some similar quantity. This essentially simplifies the task here and makes it feasible to be applied to calculations of nuclear reactions. We have adopted this way and illustrated the influence of angular couplings below.

For the calculations, we have chosen (p,α) reactions, which have been already calculated in the spin-independent case [16, 25], namely on ^{90}Zr, ^{197}Au and ^{209}Bi. In order to show the angular momentum influence unscreened by other effects, we have abstracted from the improvements to the Iwamoto-Harada model now and even we use default level density parameters, i.e. $g = A/13$ and no pairing here. Thus, the calculated energy spectra are not aimed to be compared to the data, as the parameters of the model are not "tuned" for that, but simply to illustrate the influence of angular momentum newly introduced for the pre-equilibrium cluster emission. Fig. 6 presents the energy spectra for two reactions, calculated both with and without angular momentum. The essential pre-equilibrium parameters, as the level density ones or the transition matrix element, are kept identical in both sets of calculations. Only the first emitted particle is calculated so that they do not include any consequent emissions.

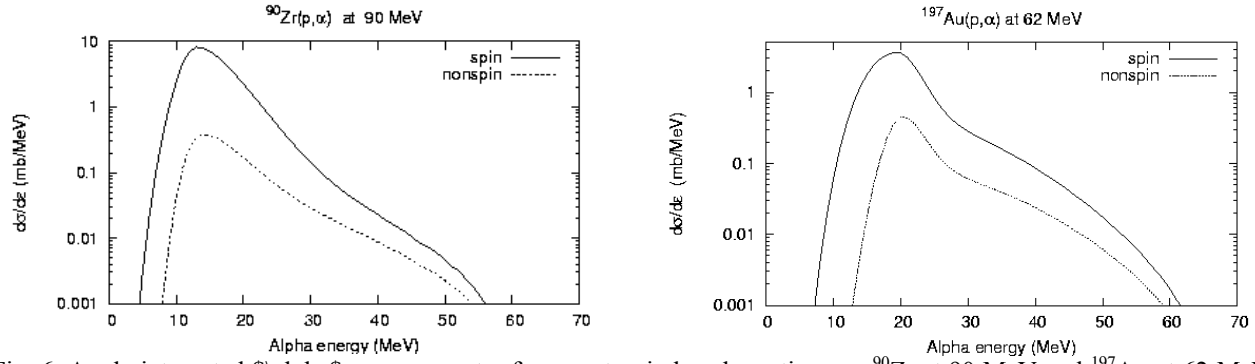

Fig. 6. Angle-integrated α energy spectra from proton-induced reactions on ^{90}Zr at 90 MeV and ^{197}Au at 62 MeV. The full curves represent the calculations with angular momentum, whereas the dotted ones are without. (From [26].)

In all cases, the introduction of angular momentum increases the cluster spectra significantly and somewhat lowers the emission of nucleons (as the reaction cross section σ_R is the same both with and without angular momentum, and it has to be split among neutron, proton, cluster and γ emissions). Thus we arrive to a result which is in similar direction as that obtained by Blann and Komoto [27] by considering deformed nuclei.

4. Conclusions

We have discussed the extensions of the pre-equilibrium models to describe the cluster emission at low energies. The model with generalizations is rather useful to yield reliably the overall trends and also correctly predict the (order of) magnitude of cross sections and related quantities without any specific parameters for the cluster emission. However, for deeper understanding and more precise description, one has to incorporate the very details of cluster formation and emission and this is obviously beyond the scope of simple statistical models.

ACKNOWLEDGMENTS

The author is grateful to late P.E. Hodgson, J. Dobeš, C. Kalbach and P. Obložinský for discussions. The work has been supported in part by the VEGA and APVV grants Nos 2/0029/20 and 0177-11, respectively.

REFERENCES

1. *Blann M., Lanzafame F.M.* // Nucl. Phys. - 1970 - Vol. A142 - P. 559.
2. *Milazzo-Colli L., Braga-Marcazzan G.M.* // Phys. Lett. - 1971 - Vol. B36 - P. 447; *Colli-Milazzo L., Marcazzan-Braga G.M.* // Ibid. - 1972 - Vol. B38 - P. 155.
3. *Cline C.K.* // Nucl. Phys. - 1972 - Vol. A193 - P. 417.
4. *Běták E., Hodgson P.E.* // Rep. Prog. Phys. - 1998 - Vol. 61 - P. 483.
5. *Gadioli E., Hodgson P.E.* Pre-Equilibrium Nuclear Reactions. - Oxford: Clarendon Press, 1992.
6. *Ribanský I., Obložinský P.* // Phys. Lett. - 1973 - Vol. B45 - P. 318.
7. *Dobeš J., Běták E.* Emission of complex particles in the exciton model // Int. Conf. Reaction Models '77, Balatonfüred 1977 / Ed. by L.P. Csernai. - Budapest, 1977. - P. 195 - 200.
8. *Běták E., Obložinský P.* // Complex particle formation and pre-equiluibrium decay // 5th Internat. Symp. Interacts. Fast Neutrons with Nuclei, Gaussig 1975 / Ed. by D. Seeliger. - ZfK Rossendorf: Report ZfK-324, 1996. - P. 77 - 78.
9. *Machner H.* // Phys. Lett. - 1979. - Vol. B86 - P. 129.
10. *Wu J.R., Chang C.C.* // Phys. Rev. - 1978. - Vol. C17. - P. 1540.
11. *Kalbach C.* // Z. Phys. - 1978. - Vol. A283. - P. 401.
12. *Kalbach C.* // Phys. Rev. - 1979. - Vol. C19. - P. 1548.
13. *Kalbach C.* // Phys. Rev. - 1988. - Vol. C37. - P. 2350.
14. *Iwamoto A., Harada K.* // Phys. Rev. - 1982. - Vol. C26. - P. 1821.
15. *Bisplinghoff J.* // Phys. Rev. - 1994. - Vol. C50. - P. 1611.
16. *Běták E.* // AIP Conf. Proc. - 2005. - Vol. 769. - P. 1168 - 1171.
17. *Běták E.* // Clusters in the pre-equilibrium exciton model. // 9th Internat. Conf. Nucl. React. Mechanisms (Varenna, Italy, 2000) / Ed. by E. Gadioli. - Milano: University, 2000 - P. 591 - 600.
18. *Běták E.* // Int. J. Mod. Phys. - 2004. - Vol. E13. - P. 63.
19. *Ribanský I., Obložinský P., Běták E.* // Nucl. Phys. - 1973. - Vol. A205. - P. 545.
20. *Běták E.* // PEQAG: A PC version of fully pre-equilibrium computer code with gamma emission // Report INDC(CSR)-016/LJ. - Vienna: IAEA, 1989.
21. *Kalbach C.* // Phys. Rev. - 2005. - Vol. C71. - P. 034606.
22. *Xiangjun Shi, Gruppelaar H., Akkermans J.M.* // Nucl. Phys. - 1987. - Vol. A466. - P. 333.
23. *Obložinský P.* // Phys. Rev. - 1987. - Vol. C35. - P. 407; *Obložinský P., Chadwick M.B.* // Ibid. - 1990. - Vol. C42. - P. 1652.
24. *Běták E., Obložinský P.* // PEGAS: Pre-Equilibrium--Equilibrium Gamma-And-Spin Code (PC Version) // Report INDC(SLK)-001. - Vienna: IAEA, 1993.
25. *Běták E. //* Complex particle emission - statistical picture of direct reactions // Proc. XXIV Int. Workshop on Nuclear Theory (Rila Mountains, Bulgaria, 2005) / Ed. by S. Dimitrova. - Sofia: Heron Press, 2006. - P. 40 - 47.
26. *Běták, E.* // EPJ Web Conf. - 2012. - Vol. 21. - P. 012021
27. *Blann M.* // Phys. Rev. - 1980. - Vol. C21. - 1770; *Blann M., Komoto T.T.* // Ibid. - 1981. - Vol. C24. - P. 426.

SUPERHEAVY ELEMENT RESEARCH AT THE VELOCITY FILTER SHIP

S. Heinz[1,2] (for the SHIP and IONAS collaborations)

[1] *GSI Helmholtzzentrum für Schwerionenforschung, Darmstadt, Germany*
[2] *II. Physikalisches Institut, Justus-Liebig-Universität Gießen, Gießen, Germany*

The Separator for Heavy Ion Reaction Products (SHIP) is a velocity filter located at the UNILAC accelerator of GSI Darmstadt, Germany. For about 35 years a broad experimental program in the field of superheavy element research is running at SHIP. During the last years particularly investigations in the region of the heaviest known nuclei were performed. In fusion reactions of ^{48}Ca + ^{248}Cm → ^{296}116* a total of six decay chains was observed which could be attributed to the evaporation residues ^{292}116 and ^{293}116. In this experiment, data measured previously on the same isotopes in Dubna were well confirmed. Besides, two attempts were made to synthesize isotopes of the still unobserved element Z = 120 in reactions of ^{64}Ni + ^{238}U and ^{54}Cr + ^{248}Cm. No events were observed in these experiments leading to one-event cross-section limits of 90 fb and 560 fb, respectively. For future superheavy element research, a new superconducting continuous wave LINAC is planned at GSI which shall deliver beam intensities of up to 10^{14} particles per second. In this context we are developing a next generation separator and new detection techniques.

1. Introduction

Until the year 2005, so-called cold fusion reactions using doubly magic Pb or Bi targets were applied at SHIP for the synthesis of superheavy elements and lead to the discovery of the elements Z = 107 - 112 [1 - 6]. Starting in 2005, hot fusion reactions with actinide targets (^{238}U, ^{248}Cm) were introduced at SHIP. This was motivated by experimental results from the Dubna gas-filled separator (DGFRS) [7] at the Flerov Laboratory of Nuclear Reactions where relatively large cross-sections on the order of 1 pb were observed for nuclei with Z = 114 - 118 in hot fusion [8]. In contrast, the cross-sections in cold fusion reactions drop by about one order of magnitude for every two protons more in the compound nucleus and become already as low as 30 fb for Z = 113 [9]. The application of hot fusion reactions at SHIP is an important step not only for the synthesis of new elements with Z > 118 but equally for the confirmation of existing data from hot fusion on 112 ≤ Z ≤ 118. The latter have been synthesized until recently only at gas-filled separators, mainly in Dubna. SHIP is presently the only velocity filter applied for the synthesis of the heaviest elements with exception of the energy filter VASSILISSA [10] in Dubna. Therefore, the cross-sections and decay properties of superheavy nuclei measured at SHIP represent an important cross-check of the existing data with respect to possible systematic errors. Additionally, SHIP allows the identification of the reaction channel (xn, αxn, transfer etc.) with good resolution by measuring the velocity spectra of the reaction products [11]. The knowledge of the reaction channel is crucial for assigning an observed decay chain to the correct mother isotope since the mass and nuclear charge of the superheavy nuclei are not measured directly.

The production cross-sections of superheavy nuclei are small and reach the sub-picobarn region for the heaviest known isotopes. This presently limits the synthesis of new elements with the available beam intensities of $5 \cdot 10^{12}$ ions per second. Reaction cross-sections on the order of 100 fb require several months of beam time to reach the one-event cross-section limit for the desired isotope. Therefore, the availability of higher beam intensities and the related necessary upgrades of the separation and detection techniques are decisive steps for the future research in this field. At GSI, a new superconducting continuous wave LINAC is planned. The beam intensities are expected to be 10 to 50 times larger than the presently available currents. Within this frame, we are developing a concept for a new separator which allows a strong suppression of primary beams with intensities up to several 10^{14} particles per second. In parallel to the separator design, we are testing and developing new detection techniques for nuclei which are long-lived and/or undergo beta-decay or spontaneous fission and are therefore not accessible with the available techniques.

2. SHIP: Experimental Setup

A scheme of the experimental setup is shown in Fig. 1. SHIP is a Wien filter which separates the ions according to their velocities [12]. Reaction products which leave the target at forward angles of (0 ± 2) degree with respect to the beam direction are accepted by the entrance aperture of SHIP. The electric and magnetic fields are chosen such that the relatively light and fast projectiles and projectile-like reaction products are deflected to the beam stop while the much slower evaporation residues pass SHIP and reach the focal plane detector. The accepted velocity window at a given setting is Δv/v = 0.1 (FWHM). All reaction products which pass the velocity filter are implanted in a position sensitive 16 strip silicon detector (”stop detector”) where their time of implantation, position, kinetic energy and radioactive decays are registered [13]. Such, especially the alpha decay properties allow for an unambiguous identification of single isotopes. Six further Si detectors are installed in a box-like arrangement (“box detector”) in front of the stop detector and cover 85 % of the backward hemisphere in order to register alpha particles and fission fragments escaping from the stop detector.

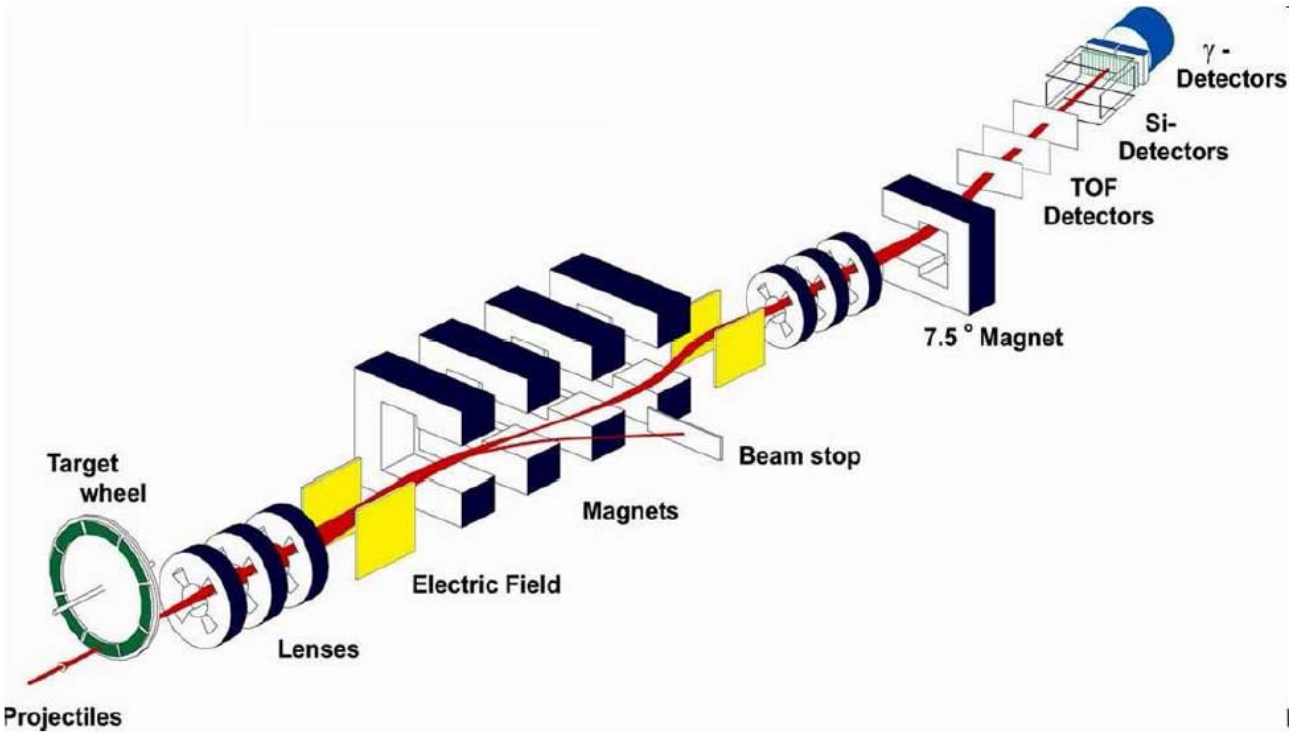

Fig. 1 The velocity filter SHIP and detection system. For details see text.

Finally, a germanium clover detector is mounted behind the stop detector. It consists of four germanium crystals which register gamma rays from excited reaction products implanted in the stop detector. Three time-of-flight (TOF) detectors [14] are installed in front of the silicon detectors. They fulfill two tasks: On one hand the measured TOF together with the energy deposited in the silicon detector allows to distinguish between projectile-like nuclei, target-like nuclei and fusion evaporation residues. Secondly, they allow to distinguish between ions which have been produced in the target and radioactive decay products (alpha particles or fission fragments) which have been created in the silicon detector by decays of implanted mother isotopes. In the first case the particles have to pass the TOF detectors and create a TOF signal while in the latter case they don't. Further details concerning the experimental setup can be found in [15].

The combination of isotope identification via radioactive decays and the strong background suppression by the separator allows the identification of single nuclei where cross-section limits of 10 pb can be reached within one day of beam time by applying usual beam intensities of several 10^{12} particles per second. For additional suppression of alpha-like and fission-like background events the beam-off periods are used which are provided by the pulsed structure of the beam consisting of 5 ms long beam-on periods followed by 15 ms long beam-off periods.

3. Hot fusion reactions at SHIP

3.1 The reaction $^{48}Ca + ^{248}Cm \rightarrow ^{296}116^*$

The nuclei with the largest proton numbers synthesized so far at SHIP, and also at GSI, are isotopes of element Z = 116 in reactions of $^{48}Ca + ^{248}Cm \rightarrow ^{296}116^*$ [16] (June 25 - July 26, 2010). The same reaction was already studied earlier at the Dubna gas-filled separator in several experiments during the years 2000 to 2004 at compound nucleus excitation energies of 33 and 39 MeV [17, 18]. In the Dubna experiments five decay chains were observed which were attributed to the decay of the isotope $^{293}116$ (3n evaporation channel) and six decay chains which were attributed to $^{292}116$ (4n channel). At SHIP, we continued the excitation function to higher energies of 41 and 45 MeV. At 41 MeV we observed six alpha decay chains of different lengths, all of them terminated by a spontaneously fissioning nucleus (Fig. 2). Four of the chains consist of an implanted recoil nucleus followed by two alpha decays and a fission event. The length of these chains as well as the half-lives and alpha energies of the chain members are well in agreement with the data measured in Dubna for the isotope $^{292}116$. Also the corresponding cross-section of 3.4 pb well continues the excitation function measured in Dubna as shown in Fig. 3. Fig. 3 shows also the expected excitation functions from model calculations [19]. The good agreement between experimental data and theoretical expectations further supports the attribution of the four decay chains to the mother isotope $^{292}116$.

Besides, two further chains were observed. One of them consists of an implanted recoil nucleus followed by three α-decays and fission decay. This decay sequence, the α-energies and half-lives are consistent with the data measured in Dubna for the isotope $^{293}116$ (3n channel). Also the related cross-section of 0.9 pb agrees well with these data and with theoretical predictions (Fig. 3). In the other decay chain the recoil nucleus was followed by four α-decays and a fission event. In this chain only the energy of the first α-particle was in agreement with the values measured in Dubna for the

nucleus ^{293}116. Therefore, we attributed this chain preliminary also to the mother isotope ^{293}116. The last α-decay in the chain, with the energy of 9.315 MeV would then originate from an alpha branch of the isotope ^{281}Ds. An α-decay of ^{281}Ds was so far only observed in an experiment at the gas-filled separator TASCA at GSI [20], however with an energy of 8.727 MeV which is 588 keV less than the energy observed at SHIP. The half-lives of the four α-decays observed at SHIP and attributed to ^{293}116, ^{289}114, ^{285}Cn and ^{281}Ds are in agreement with the literature values within statistical fluctuations. But the α-decay energies of the daughter nuclei ^{289}114 and ^{285}Cn are 211 keV and 523 keV larger than the literature values.

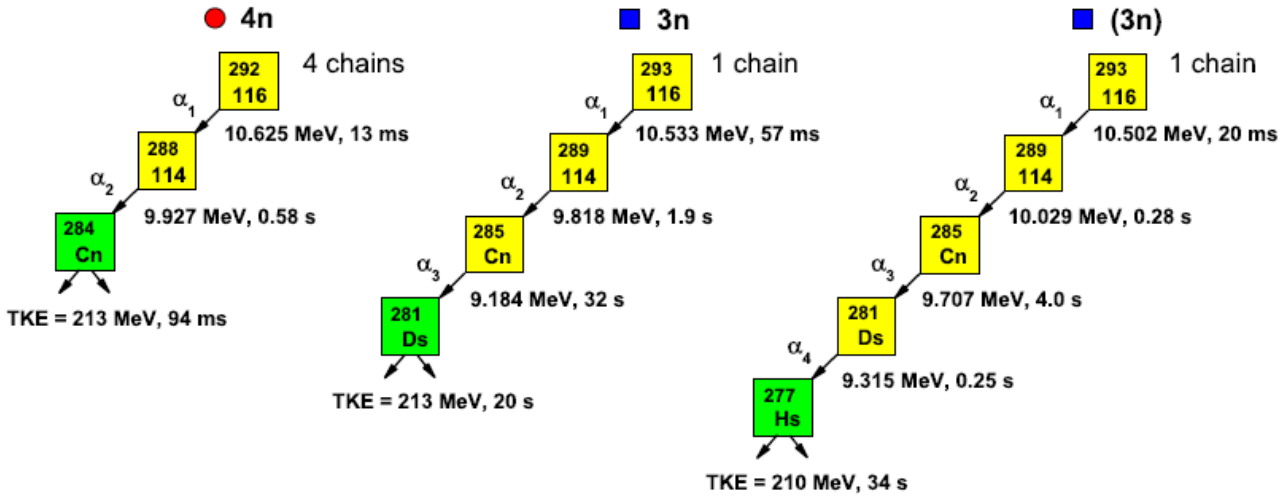

Fig. 2 Decay chains observed at SHIP in fusion reactions of ^{48}Ca + ^{248}Cm leading to the compound nucleus ^{296}116* at an excitation energy of 41 MeV. The given half-lives and alpha decay energies include all available data from different experiments. The decay sequence (α–α–α–α–fission) was so far only observed at SHIP and preliminary attributed to the 3n evaporation channel. For this case the half-lives and decay energies represent the values measured at SHIP.

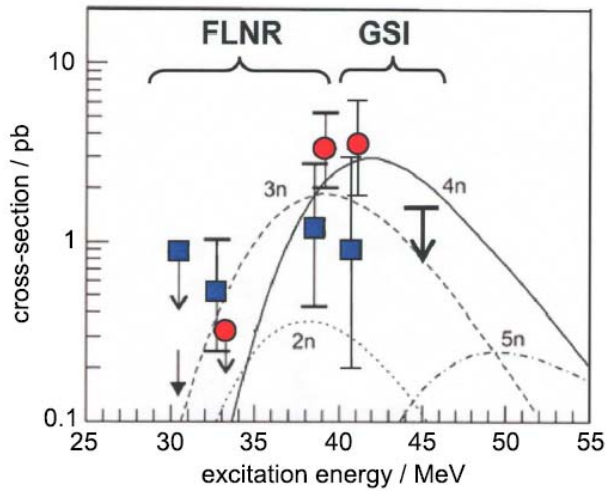

Fig. 3. Measured cross-sections for the 3n (squares) and 4n (circles) evaporation channels of the reaction ^{48}Ca + ^{248}Cm → ^{296}116*. The Figure shows both, the data measured in Dubna [17, 18] and at SHIP. Also shown are the calculated excitation functions for the 2n, 3n, 4n and 5n evaporation channels [19].

A possible explanation for the deviating α-energies observed at SHIP might be the population of isomeric states which are located rather close to the ground state. Theoretical calculations for the decay chain of ^{293}116 [21] result in the existence of high and low spin states close to the ground state which would enable the existence of isomeric states. The observation of very similar half-lives for the decay chains from the hypothetical ground and isomeric states is not contradicting according to the calculations in [21] since they allow for the existence of decay chains from the ground as well as from isomeric states with similar angular momentum leading to similar half-lives. However, an assignment of the observed transitions by comparing experimental and theoretical data was not possible.

3.2 Search for Z = 120

The reaction ^{64}Ni + ^{238}U was studied at SHIP to search for evaporation residues of the compound nucleus ^{302}120*. This proton number is particularly interesting because in some theoretical models a spherical shell closure is expected there. The compound nucleus ^{302}120* formed in fusion reactions of ^{64}Ni and ^{238}U has 182 neutrons. This would be the closest approach to the predicted closed neutron shell N = 184 reached so far in superheavy element experiments. Calculations within different models have been performed for this reaction which resulted in strongly different production cross-sections. The calculated values for the 4n channel are compared in the Table, column 1 for several models.

Expected cross-sections for the isotope $^{298}120$ according to different model calculations. The nuclei are produced in 4n evaporation channels from excited $^{302}120^*$ compound nuclei created in fusion reactions with different projectile-target combinations. References are given in the Table.

$^{64}Ni + ^{238}U$	$^{58}Fe + ^{244}Pu$	$^{54}Cr + ^{248}Cm$	ref.
3.2 fb	5.3 fb	25 fb	[22]
0.022 fb	1 fb	800 fb	[23]
0.02 fb	0.015 fb	0.07 fb	[24]
5 fb	32 fb	54 fb	[24]
< 90 fb [25]	< 400 fb [26]	< 560 fb [27]	experiment

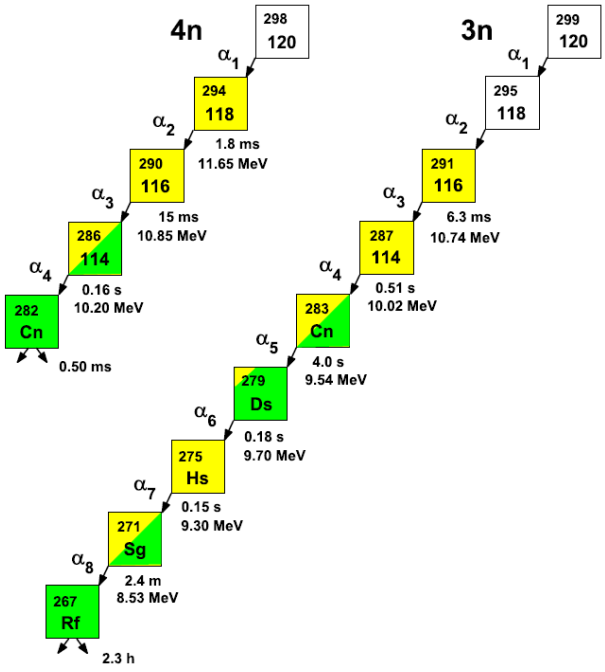

Fig. 4 Expected decay chains of the isotopes $^{298}120$ and $^{299}120$. The white squares represent still unobserved isotopes.

They differ by more than three orders of magnitude which reflect the high sensitivity of the cross-sections to the entrance and exit channel parameters like fusion barriers and shell correction energies which vary in the different models or have different impact, respectively. One has to note that all models named in the Table were able to reasonably reproduce the cross-sections for lighter superheavy nuclei measured in Dubna. The models underlying the values in the Table assumed fission barriers of about 7 MeV and a proton shell closure at Z = 114. However, if the fission barriers are actually higher and/or the shell closure is located at Z = 120, much higher cross-sections can be expected. Concerning the strength of the shell corrections the model predictions vary on a large scale resulting in values for the shell correction energies from -6 MeV to -12 MeV which corresponds to fission barriers of (6 - 12) MeV [28]. By trend, one can assume that the cross-section increases by one order of magnitude if the fission barrier increases by 1 MeV. This was the motivation to investigate this reaction. A total of 120 days of beam time was applied in 2007 and 2008. The beam energy was chosen such that the compound nuclei would be created with excitation energy of 36 MeV which should predominantly lead to the evaporation residues $^{298}120$ and $^{299}120$. From both isotopes long α-decay chains can be expected which join the already known decay chains of $^{294}118$ and $^{291}116$, respectively (Fig. 4). Finally, no event was observed which showed the expected signatures of the decay of a Z = 120 isotope. The upper cross-section limit reached in this experiment is 90 fb at a total number of $2.64 \cdot 10^{19}$ projectiles on target [25]. This indicates that the fission barriers are not higher than 8.3 MeV for the isotopes $^{298,299}120$.

Besides in fusion reactions of $^{64}Ni + ^{238}U$, the same compound nucleus, $^{302}120^*$, can also be created in collisions of $^{58}Fe + ^{244}Pu$ and $^{54}Cr + ^{248}Cm$. The respective calculated cross-sections for the 3n channel are listed in the Table, column 2 and 3. The reaction $^{58}Fe + ^{244}Pu \rightarrow ^{302}120^*$ was investigated in Dubna [26]. No event was observed which could be attributed to the decay of a Z = 120 isotope. The corresponding upper cross-section limit for the observation of one event was 400 fb.

At SHIP, the reaction $^{54}Cr + ^{248}Cm$ was investigated from April 23 to June 1st, 2011, with a total of $7.9 \cdot 10^{18}$ projectiles on target [27]. Also here no event was observed leading to an upper cross-section limit of 560 fb. The limit cross-sections reached so far in the experiments are still not low enough to meet the cross-sections predicted by most of the models. However, the experimental data allow the exclusion of extraordinary high fission barriers as predicted by some models. From the experimental cross-section limits one can deduce that the barriers do not significantly exceed the value of 8 MeV.

The expected half-lives for isotopes with Z = 120 deserve special attention. The Q-values for α-decay are increasing with the proton number which leads to a decrease in the half-lives. According to the macroscopic-microscopic model which assumes the shell closure at Z = 114 the Q-values are about 13 MeV leading to half-lives on the order of (1 – 10) μs for the isotopes $^{298,299}120$. This is already on the same range as the flight time of the fusion products through the separator. Therefore one has to keep in mind that the evaporation residues could already decay before the detector is reached. If, however, the shell closure is assumed at Z = 120 one can expect significantly longer half-lives on the order of 1 s. The related Q-values are around 11 MeV. Therefore, the observation of relatively long half-lives and α-decay energies around 11 MeV would be a strong hint for a shell closure at Z = 120.

4. Perspectives for the future of superheavy element research

The small production cross-sections of the heaviest nuclei presently limit the synthesis of new isotopes or elements, respectively. Presently available typical beam intensities are on the scale of $5 \cdot 10^{12}$ ions / s which leads to the situation that cross-sections on the order of 100 fb require already several months of beam time to reach the one-event cross-section limit for the desired isotope. Therefore, the availability of more intense ion beams and the related necessary upgrades of the separation and detection techniques are decisive steps for the future research in this field. This concerns equally, beside the synthesis of new isotopes, all experiments in the field of superheavy nuclei like spectroscopic and chemical investigations, precision mass measurements and nuclear reaction studies.

At GSI, a new superconducting continuous wave (cw) LINAC is planned which shall provide ion beams with intensities up to 10^{14} particles / s. Presently, a so-called demonstrator, consisting of a superconducting CH-cavity and two superconducting solenoids is built and shall be tested with beam in 2013 / 2014 at GSI [29]. In parallel, we are developing a new separator for the future superheavy element experimental program which will be adjusted to the requirements arising with the higher beam intensities, namely, it must be capable of strong background suppression to handle the 10 to 50 times higher beam intensities. The new separator will also be based on the concept of a velocity filter like the present SHIP following from the positive long-term experience with SHIP. Velocity filters provide several advantages in comparison to gas-filled separators: (i) the separation according to velocities is, for the typical reactions applied here, about five times stronger than the separation according to magnetic rigidity in gas. Therefore, velocity filters provide a stronger suppression especially of target-like quasi-elastic and deep inelastic background events; (ii) velocity filters allow the determination of the reaction channel in which a certain isotope was created by measuring the velocity spectra of the reaction products; (iii) due to the relatively strong separation of different reaction channels, velocity filters are also suitable for the study of transfer reactions with low cross-sections, especially at beam energies below and close to the Coulomb barrier. The study of transfer reactions is very interesting since in recent times new theoretical calculations suggest to produce new neutron-rich heavy and superheavy nuclei in multi-nucleon transfer reactions which are not accessible in other reactions (see e. g. [22, 30]).

For the new separator we plan a more compact design in comparison to SHIP. It will also be a two-stage separator but the condenser field shall be placed inside the magnetic dipole field while SHIP has separated electric and magnetic fields. To enhance especially the angular efficiency for transfer products, the acceptance angle will be increased by a factor of 2 to 3 with respect to the present acceptance of SHIP which is 10 msr.

In parallel to the separator design, we are testing and developing detection techniques for heavy long-lived nuclei and for nuclei which do not undergo α-decays and are therefore not accessible with the present technique of α-decay tagging. One possibility is the application of high-precision mass measurements. Penning traps or multiple reflection time-of-flight mass spectrometers have mass resolving powers up to $m/\Delta m \approx 10^7$ where, however, a resolving power of 10^5 is already sufficient for an isobaric separation of most of the isotopes. The mass measurement is performed after the separation stage. Penning traps and TOF spectrometers can only trap ions with low energies on the scale of (100 - 1000) eV therefore a buffer gas cell and an ion guide system has to be used after the separator for stopping, extracting and transporting the ions to the mass measurement device. The presently running gas cells which are applied for ions in the required mass and energy range have overall (i. e. stopping and extraction) efficiencies of ≈1 %. This leads to a rather strong loss of ions which presently requires production cross-sections of at least 10 nb. However, the new generation of cryogenic gas cells [31, 32] shows at least a factor of 10 more efficiency which has been demonstrated in the commissioning of such a cell at the Fragment Separator at GSI. Further, a newly developed multiple reflection time-of-flight mass spectrometer (MR-TOF-MS [33]) at the University of Gießen has promising features for the application as detection system since it allows for a broadband detection. This is especially for transfer products very efficient since a large number of them with rather different mass numbers can pass the separator at the same setting.

Besides, we are investigating the applicability of calorimetric low temperature detectors (bolometers) [34] for energy measurement of very heavy nuclei. These detectors register the increase of temperature when an ion deposits its energy in the detector. In this case, the usually occurring plasma effects which lead to a pulse height deficit can be circumvented. As a consequence, a considerably better energy resolution can be obtained than with the usually applied semiconductor detectors.

REFERENCES

1. *Münzenberg G., Hofmann S., Heßberger F.P. et al.* // Z. Phys. - 1981. - Vol. A300. - P. 107 - 108.
2. *Münzenberg G., Armbruster P., Heßberger F.P. et al.* // Z. Phys. - 1982. - Vol. A309. - P. 89 - 90.
3. *Münzenberg G., Armbruster P., Folger H. et al.* // Z. Phys. - 1984. - Vol. A317. - P. 235 - 236.
4. Hofmann S., Ninov V., Heßberger F.P. et al. // Z. Phys. - 1995. - Vol. A350. - P. 277 - 280.
5. *Hofmann S., Ninov V., Heßberger F.P. et al.* // Z. Phys. - 1995. - Vol. A350. - P. 281 - 282.
6. *Hofmann S., Ninov V., Heßberger F.P. et al.* // Z. Phys. - 1996. - Vol. A354. - P. 229 - 230.
7. *Subotic K., Oganessian Y.T., Utyonkov V.K. et al.* // Nucl. Instr. Meth. - 2002. - Vol. A481. - P. 71.
8. *Oganessian Yu.* // J. Phys. - 2007. - Vol. G34. - P. R165 - R242.
9. *Morita K., et al.* // J. Phys. Soc. Jpn., - 2004. - Vol. 73. - P. 2593 - 2596.
10. *Yeremin A.V., Bogdanov D.D., Chepigin V.I. et al.* // Nucl. Instr. Meth. - 1997. - Vol. B126. - P. 329.

11. *Heinz S., Hofmann S., Comas V. et al.* // Eur. Phys. Jour. - 2012. - Vol. A48. - P. 32.
12. *Münzenberg G., Faust W., Hofmann S. et al.* // Nucl. Instr. Meth. - 1979. - Vol. 161. - P. 65.
13. *Hofmann S., Faust W., Münzenberg G. et al.* // Z. Phys. - 1979. - Vol. A291. - P.53 - 70.
14. *Saro S., Janik R., Hofmann S. et al.* // Nucl. Instr. Meth. - 1996. - Vol. 381. - P. 520.
15. *Hofmann S., Münzenberg G.* // Rev. Mod. Phys. - 2000. - Vol. 72. - P. 733.
16. *Hofmann S., Heinz S., Mann R. et al.* // Eur. Phys. Jour. - 2012. - Vol. A48. - P. 62.
17. *Oganessian Yu.Ts., Utyonkov V.K., Lobanov Yu.V. et al.* // Phys. Rev. - 2000. - Vol. C63. - P. 011301.
18. Oganessian Yu.Ts., Utyonkov V.K., Lobanov Yu.V. et al. // Phys. Rev. - 2004. - Vol. C70. - P. 064609.
19. *Zagrebaev V.I.* // Nucl. Phys. - 2004. - Vol. A734. - P. 164.
20. *Düllmann Ch.E., Schädel M., Yakushev A. et al.* // Phys. Rev. Lett. - 2010. - Vol. 104. - P. 252701.
21. *Cwiok S., Nazarewicz W., Heenen P.H.* // Phys. Rev. Lett. - 1999. - Vol. 83. - P. 1108.
22. *Zagrebaev V., Greiner W.* // Phys. Rev. - 2008. - Vol. C78. - P. 34610.
23. *Nasirov A.K., Giardina G., Mandaglio G. et al.* // Phys. Rev. - 2009. - Vol. C79. - P. 024606.
24. *Adamian G.G., Antonenko N.V., Scheid W.* // Eur. Phys. Jour. - 2009. - Vol. A41. - P. 235.
25. *Hofmann S., Ackermann D., Antalic S. et al.* // GSI Sci. Rep. 2008. - 2009. - P. 131.
26. *Oganessian Yu.Ts., Utyonkov V.K., Lobanov Yu.V. et al.* // Phys. Rev. - 2009. - Vol. C79. - P. 024603.
27. *Hofmann S., Heinz S., Ackermann D. et al.* // Sci. Rep. 2011. - 2012. - P. 205.
28. *Bender M., Nazarewicz W., Reinhard P.-G.* // Phys. Lett. - 2001. - Vol. 515. - P. 42 - 48.
29. *Mickat S., Amberg M., Aulenbacher K. et al.* The SC CW-LINAC-Demonstrator - SRF technology finds the way to GSI // Proc. of the SRF Conference 2011. - Chicago, 2011.
30. *Adamian G.G., Antonenko N.V., Zubov A.S.* // Phys. Rev. - 2005. - Vol. C71. - P. 034603.
31. *Dendoven P., Purushothaman S., Gloos K.* // Nucl. Instr. Meth. - 2006. - Vol. A558. - P. 580.
32. *Purushothaman S., Dendooven P., Moore I. et al.* // Nucl. Instr. Meth. - 2008. - Vol. B266. - P. 4488.
33. *Plaß W.R., Dickel T., Czok U. et al.* // Nucl. Instr. Meth. - 2008. - Vol. B266. - P. 4560.
34. *Egelhof P., Kraft-Bermuth S.* // Topics in Applied Physics. - 2005. - Vol. 99. - P. 469 - 500.

REGGEOMETRY OF DEEPLY VIRTUAL COMPTON SCATTERING AND EXCLUSIVE DIFFRACTIVE VECTOR MESON PRODUCTION

L. Jenkovszky[1,2], A. Salii[1], J. Turóci[3], D. Himics[3]

[1] *M. M. Bogolyubov Institute for Theoretical Physics, National Academy of Sciences of Ukraine, Kyiv, Ukraine*
[2] *Wigner Research Centre for Physics, Hungarian Academy of Sciences, Budapest, Hungary*
[3] *Uzhgorod National University, Uzhgorod, Ukraine*

We extend a simple Pomeron pole amplitude by t and Q^2, M_V dependencies inspired by geometrical ideas. The experimentally transition from *soft* to *hard* dynamics is realized by the introduction of two Pomeron poles with different Q^2, M_V - dependent residue. A unified description of deeply virtual Compton scattering as well as the elastic electroproduction of all vector meson is suggested.

1. Introduction

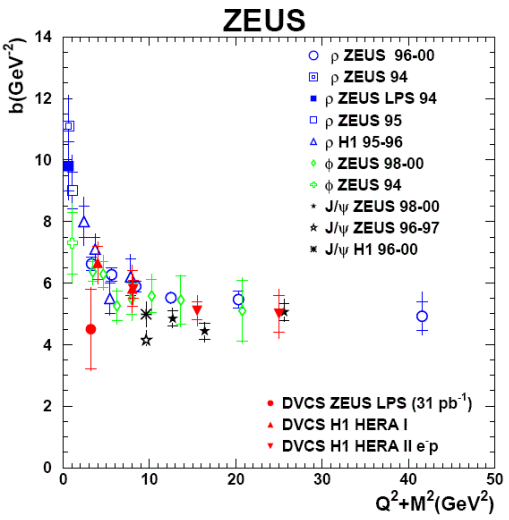

Fig. 1. The B-slope as a function of $\tilde{Q}^2$. Compilation of data for VMP and DVCS process ([10]).

The forward slope of the differential cross sections for elastic scattering is known to be related to the masses/virtualities of the interacting particles. This phenomenon is well known (Fig. 1), where the forward slope $B(\tilde{Q}^2)=\frac{d}{dt}\ln\frac{d\sigma}{dt}$ is plotted as a function of $\tilde{Q}^2=Q^2+M_V^2$ [1]. One of the basic idea of diffraction processes is that the slope of differential cross section $\frac{d\sigma}{dt}$ is proportional to the *interaction radius* R [1]. In our case R depends on $\tilde{Q}^2$ and decreases with increasing of $\tilde{Q}^2$, reaching some saturation value, determined by the finite mass of the nucleons. In this *geometric* picture, the largest slope (radius) is expected for real Compton scattering at $Q^2=0$, which may require a separate treatment.

In the present paper we consider exclusive diffractive electroproduction of real photons and vector mesons as well as elastic proton-proton scattering by making use of the above *geometric* considerations, by writing the scattering amplitude in the form:

$$A(s,t)\sim e^{B(s,M_V^2)t} \tag{1}$$

with $B(M^2)\sim 1/f(M_V^2)$. This approach was used in ref. [2] for the case of photoproduction $\tilde{Q}^2=0$, excluding real Compton scattering, and without considering nucleon scattering, to be also included below.

While the geometric considerations was proved to be efficient [3] for photoproduction, they are not sufficient in the case of electroproduction $Q^2=0$, since the relevant cross sections will increase with $\tilde{Q}^2$ contradicting the experimental data. To remedy this deficiency, this rise must be compensated by multiplying the amplitude by a function decreasing with $\tilde{Q}^2$. To cope with the observed trend of *hardening* of dynamics with $\tilde{Q}^2$ increasing, and following ref. [4, 5], we expect to introduce two components for the diffractive (Pomeron) amplitude of the type Eq. (1), soft A_s and hard A_h, each one to be multiplied by a relevant $\tilde{Q}^2$ - dependent factor $H_i(\tilde{Q}^2)$, $i=s,h$. These factors are chosen in such a way as provide for the increasing weight of the hard component as the mass (virtuality) increases. To avoid conflict with unitarity, the rise with $\tilde{Q}^2$ of the hard component is finite, and it terminates at some *saturation* scale $\tilde{Q}^2$, whose value will be determined phenomenologically. Explicit examples of these functions will be given below.

Recently a model for exclusive production of vector particles at HERA was suggested and successfully fitted to the HERA data [2 - 4]. In that model, the interplay between t and $\tilde{Q}^2$ is achieved by introducing a new variable $z=t-\tilde{Q}^2$. Good fits were obtained at those papers, however the specific interplay between the variables t and $\tilde{Q}^2$ there waits for a better understanding and physical interpretation.

---

[1] The use of the variable $\tilde{Q}^2=\left(M_V^2+Q^2\right)$ implies symmetry between the mass M_V^2 and virturality Q^2, which should imply equal slopes (radii) for e.g. J/Ψ production near $Q^2=0$ and ρ electroproduction near $Q^2\approx 9\ GeV^2$, which is not supported by the data.

2. The Model

2.1. Regge + geometry = Reggeometry

Quite generally, the Regge-pole scattering amplitude can be written as:

$$A(s,t,M,Q^2)=\xi(t)\beta(t,M,Q^2)(s/s_0)^{\alpha(t)}, \tag{2}$$

where $\xi(t)=e^{-i\pi\alpha(t)}$ is the signature factor and $\beta(t,M,Q^2)$ is the residue factor written in the following geometrical form:

$$\beta(t,M,Q^2)=\exp\left[2\left(\frac{a}{M_V^2+Q^2}+\frac{b}{2m_N^2}\right)t\right]. \tag{3}$$

Hence

$$A(s,t,M,Q^2)=\tilde{A}_0 e^{-i\pi\alpha(t)}e^{-2\left(\frac{a}{M_V^2+Q^2}+\frac{b}{2m_N^2}\right)|t|}(s/s_0)^{\alpha(t)}. \tag{4}$$

The differential cross section is

$$\frac{d\sigma}{d|t|}=\frac{\pi}{s^2}\left|A(s,t,M,Q^2)\right|^2=A_0^2(s/s_0)^{2(\alpha_0-1-\alpha'|t|)}e^{-4\left(\frac{a}{M_V^2+Q^2}+\frac{b}{2m_N^2}\right)|t|}, \tag{5}$$

or

$$\frac{d\sigma}{d|t|}=A_0^2(s/s_0)^{2(\alpha_0-1)}e^{-\left[2\alpha'\ln(s/s_0)+4\left(\frac{a}{M_V^2+Q^2}+\frac{b}{2m_N^2}\right)\right]|t|}=Ce^{-B|t|}. \tag{6}$$

The local slope parameter is defined as

$$B(s,\tilde{Q}^2)=\frac{d}{dt}\ln\frac{d\sigma}{d|t|}=2\alpha'\ln(s/s_0)+2\left(\frac{a}{M_V^2+Q^2}+\frac{b}{2m_N^2}\right), \tag{7}$$

and the integrated elastic scattering amplitude is

$$\sigma_{el}=\frac{1}{B}\frac{d\sigma}{dt}\bigg|_{t=0}=\frac{C}{B}, \tag{8}$$

or

$$\sigma=\frac{A_0^2(s/s_0)^{2(\alpha_0-1)}}{2\alpha'\ln(s/s_0)+4\left(\frac{a}{M_V^2+Q^2}+\frac{b}{2m_N^2}\right)}. \tag{9}$$

In the case a > 0 when $\tilde{Q}^2=\left(M_V^2+Q^2\right)$ grows, $B(s,\tilde{Q}^2)$ falls, but $\frac{d\sigma}{d|t|}$ and σ become larger. While the behavior of $B(s,\tilde{Q}^2)$ is consistent with the experimental data, the behavior of $\frac{d\sigma}{d|t|}$ and σ are not.

2.2. Soft and Hard components of the unique Pomeron

We build the scattering amplitude that consist of two terms, soft and hard, with two different $\tilde{Q}^2$-dependent factors:

$$\begin{aligned}A(s,t,Q^2,M_V^2)=&\frac{\tilde{A}_s}{\left(1+\frac{\tilde{Q}^2}{\tilde{Q}_s^2}\right)^{n_s}}e^{-i\frac{\pi}{2}\alpha_s(t)}\left(\frac{s}{s_{0s}}\right)^{\alpha_s(t)}e^{2\left(\frac{a_s}{\tilde{Q}^2}+\frac{b_s}{2m_p^2}\right)t}+\\&+\frac{\tilde{A}_h\left(\frac{\tilde{Q}^2}{\tilde{Q}_h^2}\right)}{\left(1+\frac{\tilde{Q}^2}{\tilde{Q}_h^2}\right)^{n_h+1}}e^{-i\frac{\pi}{2}\alpha_h(t)}e^{2\left(\frac{a_h}{\tilde{Q}^2}+\frac{b_h}{2m_p^2}\right)t}.\end{aligned} \tag{10}$$

The $\tilde{Q}^2$ – dependent factors were introduced in such a way as to provide for a proper balance between the soft and hard components of the Pomeron, namely that the hard one increases with increasing $\tilde{Q}^2$, up to the saturation point, thus securing unitarity. The extra $\tilde{Q}^2$ – dependent (but t – independent!) factor does not violate the geometrical structure of the amplitude. The differential and integrated cross sections now are:

$$\frac{d\sigma_{el}}{d|t|} = H_s^2 e^{2\{L_s(\alpha_s(t)-1)+g_s t\}} + H_h^2 e^{2\{L_h(\alpha_h(t)-1)+g_h t\}} + 2H_s H_h e^{\{L_s(\alpha_s(t)-1)+L_h(\alpha_h(t)-)+(g_s+g_h)t\}} \cos\left(\frac{\pi}{2}(\alpha_s(t)-\alpha_h(t))\right), \quad (11)$$

$$\sigma_{el} = \frac{H_s^2 e^{2\{L_s(\alpha_{0s}-1\}}}{2(\alpha_s' L_s + g_s)} + \frac{H_h^2 e^{2\{l_H(\alpha_{0h}-1)\}}}{2(\alpha_h' L_h + g_h)} + 2H_s H_h e^{L_s(\alpha_{0s}-1)+L_h(\alpha_{0h}-1)} \frac{\mathrm{B}\cos\varphi_0 + \mathrm{A}\sin\varphi_0}{B^2 + A^2}, \quad (12)$$

where:

$$H_s = \frac{A_s}{\left(1+\frac{\tilde{Q}^2}{\tilde{Q}_s^2}\right)^{n_s}},\ H_h = \frac{A_h\left(\frac{\tilde{Q}^2}{\tilde{Q}_h^2}\right)}{\left(1+\frac{\tilde{Q}^2}{\tilde{Q}_h^2}\right)^{n_s+1}},$$

$$L_s = \ln\left(\frac{s}{s_{0s}}\right),\quad g_s = 2\left(\frac{a_s}{\tilde{Q}^2}+\frac{b_s}{2m_p^2}\right),\quad \alpha_s(t) = \alpha_{0s} + \alpha_s' t,$$

$$L_h = \ln\left(\frac{s}{s_{0h}}\right),\quad g_h = 2\left(\frac{a_h}{\tilde{Q}^2}+\frac{b_h}{2m_p^2}\right),\quad \alpha_h(t) = \alpha_{0h} + \alpha_h' t$$

$$\mathrm{B} = L_s\alpha_s' + L_h\alpha_h' + (g_s + g_h),$$

$$A = \frac{\pi}{2}(\alpha_s' - \alpha_h'),$$

$$\varphi_0 = \frac{\pi}{2}(\alpha_{0s} - \alpha_{0h})$$

was introduced.

For the soft and hard components of the Pomeron trajectory we use the Donnachie-Landshoff parameterization [5, 6]:

$$\alpha_s(t) = 1.08 + 0.25t,$$

$$\alpha_h(t) = 1.44 + 0.01t \quad (\textit{DL pomeron}).$$

3. Fits to the data

Although there are 16 fitting parameters, almost all of them can be fixed.

$$\begin{pmatrix} & fix, & fix, & fix, & fix, & fix, & fix \\ A_s, & \tilde{Q}_s^2, & n_s, & s_{0s}, & \alpha_{0s}, & \alpha_s', & a_s, & b_s \\ A_h, & \tilde{Q}_h^2, & n_h, & s_{0h}, & \alpha_{0h}, & \alpha_h', & a_h, & b_h \end{pmatrix}.$$

The values of the parameters obtained form fitting the DVCS differential elastic cross section are

	A_s	$\tilde{Q}_s^2$	n_s	s_{0s}	α_{0s}	α_s'	a_s	b_s
soft :	3.437 ± 3.587;	23.724 ± 36.520;	2;	7.0;	1.08;	0.25;	1.0;	1.0;
hard :	2.466 ± 27.216;	1.535 ± 7.243;	2;	7.0;	1.44;	0.01;	1.0;	1.0;

and those form fitting the integrated elastic DVCS cross section are:

	A_s	$\tilde{Q}_s^2$	n_s	s_{0s}	α_{0s}	α_s'	a_s	b_s
soft :	2.448 ± 2.118;	29.683 ± 38.633;	2;	7.0;	1.08;	0.25;	1.0;	1.0;
hard :	2.466 ± 27.216;	1.705 ± 2.089;	2;	7.0;	1.44;	0.01;	1.0;	1.0;

These two fits were performed separately, giving similar results. The experimental data for the fits are from Refs. [7 - 10]. The results of the fit are shown in the Figs. 2 and 3.

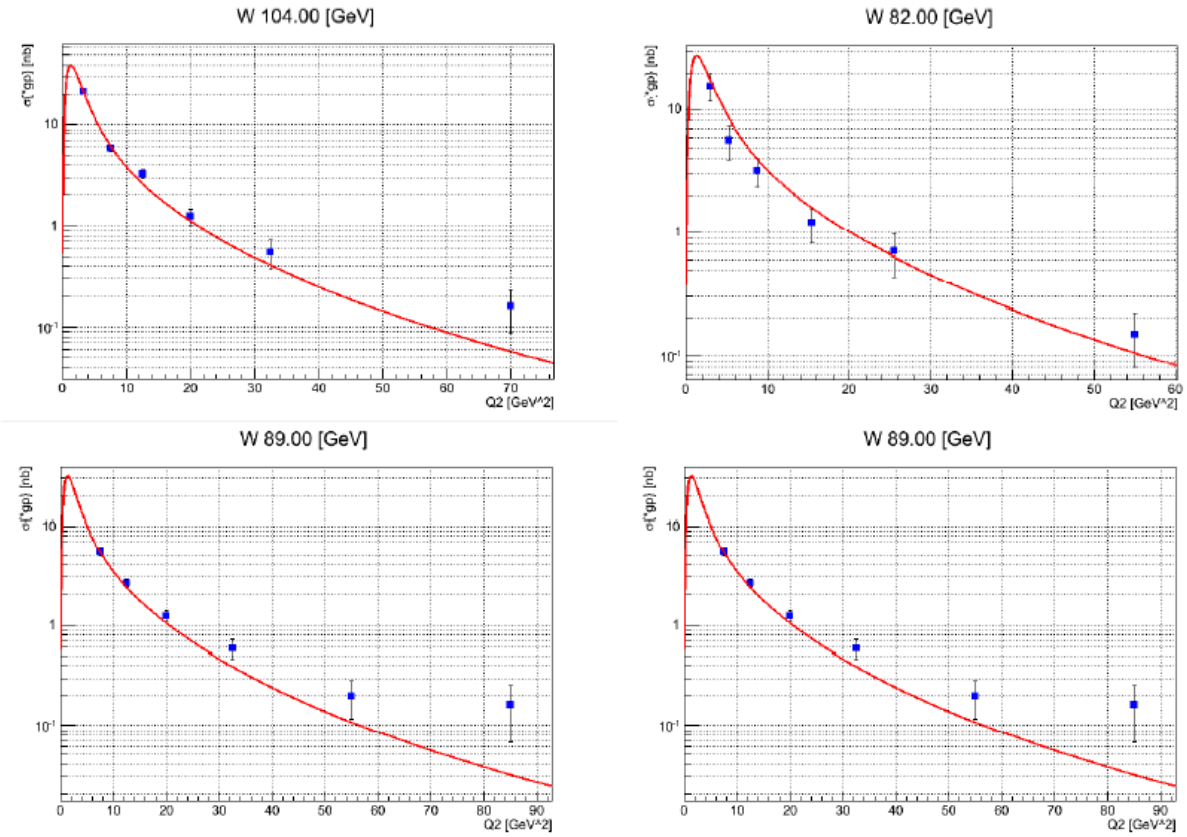

Fig. 2. Results of our fit to $\gamma^* p \to \gamma p$ elastic cross-section as a function of Q^2 for ZEUS 99-00 (upper, left icon) and H1 96-00 (upper, right icon); for ZEUS 96-00 (lower left and right icons).

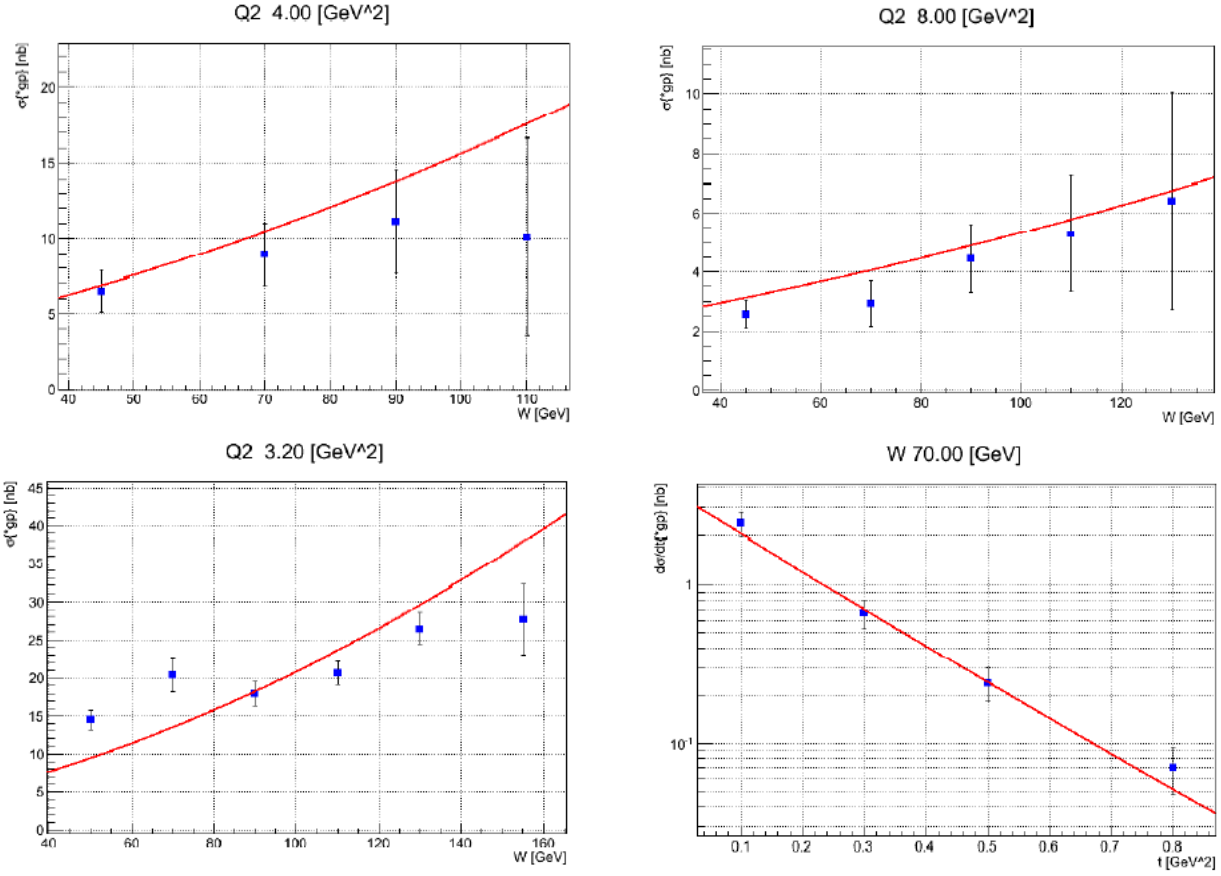

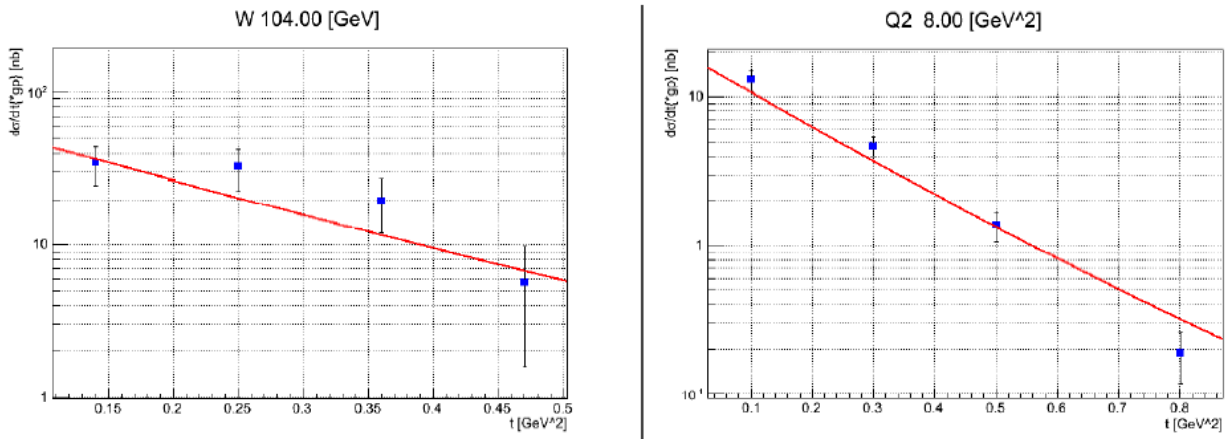

Fig. 3. Results of our fit to $\gamma^* p \to \gamma p$ elastic cross-section as a function of W for ZEUS 99-00 (upper left and middle left icons) and H1 05-06 (upper right, icon); $\gamma^* p \to \gamma p$ differential cross-section as a function of t for ZEUS 99-00 (down-left) and H1 05-06 (middle and lower, right icons).

ACKNOWLEDGMENTS

L.J. thanks the Organizers of the NPAE Conference for the creative atmosphere there.

REFERENCES

1. *Goulianos K.* Diffractive interactions of hadrons at high energies // Phys. Lett. - 1983. - Vol. 101, No. 3. - P. 161 - 219;
2. *Capua M., Fazio S., Fiore R.et al.* // Phys. Letters. - 2007. - Vol. B645. - P. 161; hep-ph/0605319.
3. *Fiore R., Jenkovszky L.L., Paccanoni F.* // arXiv:hep-ph/9812458 [pdf, ps, other] Photoproduction of Heavy Vector Mesons at HERA - A Testfield for Diffraction // Eur. Phys. J. - 1999. - Vol. C10. - P. 461-467; hep-ph/9812458.
4. *Fazio S., Fiore R., Jenkovszky L.L., Lavorini A.A.* // Phys. Rev. - 2012. - Vol. C85. - P. 5; hep-ph/1109.6374.
5. *Landshoff P.* // hep-ph/0903.1523.
6. *Donnachie A., Landshoff P.V.* // hep-ph/0803.0686.
7. *Atkas A. et al.* [H1 Collaboration] // Eur. Phys. J. - 2005. - Vol. C44. - P. 1.
8. *Aaron F.D. et al.* [H1 Collaboration] // Phys. Lett. - 2008. - Vol. B659. - P. 796.
9. *Aaron F.D. et al.* [H1 Collaboration] // Phys. Lett. - 2009. - Vol. B681. - P. 391.
10. *Chekanov S. et al.* [ZEUS Collaboration] // JHEP. - 2009. - Vol. 0905. - P. 108.

PREDICTIVE POWER OF NUCLEAR-MASS MODELS

Yu. A. Litvinov[1], A. Sobiczewski[2,1], E. A. Cherepanov[3]

[1] *GSI Helmholtzzentrum für Schwerionenforschung, Darmstadt, Germany*
[2] *National Centre for Nuclear Research, Warsaw, Poland*
[3] *Joint Institute for Nuclear Research, Dubna, Moscow region, Russia*

Ten different theoretical models are tested for their predictive power in the description of nuclear masses. Two sets of experimental masses are used for the test: the older set of 2003 and the newer one of 2011. The predictive power is studied in two regions of nuclei: the global region (Z, $N \geq 8$) and the heavy-nuclei region ($Z \geq 82$, $N \geq 126$). No clear correlation is found between the predictive power of a model and the accuracy of its description of the masses.

1. Introduction

Mass of a nucleus is a fundamental property of it. It is decisive for its other properties and also for the properties of various nuclear processes. A realistic description of the mass is an important question for nuclear models.

The objective of this paper is to test the quality of the description of measured masses by various theoretical models and also to test the predictive power of the models in this description. An interesting question is also the relation between these two properties of a model.

Ten models of various nature are considered: semi-empirical, macroscopic-microscopic, purely microscopic (self-consistent) and others. The quality of the description is tested with the use of experimental masses evaluated recently [1]. The predictive power of a model is studied by comparing its description of the older mass data [2] with that of the new data [1], to which the model was not adjusted. Between the older evaluation [2] and the new one [1], masses of more than 140 nuclei have been measured. Also the accuracy of the newly measured masses has been improved for many nuclei. The present study is an extension of our discussion on the description of the heavy-nuclei masses by macroscopic-microscopic models [3].

2. Considered models

Ten various models are considered in the study. These are: one semi-empirical (LMZ) [4], five macroscopic-microscopic, two purely microscopic (self-consistent) and two models of other kind. The macroscopic-microscopic models are: the Finite-Range Droplet Model (FRDM) [5], the Finite-Range Liquid Drop Model (FRLDM) [5], the nuclear Thomas-Fermi (TF) [6], the Warsaw model for Heavy Nuclei (HN) [7] (see also [8]), and the Lublin-Strasbourg (LSD) model [9]. The purely microscopic models are: the most recent (21st) version of the Hartree - Fock - Bogoliubov approach (HFB21) [10], which uses the Skyrme interactions, and the HFB approach exploiting the Gogny forces (GHFB) [11]. Two other models are the following: the model of Duflo and Zuker (DZ) [12] and that of Koura et al. (KTUY) [13].

Eight of the models are of a global character describing all nuclei with Z, $N \geq 8$. Two of the models (LMZ and HN) are of a local type, specially adapted to describe heavy nuclei with proton number $Z \geq 82$ and neutron number $N \geq 126$.

3. Quality of the description of masses

In this section, we illustrate the quality of the description of nuclear masses by the considered models in two regions of nuclei: the whole (global) region (Z, $N \geq 8$) and in its part corresponding to heavy nuclei ($Z \geq 82$, $N \geq 126$). Three quantities characterizing the quality are calculated: rout-mean-square (rms) of the discrepancies between

Table 1: Results for all (global) and heavy nuclei.

Model	LMZ	HN	LSD	FRDM	TF	FRLDM	HFB21	GHFB	DZ	KTUY
(Year)	(2000)	(2001)	(2003)	(1995)	(1996)	(1995)	(2010)	(2009)	(1995)	(2005)
						GLOBAL				
N_{nucl}	-	-	2267	2294	2293	2294	2294	2294	2294	2294
Rms	-	-	0.600	0.645	0.629	0.768	0.573	0.784	0.373	0.690
$\bar{\delta}$	-	-	-0.029	-0.062	0.027	0.057	0.030	-0.108	-0.030	-0.048
Max $\mid \delta \mid$	-	-	4.34	3.64	4.61	4.17	3.20	3.23	3.01	2.63
						HEAVY				
N_{nucl}	297	297	289	297	296	297	297	297	297	297
Rms	0.202	0.358	0.352	0.455	0.476	0.731	0.484	1.057	0.333	0.986
$\bar{\delta}$	0.028	-0.133	0.163	0.131	0.340	0.562	0.132	-0.118	-0.011	-0.307
Max $\mid \delta \mid$	1.12	1.13	1.43	1.95	1.75	1.92	1.33	3.23	3.01	2.38

theoretical and experimental masses, the average value of the discrepancies, $\bar{\delta}$, and the maximum of the absolute values of the discrepancies, max |δ|. The experimental masses are taken from Ref. [1]. The results are given in Table 1, where the year of publication of each model and the number of nuclei with both measured and calculated masses in each of the considered regions, N_{nucl}, are also indicated. The most important quantities, rms, are also illustrated in a graphical form in Figs. 1 and 2.

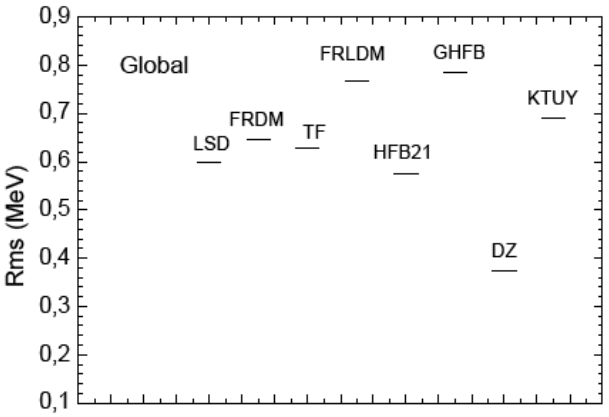

Fig. 1. Rms values of the discrepancies between the mass values calculated with 8 global models (see text for the notation of the models) and the experimental ones.

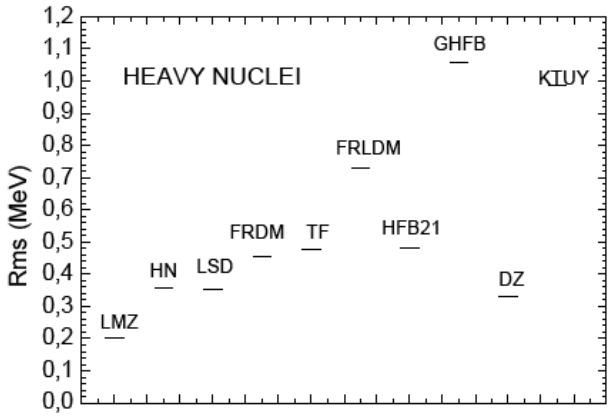

Fig. 2. Same as in Fig. 1, but for the heavy-nuclei region. Results for the two local models (LMZ and HN) are also shown.

One can see in Fig. 1 that the rms values may be divided into three groups. The lowest value is obtained for the DZ model. Medium values, close to each other, appear for the LSD, FRDM, TF and HFB21 approaches. The largest values are obtained for the three remaining models.

The results obtained for the heavy nuclei (Fig. 2) differ significantly from those of Fig. 1. Rms of the LSD, FRDM, TF and HFB21 models decrease significantly, while those of the GHFB and KTUY approaches significantly increase, with respect to the rms values of Fig. 1. The rms values of the LMZ and HN approaches are small, as could be expected for these local models, specially adapted for heavy nuclei.

The results presented in this Section show that the accuracy of the description of nuclear masses by a given model significantly depends on the region of nuclei to which the model is applied.

4. Predictive power of the models

Let us test the predictive power of the considered models in description of masses in both studied regions of nuclei.

Table 2 shows the results for the global region. The first row gives the number of nuclei, the masses of which are described by each model in the case of data evaluated in Ref. [2]. The second row specifies the same quantity in the case of using Ref. [1]. In the third row, the difference, δN_{nucl}, between the number of nuclei with measured masses in the later evaluation of Ref. [1] and the earlier one of Ref. [2], is shown. The respective difference in the rms, δRms, given in the last row, is also illustrated in a graphical form in Fig. 3.

Table 2: Predictive power of the models in description of global masses.

Model	LSD	FRDM	TF	FRLDM	HFB-21	GHFB	DZ	KTUY
$N_{nucl}(03)$	2141	2149	2149	2149	2149	2149	2149	2149
$N_{nucl}(11)$	2267	2294	2293	2294	2294	2294	2294	2294
δN_{nucl}	126	145	144	145	145	145	145	145
Rms (03)	0.621	0.655	0.637	0.769	0.577	0.798	0.360	0.653
Rms (11)	0.600	0.645	0.629	0.768	0.574	0.784	0.374	0.690
δRms	-0.021	-0.010	-0.008	-0.001	-0.003	-0.014	0.014	0.037

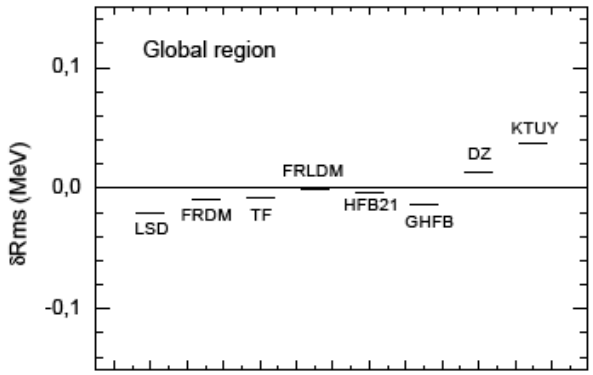

Fig. 3. Difference, δRms, between the rms values obtained with the larger set of experimental masses [1] and the smaller one [2], for the global region of nuclei.

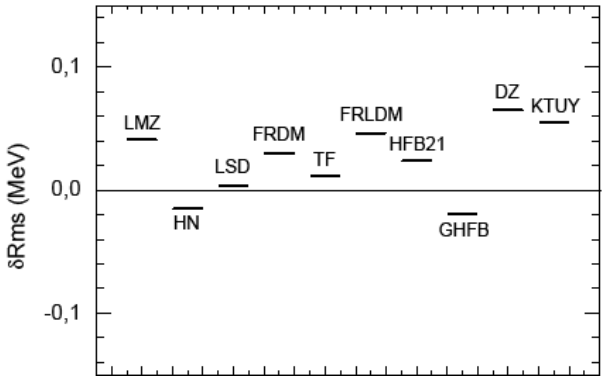

Fig. 4. Same as in Fig. 3, but for the region of heavy nuclei.

Table 3: Predictive power of the models in description of the heavy-nuclei masses.

Model	LMZ	HN	LSD	FRDM	TF	FRLDM	HFB-21	GHFB	DZ	KTUY
$N_{nucl}(03)$	264	264	262	264	264	264	264	264	264	264
$N_{nucl}(11)$	297	297	289	297	296	297	297	297	297	297
δN_{nucl}	33	33	27	33	32	33	33	33	33	33
Rms (03)	0.161	0.373	0.348	0.425	0.464	0.685	0.460	1.076	0.268	0.931
Rms (11)	0.202	0.358	0.352	0.455	0.476	0.731	0.484	1.057	0.333	0.986
δRms	0.041	-0.015	0.004	0.030	0.012	0.046	0.024	-0.019	0.065	0.055

Respective results for the region of the heavy nuclei are presented in Table 3 and Fig. 4.

One can see in Fig. 3 that δRms is negative for five models (this means that the models better describe the larger set of nuclear masses, which includes masses unknown in the time when the model was elaborated), one model (FRLDM) describes equally well the larger and the smaller sets of masses, and two models (DZ and KTUY) have higher Rms for the larger set than for the smaller one (smaller predictive power).

For the heavy-nuclei region (Table 3 and Fig. 4), the results are much different: most of the models show a poorer predictive power in the heavy-nuclei region than in the global one.

Comparing Fig. 1 with Fig. 3 and Fig. 2 with Fig. 4, one can hardly see a clear correlation between the quality of the description of masses of a model and its predictive power.

5. Detailed description of the discrepancy

Fig. 5 shows a detailed map of the discrepancy δ *(Z, N)* in the heavy-nuclei region for the DZ model. This is the model which gives relatively small rms in both the global and the heavy-nuclei regions.

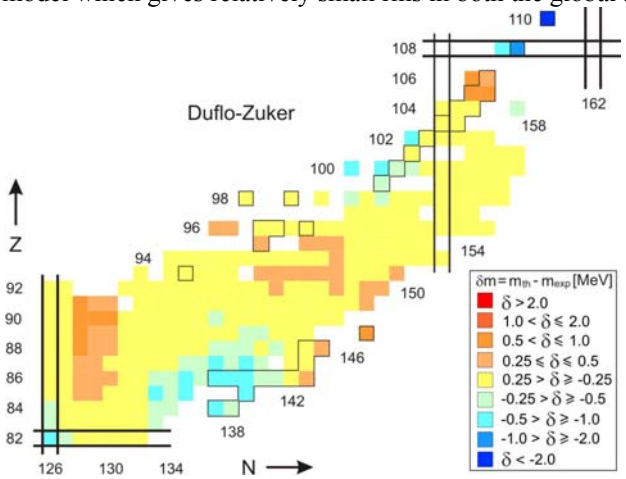

Fig. 5. (Color-online) Detailed map of the discrepancies obtained for the DZ model in the heavy-nuclei region. New masses of Ref. [1], which are absent in Ref. [2], are indicated by thin black contours.

6. Conclusions

Two main conclusions may be drawn from our study:

(1) The quality of the description of nuclear masses by a given model as well as its predictive power depend significantly on the region of nuclei for which they are calculated.

(2) No clear correlation between these two quantities is observed.

ACKNOWLEDGEMENTS

The authors would like to thank Dieter Ackermann, Michael Block, Fritz Bosch, Hans Geissel, Stephane Goriely, Fritz Hessberger, Sigurd Hofmann, Christophor Kozhuharov, and Christoph Scheidenberger for helpful discussions and correspondence. Support by the Helmholtzinstitut Mainz (HIM), the Polish National Centre of Science (within the research project No. N N 202 204938), the European Science Foundation (within the EuroGenesis programme), and the Polish-JINR (Dubna) Cooperation Programme is gratefully acknowledged.

REFERENCES

1. *Audi G., Wang Meng* // Private communication (April 2011).
2. *Audi G., Wapstra A.H., Thibault C.* // Nucl. Phys. - 2003. - Vol. 729. - P. 337.
3. *Litvinov Yu.A., Sobiczewski A., Parkhomenko A., Cherepanov E.A.* // Int. J. Mod. Phys. - 2012 - Vol. E21. - P. 1250038.
4. *Liran S., Marinov A., Zeldes N.* // Phys. Rev. - 2000. - Vol. C62. - P. 047301.
5. *Möller P., Nix J.R., Myers W.D., Świątecki W.J.* // At. Data Nucl. Data Tables. - 1995. - Vol. 59. - P. 185.
6. *Myers W.D., Świątecki W.J.* // Nucl. Phys. - 1996. - Vol. A601. - P. 141.
7. *Muntian I., Patyk Z., Sobiczewski A.* // Acta Phys. Pol. - 2001. - Vol. B32. - P. 691.
8. *Sobiczewski A., Pomorski K.* // Prog. Part. Nucl. Phys. - 2007. - Vol. 58. - P. 292.
9. *Pomorski K., Dudek J.* // Phys. Rev. - 2003. - Vol. C67. - P. 044316.
10. *Goriely S., Chamel N., Pearson J.M.* // Phys. Rev. - 2010. - Vol. C82. - P. 035804.
11. *Goriely S., Hilaire S., Girod M., Peru S.* // Phys. Rev. Lett. - 2009. - Vol. 102. - P. 242501.
12. *Duflo J., Zuker A.P.* // Phys. Rev. - 1995. - Vol. C52. - P. R23.
13. *Koura H., Tachibana T., Uno M., Yamada M.* // Prog. Theor. Phys. - 2005. - Vol. 113. - P. 305.

SPONTANEOUS FISSION OF SUPERHEAVY NUCLEI IN A MACROSCOPIC-MICROSCOPIC MODEL

Z. Łojewski

Department of Computer Science, M. Curie-Skłodowska University, Lublin, Poland

A systematic study of spontaneous fission half-lives of superheavy nuclei in the framework of the macroscopic-microscopic method was performed. The macroscopic-microscopic calculations of the half-lives consist in determining the collective potential energy V which splits into microscopic and smooth average macroscopic parts as well as into a nucleus mass tensor of the nucleus undergoing the fission process. The microscopic part of the energy is calculated using the single-particle Woods-Saxon potential with a *universal* set of parameters. Two models of the residual pairing interaction were studied. In the first approach we used monopole pairing (with constant matrix elements G). In the second approximation the pairing matrix elements were calculated with δ-force and are state dependent. As the macroscopic part of collective energy we examined four different macroscopic models of nuclear energy: Myers - Swiatecki liquid drop, Droplet expansion, Yukawa-plus-Exponential and the Lublin-Strasbourg Drop (*LSD*) model. The analysis covers a wide range of even-even superheavy nuclei from Z = 100 to Z = 126. The calculations of spontaneous fission half-lives (T_{sf}) were performed by means of a *WKB* approximation, in the multi-dimensional dynamical-programming method (*MDP*) within parameters describe the shape of nuclei. The studies offer an opportunity of a comprehensive approach to a very interesting group of exotic heavier nuclei, which are currently investigated by experimenters.

1. Introduction

The region of superheavy nuclei is one of the most intensely studied ones in recent years. The authors of papers recently published [1 - 3] that overcome the barrier of the island of stability placed in the vicinity of the magic number Z = 114.

It is believed that experiments in the near future will focus on nuclei in the neighborhood of Z = 112 - 122 and N ~ 170 - 190. Nevertheless, experimental evidence is still far from complete. Therefore, in preparing the experimental setups theoretical estimations are mainly used.

The aim of this work is the evaluation of the properties of superheavy nuclei using different macroscopic-microscopic models and a critical analysis of the results. Comparisons of these properties for different models allow for easier determination of identifying the interesting areas of superheavy nuclei.

According to the Strutinsky [4] model, the collective potential energy V is split into a shell δE_{shell}, the pairing correction parts, δE_{pair} and the smooth average background energy E_{smooth} (macroscopic part).

The shell correction energy [5] depends on the form of the single-particle potential used and we believe that the deformed Woods-Saxon potential with universal parameters [6] guarantees good behavior of the fission barrier with deformation.

Literature offers many models of smooth energy. More popular ones include the drop model [7], droplet model [8], the so called Folded-Yukawa with an exponential model [9] and the Lublin-Strasburg Drop model (LSD-drop) [10]. The latter model (i.e. LSD-drop) is a revised and improved nuclear liquid drop, in which the corresponding parameter of the extended classical energy formula was adjusted to the currently known nuclear masses and fission barriers heights.

2. Theory

2.1. Nuclear Shape Parameterisation

The shape of the nucleus is defined by the surface $\sum$:

$$\sum : f(r,\theta,\phi) = 0 \tag{1}$$

There are many multi-parameter descriptions of nuclear shapes in literature. One of the most recognised and comprehensive is the expansion of the radius R into spherical harmonics:

$$R(\theta,\phi,\hat{\alpha}) = R_0[1 + \sum_{\lambda\geq 2}\sum_{\mu}\alpha_{\lambda\mu}Y_{\lambda\mu}(\theta,\phi)] \tag{2}$$

In above equation $R_0 = r_0 A^{1/3}$ is the radius of the spherical nucleus with an atomic number A and $\hat{\alpha}$ denotes the full set of deformation parameters. For the axial shapes only Eq. 2 simplifies to:

$$R(\theta,\hat{\beta}) = R_0[1 + \sum_{\lambda\geq 2}\beta_{\lambda}Y_{\lambda 0}(\theta)] \tag{3}$$

The β-expansion defined by Eq. (3) is usually limited to the low order coefficients: β_2 (quadrupole), β_3 (octupole) and β_4 (hexadecapole) degrees of freedom. However, for significantly elongated and mass-asymmetric shapes, it is necessary to have liberty to choose higher order multiples. In our code the upper limit on the multiples is $\lambda_{max} = 9$.

2.2. Collective energy

Collective energy V is calculated for a given nucleus by the macroscopic--microscopic model developed by Strutinsky [4]. In this model the fission barrier energy is split into two parts: the smooth macroscopic E_{macr} part and the microscopic energy consisting of the shell δE_{shell} and pairing δE_{pair} energies.

$$V = E_{macr}(\beta) + \delta E_{shell}(\beta) + \delta E_{pair}(\beta, \Delta) \tag{4}$$

The smooth part of energy E_{macr} includes various nuclear drop models. In this study we tested the Myers - Swiatecki drop model [7], the droplet model [8], the Folded - Yukawa plus exponential model [9] and the Lublin-Strasburg drop model (LSD) [10].

The latest and most promising LSD model constitutes a revised and improved version of the nuclear liquid drop, in which the corresponding parameters of the extended classical energy formula were adjusted to the currently known nuclear masses and fission barrier heights.

The shell energy correction δE_{shell} depends on the form of the single-particle potential. There is a common belief that the deformed Woods-Saxon potential with a universal set of parameters [6] reflects the proper behavior of the fission barrier as a function of the deformation.

Pairing energy δE_{pair} is the third component of total energy. Two residual pairing interaction models were examined. In the first approach we used the monopole pairing (with constant matrix elements $< \nu\bar{\nu} | \hat{V}_{pair} | \mu\bar{\mu} >= const$). In the second approximation, the pairing matrix elements were calculated with the δ force [11].

2.3. Various nuclear liquid-drop models.

If we normalize the energy to zero at spherical shape [8], the formulae for liquid drop model [3] comprising the surface and Coulomb energy can be written:

$$E_{LD}(\hat{\beta}) = E_0^C (B_C(\hat{\beta}) - 1) + E_0^S (B_S(\hat{\beta}) - 1) \tag{5}$$

The numerical value of the parameters E_0^C and E_0^S is taken from a mass formula [3]. The entire deformation dependence is contained in $B_S(\hat{\beta})$ and $B_C(\hat{\beta})$ coefficients. They both can be expressed by two or three dimensional integrals:

$$B_S = \frac{1}{4\pi R_0^2} \oint_S dS \tag{6}$$

$$B_C = \frac{1}{32\pi^2 R_0^5} \oint_V W(r) dV \tag{7}$$

where W(r) denote the Coulomb potential:

$$W(r) = \oint_V \frac{dr'}{|\vec{r} - \vec{r}'|} \tag{8}$$

The improved version of the liquid drop model was proposed by Myers and Świątecki [5] in 1969 as the liquid drop model extension in the form of curvatures and corrections resulting from non – uniform distribution of charges on nucleus surface.

Macroscopic energy can express in that model as:

$$E_{DROPLET}(\hat{\beta}) = b_S (B_S(\hat{\beta}) - 1) + b_{CUR} (B_{CUR}(\hat{\beta}) - 1) + b_C (B_C(\hat{\beta}) - 1) +$$

$$+ b_R (B_R(\hat{\beta}) - 1) + b_w (B_W(\hat{\beta}) - 1) \tag{9}$$

The free parameters included in this Equation (b_i, i = s, c, cur, r, w) are determined phenomenologically by their adjustment to nuclear masses, multipolar moments and barriers for fission. The functions B_i (i = s, c, cur, r, w) depend

on shapes of nuclei only. Two of them i.e. relative surface energy B_S and relative Coulomb energy B_C are defined as in the liquid drop model (Eqs. 5, 6).

Coefficients B_{CUR} is associated with the average curvature of nucleus surface, B_R is associated with non-uniform charge distribution, and B_W is used to describe the non-uniformity of charge distribution on the nucleus surface. The explicit equations for function B_i in the liquid droplet model are performed in [8].

The Yukawa - plus - exponential model [9] developed in 1979 it is a more universal model of macroscopic energy of nucleus. The following term describing the broadening of nucleus surface is added to the surface energy E_S and relative Coulomb energy E_C in that model:

$$E_Y = -\frac{c_S}{8\pi^2 R_0^2 a^3}\int \frac{e^{-\frac{|r-r'|}{a}}}{|r-r'|} d^3r d^3r' \tag{10}$$

with R_0 constituting the nucleus radius with sharp cut-off of matter density on the surface and a constituting the broadening function range (for $a \to 0$ this term disappears). The well-known fact that the matter density on the surface of actual nuclei is not changed abruptly, but it decreases in accordance with the Yukawa model was considered in the present model.

The macroscopic nuclear energy according to the curvature dependent LSD model proposed in [10] is provided in the formula bellow:

$$E_{LSD}(\hat{\beta}) = b_S(1-\kappa_S I^2)A^{\frac{2}{3}}(B_S(\hat{\beta})-1) +$$

$$+b_{CUR}(1-\kappa_{CUR} I^2)A^{\frac{1}{3}}(B_{CUR}(\hat{\beta})-1) + E_0^C(B_C(\hat{\beta})-1) \tag{11}$$

Definitions of the curvature B_{CUR}, Coulomb B_C and surface B_S coefficients remain the same as in the standard drop model (Coulomb and surface coefficients) or in the Droplet model (curvature coefficient B_{CUR}).

Such a liquid drop formula results in rms mass deviations equal to 0.698~MeV for binding energies of 2766 nuclei with Z > 8 and N > 8$ and rms = 0.88 MeV for 40 fission barrier heights experimentally known [10]. As it was shown in [12], the LSD model seems to be comparable in accuracy to the Thomas - Fermi macroscopic model and can be used as a fast and exact tool for calculation of the properties of the nuclei.

2.4. Pairing model

Two models of residual pairing interaction are studied in our work. The first approach is based on the use of monopole pairing, with constant matrix elements $<\nu\bar{\nu}|\hat{V}_{pair}|\mu\bar{\mu}>=G$, while in the other approximation the pairing matrix elements are calculated with the δ-force, and they are state dependent [11].

The first approximation of the monopole type leads to the averaging of the superconductive properties of nuclei and reflects the structure of nucleon pairs rather weakly. A more realistic model consists of state-dependent pairing matrix elements $G_{\mu\nu} = <\nu\bar{\nu}|\hat{V}_{pair}|\mu\bar{\mu}>$, where the pairing interaction $\hat{V}_{pair}$ takes the following form: [13]

$$\hat{V}_{pair} = -V_0 \frac{1-\sigma_1 * \sigma_2}{4}\delta(\vec{r}_{12}) \tag{12}$$

The following values of pairing strengths V_0 were used [11]:

$$V_0^p = 216 MeV\, fm^3 \text{ and } V_0^n = 218 MeV\, fm^3 \tag{13}$$

for protons and neutrons respectively.

The residual pairing interaction is treated in the BCS and Lipkin-Nogami (LN) approximation. In the case of the Lipkin-Nogami (LN) [14, 15] model the fluctuations of the particle number are reduced by adding the quadratic term $-\lambda_2\left(\hat{N}-\left\langle\hat{N}\right\rangle\right)^2$ to the Hamiltonian $\hat{H}$ and by minimizing the average energy with respect to λ_2

The procedure offers the following expression for the newly corrected energy:

$$E_{LN} = E - \lambda_2\left\langle\Psi\middle|\Delta\hat{N}\middle|\Psi\right\rangle \tag{14}$$

where

$$\lambda_2 = \frac{\left\langle\Psi\middle|\left(\Delta\hat{N}\right)^2\middle|\Psi\right\rangle}{\left\langle\Psi\middle|\left(\Delta\hat{N}\right)\middle|\Psi\right\rangle}, \quad \Delta\hat{N} = \hat{N} - \left\langle\Psi\middle|\hat{N}\middle|\Psi\right\rangle \tag{15}$$

and $\hat{N}$ the number operator and Ψ is the BCS ground state.

2.5. Woods-Saxon potential

The one-body Woods-Saxon Hamiltonian formula consists of the kinetic energy term T, the potential energy V^{WS}, the spin-orbit term V_{so}^{WS} and the Coulomb potential V_{Coul} for protons:

$$H^{WS} = T + V^{WS}(\vec{r};\beta) + V_{so}^{WS}(\vec{r};\beta) + \frac{1}{2}(1+\sigma_3)V_{Coul}(\vec{r};\beta) \tag{16}$$

In the above equation

$$V^{WS}(\vec{r};\beta) = \frac{V_0\left[1 \pm \kappa\frac{N-Z}{N+Z}\right]}{1+\exp\left[\frac{dist(\vec{r};\beta)}{a}\right]}, \tag{17}$$

and

$$V_{so}^{WS}(\vec{r};\beta) = -\lambda\left(V^{WS}\cdot\vec{p}\cdot\vec{s}\right), \tag{18}$$

where $dist(\vec{r};\beta)$ denotes the distance of a point $\vec{r}$ from the surface of the nucleus whereas V_0, κ, a, λ, are adjustable constants.

The Coulomb potential V_{Coul} is assumed to be that of the nuclear charge equal to $(Z-1)e$ and uniformly distributed inside the nuclear surface. In our calculations, we used the Woods-Saxon Hamiltonian formula with the so-called *"universal"* set of its parameters [6] which were adjusted to the single – particle levels of odd-A nuclei with $A \geq 40$.

2.6. Fission process

Fission is treated as a tunneling through the collective potential energy barrier within the multidimensional deformation parameter space. The spontaneous-fission half-life is inversely proportional to the probability of penetration of the barrier:

$$T_{sf} = \frac{\log 2}{n}\frac{1}{P} \tag{19}$$

Here, *n* is the number of *assaults* of the nucleus on the fission barrier per unit of time. For the vibration frequency $\hbar\omega_0 = 1\,\text{MeV}$ assumed in our study one can obtains $n = 10^{20.28}s^{-1}$. The tunneling probability P in a one-dimensional WKB [] semi-classical approximation is derived using the following formula:

$$P = \left(1+e^{2S}\right)^{-1} \tag{20}$$

where *S(L)* is the action integral evaluated along the fission path *L*(*s*), which minimizes the reduced action in the multidimensional collective space:

$$S(L) = \int_{s_2}^{s_1}\left\{\frac{2}{\hbar^2}B_{eff}(s)\left[V(s)-E\right]\right\}^{1/2} ds \tag{21}$$

Effective inertia associated with the fission motion along the path *L*(*s*) is

$$B_{eff}(s) = \sum_{k,l} B_{kl}\left(\{\beta_\lambda\}\right)\frac{d\beta_k}{ds}\frac{d\beta_l}{ds} \tag{22}$$

where *ds* denotes the path-length element in the collective space. The integration limits s_1 and s_2 correspond to the classical turning points, determined by the equation $V(s) = E$, where E is the total energy of the nucleus. Collective tensor components B_{kl} are calculated In the adiabatic cranking model [17] and are dependent on collective coordinates.

The dynamic calculation of the T_{sf} means a quest for the trajectory $L_{\min}$ which fulfills the principle of stationary action:

$$\delta S(L) = 0 \tag{23}$$

To minimize the action integral we used the multi-dimensional dynamic-programming method (MDP) [18].

3. Results

3.1. Macroscopic models

Parameters of the macroscopic part of the energy of the atomic nuclei are usually fitted to experimental masses of nuclei (small deformations). Only the LSD-drop model [10] takes into account the heights of fission barriers. This leads to the effect of good conformities of each model for small deformations and divergences for deformations leading to the fission. This problem is illustrated in Fig. 1. where as an example, the diagrams for potential barriers for various models were made [12].

It can be sees that fission barriers in the liquid drop model [7] are relatively high and wide. It is especially visible in heavier isotopes. This effect leads to considerably longer spontaneous fission half-lives for heavier isotopes [19].

An interesting behaviour of fission barriers obtained with the droplet model [8] can be observed. For lighter isotopes, the barriers are in agreement with the liquid drop ones while for heavier nuclei a tendency to a large reduction of the height and thickness of the barrier can be noticed. In earlier papers dealing with the spontaneous fission half-lives this tendency was connected with an abrupt reduction of T_{sf} of heavier isotopes [20].

The Yukawa – plus - exponential model offers the macroscopic fission barriers similar to that of the drop model. However, the barrier heights are slightly lower in the case of heavy isotopes. This decrease in barrier heights influences spontaneous fission half-lives T_{sf} : for heavier isotopes T_{sf} becomes considerably longer. A similar effect was observed in this study [21, 22].

The barriers for the new LSD model [10] change very weakly with the increasing neutron number *N* and become only slightly higher and wider.

The studies conducted show that different models for the smooth part of the energy significantly modify the height and the width of the fission barrier and consequently spontaneous fission half life.

Therefore it is important to use the correct model especially for large deformations. It seems that the LSD-drop model is the best.

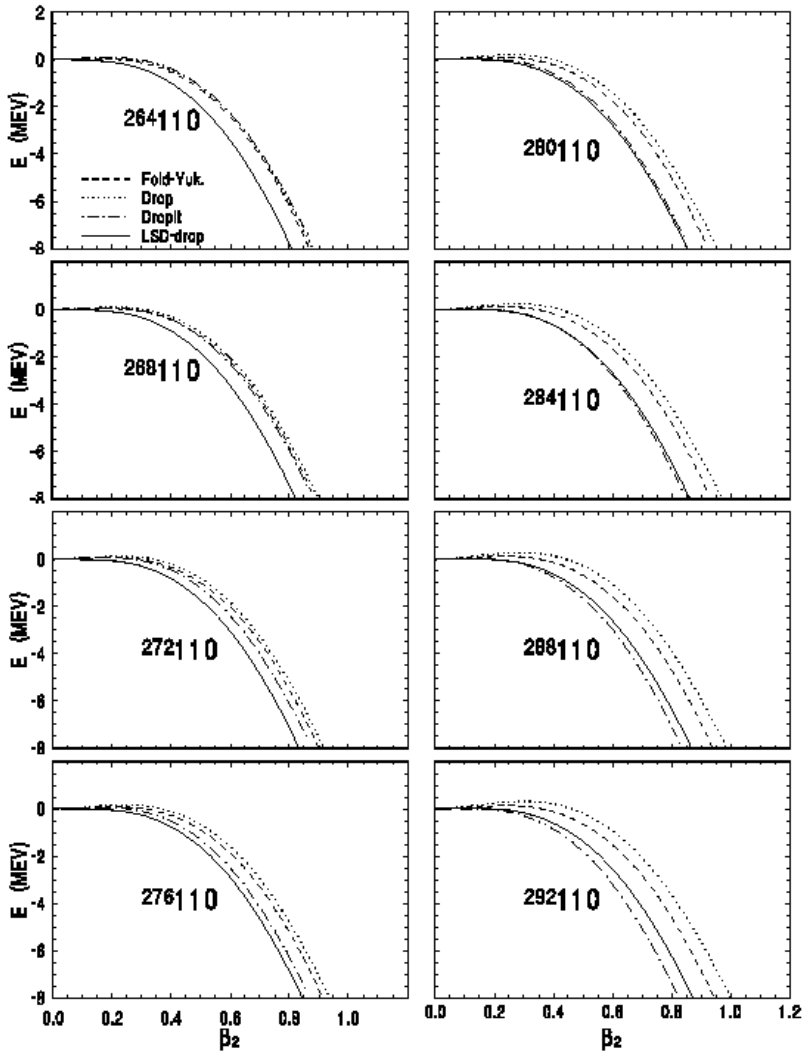

Fig. 1. Diagrams illustrating macroscopic barriers in Drop, Droplet, Folded-Yukawa (Fold-Yuk) and Lublin - Strasbourg (LSD-drop) models for various isotopes of nucleus Z = 110.

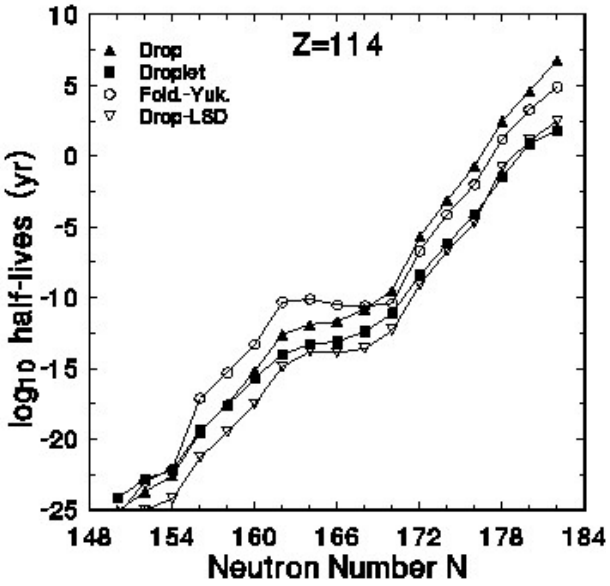

Fig. 2. Spontaneous fission half-lives T_{sf} (in years) for even-even isotopes with the atomic number Z = 114 plotted as a function of the neutron number N.

In Fig. 2 the estimates of the spontaneous fission half-lives T_{sf} for isotopes Z = 114 are showed. Theoretical results are obtained using the four models for macroscopic energy as referred to above.

The data obtained in the liquid drop model are represented by full triangles and the results obtained with the droplet model by squares. The estimates made with the LSD are marked with open triangles. It is seen that the spontaneous fission half-lives differ considerably depending on the model used (1-5 orders of magnitude).

The calculations for the whole region showed that for the liquid drop and folded Yukawa models the results are too large as compared to the experiment, while these for the droplet and LSD models are closer to the measured T_{sf} .

3.2 Influence of pairing forces on fission

Pairing plays an important role in macroscopic-microscopic description of the fission process. We discuss two kinds of pairing models: monopole (G = const) and state dependent (δ -type force). As an illustration of the effect of different pairing models we show the barriers and spontaneous fission half lives for Z = 112 and Z = 116 isotopes. The barriers of Z= 1 12 and 116 isotopes are shown in Fig. 2 for both models: G=const and δ - interaction). Unprojected (G = const and δ + BCS) and particle number projected (G = const + LN and δ + LN) methods are taken into account.

One can see that in all pairing models examined barriers height changes are approximately similar together along the neutrons number N.

In the case of δ - pairing interaction, spontaneous fission barriers become higher (the coupling constant V_0 estimated in [11] is probably too high) than in the case of the G = const model. Our study indicates that model pairing forces weakly influences on the height of fission barriers. The barrier heights shown in Fig. 3 change more smoothly as a function of N in the case of LN projected energies, as compared to the case without projection.

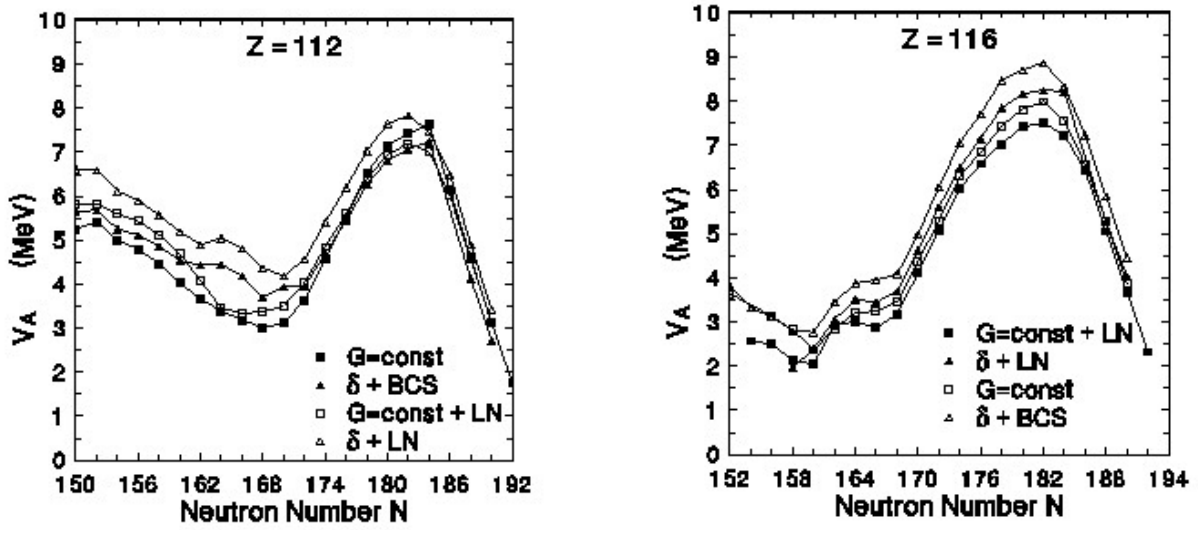

Fig. 3. Barrier height of Z = 112 and 116 isotopes for the case of different pairing models.

The spontaneous fission half-lives of the Z = 112 and 116 isotopes are shown in Fig. 4. As in the case of fission barriers, the LN projected T_{sf} results are smoother, as compared to the unprojected ones. The most important finding is that different pairing models substantially influence the spontaneous fission half-lives (3-5 orders of magnitude). The differences between the projected and unprojected models are smaller (1 - 2 orders). Projected results are a quite close to the experimental data.

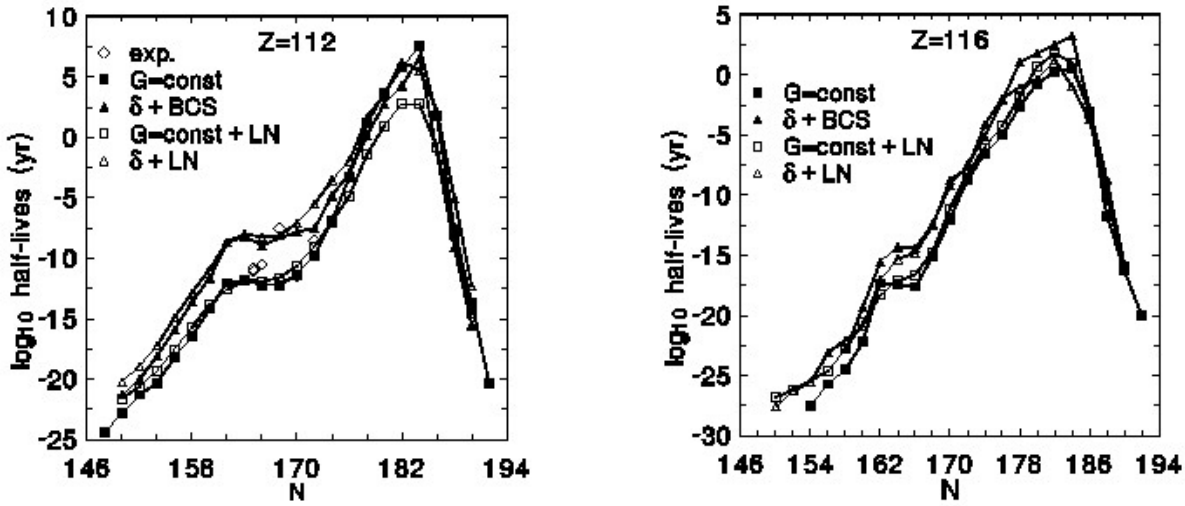

Fig. 4. Spontaneous fission half-lives T_{sf} (in years) for even-even isotopes with atomic number Z = 112 and 116 plotted as a function of the neutron number N.

4. Conclusions

Spontaneous fission half lives strongly depended on two main factors: potential energy represented by the collective energy V_{coll} and kinetic energy proportional inversely to the so called collective mass parameter B_{kl} for multipole vibrations.

In our paper in the MM model we examined different forms of collective energy V_{coll}. Our studies show that macroscopic energy influences significantly calculated spontaneous fission half-lives T_{sf} (1 - 5 orders of magnitude).

For the liquid drop and folded Yukawa models the results of T_{sf} are too large as compared to the experiment, while these for the droplet and LSD models are closer to the measured T_{sf}.

The LSD and droplet model seems to be suitable and can be used as a fast and exact tool for calculation of the spontaneous fission half lives T_{sf}.

The different pairing models substantially influence the spontaneous fission half-lives (3 - 5 orders of magnitude).

The fission barriers of the δ-pairing force model are similar to that of the classical pairing, although they are slightly higher.

The differences between the projected and unprojected models are smaller (1 - 2 orders).The state dependent δ-type force, significantly influences the spontaneous fission half lives. At the same time, the isotopic systematic of T_{sf} does not change.

The LN fission barriers are few hundreds of keV lower than the barriers calculated within the BCS approach. Differences between projected and unprojected results of T_{sf} are 1 - 2 orders of magnitude.

Investigations of the pairing interaction and the macroscopic nuclear energy should continue in order to obtain the proper coupling constants and the most appropriate fission barriers and spontaneous fission half lives.

REFERENCES

1. *Oganessian Yu.Ts.* // J. Phys. - 2007. - Vol. G34. - P. R165.
2. *Oganessian Yu.Ts. et al.* // Phys. Rev. Lett. - 2010. - Vol. 104. - P. 142502.
3. *Hofmann S.* // Radiochim. Acta. - 2011. - Vol. 99. - P. 405.
4. *Strutinsky V.M.* // Nucl. Phys. - 1968. - Vol. A122. - P. 1.
5. *Pauli H.C.* // Phys. Rep. - 1972. - Vol. 7, No. 2. - P. 35.
6. *Ćwiok S. et al.* // Comput. Phys. Commun. - 1987. - Vol. 46. - P. 379.
7. *Myers W.D., Świątecki W.J.* // Nucl. Phys. - 1966. - Vol. 81. - P. 1.
8. *Myers W.D., Świątecki W.J.* // Ann. Phys. - 1974. - Vol. 84. - P. 186.
9. *Krappe H.J., Nix J.R., Sierk A.J.* // Phys. Rev. - 1979. - Vol. C20. - P. 992.
10. *Dudek J. Pomorski K.* // Phys. Rev. - 2003. - Vol. C67. - P. 044316.
11. *Sieja K., Baran A.* // Phys. Rev. - 2003. - Vol. C68. - P. 044308.
12. *Łojewski Z., Baran A., Pomorski K.* // Acta Phys. Pol. - 2003. - Vol. B34. - P. 1801.
13. *Kriege S.J., Bonche P., Flocard H. et al.* // Nucl. Phys. - 1990. - Vol. A517. - P. 275.
14. *Lipkin H.J.* // Ann. Phys. - 1960. -Vol. 31. - P. 525.
15. *Nogami Y.* // Phys. Rev. - 1964. - Vol. B313. - P. 134.

16. *Froman P.O., Froman N.* JWKB Approximation, Contribution to the theory. - North Holland Press, 1965.
17. *Belayev S.* // Nucl. Phys. - 1961. - Vol. 24. - P. 322.
18. *Łojewski Z., Baran A.* // Z. Phys. - 1988. - Vol. A329. - P. 161.
19. *Baran A. et al.* // Proc. of the 3-rd Int. Conf. on Nuclei Far from Stability. - Cargese, Geneva, 1976. - P. 537.
20. *Baran A.* // Phys. Lett. - 1978. - Vol. 76. - P. 8.
21. *Staszczak A., Łojewski Z.* // Proc. Inter. Workshop XXIV. - Hirschegg, 1997.
22. *Łojewski Z; Staszczak A.* // Nucl. Phys. - 1999. - Vol. A657. - P. 134.

CLUSTER RADIOACTIVITY AND ALPHA DECAY OF SUPERHEAVY NUCLEI

D. N. Poenaru[1,2], R. A. Gherghescu[1,2], W. Greiner[2]

[1] *Horia Hulubei National Institute for Physics and Nuclear Engineering, Bucharest-Magurele, Romania*
[2] *Frankfurt Institute for Advanced Studies, Frankfurt/Main, Germany*

The competition of cluster radioactivity (CR) and α decay is investigated in the region of superheavy (SH) nuclei with atomic numbers Z = 104 - 124. Calculations of half-lives within analytical superasymmetrical fission (ASAF) model are performed by using different theoretical mass tables to determine the energy released, Q. For α decay the ASAF calculations are compared with semFIS (semi-empirical fission model). A trend toward shorter half-lives and larger branching ratios relative to alpha decay for heavier SHs was observed**.**

1. Introduction

The first theoretical explanation of α decay, as a quantum tunneling phenomenon was given by G. Gamow [1] — a famous physicist born in Ukraine. This was the first application of newly developed quantum mechanics to nuclei. Another renowned theorist who has been working in the host Institute of the present Conference was V.M. Strutinsky. I had the privilege to meet him in Kiev in 1983. Our fission models are mainly based on his macroscopic-microscopic method [2, 3].

Superheavy (SH) elements with atomic numbers Z = 104 - 118 (see the review paper [4] and the invited talks at this Conference by S. Heinz, A. Sobiczewski, G. Royer and Z. Lojewski) have been synthesized with cold fusion reactions [5, 6] or with hot fusion induced by ^{48}Ca projectiles [7]. Many of them have already names and symbols: Rf, Db, Sg, Bh, Hs, Mt, Ds, Rg, Cn, Fl, and Lv. The elements 113, 115, 117, and 118 are still waiting to be named. Many of them are identified through the α decay chains. Previously we also discussed the competition of a decay and cluster radioactivity (CR) [8], which may be important [9, 10] in the region of the heaviest SHs. In this process, from one parent nucleus ^{A}Z, one obtains an emitted particle ^{Ae}Z$_e$, and a daughter ^{Ad} Z$_d$: ^{A}Z → ^{Ae}Z$_e$ + ^{Ad}Z$_d$. Alternating theory of α-decay [11, 12] and of SH production [13 - 16] was developed by V.Yu. Denisov. A universal decay law for α emission and CR was recently introduced [17] based on R-matrix theory.

Starting with 1984 [18] many CR have been experimentally confirmed [19, 20] in heavy parent nuclei with Z = 87 to 96: ^{14}C, ^{20}O, ^{23}F, $^{22,24\text{-}26}$Ne, ^{28,30}Mg, and ^{32,34}Si. The measured half-lives are in good agreement with predicted values within the ASAF model (see the review [21] and references therein). The largest branching ratio relative to α decay, $b_\alpha = T_\alpha / T_c$, of $10^{-8.9}$ was observed for ^{14}C radioactivity of ^{223}Ra. Usually in this region of the nuclear chart CR is a rare process in a huge background of α particles. The strong shell effect of the doubly magic daughter $^{208}_{82}Pb_{126}$ was observed. In order to study his importance in the region of SHs with $Z > 110$ we changed the concept of CR, previously [22] associated with a maximum $Z_e^{\max}|_{old} = 28$. Now we allow $Z_e^{\max} = Z - 82$.

2. The ASAF model

The accuracy of half-life calculation is very much dependent on the precision with which we know the Q-value

$$Q = \left[M - \left(M_e + M_d \right) \right] c^2 \tag{1}$$

obtained as a difference between the parent, M, and the two decay product masses, M_e and M_d, in units of energy; c is the light velocity.

The decay constant $\lambda = \ln 2/T_c$ is expressed by a product of three model dependent quantities v, S and P_s where v is the frequency of assaults on the barrier per second, S is the preformation probability and P_s is penetrability of external barrier. According to our method [23] the preformation in a fission theory is given by the penetrability of the internal part of the barrier.

We developed our ASAF model starting with the Myers - Swiatecki's liquid drop model [24] adjusted with a phenomenological correction.

The half-life is given by

$$T = [(h \ln 2)/(2E_v)]\exp(K_{ov} + K_s) \tag{2}$$

It is calculated by using the WKB quasi classical approximation

$$K = \frac{2}{h} \int_{R_a}^{R_b} \sqrt{2B(R)E(R)}\, dR \tag{3}$$

with $B = \mu$, $K = K_{ov} + K_s$, and $E(R)$ replaced by [E(R) - E_{corr}] - Q where E_{corr} is a correction energy similar to the Strutinsky shell correction. The turning points of the WKB integral are: $R_\alpha = R_i + (R_t - R_i)[(E_v + E^*)/E_b^0]^{1/2}$ and

$R_b = R_t E_c \{1/2+[1/4+(Q + E_v + E^*)E_l/ E_c^2]^{1/2}\}/(Q + E_v + E^*)$ where E^* is the excitation energy concentrated in the separation degree of freedom, $R_i = R_0 - R_e$ is the initial separation distance, $R_t = R_e + R_d$ is the touching point separation distance, $R_j = r_0 A_j^{1/3}$ (j = 0, e, d; r_0 = 1.2249 fm) are the radii of parent, emitted, and daughter nuclei, respectively, and $E_b^0 = E_i - Q$ is the barrier height before correction. The interaction energy at the top of the barrier, in the presence of a non-negligible angular momentum, $l\hbar$, is given by $E_i = E_c + E_l = e^2 Z_e Z_d / R_t + \hbar^2/(l + 1)/(2\mu R_t^2)$. The two terms of the action integral K, corresponding to the overlapping K_{ov} and separated K_s fragments, are calculated analytically [10, 22]. The potential barrier shape similar to that which we considered within the ASAF model was calculated by using the macroscopic-microscopic method [25].

3. Mass tables

Half-life calculations are very sensitive to the Q-values. The closest to reality are the updated table of evaluated experimental masses AME11 [26], but many masses are still not available for new SH_s in this table. We have also used some calculated masses: LiMaZe01 Liran - Marinov - Zeldes [27, 28] (semi empirical shell model), KTUY05 Koura - Tachibana - Uno - Yamada [29] (phenomenological) and FRDM95 the finite-range droplet model [30] (macroscopic-microscopic). To these we may add: MySw94 Myers-Swiatecki [31] (macroscopic-microscopic), APDT95 Aboussir-Pearson-Dutta-Tondeur [32] (microscopic), DuZu96 Duflo-Zuker [33] (shell model). Other alternatives are presented by A. Sobiczewski at this Conference.

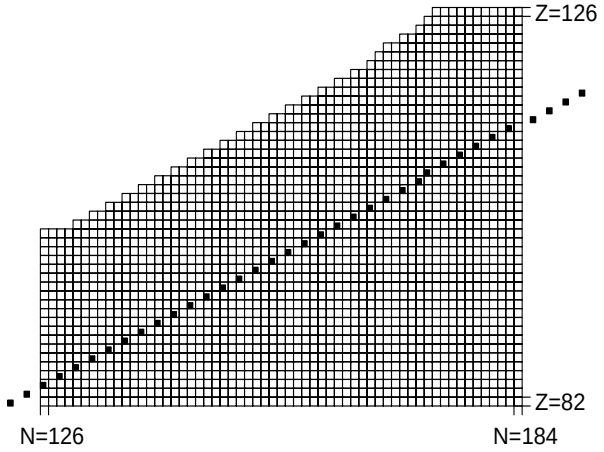

Fig. 1. Chart of nuclides with calculated LiMaZe01 masses. 1969 masses for Z = 82 - 126, N = 126 - 184. The Green approximation of the beta stability is marked by full squares.

We show in Figs. 1, 2, and 3 the nuclides for which calculated masses are available according to the tables LiMaZe01, KTUY05, and FRDM95, respectively. For the region of interest Z = 104 - 124 the beta stability line goes through N_g = 106 for Z = 104 and N_g = 206 for Z = 124. It is clearly seen that the most complete mass table of these three is FRDM95. The other two will allow us to make calculations only for some of the neutron deficient heaviest SHs.

When using calculated masses for parent and daughter nuclei we take into account the nuclides stable against one proton, two protons, one neutron and two neutrons spontaneous emissions which leads to a smaller number of parent nuclides than those shown in Figs. 1, 2, and 3.

4. Shorter half-lives for heavy superheavies

Besides the emitted clusters with $Z_e \leq 28$ (Be, C, Ar, Ti, V, Cr, Mn, Fe, Co, and Ni), many other types of new CR with $Z_e > 28$ appear when we use the FRDM95 calculated mass table to determine the Q-values: Cu, Zn, Ga, Ge, As, Se, Br, Kr, Rb, Sr, Y, Zr, Nb, and Mo. Many of the SH nuclides are ^{8}Be emitters, but they have a very low branching ratio b_α. Most frequently occurs the doubly magic ^{78}Ni radioactivity.

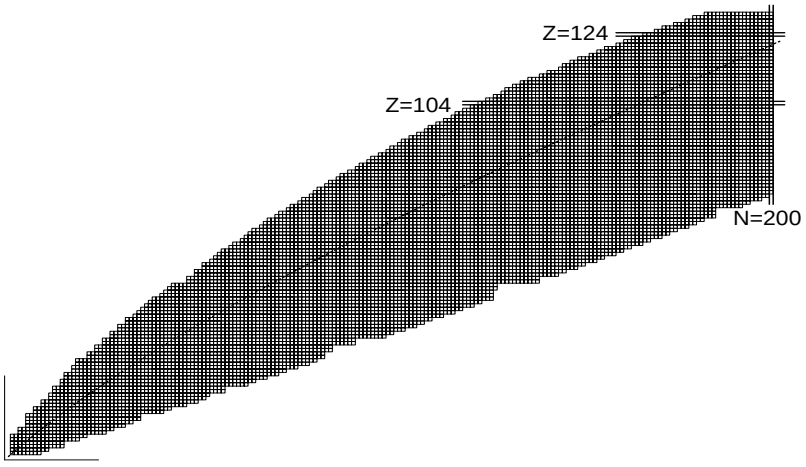

Fig. 2. Chart of nuclides with calculated KTUY05 masses. 9441 masses for Z = 2 - 130, N ≤ 200. The Green approximation of the beta stability is marked by full squares.

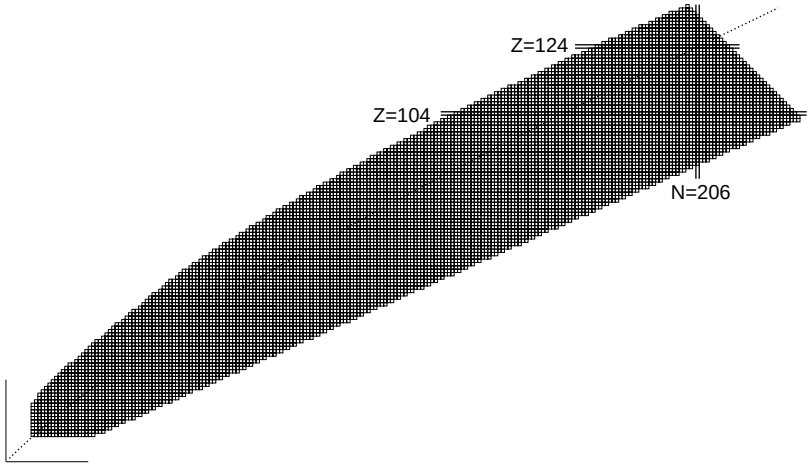

Fig. 3. Chart of nuclides with calculated FRDM95 masses. 8979 masses for Z = 8 - 136, N ≤ 236. The Green approximation of the beta stability is marked by full squares.

An even-odd staggering of CR half-lives was observed [10] leading to shorter T_c for even N nuclides compared to the neighboring odd N ones. In order to avoid such a complication we consider in Fig. 4 for cluster decay only the odd N isotopes. Two important trends are observed: (1) both T_c and T_α are shorter for SHs with larger atomic number, and (2) for some of the isotopes of $Z = 123$ and $Z = 124$ elements cluster decay half-life may be shorter than that of a decay: $T_c < T_\alpha$ (or the branching ratio $b_\alpha = T_\alpha/T_c$ becomes larger than unity when the atomic number of the parent nucleus increases over 122).

We observed [10] that large differences in Q-values for α decay calculated with various mass tables occur very frequently and make an important contribution to the broad range of branching ratios b_α for any particular nucleus. Even the most probable emitted cluster can differ as in the case of the ^{304}124 parent for which ^{98}Mo results in calculations of released energy based on LiMaZe01, ^{95}Zr based on KTUY05, and ^{96}Zr based on FRDM95.

More elaborate models should be used (see, e.g., [34]) in order to estimate the competition of spontaneous fission.

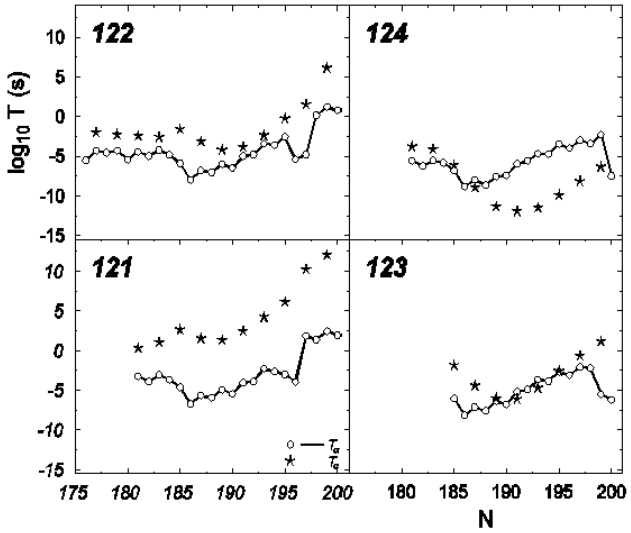

Fig. 4. Decimal logarithm of the half-lives of superheavy nuclei with atomic numbers 121 - 124 against α decay (open circles) and CR for odd-neutron isotopes (stars) versus the neutron number of the parent nucleus. Q values are calculated using the KTUY05 mass tables

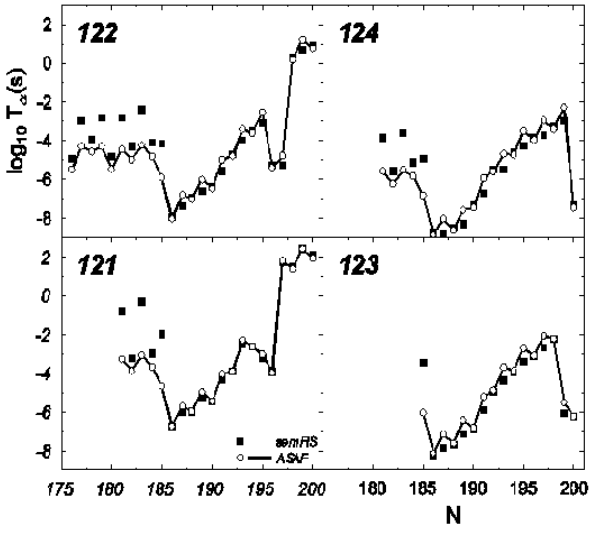

Fig. 5. Comparison of alpha-decay half-lives calculated with ASAF (open circles) and semFIS (full squares) models vs. the neutron number of the parent nucleus. Q-values calculated using the KTUY05 mass table. The largest deviations are around the neutron magic number 184.

5. Accuracy of calculated half-lives for α decay

An estimation of the accuracy gives the standard rms deviation of log10 T values:

$$\sigma = \{\sum_{i=1}^{n}[\log_{10}(T_i / T_{\exp})]^2 / (n-1)\}^{1/2}. \quad (4)$$

Compared to calculations within ASAF model, lower values of σ for α decay half-lives may be obtained [35] within our UNIV (universal curve) [36] and semFIS (semi empirical) models. For 44 even-even nuclei we obtained σ = 0.164 within semFIS, σ = 0.267 within UNIV and σ = 0.402 within ASAF model. For 25 odd-odd nuclei σ = 0.451, 0.456 and 0.795, respectively.

A comparison of $\log_{10} T_{ASAF}$ with $\log_{10} T_{semFIS}$ is shown in Fig. 5. We assume that semFIS calculations are closer to reality, particularly in the vicinity of the neutron and proton magic numbers. From Fig. 5 one can see that large discrepancies are observed for odd-*N* values in the neighborhood of $N = 184$ when $N \leq 184$.

In conclusion we found that calculated half-lives T_c against CR and the branching ratios relative to α decay are showing a trend toward shorter T_c and larger b_α for the heaviest SHs. In the vicinity of neutron magic number $N = 184$ the half-lives for α decay calculated within ASAF model are shorter than those determined with semFIS which takes into account the influence of closed shells. The accuracy of calculated masses in the region of heaviest SHs should be improved in order to make reliable predictions of half-lives.

This work was partially supported within the IDEI Programme under Contracts No. 43/05.10.2011 and No. 42/05.10.2011 with UEFISCDI, Bucharest.

REFERENCES

1. *Gamow. G.* Zur Quantentheorie des Atomkernes // Z. Phys. - 1928. Vol. - 51. - P. 204 - 212.
2. *Strutinsky V.M.* Shell effects in nuclear masses and deformation energies // Nucl. Phys. - 1967. - Vol. A95. -P. 420 - 442.
3. *Ivanyuk F.A., Ivascu M., Poenaru D.N.* Shell and pairing corrections // Particle Emission from Nuclei. Vol. I: Nuclear Deformation Energy / Ed. by D. N. Poenaru and M. Ivascu. - Boca Raton, Florida: CRC Press, 1989. - P. 141 - 175.
4. *Sobiczewski. A.* Theoretical description of superheavy nuclei // Radiochim. Acta. - 2011. - Vol. 99. - P. 395 - 404.
5. *Hofmann S.* Synthesis of superheavy elements by cold fusion // Radiochim. Acta. - 2011. - Vol. 99. - P. 405 - 428.
6. *Morita K. et al.* Observation of second decay chain from $^{278}113$ // J. Phys. Soc. Jpn. - 2007. - Vol. 76. - P. 045001.
7. *Oganessian. Yu.Ts.* Synthesis of the heaviest elements in ^{48}Ca-induced reactions // Ra-diochim. Acta. - 2011. - Vol. 99. - P. 429 - 439.
8. Encyclopaedia Britannica Online, 2011. Web http:/ / www.britannica.com/EBchecked / topic /465998/.
9. *Poenaru D., Gherghescu R.A., Greiner W.* Heavy-particle radioactivity of super-heavy nuclei // Phys. Rev. Lett. - 2011. - Vol. 107. - P. 062503.
10. *Poenaru D.N., Gherghescu R.A., Greiner W.* Cluster decay of superheavy nuclei // Phys. Rev. - 2012. - Vol.C85. - P. 034615.
11. *Denisov V.Yu., Khudenko A.A.* α-decay half-lives, α-capture, and α-nucleus potential // Atomic Data Nucl. Data Tables. - 2009. - Vol. 95. - P. 815 - 835.
12. *Denisov V.Yu., Khudenko A.A.* Alpha-decay half-lives: Empirical relations // Phys. Rev. - 2010. - Vol. C82. - P. 054614.
13. *Denisov V.Yu., Hofmann S.* Formation of superheavy elements in cold fusion reactions // Phys. Rev. - 2000. - Vol. C61. - P. 034606.
14. *Denisov V.Yu., Norenberg W.* Entrance-channel potentials in the synthesis of the heaviest nuclei // Eur. Phys. J. - 2002. - Vol. A15. - P. 375 - 388.
15. *Denisov V.Yu.* Magic numbers of ultraheavy nuclei // Phys. At. Nucl. - 2005. - Vol. 68. - P. 1133 - 1137.
16. *Denisov V.Yu.*, *Ikezoe H.* α-nucleus potential for α-decay and sub-barrier fusion // Phys. Rev. - 2005. - Vol. C 72. - P. 064613.
17. *Qi C., Xu F.R., Liotta R.J., Wyss R.* Universal decay law in charged-particle emission and exotic cluster radioactivity // Phys. Rev. Lett. - 2009. - Vol. 103. - P. 072501.
18. *Rose H.J., Jones G.A.* A new kind of natural radioactivity // Nature. - 1984. - Vol. 307. - P. 245 - 247.
19. *Bonetti R., Guglielmetti A.* Cluster radioactivity: an overview after twenty years. // Rom. Rep. Phys. - 2007. - Vol. 59. - P. 301 - 310.
20. *Poenaru D.N., Nagame Y., Gherghescu R.A., Greiner W.* Systematics of cluster decay modes // Phys. Rev. - 2002. - Vol. C65. - P. 054308. Erratum: Phys. Rev. - 2002. - Vol. C66. - P. 049902.
21. *Poenaru D.N., Greiner W.* Cluster radioactivity // Clusters in Nuclei. Vol. 1. Lecture Notes in Physics Vol. 818 / Ed. by C. Beck. - Berlin: Springer, 2010. - P. 1 - 56.
22. *Poenaru D.N., Schnabel D., Greiner W. et al.* Nuclear lifetimes for cluster radioactivities // Atomic Data Nucl. Data Tables. - 1991. - Vol. 48. - P. 231 - 327.
23. *Poenaru D.N., Greiner W.* Cluster preformation as barrier penetrability // Physica Scripta. - 1991. - Vol. 44. - P. 427 - 429.
24. *Myers W.D., Swiatecki W.J.* Nuclear masses and deformations // Nucl. Phys. - 1966. - Vol. A81. - P. 1 - 60.
25. *Poenaru D.N., Gherghescu R.A., Greiner W.* Potential energy surfaces for cluster emitting nuclei // Phys. Rev. - 2006. - Vol. C73. - P. 014608.
26. *Audi Georges, Meng Wang*. Private communication. April 2011.
27. *Liran S., Marinov A., Zeldes N.* Semiempirical shell model masses with magic number Z = 126 for superheavy elements // Phys. Rev. - 2000. - Vol. C62. - P. 047301.

28. *Liran S., Marinov A., Zeldes N.* Applications of semiempirical shell model masses based on proton magic number Z = 126 to superheavy nuclei // Phys. Rev. - 2002. - Vol. C66. - P. 024303.
29. *Koura Hiroyuki, Tachibana Takahiro, Uno Masahiro, Yamada Masami.* Nuclidic mass formula on a spherical basis with an improved even-odd term // Prog. Theor. Phys. - 2005. - Vol. 113. - P. 305 - 325.
30. *Moller P., Nix J. R., Myers W. D., Swiatecki W. J.* Nuclear ground-state masses and deformations // Atomic Data Nucl. Data Tables. - 1995. - Vol.59. - P. 185-381.
31. *Myers W.D., Swiatecki W.J.* Table of nuclear masses according to the 1994 Thomas - Fermi model. Report LBL-36803. - Lawrence Berkeley Laboratory, 1994.
32. *Aboussir Y., Pearson J.M., Dutta A.K., Tondeur F.* Nuclear-mass formula via an approximation to the Hartree - Fock method // Atomic Data Nucl. Data Tables. - 1995. - Vol. 61. - P. 127 - 176.
33. *Duflo J., Zuker A.P.* Microscopic mass formulas // Phys. Rev. - 1995. - Vol. C52. - P. R23 - R27; Private Communication to AMDC, February 1996.
34. *Smolanczuk R., Skalski J., Sobiczewski A.* Spontaneous-fission half-lives of deformed superheavy nuclei // Phys. Rev. - 1995. - Vol. C52. - P. 1871 - 1880.
35. *Poenaru D.N., Plonski I.H., Greiner W.* α-decay half-lives of superheavy nuclei // Phys. Rev. - 2006. - Vol. C74. - P. 014312.
36. *Poenaru D.N., Gherghescu R.A., Greiner W.* Simple relationships for α-decay half-lives // J. Phys. G: Nucl. Part. Phys. - 2012. - Vol. 39. - P. 015105.

GENERALIZED LIQUID DROP MODEL AND FISSION, FUSION, ALPHA AND CLUSTER RADIOACTIVITY AND SUPERHEAVY NUCLEI

G. Royer

Laboratoire Subatech, UMR: IN2P3/CNRS-Université-Ecole des Mines, Nantes, France

A particular version of the liquid drop model taking into account both the mass and charge asymmetries, the proximity energy, the rotational energy, the shell and pairing energies and the temperature has been developed to describe smoothly the transition between one and two-body shapes in entrance and exit channels of nuclear reactions. In the quasi-molecular shape valley where the proximity energy is optimized, the calculated l-dependent fusion and fission barriers, alpha and cluster radioactivity half-lives as well as actinide half-lives are in good agreement with the available experimental data. In this particular deformation path, double-humped potential barriers begin to appear even macroscopically for heavy nuclear systems due to the influence of the proximity forces and, consequently, quasi-molecular isomeric states can survive in the second minimum of the potential barriers in a large angular momentum range.

1. Introduction

The fission shapes were firstly investigated long time ago by minimizing the sum of the Coulomb and surface energies using mainly a development of the radius in Legendre polynomials. This leads to fission valley through very elongated shapes with shallow necks and difficulties to precise the position of the scission point where the rupture of the bridge of matter between the nascent fragments occurs.

More recently, the fusion studies have shown that the picture of the pure Coulomb barrier is not sufficient to obtain correct fusion cross sections. It is necessary to take into account the effects of the nuclear forces in the gap between the incoming close nuclei or in the crevice where the neck is formed in adding a proximity energy term.

So we have defined a Generalized Liquid Drop Model (GLDM) including this proximity energy and a quasi-molecular shape sequence to describe firstly the fusion process and, later on, to study whether, in this deformation valley which optimizes the proximity energy, the fission data may also be reproduced. Calculations show that degeneracy exists effectively between the energy of elongated shapes found by the liquid drop model without proximity energy and the energy of compact and necked shapes which is lowered by the introduction of the nuclear proximity effects. The agreement with the fusion and fission data has finally led to the study of the alpha and cluster radioactivity and the entrance and exit channels of superheavy nuclei.

2. Generalized Liquid Drop Model

For an arbitrary deformed nucleus, the macroscopic total energy is the sum of the Rotational Liquid-Drop Model energy and the nuclear proximity energy [1]. Constant density and volume conservation are assumed.

$$E_{RLDM} = E_V + E_S + E_C + E_{Rot} . \tag{1}$$

For one-body shapes, the volume E_V, surface E_S and Coulomb E_C energies are given by :

$$E_V = -a_v(1-k_v I^2)A , \tag{2}$$

$$E_S = a_s(1-k_s I^2)A^{2/3}(S/4\pi R_0^2) , \tag{3}$$

$$E_C = 0.6e^2(Z^2/R_0)\cdot 0.5\int (V(\theta)/V_0)(R(\theta)/R_0)^3 \sin\theta\, d\theta \tag{4}$$

where A, Z and I = (N - Z)/A are the mass, charge and relative neutron excess of the compound nucleus. $V(\theta)$ is the electrostatic potential at the surface of the shape and V_0 the surface potential of the sphere. The volume and surface coefficients a_v, a_s and the effective sharp radius R_0 are defined as :

$$a_v(T) = 15.494(1+0.00337T^2)\ \text{MeV} , \tag{5}$$

$$a_s(T) = 17.9439\ (1+1.5T/17)(1-T/17)^{3/2}\ \text{MeV} , \tag{6}$$

$$R_0(T) = (1.28A^{1/3} - 0.76 + 0.8A^{-1/3})(1+0.0007\ T^2)\ \text{fm} . \tag{7}$$

This later formula leads to an increase of the ratio $r_0 = R_0/A^{1/3}$ with the mass; for example, $r_0 =$ 1.11 fm for ^{20}Ne and $r_0 =$ 1.18 fm for ^{240}Pu. For comparison, the potential defined by Krappe, Nix and Sierk [2] assumes $a_s =$ 21.7 MeV

and $r_0 =$ 1.18 fm while the recent version of the Thomas-Fermi model [3] supposes $a_s =$ 18.63 MeV and $r_0 =$ 1.14 fm. The surface and volume asymmetry coefficients take on the values:

$$k_s = 2.6 \qquad \text{and} \qquad k_v = 1.8 \,. \tag{8}$$

Discussions on the different possible coefficients of the macro-microscopic mass formulas can be found in Ref. [4].

When the two fragments (or colliding nuclei) are separated:

$$E_V = -a_v \left[(1 - k_v I_1^2) A_1 + (1 - k_v I_2^2) A_2 \right], \tag{9}$$

$$E_S = a_s \left[(1 - k_s I_1^2) A_1^{2/3} + (1 - k_s I_2^2) A_2^{2/3} \right], \tag{10}$$

$$E_c = \frac{3}{5} e^2 Z_1^2 / R_1 + \frac{3}{5} e^2 Z_2^2 / R_2 + e^2 Z_1 Z_2 / r \,, \tag{11}$$

where A_i, Z_i, R_i and I_i are the masses, charges, radii and relative neutron excesses of the fragments and r the distance between the mass centers. The discontinuity of a few MeV which appears at the contact point when Z_1/A_1 and Z_2/A_2 are very different has been removed linearly from the contact point to the sphere since it is due to the progressive rearrangement of the nuclear matter.

The surface energy E_S takes only into account the effects of the surface tension forces in an half space and does not include the contribution due to the attractive nuclear forces between the surfaces in regard in the neck or the gap between nascent fragments or incoming nuclei. The nuclear proximity energy term E_N takes into account these additional surface effects when crevices appear in the deformation path [1].

$$E_N = 2\gamma \int_{h_{\min}}^{h_{\max}} \varphi(D/b) 2\pi h dh \,. \tag{12}$$

h is the ring radius in the plane perpendicular to the fission axis and D the distance between the infinitesimal surfaces in regard. b is the surface width fixed at 0.99 fm. ϕ is the proximity function. The surface parameter γ is given by a geometric mean between the surface parameters of the two fragments:

$$\gamma = 0.9517 \sqrt{(1 - k_s I_1^2)(1 - k_s I_2^2)} \ \text{MeV.fm}^{-2}. \tag{13}$$

In this GLDM the surface diffuseness is not considered and the proximity energy vanishes when there is no neck.

The rotational energy has been determined within the rigid body ansatz. Indeed, it has been shown that corrective terms arising from the orbital motion and the spin degrees of freedom roughly cancel each other, particularly at large deformations.

$$E_{Rot} = \frac{\hbar^2 l(l+1)}{2 I_\perp} \,. \tag{14}$$

Microscopic corrections have been added to this macroscopic energy. The shell corrections have been introduced [5] as defined in the Droplet Model with an attenuation factor given by

$$E_{Shell} = E_{Shell}^{sphere} (1 - 2.6\alpha^2) \exp(-\alpha^2), \quad \text{where} \quad \alpha^2 = (\delta R)^2 / a^2 \,. \tag{15}$$

The distortion αa is the root mean square of the deviation of the surface from a sphere, a quantity which incorporates all types of deformation indiscriminately. Using this approach, shell corrections only play a role near the ground state of the compound nucleus and not at the saddle-point (where they are expected to be of the order of 1 MeV or smaller). The pairing energy of the recent Thomas - Fermi model [3] has been selected.

A two parameter shape sequence has been defined [1] to describe the continuous transition from one spherical nucleus to two tangent spherical nuclei (see Fig. 1).

$$R(\theta)^2 = \begin{cases} a^2 \sin^2\theta + c_1^2 \cos^2\theta & (0 \le \theta \le \pi/2) \\ a^2 \sin^2\theta + c_2^2 \cos^2\theta & (\pi/2 \le \theta \le \pi) \end{cases}. \tag{16}$$

c_1 and c_2 are the two radial elongations and a the neck radius. Assuming volume conservation, the two parameters $s_1 = a / c_1$ and $s_2 = a / c_2$ completely define the shape. When s_1 decreases from 1 to 0 the shape evolves from one sphere

to two touching spheres with the formation of a deep neck while keeping almost spherical ends. Using the axial symmetry, analytical expressions have been obtained for the various shape-dependent functions: volume, surface, moment of inertia, distance between the mass centres of each fragment and quadrupole moment.

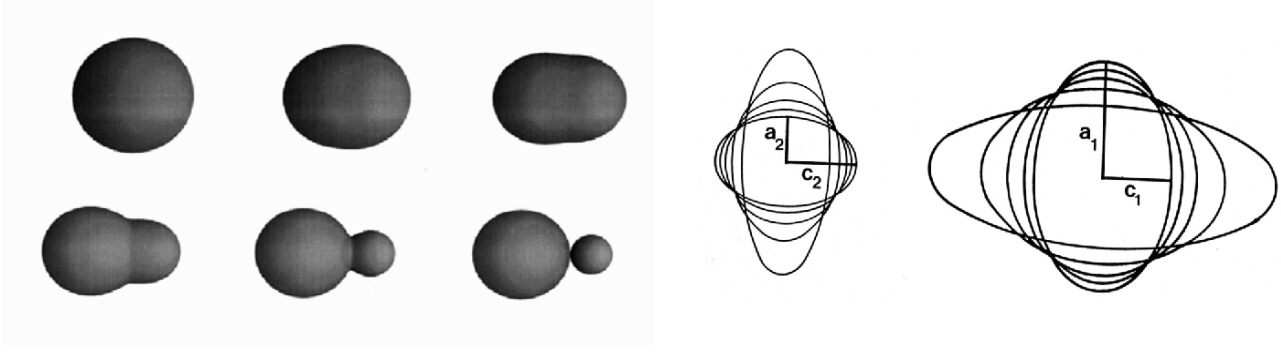

Fig. 1. Shape sequences describing the one-body shape evolution and the two coaxial ellipsoid configurations. The fission axis is the common axis of revolution.

The two coaxial ellipsoid configurations or simply the two-sphere approximation have been used to describe the two-body shapes.

3. Fusion

The main characteristics which govern the fusion process are the barrier height and the position of its maximum. The GLDM allows a correct reproduction of these empirical data deduced from the fusion cross sections ([1, 6] and Table 1). Double-humped fusion barriers appear when $Z_1Z_2 \geq 1800 \pm 100$. The inner barrier is the highest for $Z_1Z_2 \geq 2300 \pm 100$. The existence and the shape of the external minimum due to the proximity energy is at the origin of the development of fusion-fission and fast fission phenomena. Using a simple dynamic model it has been shown that a dynamic fusion barrier appears for very heavy systems ($Z_1Z_2 \geq 2100 \pm 100$), significantly higher than the static one and in close agreement with the experimental data. This dynamic barrier is mostly governed by the entrance channel. The possibility of forming superheavy elements in almost symmetric reactions is strongly hindered by this double-humped dynamic barrier.

Table 1. **Comparison between the experimental fusion barrier heights E_{0f} and positions R_{0f} and the theoretical predictions of the Krappe, Nix and Sierk potential and of the GLDM**

Reaction	Z_1Z_2	$E_{of,Exp}$ (MeV)	$R_{of,Exp}$ (fm)	$E_{of,Th}$ (KNS)	$R_{of,Th}$ (KNS)	$E_{of,Th}$ (GLDM)	$R_{of,Th}$ (GLDM)
$^{9}Be + ^{10}B$	20	3.4	7.65	3.36	7.77	3.36	7.79
$^{4}He + ^{44}Ca$	40	6.37	8.25	6.19	8.5	6.2	8.51
$^{16}O + ^{26}Mg$	96	15.24	8.29	14.69	8.59	14.82	8.56
$^{4}He + ^{209}Bi$	166	20.52	10.88	20.58	10.77	20.46	10.93
$^{34}S + ^{26}Mg$	192	27.11	9.5	27.63	9.16	27.84	9.17
$^{16}O + ^{110}Pd$	368	46.2	-	48.0	10.17	48.05	10.26
$^{40}Ar + ^{58}Ni$	504	65.3	-	66.74	9.99	66.76	10.07
$^{40}Ca + ^{58}Ni$	560	73.36	10.2	73.89	10.02	74.72	9.98
$^{35}Cl + ^{90}Zr$	680	84.87	10.74	86.73	10.39	86.5	10.51
$^{86}Kr + ^{58}Ni$	1008	120.8	-	123.55	10.82	122.77	10.95
$^{40}Ar + ^{144}Sm$	1116	130.2	-	132.01	11.23	130.96	11.37
$^{40}Ar + ^{174}Yb$	1260	139	-	144.83	11.58	143.39	11.76
$^{40}Ar + ^{177}Hf$	1296	145	-	148.67	11.6	147.19	11.76
$^{81}Br + ^{90}Zr$	1400	156	-	164.79	11.26	163.29	11.42
$^{81}Br + ^{104}Ru$	1540	174	-	178.01	11.48	176.18	11.61

For light systems and energy around the Coulomb barrier the static approach is sufficient to reproduce the fusion cross sections. At higher energies the increase of the fusion cross section with incident energy is limited by a strong dissipation occurring around the contact point. With increasing mass the slope of the fusion cross sections is better reproduced if the angular momentum dissipation rule varies from the sticking limit for medium systems to the sliding limit for very heavy systems [1].

4. Fission

The different contributions to the deformation energy are given for the ^{160}Dy nucleus in Fig. 2. The E_s and E_n curves change drastically at the contact point since the surface is constant after the separation and the nuclear attraction is greatest at the contact point. Nevertheless, the total energy varies gently even around the contact point. Moreover the barrier height corresponds to the fission barrier height [7]. In the right part of Fig. 2 the deformation energies of the ^{234}U nucleus corresponding to different shape sequences with and without proximity energy contribution are compared. The potential energy calculated using quasi-molecular shapes without taking into account the proximity energy is very energetically unfavourable . On the contrary, when the proximity energy is included for the same shape sequence, the barrier height may be compared with the barrier height of the potential energy for usual elongated and little or not creviced shapes [5]. Furthermore, a double-humped barrier appears even macroscopically for the compact and necked shapes. This shows clearly that the comparison between the two shape sequences must be re-examined when the additional proximity energy term is introduced. The two spheroid shapes would be also highly competitive with regard to the usual elongated shapes if the proximity energy was included since this term is large when there is a deep gap and negligible for elongated shapes with a shallow neck.

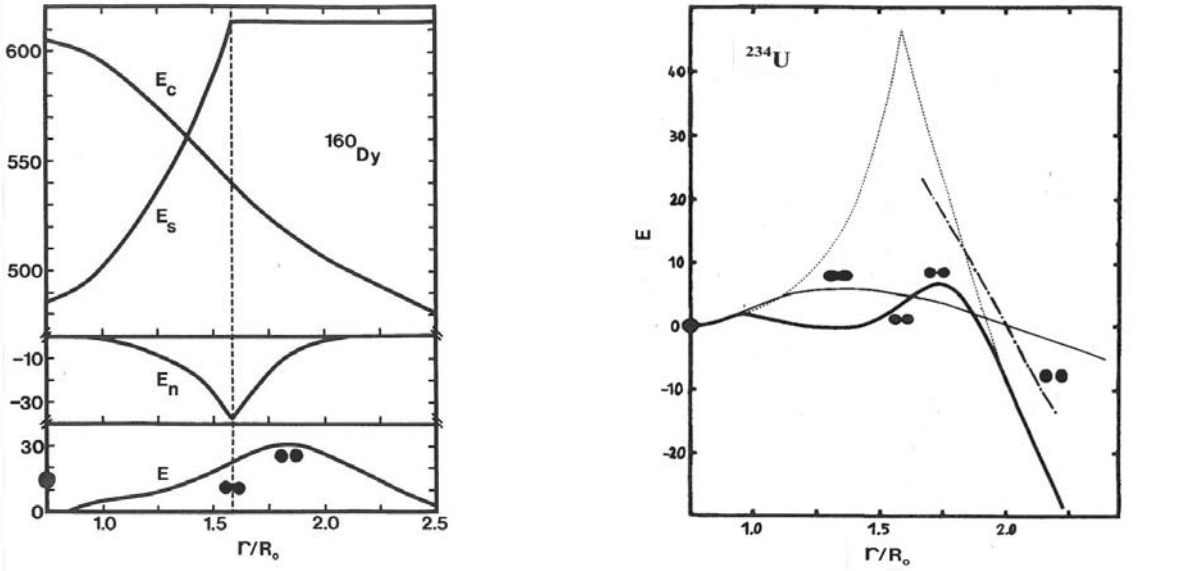

Fig. 2. On the *left part*, contribution of the Coulomb, surface and nuclear proximity energies to the total deformation energy E of the ^{160}Dy. The dotted line indicates the contact point between spherical fragments. On the *right part*, the thick full curve and the dotted curve are respectively the potential energies using our quasi-molecular shape sequence with and without proximity energy. The thin full curve is the energy of elongated shapes while the chain curve gives the energy of two separated oblate spheroids with no proximity contribution.

The usual picture of the Businaro - Gallone point assuming that, macroscopically, asymmetric fission is favoured for light systems and symmetric fission for heavy nuclei is also observed in the quasi-molecular shape path (see Fig. 3). More generally, it has been proved that the deformation barrier heights in this valley correspond precisely to the experimental fission barrier heights [5].

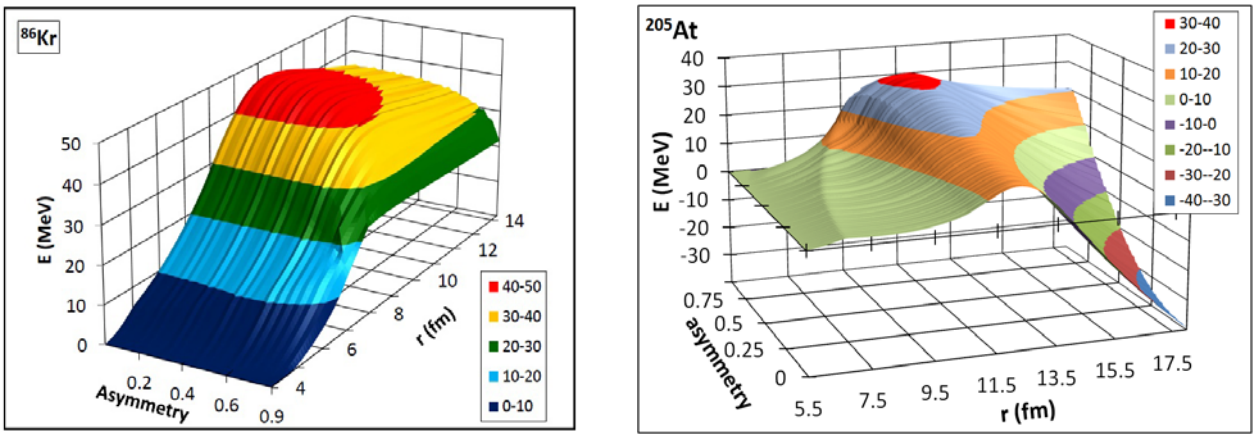

Fig. 3. Macroscopic fission barriers as functions of the decay asymmetry $(A_1 - A_2)/(A_1 + A_2)$ and the distance between the mass centers r for the two ^{86}Kr and ^{205}At nuclei.

In the *left part* of Fig. 4 the mass evolution of the barrier profile is displayed. With increasing mass appear macroscopically a plateau and a second external relative minimum and internal peak due to the proximity energy and then the possibility of isomeric states. On the right, for ^{152}Dy but this is a general behaviour, it is shown that the rotation of a quasi-molecular shape creates also strongly deformed rotating isomeric states [6, 8].

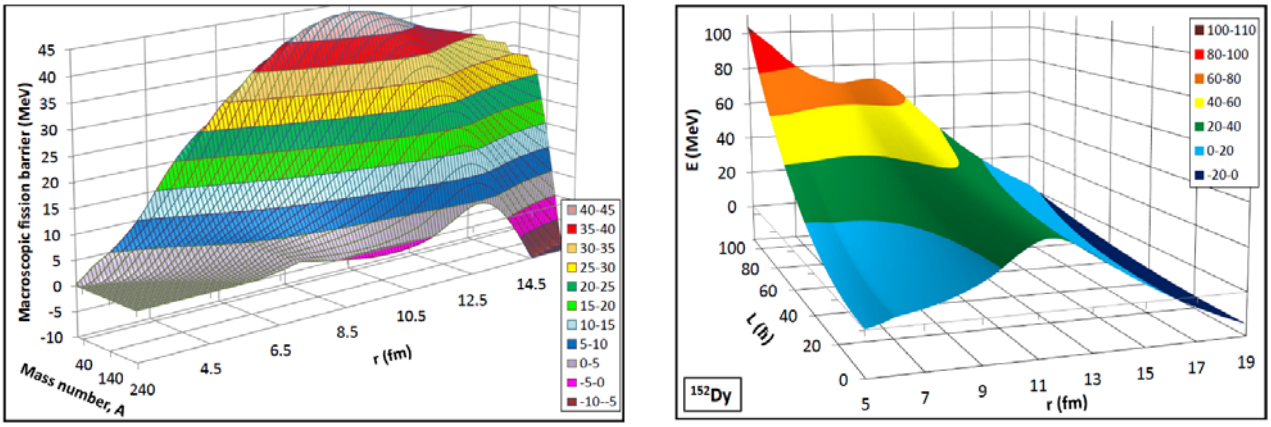

Fig. 4. Symmetric fission barrier as functions of the mass in the β-stability valley (on the *left*) and symmetric fission barrier of the ^{152}Dy nucleus versus the angular momentum (on the *right*).

In Fig. 5 the shell and pairing energies have been introduced as well as the ellipsoidal deformations to calculate the fission barriers of ^{240}Pu, as an example. Multiple-humped potential barriers appear. The second maximum corresponds to the transition from compact and creviced one-body shapes to two touching ellipsoids. Shallow third minimum and peak appear in specific asymmetric exit channels where one fragment is close to a double magic quasi-spherical nucleus while the other one evolves from oblate to prolate shapes. The heights of the potential barriers agree with the experimental data and the calculated half-lives follow the trend of the experimental values. The complete separation of the fragments corresponds to a sudden shape change and to the vanishing of the proximity energy. It occurs on an energy plateau corresponding to the fragment kinetic energy plus excitation energy.

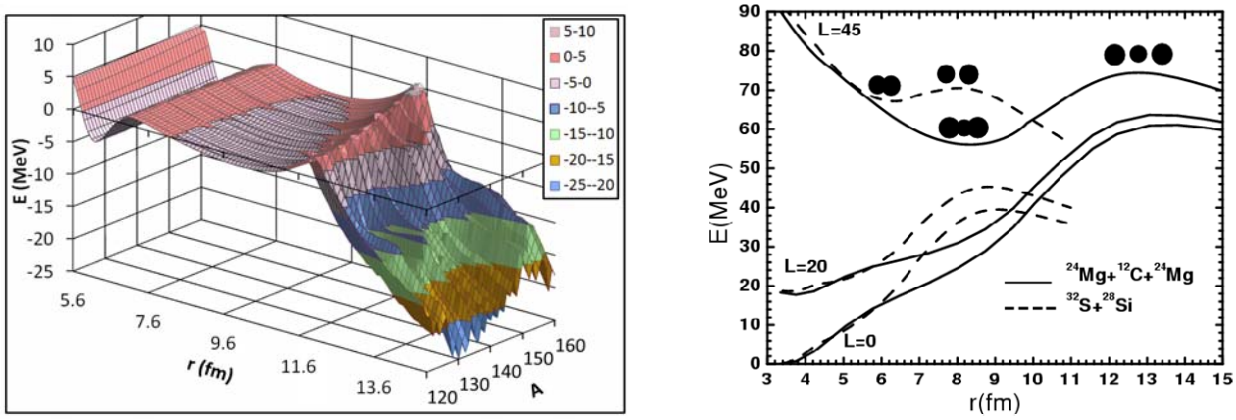

Fig. 5. Multiple-humped macro-microscopic barriers for ^{240}Pu as a function of the heaviest fragment mass (on the *left*) and binary and ternary fission barriers for ^{60}Zn as a function of the angular momentum (on the right).

In the experiments ^{32}S + ^{24}Mg → ^{56}Ni (E*= 84 MeV) and ^{36}Ar + ^{24}Mg → ^{60}Zn (E*= 88 MeV) narrow out-of-plane correlations corresponding to coplanar decay are observed when two fragments are emitted with missing charges from 4 up to 8. This ternary fission have been interpreted as the decay of hyper-deformed states with angular momenta around 45 - 50 $\hbar$ [8].

The Fig. 5 (*right part*) indicates that the very asymmetric ternary fission is favoured relatively to the symmetric ternary one. At high angular momenta around 45 $\hbar$ the potential energy minima is lower in the ternary fission path than in the binary fission path. The more negative Q-value for ternary fission is compensated for the smaller value of the rotational energy at the saddle point. Thus, the GLDM indicates simply that the ternary cluster fission of light nuclei becomes competitive with binary cluster fission at the highest angular momenta.

5. Alpha and Cluster radioactivity

α decay and cluster radioactivity are, as the spontaneous fission, quantum tunneling processes through the potential barrier leading from the mother nucleus to the two emitted fragments. An open question is whether these three decay

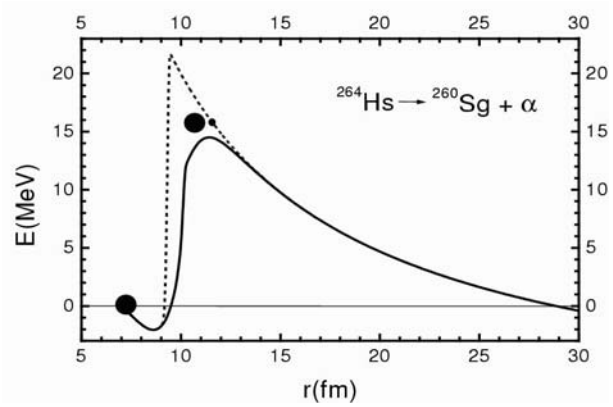

Fig. 6. Potential barriers against alpha emission for the ^{264}Hs nucleus. The dashed curve corresponds to the pure Coulomb barrier without including the proximity energy while the solid line takes into account the proximity effects.

modes can be described within a fission process but for three very different mass asymmetries or whether α and cluster radioactivities correspond to the emission of preformed clusters.

The same GLDM and quasi-molecular shapes has been used [9, 10] to determine the potential barriers for these two decay modes since it is unlikely that the α and cluster emissions lead to elongated fragments contracting after separation. An α decay barrier is displayed in Fig. 6. The difference between the experimental Q value and the theoretical GLDM Q value has been added at the macroscopic energy of the mother nucleus with a linear attenuation factor vanishing at the contact point of the nascent fragments. The proximity forces lower the barriers of 7.3 MeV and the displacement of the maximum is of 2.1 fm.

In the picture of an unified fission model the decay constant has been simply defined as the product of the assault frequency by the barrier penetrability calculated within the WKB method. The main part of the potential barriers corresponding to two-body shapes it has been assumed that the entrance of the tunnel corresponds to the contact point while the inertia parameter is simply the reduced mass. For the cluster emission, these approximations are not possible and the position of the tunnel entrance is the initial sphere while a more sophisticated expression has been selected for the inertia [10, 11]. The Fig. 7 and the Table 2 indicate that this approach allows to determine accurately the half-lives of the α decay and cluster radioactivity. Simple accurate analytical formulas depending on the mass and charge of the α emitter and the experimental or theoretical Q value have been proposed [9] to reproduce the known α decay half-lives and also to predict the half-lives of other possible but still unknown α decays particularly for the superheavy nuclei. Predictions for other cluster emissions have been also provided meeting two criteria: partial half-life $\leq 10^{30}$ s and branching ratio relative to α emission $\geq 10^{-24}$.

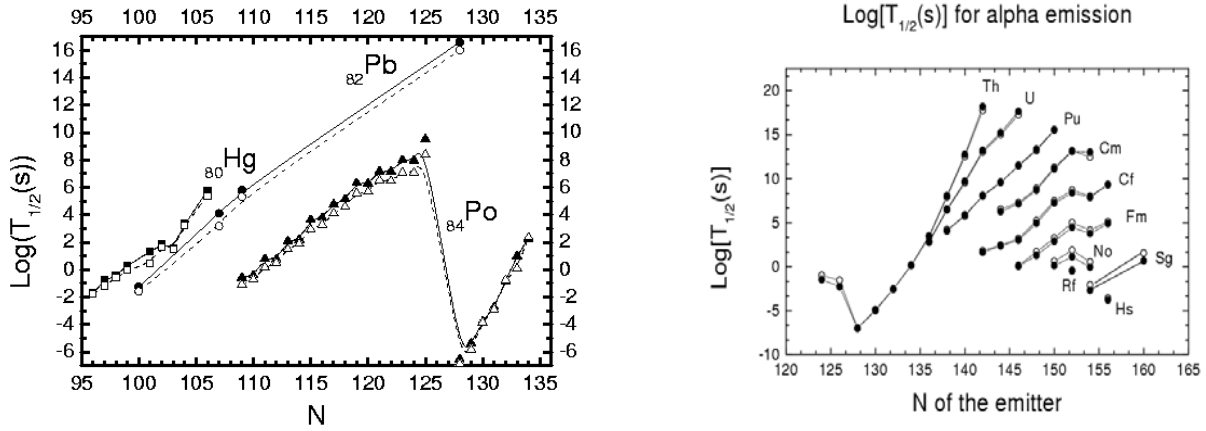

Fig. 7. Comparison between the theoretical and experimental alpha-decay half-lives of the Hg, Pb, Po, Th, U, Pu, Cm, Cf, Fm, No, Rf, Sg and Hs isotopes.

The preformation of clusters and α particle in heavy nuclei has also been investigated [12]. Recently the angular momentum dependence of the partial α decay half-lives has been taken into account and new formulas are proposed.

Table 2. **Comparison between the experimental and theoretical half-lives for the cluster radioactivity**

Emitter and fragments	GLDM-$T_{1/2}$(s)	Experimental $T_{1/2}$(s)
^{222}Ra → ^{14}C + ^{208}Pb	$3.9 \cdot 10^{10}$	$1.0 \cdot 10^{11}$
^{223}Ra → ^{14}C + ^{209}Pb	$2.8 \cdot 10^{13}$	$1.4 \cdot 10^{15}$
^{224}Ra → ^{14}C + ^{210}Pb	$3.9 \cdot 10^{16}$	$5.9 \cdot 10^{15}$
^{226}Ra → ^{14}C + ^{212}Pb	$3.2 \cdot 10^{22}$	$1.8 \cdot 10^{21}$
^{228}Th → ^{20}O + ^{208}Pb	$4.1 \cdot 10^{21}$	$5.0 \cdot 10^{20}$
^{230}Th → ^{24}Ne + ^{206}Hg	$2.8 \cdot 10^{25}$	$4.1 \cdot 10^{24}$
^{231}Pa → ^{24}Ne + ^{207}Tl	$8.6 \cdot 10^{21}$	$7.9 \cdot 10^{22}$
^{232}U → ^{24}Ne + ^{208}Pb	$9.7 \cdot 10^{19}$	$2.5 \cdot 10^{20}$

Continuation of Table 2

Emitter and fragments	GLDM-$T_{1/2}$(s)	Experimental $T_{1/2}$(s)
$^{233}U \rightarrow {}^{24}Ne + {}^{209}Pb$	$2.3 \cdot 10^{23}$	$6.8 \cdot 10^{24}$
$^{234}U \rightarrow {}^{24}Ne + {}^{210}Pb$	$3.5 \cdot 10^{26}$	$7.9 \cdot 10^{25}$
$^{235}U \rightarrow {}^{28}Mg + {}^{207}Hg$	$1.8 \cdot 10^{29}$	$2.8 \cdot 10^{28}$
$^{236}Pu \rightarrow {}^{28}Mg + {}^{208}Pb$	$1.0 \cdot 10^{20}$	$4.7 \cdot 10^{21}$
$^{238}Pu \rightarrow {}^{28}Mg + {}^{210}Pb$	$2.2 \cdot 10^{26}$	$4.7 \cdot 10^{25}$
$^{238}Pu \rightarrow {}^{32}Si + {}^{206}Hg$	$5.4 \cdot 10^{25}$	$1.9 \cdot 10^{25}$

6. Superheavy elements

Using heavy-ion reactions of mean asymmetry (Cr, Fe, Ni, Zn on Bi and Fe, Ni, Zn on Pb) and more recently highly asymmetric reactions (Ca on Np, Pu, Am, Cm, Bk, Cf) new very heavy elements have been synthesized. Actually it is assumed that the lower limit for the fission barrier heights of these heaviest elements is around 6 MeV. The main observed decay mode is the α decay.

Within this GLDM the potential barriers governing these reactions have been determined (see [13] and Fig. 8). For the cold fusion reactions a wide potential pocket due mainly to a high proximity energy and high Coulomb repulsion appears at large deformations. Whatever the microscopic correction assumptions are, double-humped barriers exist. The quasispherical system can be reached by tunnelling even if the shells and pairs are not completely built. Incomplete fusion and fast fission events in the external pocket are the main exit channels since the neck between the two nuclei is formed and exchanges of nucleons can occur. If the reorganization of the single particle levels is very rapid then the value of the proton magic number begins to play some role. So an open question is whether at large deformations the nucleons shells can take form to stabilize the nuclear system before investigating a peculiar exit channel. The pre or post equilibrium nature of the neutron evaporation process is also crucial.

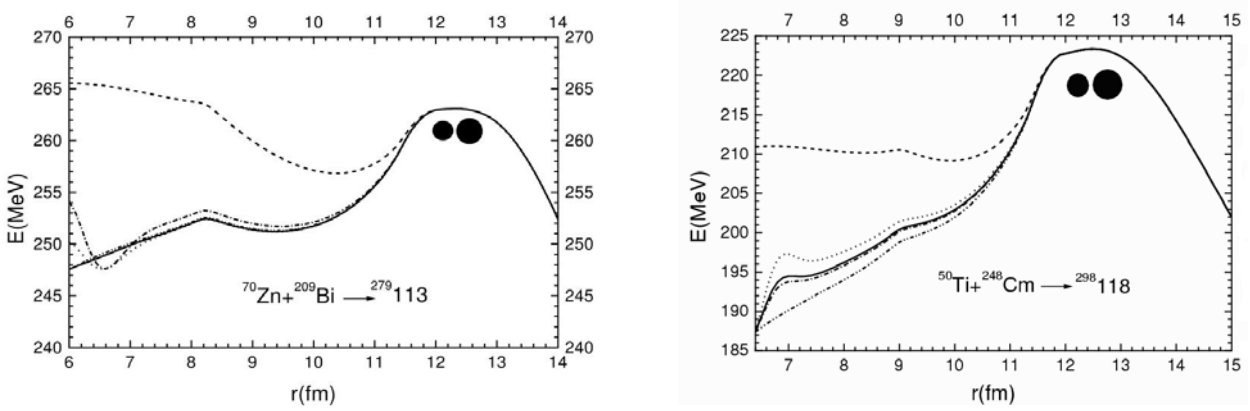

Fig. 8. Potential barriers for the cold $^{70}Zn + {}^{209}Bi$ fusion reaction and the warm $^{50}Ti + {}^{248}Cm$ fusion reaction. The dashed curve corresponds to the macroscopic barrier. The full line, dotted curve and dashed and dotted curve include the shell effects assuming a proton magic number of 114, 120 and 126 and an adjustment to reproduce the Q value.

For the warm fusion reactions the Coulomb repulsion and the proximity energy are lower than for the cold fusion reactions and the barrier against reseparation is wide and high. There is no double-humped barriers. Even for a subbarrier tunnelling of 6 MeV in the entrance channel and even if the shells and pairs have not enough time to develop the nuclear system has enough energy to reach a quasispherical compound system. The excitation energy is more than 30 MeV allowing the emission of several neutrons or an α particle. The different hypotheses on the proton magic number do not change the global predictions in the entrance path.

Using the above mentioned general formulas giving the α decay half-lives and with the help of an accurate Q value our theoretical half-lives agree with the experimental data for the known superheavy nuclei. Thus, predictions of the α decay half-lives of other possible superheavy isotopes have been provided, some of which reaching more than one hour [14].

Recently, the systems ^{238}U + Ni and ^{238}U + Ge have been studied at high excitation energy of 6.62 MeV/u and 6.09 MeV/u possibly leading to nuclear systems of charge 120 and 124 [15]. A coupled analysis of the nuclear reaction time distributions and of the measured K x rays provides evidence for nuclei with Z = 120 and 124 living longer than 10^{-18} s and arising from highly excited compound nuclei.

In Fig. 9 the capture barriers for these reactions have been calculated as a function of the angular momentum within this GLDM. The excitation energy is very large and very high angular momenta are populated while the shell effects are probably very small at these energies. For these very heavy systems the potential energy profile is very flat once the external barrier is passed allowing the possible formation and stability of rapidly rotating isomeric states without necessarily reaching a quasi-spherical nuclear shape and even though the shell effects vanish and the inner barrier is destroyed.

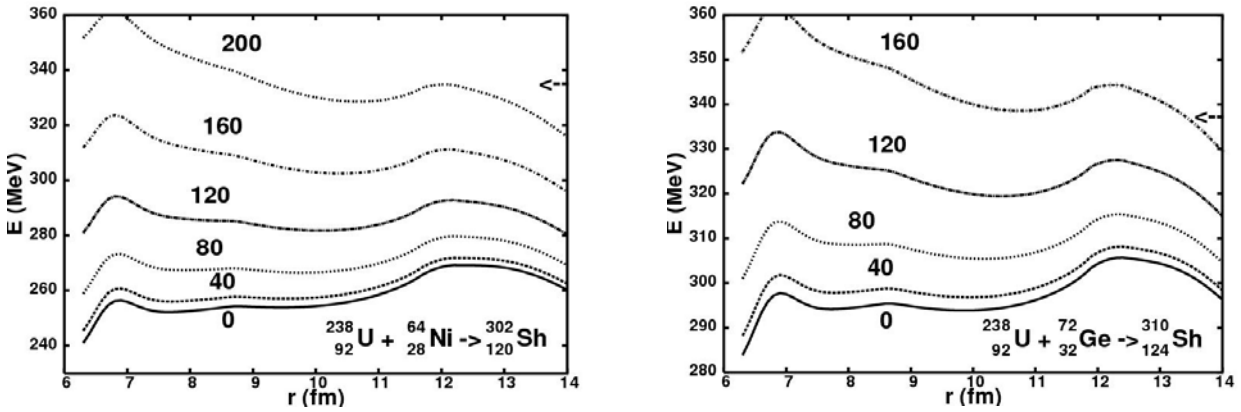

Fig. 9. L-dependent capture barriers for the U + Ni and U + Ge reactions. The arrows indicate the beam energy. The shell effects are taken into account assuming that the next proton magic number is Z = 114.

7. Summary and Conclusions

A generalized liquid drop model including both the mass and charge asymmetries, the proximity energy, a particular nuclear radius, the rotational energy, the shell and pairing energies and the temperature has been defined and used to describe smoothly the transition between two-body and one-body shapes in entrance and exit channels of nuclear reactions.

In the compact and creviced shape valley where the proximity energy is maximal at the contact point, the calculated l-dependent fusion and fission barrier heights and the half-lives of alpha and cluster radioactivities as well as actinides are in agreement with the available experimental data. In this quasi-molecular shape path, double-humped potential barriers begin to appear even macroscopically for heavy nuclear systems in entrance and exit channels due to the influence of the proximity forces and, consequently, quasi-molecular isomeric states can survive in the second minimum of the potential barriers, particularly at intermediate angular momenta.

ACKNOWLEDGMENTS

I thank warmly my colleagues C. Beck, C. Bonilla, V. Yu Denisov, R. Gherghescu, R. K. Gupta, F. Haddad, W. von Oertzen, A. Onillon and H. F. Zhang.

REFERENCES

1. *Royer G., Remaud B.* Static and dynamic fusion barriers in heavy-ion reactions // Nucl. Phys. - 1985. - Vol. A444. - P. 477 - 497.
2. *Krappe H.J., Nix J.R., Sierk A.J.* Unified nuclear potential for heavy-ion elastic scattering, fusion, fission, and ground states masses and deformations // Phys. Rev. - 1979. - Vol. C20. - P. 992 - 1013.
3. *Myers W.D., Swiatecki W.J.* Nuclear properties according to the Thomas - Fermi model // Nucl. Phys. - 1996. - Vol. A601. - P. 141 - 167.
4. *Royer G., Guilbaud M., Onillon A.* Macro-microscopic mass formulae and nuclear mass predictions // Nucl. Phys. - 2010. - Vol. A847. - P. 24 - 41.
5. *Royer G., Remaud B.* Fission processes through compact and creviced shapes // J. Phys. - 1984. - Vol. G10. - P. 1057 - 1070.
6. *Royer G., Gaudillot J.* Rotating hyperdeformed states in light nuclear systems // Phys. Rev. - 2011. - Vol. C84. - P. 044602(6).
7. *Royer G.* Heavy elements and related new phenomena // Fission through quasi-molecular shapes and fragmentation / Ed. by R. K. Gupta, W. Greiner. - Singapure: World Scientific, 1999. - P. 591 - 631.
8. *Von Oertzen W. et al.* Fission decay of N = Z nuclei at high angular momentum: ^{60}Zn // Phys. Rev. - 2008. - Vol. C78. - P. 044615(19).
9. *Royer G.* Alpha emission and spontaneous fission through quasi-molecular shapes // J. Phys. - 2000. - Vol. G26. - P. 1149 - 1170.
10. *Royer G., Gupta R.K., Denisov V.Yu.* Cluster radioactivity and very asymmetric fission through compact and creviced shapes // Nucl. Phys. - 1998. - Vol. A632. - P. 275 - 284.
11. *Bao X.J. et al.* Half-lives of cluster radioactivity with a generalized liquid-drop model // J. Phys. - 2012. - Vol. G39. - P. 095103(11).
12. *Zhang H.F. et al.* Preformation of clusters in heavy nuclei and cluster radioactivity // Phys. Rev. - 2009. - Vol. C80. - P. 037307(4).
13. *Royer G., Zbiri K., Bonilla C.* Entrance channels and alpha decay half-lives of the heaviest elements // Nucl. Phys. - 2004. - Vol. A730. - P. 355 - 376.
14. *Royer G., Zhang H. F.* Recent alpha decay half-lives and analytic expression predictions including the heaviest nuclei // Phys. Rev. - 2008. - Vol. C77. - P. 037602(4).
15. *Frégeau M. O. et al.* X-Ray fluorescence from the element with atomic number Z = 120 // Phys. Rev. Lett. - 2012. - Vol. 108. - P. 122701(5).

MODERN ENERGY DENSITY FUNCTIONAL FOR PROPERTIES OF FINITE NUCLEI AND NUCLEAR MATTER

S. Shlomo

Cyclotron Institute, Texas A&M University, College Station, TX, USA

We describe a method, based on the simulated annealing approach, for determining a modern energy density functional within the Skyrme Hartree - Fock (HF) theory by carrying out a fit to extensive set of experimental data and including important constraints on the Skyrme parameters. We then present results of calculations for the excitation strength functions and centroid energies of giant resonances within the HF-based random phase approximation and discuss the current status of the nuclear matter (NM) incompressibility coefficient and the symmetry energy density, which are the needed ingredients for extending our knowledge of the equation of state (energy as a function of neutron and proton densities) of symmetric and asymmetric NM beyond the saturation point of the symmetric NM.

1. Introduction

Density functional theory, which is based on a theorem [1] for the existence of an energy density functional (EDF) that depends on the densities of the constituents and their derivatives, provides a powerful approach for theoretical calculations of properties of many body systems. Thus it is very important to develop a modern EDF which provides enhanced predictive power for properties of rare nuclei with unusual neutron-to-proton ratios that are difficult to produce experimentally and likely to exhibit interesting new phenomena associated with effects of isospin, clusterization, and the continuum. Since determining the EDF of an interacting many body system from first principles is a difficult problem, it is common to assume a certain form for the EDF with parameters determined by experimental data. Following the pioneering work of Brink and Vautherin [2], continuous efforts have been made to readjust the parameters of the EDF associated with the Skyrme-type effective nucleon-nucleon (NN) interaction [3, 4] to better reproduce experimental data [5 - 8]. There exist more than 200 parameterizations of the Skyrme type interactions [8]. The values of the parameters of the Skyrme interactions available in the literature were obtained by fitting the Hartree - Fock (HF) results to experimental data on bulk properties of a few stable closed-shell nuclei. In our work [9] we further enhanced the applicability of the Skyrme-type EDF by including data on nuclei away from the valley of stability, and including in the fit, for the first time, the data on the constraint energies of the isoscalar giant monopole resonances (ISGMR) of nuclei. We have also imposed additional constraints, such as a non-negative value for the slope of the symmetry energy density at high nuclear matter (NM) density (at three times the saturation density of NM) and the Landau's stability conditions for NM. Adopting the standard parameterization of the Skyrme type interaction, we have implemented, for the first time, the simulated annealing method (SAM) together with an advanced least square method to search for the global minima.

The study of collective modes in nuclei has been the subject of extensive theoretical and experimental investigations for over 60 years, since it contributes significantly to our understanding of properties of nuclei and NM, their non-equilibrium properties and properties of the nuclear force [10 - 12]. Of particular interest is the equation of state (EOS), i.e., the energy as a function of neutron and proton densities, which is an important ingredient in the study of properties of nuclei at and away from stability, structure and evolution of compact astrophysical objects, such as neutron stars and core-collapse supernovae, and of heavy-ion collisions [13, 14]. The saturation point of the EOS for the symmetric nuclear matter (SNM) at zero temperature (T = 0) is well determined from ground state properties of nuclei, such as binding energies and central matter densities, by extrapolation to infinite NM. To extend our knowledge of the EOS beyond the saturation point of the SNM, an accurate value of the NM incompressibility coefficient K, which is directly related to the curvature of the EOS at saturation density, is needed. An accurate determination of the density dependence of the symmetry energy, $E_{sym}(\rho)$, is needed for the EOS of asymmetric NM. It is well known that the energies of compression modes in nuclei, such as the ISGMR and the isoscalar giant dipole resonance (ISGDR), are sensitive to the value of K [10, 15, 16] and the energies of the isovector resonances, in particular, the giant dipole resonance (IVGDR), are sensitive to $E_{sym}(\rho)$ [17, 18].

In the following, we first describe a method, based on the simulated annealing method (SAM), for determining a modern energy density functional within the Skyrme HF theory by carrying out a fit to extensive set of experimental data and including important constraints on the Skyrme parameters. We then present results of fully self-consistent HF-based random phase approximation (RPA) calculations for the excitation strength functions and centroid energies of giant resonances (GR) and discuss the current status of K and $E_{sym}(\rho)$, which are needed for extending our knowledge of the EOS of symmetric and asymmetric NM beyond the saturation point of the symmetric NM.

2. Determination of the Skyrme Energy Density Functional

We have recently considered the EDF associated with the Skyrme type effective nucleon-nucleon interaction, adopting the following form for the Skyrme interaction [4 - 6]:

$$V_{12} = t_0(1 + x_0\ P_{12}^{\sigma})\delta(\vec{r}_1 - \vec{r}_2) + \frac{1}{2}t_1(1 + x_1 P_{12}^{\sigma})[\overleftarrow{k}_{12}^2\delta(\vec{r}_1 - \vec{r}_2) + \delta(\vec{r}_1 - \vec{r}_2)\vec{k}_{12}^2] +$$

$$+t_2(1 + x_2 P_{12}^{\sigma})\overleftarrow{k}_{12}\delta(\vec{r}_1 - \vec{r}_2)\vec{k}_{12} + \frac{1}{6}t_3(1 + x_3 P_{12}^{\sigma})\rho^{\alpha}\left(\frac{\vec{r}_1 + \vec{r}_2}{2}\right)\delta(\vec{r}_1 - \vec{r}_2) +$$

$$+iW_0\overleftarrow{k}_{12}\delta(\vec{r}_1 - \vec{r}_2)(\vec{\sigma}_1 + \vec{\sigma}_2)\cdot\vec{k}_{12}. \tag{1}$$

where t_i, x_i, α, and W_0 are the parameters of the interaction and P_{12}^{σ} is the spin exchange operator; $\vec{\sigma}_i$ is the Pauli spin operator; $\vec{k}_{12} = -i\left(\vec{\nabla}_1 - \vec{\nabla}_2\right)/2$, and $\overleftarrow{k}_{12} = -i\left(\overleftarrow{\nabla}_1 - \overleftarrow{\nabla}_2\right)/2$. Here, the right and left arrows indicate that the momentum operators act on the right and on the left, respectively. The corresponding mean-field V_{HF} and the total energy E of the system are given by

$$V_{HF} = \frac{\delta H}{\delta\rho}, \quad E = \int H(r)d^3r, \tag{2}$$

respectively. Here, $H(r)$ is the energy density functional associated with the Skyrme interaction and is obtained using Eq. (1). The HF equations are derived by minimizing the energy E,

$$\frac{\delta}{\delta\rho_{\sigma,\tau}}\left[E - \sum_i \epsilon_i \int \rho_{\sigma,\tau} d\vec{r}\right] = \frac{\delta E}{\delta\rho_{\sigma,\tau}} - \frac{\delta\left[\sum_i \epsilon_i \int \rho_{\sigma,\tau} d\vec{r}\right]}{\delta\rho_{\sigma,\tau}} = 0. \tag{3}$$

Here ϵ_i are the Lagrange multipliers and $\delta\rho_{\sigma,\tau}$ is the density increment which is given in terms of single particle wave functions. For the spherical case one obtains the HF equations,

$$\frac{\hbar^2}{2m_{\tau}^*(r)}\left[-R_{\alpha}^{''}(r) + \frac{l_{\alpha}(l_{\alpha}+1)}{r^2}R_{\alpha}(r)\right] - \frac{d}{dr}\left(\frac{\hbar^2}{2m_{\tau}^*(r)}\right)R_{\alpha}^{'}(r) +$$

$$+\left[U_{\tau}(r) + \frac{1}{r}\frac{d}{dr}\frac{\hbar^2}{2m_{\tau}^*(r)} + \frac{\left[j_{\alpha}(j_{\alpha}+1) - l_{\alpha}(l_{\alpha}+1) - \frac{3}{4}\right]}{r}W_{\tau}(r)\right]R_{\alpha}(r) = \epsilon_{\alpha}R_{\alpha}(r), \tag{4}$$

where $m_{\tau}^*(r)$, $U_{\tau}(r)$, and $W_{\tau}(r)$ are the effective mass, central potential and spin-orbit potential, which are given in terms of the Skyrme parameters and the neutron and proton densities and their derivatives [2]. Equations (4) are numerically solved by iteration, starting, for example, with the results of commonly used Wood Saxon potential.

2.1. Simulated annealing based algorithm

From the literature [7, 8] one finds that the value of each Skyrme parameter vary over a wide range. Therefore, to make the search process more efficient, we take advantage of the fact that the Skyrme parameters can be expressed in terms of the various quantities which are related to the nuclear matter, since these nuclear matter quantities are known empirically within 10 % - 20 %. For convenience, we have defined a vector v with the components as

$$v \equiv \left(B/A, K, \rho_0, m^*/m, E_s, J, L, \kappa, G_0^{'}, W_0\right). \tag{5}$$

Here $B/A, K, \rho_0, m^*/m, E_s, J, L, \kappa, G_0^{'}$, and W_0 are the binding energy per nucleon, NM incompressibility coefficient, nuclear matter density, effective mass, surface energy, symmetry energy coefficient, the quantity which is related to the slope of the symmetry energy coefficient ($L = 3\rho dJ/d\rho$), the enhancement factor in the energy weighted sum rule (EWSR) of the isovector giant dipole resonance (IVGDR), the spin-isospin Landau parameter of the particle-hole interaction, and the Skyrme spin-orbit parameter, respectively.

Once the vector v is known one can calculate the values of all the Skyrme parameters. We have also defined the vectors v_0, v_1 and d. The vector v_0 and v_1 contain the lower and the upper limits of each of the components of the vector v. The vector d represents the maximum displacement allowed in a single step for the components of the vector v. For a given set of experimental data, we have implemented the SAM algorithm using the following basic steps: Starting with a guess for the vector v we calculate χ^2 (say, χ_{old}^2). We use random numbers to select an element of v of and change it slightly. Using the new v we determine the new Skyrme parameters and calculate the new χ_{new}^2. We then calculate the quantity

$$P\left(\chi^2\right) = e^{\left(\chi_{old}^2 - \chi_{new}^2\right)/T}, \tag{6}$$

where T is an effective temperature and accept new set of Skyrme parameters only if

$$P\left(\chi^2\right) > \beta, \tag{7}$$

where $\beta < 1$ is a random number. To search for the global minimum of χ^2 we begin with some reasonable value of an effective temperature $T = T_i$ and repeat the process described above more than 1000 times. Then, we reduce the temperature and repeat the process until the value of χ^2 converges.

2.2. Experimental data and some constraints

In Table 1 we summarize the choice of the experimental data used in the fit for determining the Skyrme parameters. It must be noted that, in addition to the typically used data on the binding energy, charge rms radii and spin-orbit splitting, we have also included in our fit the experimental data for the rms radii of valence neutron orbits and the breathing-mode constraint energies of several nuclei. For the binding energy we have used in the fit the error of 1.0 MeV except for the ^{100}Sn nuclei, in which we have used 2.0 MeV since the binding energy for the ^{100}Sn nucleus is determined from systematic. For the charge rms radii we have adopted the theoretical error of 0.02 fm except for the case of ^{56}Ni nucleus. The charge rms radius for the ^{56}Ni nucleus is obtained from systematic and we use the theoretical error of 0.04 fm. We considered in the fit the experimental data for the spin-orbit splittings for the 2p neutrons and protons in the ^{56}Ni nucleus and the rms radii for the $1d_{5/2}$ and $1f_{7/2}$ neutron orbits in ^{17}O and ^{41}Ca nuclei, respectively. The theoretical error taken for the spin-orbit splitting data is 0.2 MeV, and for the rms radii for the valence neutron orbits the experimental error of 0.06 fm was adopted. To be consistent with the way these valence neutron radii are determined, the CM correction to these data was not included. The experimental data for the breathing-mode constraint energies E_0 for the ^{90}Zr, ^{116}Sn, ^{144}Sm and ^{208}Pb nuclei were included in the fit with the theoretical error taken to be 0.5 MeV for the ^{90}Zr nucleus and 0.3 MeV for the other nuclei. We have also included in the fit the critical density ρ_{cr}, defined as the highest density for which the Landau stability conditions are maintained, assuming a value of $2.5\,\rho_0$ with an error of $0.5\,\rho_0$. Further the values of the Skyrme parameters were constrained by requiring (i) a positive slope for the symmetry energy density for $\rho \le 3\rho_0$, (ii) $\kappa = 0.1 - 0.5$ and (iii) $G_0' \ge 0$ at $\rho = \rho_0$ (see Ref. [9] for details).

Table 1: **Selected experimental data for the binding energy *B*, charge rms radius r_{ch}, rms radii of valence neutron orbits r_v, spin-orbit splitting S-O, breathing-mode constraint energy E_0, and critical density ρ_{cr} used in the fit to determine the parameters of the Skyrme interaction**

Properties	Nuclei
B	^{16,24}O, ^{34}Si, ^{40,48}Ca, ^{48,56,68,78}Ni, ^{88}Sr, ^{90}Zr, ^{100,132}Sn, ^{208}Pb
r_{ch}	^{16}O, ^{40,48}Ca, ^{56}Ni, ^{88}Sr, ^{90}Zr, ^{208}Pb
$r_v(\nu 1d_{5/2})$	^{17}O
$r_v(\nu 1f_{7/2})$	^{41}Ca
S-0	2p orbits in ^{56}Ni
E_0	^{90}Zr, ^{116,132}Sn, ^{144}Sm, ^{208}Pb
ρ_{cr}	Nuclear matter

3. Equation of State of Symmetric and Asymmetric Nuclear Matter

In the vicinity of the saturation density ρ_0 of symmetric NM, the EOS can be approximated by

$$E_0[\rho] = E[\rho_0] + \frac{1}{18} K \left(\frac{\rho - \rho_0}{\rho_0} \right)^2, \tag{8}$$

where $E_0[\rho]$ is the binding energy per nucleon and K is the incompressibility coefficient which is directly related to the curvature of the EOS, $K = 9\rho_0^2 \frac{\partial^2 E_0}{\partial \rho^2}\Big|_{\rho_0}$. Similarly, the EOS of asymmetric NM, with proton density ρ_p and neutron density ρ_n, can be approximated by

$$E\left[\rho_p, \rho_n\right] = E_0[\rho] + E_{sym}[\rho] \left(\frac{\rho_n - \rho_p}{\rho} \right)^2, \tag{9}$$

where $E_{sym}[\rho]$ is the symmetry energy at matter density ρ commonly approximated by,

$$E_{sym}[\rho] = J + \frac{1}{3} L \left(\frac{\rho - \rho_0}{\rho_0} \right) + \frac{1}{18} K_{sym} \left(\frac{\rho - \rho_0}{\rho_0} \right)^2, \tag{10}$$

where $J = E_{sym}[\rho_0]$ is the symmetry energy at saturation density ρ_0, $L = 3\rho_0 \left.\frac{\partial E_{sym}}{\partial \rho}\right|_{\rho_0}$, and $K_{sym} = 9\rho_0 \left.\frac{\partial^2 E_{sym}}{\partial \rho^2}\right|_{\rho_0}$.

There have been many attempts over the years to determine K and $E_{sym}(\rho)$ by considering physical quantities which are sensitive to the values of K and $E_{sym}(\rho)$ [12,13,19,20]. Here we consider the sensitivity of the centroid energies of the isoscalar and isovector giant resonances to bulk properties of NM, such as K, E_{sym} and the effective mass m^*. It is well known that the energies of the isoscalar compression modes are very sensitive to the value of K and the energies of the isovector giant resonances are sensitive to the density dependence of E_{sym}. Furthermore, information on the density dependence of E_{sym} can also be obtained by studying the isotopic dependence of strength functions, such as the difference between the strength functions of ^{40}Ca and ^{48}Ca and between ^{112}Sn and ^{124}Sn. Other physical quantities that are sensitive to the $E_{sym}(\rho)$ below the saturation density are: the neutron skin thickness, r_n - r_p [21 - 23], the difference between the root mean square radii (rms) of the neutron and proton density distributions; and the electric isovector dipole polarizability α_D [24], which is directly related to the inverse energy moment (m_{-1}) of the strength function of the IVGDR.

4. Hartree - Fock-based Random Phase Approximation

In the numerical calculations of the properties of giant resonances in nuclei within the HF-based RPA theory, one starts by adopting an effective nucleon-nucleon interaction V_{12}, such as the Skyrme interaction, with parameters determined by a fit [9] of the HF predictions to experimental data on ground state properties, such as binding energies and radii, of a selected set of a wide range of nuclei. Then, the RPA equations are solved using the particle-hole (p-h) interaction deduced from V_{12}, by employing a certain numerical method [25 - 27], and the physical quantities of interest, such as the strength functions $S(E)$ and transition densities, are calculated. For example, within the Green's function RPA approach the response $S(E)$ of the many-body system to an external field described by the single-particle operator $F = \sum f(r_i)$, is given by [25],

$$S(E) = \sum_n |\langle 0|F|n\rangle|^2 \delta(E - E_n) = \frac{1}{\pi} \mathrm{Im} \int_0^\infty dr dr' f(r) G(r, r', E) f(r'), \tag{11}$$

where G is the particle-hole Green's function. The transition density, ρ_t is obtained from

$$\rho_t(r, E) = \frac{\Delta E}{\sqrt{S(E)\Delta E}} \int_0^\infty f(r') \left[\frac{1}{\pi} \mathrm{Im} G(r', r, E)\right] dr'. \tag{12}$$

In RPA theory the Green's function is given by

$$G^{RPA} = G^{(0)}\left(1 - \frac{\delta V}{\delta \rho} G^{(0)}\right)^{-1}, \tag{13}$$

where V is the Hartree - Fock potential, having a functional dependence on ρ, the matter density. The unperturbed Green function $G^{(0)}$ is given in terms of the Hartree - Fock Hamiltonian H_0, its occupied eigenstates ϕ_h, and the associated eigen-energies ϵ_h, as

$$G^{(0)}(r_1, r_2, \omega) = -\sum_h \phi_h(r_1)\left(\frac{1}{H_0 - \epsilon_h - \omega} + \frac{1}{H_0 - \epsilon_h + \omega}\right)\phi_h(r_2). \tag{14}$$

The sum in (14) is on the occupied states; $(H_0 - E)^{-1}$ is the Hartree - Fock Green function for a single particle propagated from r_2 to r_1.

We point out that in fully self-consistent calculations, one should employ all the components of the p-h interactions obtained from the V_{12} used in the HF calculations [16, 28, 20], In our calculations we employed the fully self-consistent method based on the Q-P representation described in detail in Refs. [26, 30] and calculate the strength function

$$S(E) = \sum_j |\langle 0|F_L|j\rangle|^2 \delta(E_j - E_0). \tag{15}$$

Here, $|0\rangle$ is the RPA ground state and the sum is over all RPA excited states $|j\rangle$ with the corresponding excitation energies E_j. We adopt the single particle scattering operator

$$F_L = \sum_i f(r_i) Y_{L0}(i) \tag{16}$$

for isoscalar ($T = 0$) excitations and

$$F_L = \frac{Z}{A}\sum_n f(r_n) Y_{L0}(n) - \frac{N}{A}\sum_p f(r_p) Y_{L0}(p) \tag{17}$$

for isovector ($T = 1$) excitations. In Eqs. (16) and (17) we use the operator $f(r) = r$, for the isovector dipole ($T = 1$, $L = 1$) and $f(r) = r^3 - (5/3)\langle r^2 \rangle r$ for the isoscalar dipole ($T = 0$, $L = 1$), to eliminate possible contribution of the spurious state mixing [16, 28, 29]. For the isoscalar and isovector monopole ($L = 0$), quadrupole ($L = 2$) and octopole ($L = 3$) excitations we use the operators $f(r) = r^2$, r^2, and r^3, respectively. We then determine the energy moments of the strength function,

$$m_k = \int_0^\infty E^k S(E)\, dE. \tag{18}$$

The centroid energy, E_{CEN}, and the constraint energy, $E_0 = E_{CON}$, are then obtained from

$$E_{CEN} = \frac{m_1}{m_0}, \tag{19}$$

$$E_{CON} = \sqrt{\frac{m_1}{m_{-1}}}, \tag{20}$$

respectively.

We have carried out fully self-consistent Hartree - Fock (HF) based RPA calculations of the isoscalar giant monopole resonance (ISGMR), dipole (ISGDR), quadrupole (ISGQR), and the octopole (ISGOR) strength functions and for the isovector giant monopole resonance (IVGMR), dipole (IVGDR), quadrupole (IVGQR) and octopole (IVGOR) strength functions using a wide range of Skyrme type effective interactions. In the next section we present the results of our calculations and compare with available experimental data.

5. Results and discussion

In Table 2 we give the values for the resulting Skyrme parameters obtained at the minimum value of the $\langle \chi^2 \rangle$ together with the various quantities characterizing the nuclear matter; binding energy per particle B/A, incompressibility coefficient K, saturation density ρ_0, effective mass, m^*, and symmetry energy coefficient $J = E_{sym}(\rho_0)$. Also shown in Table 2 are the coefficient L which is directly related to the derivative of the symmetry energy, the enhancement factor, κ, associated with the IVGDR and the Landau spin-isospin particle-hole interaction parameter G'_0. The KDE0 and KDE0v1 Skyrme interactions where obtained by fits the HF results, taking into account only the direct Coulomb term [9, 31]. The KDEX interaction was determined [32] by taking into account the contribution of the ground state RPA correlations to binding energies and charge radii.

Table 2. **Values of the Skyrme parameters and the corresponding physical quantities of nuclear matter for the KDE0 and KDE0v1 and KDEX interactions**

Parameter	KDE0	KDE0v1	KDEX
t_0 (MeV fm^3)	-2526.5110	-2553.0843	-1419.8304
t_1 (MeV fm^5)	430.9418	411.6963	309.1373
t_2 (MeV fm^5)	-398.3775	-419.8712	-172.9562
t_3(MeVfm$^{3(1+\alpha)}$)	14235.5193	14603.6069	10465.3523
x_0	0.7583	0.6483	0.1474
x_1	-0.3087	-0.3472	-0.0853
x_2	-0.9495	-0.9268	-0.6144
x_3	1.1445	0.9475	0.0220
W_0(MeV fm^5)	128.9649	124.4100	98.8973
α	0.1676	0.1673	0.4989
B/A (MeV)	16.11	16.23	15.96
K (MeV)	228.82	227.54	274.20
ρ_0 (fm^{-3})	0.161	0.165	0.155
m^*/m	0.72	0.74	0.81
J (MeV)	33.00	34.58	32.76
L (MeV)	45.22	54.69	63.70
κ	0.30	0.23	0.33
G'_0	0.05	0.00	0.41

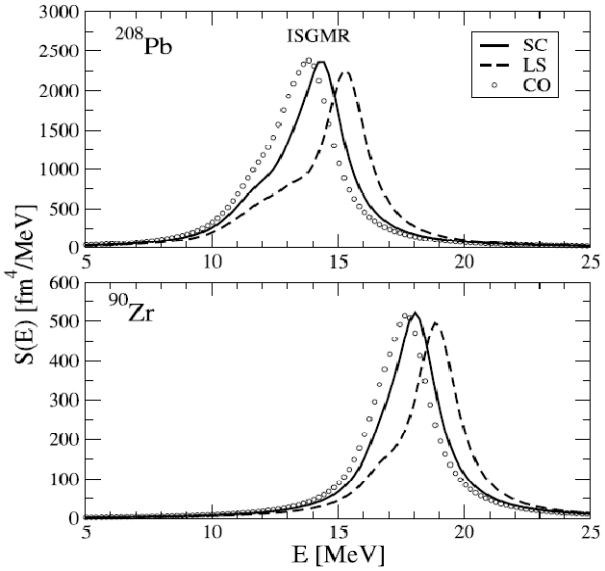

Fig. 1. Strength functions of isoscalar giant monopole for ^{208}Pb and ^{90}Zr nuclei calculated using the KDE0 interaction [9]. SC (full line) corresponds to the fully self-consistent calculation where LS (dashed line) and CO (open circle) represent the calculations without the ph spin-orbit and Coulomb interactions in the RPA, respectively.

In Fig. 1 we present the HF-based RPA results for the strength functions of the ISGMR in ^{208}Pb and ^{90}Zr, using the KDE0 Skyrme interaction [9]. The full line (SC) corresponds to the fully self-consistent calculations. The dashed line and the open circle line represent the results obtained with violation of self consistency in the RPA calculations, by neglected the particle-hole spin-orbit (SO) and Coulomb (CO) interactions. Note the shift of about 1 MeV in the ISGMR energy, which corresponds to a shift of 30 MeV in the value of the nuclear matter incompressibility coefficient K.

In Table 3 we present the results of fully self-consistent HF-based RPA for the centroid energies of the ISGMR (see Refs. [26, 30]) for several nuclei, using the KDE0 [9], SK255 [34], and SGII [33] Skyrme interactions and the results obtained within the relativistic mean-field (RMF)-based RPA using the NL3 interaction [35], and compare with the experimental data of Refs. [36, 37] with the proper excitation energy range (ω_1 - ω_2). We point out that the centroid energy of the ISGMR for the SGII interaction is lower than that of the KDE0 interaction (shown in Table 3) and is also significantly lower than that obtained in RPA calculations with violations of self-consistency, demonstrating the importance of carrying out fully self-consistent HF-based RPA calculations. Moreover, considering the results for the SK255 and NL3, we conclude that it is possible to build *bona fide* Skyrme forces with K close to that obtained in relativistic models which also reproduce the experimental data for the centroid energies of the ISGMR (i.e. demonstrating model independence in determining *K*). We have also found that $K = 240 \pm 20$ MeV. The uncertainty of 20 MeV is mainly due to the uncertainty in $E_{sym}(\rho)$ (see the review in Ref. [12]).

Table 3. **Results of fully self-consistent RPA calculations for the centroid energies of the ISGMR for interactions with various values of the incompressibility *K* and symmetry *J* coefficients (in MeV), compared with experimental data [36, 37]**

Nucleus	$\omega_1 - \omega_2$	Expt.	NL3	SK255	SGII	KDE0
^{90}Zr	0-60		18.7	18.90	17.89	18.03
	10-35	17.81± 0.30		18.85	17.87	17.98
^{116}Sn	0-60		17.1	17.31	16.36	16.58
	10-35	15.85± 0.20		17.33	16.38	16.61
^{144}Sm	0-60		16.1	16.21	15.26	15.46
	10-35	15.40± 0.40		16.19	15.22	15.44
^{208}Pb	0-60		14.2	14.34	13.57	13.79
	10-35	13.96± 0.20		14.38	13.58	13.84
K (MeV)			272	255	215	229
J (MeV)			37.4	37.4	26.8	33.0

In Fig. 2, we show our results [38], of fully self-consistent HF-based RPA calculations using 15 commonly employed Skyrme type interactions, for the centroid energies of the IVGDR in ^{40}Ca and ^{48}Ca, and their differences, as functions of $J(0.1)/J$, where $J(0.1)=E_{sym}(0.1)$ is the symmetry energy at matter density of 0.1 fm^{-3} (about $(2/3)\rho_0$). An agreement with experimental data [39 - 41] is obtained for several interactions. However, a very weak correlation is obtained between the centroid energies and $J(0.1)/J$. We point out that similar results were obtained when using, instead of $J(0.1)/J$, the quantities L and K_{sym}.

Recent high-resolution measurement [24] of the electric isovector dipole polarizibility α_D in ^{208}Pb was used to determine the magnitude of the neutron skin thickness in this nucleus, resulting in the value of $r_n - r_p = 0.156$ (.025) fm. However, the analysis in this work was based on only one form of energy density functional (EDF), associated with the Skyrme SV-min interaction. Here we examine the conclusion of the work of Ref. [24]. For this purpose, we have carried out [38] fully self-consistent Hartree - Fock (HF) based RPA calculations of the electric isovector dipole polarizability (directly related to m_{-1} of the IVGDR strength function) in ^{208}Pb, using over 27 commonly employed Skyrme type interaction.

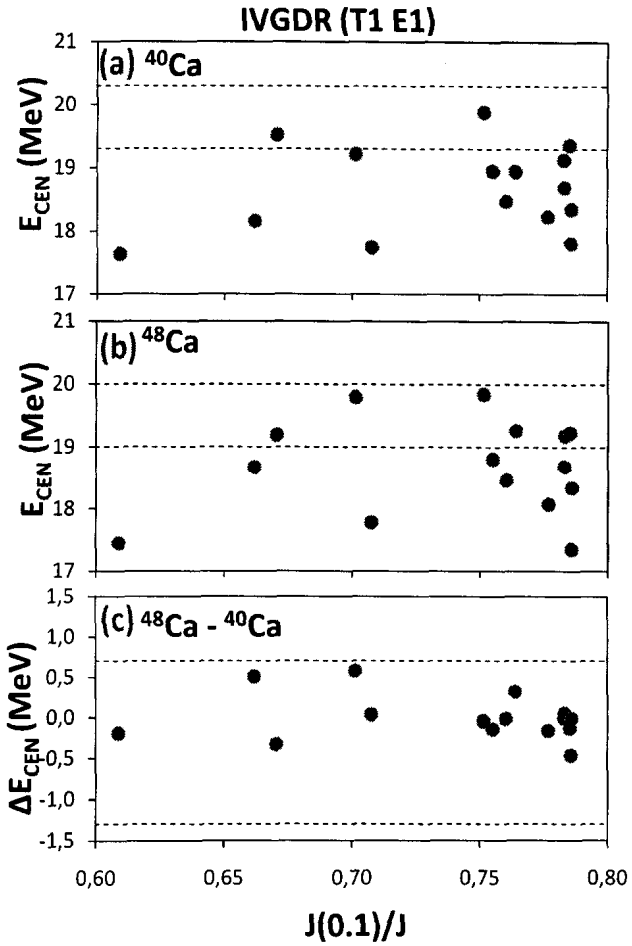

Fig. 2. Centroid energies and their differences of the IVGDR in ^{40}Ca and ^{48}Ca as functions of $J(0.1)/J$. The experimental data [39 - 41] are shown as the regions between the dashed lines

In Fig. 3 we present the predictions [38] of these interactions for the polarizability α_D and $r_n - r_p$. The experimental data [24] on α_D is shown as the region between the dashed lines. Also shown is the Pearson correlation coefficient $C_{AB} = 0.55$, which indicates a weak correlation between α_D and $r_n - r_p$. We thus conclude that EDFs associated with theoretical predictions of values of $r_n - r_p$ in the range of 0.14 to 0.20 fm are consistent with the experimental data on α_D.

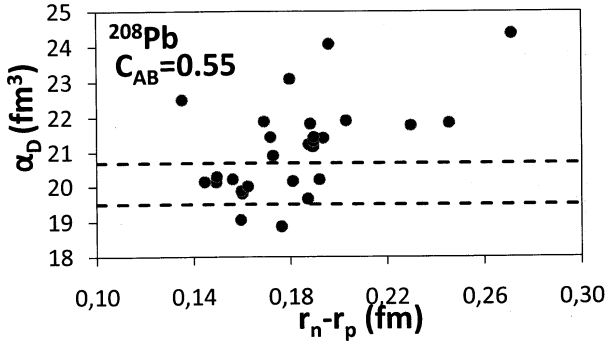

Fig. 3. The IVGDR electric polarizability α_D as a function of $r_n - r_p$. The experimental data on α_D [24] is shown as the region between the dashed lines. The results of fully self-consistent HF-based RPA calculation of 37 commonly used Skyrme interaction are shown as solid points. Also shown is the Pearson correlation coefficient C_{AB}.

6. Conclusions

We have described a method, based on the simulated annealing approach, for determining a modern energy density functional within the Skyrme Hartree - Fock (HF) theory by carrying out a fit to extensive set of experimental data and further include constraints on the Skyrme parameters. We then presented results of calculations for the excitation strength functions and centroid energies of giant resonances within the HF-RPA approach. In particular:

- We have developed new energy density functionals based on Skyrme type effective nucleon-nucleon interactions (KDE0, KDE0v1, KDEX,) which are applicable for calculating properties of rare nuclei and neutron stars.
- We have demonstrated the importance of carrying out fully self-consistent HF-based RPA calculations of strength function of giant resonances.
- We have demonstrated that calculations of the energies of the isoscalar compression modes (ISGMR and ISGDR) within HF-based RPA using Skyrme forces and within relativistic model lead to the model independent value of $K = 240 \pm 20$ MeV for incompressibility coefficient of symmetric nuclear matter. The uncertainty of 20 MeV is due to the uncertainty in the density dependence of the symmetry energy.

- We pointed out the weak dependence of the isotopic dependence of the energy of the IVGDR on the density dependence of the symmetry energy
- We pointed out the weak dependence of the energies and electric polarizability associated with the IVGDR, the isotopic dependence of the energies of giant resonances and the neutron skins, $r_n - r_p$, in neutron rich nuclei on the density dependence of the symmetry energy. These are still open problems.

We add that for possible improvements for the EDF we have to:

- Account for the isospin dependence of the spin-orbit interaction.
- Include additional data, such as the IVGDR (sensitive to $E_{sym}(\rho)$) and the isoscalar giant quadrupole resonance (sensitive to m^*), for the EDF fit.

ACKNOWLEDGEMENTS

This work was supported in part by the US Department of Energy under Grant Nos. DE-FG02-93ER40773. We thank V.M. Kolomietz, B.K. Agrawal, T. Sil, D.C. Fuls, M.R. Anders and D.H. Youngblood, for discussions and collaboration on work reported here.

REFERENCES

1. *Kohn W.* // Rev. Mod. Phys. - 1999. - Vol. 71. - P. 1999.
2. *Vautherin D., Brink D.M.* // Phys. Rev. - 1972. - Vol. C5. - P. 626.
3. *Skyrme T.H.R. //* Phil. Mag. - 1956. - Vol. 1. - P. 1043.
4. *Skyrme T.H.R.* // Nucl. Phys. - 1959. - Vol. 9. - P. 615.
5. *Chabanat E., Bonche R., Haensel R. et al.* // Nucl. Phys. - 1997. - Vol. A627. - P. 710.
6. *Chabanat E., Bonche R., Haensel R. et al.* // Nucl. Phys. - 1998. - Vol. A635. - P. 231.
7. *Bender M., Heenen R.H., Reinhard R-G.* // Rev Mod. Phys. - 2003. - Vol. 75. - P. 121.
8. *Dutta M., Lourenco O., Sa Martins J.S. et al.* // Phys. Rev. - 2012. - Vol. C85. - P. 035201.
9. *Agrawal B.K., Shlomo S., Kim V.Au.* // Phys. Rev. - 2005. - Vol. C72. - P. 014310.
10. *Bohr A., Mottelson B.M.* // Nuclear Structure II. - New York: Benjamin, 1975.
11. *Ring P., Schuck P.* The nuclear many-body problem. - New York - Heidelberg - Berlin: Springer, 1980.
12. *Shlomo S., Kolomietz V.M., Colo G.* // Eur. Phys. J. - 2006. - Vol. A30. - P. 23 and references therein.
13. *Glendening N.K.* // Phys. Rev. - 1988. - Vol. C37. - P. 2733.
14. *Lattimer J.M., Prakash M.* // Phys. Rep. - 2007. - Vol. 442. - P. 109.
15. *Blaizot J.P.* // Phys. Rep. - 1980. - Vol. 64. - P. 171.
16. *Shlomo S., Sanzhur A.I.* // Phys. Rev. - 2002. - Vol. C65. - P. 044310.
17. *Krivine H., Treiner J., Bohigas O.* // Nucl. Phys. - 1980. - Vol. A336. - P. 155.
18. *Lipparini E., Stringari S.* // Phys. Rep. - 1989. - Vol. 175. - P. 103.
19. *Myers W.D., Swiatecki W.J.* // Phys. Rev. - 1998. - Vol. C57. - P. 3020.
20. *Satpathy L., Maheshwari V.S.U., Nayak R.C.* // Phys. Rep. - 1999. - Vol. 319. - P. 85.
21. *Shlomo S., Friedman E.* // Phys. Rev. Lett. - 1977. - Vol. 39. - P. 1180.
22. *Shlomo S., Schaeffer R.* // Phys. Lett. - 1979. - Vol. B83. - P. 5.
23. *Friedman E., Shlomo S.* // Z. Physik. - 1977. - Vol. A283. - P. 67.
24. *Tamii A. et al.* // Phys. Rev. Lett. - 2011. - Vol. 107. - P. 062502.
25. *Shlomo S., Bertsch G.* // Nucl. Phys. - 1975. - Vol. A243. - P. 507.
26. *Reinhardt P.-G.* // Ann. Phys. (Leipzig). - 1992. - Vol. 1. - P. 632.
27. *Nakatsukasa T., Inakura T., Yabana K.* // Phys. Rev. - 2007. - Vol. C76. - P. 024318.
28. *Agrawal B.K., Shlomo S., Sanzhur A.I.* // Phys. Rev. - 2003. - Vol. C67. - P. 034314.
29. *Agrawal B.K., Shlomo S.* // Phys. Rev. - 2004. - Vol. C70. - P. 014308.
30. *Sil Tapas, Shlomo S., Agrwal B.K., Reinhard P.-G.* // Phys. Rev. - 2006. - Vol. C73. - P. 034316.
31. *Shlomo S.* // Rep. Prog. Phys. - 1978. - Vol. 41. - P. 957.
32. *Fuls D.C.*, unpublished.
33. *Giai N.V., Sagawa H.* // Phys. Lett. - 1981. - Vol. B106. - P. 379.
34. *Agrawal B.K., Shlomo S., Kim Au V.* // Phys. Rev. - 2003. Vol. C68. - P. 031304R.
35. *Lalalazissis G.A., Konig J., Ring P.* // Phys. Rev. - 1997. - Vol. C55. - P. 540.
36. *Youngblood D.H. et al.* // Phys. Rev. - 2004. - Vol. C69. - P. 034315.
37. *Youngblood D.H. et al.* // Phys. Rev. - 2004. - Vol. C69. - P. 054312.
38. *Anders M.R. et al.* In preparation.
39. Center For Photonuclear Experiments Data // http://cdfe.sinp.msu.ru/
40. *O'keefe G.J., Thompson M.N., Assafiri Y.I. et al.* // Nucl. Phys. - 1987. - Vol. A469. - P. 239.
41. *Veyssiere A. et al.* // Nucl. Phys. - 1974. - Vol. A277. - P. 513.

HOW DOES THE CARBON FUSION REACTION HAPPEN IN STARS?

X. Tang[1], B. Bucher[1], X. Fang[1], M. Notani[1], W. P. Tan[1], Y. Li[1,3], P. Mooney[1], H. Esbensen[2], C. L. Jiang[2], K. E. Rehm[2], C. J. Lin[3], E. Brown[4]

[1] Department of Physics and Joint Institute for Nuclear Astrophysics, University of Notre Dame, Notre Dame, IN, USA
[2] Physics Division, Argonne National Laboratory, Argonne, IL, USA
[3] China Institute of Atomic Energy, Beijing, China
[4] Department of Physics and Astronomy, National Superconducting Cyclotron Laboratory, and the Joint Institute for Nuclear Astrophysics, Michigan State University, East Lansing, Michigan, USA

The $^{12}C + ^{12}C$ fusion reaction is one of the most important reactions in the stellar evolution. Due to its complicated reaction mechanism, there is great uncertainty in the reaction rate which limits our understanding of various stellar objects, such as massive stellar evolution, explosions on neutron stars, and supernovae from accreting white dwarf stars. In this paper, I will review the challenges in the study of carbon burning. I will also report recent results from our studies: 1) an upper limit for the $^{12}C + ^{12}C$ fusion cross sections, 2) measurement of the $^{12}C + ^{12}C$ at deep sub-barrier energies, and 3) a new measurement of the $^{12}C(^{12}C, n)$ reaction. The outlook for the studies of the astrophysical heavy-ion fusion reactions will also be presented.

1. Introduction

In 1960 Almqvist, Kuehner and Bromley discovered several resonances in collisions between ^{12}C nuclei. For at least three energies, $E_{c.m.} = 5.68$, 6.00 and 6.32 MeV, they observed increased yields for the reaction products: p, α, n and γ. These resonances have characteristic widths of about 100 keV and were interpreted as signatures for the formation of nuclear molecules [1, 2, 3]. In the following years, the discoveries of such resonances continued down to the lowest energies. For instance, the most recent published measurement of the $^{12}C+^{12}C$ fusion reported a strong resonance at $E_{c.m.} = 2.14$ MeV [4].

Apart from its interest to nuclear reaction studies, the $^{12}C + ^{12}C$ fusion reaction also plays a crucial role in a number of important astrophysical scenarios, such as explosions on the surface of neutron stars, white dwarf (type Ia) supernovae, and massive stellar evolution [5]. For astrophysics, the important energy range extends from 1 MeV to 3 MeV in the center of mass frame, which is only partially covered by experiments. Therefore, an extrapolation is the only resource available to obtain the reaction rate for astrophysical applications. The currently adopted reaction rate is established based on the modified S factor

$$S^*(E_{c.m.}) = \sigma(E_{c.m.})\,E_{c.m.}\exp\left(\frac{87.21}{\sqrt{E}_{c.m.}} + 0.46E_{c.m.}\right). \quad (1)$$

An S* factor of $3 \cdot 10^{16}$ MeV*b was obtained by fitting the data measured by Patterson [6], Spinka [7] and Becker [8]. This averaged value was extrapolated towards lower energies by assuming that the averaged S* factor remains constant at sub-barrier energies [6, 9]. At present, there is nothing known about the energies and strengths of resonances in the energy region below $E_{c.m.} = 2$ MeV. Besides this uncertainty, the recent study of fusion hindrance has suggested a new extrapolation which is smaller than the adopted one [5, 10]. Therefore, our understanding of the $^{12}C + ^{12}C$ fusion rate is highly uncertain.

2. The experimental efforts at Notre Dame

To aid in the understanding of this reaction, the carbon fusion project at Notre Dame was established in 2007 with the aim of measuring the reaction cross section and decay branches at low energies as well as providing a reliable extrapolation into the energies that cannot be reached by experiment. In this paper, we report on three studies: 1) an upper limit for the $^{12}C + ^{12}C$ total fusion cross section at astrophysical energies, 2) the measurement of the $^{12}C + ^{12}C$ fusion cross sections at deep sub-barrier energies, and 3) a measurement of the neutron branching at low-energy with an improved extrapolation based on the mirror reaction channel, $^{12}C(^{12}C, p)$.

2.1. An upper limit for the $^{12}C+^{12}C$ fusion cross sections

The primary goal of this work was to study the carbon isotope fusion reactions, which display a much smoother excitation function than $^{12}C + ^{12}C$, at sub-barrier energies in hope to find a better model for the general behavior of $^{12}C + ^{12}C$ at these energies. The modeling of $^{12}C + ^{12}C$ itself is complicated by the potential existence of large resonances, whereas this complication appears to be absent from the isotope reactions. For example, the most recently published measurement at energies below 3 MeV center-of-mass (the energy range of astrophysical interest is 1 - 3 MeV) by Spillane et al. shows a large, narrow resonance at 2.14 MeV [4]. An even stronger resonance at 1.5 MeV is predicted by Cooper et al. based on comparisons between superburst models and observations [10]. By looking at the isotope systems, one can effectively remove the added complication from the resonant structure and more easily study

the general behavior of the $^{12}C+^{12}C$ fusion reaction.

The $^{12}C + ^{13}C$ fusion reaction was measured at Notre Dame with the goal of extending the already existing data from [12] to lower energies. The 11 MV FN tandem accelerator at Notre Dame was used to provide beams of ^{13}C ions with intensities up to 1 pμA for bombardment on a thick graphite target. The details of the measurement are given in [13], but the main idea was to measure $^{13}C(^{12}C, p)^{24}Na$ by counting the beta decays from the residual ^{24}Na ($t_{1/2}$ = 15 h) using the beta-gamma coincidence technique. After correcting for the contributions from the other decay branches, the total fusion cross section measurements were extended down below 2.7 MeV c.m. where the cross section value drops to 20 nb (a factor of 50 less than the previous lowest measurement). The new data shows good agreement with the data from [12] in the overlapping energies (Fig. 1).

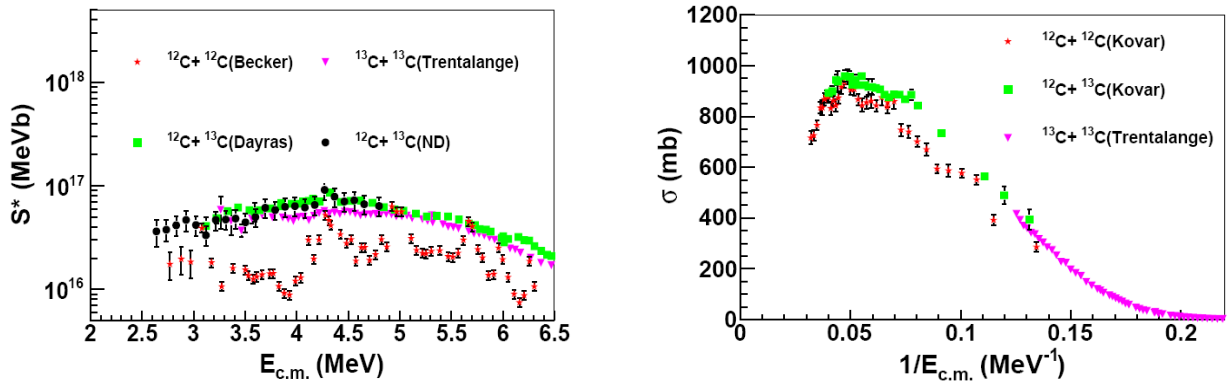

Fig. 1. *Left* - The experimental S* factors of three carbon-isotope fusion reactions around or below the Coulomb barrier: $^{12}C + ^{12}C$ (red stars) [8], $^{12}C + ^{13}C$ from Ref. [13] (black points) and Ref. [12] (green squares), and $^{13}C + ^{13}C$ [14] (magenta triangles). The systematic uncertainties, 30 % for the $^{12}C+^{12}C$ data, 15 % for the $^{13}C+^{13}C$data, and 30 % for the $^{12}C + ^{13}C$data from Ref. [12] [$^{12}C + ^{13}C$ (Dayras)], are not shown in the graph. The $^{12}C + ^{13}C$ data reported in Ref. [13] [$^{12}C + ^{13}C$(ND)] are dominated by a 20 % systematic uncertainty, which is included in this graph. *Right* - The experimental cross sections of three carbon-isotope fusion reactions above the Coulomb barrier: $^{12}C + ^{12}C$ (red points) [15], $^{12}C + ^{13}C$ (green squares) [15] and $^{13}C + ^{13}C$ [14] (magenta triangles).

When the $^{13}C + ^{13}C$ and $^{12}C + ^{12}C$ excitation functions from [14] and [8], respectively, are plotted together with the $^{12}C + ^{13}C$ using the cross section factor defined by equation (1), which is traditionally used to study the $^{12}C + ^{12}C$ fusion reaction [6], a striking correlation is realized. The $^{12}C + ^{12}C$ cross section is suppressed relative to the isotope fusion reactions except at the resonant energies where the cross sections are in an excellent agreement! The two isotope systems agree with each other within the systematic uncertainties of the measurements. Considering a systematic uncertainty of 15 - 30 % for the data from Refs. [8, 12, 14] (not shown in Fig. 1), the major resonant cross sections of $^{12}C + ^{12}C$ (Er = 3.1, 4.3, 4.9, 5.7, 6.0, and 6.3 MeV) match remarkably well with the fusion cross sections of the other two carbon isotope combinations within their quoted uncertainties. This correlation between $^{12}C + ^{12}C$ and the isotope reactions holds from the highest measured energy, ~40 MeV, down to the lowest measured energies, 2.7 MeV, in Ref. [8]. In other words, the isotope fusion reactions provide an upper bound on the $^{12}C+^{12}C$ fusion within the measured energy ranges [13].

Since the isotope excitation functions behave relatively smoothly with energy, they are much more easily modeled. In order to extrapolate the isotope reactions down to the lower, unmeasured energies, a coupled-channels calculation was performed based on the M3Y+repulsion double-folding potential with ingoing-wave-boundary-conditions (IWBC), where the details of the calculation are given in [16]. The results of the calculation agree with the experimental data within the systematic uncertainty over the measured energy range (Fig. 2). The parameters for the nuclear potentials used in the isotope fusion calculations were then used to constrain the potential for $^{12}C + ^{12}C$. The result of this calculation is in very good agreement with the experimental resonant cross section values except for the lowest few data points defining the large 2.14 MeV resonance measured in [4]. Considering the difficulty of this measurement, peculiarities raised in [13], and the fact that a subsequent measurement by the same group observed a much weaker resonance [17] (within the upper limit established here), these last few data points are questionable and in need of further experimental confirmation. The hypothetical resonance predicted in [11] deviates to even larger values above our upper limit leaving its existence in doubt at this moment.

It is interesting to note that the coupled channel prediction based on IWBC does not describe the average trend of the cross sections, but rather matches the observed $^{12}C + ^{12}C$ peak cross sections. Here we provide a qualitative explanation for our results, which is based on the intrinsic excited nuclear molecule model (Nogami - Imanishi model) [18]. In this model, the resonances of $^{12}C + ^{12}C$ are explained as the result of a coupling effect between the elastic channel and the inelastic channels, such as $^{12}C(0^+, g.s.) + ^{12}C(2^+,4.44\ MeV)$ and $^{12}C(2^+, 4.44\ MeV) + ^{12}C(2^+,4.44\ MeV)$. The resonances only happen at certain energies when the ingoing wave matches the inner boundaries for the formation of molecular states. For $^{12}C + ^{12}C$, the resonances are isolated because of the low level density for the molecular states. For the isotope systems ($^{12}C + ^{13}C$ and $^{13}C + ^{13}C$), the $^{12}C + ^{12}C$ core or ^{12}C core + ^{12}C core may still behave in a way

similar to the $^{12}C + ^{12}C$ system. The addition of one or two valence neutrons significantly increases the level density of the molecular states and leads to much more relaxed boundary condition to be matched with the ingoing wave. Therefore, the coupled-channels calculation with IWBC becomes a reasonable approximation for the isotope systems because of their higher level densities than the $^{12}C + ^{12}C$ system. However, the $^{12}C + ^{12}C$ fusion cross sections could only match with the isotope systems at several resonant energies because the level density of the molecular states is low. To verify this qualitative explanation, detailed coupled channel calculations are urgently needed to investigate the role of the valence neutron in the carbon isotope fusion process.

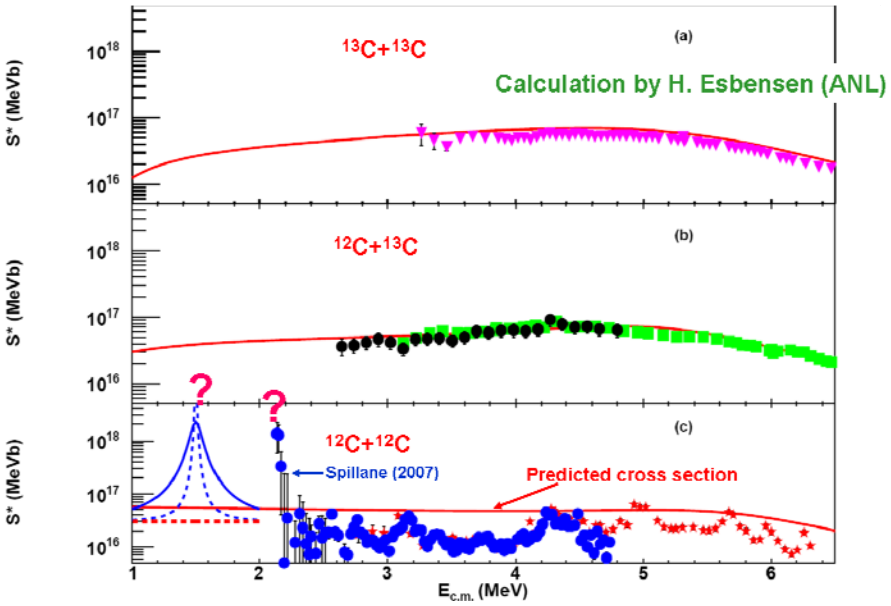

Fig. 2. The coupled channels calculations for: *a* – $^{13}C + ^{13}C$ with data from [14]; *b* – $^{12}C + ^{13}C$ with data from [12] (squares) and new ND data (circles) [13]; *c* – $^{12}C + ^{12}C$ with data from [8] (stars) and [4] (circles). The calculations show good agreement with the experimental data of the isotope systems down to the lowest measured energies. For the $^{12}C + ^{12}C$ system, the calculation matches very well at the resonance energies excepting the last two points of the Spillane et al. data set [4] and the hypothetical Cooper resonance [11].

2.2. Measurements at deep sub-barrier energies

The measurements at deep sub-barrier energies are important for us to understand the reaction mechanism and provide a more reliable extrapolation towards the region which cannot be covered by current experiments. It is also interesting to test the upper limit we have proposed based on our study on carbon isotope fusions. There are two difficulties in measurements. 1) How to identify the few fusion events from the intense background? 2) How to connect the observable reaction channels with the total fusion cross section?

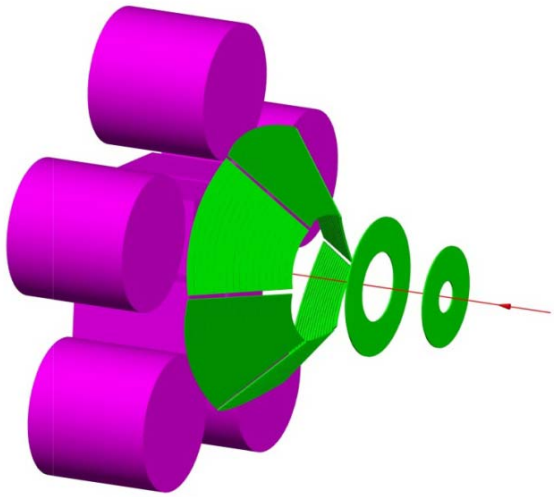

Fig. 3. Setup for SAND silicon detector array (green) in coincidence with GEORGINA gamma array (magenta). The direction of ^{12}C beam is indicated by the red arrow. The thick target on the surface of gamma detectors is blocked by the silicon detectors.

At Notre Dame, we are preparing two experiments: 1) particle-gamma coincidence with GEORGINA (a compact Ge detector array) and SAND (a silicon array covering 2π solid angle) and 2) charged particle detection with a HELIOS-type solenoid spectrometer [19]. In the first approach, the SAND array provides the energy and angle of the light charged particles with which a unique reaction Q-value can be constructed for each decay channel while the GEORGINA array records the energies of emitted gamma-rays. With the coincidence between the two detector arrays, we can greatly suppress contributions from cosmic and room background. To avoid the target thickness variation during the experiment, a 1-mm thick HOPG (Highly Ordered Pyrolytic Graphite) target will be used in the experiment. A test experiment has been done at $E_{c.m.}$ = 4, 4.5 and 5 MeV using the ATLAS facility at ANL [20]. In this test, a 20 $\mu g/cm^2$ thin ^{12}C target was used. The light charged particles and the emitted gamma rays were detected by a large area strip detector and Gammasphere, respectively. The particle-gamma coincidence expe-

riment with GEORGINA and SAND will take place later this year at Notre Dame when the new 5 MV single end accelerator delivers high intensity ^{12}C beam.

Even though the particle-gamma conincidence provides a much cleaner background than any past experiments using either particle detectors or Ge detectors, there are transitions that only emit particles without gamma-rays (e.g. Transition to ground states of fusion residues) for which the solenoid spectrometer seems to be a better approach. In this approach, both the target and detector are placed on the axis of a uniform magnetic field while the light charged particles generated at the target move on helical orbits and are bent back to the axis after one cyclotron period. The position-sensitive silicon detector array, located on the axis, records energy, target-to-detector position and TOF with respect to beam pulses. The position and the energy of the particles translate into the desired information of excitation energy and center-of-mass angle. A study of the $^{12}C + ^{12}C$ fusion reaction has been done at $E_{c.m.} = 4$, 5 and 6 MeV using one of the existing solenoids of the TWINSOL facility at Notre Dame. Two 1×5 cm^2 1-D position sensitive detectors were placed around the axis at the upstream direction with respect to the 20 μg/cm^2 thick carbon foil. The closest distance between the detectors and target were set as 8 cm initially and latter increased to 23 cm to cover longer distance. To stop the scattered ^{12}C particles from reaching the detectors, a 5.7 μm Aluminum degrader was placed on the surface of detectors. The spectrum of the detected energy vs. position plot shown in Fig. 4 indicates that a clean observation of the transitions to the ground state of ^{23}Na has been achieved. We are working on the beam collimation system with a hope to get clean observation of the α_0 channel in the near future. Meanwhile, it is necessary to look for funding to build a complete silicon array so that the measurement can be efficiently carried out at lower energies.

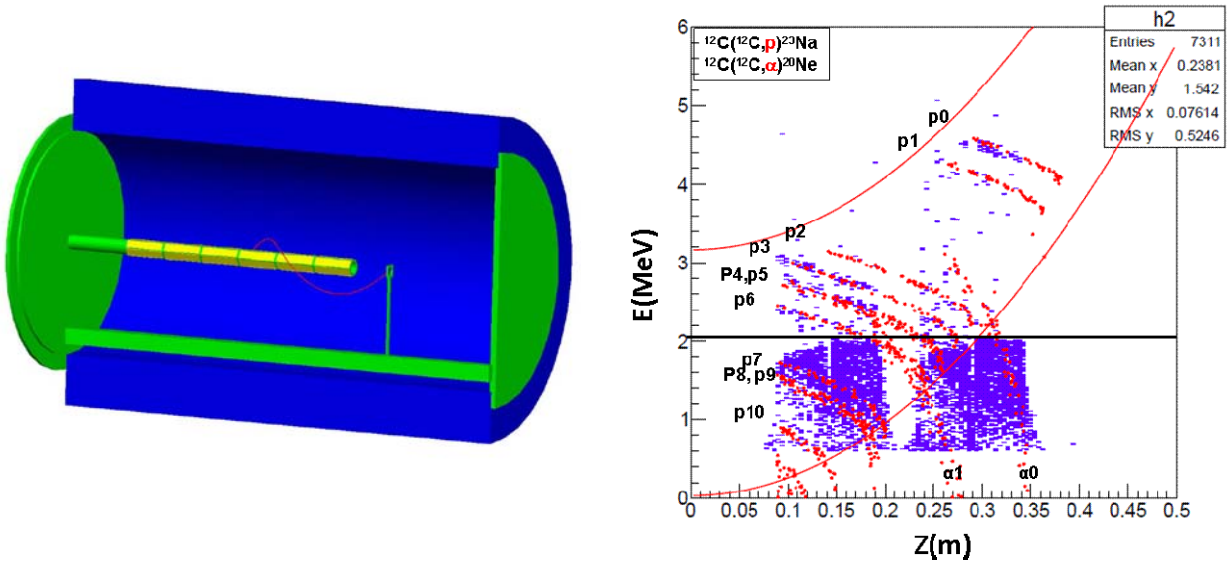

Fig. 4. *Left* - The SSNAP solenoid spectrometer at Notre Dame. The beam goes from left to right through the hollow tube and hits the target. A reaction product is emitted at a backward angle and bent back to the axis after one cyclotron period. The 31-cm long position-sensitive Silicon detector located on the axis, records energy, target-to-detector position and TOF with respect to beam pulses. There was only two silicon detectors used in our test. The target distance from the beginning of detector array was set as 8 cm and 23 cm, respectively, to cover a longer distance. The diameter of the vacuum chamber is 28 cm. *Right* - The energy vs. position spectrum measured for $^{12}C + ^{12}C$ fusion reaction at $E_{c.m.} = 4$ MeV. A 5.7 mm thick aluminum foil was placed before the detectors to stop scattered ^{12}C particles. The blue points are the experimental result while the red points are produced by a GEANT4 simulation. The p_0 and p_1 channels are clearly separated from the background which dominates the region below 2 MeV. The scattered points between the p_1 and p_2 groups may come from the $^{12}C + ^{13}C$ reaction. The two red lines show the acceptance of the spectrometer.

Because of the complication of the decay schemes of the fusion residues, it is a great challenge to get the total fusion cross section from the observable decay channels. For example, in the past, gamma ray measurements were only focused on the cross sections to two characteristic lines, 440 keV for ^{23}Na and 1634 keV for ^{20}Ne. The charged particle measurements were limited to the channels above the huge background incurred by the H/D contaminants in target. In most analyses in the past, the total $^{12}C + ^{12}C$ fusion cross sections were obtained by a simple summation of the observed decay channels. Using a statistical model, we have estimated the contribution from those unobserved channels. The theoretical result was compared with the predicted cross section based on the partial cross sections measured by Becker et al. [8]. The results shown in Figs. 5 and 6 suggest that the total fusion cross section between the range of 1 to 3 MeV can be determined by combining the information from both particle detection and gamma-ray detections. The fraction for the missing decay channels is well controlled below 4 % at astrophysical relevant energies.

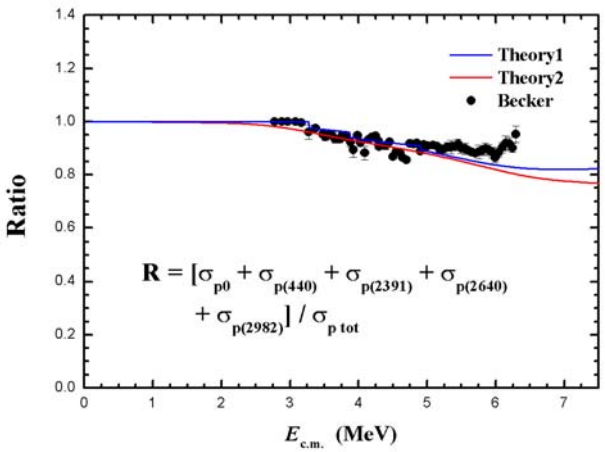

Fig. 5. The ratio of the sum of several observable proton channels to the total cross section of the proton channel (σ_{ptot}). In the graph, σ_{p0} is the cross section for the proton channel to the ground state of ^{23}Na. $\sigma_{p(440)}$, $\sigma_{p(2391)}$, $\sigma_{p(2640)}$ and $\sigma_{p(2982)}$ are corresponding to the cross sections of the gamma transitions of ^{23}Na, (440 keV→0), (2390 keV→0), (2639 keV→0) and (2982 keV→0), respectively. The black points are the predicted ratio based on the observed proton cross sections by Becker et al. [8] and the known level scheme. The red line (Theory 1) is a prediction by TALYS [21]. In the experimental data, there are various energy limits for different channels because of the complicated background. To simulate the effect, the experimental energy limits are included in the TALYS calculation and the result is shown as the blue line (Theory 2).

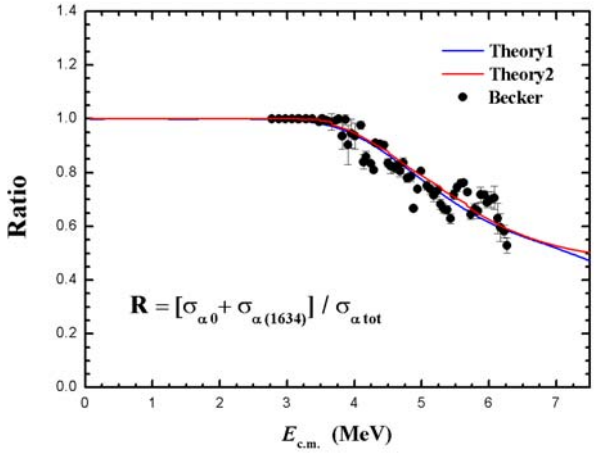

Fig. 6. The ratio of the sum of two observable alpha channels to the total cross section of the alpha channel. In the graph, $\sigma_{\alpha 0}$ is the cross section for the alpha channel to the ground state of ^{20}Ne. $\sigma_{\alpha(1634)}$ is the cross sections for the gamma transition of ^{20}Ne, (1634 keV→0). The blue and red lines are the predications with TALYS [21]. See the caption of Fig. 5 for more details.

With the combinations of the new high current 5 MV accelerator at Notre Dame and the two new highly efficient detection techniques, a great improvement in the detection yield will be achieved. By comparing our approaches with the Naples experiment [17], we expect the detection yield will be improved by one or two orders of magnitudes, depending on the details of the detector configuration. The lowest event rate measured by the Naples experiment is 0.5 evt/day when $E_{c.m.}$ = 2.1 MeV. If we were lucky and achieved an improvement on the detection yield by two orders of magnitude, this would bring the lowest measured energy down to 1.7 MeV. To map the ^{12}C + ^{12}C resonance below 1.7 MeV, we are collaborating with collaborators at the Research Center for Nuclear Physics (RCNP) at Osaka University on a complimentary approach of using the ^{24}Mg(α, α') reaction to search the resonances in ^{24}Mg which may contribute to the ^{12}C fusion cross section at astrophysical energies.

2.3. The low-energy resonances in the ^{12}C(^{12}C,n)^{23}Mg reaction cross section

Carbon burning in the various astrophysical environments proceeds through 3 main reaction channels: ^{12}C(^{12}C, α)^{20}Ne (Q = 4.6 MeV), ^{12}C(^{12}C, p)^{23}Na (Q = 2.2 MeV), and ^{12}C(^{12}C, n)^{23}Mg (Q = -2.6 MeV). At typical astrophysical energies, the contribution from the neutron branch is estimated to be less than 1 % of the total fusion yield. However, this still may be a significant amount to aid in the nucleosynthesis of heavy elements during the weak s-process occurring in massive stars. 1-D massive star models indicate a sensitivity of the abundances produced during shell-carbon burning to this reaction [22]. Isotopes between 60 < A < 110 are most affected with a typical production increase of ~30 % for a factor of 5 enhancement over the standard Dayras et al. branching ratio [23], depending on the specifics of the model. A typical temperature in the shell-carbon burning environment is 1.1 GK which means the relevant astrophysical energies are from ~3.2 MeV down to threshold at 2.6 MeV. The currently existing experimental data stops above 3.5 MeV [6, 21], so stellar models must rely on an extrapolation of the data to the relevant energies. The standard extrapolation is based on a statistical model calculation which is unable to account for the resonant contribution to the rate that is likely important (Fig. 7).

The reaction cross section was measured from 6.5 MeV down to 3.1 MeV using ^{12}C beams produced with the FN tandem accelerator at Notre Dame. Two different approaches have been used to study the neutron channel. The first approach is to detect the ^{23}Mg ($t_{1/2}$ = 11.317 s) β^+ decay using a plastic scintillator. In the experiment, a thin carbon target (thickness 20 μg/cm2) was used, and the ^{23}Mg reaction product was collected using an aluminum catcher placed behind the target. After 20 s of target irradiation, the ^{23}Mg β^+ decays were counted for 40 s after which the process was repeated until sufficient statistics were achieved. The combination of high background yield arising from the hydrogen

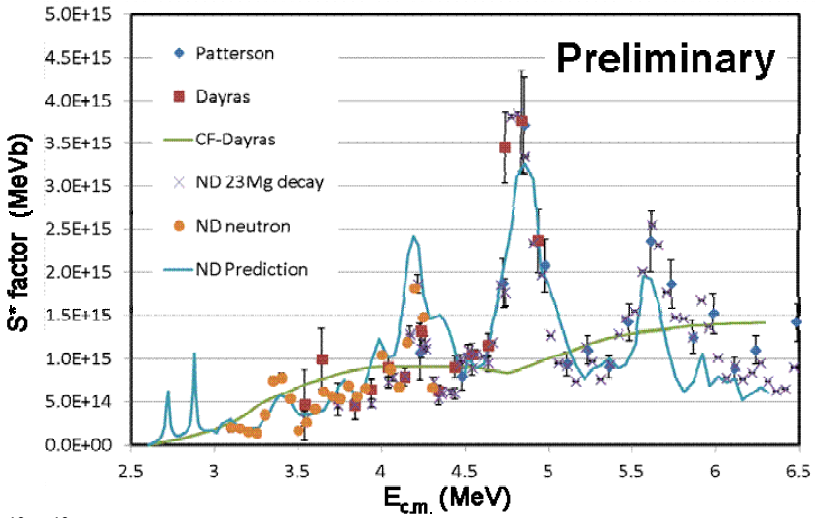

Fig. 7. The existing $^{12}C(^{12}C,p)$ data from Ref. [6] (Patterson) and [23] (Dayras). The statistical model prediction by Dayras et al. is shown as the green line. The important energy range for shell carbon burning extends from 2.8 MeV to 3.2 MeV. Our new prediction based on the measured proton channel data is shown in the blue line. For $E_{c.m.}>3$ MeV, the proton data used in the prediction were measured at Notre Dame. The two resonances at the energies below 3 MeV is predicted with resonance information obtained from the observation of the p_0 and p_1 channels reported in Ref.[17]. The new measurements from Notre Dame are labeled as purple crosses and orange circles.

contaminant in targets and low fusion yield prevented useful measurements below 3.5 MeV. The second method is to detect the neutron directly with a highly efficient ^{3}He detector array. To minimize the hydrogen contaminant, a 1-mm thick HOPG target was used. A LN_2 cooled cooper tube was placed just before the target to prevent hydrogen contamination from the vacuum. With these measurements, the measurement was pushed down to 3.1 MeV.

We also developed a new extrapolation method to accommodate the complicated resonant feature in the $^{12}C + ^{12}C$ fusion reaction and provide a more reliable prediction for the cross sections at the energies below the experimental limit. In this new method, we take the advantage that any neutron branch n_i (i is corresponding to the i^{th} excited state in ^{23}Mg) is exactly the mirror reaction channel for the proton branch p_i (i is corresponding to the i^{th} excited state in ^{23}Na). Any resonance existing in the $^{12}C + ^{12}C$ channel would imprint itself in both proton and the corresponding neutron channels. The code EMPIRE [24] was used to calculate the corresponding ratios between the mirror branches, p_i and n_i. Then considering all the open n_i's for a given energy (below 4.6 MeV, only n_0 and n_1 are open), a total neutron production cross section is generated based on the corresponding p_i production cross sections. The predicted cross sections based on the proton channels are shown in Fig. 7. The results show remarkable accuracy with the measured neutron data and extend into the experimentally inaccessible energy range (Fig. 2). For most data points, the deviations between the prediction and the measurement are less than 40 %. This discrepancy is not surprising because the optical models used in EMPIRE only describe the average penetrabilties for the $p_i + ^{23}$Na and $n_i + ^{23}$Mg. The predicted resonance at 3.4 MeV has been confirmed by our recent measurement using neutron detection. Two more sharp resonances are predicted at energies below 3 MeV based on the experimental data from Ref. [17]. The corresponding new reaction rate is about a factor of 2 of what Dayras has recommended. This leads to the conclusion that the $^{12}C(^{12}C, n)$ role in the weak s-process of Population I massive stars is quite limited compared with the major neutron source, $^{22}Ne(\alpha, n)$. The impact to other relevant astrophysical scenarios, such as the nucleosynthesis in metal poor massive stars and explosive carbon burning, is being studied.

3. Summary and outlook

The study of the $^{12}C+^{12}C$ fusion process at deep sub-barrier energies represents a main challenge in nuclear astrophysics. At Notre Dame, we have established an upper limit for the $^{12}C + ^{12}C$ fusion cross sections within the astrophysical energy range. We are developing two different approaches which will enable us to precisely study this important fusion process at lowest energies than have ever been reached in any past experiments. We also collaborate with collaborators at the Research Center for Nuclear Physics (RCNP) at Osaka University on a complimentary approach of using the $^{24}Mg(\alpha, \alpha')$ reaction to search the resonances in ^{24}Mg which may contribute to the ^{12}C fusion cross section at astrophysical energies. The new measurement of the $^{12}C(^{12}C, n)$ channel and the new extrapolation technique reduced the existing ambiguities in the weak s-process for Population I massive stars.

Besides $^{12}C + ^{12}C$, the $^{12}C + ^{16}O$ and $^{16}O + ^{16}O$ fusion reactions are also important for nuclear astrophysics. At sub-barrier energies, there are still many mysteries, such as the molecular resonance, hindrance effect and correlation within the isotope systems, which can only be addressed with better experimental data. The new 5 MV single end accelerator with an Electron Cyclotron Resonance source will soon provide high-current heavy ion beams at Notre Dame. With improvements of the detection techniques discussed in this paper, better experimental data can be expected in the near future.

ACKNOWLEDGEMENT

This work was supported by the NSF under Grants No. PHY-0758100 and No. PHY-0822648, the DOE office of Science through Grant No. DE-AC02-06CH11357, the National Natural Science Foundation of China under Grant No. 11021504, and the University of Notre Dame.

REFERENCES

1. *Almqvist E., Kuehner J.A., Bromley D.A.* Resonances in ^{12}C on Carbon Reactions // Phys. Rev. Lett. - 1960. - Vol. 4. - P. 515 - 517.
2. *Bromley D.A.* Nuclear Molecules // Sci. Am. - 1978. - Vol. 239. - P. 58 - 68.
3. *Erb K.A., Bromley D.A.* Heavy Ion Resonances // Treatise on Heavy-Ion Science / Ed. by D.A. Bromley - New York: Plenum Press, 1985. - Vol. 3. - P. 201 - 310.
4. *Spillane T. et al.* $^{12}C + ^{12}C$ Fusion Reactions near the Gamow Energy // Phys. Rev. Lett. - 2007. - Vol. 98. - P. 122501.
5. *Gasques L.R. et al.* Implications of low-energy fusion hindrance on stellar burning and nucleosynthesis // Phys. Rev. - 2007. - Vol. C76. - P. 035802.
6. *Patterson J.R., Winkler H., Zaidins C.S.* Experimental Investigation of the Stellar Nuclear Reaction $^{12}C + ^{12}C$ at Low Energies // Astrophys. J. - 1969. - Vol. 157. - P. 367.
7. *Spinka H., Winkler H.* Experimental determination of the total reaction cross section of the stellar nuclear reaction $^{16}O + ^{16}O$ // Nucl. Phys. - 1974. - Vol. A233. - P. 456.
8. *Becker H.W., Kettner K.U., Rolfs C., Trautvetter H.P.* The $^{12}C + ^{12}C$ reaction at subcoulomb energies (II) // Z. Phys. - 1981. - Vol. A 303. - P. 305.
9. *Caughlan G.R., Fowler W.A.* Thermonuclear reaction rates V // At. Data Nucl. Data Tables - 1988. - Vol. 40. - P. 283.
10. *Jiang C.L., Rehm K.E., Back B.B., Janssens R.V.F.* Expectations for ^{12}C and ^{16}O induced fusion cross sections at energies of astrophysical interest // Phys. Rev. - 2007. - Vol. C75. - P. 015803.
11. *Cooper R.L., Steiner A.W., Brown E.F.* Possible Resonances in the $^{12}C + ^{12}C$ Fusion Rate and Superburst Ignition // Astrophys. J. - 2009. - Vol. 702. - P. 660.
12. *Dayras R.A., Stokstad R.G., Switkowski Z.E., Wieland R.M.* Gamma-ray yields from $^{12}C + ^{13}C$ reactions near and below the coulomb barrier // Nucl. Phys. - 1976. - Vol. A 265. - P. 153.
13. *Notani M., Esbensen H., Fang X. et al.* Correlation between the $^{12}C + ^{12}C$, $^{12}C + ^{13}C$, and $^{13}C + ^{13}C$ fusion cross sections // Phys. Rev. - 1976. - Vol. C 85. - P. 014607.
14. *Trentalange S., Wu S.C., Osborne J.L., Barnes C.A.* Elastic scattering and fusion cross sections of $^{13}C + ^{13}C$ // Nucl. Phys. - 1988. - Vol. C 483. - P. 406.
15. *Kovar D.G. et al.* Systematics of carbon- and oxygen-induced fusion on nuclei with $12 \leq A \leq 19$ // Phys. Rev. - 1979. - Vol. C 20. - P. 1305.
16. *Esbensen H., Tang X., Jiang C.L.* Effects of mutual excitations in the fusion of carbon isotopes // Phys. Rev. - 2011. - Vol. C 84. - P. 064613.
17. *Zickefoose J.* $^{12}C + ^{12}C$ Fusion: Measurement and Advances Toward the Gamow Energy - Ph.D. thesis - University of Connecticut, 2010.
18. *Imanishi B.* Resonance energies and partial widths of quasimolecular states formed by the two carbon nuclei // Phys. Lett. - 1968. - Vol. B 27. - P. 267.
19. *Lighthall J.C. et al.* Commissioning of the HELIOS Spectrometer // Nucl. Instr. and Meth. in Phys. Res. - 2010. - Vol. A622. - P. 97.
20. *Jiang C.L., Rehm K.E., Fang X. et al.* Measurements of fusion cross-sections in $^{12}C+^{12}C$ at low beam energies using a particle-γ coincidence technique // Nucl. Instr. Meth. - 2012. - Vol. A682. - P. 12.
21. *Koning A.J., Hilaire S., Duijvestijn M.C.* TALYS-1.0 // Proc. of the Int. Conf. on Nuclear Data for Science and Technology / Ed. by O. Bersillon, F. Gunsing, E. Bauge, R. Jacqmin, S. Leray - Nice, France, 2007. - P. 211 - 214.
22. *Pignatari M., Gallino R., Heil M. et al.* The Weak s-process in Massive Stars and Its Dependence on the Neutron Capture Cross Sections // Astrophys. J. - 2010. - Vol. 710. - P. 1557.
23. *Dayras R., Switkowski Z.E., Woosley S.E.* Neutron branching in the reaction $^{12}C + ^{12}C$ // Nucl. Phys. - 1977. - Vol. A279. - P. 70.
24. *Herman M., Capote R., Carlson B.V. et al.* EMPIRE: Nuclear Reaction Model Code System for Data Evaluation // Nucl. Data Sheets. - 2007. - Vol. 108. - P. 2655.

SURFACE BOILING – AN OBVIOUS BUT LIKE NO OTHER DECAY MODE OF HIGHLY EXCITED ATOMIC NUCLEI

J. Tõke

Department of Chemistry, University of Rochester, Rochester, NY, USA

Essentials of a generalized compound nucleus model are introduced based on a concept of an open microcanonical ensemble which considers explicitly the role of the diffuse surface domain and of the thermal expansion of nuclear systems in the quest for maximum entropy. This obvious generalization offers a unique and universal thermodynamic framework for understanding the changes in the gross behavior of excited nuclear systems with increasing excitation energy and, specifically, the competition between different statistical decay modes, including classical evaporation and binary fission, but also the Coulomb fragmentation of excited systems into multiple fragments – the famed multifragmentation. Importantly, the formalism offers a natural explanation, in terms of boiling or *spinodal vaporization*, for the experimentally observed appearance of limiting excitation energy that can be thermalized by an exited nuclear system and the associated limiting temperature. It is shown that it is the thermal expansion that leads to volume boiling in an infinite matter and surface boiling in finite nuclei. The latter constitutes an important and universal, but hitherto unappreciated decay mode of highly excited nuclei, a mode here named *surface spinodal vaporization*. It is also shown that in iso-asymmetric systems, thermal expansion leads to what constitutes distillation – a decay mode here named *distillative spinodal vaporization*.

1. Introduction

The concept of a compound nucleus [1, 2] is one of the most fundamental concepts in nuclear theory, which has not faced serious challenges in its over 70 years of existence. Implemented in numerous computer codes, such as e.g., PACE[3] and GEMINI [4, 5] this concept has consistently provided a sound framework for interpreting a whole host of experimental observations, but has also provided a sound basis for nuclear microcanonical thermodynamics.[1] The concept of a compound nucleus rests on the assumption that an excited nucleus is a metastable object that is able to reach approximate microcanonical equilibrium, before finite fluctuations in particle energies and in the global shape bring it to one of the possible transition states for particle emission or binary Coulomb fragmentation, i.e., fission. One may view the collection of all possible transition states as a hypersurface in the whole 6N-dimensional phase space of particle coordinates and particle momenta, and the microcanonical equilibrium refers then to a part of the total phase space confined by the said hypersurface [6]. Obviously, no true microcanonical equilibrium is possible for nuclei excited in excess of particle separation energies, while such is possible for confined systems. We call here the system confined only by the hypersurface of transition states an "open microcanonical" system, acknowledging the fact that such a system is allowed to decay into the continuum whenever it reaches any (microscopic) state on this hypersurface. While not spelled out explicitly in the theory of compound nucleus, the existence of such a hypersurface is implied by the very use of Boltzmann's entropy in the quantification of decay rates. The reason it is spelled out here is to contrast this kind of "liberal" self-confinement with the purely hypothetical "rigid" confinement in the global 3-dimensional coordinate space at the crux of most mainstream models and, more importantly, to stress the fact that the said "liberalism" of such a (thought) confinement has consequences far beyond those contemplated by standard implementations of the concept of a compound nucleus.

In its classical form, the theory of compound-nucleus recognizes two fundamental modes of statistical decay – particle evaporation and fission. In terms of the hypersurface of transition states, the former happens whenever statistical fluctuations bring the system to a point on the hypersurface which is associated with any particular particle continuum state. The latter happens when the point in question is a fragmentation saddle-point configuration. In its classical form, the model predicts Boltzmann-like scaling for the yields of decay products both, evaporative and fragmentation-like, with quantitative trends depending on transition-state energy for any particular decay channel.

While it is generally understood that the metastability at the crux of this model becomes not quite so well justifiable at elevated excitations, there has been no concerted theoretical effort undertaken to actually study quantitative criteria for the absolute loss of validity of this concept, should such criteria exist. Rather, to account for some important and intriguing experimental observations, vague and relative narratives have been proposed [7 - 9] for why the classical compound nucleus picture should be replaced with one that would apparently explain not only the appearance of certain modes of decay (such as , e.g., nuclear multifragmentation) but also their non-Boltzmannian, phase-transition-like scaling. These narratives fail to identify any particular "cross-over" point on the excitation energy or temperature scale, even as some experimental observations appear to be identifying such candidate points as, e.g., the point of the (rapid on the energy scale) onset of multifragmentation and the point where the limiting temperature would be reached.[7, 10, 11].

As revealed in a series of studies [6, 12 - 17], thermal expansion has profound qualitative effects on the behavior of excited nuclei some of which are only indirectly reflected in experimental observations but some other are directly observable in the decay modes and their interplay. At low excitations, the effects of thermal expansion appear insignificant, and it appears well justified to neglect them. However, as the excitation energy is raised, the compound system expands more and more and, as a result, lowers somewhat its temperature with respect to the non-expanded configuration. As shown in Ref. [15], this reduction in temperature leads to a reduction in Weisskopf's [1] (evaporative)

decay rates and helps the system to maintain metastability. Additionally, thermal expansion allows for stronger local matter density fluctuations and global shape fluctuations which tend to further lower the system temperature. This kind of action by thermal expansion is consistent with Le Chatelier's principle requiring the system to respond to a stimulus (here, excitation energy) in a way that minimizes the effects of this stimulus (here, the increase in temperature). Further, the fact that the surface domain also expands thermally helps in reducing the surface tension beyond what results from a simple increase in surface entropy.[13] The latter then results in an increase in the magnitude of the global shape fluctuations and the relative enhancement of Coulomb fragmentation, [12, 13] as compared with particle evaporation. Such global shape fluctuations further contribute to the reduction of temperature and the retardation of statistical evaporation. In the light of the Le Chatelier's principle, one may then view at moderate excitation energies thermal expansion and fluctuations as a blessing for the concept of compound nucleus in that they appear to extend the time scales of statistical decay and, thus, allow for a more profound thermalization of the excitation energy.

Interestingly, thermal expansion of the surface domain and the resulting reduction in surface tension and, thus in fragmentation saddle energies, affect the fragmentation decay rates in a way that makes these rates to deviate substantially from the Boltzmann scaling and to resemble more phase-transition like scaling.[6] The latter scaling is characterized by a rapid onset on the energy scale, as it has been observed with respect to the onset of Coulomb fragmentation, usually called multifragmentation. One may posit that it is this action of thermal expansion on the Coulomb fragmentation rates that has given rise to numerous speculations linking nuclear multifragmentation to phase transitions.

The present study concentrates on the boiling phenomenon which appears tightly associated with thermal and not purely mechanical expansion.[16, 17] Boiling reflects the system becoming spinodally unstable with respect to local thermal fluctuation as the heat capacity of the system turns formally negative (because of expansion cooling). By boiling here is meant a phenomenon similar to that known from everyday life to occur to water heated in an open kettle. In a "run-up" to boiling, water is seen first to evaporate while remaining metastable, with the evaporation rate increasing with increasing temperature. What is less conspicuous but equally well known is that in the course of heating water expands. And then, upon reaching the boiling point specific energy, bubbles are seen to form chaotically throughout the volume, expand, and separate from water and finally, are seen to disappear into the surrounding open space. Also, temperature is seen to stay constant until the last drop has vaporized.

The present paper is constructed as follows: in Section 2, the employed theoretical formalism is discussed in terms of Fermi gas model in Thomas Fermi approximation followed by a revisiting of the essentials of spinodal instabilities in uniform matter. Then, results of calculations are presented as pertaining to boiling instabilities in infinite (Section 3, Subsection 1) and finite (Section 3, Subsection 2) iso-neutral matter, and in iso-asymmetric infinite matter (Section 3, Subsection 3). Then, Section 4 presents a discussion and summary.

2. Theoretical Formalism

The formalism employed in this study is described in detail in series of papers, [12 - 17, 6] all based on an expression for the level density parameter of little *a* as proposed in Ref. [18]. It aims at identifying the configuration of maximum entropy for any given excitation energy and then inspecting characteristics of interest for such configuration. By a configuration here is understood a particular macroscopic distribution of nuclear matter that is parameterized in terms of one or more parameters. The configuration entropy is written as:

$$S_{config} = 2\sqrt{a_{config}(E - E_{config})}\,, \tag{1}$$

where E is the system energy, E_{config} is the zero-temperature configuration energy and a_{config} is the level density parameter for the configuration of interest. Equation 1 is the base equation of the formalism, allowing one to evaluate entropy for any spatial matter density distribution $\rho_{config}(\boldsymbol{r})$. For a_{config} one writes: [18]

$$a_{config} = \alpha_o \rho_o^{2/3} R(I) \iiint \rho^{1/3}(\vec{r}) d\vec{r}\,, \tag{2}$$

where α_o expresses the value of the level density parameter per nucleon at normal matter density ρ_o, I is the iso-asymmetry factor $I = (N - Z)/(N + Z)$, and $R(I)$ is the asymmetry-dependent factor[18] equal to $(1 - 1/9I^2)$.

The zero-temperature energy of a given configuration E_{config} was calculated by folding a Skyrme-type interaction energy density with a Gaussian folding function emulating the finite range of nuclear interaction [16]. Note that the folding is essential only in the case of finite nuclei and is not consequential for the bulk infinite matter.

The characteristic property of central interest in the present study is the curvature of the entropy function with respect to its arguments E and I. It is this curvature that decides whether the system can persist as metastable or will be forced to promptly decay via *spinodal vaporization* of a part of itself into the surrounding open space. Mathematically, this curvature is determined by the eigenvalues of the Hessian (a symmetric non-diagonal matrix built of second derivatives) of the entropy function, which is here defined as:

$$H(S)=\begin{bmatrix} \dfrac{\partial^2 S}{\partial E^2} & \dfrac{\partial^2 S}{\partial E \partial I} \\ \dfrac{\partial^2 S}{\partial I \partial E} & \dfrac{\partial^2 S}{\partial I^2} \end{bmatrix}. \tag{3}$$

For the uniform configuration of interest to be stable, the entropy function must be a concave function of its arguments and this means that both eigenvalues of Hessian must be negative and, thus, Hessian must be a negative definite matrix. Note that for symmetric or one-component matter, Hessian degenerates into a trivial 1x1 matrix with the second derivative of entropy with respect to energy as the only element and also the sole eigenvalue. Here, a practical condition for the entropy being a concave function of energy is the heat capacity to be positive and this condition is usually visualized in the form of a caloric curve of the temperature *T* plotted as a function of the excitation energy *E*.

Note that were the entropy a convex function of its arguments, the (uniform) configuration would be thermally unstable such that local fluctuations in the excitation energy would fail to generate restoring forces returning the system to the uniformity presumed for the configuration of maximum entropy. Rather, a driving force would be generated that would drive the system even further away from uniformity. Note also that the kind of instability associated with the "wrong" curvature of the characteristic thermodynamic function for a given type of ensemble is termed "spinodal instability" [19 - 21] and that its character depends on the type of (idealized) thermodynamic ensemble considered. For example, the most commonly discussed spinodal instability in a canonical ensemble is of mechanical type, associated in a synchronous manner with both, the negative compressibility and the negative chemical susceptibility (first derivative of the chemical potential with respect to concentration). The boiling phenomenon appears only in open microcanonical systems, is of thermal type and associated with negative heat capacity. It shows also negative chemical susceptibility as the entropy function depends in a nontrivial linear manner only on the energy per nucleon and not on the energy and the number of nucleons taken separately.

3. Results of calculations

3.1. Thermal instabilities in infinite systems

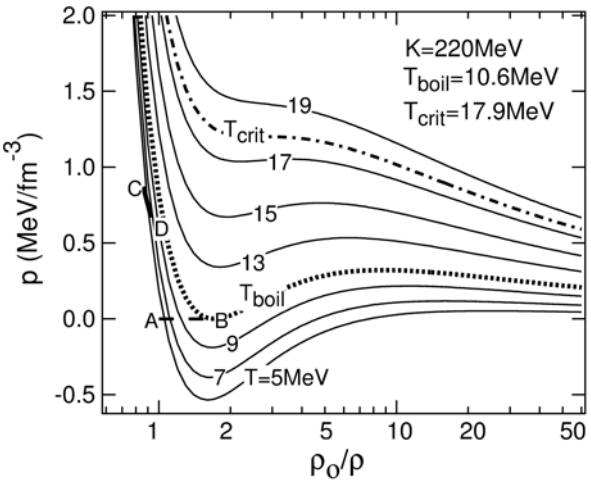

Fig. 1. Isotherms for the model matter. The isotherm corresponding to zero-pressure boiling-point temperature is shown in dotted line and the critical isotherm is shown in dash-dotted line. The adiabatic thermal expansion trajectory for the system at zero-pressure is shown in dashes as line AB, with B being the boiling point. The bulk interior expansion trajectory for finite system is shown in bold solid line CD.

Fig. 1 illustrates isotherms obtained by evaluating the temperature T and pressure p by taking proper partial derivatives of the (uniform) configuration entropy given by Eq. 1, i.e.,

$$T = 1/\left(\frac{\partial S}{\partial E}\right)_{V,N} \quad \text{and} \quad p = T\left(\frac{\partial S}{\partial V}\right)_{E,N}. \tag{4}$$

The calculations were done assuming a Skyrme-type equation of state with the incompressibility modulus of K = 220 MeV. As seen in Fig. 1, as the system expands with increasing excitation energy per nucleon starting from point A, its temperature first rises, what is evidenced by crossing of isotherms with progressively higher temperature labels. Then, beginning at point B, the temperature is seen to drop with a further increase of excitation energy and the induced expansion, an indication of spinodal instability of thermal type. The purpose of Fig. 1 is to demonstrate that the appearance of spinodal instability in an open microcanonical system is both, trivial and unavoidable for any system characterized by a van der Waals-type equation of state.

Fig. 2 illustrates in more detail thermal expansion (panel *a*), the appearance of negative heat capacity (panel *b*), and the appearance of convexity in the entropy (panels c and d), all as function of excitation energy per nucleon. The reduced entropy S_{red} shown in panel d is obtained by first subtracting a linear function in energy per nucleon from the entropy per nucleon shown in panel c, and then multiplying the result by a suitable normalization factor. Obviously, a subtraction of a linear function does not change the second derivative of the function, which is of interest here.

A simple explanation for the instability rests on the fact that when in the negative heat capacity domain, any fluctuation in local excitation energy per nucleon results in the recipient of the energy to cool down and the donor to heat up in terms of temperature. Subsequently, the colder recipient draws even more energy from the hotter donor in the quest for maximum entropy. This entropy driven transfer of heat and the resulting expansion of the colder, already

expanded part is the essence of the boiling process. The onset of thermal instability can be seen also in a purely microcanonical representation, without recourse to the notion of (microcanonical) temperature. This is seen in Fig. 3, where the entropy is shown as a function of the excitation energy per nucleon and the asymmetry in the excitation energy division between two hypothetical equal-size subsystems.

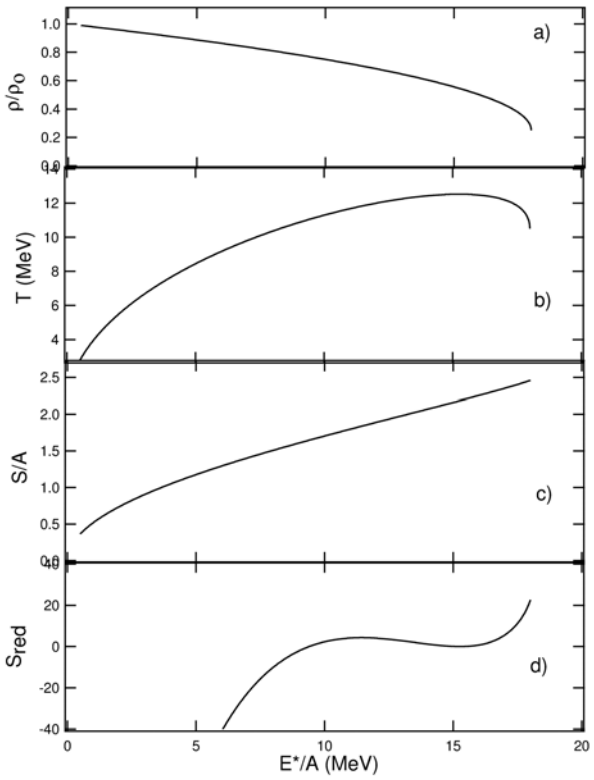

Fig. 2. Evolution of the matter density (*a*); the micro-canonical temperature (*b*); the entropy (*c*), and the reduced entropy (*d*) with the excitation energy per nucleon. The appearance of convexity is made conspicuous in panel (*d*) through a suitable curvature-neutral linear transformation.

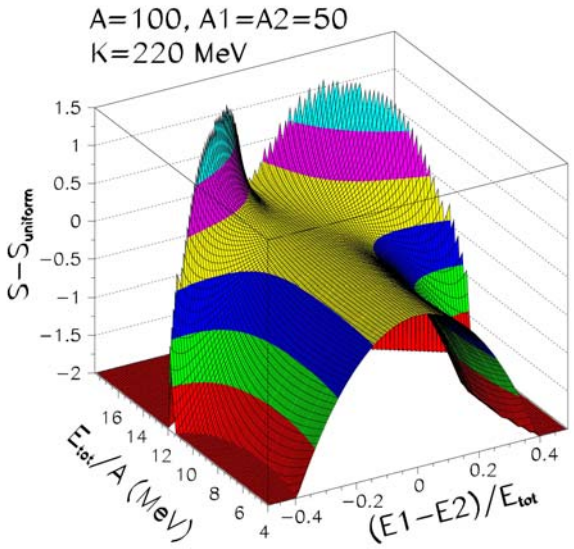

Fig. 3. (Color online) Entropy of a two-phase system with respect to that of the uniform system, plotted as a function of total excitation energy per nucleon and the asymmetry in energy distribution between the two equal-size subsystems.

As is seen in Fig 3, at lower excitations, the entropy favors a uniform distribution of the excitation energy, while allowing for finite fluctuations in excitation energy division between the arbitrarily chosen split of the entire system into two equal-size subsystems. At elevated energies, this trend is reversed and the entropy now favors unequal energy distribution – the essence of spinodal instability.

It is important to note that once the convexity sets in for the entropy function at the boiling-point excitation energy per nucleon, it stays there up to the end point of the curves shown in Fig. 2, where the system becomes unstable with respect to uniform expansion. This means that part of the system must separate physically from the surviving metastable residue with the "departing" temperature lower than that of the residue. Here, the boiling process is named also as *spinodal vaporization*, to reflect its prompt character and its roots in spinodal instability.

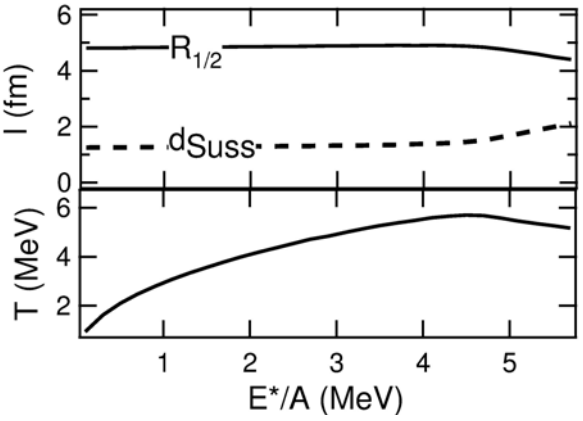

Fig. 4. Matter density distribution parameters (top panel) and the microcanonical temperature (bottom panel) as functions of the excitation energy per nucleon. (See text).

3.2. Boiling in finite nuclei

Calculations for finite nuclei were performed assuming a matter density profile given by the error function, [18] with the half-density radius R_{half} and the surface width d as the two parameters:

$$\frac{\rho(r)}{\rho_o} = C(R_{half}, d)\left[1 - erf\left(\frac{r - R_{half}}{\sqrt{2}d}\right)\right], \qquad (5)$$

The results of maximizing entropy for the excitation energy range for which the maximum of entropy as a function of R_{half} and d exists, are shown in Fig. 4.

As seen in Fig. 4, with increasing excitation energy, both the half-density radius and the surface domain width

(Sűssman width) first increase, as does the microcanonical temperature *T*. Then, beginning around 4.5 MeV/nucleon, T reverses the trend, indicating the onset of thermal spinodal instability – in this case, the surface boiling. At the same time the surface diffuseness begins increasing more rapidly. The trends seen in Fig. 4 are indicative of a thermal instability where one section of surface domain increases its diffuseness by drawing energy from the neighboring section and by cooling down as a result. It is obvious from Fig. 4 that once the system enters the spinodal domain, it cannot regain stability before the excess energy is shed along with a portion of the system itself. The boiling here constitutes a prompt decay of the excited system via diffusion of some parts of the surface away. By diffusion, it is here understood a process of a steady increase in surface diffuseness, until parts of the system separate.

Note that the surface boiling is a novel and important mode of decay of realistic nuclei, with many real and potential consequences. It is also a new kind of spinodal instability, different from the classical one where the instability applies uniformly to every infinitesimally small part of the uniform system. Here the system is uniform only in the sense of having an isotropic matter density profile and, accordingly, the instability applies here to portions of matter enclosed in infinitesimally small solid angles as viewed from the center of the system. Here, it is proposed to name this process as *surface spinodal vaporization.*

3.3. Distillative boiling in iso-asymmetric matter

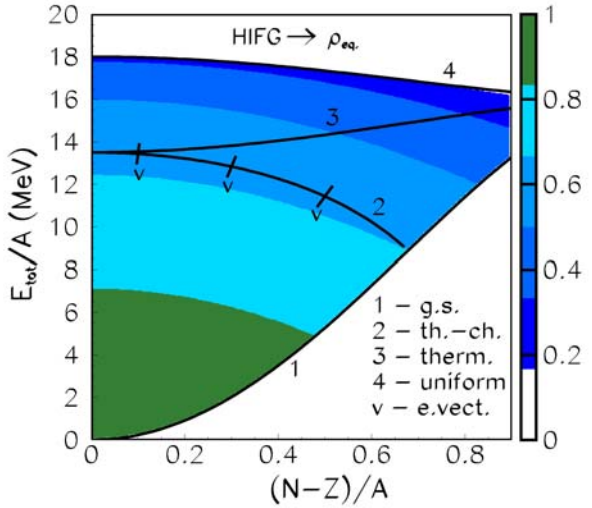

Fig. 5. (Color online) Contour plot of the equilibrium matter density as a function of iso-asymmetry, $(N - Z)/A$, and energy per nucleon E_{tot}/A. Shown are in solid lines the ground-state energy (*1*), the boundary of the metastability domain (*2*), the boundary of the domain of positive heat capacity (*3*), and the boundary of the domain stable against uniform expansion (*4*).

Iso-asymmetric self-confined matter is characterized by an entropy that is a function of two extensive arguments, energy *E* and iso-spin asymmetry *I*. Accordingly, the Hessian of entropy is a 2 × 2 non-diagonal matrix, which has two eigenvalues and two eigenvectors, with the latter not aligned with the argument axes *E* or *I*.

Results of calculations for such a model system are displayed in Fig. 5 in the form of a contour plot of the matter equilibrium density as a function of energy and iso-spin parameter. They were obtained assuming a harmonic-interaction EOS with a symmetry term linear in matter density:

$$E_{config} = c_V(1-\frac{\rho}{\rho_o})^2 + c_I\frac{\rho}{\rho_o}I^2, \qquad (6)$$

where the parameters c_V and c_I were assumed to be -16 MeV and 23 MeV, respectively.

In Fig. 5, overlaid on the contour plot are several boundary lines of significance here.

As seen in Fig. 5, the matter density decreases with increasing energy and, eventually, at the boundary line *4* becomes unstable (globally) against uniform expansion. Line *4* in this Figure is a line of "no return" for any portion of matter that manages to reach it, such that the portion of matter in question would expand indefinitely purely on the account of its own energy. Line *2* in this Figure represents the locus of points where one of the eigenvalues of the Hessian of entropy $H(S)$ turns zero, both eigenvalues being duly negative in the domain of metastability enclosed between the line *1* illustrating the ground state energy as a function of iso-asymmetry *I*, and the spinodal boundary line *2*. Line *3* on this plot serves illustrative purpose only and represents the locus of points where the heat capacity turns infinite, i.e, where the purely thermal instability would set in had it not been preempted by the thermo-chemical instability at line *2*. The fact that the latter instability is, indeed, thermo-chemical is evidenced by the orientation of eigenvectors associated with the zero eigenvalues and represented in Fig. 5 by short bars labeled as **v**. And, again, as in the case of iso-neutral matter, once the system enters the domain of thermo-chemical spinodal stability above line *2*, it never regains stability as a whole. As indicated by the short bars, the less dense matter that eventually ends up boiling off at line *4* is more neutron-rich and colder than the residue. Note that line *2* may be considered an attractor line, i.e., a collection of points describing the metastable state of the residue left after the excess energy is boiled off, an entity that can be probed experimentally, in principle.

It is worth noting that the "asymmetric" (in iso-asymmetry) boiling is reminiscent of isospin fractionation in confined hypothetical systems, except that in open systems no equilibrated gas phase is ever present. Here, it is proposed to name such a process as *distillative spinodal vaporization.*

4. Summary

Boiling is an obvious and a very common phenomenon that must happen in highly excited systems featuring a van der Waals-type equation of state. Boiling is known from everyday life as a state where bubbles are appearing chaotically throughout the volume of water, growing, and then separating from water and disappearing in the

surrounding open space. In self-bound infinite nuclear matter brought to boiling, also bubbles are expected to be formed and growing indefinitely and never in thermal equilibrium with the liquid phase. While such bubble formation in infinite systems may be of a true academic interest, it is the surface boiling that has implications as far as the "life" of a realistic highly excited nuclear system is concerned. As revealed in the present paper, the surface boiling occurs via spontaneous unrestrained expansion of parts of the surface domain at the expense of the energy derived from the neighboring parts. This expansion results in forced prompt *spinodal vaporization* of a part of the system into surrounding open space, clearly a decay process different from all other decay modes so far considered. The decay here is different from classical pre-equilibrium decay as it does not rely on any particular initial distribution of particle momenta and coordinates in the system. As is clear from the presented formalism, even if one could purely hypothetically manage to form a seemingly equilibrated "dream" system at maximum entropy with isotropic density profile, such a system would still decay promptly via *spinodal vaporization* - shedding of the excess excitation energy along with a definite part of itself. And it will do so in an isotropic manner (assuming that the system has zero angular momentum) with vapors being colder than the surviving metastable residue.

Decay via surface boiling, or *surface spinodal vaporization*, is intimately linked to thermal expansion and sets in rapidly on the excitation energy scale, in a stark contrast to Boltzmann-like scaling of yields in classical model implementations of the concept of a compound nucleus. It is then reasonable to assume that the decay processes commonly identified as statistical occur only after the prompt boiling process has completed and has left the metastable residue to decay via particle evaporation and Coulomb fragmentation, both, binary and multifragment.

The most prominent experimental observation that is trivially explained in terms of boiling, but has no other plausible explanation, is the appearance of limiting temperature in the measured caloric curves. Clearly, it will be of great interest to carry out experiments involving systems with different initial N/Z asymmetries to get handle on iso-spin dependence of nuclear EOS at sub-normal densities. To interpret the experimental data from such experiments, one would have to carry out very CPU-intensive calculations for finite iso-asymmetric systems, possibly including Coulomb interaction.

In summary, boiling is a prompt decay mode of highly excited nuclear systems rich in detectable, experimentally verifiable consequences. Because of its nature, it may be called *spinodal vaporization*. It is also rich in theoretical implications and offers a fertile ground for reasonable and stimulating scientific speculations. One may posit that it is one of the most overlooked phenomena in nuclear thermodynamics in recent memory and the one which, while being obvious and having a robust confirmation in a unique set of experimental observations, still awaits recognition by the nuclear science community.

ACKNOWLEDGMENTS

This work was supported by the U.S. Department of Energy grant No.DE-FG02-88ER40414.

REFERENCES

1. *Weisskopf V.* Statistics and nuclear reactions // Phys. Rev. - 1937. - Vol. 52. - P. 295 - 303.
2. *Bohr N., Wheeler J.A.* The mechanism of nuclear fission // Phys. Rev. - 1939. - Vol. 56. - P. 426 - 450.
3. *Gavron A.* Statistical model calculations in heavy ion reactions // Phys. Rev. C. - 1980 - Vol. 21. - P. 230 - 236.
4. *Charity R.J.* Systematic description of evaporation for light and heavy compound nuclei // Phys. Rev. C. - 2010. - P. 014610-1 - 014610-16.
5. *Charity R.J.* Unified description of fission in fusion and spallation reactions // Phys. Rev. C - 2010. - P. 044610-1 - 044610-14.
6. *Tõke J., Schröder W.U.* Common signatures of statistical Coulomb fragmentation of highly excited nuclei and phase transitions in confined microcanonical systems // Phys. Rev. C. - 2009. - Vol. 79. - P. 064622-1 - 064622-11.
7. *Friedman W.A.* Basis for a characteristic temperature in nuclear fragmentation // Phys. Rev. Lett. - 1988. - Vol. 60. - P. 2125 - 2128.
8. *Gross D.H.E.* Statistical decay of very hot nuclei - the production of large clusters // Rep. Prog. Phys. - 1990. - Vol. 53. - P. 605 - 658.
9. *Bondorf J.P. et al.* Statistical multifragmentation of nuclei // Phys. Rep. - 1995. - Vol. 133. - P. 133 - 221.
10. *Wada R. et al.* Temperatures and excitation energies of hot nuclei in the reactions of 32S + Ag and 16O + Ag at 30 MeV/nucleon // Phys. Rev. C - 1989. - Vol. 39. - P. 497 - 515.
11. *Natowitz J.B. et al.* Caloric curves and critical behavior in nuclei // Phys. Rev. C. - 2002 - Vol. 65. - P. 34618-1 - 34618-9.
12. *Tõke J., Schröder W.U.* New type of shape instability of hot nuclei and nuclear fragmentation // Phys. Rev. Lett. - 1999. - Vol. 82. - P. 5008 - 5011.
13. *Tõke J., Lu J., Schröder W.U.* Surface entropy in statistical emission of massive fragments from equilibrated nuclear systems // Phys. Rev. C. - 2003. - Vol. 67. - P. 034609-1 - 034609-6 .
14. *Tõke J., Lu J., Schröder W.U.* Liquid-gas coexistence and critical behavior in boxed neutral, isosymmetric pseudo-Fermi matter // Phys. Rev. C. - 2003. - Vol. 67. - P. 044307 -1 - 044307-4.
15. *Tõke J., Pieńkowski L., Sobotka L.G. et al.* Retardation of particle evaporation from excited nuclear systems due to thermal expansion // Phys. Rev. C. - 2005. - Vol. 72. - P. 031601-1 - 031601-4.

16. *Tõke J., Schröder W.U.* Surface boiling - a new type of instability of highly excited atomic nuclei // arXiv: - 2012. - 1207.3828v1.
17. *Tõke J.* Surface boiling - an “obvious” explanation for the observed limited temperature of finite nuclei // Proc. of the Int. Workshop on Multifragmentation and Related Topics / Ed. by J.D. Frankland et al. - Caen, France, 2011. - EPJ Web of Conferences Vol. 31 0006.
18. *Tõke J., Swiatecki W.J.* Surface-layer corrections to the level-density formula for a diffuse Fermi gas // Nucl. Phys. - 1981. - Vol. A372. - P. 141 - 149.
19. *Chomaz P., Colonna M., Randrup J.* Nuclear spinodal fragmentation // Phys. Rep. - 2004. - Vol. 389. - P. 263 - 440.
20. *Műller H., Serot B.* Phase transitions in warm, asymmetric nuclear matter // Phys. Rev. C. - 1995. - Vol. 52. - P. 2072 - 2091.
21. *Barranco M., Buchler J.* Thermodynamic properties of hot nucleonic matter // Phys. Rev. C. - 1980. - Vol. 22. - P. 1729 - 1737.

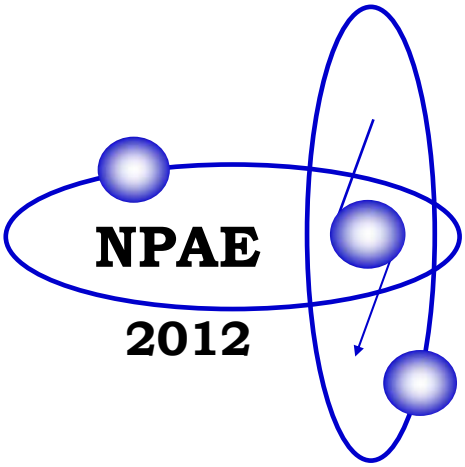

Section 1

Collective Processes in Atomic Nuclei

PAIRING COLLECTIVE EXCITATIONS IN NUCLEI: A SEMICLASSICAL APPROACH

V. I. Abrosimov[1], D. M. Brink[2], A. Dellafiore[3], F. Matera[3,4]

[1] *Institute for Nuclear Research, National Academy of Sciences of Ukraine, Kyiv, Ukraine*
[2] *Oxford University, Oxford, United Kingdom*
[3] *Istituto Nazionale di Fisica Nucleare, Sezione di Firenze, Firenze, Italy*
[4] *Dipartimento di Fisica, Universita degli Studi di Firenze, Firenze, Italy*

We study the solutions of the semiclassical time-dependent Hartree - Fock - Bogoliubov equations of motion in an improved linear approximation in which the pairing field fluctuations are taken into account. The static pairing field is approximated with a phenomenological constant Δ, hence our approach is not fully self-consistent, however, the pairing field fluctuations are derived from the self-consistent relations. The self-consistent pairing-field fluctuations introduce possibility of new collective modes of the system, generated by the pairing interaction. We have found out the dispersion relation which determines pairing collective modes. The solutions of dispersion relation have been studied in a simple model, in which nuclei are represented as a system of *A* nucleons enclosed in a spherical cavity characterized by parameters (size, density, pairing gap) typical of heavy nuclei. We have found that our semiclassical dispersion relation has approximate solution at $\circ\omega \approx 2\Delta$ for the monopole and quadrupole channels. Found solution is in good agreement with the result of well-known quantum approaches.

1. Introduction

Collective phenomena associated with the pairing interaction are of current interest both in the physics of nuclei [1] and of other mesoscopic systems [2]. Here we address this problem by using a semiclassical approximation for the time-dependent Hartree - Fock - Bogoliubov equations of motion for finite Fermi systems.

The semiclassical approximation is valid for small or mesoscopic Fermi systems with a characteristic size *R*, provided $p_F R/\circ >> 1$, where p_F is the Fermi momentum. Since in heavy nuclei the condition $p_F R/\circ >> 1$ is well satisfied, in [3,4] we have proposed a semiclassical approach to study of pairing effects in collective nuclear excitations.

We use the improved linear approximation in which the pairing field $\Delta(\mathbf{r}, \mathbf{p}, t)$ is allowed to oscillate and to become complex [4]. In present approach the static pairing field $\Delta_0(\mathbf{r}, \mathbf{p})$ is approximated with a real, constant, phenomenological parameter Δ, hence our approach is not fully self-consistent, however, the (complex) pairing-field fluctuations $\delta\Delta(\mathbf{r}, \mathbf{p}, t)$ are derived from self-consistency relation (the gap equation of the BCS type). We study the new set of equations of motion that arise in this improved approximation. The resulting equations allow for the study of collective effects associated with the pairing interaction.

2. Semiclassical model with pairing for small amplitudes

We use the time-dependent Hartree - Fock - Bogoliubov equations in the semiclassical approximation as dynamical equations. We assume that our system is saturated both in spin and isospin space, so we do not need to introduce explicitly these variables. Thus for small amplitudes our dynamical equations can be written as [4]

$$i\hbar\partial_t \delta\rho^{ev} = i\hbar\{h_0, \delta\rho^{od}\} - i2\ (\Delta\delta\kappa^i - \kappa_0\delta\Delta^i), \tag{1}$$

$$i\hbar\partial_t \delta\rho^{od} = i\hbar\{h_0, \delta\rho^{ev}\} + i\hbar\{\delta h, \rho_0\} + i\hbar\{\delta\Delta^r, \kappa_0\}, \tag{2}$$

$$i\hbar\partial_t \delta\kappa = 2(h_0 - \mu)\delta\kappa - (2\rho_0 - 1)\delta\Delta + 2\kappa_0\delta h - 2\Delta\delta\rho^{ev} \tag{3}$$

with

$$\delta\rho^{ev(od)}(\mathbf{r}, \mathbf{p}, t) = \frac{1}{2}\left[\delta\rho(\mathbf{r}, \mathbf{p}, t) \pm \delta\rho(\mathbf{r}, -\mathbf{p}, t)\right], \tag{4}$$

$$\delta\kappa(\mathbf{r}, \mathbf{p}, t) = \delta\kappa^r(\mathbf{r}, \mathbf{p}, t) + i\delta\kappa^i(\mathbf{r}, \mathbf{p}, t). \tag{5}$$

We have the equations of motion for the variations of the normal phase-space distribution function $\delta\rho(\mathbf{r}, \mathbf{p}, t)$ and the anomalous one $\delta\kappa(\mathbf{r}, \mathbf{p}, t)$ from equilibrium distribution $\rho_0(\mathbf{r}, \mathbf{p})$ and $\kappa_0(\mathbf{r}, \mathbf{p})$. The variation $\delta\rho(\mathbf{r}, \mathbf{p}, t)$ is a real function while $\delta\kappa(\mathbf{r}, \mathbf{p}, t)$ is a complex one.

The equilibrium phase-space distributions $\rho_0(\mathbf{r}, \mathbf{p})$ and $\kappa_0(\mathbf{r}, \mathbf{p})$ are given by [5] (note the opposite sign of our function κ_0, compared to the function κ in Ref. [5])

$$\rho_0(\mathbf{r},\mathbf{p}) = \frac{1}{2}\left(1 - \frac{h_0(\mathbf{r},\mathbf{p}) - \mu}{E(\mathbf{r},\mathbf{p})}\right), \qquad \kappa_0(\mathbf{r},\mathbf{p}) = -\frac{\Delta_0(\mathbf{r},\mathbf{p})}{2E(\mathbf{r},\mathbf{p})} \tag{6}$$

with the quasiparticle energy

$$\rho_0(\mathbf{r},\mathbf{p}) = \frac{1}{2}\left(1 - \frac{h_0(\mathbf{r},\mathbf{p}) - \mu}{E(\mathbf{r},\mathbf{p})}\right), \tag{7}$$

The chemical potential μ is determined by the number of nucleons A. The equilibrium Hamiltonian $h_0(\mathbf{r}, \mathbf{p})$ contains the (Hartree) mean field $V_0(\mathbf{r})$, which should be evaluated self-consistently, however in the following we use a phenomenological potential well instead.

We want to use the linear response function formalism, thus we assume that our system is initially at equilibrium and that at time $t = 0$ it is perturbed by a weak external driving field $\delta V^{ext}(\mathbf{r}, t) = \eta\delta(t)Q(\mathbf{r})$, where $\delta(t)$ is a Dirac δ-function in time and η is a parameter specifying the strength of the external field. We shall consider the zero-order approximation for the normal mean-field, so the mean-field fluctuations $\delta h(\mathbf{r}, t)$ are given by $\delta h(\mathbf{r}, t) \approx \delta V^{ext}(\mathbf{r}, t)$, while the pairing field is treated more carefully.

We consider the approximation in which the static pairing field $\Delta_0(\mathbf{r}, \mathbf{p})$ is approximated with a phenomenological energy gap Δ, while the pairing field fluctuations $\delta\Delta^{r,i}(\mathbf{r}, \mathbf{p}, t)$ are derived from self-consistency relations. Thus, in the present approach, the pairing field is approximated as

$$\Delta(\mathbf{r},\mathbf{p},t) \approx \Delta + \delta\Delta^{r}(\mathbf{r},t) + i\delta\Delta^{i}(\mathbf{r},t). \tag{8}$$

The possible momentum dependence of the complex fluctuations is neglected in order to simplify the theory.

In a self-consistent theory, the changes in the pairing field are related to the changes in the anomalous density $\delta\kappa^{r,i}$. There are many possible choices for the self-consistency relation. Two minimum requirements are that the total particle number should be conserved and that the value of the energy weighted sum rule should be correct (the same as in normal systems). A choice that satisfies both requirements is obtained from the self-consistency relation (the gap equation of the BCS type) written in the form [7]

$$g\int \frac{d\mathbf{p}}{(2\pi\hbar)^3}\left(\frac{\kappa(\mathbf{r},\mathbf{p},t)}{\Delta(\mathbf{r},t)} + \frac{1}{p^2/m}\right) = 1. \tag{9}$$

Here g is a parameter determining the strength of the pairing interaction. By differentiating Eq. (9), we get the first-order relation

$$\int \frac{d\mathbf{p}}{(2\pi\hbar)^3}\left(\delta\kappa(\mathbf{r},\mathbf{p},t) - \kappa_0(\mathbf{r},\mathbf{p})\frac{\delta\Delta(\mathbf{r},t)}{\Delta}\right) = 0, \tag{10}$$

where $\kappa_0(\mathbf{r}, \mathbf{p})$ and Δ are real equilibrium quantities, while $\delta\kappa(\mathbf{r}, \mathbf{p}, t)$ and $\delta\Delta(\mathbf{r}, t)$ are their complex fluctuations. The self-consistency condition similar to (10) have been used by the authors of Ref. [2] in their quantum calculations for infinite homogeneous systems.

The integral relation (10), together with equations of motion (1 - 3), are not sufficient to determine a unique solution of our problem; hence we need to introduce a further assumption, or 'Ansatz': we assume that the pairing field fluctuations are proportional to the fluctuations of the mean field, that is

$$\delta\Delta^{r,i}(\mathbf{r},\omega) = \eta R^{r,i}(\omega)\delta h(\mathbf{r},\omega). \tag{11}$$

The two response functions $R^{r,i}(\omega)$ can be determined from the equations of motion and from the self-consistency integral relation.

Instead of the self-consistency relation (10), it is more convenient to use the weaker relations

$$\int d\mathbf{r}\int \frac{d\mathbf{p}}{(2\pi\hbar)^3}\left(\delta\kappa(\mathbf{r},\mathbf{p},t) + \frac{\delta\Delta(\mathbf{r},t)}{2E(\quad)}\right) = 0, \tag{12}$$

that follows immediately from (10) taking into account Eqs. (6) and (8).

The approximations (11) and (12) concerning the self-consistency relation make it possible to reduce the problem of solving of the integral relations to the solution of a system of coupled algebraic equations.

3. Pairing vibrations

The equations of motion (1 - 3) together with the self-consistency relation (10) can be solved for finite systems with the method of action-angle variables [3, 8].

The method of action-angle variables has proved to be very useful for solving the Vlasov equation in normal systems; hence we use the same method also for systems with pairing correlations. The action-angle variables (**I, Φ**) have a very useful property. Any one-valued function $F(\mathbf{r}, \mathbf{p})$ of the state of the system, expressed in terms of the canonical variables (**r**, **p**), is a periodic function of the angle variables **Φ**, and its period in each variable is 2π. It can be expanded as a multiple Fourier series:

$$F(\mathbf{r},\mathbf{p}) = \sum_{\mathbf{n}} F_{\mathbf{n}}(\mathbf{I}) e^{i\mathbf{n}\Phi}, \tag{13}$$

in our case the vector **n** has three integer components $\mathbf{n} = (n_1, n_2, n_3)$. In principle the sum over the components n_i runs from $-\infty$ to $+\infty$, however, in practice it is sufficient to include only a few terms around $n_i = 0$, moreover, for spherical systems, the vector **n** is effectively two-dimensional.

We take the Fourier transform in time of the equations of motion (1 - 3) and introduce the following Fourier expansions based on the method of action-angle variables:

$$\delta h(\mathbf{r},\omega) = \sum_{\mathbf{n}} \delta h_{\mathbf{n}}(\mathbf{I},\omega) e^{i\mathbf{n}\Phi}, \tag{14}$$

$$\delta\rho^{ev(od)}(\mathbf{r},\mathbf{p},\omega) = \sum_{\mathbf{n}} \delta\rho_{\mathbf{n}}{}^{ev(od)}(\mathbf{I},\omega) e^{i\mathbf{n}\Phi}, \tag{15}$$

$$\delta\kappa^{r,i}(\mathbf{r},\mathbf{p},\omega) = \sum_{\mathbf{n}} \delta\kappa_{\mathbf{n}}{}^{r,i}(\mathbf{I},\omega) e^{i\mathbf{n}\Phi}, \tag{16}$$

$$\delta\Delta^{r,i}(\mathbf{r},\omega) = \sum_{\mathbf{n}} \delta\Delta_{\mathbf{n}}{}^{r,i}(\mathbf{I},\omega) e^{i\mathbf{n}\Phi}. \tag{17}$$

Moreover we use the relation

$$\{f, h_0\} = \sum_{\mathbf{n}} i\omega_{\mathbf{n}}(\mathbf{I})\, f_{\mathbf{n}}(\mathbf{I}) e^{i\mathbf{n}\Phi}. \tag{18}$$

where $\omega_{\mathbf{n}}(\mathbf{I}) = \Sigma_\alpha n_\alpha \omega_\alpha$ are the eigenfrequencies of the uncorrelated system [8], to obtain from the dynamic equations (1 - 3) the system of algebraic equations. By using this set of coupled algebraic equations, we can express the quantities $\delta\kappa^{r,i}$ and $\delta\rho^{ev,od}$ in terms of the pairing field fluctuations $\delta\Delta^{r,i}$ and δV^{ext}.

The expressions for the quantities $\delta\kappa^{r,i}$ in terms of the pairing field fluctuations $\delta\Delta^{r,i}$ allow us to write the weaker self-consistency relation (10) as

$$\left[\int d\mathbf{I}\; a_{11}(\mathbf{n},\mathbf{I},\omega)\;\delta\Delta^{r}_{\mathbf{n}}(\mathbf{I},\omega) + \int d\mathbf{I}\; a_{12}(\mathbf{n},\mathbf{I},\omega)\;\delta\Delta^{i}_{\mathbf{n}}(\mathbf{I},\omega)\right]\delta_{\mathbf{n},0} = \eta \int d\mathbf{I}\; b_1(\mathbf{n},\mathbf{I},\omega)\; Q_{\mathbf{n}}(\mathbf{I})\;\delta_{\mathbf{n},0}, \tag{19}$$

$$\left[\int d\mathbf{I}\; a_{21}(\mathbf{n},\mathbf{I},\omega)\;\delta\Delta^{r}_{\mathbf{n}}(\mathbf{I},\omega) + \int d\mathbf{I}\; a_{22}(\mathbf{n},\mathbf{I},\omega)\;\delta\Delta^{i}_{\mathbf{n}}(\mathbf{I},\omega)\right]\delta_{\mathbf{n},0} = \eta \int d\mathbf{I}\; b_2(\mathbf{n},\mathbf{I},\omega)\; Q_{\mathbf{n}}(\mathbf{I})\;\delta_{\mathbf{n},0}, \tag{20}$$

The expressions for the functions $a_{ik}(\mathbf{n}, \mathbf{I}, \omega)$ and $b_i(\mathbf{n}, \mathbf{I}, \omega)$ are given by Eqs. (79 - 83) of [4].

Using the 'Ansatz' (11), in self-consistency relations (19 - 20) gives a system of coupled algebraic equations for the response functions $R^{r,i}(\omega)$. This system has two kind solutions. If the determinant is non- vanishing, the system of coupled algebraic equations (19 - 20) can be solved, giving $R^r(\omega) = 0$ and $R^i(\omega) = 2\Delta/i\circ\omega$ [4]. However there are also other solutions corresponding to the roots of vanishing determinant. They give frequencies of collective modes related to pairing.

The self-consistent fluctuations of the pairing-field introduce the possibility of extra collective modes of the system induced by the pairing interaction. The possible frequencies of these collective modes are given by the roots of vanishing determinant of coupled algebraic equations (19 - 20) that can be written as [4]

$$\omega^2 K(L,\omega) = 0. \tag{21}$$

The dispersion relation (21) has the obvious solution at $\omega=0$ that is related to gauge symmetry [1]. We study the possible solutions of the dispersion relation (21) to establish if, for a system with size, density and pairing parameters

typical of heavy nuclei, pairing collective modes are to be expected.

We get an explicit expression of the dispersion relation (21) for the monopole channel by using a simple model of nucleus, in which nucleons are confined to a spherical cavity characterized by parameters typical of heavy nuclei [5]. It reads

$$K(L=0,\omega)=\left[I_1(\omega)\right]^2-\left[(\hbar\omega)^2-4\Delta^2\right]\left[I_2(\omega)\right]^2=0 \tag{22}$$

with

$$I_2(\omega)=\int_0^\infty d\epsilon\, g(\epsilon)\frac{1}{2E(\epsilon)}\frac{1}{(\hbar\omega+\imath\varepsilon)^2-4E^2(\epsilon)}, \tag{23}$$

$$I_1(\omega)=\int_0^\infty d\epsilon\, g(\epsilon)\frac{\epsilon-\mu}{E(\epsilon)}\frac{1}{(\hbar\omega+\imath\varepsilon)^2-4E^2(\epsilon)}, \tag{24}$$

where $g(\varepsilon)$ is the single-particle level density for the equilibrium mean field. In our model the equilibrium mean field is approximated by a spherical square-well potential of radius $R = 1.2A^{1/3}$fm (and infinite depth) so that $g(\varepsilon)\propto\varepsilon^{1/2}$. For the monopole channel we put in the external field $Q_{L=0}(\mathbf{r}) = r^2Y_{00}(\theta, \varphi)$. The integrals (23, 24) are the semiclassical versions of similar quantities which have been studied in analogous quantum approaches to the problem of pairing vibrations [1]. In the quantum theory, the integrals (23, 24) are replaced by sum over discrete nuclear levels.

The possible solutions of Eq. (22) are complex. The real part of the solution is defined by the minimum of the absolute value of the function $K(L, \omega)$. In figure (on the *left*) the absolute value of the function $K(L = 0, \omega)$ is shown for the monopole channel. We assume $A = 208$ and the Fermi energy is determined by the parameterization chosen for the radius as $\varepsilon_F \approx 33$ MeV. The value of μ is practically coincident with that of ε_F, so we have used $\mu = \varepsilon_F$. The deep dent of the quantity $K(L = 0, \omega)$ at $\omega \approx 2$ MeV means that the dispersion relation (22) has an approximate solution at $\omega \approx 2\Delta$ (the value of $\Delta = 1$ MeV was used in our calculations).

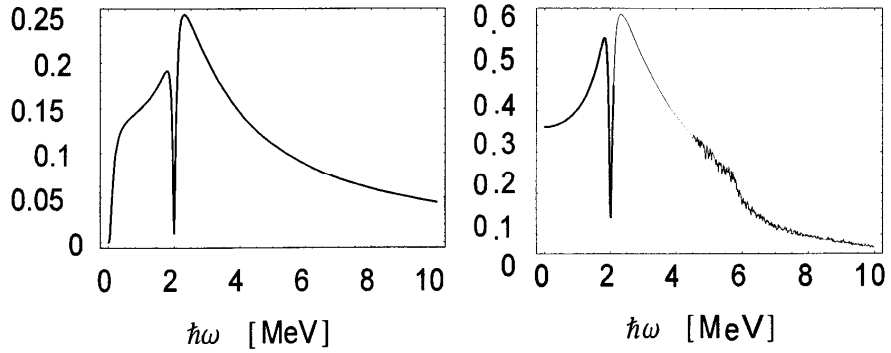

Absolute value of the quantity $K(L, \omega)$ for the monopole (on the *left*) and quadrupole (on the *right*) channels.

The quadrupole channel is also interesting. The expression of the dispersion relation (21) for the quadrupole channel is more complicated than for the monopole one, see [4]. In this case the external field is assumed to be of the form $Q_{L=2}(\mathbf{r}) = r^2Y_{20}(\theta, \varphi)$. The figure (on the *right*) shows the absolute value of $K(L = 2, \omega)$ for the quadrupole channel. The sharp drop of $K(L = 2, \omega)$ at $\omega \approx 2$ MeV is still present. The origin of this dent is the same as that for the monopole channel because $K(L = 2, \omega)$ contains a part which is proportional to $K(L = 0, \omega)$. The small wiggles above 4 MeV are of numerical origin and have no physical meaning.

4. Conclusions

We have studied the solutions of the semiclassical time-dependent Hartree - Fock - Bogoliubov equations of motion for finite Fermi systems in a linear approximation in which the pairing field is allowed to oscillate. The pairing field fluctuations are derived from the self-consistency relation.

The self-consistent pairing-field fluctuations introduce possibility of new collective modes of the system, generated by the pairing interaction. We have found out the dispersion relation which determines pairing collective modes. Our semiclassical dispersion relation for pairing vibration in heavy nuclei has approximate solution at $\omega \approx 2\Delta$ for the monopole and quadrupole channels.

It is known that collective pairing modes in nuclei can be strongly excited by two-neutron transfer reactions. To study these processes within the quasiparticle random phase approximation, the response function is used that is related to the external field which changes the number of particles in the system. It is of interest to introduce a corresponding external field in our semiclassical approach in order to get a suitable response function for studying of collective pairing effects.

REFERENCES

1. *Brink D.M., Broglia R.A.* Nuclear Superfluidity. - Cambridge University Press, UK, 2005. - 377 p.
2. *Combescot R., M. Yu. Kagan M. Yu., Stringari S.* Collective mode of homogeneous superfluid Fermi gases in the BEC-BCS crossover. // Phys. Rev. - 2006. - Vol. A74. - P. 042717 - 042730.
3. *Abrosimov V.I., Brink D.M., Dellafiore A., Matera F.* Kinetic equation for finite systems of fermions with pairing // Nucl. Phys. - 2008. - Vol. A800. - P. 1 - 20.
4. *Abrosimov V.I., Brink D.M., Dellafiore A., Matera F.* Self-consistency and search for collective effects in semiclassical pairing theory // Nucl. Phys. - 2011. - Vol. A864. - P. 38 - 62.
5. *Ring P., Schuck P.* The Nuclear Many-Body Problem. - New York: Springer-Verlag, 1980. - 716 p.
6. *Bohr A., Mottelson B.R.* Nuclear Structure. Vol. 2. Nuclear Deformations. - New York: W.A. Benjamin, 1975. - 748 p.
7. *Urban M., Schuck P.* Dynamics of a trapped Fermi gas in the BCS phase. // Phys. Rev. - 2006. - Vol. A73. - P. 013621 - 013635.
8. *Brink D.M., Dellafiore A., Di Toro M.* Solution of the Vlasov equation for collective modes in nuclei. // Nucl. Phys. - 1986. - Vol. A456. - P. 205 - 234.

NEW TYPE OF NUCLEAR COLLECTIVE MOTION - SPIN SCISSORS

E. B. Balbutsev, I. V. Molodtsova

Joint Institute for Nuclear Research, Dubna, Moscow region, Russia

The coupled dynamics of low lying modes and various giant resonances are studied with the help of the Wigner Function Moments method on the basis of Time Dependent Hartree - Fock equations in the harmonic oscillator model including spin orbit potential plus quadrupole-quadrupole and spin-spin residual interaction. New low lying spin dependent modes are analyzed.

1. Introduction

In the paper [1] the Wigner Function Moments (WFM) method was applied for a first time to solve the TDHF equations including spin dynamics. The most remarkable result was the discovery of the new type of the nuclear collective motion - rotational oscillations of "spin-up" nucleons with respect of "spin-down" nucleons (spin scissors). Three low lying excitations of the new nature were found: isovector and isoscalar spin scissors and the excitation generated by the relative motion of the orbital angular momentum and spin of the nucleus (they can change their absolute values and directions keeping the total angular momentum unchanged).

In the frame of the same approach ten high lying excitations were obtained: well known isoscalar and isovector GQR, two resonances of the new nature describing isoscalar and isovector quadrupole vibrations of "spin-up" nucleons with respect of "spin-down" nucleons, and six resonances which can be interpreted as spin flip modes of various nature and multipolarity. In the absence of proper residual interactions the last eight modes have very small excitation probabilities and the standard shell model energies $E = 2\hbar\omega(\delta)$.

Only spin orbital interaction was taken into account in the paper [1], as the most important one among all possible spin dependent interactions because it enters into the mean field. The aim of this work is to study the influence of the spin-spin residual interaction on the energies and excitation probabilities of all found modes, especially the low lying ones, which are expected to be very sensitive to such forces.

2. Model Hamiltonian and equations of motion

The microscopic Hamiltonian of the model is the harmonic oscillator with spin orbit potential plus separable quadrupole-quadrupole and spin-spin residual interactions:

$$H = H_{osc} + H_{qq} + H_{ss}.$$

The contribution of H_{qq} to the mean field potential was found in [2]. The analogous problem for H_{ss} can be solved in a standard way, with the help of formula (5.34) of the book [3].

TDHF equations are solved by the method of phase space (or Wigner function) moments. To this end they are rewritten at first with the help of the Wigner transformation [3]. Integrating obtained equations over phase space with the weights

$$W = \{r \otimes p\}_{\lambda\mu}, \{r \otimes r\}_{\lambda\mu}, \{p \otimes p\}_{\lambda\mu} \quad \text{and 1},$$

where $\{r \otimes p\}_{\lambda\mu}$ are irreducible tensors [4], one gets the dynamic equations for multipole moments in the phase space which are the collective variables of WFM method. Except quantum numbers λ, μ these variables have also spin quantum numbers σ = +,−,↑↓,↓↑ (with $\pm$ = ↑↑$\pm$↓↓) which they acquire from Wigner functions.

We are interested in the scissors mode with quantum number $K^{\pi} = 1^{+}$. Therefore, we only need the part of dynamic equations with $\mu = 1$. These equations are nonlinear and are solved in the small amplitude approximation. Imposing the time evolution via $e^{i\Omega t}$ for all variables one transforms dynamic equations into a set of algebraic ones. Eigenfrequencies are found as the zeros of its secular equation. Excitation probabilities are calculated with the help of the linear response theory. The detailed explanation can be found in [1, 2].

3. Results of calculations and conclusions

The results of calculations with three values of the spin-spin strength constants (ξ_s - neutron-neutron and proton-proton constant, $\overline{\xi_s}$ - neutron-proton one) are given in Tables 1 and 2. The values of constants are taken from the paper [5], where the notation $\xi_s = K_s/A$, $\overline{\xi_s} = q\xi_s$ was introduced. One can see that spin-spin interaction does not change the qualitative picture of excitations described in [1]. It pushes all levels up proportionally to its strength (20 - 30 % in the case I and 40 - 60 % in the case II) without changing their order. The most interesting result in the isovector case concerns B(M1) values of both scissors - the spin-spin interaction strongly redistributes M1 strength in the favour of the spin scissors.

Table 1. **Isovector energies and excitation probabilities calculated for ^{164}Er with the spin-orbit constant η = 0.36 MeV and three sets of spin-spin interaction constants: I - K_s = 0 MeV; II - K_s = 92 MeV; q = -0.8; III - K_s = 200 MeV; q = -0.5. Quantum numbers (including indices σ =+,-,↑↓,↓↑) of variables responsible for the generation of the present level are shown in first column. For example: $(1,1)^-$ - spin scissors, $(1,1)^+$- "standard" scissors**

$(\lambda, \mu)^\sigma$	E_{iv}, *MeV*			B*(M1)*, μ_N^2			B*(E2)*, B_W		
	I	II	III	I	II	III	I	II	III
$(1,1)^-$	1.61	2.02	2.34	3.54	5.44	7.91	0.12	0.36	0.82
$(1,1)^+$	2.18	2.45	2.76	5.33	4.48	2.98	1.02	1.23	1.26
$(0,0)^{\downarrow\uparrow}$	12.80	16.81	20.02	0.01	0.01	0.04	0.04	0.13	0.52
$(2,1)^-$	14.50	18.52	21.90	0.01	0.02	0.34	0.03	0.13	4.29
$(2,2)^{\uparrow\downarrow}$	16.18	20.61	24.56	0.02	0.23	0.03	0.18	3.09	0.44
$(2,0)^{\downarrow\uparrow}$	16.20	22.65	27.67	0.00	0.03	0.00	0.00	0.39	0.02
$(2,1)^+$	20.59	21.49	22.42	2.78	2.19	1.77	35.45	30.47	27.43

It is necessary to note also that in the isoscalar case the low lying mode marked by $(1,1)^+$ is practically insensitive to the spin-spin interaction.

Table 2. **The same as in Table 1, but for isoscalar excitations**

$(\lambda, \mu)^\sigma$	E_{iv}, MeV			B*(M1)*, μ_N^2			*B(E2)*, B_W		
	I	II	III	I	II	III	I	II	III
$(1,1)^-$	1.73	2.04	2.40	0	0	0	0.65	0.39	1.12
$(1,1)^+$	0.39	0.37	0.37	0.24	0.24	0.24	117.90	118.27	117.19
$(0,0)^{\downarrow\uparrow}$	12.83	15.59	18.72	0	0	0	0.31	0.15	0.66
$(2,1)^-$	14.51	17.40	20.65	0	0	0	0.06	0.03	0.12
$(2,2)^{\uparrow\downarrow}$	16.20	19.43	23.09	0	0	0	0.07	0.04	0
$(2,0)^{\downarrow\uparrow}$	16.22	20.09	24.80	0	0	0	0.02	0.01	0.20
$(2,1)^+$	10.28	11.92	13.60	0	0	0	57.78	50.87	66.50

In conclusion, the WFM method is applied for the first time to solve the TDHF equations including spin dynamics with the model Hamiltonian consisting of a harmonic oscillator with spin orbit mean field potential plus quadrupole-quadrupole and spin-spin residual interactions. Two isovector and two isoscalar low lying eigenfrequencies and five isovector and five isoscalar high lying eigenfrequencies have been found.

Three low lying levels correspond to the excitation of new types of modes. For example the isovector level marked by $(1,1)^-$ describes rotational oscillations of nucleons with the spin projection "up" with respect of nucleons with the spin projection "down", i.e. one can talk of a nuclear spin scissors mode. Having in mind that this excitation is an isovector one, we can see that the resulting motion looks rather complex - proton spin scissors counter-rotates with respect to the neutron spin scissors. Thus the experimentally observed group of 1^+ peaks in the interval 2 - 4 MeV, associated usually with the nuclear scissors mode, in reality consists of the excitations of the "spin" scissors mode together with the 'standard' [6] scissors mode (the level $(1,1)^+$ in our case). The isoscalar level $(1,1)^-$ describes the real spin scissors: all spin up nucleons (protons together with neutrons) oscillate rotationally out of phase with all spin down nucleons.

One more new low lying mode (isoscalar, marked by $(1,1)^+$) is generated by relative motion of the orbital angular momentum and spin of the nucleus (they can change their absolute values and directions keeping the total angular momentum unchanged).

Two high lying excitations of the new nature are found. They are marked by $(2,1)^-$ and following the paper [7] can be called spin-vector giant quadrupole resonances. The isovector one corresponds to the following motion: the proton system oscillates out of phase with the neutron system, whereas inside of each system spin up nucleons oscillate out of phase with spin down nucleons. The respective isoscalar resonance describes out of phase oscillations of all spin up nucleons (protons together with neutrons) with respect of all spin down nucleons.

Six high lying modes can be interpreted as spin-flip giant monopole (marked by $(0,0)^{\downarrow\uparrow}$) and quadrupole (marked by $(2,0)^{\downarrow\uparrow}$ and $(2,2)^{\uparrow\downarrow}$) resonances.

The aim of this work was to demonstrate, that the generalization of the WFM method by including spin degrees of freedom allows one to reveal a variety of new types of nuclear collective motion involving spin degrees of freedom. Such excitations were, undoubtedly, produced by other methods, but they never were explained in such terms.

We should mention that we did not include pairing in this work. Inclusion of pairing would have complicated the formalism quite a bit. We here wanted to work out the features of spin dynamics in a most transparent way staying, however, somewhat on the qualitative side. That is why we don't try to discuss here any possible relations with experiment or to compare with the results of other theories. In the light of the above results, the study of all found (low and high lying) excitations with pairing included, will be the natural continuation of this work. Pairing is important for a quantitative description of the 'standard' scissors mode. The same is expected for the novel spin scissors mode discussed here.

REFERENCES

1. *Balbutsev E.B., Molodtsova I.V., Schuck P.* Spin scissors mode and the fine structure of M1 states in nuclei // Nucl. Phys. - 2011. - Vol. A872. - P. 42 - 68.
2. *Balbutsev E.B., Schuck P.* The nuclear scissors mode in a solvable model // Nucl. Phys. - 2003. - Vol. A720. - P. 293 - 336; *Balbutsev E. B., Schuck P.* Erratum to: "The nuclear scissors mode in a solvable model" // Nucl. Phys. - 2003. - Vol. A728. - P. 471 - 479.
3. *Ring P., Schuck P.* The Nuclear Many-Body Problem. - Berlin: Springer, 1980. - 716 p.
4. *Varshalovitch D.A., Moskalev A.N., Khersonski V. K.* Quantum Theory of Angular Momentum. - Singapore: World Scientific, 1988. - 514 p.
5. *Sarriguren P., Moya de Guerra E., Nojarov R.* Spin M1 excitations in deformed nuclei from self-consistent Hartree - Fock plus random-phase approximation // Phys. Rev. - 1996. - Vol. C54. - P. 690 - 705; *Sarriguren P., Moya de Guerra E., Nojarov R.* Test of three-body contact Skyrme forces with spin excitations in deformed nuclei // Z. Phys. - 1997. - Vol. A357. - P. 143 - 147.
6. *Heyde K., von Neuman-Cosel P., Richter A.* Magnetic dipole excitations in nuclei: elementary modes of nucleonic motion // Rev. Mod. Phys. - 2010. - Vol. 82. - P. 2365 - 2423.
7. *Osterfeld F.* Nuclear spin and isospin excitations // Rev. Mod. Phys. - 1992. - Vol. 64. - P. 491 - 557.

MECHANICAL BREAKDOWN IN THE NUCLEAR MULTIFRAGMENTATION PHENOMENA. THERMODYNAMIC ANALYSIS

L. A. Bulavin, K. V. Cherevko, V. M. Sysoev

Physics Department, Taras Shevchenko National University, Kyiv, Ukraine

Based on a similarity of the Van der Waals and nucleon-nucleon interaction the known thermodynamic relations for ordinary liquids are used to analyze the possible decay channels in the proton induced nuclear multifragmentation phenomena. The main features of the different phase trajectories in the P-V plane are compared with the experimental data on multifragmentation. It allowed choosing the phase trajectories with the correct qualitative picture of the phenomena. Based on the thermodynamic analysis of the proton-induced multifragmentation phenomena the most appropriate decay channel corresponding to the realistic phase trajectory is chosen. Macroscopic analysis of the suggested decay channel is done in order to check the possibility of the mechanical breakdown of the heated system. Based on a simple thermodynamic model preliminary quantitative calculations of corresponding macroscopic parameters (energy, pressure) are done and therefore the model verification on macroscopic level is held. It is shown that on macroscopic level the chosen decay channel through the mechanical breakdown meets the necessary conditions for describing the proton-induced multifragmentation phenomena.

1. Introduction

Disintegration when a bigger nucleus breaks into one or several nuclei and some nucleons is one of the two basic mechanisms in nature by which nuclei can be formed. The appropriate way to study this phenomenon is the experiment with proton-nucleus and nucleus-nucleus collisions. The present study to a large extent was inspired by the growing understanding of the reactions in which excited nuclei break up into intermediate size fragments. Such a phenomena is observed in collisions at energies higher than the threshold value $E_{th} \sim 2-4$ MeV/nucleon [1]. The nature of the IMF production in such experiments is of great interest for consequent understanding of the nuclear matter properties and progress in the studies of nuclear equation of state [2 - 6].

Starting from pioneering works of Finn *et al.* [7] and up to present days much effort has been put forward to investigate multifragmentation in nuclear collisions [1, 8, 9]. Some existing models are related to statistical description based on multi-body phase space calculations [10] whereas others describe the dynamic evolution of the systems via molecular dynamics [11, 12] The experimental observation of multiple intermediate mass fragments (IMF) is also often linked to the nuclear liquid-gas transition [13].

In spite of a long history and a high number of different approaches used there is still a number of problems left that have no explanation. For example, models involving the phase transition have the strong position based on the recent works dealing with the bimodality [14 - 16], but at the same time they are insensitive to many initial parameters [17] when it is known for ordinary liquids that the phase transition is usually the quality difficult to prepare. The most successful models in describing the observed fragment mass distribution nowadays are the statistical equilibrium models [18, 19]. They are used for intermediate energy heavy ion collisions in many substantial variations [20]. At the same time such models have a number of problems [17, 19].The question with the equilibrium at low freeze-out density that lies in the basis of such theories is not confirmed by some microscopic approaches. Another problem is the predicted kinetic energy of the fragments being lower than the observed experimental values. Therefore the determination of the macroscopic model suitable for the multifragmentation phenomenon and able to solve the existing problems in natural way is of particular interest as this issue has not been settled up to now.

From this point of view it is important that the thermodynamic behavior of the nuclear matter has much in common with that of the fluids. The physical reason is the qualitative similarity of the Van der Waals and nucleon-nucleon interaction [21]. It allows using the knowledge of the ordinary liquid behavior for revealing the underlying mechanism of the nuclear multifragmentation.

In this work we focus our analysis on the proton-induced nuclear multifragmentation. In subsequent parts of the paper we will study different possible phase trajectories of the excited nuclear system at P-V plane. Our aim here is to get a qualitative picture of the phenomenon from the macroscopic analysis of the thermodynamic system considering the boundedness of the system. And to check the suggested decay channel for any restrictions on the macroscopic level (energy, pressure, volume) prohibiting its realization in real experiments.

2. Phase diagram analysis

Analyzing possible phase trajectories of the nuclear system in the Pressure-Volume (P-V) plane one can find two different groups of phase trajectories, namely: the single-phase transitions and two-phase transitions. Let us assume our system before the collision to be in point L of the phase diagram (Fig. 1). This position suggests either the single-phase transition (dashed line) or two-phase transitions (solid line). It is obvious that there could be a mixture of two decay channels when different parts of the system are found indifferent areas of the phase diagram.

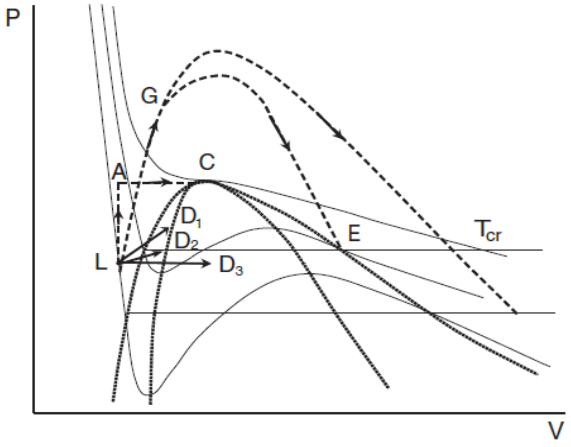

Fig. 1. Possible phase trajectories of the nuclear system in theproton-induced multifragmentation phenomenon.

A particularly interesting set of phase trajectories that stands up in the study of multifragmentation phenomenon is that where the trajectories do not cross the binodal (LAC and LGE type curves in Fig. 1) [22]. The necessary condition for realizing the above trajectories is heating the system to supercritical temperature in order to get over the critical point and binodal line. This mechanism can be realized either in the whole system or in a part of it when the other parts follow the different trajectories.

The next decay mechanism we are going to discuss here could be represented by a number of different trajectories leading to the metastable region (*e.g.* LD_1, LD_2-type transitions in Fig. 1). It is a two-phase mechanism that can be switched on either by overheating under the equilibrium pressure or by liquid stretching due to the gas-dynamic expansion of the high pressure regions.

As for the second group among the two-phase trajectories one should consider spinodal decomposition which means the instability of the system to the small fluctuations [23]. Unfortunately there are some peculiarities restricting the validity of spinodal decomposition model. Cahn's theory of spinodal decomposition [23] for the changes in free energy presents the following:

$$\Delta F = \int \left[\frac{1}{2} \left(\frac{\partial^2 f}{\partial c^2} (c - c_0)^2 \right) + K (\nabla c)^2 \right] dV \qquad (1)$$

And therefore the system is unstable to the Fourier components with $\beta < \beta_c = \left(-\frac{\partial^2 f / \partial c^2}{2K} \right)^{1/2}$ or sufficiently large wavelength as it decreases the system free energy when it is in the unstable region. This result shows that for the smaller wavelengths there is no decrease in the system free energy. As nucleus is quite a bounded system the question arises if it is big enough to have wavelengths needed for the spinodal decomposition?

As stated in the Introduction we dwelt on the qualitative picture which should be the first step in choosing the most appropriate phase trajectory. In the Table 1 pros and cons of different groups of trajectories are compared.

Table 1. **Comparison of the decay mechanisms**

	Single-phase transitions	Metastable boiling	Spinodal decomposition
Pros	Most effective one regarding the time required. Doesn't require thermalization of the system. Might be responsible for the high kinetic energies of the fragments. Can explain IMF + gas of nucleons Polydisperse spectrum.	Might be responsible for the high kinetic energies of the fragments. Can explain IMF + gas of nucleons Polydisperse spectrum	Can explain IMF + gas of nucleons Polydisperse spectra of fragments close to the experimental data.
Cons	If observed in the whole volume condensed fragments come only from the recondensation in the metastable region. Seems to be doubtful for small systems.	Long process timescale. System thermalization required Wrong fragments mass spectra for bounded systems.	System thermalization required The boundness of the systems could lead to the impossibility of the small fluctuations to be amplified. Long process timescale.

Summing up all pros and cons of different decay channels qualitative characteristics we suggest that the most appropriate decay channel is the mechanical breakdown of the shell in the single-phase process (in the small inner part of the system) that may be followed by the metastable boiling of the shell.

3. Mechanical breakdown

This decay channel corresponds to the LAC or LGE type phase trajectories in the P-V plane for the excited inner part of the system and possibly LD_1 or LD_2 trajectories for the shell (Fig. 1 [24]). In subsequent parts of the paper we check this decay channel for any restrictions on the macroscopic level (energy, pressure, volume) prohibiting its realization in real experiments.

3.1. Nuclear matter ultimate strength and the breakdown pressure

When analyzing the possible mechanical breakdown of the system within the elasticity theory one should now the ultimate strength of the matter which is the quantity defining the maximum tension the matter can withstand without braking.

In our work we have done rough estimates for the nuclear matter ultimate strength based on the study of the ^{235}U decay in the approximation of the uniform charge distribution. The idea is that the only destroying force is the Coulomb force. We haven't studied Skyrme, surface, etc. terms separately but we rather suggested an integral value of the ultimate strength. From our calculations we have got $\sigma = 6.2 \cdot 10^{21}\ N/m^2$.

In our model the necessary pressure P for destroying the shell Δ in dependence on the size R of the heated inner part of the system might be found from the elasticity theory and has the form:

$$P = \sigma \frac{R^2 - (R-\Delta)^2}{(R-\Delta)^2} \tag{2}$$

3.2. Temperature of the inner part and corresponding pressure

There are different values of the temperature reported in the literature within the range of 5 - 8 MeV [25] Our point is that all those calculations are model dependant. For example, many of them use he hypothesis of the equilibrated source at freeze-out, when it is not strictly proved [19]. This suggests that there is a possibility of different mechanism being responsible for the multifragmentation. We tried to obtain the temperature values that are more or less model independent. It should be taken into account that we suggest this temperature not for the whole system, but only for the "hot" small inner part. In our article we do an attempt to analyze the INC calculations results and in such a way to define the macroscopic parameters of the system.

Table 2. **Deposited energy**

Projectile energy, Gev	Method	E^*, GeV	T, MeV
3.7	INC	1.2	20.5
8.1	INC	1.4	22.1
3.7	INC + fast	0.95	18.0
8.1	INC + fast	1.11	19.7

In the Table 2 there estimations for the temperatures from the two approaches in analyzing the INC calculations data from [26]. First is the straight forward calculation not considering the "fast particles" when the second considers the energy taken away by the "fast particles" (first emitted particles within the $\tau \sim 5-10\ fm/c$ [26] that are much more energetic than the latest one).

The obtained temperature values were used to compare the pressure in the "hot" inner part of the nuclei with the breakdown pressure. For calculating the pressure we used EOS in the following form [27]:

$$P(T,\rho,X) = \tilde{P}(T,\rho) + P_{sym}(T,\rho,\alpha) + \left(\frac{4\pi\rho}{3A}\right)^{1/3} \frac{Z^2 e^2}{5A}\rho \tag{3}$$

$$\tilde{P}(T,\rho) = -a_0\rho^2 + a_3(1+\sigma)\rho^{2+\sigma} + T\rho\left[1 + \sum_{n=1}^{5} b_n \left(\left(\frac{2\pi\hbar^2}{mT}\right)^{3/2} \frac{\rho}{g}\right)^n\right]$$

$$P_{sym}(T,\rho,X) = \left[\frac{2}{3}\left(x_0 + \frac{1}{2}\right)a_0\rho^2 - (1+\sigma)a_3\rho^{2+\sigma} + +T\rho\sum_{n=1}^{5}\frac{n(n+1)}{2} b_n \left(\left(\frac{2\pi\hbar^2}{mT}\right)^{3/2} \frac{\rho}{g}\right)^n\right] X^2 .$$

As for the parametrization we considered the soft EOS with the incompressibility module $K = 222$ MeV . The parameters used are $t_0 = -2112.248, t_3 = 13988.567, \sigma = 0.2554,\ x_0 = 0.244$ [28].

The comparison of the pressure required for the shell breakdown and the possible pressure in the proton induced multifragmentation is shown in the Figs. 2 and 3.

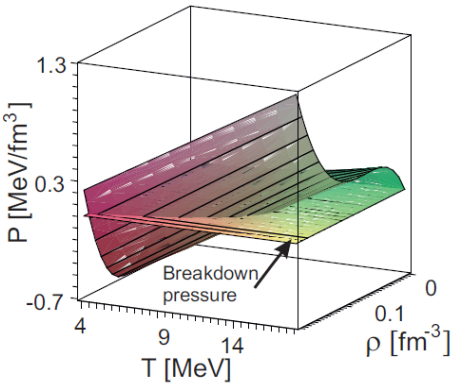

Fig. 2. Nuclear matter pressure from the EOS and the outer shell breakdown pressure dependence on temperature and density.

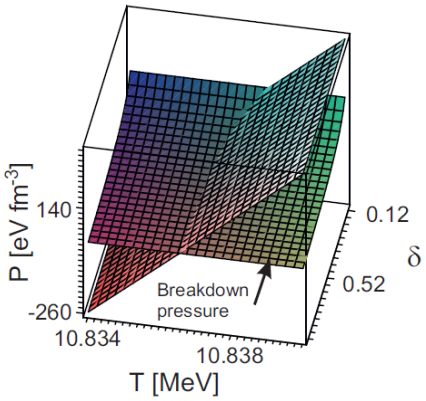

Fig. 3. Nuclear matter pressure from the EOS and the outer shell breakdown pressure dependence on temperature and evaporation level.

One may see that for the inner part densities in the range $\rho = 0.8 \div 1\rho_0$ it's enough to have the temperature above 10.8 MeV in order to realize the breakdown of the shell. Comparison with the data from Table 2 suggests that the energy deposited into the system in the multifragmentation phenomena experiments is enough for the realization of the studied decay channel. It is worth mentioning that in our calculations we treated only a small inner part being "thermalized" rather than the whole volume.

Conclusions

1) Not all of the phase trajectories could be realized in nuclear systems because of their size.
2) Some phase trajectories does not meet the requirements for the time needed for the process.
3) Spinodal decomposition could not be responsible for the multifragmentation phenomena because of the system size.
4) On macroscopic level the mechanical breakdown of the thermodynamic system in a single-phase process that may be followed by metastable boiling of the shell is a good and quite adequate candidate for explaining the proton-induced multifragmentation phenomena
5) Analysis of our "thermodynamic" model on macroscopic level shows that there is enough energy in the system for the mechanical breakdown of the shell and it possibly allows to resolve some existing controversies in standard models (*e.g.* the question with the equilibrium at low freeze-out density, the problem with the predicted kinetic energy of the fragments being lower than the observed experimental values)

REFERENCES

1. *Botvina A.S., Mishustin I.N.* Statistical description of nuclear break-up // Eur. Phys. J. A. - 2006. - Vol. 30. - P. 121 - 128.
2. *Pan J., Das Gupta S.* Unified description for the nuclear equation of state and fragmentation in heavy-ion collisions // Phys. Rev. C. - 1995. - Vol. 51. - P. 1384 - 1392.
3. *Viola V.E, Kwiatkowski K., Natowitz J.B., Yennello S.J.* // Phys. Rev. Lett. - 2004. - Vol. 93. - P. 132701.
4. *Chase K. C., Mekjian A. Z.* Heated Nuclear Matter, Condensation Phenomena, and the Hadronic Equation of State // Phys. Rev. Lett. - 1995. - Vol. 75. - P. 4732 - 4735.
5. *Fuchs C., Wolter H.H.* Modelization of the EOS // Eur. Phys. J. A. - 2006. - Vol. 30. - P. 5 - 21.
6. *Chaudhuri G., Das Gupta S.* Phase diagram for asymmetric nuclear matter in the multifragmentation model // Phys. Rev. C. - 2009. - Vol. 80. - P. 044609.
7. *Finn J.E. et al.* Nuclear Fragment Mass Yields from High-Energy Proton-Nucleus Interactions // Phys. Rev. Lett. - 1982. - Vol. 49. - P. 1321.
8. *Siemens P.J.* // Nature. - 1983. - Vol. 305. - P. 410.
9. *Lee S.J., Mekjian A.Z.* Nuclear, chemical and mechanical instability and the liquid-gas phase transition in nuclei // Phys. Rev. C. - 2008. - Vol. 77. - P. 054612.
10. *Gulminelli F., Durand D.* Theoretical comparison of different thermometers for the determination of the nuclear caloric curve // Nucl. Phys. A. - 1997. - Vol. 615. - P. 117 - 134.
11. *Zhang F.-S.* // Z. Phys. A. - 1996. - Vol. 356. - P. 163.
12. *Nebauer R. et al.* (*INDRA Collaboration*). Multifragmentation in Xe(50 AMeV) + Sn: Confrontation of theory and data // Nucl. Phys. A. - 1999. - Vol. 658. - P. 67 - 93.
13. *Cussol D., Suraud E., Gregoire C., Pi M.* // Nuovo Cim. - 1991. - Vol. 104. - P. 611.
14. *Bonnet E. et al.* (*INDRA and ALADIN Collaborations*). Bimodal Behavior of the Heaviest Fragment Distribution in Projectile Fragmentation // Phys. Rev. Lett. - 2009. - Vol. 103. - P. 072701.

15. *Chaudhuri G., Das Gupta S., Gulminelli F.* Bimodality and Coulomb effects with a canonical thermodynamic model // Nucl. Phys. A. - 2009. - Vol. 815. - P. 89 - 99.
16. *Le Fevre A., Aichelin J.* Bimodality: A Sign of Critical Behavior in Nuclear Reactions // Phys. Rev. Lett. - 2008. - Vol. 100. - P. 042701.
17. *Hufner J.* // Phys. Rep. - 1985. - Vol. 125. - P. 129.
18. *Botvina A. S. et al.* Multifragmentation of spectators in relativistic heavy-ion reactions // Nucl. Phys. A. - 1995. - Vol. 584. - P. 737 - 756.
19. *Campi X., Krivine H., Plagnol E., Sator N.* "Little big bang" scenario of multifragmentation // Phys. Rev. C. - 2003. - Vol. 67. - P. 044610.
20. *Das C. B., Das Gupta S., Mekjian A. Z.* Model of multifragmentation, equation of state, and phase transition // Phys. Rev. C. - 2003. - Vol. 67. - P. 064607.
21. *Shlomo S., Kolomietz V.M.* Hot nuclei // Rep. Prog. Phys. - 2005. - Vol. 68. - P. 1.
22. *Zemlianov A.A., Kuzikovsky A.V.* // Sov. J. Quant. Electronics. - 1980. - Vol. 7. - P. 1523.
23. *Cahn J.W.* // J. Chem. Phys. - 1965. - Vol. 42. - P. 93.
24. *Cherevko K. V., Bulavin L. A., Sysoev V. M.* Thermodynamic analysis of multifragmentation phenomena // Phys. Rev. C. - 2011. - Vol. 84. - P. 044603.
25. *Kelic A., Natowitz J.B., Schmidt K.-H.* // Eur. Phys. J. A. - 2006. - Vol. 30. - P. 203.
26. *Cugnon J.* // Nucl. Phys. A. - 1987. - Vol. 462. - P. 751.
27. *Jaqaman H.R.* Coulomb instability of hot nuclei // Phys. Rev. C. - 1989. - Vol. 39. - P. 169.
28. *Klupfel P., Reinhard P.-G., Burvenich T.J., Maruhn J.A.* Variations on a theme by Skyrme: A systematic study of adjustments of model parameters // Phys. Rev. C. - 2009. - Vol. 79. - P. 034310.

INERTIA MOMENT OSCILLATING COMPONENT OF QUANTUM HARMONIC OSCILLATOR

A. A. Khamzin[1], A. S. Sitdikov[1,2], A. S. Nikitin[2], D. A. Roganov[3]

[1] *Kazan State Federal* (*Volga region*) *University, Kazan, Russia*
[2] *Kazan State Power-Engineering University, Kazan, Russia*
[3] *ОАО "Акционерный инвестиционный коммерческий Банк "Татфондбанк"", Казань, Россия*

The original method for the calculation of inertia moment of nucleus at arbitrary frequencies and finite temperatures in framework of cranking model with harmonic oscillator potential is suggested. In the adiabatic case the analytical calculations show oscillations of inertia moment depending on chemical potential. Are oscillations moment of inertia is increase at spherical limit of deformation and exponentially decrease at increase of temperature

1. Introduction

One of the fruitful approaches considering the rotating nucleus and finite Fermi-systems is the Cranking model [1 - 3]. At the same time the most of significant phenomena that appear at collective rotation, are caused by particles near Fermi surface, i.e. shell effects appear. This fact allows avoiding the solutions of complicated nonlinear equations of cranking model and essentially simplifies the description of the collective nuclear dynamics. All that is possible due to possibility of separating the most of physical quantities into smooth (averaged, i.e. the Thomas - Fermi) and shell correction (oscillating) parts. In particular, Pashkevich and Frauendorf [5] represent the moment of inertia as the sum of smooth and oscillating parts on the basis of shell correction Strutinsky's method [4].

The next important step has been made by Strutinsky and Magner and they have developed the semiclassical theory of Gutzwiller [6] to calculate the oscillating components by using fruitful periodic orbit theory [7, 8]. In [9 - 11] this method was applied to calculate the shell corrections for the moments of inertia of finite Fermi systems in deformed harmonic oscillator potential and was demonstrated the comparison semiclassical calculations with quantum mechanical results. Large oscillations depending on chemical potential are shown, decreasing with a deformation from spherical to deformed shapes.

The purpose of this work is analytical investigations of large scale oscillations [11] of inertia moment shell corrections depending on chemical potential at fixed deformations.

2. Analytical calculations moment of inertia oscillating component

In [11] we obtain generalization of Zelevinski's formula [3] for the inertia moment of quantum harmonic oscillator for finite temperatures case:

$$\Theta_x(\omega)=\sum_{\xi} f(\varepsilon_{\xi}^{\omega}-\lambda)\frac{<l_x>_{\xi}}{\omega}=\hbar\left\{\frac{2(\omega_y^2+\omega_z^2)}{\omega_+^2-\omega_-^2}\left(\frac{\bar{N}_-}{\omega_-}-\frac{\bar{N}_+}{\omega_+}\right)-\left(\frac{\bar{N}_-}{\omega_-}+\frac{\bar{N}_+}{\omega_+}\right)\right\}. \quad (1)$$

Where $f(x)=(\exp(x/T)+1)^{-1}$ – the Fermi function, $\bar{N}_{\alpha}=\sum_{\xi} f(\varepsilon_{\xi}^{\omega}-\lambda)\left(n_{\alpha\xi}+1/2\right)$ ($\alpha=\pm$) and λ – Fermi-energy.

The oscillating behavior of inertia moment depending on chemical potential is revealed at fixed deformation parameters [11]. It is very interesting to investigate such oscillations analytically.

In this connection we analyze the dependence of moment of inertia on chemical potential in the adiabatic limit at low temperatures. It is assumed that under this limit the angular velocity $\omega\to 0$ and spectrum is not depend from angular velocity

$$\varepsilon_{\xi}=\hbar\omega_{\perp}(n_{\perp\xi}+1)+\hbar\omega_z(n_{z\xi}+1/2),\quad n_{\perp\xi}=n_{x\xi}+n_{y\xi}, \quad (2)$$

where $\omega_x=\omega_y=\omega_{\perp}$ at axial symmetry, $\omega_{\perp}=\omega_0\eta^{1/3}$, $\omega_z=\omega_0\eta^{-2/3}$, $\eta=\omega_{\perp}/\omega_z$ – deformation parameter. From (1) we obtain the following expression for the inertia moment

$$\Theta_x=\frac{d_s\hbar}{2\omega_{\perp}\omega_z}\left[\frac{(\omega_z-\omega_{\perp})^2}{\omega_{\perp}+\omega_z}(\overline{N}_y+\overline{N}_z)+\frac{(\omega_z+\omega_{\perp})^2}{\omega_{\perp}-\omega_z}(\overline{N}_z-\overline{N}_y)\right], \quad (3)$$

where $\bar{N}_{\alpha}=\sum_{\xi} f(\varepsilon_{\xi}-\lambda)\left(n_{\alpha\xi}+1/2\right)$, d_s – spin degeneration.

The results of numerical calculations of inertia moment (3) for various values of deformations η at the tempera-

ture $T = 0{,}1\,\hbar\omega_0$ have been presented in Fig. 1. The Figure clearly demonstrates the presence of oscillations in behavior of inertia moment depending on chemical potential, increasing sharply with deformation to spherical shape. In this picture for comparison we reduce also quantum mechanical rigid-body inertia moment Θ_x^{rig}

$$\Theta_x^{\text{rig}} = d_s m \sum_{\xi} f(\varepsilon_\xi - \lambda) \left\langle \xi \left| y^2 + z^2 \right| \xi \right\rangle = d_s \hbar \left(\frac{\overline{N}_y}{\omega_\perp} + \frac{\overline{N}_z}{\omega_z} \right). \tag{4}$$

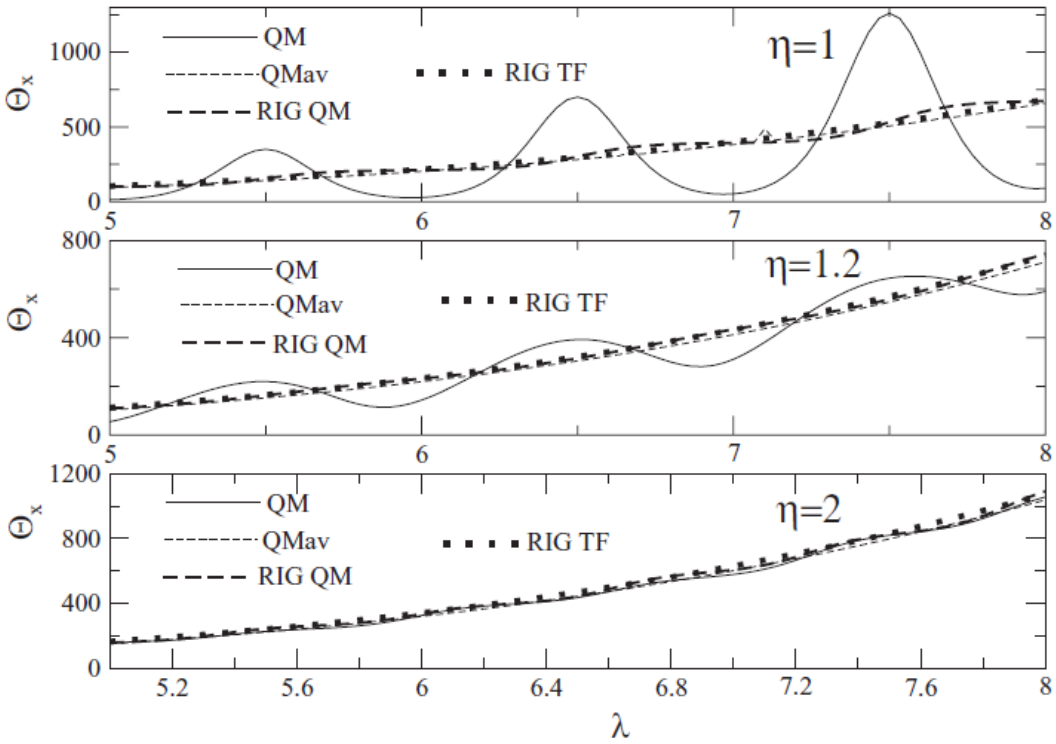

Inertia moment (22) (quantum; QM), its Strutinski's averaged (QMav), quantum rigid-body inertia moment (23) (RIG QM) and its Thomas-Fermi approximation (24) (RIG TF) as function of chemical potential λ for the same values of deformation parameter and temperature $T = 0{,}1\,\hbar\omega_0$. All moments of inertia in units $\hbar/\omega_0$, λ – in units $\hbar\omega_0$.

Fig. 1 demonstrates that oscillations of $\Theta_x^{\text{rig}}(\lambda)$ detached from Thomas-Fermi rigid-body inertia moment $\Theta_{x\,\text{TF}}^{\text{rig}}(\lambda)$:

$$\Theta_{x\,\text{TF}}^{\text{rig}} = m \int \mathbf{dr} r_{\perp x}^2 \rho_{\text{TF}}(\vec{r}) = \frac{m d_s}{6\pi^2\hbar^3} \int \mathbf{dr} (y^2 + z^2) p_{\text{F}}^2(r) = \left(\frac{1+\eta^2}{3\omega_\perp^2} \right) \frac{\lambda^4}{4(\hbar\omega_0)^3}, \tag{5}$$

where $p_{\text{F}}(r) = \sqrt{2m\left(\varepsilon_{\text{F}} - m\left[(x^2+y^2)\omega_\perp^2 + \omega_z^2 z^2\right]/2\right)}$, $\rho_{\text{TF}}(\vec{r}) = d_s p_{\text{F}}^3 / (6\pi^2\hbar^3)$-Thomas-Fermi density.

Large-scale oscillations of full inertia moment Θ_x in comparison with the oscillations of Θ_x^{rig} at small deformations can be easily understood from expression (3) that can be rewrited in the following way

$$\Theta_x = \Theta_x^{\text{rig}} + \frac{4\eta^2}{\omega_\perp^2(\eta^2 - 1)} q, \tag{6}$$

where $q = \omega_z \overline{N}_z - \omega_\perp \overline{N}_\perp$. Accordingly, shell correction $\delta\Theta_x$ is determined by expression:

$$\delta\Theta_x = \delta\Theta_x^{\text{rig}} + \frac{4\eta^2}{\omega_\perp^2(\eta^2 - 1)} \delta q, \tag{7}$$

i.e. are determined by shell corrections to the $\delta\Theta_x^{\mathrm{rig}}$ and δq. The function q characterize the breaking of statistically equilibrium rotation ($\omega_x \overline{N}_x = \omega_y \overline{N}_y = \omega_z \overline{N}_z$) and the presence of even small shell corrections due to multiplier $\eta^2 - 1$ in denominator leads to the significant increase of amplitude of oscillations at spherical limit.

The oscillating behavior of inertia moment is some analogue of the oscillations of van Alphen-de Haase in electronic gas, that is the consequence of quantized Landau levels in magnetic field. Similar oscillations of other thermodynamic quantities appear in many quantum finite Fermi systems [12] as consequence of discretness of states, when temperature becomes order of space $\delta \sim E_F / N$ ($\mathrm{E_F}$ – Fermi energy of the system, N – number of particles) between the levels. In this connection now we analyze the oscillations in behavior of inertia moment depending on chemical potential using the methods of calculating the oscillating components of the physical quantities of electronic gas in magnetic field [13, 14].

Now we rewrite the expression (3) in the form

$$\Theta_x = \frac{\hbar}{\omega_\perp(\eta^2-1)}\left[(\eta-1)^3\overline{N}_+ + (\eta+1)^3\overline{N}_-\right], \tag{8}$$

where

$$\overline{N}_\pm = \overline{N}_z \pm \overline{N}_y = \sum_\xi f(\varepsilon_\xi - \lambda)\left(n_{z\xi} + \frac{1}{2} \pm \left(n_{y\xi} + \frac{1}{2}\right)\right) =$$

$$= \sum_{n_\perp, n_z} (n_\perp + 1) f(\varepsilon_{n_\perp, n_z} - \lambda)\left(n_z + \frac{1}{2} \pm \frac{1}{2}(n_\perp + 1)\right) \tag{9}$$

($d_s = 2$). For extracting the oscillating component in (8) we use the well-known summation formula of Poisson:

$$\frac{1}{2}\varphi(0) + \sum_{n=0}^{\infty}\varphi(n) = \int_0^\infty \varphi(n)dn + 2\,\mathrm{Re}\sum_{k=1}^{\infty}\int_0^\infty \varphi(n)\exp(2\pi i k n)\,dn\,. \tag{10}$$

Now we apply this formula to the sum $n_\perp$ in double-sums in (9) (we assume, that number of quants in direction $\perp$ can be exchanged unlimitedly). At such approach is the sum separated on two integrals and only the second integral in (10) gives the oscillating contribution. Then for the oscillating parts of $\overline{N}_\pm$ we have:

$$\widetilde{\overline{N}_\pm} = \mathrm{Re}\sum_{n_z}\sum_{k=1}^{\infty} J_k^\pm\,, \tag{11}$$

where $\widetilde{\overline{N}_\pm}$ denote the oscillating part of $\overline{N}_\pm$, and

$$J_k^\pm = \int_0^\infty (n_\perp + 1)(2n_z + 1 \pm (n_\perp + 1)) f(\varepsilon_{n_\perp n_z} - \lambda)\exp(2\pi i k n_\perp)\,dn_\perp\,. \tag{12}$$

At further integration it is convenient to pass to integration over energy ε. Then we get

$$J_k^\pm = \pm\frac{1}{\omega_\perp}\exp\left(-\frac{2\pi i k}{\eta}\left[n_z + \frac{1}{2}\right]\right)\int_0^\infty d\varepsilon \frac{\exp(2\pi i k\varepsilon/\omega_\perp)}{\exp((\varepsilon-\lambda)/T)+1}\left(\frac{\varepsilon}{\omega_\perp} - \left[\frac{\varepsilon_{0n_z}}{\omega_\perp} - 1\right]\right)\times$$

$$\times\left(\frac{\varepsilon}{\omega_\perp} \pm (2\eta \mp 1)\left[\frac{\varepsilon_{0n_z}}{\omega_\perp} - 1\right]\right). \tag{13}$$

We take the bottom limit equal to zero, because neighbourhood of Fermi surface only important. Therefore the choice of bottom limit is arbitrary. Further we pass to the new variable $\zeta = (\varepsilon - \lambda)/T$ and replace the bottom limit $-\lambda/T$ to $-\infty$ (because we suppose, that $\lambda/T >> 1$):

$$J_k^{\pm} = \pm\left(\frac{T}{\omega_\perp}\right)^3 \exp\left(2\pi i k\left\{\frac{\lambda}{\omega_\perp} - \frac{1}{\eta}\left[n_z + \frac{1}{2}\right]\right\}\right)\int_{-\infty}^{\infty} d\zeta \frac{\exp\left(2\pi i k T\zeta/\omega_\perp\right)}{\exp(\zeta)+1}\left(\zeta + \frac{\lambda}{T} - \frac{1}{T}\left[\varepsilon_{0n_z} - \omega_\perp\right]\right)\times$$

$$\times\left(\zeta + \frac{\lambda}{T} \pm \frac{2\eta \mp 1}{T}\left[\varepsilon_{0n_z} - \omega_\perp\right]\right). \qquad (14)$$

We take into account that only neighbourhood of Fermi surface is important, we reduce the formula (14) to the expression

$$J_k^{\pm} \simeq \pm\frac{T\lambda^2}{\omega_\perp^3}\exp\left(2\pi i k\left\{\frac{\lambda}{\omega_\perp} - \frac{1}{\eta}\left[n_z + \frac{1}{2}\right]\right\}\right)\int_{-\infty}^{\infty}\frac{\exp\left(2\pi i k T\zeta/\omega_\perp\right)}{\exp(\zeta)+1}d\zeta. \qquad (15)$$

Using the formula

$$\int_{-\infty}^{\infty}\frac{e^{i\alpha\zeta}}{e^{\zeta}+1}d\zeta = \frac{-i\pi}{\mathrm{sh}(\pi\alpha)},$$

we finally obtain for $J_k^{\pm}$:

$$J_k^{\pm} \simeq \mp\frac{i\pi T\lambda^2}{\omega_\perp^3}\frac{\exp\left(2\pi i k\left\{\frac{\lambda}{\omega_\perp} - \frac{1}{\eta}\left[n_z + \frac{1}{2}\right]\right\}\right)}{\mathrm{sh}\left(2\pi^2 Tk/\omega_\perp\right)}. \qquad (16)$$

As a result the expressions for sums $\widetilde{\widetilde{N}}_{\pm}$ are:

$$\widetilde{\widetilde{N}}_{\pm} = \mp\frac{\pi T\lambda^2}{\omega_\perp^3}\sum_{k=1}^{\infty}\mathrm{Re}\left\{\frac{i\exp\left(2\pi i k\lambda/\omega_\perp\right)}{\mathrm{sh}\left(2\pi^2 Tk/\omega_\perp\right)}\sum_{n_z}\exp\left(-\frac{2\pi i k}{\eta}\left[n_z + \frac{1}{2}\right]\right)\right\}. \qquad (17)$$

We make up summation over n_z in (17) and deformation parameter η regards as irrational, we have

$$\sum_{n_z}\exp\left(-\frac{2\pi i k}{\eta}\left[n_z + \frac{1}{2}\right]\right) = -\frac{i}{2\sin\left(\pi k/\eta\right)},$$

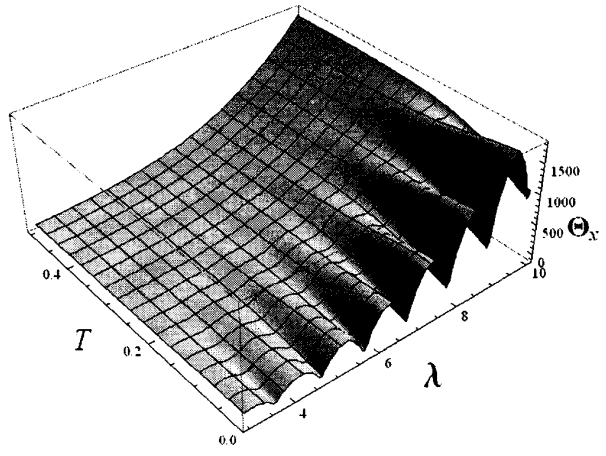

Fig. 2. Inertia moment $\Theta_x = \overline{\Theta}_x + \widetilde{\Theta}_x$, where $\overline{\Theta}_x \approx \Theta_{x\,\mathrm{TF}}^{\mathrm{rig}}$ (24) and $\widetilde{\Theta}_x$ (38), as function of chemical potential λ and temperature T at $\eta = 1.15$. Moment of inertia in units $\hbar/\omega_0$, λ and T – in units $\hbar\omega_0$.

and

$$\widetilde{\widetilde{N}}_{\pm} \simeq \mp\frac{\pi T\lambda^2}{2\omega_\perp^3}\sum_{k=1}^{\infty}\frac{\cos\left(2\pi k\lambda/\omega_\perp\right)}{\mathrm{sh}\left(2\pi^2 Tk/\omega_\perp\right)\sin\left(\pi k/\eta\right)}. \qquad (18)$$

Substitution (18) to (8) leads to the expression:

$$\widetilde{\Theta}_x \simeq \frac{\hbar\pi(1+3\eta^2)T\lambda^2}{\omega_\perp^4(\eta^2-1)}\sum_{k=1}^{\infty}\frac{\cos\left(2\pi k\lambda/\omega_\perp\right)}{\mathrm{sh}\left(2\pi^2 Tk/\omega_\perp\right)\sin\left(\pi k/\eta\right)}. \qquad (19)$$

So, accordingly to (19), inertia moment is really oscillating function of the Fermi energy λ with period $\Delta = \omega_\perp$. We note, that period of oscillations does not depend on temperature. The monotonous part of inertia moment (we denote it by $\overline{\Theta}_x$) can be approximated with rigid-body Thomas-Fermi moment of inertia (5): $\overline{\Theta}_x \approx \Theta_{x\,\mathrm{TF}}^{\mathrm{rig}}(\lambda)$.

At $T >> \omega_\perp$ the amplitude decreases exponentially (as $\exp\left(-2\pi^2 T/\omega_\perp\right)$) and can be neglected. In Fig. 2 we demonstrate the dependence of inertia moment $\Theta_x = \overline{\Theta}_x + \widetilde{\Theta}_x$ (where $\overline{\Theta}_x \approx \Theta_{x\,\mathrm{TF}}^{\mathrm{rig}}$ (5) and $\widetilde{\Theta}_x$ is determined by (19)) from the chemical potential and temperature at $\eta = 1.15$. As we see, the oscillations decrease at increase of temperature.

3. Concluding remarks

In this work we investigate the oscillations of the inertia moment of finite Fermi system in the cranking model formalism in deformed harmonic oscillator potential and obtain analytical formula for oscillating part of this inertia moment. We show that oscillating component as function of chemical potential has period $\omega_\perp = \omega_0 \eta^{1/3}$ and does not depend on temperature. At given temperature amplitude of oscillations increases sharply at spherical limit and exponentially decreases when temperature enlarges.

REFERENCES

1. *Inglis D.R.* Particle Derivation of Nuclear Rotation Properties Associated with a Surface Wave // Phys. Rev. - 1954. - Vol. 96. - P. 1059 - 1062.
2. *Bohr A., Mottelson B.* Invited Lecture at the International Conference on Nuclear Structure // J. Phys. Soc. Japan. - 1978. - Vol. 44. - P. 157.
3. *Zelevinsky V.G.* The simple model for fast-rotating nucleus // Yad. Phys. - 1975. - Vol. 22. - P. 1085 - 1095. [Sov. J. Nucl. Phys. - 1975. - Vol. 22. - P. 565].
4. *Strutinsky V.M.* Shell Effects in Nuclear Masses and Deformation Energies // Nucl. Phys. - 1967. - Vol. A95. - P. 420 - 442.
5. *Pashkevich V.V., Frauendorf S.* // Yad. Phys. - 1974. - Vol. 20. - P. 1122. [Sov. J. Nucl. Phys. - 1974. - Vol. 20. - P. 588].
6. *Gutzwiller M.J.* // Math. Phys. - 1967. - Vol. 12. - P. 343.
7. *Brack M., Bhaduri R.K.* Semiclassical Physics // Frontiers in Physics. - 2003. - No. 96 (Westview Press, Boulder).
8. *Strutinsky V.M., Magner A.G.* Semiclassical theory of atomic nuclei // ECHAYA. - 1976. - Vol. 7. - P. 138. [Sov. J. Part. Nucl. - 1976. - Vol. 7. - P. 138].
9. *Magner A.G., Sitdikov A.S., Khamzin A.A. et al.* Semiclassical Shell Structure of Moments of Inertia in Deformed Fermy Systems // Int. J. Mod. Phys. - 2010. - Vol. E19. - P. 735.
10. *Magner A.G., Sitdikov A.S., Khamzin A.A. et al.* Semiclassical Shell-Structure Energies in Finite Heated Fermi Systems // Yad. Phys. - 2010. - Vol. 73. - P. 1398.
11. *Magner A.G., Sitdikov A.S., Khamzin A.A., Bartel J.* Semiclassical Shell Structure in Rotating Fermi Systems // Phys. Rev. - 2010. - Vol. C81. - P. 064302 (1 - 20).
12. *Minnullin A.R., Tayursky D.A.* Magnetic Susceptibility Noninteracting Fermions in Bounded Geometry // Pis'ma v ZHETF. - 2000. - Vol. 72. - P. 891.
13. *Landau L.D., Lifshits E.M.* Course of Theoretical Physics. Vol. 5. - Moscow: Phizmatlit, 2002.
14. *Abrikosov A.A.* Theory of Metals. - Moscow: Nauka, 1987.

E1 GAMMA-TRANSITIONS IN HOT ATOMIC NUCLEI

V. A. Plujko[1], O. M. Gorbachenko[1], E. P. Rovenskykh[1], V. A. Zheltonozhskii[2]

[1] *Nuclear Physics Department, Taras Shevchenko National University, Kyiv, Ukraine*
[2] *Institute for Nuclear Research, National Academy of Sciences of Ukraine, Kyiv, Ukraine*

New version of the modified Lorentzian approach for radiative strength function is proposed. Renewed systematics for giant dipole resonance (GDR) parameters is given. The gamma-decay strength functions are calculated using renewed GDR parameters and compared with experimental data. It is demonstrated that closed-form approaches with asymmetric shape of the gamma strength provide the most reliable simple method for description of gamma-decay processes.

1. Introduction

Gamma-emission is one of the most universal channels of the nuclear de-excitation which accompany any nuclear reaction. The photoabsorption and gamma-decay processes can be described by means of gamma-ray (radiative) strength functions (RSF) [1]. These functions are involved in calculations of the observed characteristics of most nuclear reactions. They are also used for investigation of nuclear structure (nuclear deformations, energies and widths of the giant dipole resonances, contribution of velocity-dependent force, shape-transitions, etc.) as well as in studies of nuclear reaction mechanisms.

Dipole electric (E1) gamma-transitions are dominant when they occur simultaneously with transitions of other multipolarities. Isovector Giant Dipole Resonances (IVGDR or GDR) are strongly displayed in E1 gamma-transitions in processes of photoabsorption and gamma-decay of the atomic nuclei [1 - 3]. It provides possibility to obtain GDR parameters from investigations of the E1 gamma-transitions. A comprehensive experimental database of updated values of the GDR parameters with estimations of their uncertainties (one-sigma standard deviation) was presented in [3], that is especially important for nuclear reaction codes for the reliable modelling of E1 gamma-ray cascades in highly excited nuclei as well as for the verification of different theoretical approaches used to describe GDR resonances.

In this contribution, a new version of modified Lorentzian approach for RSF [1, 3] is proposed with the use of the renewed GDR width systematics. Different Lorentzian-type models of E1 strength functions [1] are tested by comparison of experimental data with theoretical calculations.

2. GDR parameters with uncertainties and systematics

The values and corresponding uncertainties of the Lorentzian-like model parameters were presented in Ref.[3] from a fit of the theoretical photoabsorption cross sections to the experimental data for 131 isotopes from ^{10}B to ^{239}Pu nuclei (262 entries) and 9 elements of natural isotopic composition (14 entries). The GDR component of the photoabsorption cross section was calculated within standard Lorentzian (SLO) model or within simplified version (SMLO) of the modified Lorentzian approach MLO1 [1, 3]. This compilation updates and extends the RIPL-3 database contained in files *gamma/gdr-parameters&errors-exp-SLO.dat* and *gamma/gdr-parameters&errors-exp-MLO.dat* [1].

In this contribution, the values of GDR parameters and their uncertainties from [3] are used to obtain renewed systematics of GDR parameters. The expression for new systematics for GDR width are taken in the following form (in units of MeV):

$$\Gamma_{r,j} = a_1 \cdot E_{r,j} + a_2 \cdot \beta_{dyn} \cdot E_{r,j} \cdot \gamma_j \,, \qquad (1)$$

where a_1, a_2 are constants, $E_{r,j}$ and $\Gamma_{r,j}$ are GDR energy and width for vibration along j-axis respectively, $\gamma_j = \left(R_0 / R_j\right)^{1.6}$, with R_j, R_0 for nuclear radiuses along j axis and for radius of equivalent spherical nuclei. Parameters of quadrupole dynamical deformation β_{dyn} were determined from systematic [5]: $\beta_{dyn} = \sqrt{1224 A^{-7/3} / E_{2_1^+}}$, where $E_{2_1^+}$ is energy of the first collective 2^+ state. The systematic $E_{2_1^+} = 65 A^{-5/6} / (1 + 0.05 E_{shell})$ was used in the absent of experimental data on $E_{2_1^+}$ with E_{shell} for shell correction energy calculated by the Myers - Swiatecki mass formula [1]. The χ^2 method was used to fit parameters for spherical and axially deformed nuclei. The value $\Delta\Gamma_{r,j} = 1$ (MeV) was taken as GDR width uncertainty. The values of constant and their uncertainties $a_1 = 0.255(20)$, $a_2 = 0.370(83)$ were obtained by the fitting within SLO model. Similar systematics is obtained also for the SMLO model.

The comparisons of the GDR widths with systematic (1) are presented in Fig. 1.

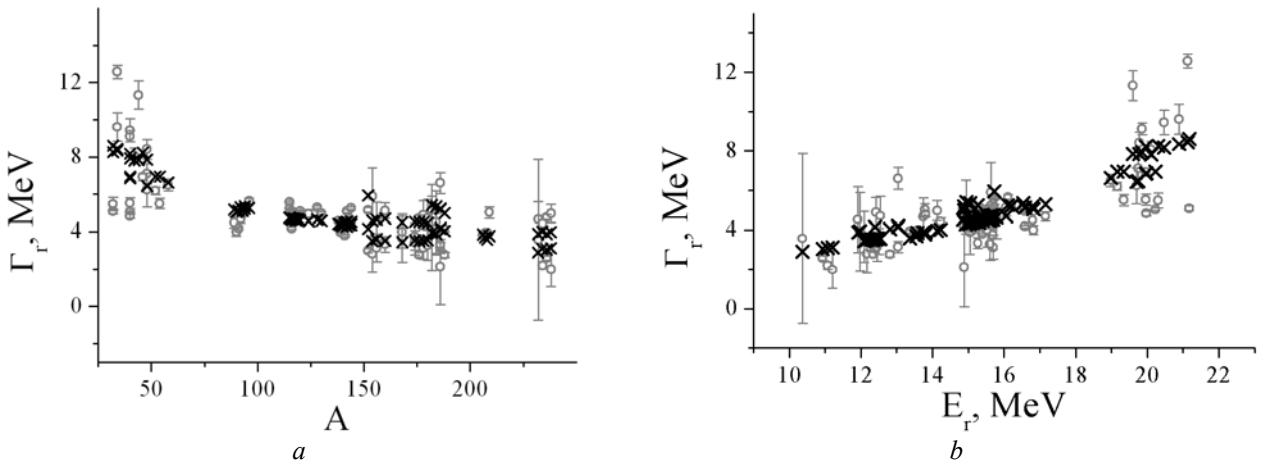

a *b*

Fig. 1. Mean GDR widths as a function of mass number (*a*) and GDR energies (*b*) calculated by the use of SLO model: open circles - renewed GDR parameters [3]; crosses - parameters obtained by the systematic (1).

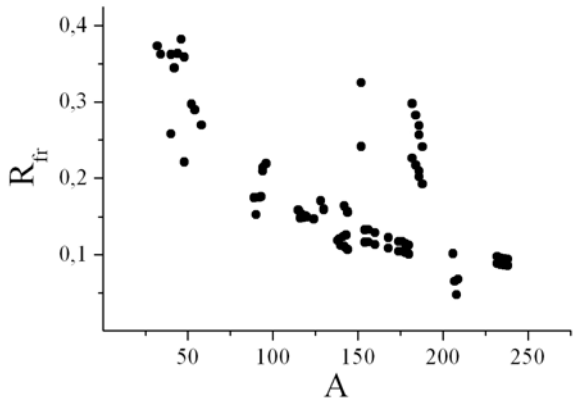

Fig. 2. Ratio $R_{fr,j} = \left(1 - a_1 E_{r,j} / \Gamma_{r,j}\right)$ of fragmentation component to the total GDR width for different nuclei.

As one can see from Fig. 1, the values of GDR widths within renewed systematic are in good agreement with experimental GDR parameters for the middle-weight and heavy atomic nuclei. Fig. 2 demonstrates contribution of the fragmentation component $R_{fr,j} = \left(1 - a_1 E_{r,j} / \Gamma_{r,j}\right)$ into the full GDR width. It can be seen that the contribution of the fragmentation component to the full width value can be up to 40 percent.

3. Verification of simplified RSF models

In order to test simplified RSF models [1], the gamma-decay radiative strength functions are calculated and compared with experimental data. The renewed GDR parameters were used: the SMLO parameters [3] were taken for calculations within MLO models (MLO1, MLO2, MLO3), and parameters of SLO model were applied for other models (SLO, the enhanced generalized Lorentzian, EGLO, and generalized Fermi-Liquid model, GFL). Variants 1 - 3 of MLO model give similar trend for photoabsorption cross sections and, therefore, only the MLO1 calculations are shown in the Figures.

On a base of the systematic (1) for the GDR width, we propose new expression for description of the energy dependent width:

$$\Gamma_j(E_\gamma, U) = b_j \left(a_1 \cdot (E_\gamma + U) + a_2 \cdot \beta_{dyn} \cdot E_{r,j} \cdot \gamma_j\right), \quad (2)$$

where E_γ and U – energy of the gamma-rays and excitation energy respectively. Parameters $b_j = 1$ in the absence of experimental data on GDR width $\Gamma_{r,j}$ and they are found from the condition $\Gamma(E_\gamma = E_{r,j}, U = 0) = \Gamma_{r,j}$ in the opposite cases. The calculations of the MLO model with this expression for energy dependent width are named below as MLO4.

The comparison of the different forms for RSF with the experimental data is shown in Figs 3 - 5.

Fig. 3 shows the dipole gamma-decay strength functions for ^{124}Te and ^{150}Sm within different RSF models in comparison with experimental data from [6, 7]. The calculations were performed for excitation energy $U = S_n$.

The Fig. 4 shows dipole gamma-decay strength functions for ^{150}Sm and ^{171}Yb within different RSF models in comparison with experimental data from [8,9]. The experimental data from [8, 9] are averaged with the excitation energy U by the following form:

$$f_{aver}(E_\gamma) = \begin{cases} \dfrac{1}{U_m - 4} \displaystyle\int_4^{U_m} \tilde{f}(E_\gamma, U_f = U_i - E_\gamma) dU_i, & 1 < E_\gamma \le 4, \\ \dfrac{1}{U_m - E_\gamma} \displaystyle\int_{E_\gamma}^{U_m} \tilde{f}(E_\gamma, U_f = U_i - E_\gamma) dU_i, & 4 < E_\gamma \le U_m, \end{cases}$$

where $U_m = 8$ MeV $\approx S_n$, S_n -neutron separation energy. This averaging on U is resulted from measurement method used in [8, 9].

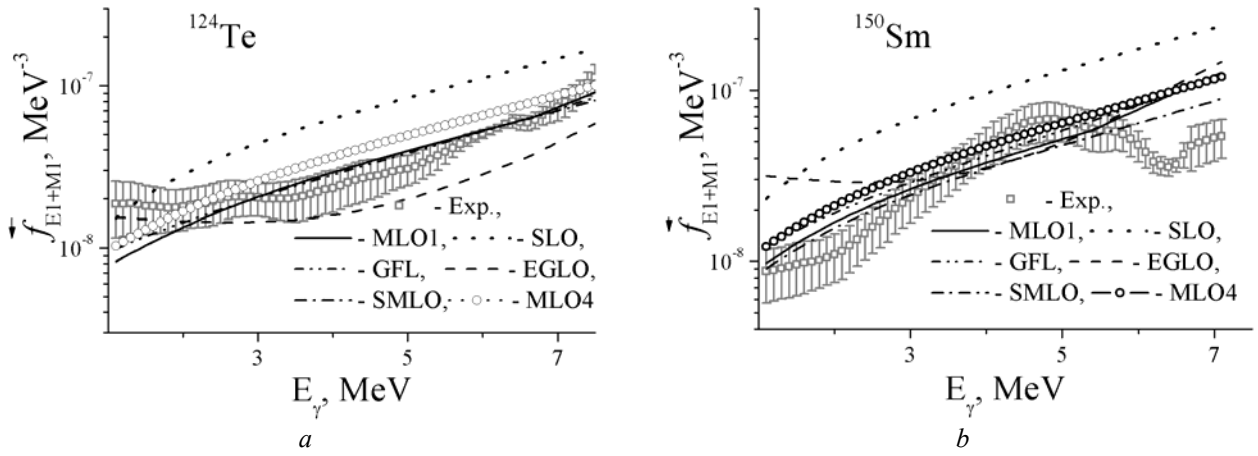

Fig. 3. The gamma-decay strength functions within different RSF models for ^{124}Te (*a*) and ^{150}Sm (*b*): $U = S_n$. Experimental data are taken from [6, 7].

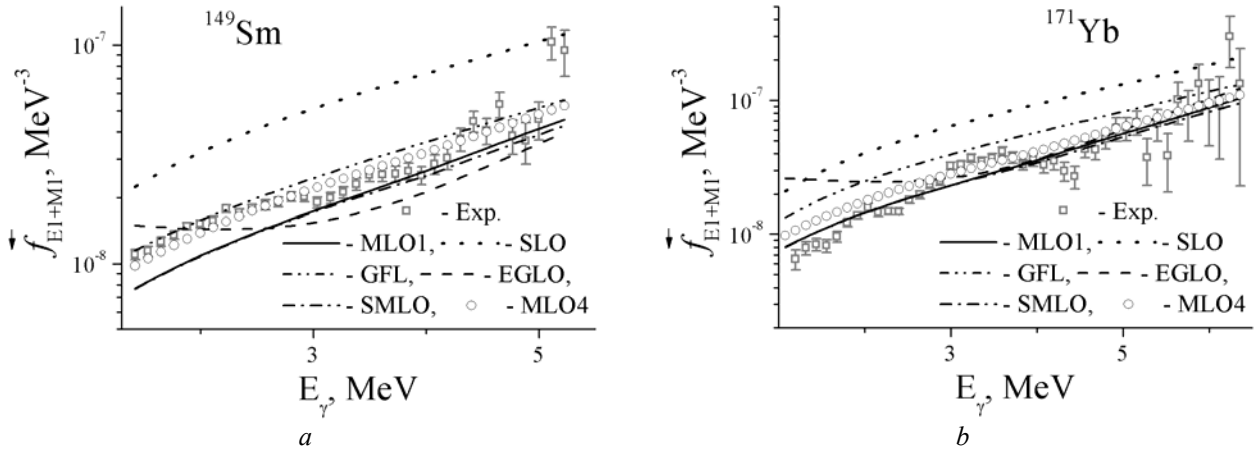

Fig. 4. The gamma-decay strength functions within different RSF models for ^{149}Sm (*a*) and for ^{171}Yb (*b*). The experimental data are taken from [8, 9].

In Fig. 5 results of the calculations for the ^{90}Zr and ^{100}Mo nuclei are compared with experimental data from [10]. The calculations were performed for excitation energy $U = S_n$.

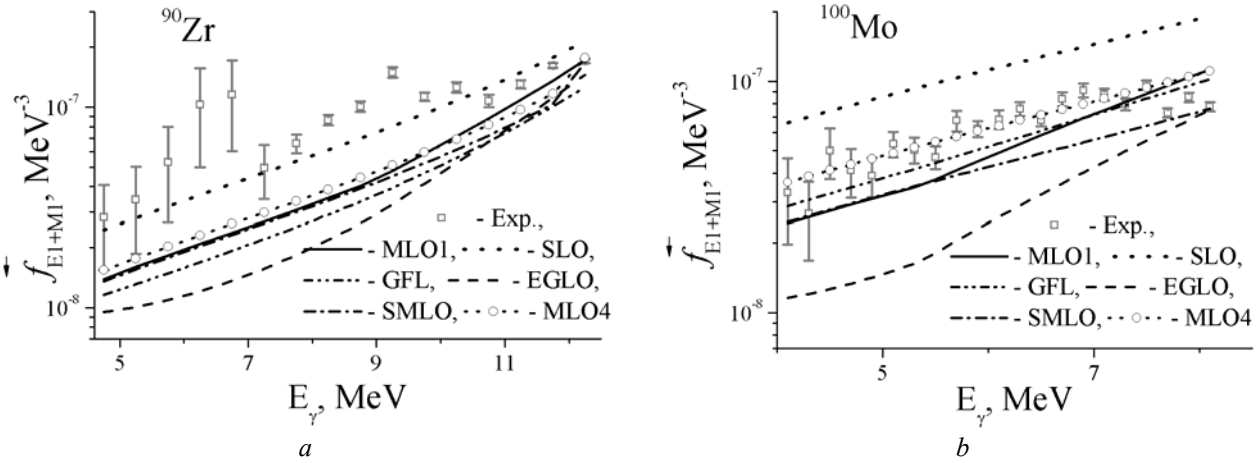

Fig. 5. The gamma-decay strength functions within different RSF models for ^{90}Zr (*a*) and ^{100}Mo (*b*): $U = S_n$. Experimental data are taken from [10]

We see from these Figures that RSF models with asymmetric shape (EGLO, GFL, MLO1, SMLO, MLO4) give better description of the experimental data than the SLO model in the low-energy region, which predict a vanishing strength function at zero gamma-ray energy. The results of the calculations of gamma-decay RSF within EGLO, GFL,

MLO, MLO4 and SMLO models are all characterized by a non-zero limit. It can be also noted that different variants of the MLO (SMLO) approach are based on general relations between the RSF and the nuclear response function [11]. Therefore, they can potentially lead to more reliable predictions among different simple models.

The Table presents the ratio $\chi^2(model)/\chi^2(\mathrm{SLO})$ of chi-square deviations of the theoretical RSF of gamma-decay from experimental data. The average values of the ratio for approximately 40 nuclei with $25 < A < 200$ were obtained. As one can see from this Table and Figures, asymmetric RSF gives better agreement with the experimental data at least in approximation of axially-deformed nuclei which is adopted in presented calculations. On the whole, proposed variant of the MLO model (MLO4) leads to the best description of the experimental data.

The average $\sum_{i=1}^{n}\left(\chi_i^2(model)/\chi_i^2(\mathrm{SLO})\right)/n$ ratio of chi-square deviations of the theoretical RSF of γ-decay from experimental data.

n - cumulative number of nuclei ([6,7]: $n = 38$, [8,9]: $n = 41$, [10]: $n = 7$)

Exp.Data	n	Model				
		EGLO	GFL	MLO	SMLO	MLO4
[6, 7]	38	1,22	0,91	0,98	1,01	0,89
[8, 9]	41	0,18	0,17	0,11	0,11	0,13
[10]	7	2,22	2,11	1,16	1,71	1,20

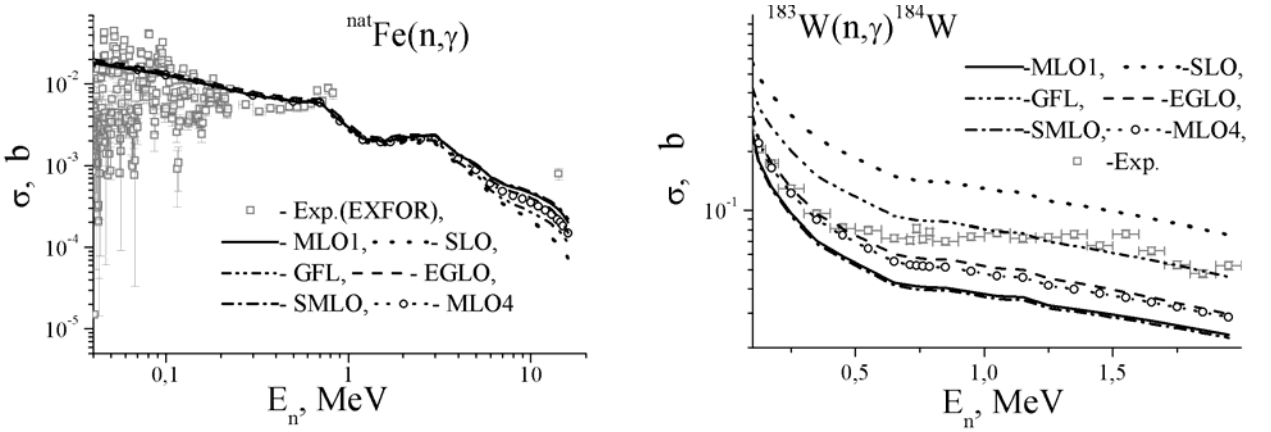

a *b*

Fig. 6. The excitation function of $^{nat}\mathrm{Fe}(n,\gamma)$ and $^{183}\mathrm{W}(n,\gamma)^{184}\mathrm{W}$ reactions using different RSF models. The experimental data are taken from EXFOR data library for panel *a* and [12] for panel *b*.

Fig. 6 shows excitation function of the $^{nat}\mathrm{Fe}(n,\gamma)$ and $^{183}\mathrm{W}(n,\gamma)^{184}\mathrm{W}$ reactions calculated by the use of different RSF models. The cross section calculations were performed by the use of EMPIRE 3.1 Rivoli code [13]. It should be mentioned that in these calculations, gamma-decay widths were normalized on their experimental values at the neutron binding energy. The difference in the calculations of excitation function by the different RSF models is growing in for heavy nuclei. It can be seen from Fig. 6, that calculations within the RSF models with asymmetric shape in general give better agreement with the experimental data for middle-weighted and heavy nuclei.

4. Conclusions

The overall comparison of the calculations within different simple models and experimental data shows that the EGLO and MLO (SMLO) approaches with asymmetric shape of the RSF provide a universal and rather reliable simple method for estimation of the dipole RSF over a relatively wide energy interval ranging from zero to slightly above the GDR peak. In generally, new version of MLO model (MLO4) leads to best description of the experimental data as for gamma-decay and for photoexcitation functions.

Reliable experimental information is needed for more accurate determination of the temperature and energy dependence of the RSF. It would give possibility to investigate the contributions of the different mechanisms responsible for the damping of the collective states and provide more reliable test of the closed-form models of the E1 RSF.

REFERENCES

1. *Capote, R., Herman M., Oblovzinsky P. et al.* Parameters for calculation of nuclear reactions of relevance for energy and non-energy nuclear applications // Nucl. Data Sheets. - 2009. - Vol. 110. - P. 3107 - 3214; see RIPL-3 web site

at http://www-nds.iaea.org/RIPL-3/.
2. *Berman B.L., Fultz S.C.* Measurements of giant dipole resonance with monoenergetic photons // Rev. Mod. Phys. - 1975. - Vol.47. - P. 713 - 761.
3. *Plujko V.A., Capote R., Gorbachenko O.M.* Giant Dipole Resonance Parameters with Uncertainties from Photonuclear Cross Sections // At. Data Nucl. Data Tables. - 2011. - Vol. 97. - P. 567 - 585.
4. *Plujko V.A., Gorbachenko O.M., Bondar V.M. et al.* Renewed data-base of GDR parameters for atomic nuclei // Journal of Korean Physical Society (JKPS). - 2011. - Vol. 59(2). - P. 1514 - 1517.
5. *Esser L., Neuneyer U., Casten R. F. et al.* Correlations of the deformation variables β and γ in even-even Hf, W, Os, Pt, and Hg nuclei // Phys. Rev. C. - 1997. - Vol. 55. - P. 206 - 210.
6. *Sukhovoj A.M., Khitrov V.A. et al.* Cascade gamma-decay of the ^{183}W compound nucleus: opportunity of developing new methods to study experimentally pecularities of heavy nucleus below B_n // Izvestiya RAN. Seriya Fiz. - 2005. - Vol. 69. - P. 641 - 647.
7. *Sukhovoj A.M., Furman W.I., Khitrov V.A.* Approximation of sums of experimental radiative strength functions of dipole gamma-transition in the region $E_\gamma \approx B_n$ fort the atomic masses $40 \le A \le 200$ // Proc. of the XV Int. Seminar on Interaction of Neutrons with Nuclei (Dubna, May 2007). - 2007. - P. 92 - 107.
8. *Melby E., Guttormsen M. et al.* Thermal and electromagnetic properties of ^{166}Er and ^{167}Er // Phys. Rev. C. - 2001. - Vol. 63. - P. 044309 - 044319.
9. *Agvaanluvsan U., Schiller A. et al.* Level densities and γ-ray strength functions in ^{170,171,172}Yb // Phys. Rev. C. - 2004. - Vol. 70. - P. 054611 - 054619; http://ocl.uio.no/compilation/.
10. *Schwengner R., Rusev G. et al.* // Phys. Rev. C. - 2008. - Vol. 78. – P. 064314; Phys. Rev. C. - 2010. - Vol. 81. - P. 034319.
11. *Plujko (Plyuiko) V.A.* The statistical description of the γ-decay width of states with fixed angular momentum // Yad. Fiz. - 1990. - Vol. 52. - P. 1004 - 1014.
12. *Macklin R.L., Drake D.M., Arthur E.D.* Neutron capture cross sections of ^{182}W, ^{183}W, ^{184}W and ^{186}W from 2.6 to 2000 keV // J. Nucl. Science and Engineering. - 1983. - Vol. 84. - P. 98.
13. *Herman M., Capote R. et al.* EMPIRE: Nuclear reaction model code system for data evaluation // Nucl. Data Sheets. - 2007. - Vol. 108. - P. 2655 - 2719.; https://ndclx4.bnl.gov/gf/project/empire/.

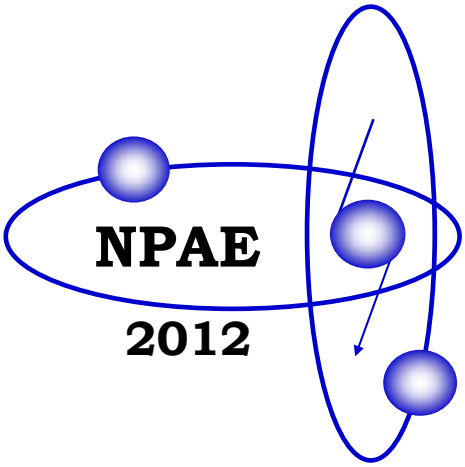

Section 2

Nuclear Reactions

SYSTEMATICS STUDIES OF (n, n'p + d) REACTION CROSS SECTIONS AT 14.5 MeV NEUTRONS ENERGY

M. Belgaid, F. Kadem, A. Amokrane, S. Sekal

Faculté de physique Université des Sciences et de la Technologie Houari Boumedienne, Alger, Algeria

A new semi-empirical formulae for the calculation of the (n, n'p) and (n, n'p + d) cross section at 14.7 MeV neutron energy are obtained. The pre-equilibrium exciton and evaporation models allow establishing these new formulae by using the Droplet model of Myers and Swiatecki to express the reaction energy Q. The systematics behavior of the different terms of the Droplet model involved in reaction energy expressions was checked individually before choosing the pertinent terms and setting up the formula. Fitting these formulae to the existing cross section data, the adjustable parameters have been determined and the systematics of the (n, n'p + d) and (n,d) reactions have been studied. The predictions of these formulae are compared with those of the existing formulae and with the experimental data and give a better fit to the data than the previous comparable formulae.

1. Introduction

The data for gas production via neutron induced reactions are of great importance in the domain of fusion reactor technology, particularly in the calculation of nuclear transmutation rates, nuclear heating and radiation damage due to gas formation. In order to determine unmeasured data, model theory calculation and systematic predictions are useful for estimating this quantity.

However, since these 14 MeV neutron induced cross sections for different nuclei vary rather smoothly with their N and Z values, several semi-empirical relations have been proposed, for example, to systematise the (n, p) and (n, α) reactions [1 - 4]. The relation for the (n, n'p + d) reaction proposed by Forrest [2] with four parameters and based on the evaporation model, is at present the best of all the existing formulas, because it results in the lowest value of χ^2, when used in fitting the (n, n'p + d) experimental data of different nuclei.

The aim of this work is to develop a semi-empirical formula, which depends only on the mass and charge numbers, in order to calculate the (n, n'p + d) reaction cross section for 14.5 MeV neutrons. The pre-equilibrium exciton and evaporation models [5 - 6] show an essentially dependence of the (n, n'p + d) cross section on the reaction energy Q. However the use of the effective reaction energy deduced from the Myers and Swiatecki [7] mass formula allows us to realize an analysis, based on the experimental data, of the (n, n'p + d) cross sections dependence to the different terms of the Droplet model involved in $Q_{(n,\, n'p\, +\, d)}$ before choosing the pertinent terms and setting up the formula.

In this work, we derive an analytical expression with seven parameters that includes the pre-equilibrium contribution, to study the systematics of (n, n'p + d) reaction cross sections and determine the values of the parameters through least-squares analysis of the existing (n, n'p + d) cross section values for different nuclei. We analyze its predictive value and compare it with the existing formulae.

2. Formalism and model parameters

Let us consider the reaction A(n, b)B with many of the symbol definitions given as follows:
E_n: the neutron kinetic energy;
S_n: neutron separation energy;
$E = E_n + S_n$: the excitation energy of the compound nucleus;
S_b: emitted particle separation energy;
E_b: emitted particle kinetic energy;
$U = E - E_b - S_b$: the excitation energy of the residual nucleus.
On the basis of Weisskopf - Ewing evaporation model the cross sections of the emitted particle is given by [8]:

$$\sigma_{nb}^{eq} = \sigma_{CN}^{a} \frac{F_b}{\sum F_{b'}}, \tag{1}$$

where σ_{CN}^{a} is the compound nucleus (CN) formation cross section through the entry channel (a) and F_b represents a quantity that is proportional to the partial decay width Γ_b of the compound nucleus for the emitted particle through the decay channel (b) calculated via the detailed balance theorem:

$$F_b = \frac{2m_b}{\hbar^2}(2I_b + 1) \int_0^{E-S_b} \sigma_{inv}^{b} E_b \rho(U) dE_b \,, \tag{2}$$

where I_b and m_b are respectively the spin and the reduced mass of the emitted particle from the compound nucleus, $\rho(U)$ is the level density of the residual nucleus B at an excitation energy U. Σ indicates the sum over all the decay channels b'. One can easily derive the expression of the evaporation cross sections [1 - 2, 9] σ_{nb} as

$$\sigma_{nb}^{eq} = \sigma_{CN}^{n} \frac{m_n}{m_b} \exp(\frac{S_n - S_b}{T} - \frac{V_b}{T}) = \sigma_{CN}^{n} \exp(\frac{Q_{nb} - V_b}{T}), \quad (3)$$

where Q_{nb} is the (n, b) reaction energy, V_b is the coulomb energy for charged emitted particle and T is the nuclear temperature assumed to be equal for particle and neutron emission.

On the other hand, the contribution of the pre-equilibrium emission based on the exciton model in his closed form, allow to write the energy spectrum of the emitted particle as [10]

$$\frac{d\sigma_{nb}^{pre}}{dE_b} = \sigma_{CN}^{n} \frac{(2S_b + 1) m_b \sigma_{inv}^{b} E_b}{\pi^2 \hbar^3 g E} \sum_{n=3} \frac{\omega(n-1, U)}{\omega(n, E)} \tau_n, \quad (4)$$

Where $\omega(n, E)$ is the exciton state density, g is the level density parameter defined in the uniform spacing model and τ_n is the life time of the n exciton state.

The expression of the exciton state density used here is given by [11]:

$$\omega(n, E) = \frac{g^n E^{n-1}}{p!h!(p+h-1)!} \quad (5)$$

where p and h are number of excited particles and number of excited holes in an exciton state n respectively, they are related to n by: $n = p + h$.

With substitution of $\omega(n, E)$ given by Eq. (5) in Eq. (4) we obtain the follow expression of the emitted particle energy spectrum for the pre-equilibrium component:

$$\frac{d\sigma_{nb}^{pre}}{dE_b} = \sigma_{CN}^{n} \frac{(2S_b + 1) m_b \sigma_{inv}^{b} E_b}{\pi^2 \hbar^3 g E} \sum_{n=3} \left(\frac{U}{E}\right)^{n-2} p(n-1) \tau_n, \quad (6)$$

where the summation is taken over the exciton number n.

The major contribution to the pre-equilibrium cross sections is essentially due to the exciton number $n = 3$. With using the sharp cutoff of the inverse cross section $\sigma_{inv}^{b} = \pi R^2 (1 - V_b / E_b)$, the pre-equilibrium cross sections can be derived after integrating over the emitted particle energy:

$$\sigma_{nb}^{pre} = \sigma_{CN}^{n} \int_{V_b}^{E_n + Q_{nb}} \frac{(2S_b + 1) m_b \pi R^2 (1 - V_b / E_b) E_b}{\pi^2 \hbar^3 g E} \left(\frac{E_n + Q_{nb} - E_b}{E}\right) 4\tau_3 dE_b. \quad (7)$$

The integration leads to:

$$\sigma_{nb}^{pre} = \sigma_{CN}^{n} \frac{(2S_b + 1) m_b \pi R^2 (E_n + Q_{nb} - V_b)^3}{\pi^2 \hbar^3 g E^2} 4\tau_3. \quad (8)$$

The cross sections due to the equilibrium (Eq. 3) and pre-equilibrium (Eq. 7) emission can be given now as:

$$\sigma_{nb} = \sigma_{CN}^{n} \left(\beta_1 \exp(\frac{Q_{nb} - V_b}{T}) + \beta_2 (E_n + Q_{nb} - V_b)^3 \right) \quad (9)$$

$$\text{with} \quad \beta_1 = \frac{m_b (2I_b + 1)}{m_n (2I_n + 1)} \text{ and } \beta_2 = \frac{(2I_b + 1) m_b \pi R^2}{\pi^2 \hbar^3 g E^2} 4\tau_3,$$

where $\sigma_{CN}^{n} = \pi \lambda\!\!\!^{-2} \sum_{\ell=0}^{\ell_{max}} (2\ell + 1) T_\ell$ around 14 MeV neutrons energy, the transmission coefficients T_ℓ for waves of orbital angular momentum $\ell \le \ell_{max} = R / \lambda\!\!\!^{-}$ (with $\lambda\!\!\!^{-} = 1/k_c$) involved in the interaction are close to unity, we can thus write the compound nucleus cross section as follows:

$$\sigma_{CN}^{n} = \pi \lambda\!\!\!^{-2} \sum_{\ell=0}^{R/\lambda\!\!\!^{-}} (2\ell + 1) \simeq \pi (R + \lambda\!\!\!^{-})^2 \quad (10)$$

with $R = r_0 A^{1/3}$ at 14 MeV neutron $\lambda\!\!\!^{-} \cong r_0$ and $\sigma_{CN}^{n} \approx \sigma_R$ that can be written as

$$\sigma_R = \pi r_0^2 (1 + A^{1/3})^2 \quad \text{with } r_0 = 1.2 \text{ fm} \tag{11}$$

Now, by using the Droplet model of Myers and Swiatecki [7, 2] Q_{nd} can be expressed as

$$Q_{n,\,n'p\,+\,d} = d_1S_1 + d_2S_2 + d_3S_3 + d_4B_1 + d_5B_2 + d_6B_3 + \text{terms} \tag{12}$$

with relatively small contributions ignored;
$S_1 = (N - Z + 0.5)/A$, the usual asymmetry term found;
$S_2 = (N - Z + 0.5)/A^{4/3}$, the surface asymmetry term;
$S_3 = [(N - Z)^4 - (N - Z + 1)^4]/A^3$, the asymmetry anharmonicity term;
$B_1 = (2Z - 1)/A^{1/3}$, the usual Coulomb term;
$B_2 = (2Z - 1)/A$, the Coulomb diffuseness term;
$B_3 = (2Z - 1)A^{1/3}$, the Coulomb volume redistribution term.
By substituting the formula of equation (12) in the expression of the (n,n'p + d) cross section we obtain:

$$\sigma_{nd} = \sigma_R \begin{Bmatrix} \exp\left[\frac{\beta_1}{T}(\alpha_1S_1 + \alpha_2S_2 + \alpha_3S_3 + \alpha_4B_1 + \alpha_5B_2 + \alpha_6B_3 - V_d)\right] + \\ \beta_2(E_n + (\alpha_1S_1 + \alpha_2S_2 + \alpha_3S_3 + \alpha_4B_1 + \alpha_5B_2 + \alpha_6B_3 - V_d)^3 \end{Bmatrix}. \tag{13}$$

Before setting up the relation for the $\sigma_{n,d}$ we checked the behaviour of these terms against the ratio $\sigma_{n,d} / \sigma_R$ for 37 nuclei (Figs. 1 - 3), where the experimental values of $\sigma_{n,d}$ cross sections were taken from EXFOR[] data compilations and were presented in Table 1. The values of σ_R were calculated with Eq. (11). In our search for a formula, we have classified the target nuclei into two groups according to the sign of $\xi + 1$ where $\xi = S_n - S_p$ is the difference between neutron and proton separation energies (see Fig. 1). We note that for the group with $\xi > -1$, the Figs. 2 and 3 show a quadratic dependence of $ln(\sigma_{nd}/\sigma_R)$ on the asymmetry term $S_1 = (N - Z + 0.5)/A$ and linear dependence on the usual Coulomb term given by $B_3 = (2Z - 1)/A^{1/3}$. For the same group, the dependence of pre-equilibrium cross section on $(Q_{nd})^3$, via the asymmetry term S_1, is illustrated in the Fig. 4. For the group with $\xi < -1$ the quadratic dependence of $ln(\sigma_{nd}/\sigma_R)$ on the surface asymmetry term is presented in Fig. 5.

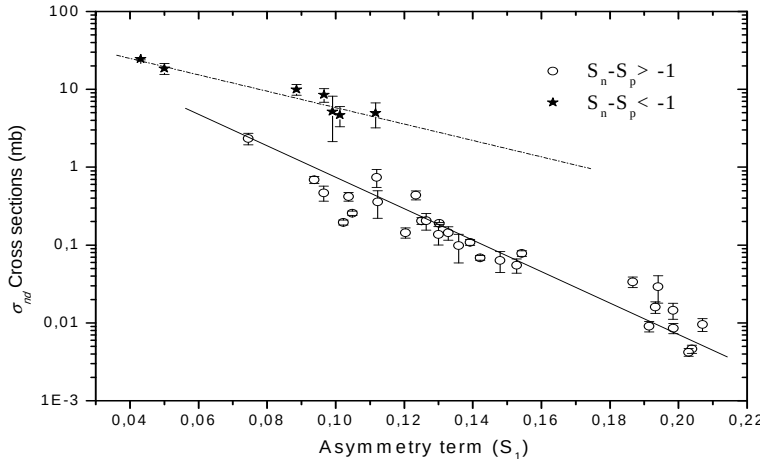

Fig. 1 σ_{nd} cross section as function of the asymmetry term S_1.

On the basis of the above analysis we can replace the linear dependence of $Q_{n,d}$ on the asymmetry term by a quadratic one in the first member of Eq. (13) describing the equilibrium contribution. While for the second member of Eq. (13) describing the pre-equilibrium component, we are retained the dependence of $Q_{n,d}$ on the asymmetry term. Then, with the dependence of σ_{nd} on V_d/T and V_d neglected and in order to develop the systematics for the (n, n'p + d) reaction cross section at 14.5 MeV the following expressions were obtained and given in mb unit as:

$$\sigma_{nd+n'p} = (1 + A^{1/3})^2 \begin{cases} \exp(C_1 + C_2S_1^2 + C_3B_1) + (C_4 + C_5S_1)^3 & \xi > -1 \\ \exp(C_6 + C_7S_2^2) & \xi < -1 \end{cases}, \tag{14}$$

$$\sigma_{nd} = (1 + A^{1/3})^2 \exp(C_1 + C_2S_1 + C_3S_2), \tag{15}$$

where C_i (i = 1, ... 7) are free parameters that could be found by using the fit of an experimental (n, n'p + d) and (n, d) cross sections at 14.5 MeV.

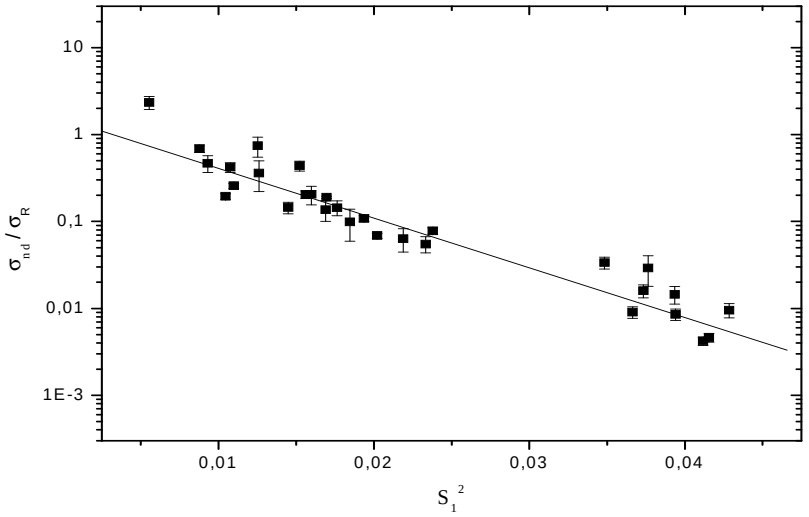

Fig. 2. Values of the ratio $\sigma_{(n,d)}/\sigma_R$ for $\xi > -1$ group showing the quadratic dependence of $ln(\sigma_{nd}/\sigma_R)$ on the asymmetry term obtained from EXFOR data and Eq. (14).

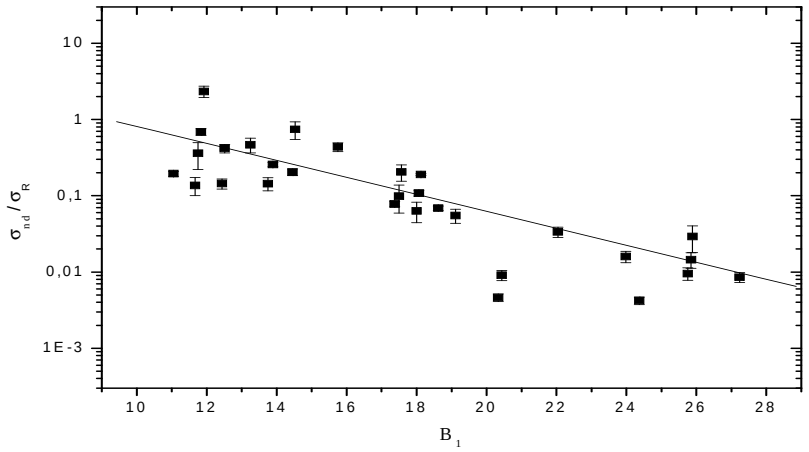

Fig. 3. Values of the ratio $\sigma_{(n,d)}/\sigma_R$ for $\xi > -1$ group showing the dependence of $ln(\sigma_{nd}/\sigma_R)$ on the usual coulomb term obtained from EXFOR data and Eq. (14).

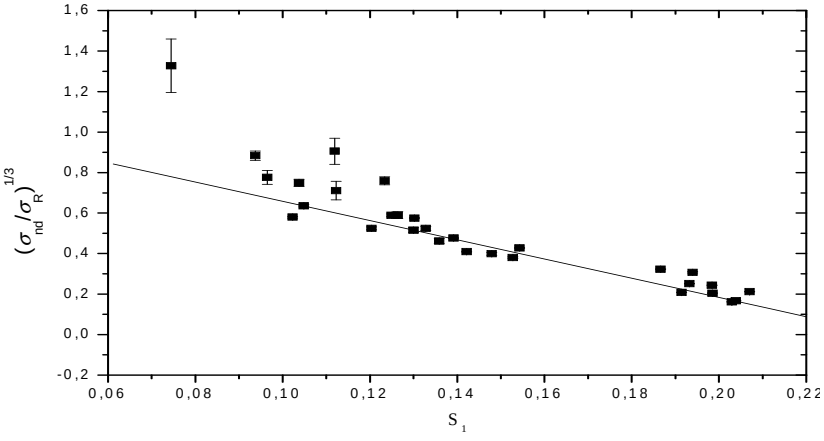

Fig. 4. Values of the ratio $\sigma_{(n,d)}/\sigma_R$ for $\xi > -1$ group showing the dependence of $(\sigma_{nd}/\sigma_R)^{1/3}$ on the asymmetry term obtained from EXFOR data and Eq. (14).

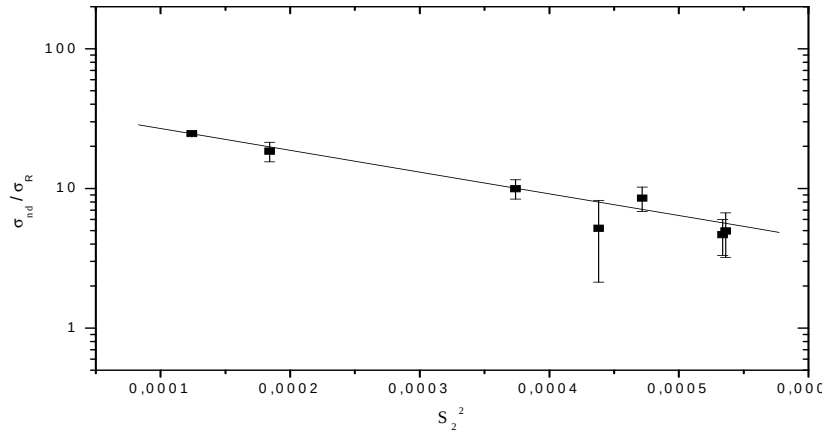

Fig. 5. Values of the ratio $\sigma_{(n,d)} / \sigma_R$ for $\xi < -1$ group showing the quadratic dependence of $ln(\sigma_{nd}/\sigma_R)$ on the surface asymmetry term obtained from EXFOR data and Eq. (14).

3. Fitting of the systematic parameters

The results fitting of the parameters of Eq. (14) to the experimental data are listed in the Table 1. The comparison between the experimental and the calculated data is shown in Fig. 6.

Table 1. **The parameters C_i of different systematics with their Σ and χ^2 resulting from the fit to the 37 experimental (n, n'p + d) cross sections**

Formule Equation	Zone	Σ	χ^2	C_1	C_2	C_3	C_4	C_5	C_6	C_7
This work	$\xi > -1$	169.96	6.79	-16.164	-1425.109	2.076	1.070	-4.425		
Eq. (14)	$\xi < -1$	2.26	0.45						3.668	-3739.391
	Total	172.22	**5.74**							
Eq. (15)	All nuclei	169	**5.48**	1.175	-44.34	52.99				
Qaim	$\xi > -1$	706.80	25.24	121.886	-30.374					
Eq. (17)	$\xi < -1$	28.47	4.74			1679.866				
	Total	735.27	**21.62**							
Forrest Eq. (16)	Total	209.91	**6.36**	449.916	0.654	48.061	99.810			
Konobeyev [15] (n, d)	All nuclei	183.73	**7.98**	1.146	-0.003	-4.33				

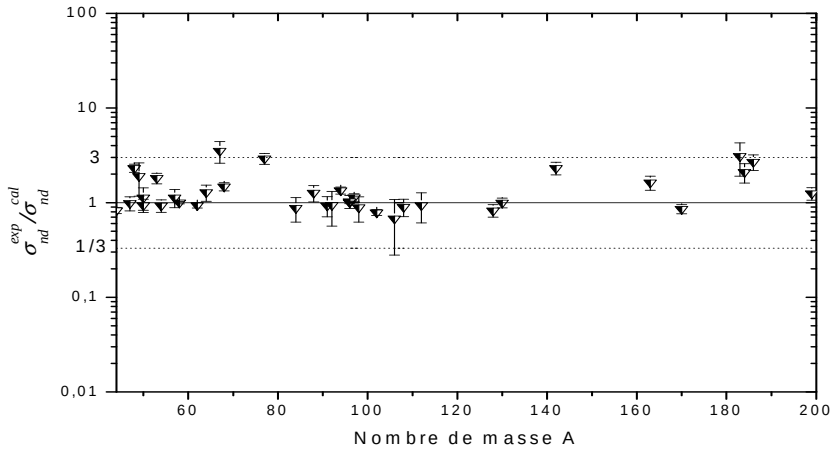

Fig. 6. Ratios of the experimental cross sections to the cross sections calculated with Eq. (14) and parameter of the Table 1.

4. Comparison with others systematics

Among the various relations proposed to describe the (n, α) cross section, the formula established by Forrest [13], for nuclei with 40 ≤ A ≤ 200, was considered to be the best systematic with the minimum χ^2:

$$\sigma_{nd} = C_1(A^{1/3}+1)^2(1-C_2\tanh(\xi+1))\exp(-C_3S-C_4 f)\,. \tag{16}$$

Qaim [14] has proposed a formula that considers only the asymmetry term and is given as follows:

$$\begin{cases} \sigma_{nd} = C_1\exp(C_2 S) & \xi > 0 \\ \sigma_{nd} = C_3 \times \sigma(\xi > 0) & \xi < 0 \end{cases}, \tag{17}$$

where $S = (N-Z)/A$ is the asymmetry term. $f = 1/A$

The parameters C_i (i = 1, 2, 3, 4, 5, 6, 7) for previous relations are given in Table 2. The predictions of formula (14) are compared with those obtained from expressions (16) and (17) by using the same experimental values of Table 1. The results are given in Table 2. We note that the chi-squares obtained with expression (14) shows significant improvement compared to the relations of Forrest [13] and Qaim [14].

The ratio of the experimental cross sections from Table 1 to the cross sections calculated through Eq. 14 is presented in Fig. 6. It should be noted that in our case the ratio of experimental to calculate data is more concentrated around the ratio equal to 1 and the all of the scatter points are included in the interval between the ratio equal to 0.5 and 3. However, we feel that the difference between experimental calculated cross sections results from the possible systematic errors in the measured (n, n'p + d) values, the approximate character of Eq. (14) and the finer nuclear structure effects that the phenomenological formulae ignore.

5. Conclusion

This work attempts to derive a new phenomenological formula to systematize (n, n'p + d) cross section values. For our case an important improvement in description of the (n, n'p + d) cross section has been obtained. This improvement is due to the simultaneous introduction of the pre-equilibrium process and the effective reaction energy deduced from the droplet model of Myers and Swiatecki. The new formula has been tested for 37 nuclei with 40 ≤ A ≤ 200. It shows an improvement in describing the (n, n'p + d) data compared with the existing relations.

REFERENCES

1. *Belgaid M., Asghar M.* Semi-empirical systematics of (n, p) cross sections for 14.5 MeV neutrons // Nucl. Instr. and Meth. B. - 2005. - Vol. 239. - P. 303.
2. *Belgaid M, Asghar M.* Semi-empirical systematics of (n, α) cross sections for 14.5 MeV neutrons // Nucl. Instr. and Meth. B. - 1999. - Vol. 149. - P. 383.
3. *Konobeyev A.Yu., Korovin Yu.A.* Semi-empirical systematics of (n, p) reaction cross sections at the energy of 14.5 MeV // Nucl. Instr. and Meth. B. - 1995. - Vol. 103. - P. 15.
4. *Konobeyev A.Yu. Lunev V.P., Shubin Yu.N.* Semi-empirical systematics of (n, α) reaction cross sections at the energy of 14.5 MeV // Nucl. Instr. and Meth. B. - 1996. - Vol. 108. - P. 233.
5. *Griffin J.J.* // Phys. Rev. Lett. - 1966. - Vol. 17. - P. 478.
6. *Weisskopf V.F., Ewing D.H.* // Phys. Rev. - 1940. - Vol. 57. - P. 472.
7. *Myers W.D., Swiatecki W.J.* Nuclear masses and deformations // Nucl. Phys. - 1966. - Vol. 81. - P. 1.
8. *Kikuchi K., Kawai M.* // Nuclear Matter and Nuclear Reactions. - Amsterdam: North Holland Publishing Company, 1968.
9. *Belgaid M., Segueni T., Kadem F., Asghar M.* Semi-empirical systematics of (n, t) cross sections for 14.5 MeV neutrons // Nucl. Instr. and Meth. B. - 2003. - Vol. 201. - P. 545.
10. *Cline C.K., Blann M.* The pre-equilibrium statistical model // Nucl. Phys. A. - 1971. - Vol. 172. - P. 225.
11. *Böhnig M.* // Nucl. Phys. A. - 1970. - Vol. 152. - P. 529.
12. http://www-nds.iaea.org/exfor/exfor.htm
13. *Forrest R.A.* // AERE R 12419. - Harwell, UK, 1986.
14. *Qaim S.M.* // Nuclear Physics. A. - 1982. - Vol. 382, Issue 2. - P. 255.
15. *Konobeyev A.Yu., Lunev V.P., Shubin Yu.N.* - Obninsk, 1996. - (Preprint / Physics and Power Institute; No. Fl3I 2494 [in Russian]).

ISOMER RATIOS FOR PRODUCTS OF PHOTONUCLEAR REACTIONS WITH ANTIMONY NUCLEI

O. A. Bezshyyko[1], A. M. Dovbnya[2], L. O. Golinka-Bezshyyko[1], I. M. Kadenko[1], V. A. Kushnir[3], V. V. Mitrochenko[3], S. M. Olejnik[2], G. E. Tuller[2], O. M. Vodin[2], Ia. O. Bezshyiko[1]

[1] Taras Shevchenko National University, Kyiv, Ukraine
[2] National Scientific Centre "Kharkiv Institute of Physics and Technology" (NSC KIPT), Kharkiv, Ukraine
[3] Research and Development Complex "Accelerator" of NSC KIPT, Kharkiv, Ukraine

Over the past several years various preequilibrium model approaches for nuclear reactions were developed. Diversified detailed experimental data in the medium excitation energy region for nucleus are needed for reasonable choice between these theoretical models. Lack of experimental data in this energy region does essentially limit the possibilities for analysis and comparison of different preequilibrium theoretical models. For photonuclear reactions this energy region extends between bremsstrahlung energies nearly 30 - 100 MeV. Experimental measurements and estimations of isomer ratios for products of photonuclear reactions with multiple particle escape on antimony have been performed using bremsstrahlung with energies 38, 43 and 53 MeV. Method of induced activity measurement was used. For acquisition of gamma spectra we used HPGe spectrometer with 20% efficiency and energy resolution 1.9 keV for 1332 keV gamma line of ^{60}Co. Linear accelerator of electrons LU-40 was a source of bremsstrahlung. Energy resolution of electron beam was about 1% and mean current was within (3.8 - 5.3) μA.

1. Introduction

Using high energy gamma-quanta as projectiles in nuclear reactions has some essential advantages for study of nuclear structure and nuclear reaction mechanisms. Indeed, gamma-quanta do not introduce large angular momentum into compound nucleus and additional contribution to excitation energy of compound nucleus due to binding energy of projectile is absent. In addition, the precise nondiscrete control of the gamma-quanta energy is possible.

Characteristics of photonuclear reactions are well studied in the energy region of Giant Dipole Resonance (GDR) and above the pion-producing threshold (PPT). The energy region between GDR and PPT (from about 30 to about 100 MeV) was studied to a smaller extent both theoretically and experimentally. The reason is due to small values of photonuclear reaction cross sections in this energy region and limited availability of high intensity quasi mono-energetic gamma ray sources with well controlled gamma-quanta energy.

During the last several years essential progress has been achieved in development of the new theoretical models for the photonuclear reactions and in improvement of the existing ones in the considered energy region. The quasi-deuteron model was further improved [1], some new pre-equilibrium models have been developed for description of the multi-particle emission [2 - 3]. Permanently growing interest in Accelerator Driven Systems and progress in the design of high intensity quasi mono-energetic gamma-quanta sources [4 - 5] also stimulates study of the photonuclear reactions above the GDR energy region. Very limited experimental data for the photonuclear reactions in the energy range (30 - 100) MeV for testing newly developed and available theoretical models was the major motivation for the present work.

The main purpose of this study is to obtain the experimental isomer ratios for nuclei ^{118m,g}Sb, ^{116m,g}Sb as the products of the ^{121}Sb(γ, 3n)^{118m,g}Sb and ^{121}Sb(γ, 5n)^{116m,g}Sb reactions.

2. Methodology

De-excitation time of nuclei by the γ-cascade irradiation usually does not exceed 10^{-12} s [6]. In some cases transitions between levels of nucleus are suppressed due to the large difference of angular momentum of these levels involved and the nucleus can live long enough in a specific state called the isomer state. Usually these isomer state doesn't have large excitation energies and its angular momentum differs from a spin of the ground state by a few units of $\hbar$.

The isomer or ground levels with large values of spin are populated mainly from highly excited states with large spins values. Population of isomer or ground levels with smaller values of spin can occur mainly from highly excited states with small values of spins. Therefore investigations of relative populations of the isomer and ground states [7 - 8] can be very useful to derive spins of highly excited levels and to study the de-excitation mechanisms via gamma emission.

For mono-energetic gamma beam with energy E the isomer ratio is determined as the cross sections ratio $\frac{\sigma_m(E)}{\sigma_g(E)}$, where $\sigma_g(E)$ is the cross section of the photonuclear reaction leading to the ground state, $\sigma_m(E)$ is the cross section for the same nucleus leading to the isomer state. Also the isomer ratio is often determined as a ratio of the cross section σ_H for state with higher spin to the cross section σ_L for state with lower spin:

$$\xi = \frac{\sigma_H(E)}{\sigma_L(E)}. \quad (1)$$

If a gamma beam is non-monoenergetic (this is the case for experiments with bremsstrahlung sources), the isomeric yield ratio is then being determined as:

$$d\left(E_{\max}\right)=\frac{Y_m}{Y_g}, \tag{2}$$

where the reaction yield is given by

$$Y_{m,g}=N_t\int_{E_{thr}^{m,g}}^{E_{\max}}\sigma_{m,g}(E)\cdot W(E,E_{\max})dE, \tag{3}$$

N_t - number of the target nuclei; $Y_{m,g}$ - reaction yield for nucleus in the isomer (m) or ground (g) state; $E_{\max}$ - maximal gamma energy; $W\left(E,E_{\max}\right)$ - bremsstrahlung spectrum; $\sigma_i(E)$ with i = m, g – the reaction cross section for nucleus to be formed in meta-stable (ground) state for gamma energy E, E_{thr}^{i}, i = m, g – the energy threshold of the reaction leading to the meta-stable (ground) state.

Production of isomeric pair and its decay can be described by the following differential equation system:

$$\begin{cases}\dfrac{dN_m}{dt}=Y_m-\lambda_m\cdot N_m\\ \dfrac{dN_g}{dt}=Y_g-\lambda_g\cdot N_g+p\cdot\lambda_m\cdot N_m\end{cases}, \tag{4}$$

where N_i - population of i-state (i = m – isomer state, i = g – ground state); Y_i - reaction yield according to (3); λ_m, λ_g - decay constants for isomer and ground state; p – branching factor (transition probability from isomer to ground state) [9 - 10]. The equation system is valid under such conditions: gamma-quanta flux is time invariable; contribution from interfering reaction may be considered as negligible; simple decay scheme, when the isomer level decays by gamma transition to the ground state in competition with β-decay and the ground state decays by β-decay branch.

Solution of system (4) is:

$$\begin{cases}\dfrac{S_m}{C\cdot\varepsilon\cdot f_m}=Y_m\Lambda_3\Lambda_6\Lambda_9\\ \dfrac{S_g}{C\cdot\varepsilon\cdot f_g}=Y_g\Lambda_2\Lambda_5\Lambda_8+\\ +Y_m(\Lambda_1\Lambda_5\Lambda_8+\Lambda_3\Lambda_4\Lambda_8+\Lambda_3\Lambda_6\Lambda_7)\end{cases}, \tag{5}$$

where S_i, i = g, m – photo-peak area (in the gamma spectrum of the activation products), coefficient C includes self-absorption factor, true coincidence effects of cascade gammas and other effects; ε - full efficiency of gamma detection for the analyzed gamma-line; f_i, i = g, m – quantum yield of gamma-line for i-state decay (transition probability for this line); coefficients Λ_j, j = 1,9 are defined by t_1, t_2, t_3, - irradiation time, cooling time and measurement time, respectively:

$$\Lambda_1=\frac{p}{\lambda_g}\left[1-\frac{\lambda_m\lambda_g}{\lambda_m-\lambda_g}\left(\frac{e^{-\lambda_g t_1}}{\lambda_g}-\frac{e^{-\lambda_m t_1^g}}{\lambda_m}\right)\right]$$

$$\Lambda_2=\frac{1}{\lambda_g}\left(1-e^{-\lambda_g t_1}\right),\quad \Lambda_3=\frac{1}{\lambda_m}\left(1-e^{-\lambda_m t_1}\right)$$

$$\Lambda_4 = p\frac{\lambda_m}{\lambda_m - \lambda_g}\left(e^{-\lambda_g t_2} - e^{-\lambda_m t_2} \right)$$

$$\Lambda_5 = e^{-\lambda_g t_2}, \qquad \Lambda_6 = e^{-\lambda_m t_2}$$

$$\Lambda_7 = p\left[1 - \frac{\lambda_m \lambda_g}{\lambda_m - \lambda_g}\left(\frac{e^{-\lambda_g t_3}}{\lambda_g} - \frac{e^{-\lambda_m t_3}}{\lambda_m} \right) \right]$$

$$\Lambda_8 = 1 - e^{-\lambda_g t_3}, \qquad \Lambda_9 = 1 - e^{-\lambda_m t_3}$$

As a result, the following expression is obtained

$$F = Y'_m X + Y'_g, \tag{6}$$

where F and X are defined as

$$F = \frac{S}{\varepsilon \cdot f_g \Lambda_2 \Lambda_5 \Lambda_8} \quad X = \frac{(\Lambda_1 \Lambda_5 \Lambda_8 + \Lambda_3 \Lambda_4 \Lambda_8 + \Lambda_3 \Lambda_6 \Lambda_7) + \frac{f_m}{f_g} \Lambda_3 \Lambda_6 \Lambda_9}{\Lambda_2 \Lambda_5 \Lambda_8}, \tag{7}$$

with $S = S_g + S_m$ peak area sum, $Y'_{m,g} = CY_{m,g}$ - values, proportional to reaction yields.

In this particular case isomer yield ratio was calculated by fitting the experimental data (X, F) using expression (6).

Experimentally, the method of induced activity was applied to obtain the isomer ratios. Irradiations of Sb target have been carried out with bremsstrahlung endpoint energies within the region (38 - 53) MeV. Linear accelerator LU-40 (Research and Development Complex "Accelerator" NSC KIPT) was used as a source of fast electrons [11]. Instability of electron beam intensity was within 2 %. Inner monitor of electron beam was calibrated by values from Faraday cup of the magnetic analyzer, placed at the accelerator outlet. The tantalum converter with 1.05 mm thickness was placed on the exit window of the accelerator facility, close to which the cylindrical aluminium gamma absorbers (thickness 5.5 and 10 cm) were installed. Diameter of beam spot on the conversion target was less than 9 mm. Energy of electron beam was determined using magnetic analyzer and was double checked in the low energy region by considering the photonuclear reaction thresholds. A distance between tantalum converter and absorber was 2 cm, between tantalum converter and target – 20 cm. We used metallic antimony target with natural isotopic abundance to study the reaction ^{121}Sb(γ, 3n)^{118m,g}Sb and the reaction ^{121}Sb(γ, 5n)^{116m,g}Sb. Irradiation time for every sample was 5 min. Then within (3 - 8) seconds the irradiated sample was moved with pneumatic transfer system to the measurement area. HPGe detector with the energy resolution <2.0 keV for ^{60}Co γ-line 1332 keV was used to acquire the instrumental gamma-ray spectra of the activation products as a set of serial measurements with various time periods. Cooling times varied from 5 s to few hours. Distances between sample and detector (dozens centimetres just after irradiation and few centimetres at the end of measurement period) were chosen to optimize both statistics and time restrictions when large contribution of interfering reactions took place, minimum distance was restricted by condition of negligible contribution of cascade gammas summing. Efficiency calibration of spectrometer was carried out for each detector-to-sample distance. The efficiency-energy dependence in double logarithmic scale showed a good quality and linearity in the energy range of interest, with deviations between experimental data and linear fitted values not exceeding 2 %.

3. Results and discussion

Isomer ratios were obtained as $IR(E_\gamma) = \frac{Y_H(E_\gamma)}{Y_L(E_\gamma)}$, where $Y_H(E_\gamma)$ is the reaction yield for the state of final nucleus with larger angular momentum (meta-stable state), $Y_L(E_\gamma)$ is the reaction yield for the state of final nucleus with smaller angular momentum (ground state). We used the decay scheme of the ^{116m,g}Sb and ^{118m,g}Sb nuclei from [6].

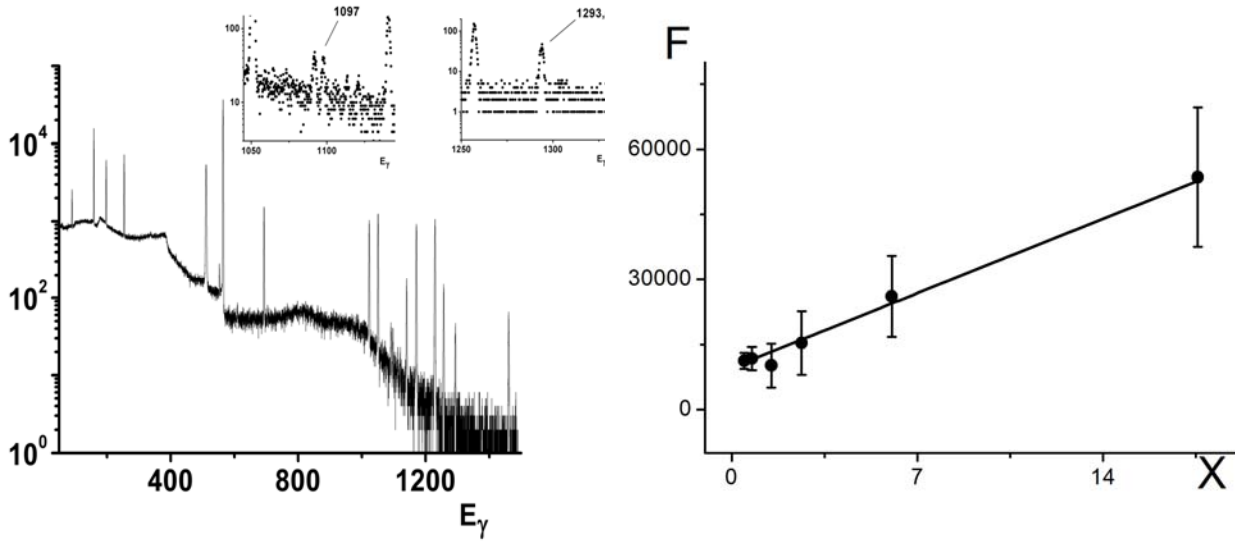

Gamma-ray spectra from the antimony activities. The analytical gamma lines used for determination of the isomer ratios are indicated separately (*left*). Fitting line for experimental points (X, F) of antimony ^{116m,g}Sb nuclei decay (reaction ^{121}Sb(γ, 5n)^{116m,g}Sb) (*right*).

Examples of spectra from the induced activities for the antimony target are shown in Figure (*left*). The gamma line 1293,5 keV (common line for EC + β + decay of the ground and isomer states) were used to obtain the isomer ratio for ^{116m,g}Sb and the gamma line 1097 keV (γ-decay of the isomer state) was used to account contribution of ^{116m,g}In (reaction ^{121}Sb(γ, nα)^{116m,g}In).

One can see (Figure, *right*) the fitting result of the decay line in presentation (X, F) according to Eqs. (6, 7).

Gamma transitions and corresponding lines with the energies 1050.7 keV (EC + β^+ decay of the isomer state) and 1229.7 keV (common line for decay of the ground and isomer states) were used to calculate the isomer ratio for ^{118m,g}Sb (reaction ^{121}Sb(γ, 3n)^{118m,g}Sb).

The gamma lines 1293.5 keV (common line EC + β^+ decay of the ground and isomer state) were used to obtain the isomer ratio for ^{116m,g}Sb (reaction ^{121}Sb(γ, 5n)^{116m,g}Sb). The gamma line 1097 keV (γ-decay of the isomer state) were used to account contribution of ^{116m,g}In (reaction ^{121}Sb(γ, nα)^{116m,g}In).

All obtained experimental values of the isomer ratios, corresponding reactions and characteristics of investigated nuclei are presented in the Table.

Reactions, the bremsstrahlung energy end-points $E\gamma_{max}$, spins of the target nuclei (*It*), spins of the meta-stable (*Im*) and ground (*Ig*) states and the experimental isomer ratios $IR = Y_H/Y_L$, obtained in experiments

Reaction	$E\gamma_{max}$, MeV	*It*	*Im*	*Ig*	*IR*
^{121}Sb(γ, 3n)^{118m,g}Sb	38	5/2+	8-	1+	0.14 ± 0.04
	43	5/2+	8-	1+	0.14 ± 0.01
^{121}Sb(γ, 5n)^{116m,g}Sb	53	5/2+	8-	3+	0.25 ± 0.03

The uncertainties given in table 1 include contributions from photopeak efficiency calibration, abundance, geometry configuration and intensities of gamma-rays (photopeak areas). Statistical uncertainties of photopeak areas made the main contribution to total uncertainty of result. Also number of experimental points of F,X dependency and range of X determination influenced total experimental error. These values were limited by experimental conditions.

4. Conclusion

Experimental values of the isomer ratios are obtained for ^{118m,g}Sb and ^{116m,g}Sb nuclei as products of the photonuclear reactions ^{121}Sb(γ, 3n)^{118m,g}Sb and ^{121}Sb(γ, 5n)^{116m,g}Sb, using bremsstrahlung endpoint energies in the region from 33 to 53 MeV. To correct deriving of isomer ratio for ^{116m,g}Sb one must account the contribution of ^{116m,g}In from reaction ^{121}Sb(γ, nα)^{116m,g}In.

REFERENCES

1. *Chadwick M.B., Oblozinsky P., Hodgson P.E., Reffo G.* Pauli-blocking in the quasideuteron model of photoabsorption // Phys. Rev. - 1991. - Vol. C44. - P. 814 - 823.
2. *Herman M., Oblozinsky P., Capote R. et al.* Recent Development of the Nuclear Reaction Model Code Empire //

Proc. of Int. Conf. on Nuclear Data for Sci. and Technology "ND2004" (Santa Fe, USA, Sept. 26 - Oct. 1, 2004). - N.-Y., 2005. - AIP Conf. Proc. - Vol. 769. - P. 1184 - 1187.
3. *Talou P., Kawano T., Young P.G., Chadwick M.B.* The McGNASH nuclear reaction code and its use for gas production cross-section calculations // Nucl. Instrum. Meth. - 2006. - Vol. A562. - P. 823 - 826.
4. *Gokhale P.A., Deokattey S., Kumar V.* Accelerator driven systems (ADS) for energy production and waste transmutation: International trends in R&D // Progr. in Nucl. Energy. - Vol. 48. - P. 91 - 102.
5. http://higs.tunl.duke.edu.
6. http://www.nndc.bnl.gov/ensdf.
7. *Ishkhanov B.C., Kapitonov I.M.* Interaction of electromagnetic radiation with nuclei. - M: MSU, 1979. - 215p. (in Russian).
8. *Gangrsky Yu.P., Tonchev A.P., Balabanov N.P.* Excitation of isomer states in photonuclear reactions // Physics of Elementary Particles and Atomic Nuclei. - 1996. - Vol. 27 No. 4 - P. 1043-1098. (in Russian)
9. *Vanska R., Rieppo R.* The experimental isomeric cross-section ratio in the nuclear activation technique // Nucl. Instr. and Meth. - 1981. - Vol. 179. - P. 525-532.
10. *Kolev D., Dobreva E., Nenov N., Todorov V.* A convenient method for experimental determination of yields and isomeric ratios in photonuclear reactions measured by the activation technique. // Nucl. Instr. and Meth. in Phys. Res. - 1995. - Vol. A356. - P. 390 - 396.
11. *Dovbnya A.N., Aizatsky M.I., Boriskin V.N. et al.* Beam parameters of an S-band electron linac with beam energy of 30...100 MeV // Problems of Atomic Science and Technology - 2006. - Vol. 2(46). - P. 11 - 13.

ISOMER RATIOS FOR ^{52}Mg - PRODUCT OF PHOTONUCLEAR REACTION ^{54}Fe(γ, np)^{52m,g}Mg

O. A. Bezshyyko[1], A. N. Dovbnya[2], L. O. Golinka-Bezshyyko[1], I. M. Kadenko[1], O. O. Kivernyk[1], V. V. Krylov[1], V. A. Kushnir[3], V. V. Mitrochenko[3], S. M. Olejnik[2], G. E. Tuller[2], A. N. Vodin[2]

[1] Taras Shevchenko National University, Kyiv, Ukraine
[2] National Scientific Centre "Kharkiv Institute of Physics and Technology" (NSC KIPT), Kharkiv, Ukraine
[3] Research and Development Complex "Accelerator" of NSC KIPT, Kharkiv, Ukraine

Photonuclear reactions with escape of neutrons for some target nuclei are often accompanied with proton emission. To derive isomer ratios for the products of ^{54}Fe(γ, np)^{52m,g}Mg reaction one has to take into account the interfering contribution of beta-decay for products of corresponding photoneutron reactions ^{54}Fe(**γ**, 2n)^{52m,g}Fe and ^{54}Fe(**γ**, n)^{53m,g}Fe. Bremsstrahlung with end-point energies within 32,8 - 43,6 MeV generated by electron linear accelerator LU-40 was used for irradiation of targets. Analytical solution for differential system of 4 equations was derived and used for correct estimation of contribution for all interfering reactions.

1. Introduction

Using high energy gamma-quanta as projectiles in nuclear reactions has some essential advantages for study of nuclear structure and nuclear reaction mechanisms. Indeed, gamma-quanta do not introduce large angular momentum into compound nucleus and additional contribution to excitation energy of compound nucleus due to binding energy of projectile is absent. In addition, the precise nondiscrete control of the gamma-quanta energy is possible.

Characteristics of photonuclear reactions are well studied in the energy region of Giant Dipole Resonance (GDR) and above the pion-producing threshold (PPT). The energy region between GDR and PPT (within 30 ÷ 100 MeV) was studied to a smaller extent both theoretically and experimentally. The reason is due to small values of photonuclear reaction cross sections in this energy region and limited availability of high intensity quasi mono-energetic gamma ray sources with well controlled gamma-quanta energy.

During the last several years essential progress has been achieved in development of the new theoretical models for the photonuclear reactions and in improvement of the existing ones in the considered energy region. The quasi-deuteron model was further improved [1], some new pre-equilibrium models have been developed for description of the multi-particle emission [2, 3]. Permanently growing interest to Accelerator Driven Systems and progress in the design of high intensity quasi mono-energetic gamma-quanta sources [4, 5] also stimulate study of the photonuclear reactions above the GDR energy region. Very limited number of experimental data for the photonuclear reactions in the energy range 30 - 100 MeV for testing newly developed and available theoretical models was the major motivation for the present work.

The main purpose of this study is to obtain the experimental isomer ratios for nuclei ^{52m,g}Mg as the product of the ^{54}Fe(γ, np)^{52m,g}Mg reactions and compare them with predictions of the modern theoretical models.

2. Theoretical background and experimental techniques

De-excitation time of nuclei by γ-cascade irradiation usually does not exceed 10^{-12} s. In some cases transitions between levels of the same nucleus are suppressed due to the large difference of angular momenta for these levels involved and the nucleus may remain long enough in a specific state called the isomer state. Usually such isomeric states have not large excitation energies and its angular momentum (named as a spin in the text below) differs from spin of ground state by a few units of $\hbar$.

The isomer or ground levels with large values of spin are populated mainly from highly excited states with large spin values. Population of isomer or ground levels with smaller values of spin can occur mainly from highly excited states with small values of spins. Therefore investigations of relative populations of the isomer and ground states [6, 7] can be very useful to derive spins of highly excited levels and to study the de-excitation mechanisms via gamma emission.

For mono-energetic gamma beam with energy E the isomer ratio is determined as the ratio of cross sections $\frac{\sigma_m(E)}{\sigma_g(E)}$, where $\sigma_g(E)$ is the cross section of the photonuclear reaction leading to the ground state, $\sigma_m(E)$ is the cross section for the same nucleus leading to the isomeric state. Also the isomer ratio is often determined as a ratio of the cross section σ_H for state with higher spin to the cross section σ_L for state with lower spin:

$$\xi = \frac{\sigma_H(E)}{\sigma_L(E)}. \quad (1)$$

If gamma beam is non-monoenergetic (that is the case for experiments with bremsstrahlung sources), the isomeric yield ratio is determined as:

$$d\left(E_{\max}\right)=\frac{Y_m}{Y_g}, \tag{2}$$

where the reaction yield is given by

$$Y_{m,g}=N_t\int_{E_{thr}^{m,g}}^{E_{\max}}\sigma_{m,g}(E)\cdot W(E,E_{\max})dE, \tag{3}$$

with N_t - number of the target nuclei; $Y_{m,g}$ - reaction yield for nucleus in the isomer (m) or ground (g) state; $E_{\max}$ - maximal gamma energy; $W\left(E,E_{\max}\right)$ - bremsstrahlung spectrum; $\sigma_i(E)$ with i = m, g – the reaction cross section for nucleus to be formed in meta-stable (m) or ground (g) state for gamma energy E, E_{thr}^{i}, i = m, g – the energy threshold of the reaction leading to the meta-stable (ground) state.

For some target nuclei photonuclear reactions with multiple escapes of neutrons are accompanied by proton emission. To study the products of these reactions one has to take into account an interfering contribution of beta-decay for products of corresponding photoneutron reactions. Often contribution of beta-decay from precursor nuclei in isobar chain (^{52m,g}Fe) is essential.

Production of isomeric pair, precursors from interfering reactions and its decay can be described by the following differential equation system (see Fig.1):

$$\begin{cases}\dfrac{dN_{Am}}{dt}=Y_{Am}(t)-\lambda_{Am}N_{Am}\\ \dfrac{dN_{Ag}}{dt}=Y_{Ag}(t)-\lambda_{Ag}N_{Ag}+p_{AmAg}\lambda_{Am}N_{Am}\\ \dfrac{dN_{Bm}}{dt}=Y_{Bm}(t)-\lambda_{Bm}N_{Bm}+p_{AmBm}\lambda_{Am}N_{Am}+p_{AgBm}\lambda_{Ag}N_{Ag}\\ \dfrac{dN_{Bg}}{dt}=Y_{Bg}(t)-\lambda_{Bg}N_{Bg}+p_{AmBg}\lambda_{Am}N_{Am}+p_{AgBg}\lambda_{Ag}N_{Ag}+p_{BmBg}\lambda_{Bm}N_{Bm}\end{cases} \tag{4}$$

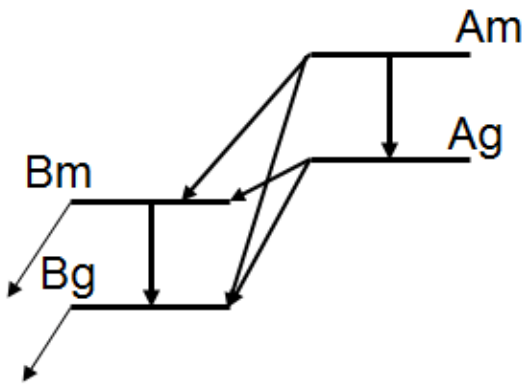

Fig. 1. General cheme of isomer nucleus (B) decay with interfering contribution of precursor nucleus (A) of isobaric chain.

where N_i - population of i-state (m - isomer state, g – ground state) of nuclei A and B; $i=Am,Ag,Bm,Bg$; Y_i - reaction yield according to (3); λ_i - decay constants for isomer and ground state; p – branching factor (transition probability from one level to other level).

Analytically solving this system the experimental values of isomer ratios were obtained by us.

Experimentally, the method of induced activity was applied to obtain the isomer ratios. Irradiations of ^{54}Fe targets have been carried out with bremsstrahlung endpoint energy 32,8, 38,3, 43,6 MeV. Linear accelerator LU-40 (Research and Development Complex “Accelerator” NSC KIPT) was used as a source of electrons [8]. Instability of electron beam intensity was within 2 %. Inner monitor of electron beam was calibrated by values from Faraday cup of the magnetic analyzer, placed at the accelerator outlet. The tantalum converter with 1.05 mm thickness was placed on the exit window of the accelerator facility, close to which the cylindrical aluminium gamma absorbers (thickness 5.5 and 10 cm) were installed. Diameter of beam spot on the conversion target was less than 9 mm. Energy of electron beam was determined using magnetic analyzer and was checked in the low energy region by reaction thresholds. A distance between tantalum converter and absorber was 2 and 4 cm, between tantalum converter and target – 20 and 30 cm (depending on electron energy). We used highly enriched ^{54}Fe targets. These target samples enriched by isotope ^{54}Fe (enrichment 99.85 %) were formed as metal disks of iron 10 mm in diameter and 236 mg mass for first sample (215 mg for second one). Then within 3 - 8 s the irradiated sample was moved by pneumatic transfer system to the measurement area. HPGe detector with the energy resolution 1.9 keV for ^{60}Co γ-line 1332 keV was used to acquire the instrumental gamma-ray spectra of the activation products as a set of serial measurements with various time periods. Distances between sample and detector (dozen centimetres just after irradiation and few centimetres at the end of

measurement period) were chosen to optimize both statistics and dead time/pile-up effects due to large contribution of interfering reactions. Minimum distance was limited by condition of negligible contribution of cascade gammas summing. Efficiency calibration of spectrometer was carried out for each detector-to-sample distance.

3. Results and discussion

Examples of spectra from the induced activities for the ^{54}Fe targets are shown in Fig. 2.

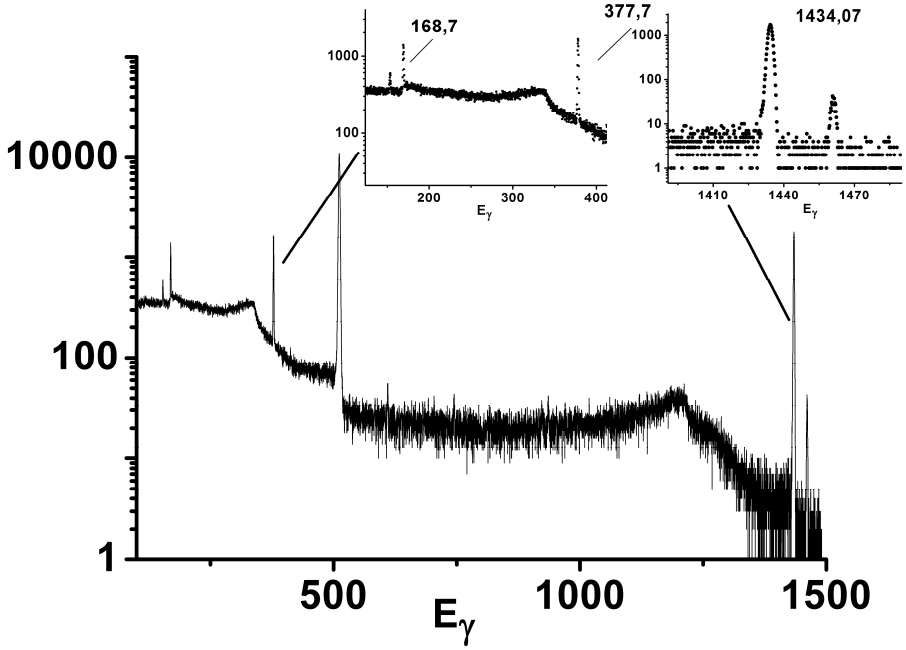

Fig. 2. Gamma-ray spectra from the induced activities in the target enriched in ^{54}Fe. The analytical gamma lines which were used for determination of the isomer ratios are indicated separately. All values of E_γ are presented in keV.

Reaction, the bremsstrahlung energy end-points $E\gamma_{max}$, spins of the target nuclei (*It*), spins of the meta-stable (*Im*) and ground (*Ig*) states and the experimental isomer ratios $IR = Y_H/Y_L$, obtained in experiments

Reaction	*It*	*Im*	*Ig*	$E\gamma_{max}$, MeV	*IR*
^{54}Fe(γ, np)^{52m,g}Mn	0+	2+	6+	32,8	0.123 ± 0.005
				38,3	0.124 ± 0.005
				43,6	0.146 ± 0.09

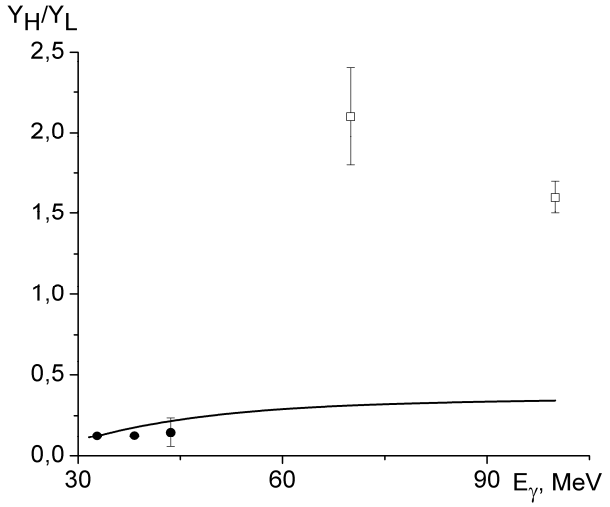

Fig. 3. Isomer ratios of yields for ^{52m,g}Mn from reaction ^{54}Fe(γ, np)^{52m,g}Mn. Solid line – calculation with using code TALYS, filled circles – experimental data obtained in this work, squares – experimental values from ref. [11].

Our subject if interest was isomer ratio of nucleus ^{52m,g}Mn, reaction product of ^{54}Fe(γ, np)^{52m,g}Mn. However, due to reaction ^{54}Fe(γ, 2n)^{52}Fe the nucleus ^{52}Fe as precursor of ^{52}Mn in isobaric decay chain may cause a significant contribution in population of isomer and ground levels of ^{52m,g}Mn. Using solution of equation system (4) we derived isomer ratios for ^{52m,g}Mn taking into account contribution of ^{52}Fe. We used for isomer ratio calculation the 1434 keV gamma line, which is generated during decay of both isomer and ground state of ^{52m,g}Mn nucleus. Gamma-line 168.7 keV (due to decay of ^{52}Fe ground state) is used to take into account a precursor contribution. Isomer state of ^{52}Fe with spin-parity 12^+ was not populated (it is confirmed by absence of decay gamma lines with energies 621.7 keV, 869.9 keV, 929.5 keV, 1416.1 keV). Using gamma line with energy 377.7 keV from ^{52m,g}Mn isomer transition is not correct, because in decay of ^{53}Fe as a product of ^{54}Fe(γ, n)^{53}Fe reaction with larger cross section, the interfering gamma line with energy 377.9 keV does overlap with 377.7 keV. Nuclides decay data for this work were taken from ENSDF database [9].

All obtained experimental values of the isomer ratios, corresponding reactions and characteristics of investigated nuclei are presented in the Table.

The uncertainties given in the Table include contributions from photopeak efficiency calibration (2 %), abundance(<1 %), geometry configuration (2 %) and intensities of gamma-rays (3 %, excluding case for 43.6 MeV). Statistical uncertainties of photopeak areas were the mojor contributors to total uncertainty of result. We used code TALYS [10] for theoretical calculations of isomer ratios for investigated nucleus (Fig. 3). Optimal default parameters were applied for calculation.

As one can see from Fig. 3 our experimental data are in rather good agreement with theoretical calculation results comparing with other experimental data given in Ref. [11].

REFERENCES

1. *Chadwick M.B., Oblozinský P., Hodgson P.E., Reffo G.* Pauli-blocking in the quasideuteron model of photoabsorption // Phys. Rev. - 1991. - Vol. C44. - P. 814 - 823.
2. *Herman M., Oblozinsky P., Capote R. et al.* Recent Development of the Nuclear Reaction Model Code Empire // Proc. of Int. Conf. on Nuclear Data for Sci. and Technology "ND2004" (Santa Fe, USA, Sept. 26 - Oct. 1, 2004). - N.-Y., 2005. - AIP Conf. Proc. - Vol. 769. - P. 1184 - 1187.
3. *Talou P., Kawano T., Young P.G., Chadwick M.B.* The McGNASH nuclear reaction code and its use for gas production cross-section calculations // Nucl. Instrum. Meth. - 2006. - Vol. A562. - P. 823 - 826.
4. *Gokhale P.A., Deokattey S., Kumar V.* Accelerator driven systems (ADS) for energy production and waste transmutation: International trends in R&D // Progr. in Nucl. Energy. - 2006. - Vol. 48. - P. 91 - 102.
5. http://www.tunl.duke.edu/higs2.php.
6. *Ishkhanov B.C., Kapitonov I.M.* Interaction of electromagnetic radiation with nuclei. - M.: MSU, 1979. - 215 p.
7. Gangrsky Yu.P., Tonchev A.P., Balabanov N.P. Excitation of isomer states in photonuclear reactions. // Physics of Elementary Particles and Atomic Nuclei. - 1996. - V. 27, No. 4. - P. 1043 - 1098.
8. *Dovbnya A.N., Aizatsky M.I., Boriskin V.N. et al.* Beam parameters of an S-band electron linac with beam energy of 30...100 MeV // Problems of Atomic Science and Technology. - 2006. - №2(46). - P. 11 - 13.
9. http://www.nndc.bnl.gov/nudat2.
10. http://www.talys.eu.
11. *Davydov M.G., Magera V.G., Trukhov A.V., Shomurodov É.M.* Isomeric ratios of the yields of photonuclear reactions for gamma-activation analysis // Atomic Energy. - 1985. - Vol. 58. - No.1. - P. 56 - 59.

REACTION ^{12}C(d, np)^{12}C AT 56 MeV IN DIFFRACTION APPROXIMATION

V. V. Davydovskyy, A. D. Foursat

Institute for Nuclear Research, National Academy of Science of Ukraine, Kyiv, Ukraine

Reaction of the deuteron breakup on ^{12}C nucleus at zero angle and the energy of 56 MeV is considered in the framework of the diffraction nuclear model using the generalized three-dimensional profile functions. Geometrical parameters of the model are determined by fitting the experimental data on elastic scattering of protons with the energy of 20 MeV on ^{12}C. Calculated dependence of the deuteron breakup differential cross section on the energy of emerging proton desribes the experimental data much better than alternative approaches. Relative contributions of the Coulomb and nuclear interactions are analyzed as well as the magnitude of the effects, related to accounting of the longitudinal component of the transferred momentum, is estimated.

1. Introduction

Investigation of the reaction of deuteron breakup by atomic nuclei in wide energy range provides valuable information on both the mechanism of reaction and the nature of interaction of the complex particles with nuclei.

Even in early studies it was shown that to describe the various characteristics of the process of the deuteron breakup requires the inclusion of both the nuclear and Coulomb interactions.

Recently, theoretical studies of (d, np) reaction developed in two ways. At relatively low energies of the incident deuterons ($E_d \sim 8-20$ MeV) various modifications of the method of distorted waves [1 - 3] are used. Application of this method leads to a rather complex numerical calculations, during which one has, as a rule, to introduce a number of additional simplifying assumptions.

In that case, where the wavelength of the relative motion of the colliding particles is small compared to the characteristic size of the interaction region, the diffraction model is widely used [4 - 6].

Despite the fact that for the fulfillment of the diffraction approximation validity criterion the incident deuterons must have energies greater than the height of the Coulomb barrier, taking into account the Coulomb interaction appears to be essential for the correct description of the observed characteristics of the breakup process [7, 8].

Diffraction theory of interaction of complex particles and nuclei used in the studies cited above, suggests that each nucleon, which is part of the deuteron scattered by the force center, leads to a phase shift that is associated only with the transfer of the transverse momentum. This assumption is valid for deuteron elastic scattering at small angles. In the case of inelastic process, including the breakup process, a certain longitudinal momentum can also be transferred to the deuteron's nucleon. This fact leads to the incoherence of the breakup process, which therefore cannot be described by a profile function corresponding to the elastic scattering. The calculations of the angular correlations in the reaction ^{3}He(p, 2p)d at the proton energy of 156 MeV [9] have shown the importance of these effects.

It is therefore of interest to examine the process of deuteron breakup by atomic nuclei in the diffraction approximation taking into account the longitudinal and transverse components of the transferred momentum.

2. General formalism

In the diffraction approximation, the deuteron breakup amplitude can be written as

$$F_{fi}(\mathbf{Q},\mathbf{p}) = \frac{ik_d}{2\pi}\int d^2B \exp\left(i\mathbf{Q}_\perp\mathbf{B}\right)\int d^3r \Psi_f^*(\mathbf{r})\widehat{\Omega}(\mathbf{B},\mathbf{r})\Psi_i(\mathbf{r}), \quad (1)$$

where k_d is the deuteron momentum in the laboratory frame; $\mathbf{Q}$ is the momentum transferred to the nucleus; $\mathbf{p}$ is the momentum of the relative motion of the nucleons, released as a result of the reaction; $\mathbf{B}$ is a two-dimensional vector, the modulus of which determines the impact parameter of the deuteron center of mass. Complete wave functions of the initial and final states of the two nucleons are given by the following expressions:

$$\Psi_i = \varphi_0(\mathbf{r})\chi_{S=1.M}(1,2)\zeta_{T=0}(1,2), \quad (2)$$

$$\Psi_f = \frac{a}{\sqrt{2}}\left\{\varphi_{\mathbf{p}}(\mathbf{r})\chi_{1/2m_1}(1)\chi_{1/2m_2}(2)\zeta_{1/2,1/2}(1)\zeta_{1/2,-1/2}(2)\right\} \quad (3)$$

Here $\varphi_0(\mathbf{r})$ and $\varphi_{\mathbf{p}}(\mathbf{r})$ are spatial components of the wave functions of the two-nucleon system, $\chi_{1/2m_j}$ and $\zeta_{1/2\mu_j}$ are the spin and isospin functions of the nucleons, correspondingly; a is antisymmetrization operator.

Following [9], if we take into account noncoherence of the process of nucleon scattering by the force center, the complete profile operator $\widehat{\Omega}(\mathbf{B},\mathbf{r})$, included in (1), can be expressed in terms of the profile operators of separate nucleons forming deuteron as follows

$$\hat{\Omega} = \hat{\Omega}_1 \exp\left(-iQ_z z_1\right) + \hat{\Omega}_2 \exp\left(-iQ_z z_2\right) - \frac{1}{2}\hat{\Omega}_1 \hat{\Omega}_2 \left[\exp\left(-iQ_z z_1\right) + \exp\left(-iQ_z z_2\right)\right], \tag{4}$$

where the "hat" over letters means that the corresponding quantities are the matrices in isospin space of both nucleons.

Thus, the mechanism of the process under study consists in the diffraction scattering of the center of mass of the neutron-proton system, whereas the process of the breakup in the interaction with the nucleus, which changes the character of the relative motion of the proton and the neutron, is incoherent and is accompanied by the transfer of longitudinal momentum.

Taking Coulomb interaction into account is carried out on the basis of the principle of the additivity of phase shifts:

$$\hat{\Omega}_j = 1 - \exp\left(i\chi_j + i\chi_j^c \hat{\pi}_j\right) = \omega_j + \hat{\omega}_j^c - \omega_j \hat{\omega}_j^c \tag{5}$$

where $\hat{\pi}_j = 1/2(1+\tau_{jz})$ is the proton state projection operator, χ_j and $\chi_j^c \equiv 2\sigma$ are nuclear and Coulomb phase shifts, correspondingly.

Neglecting the spin and isospin dependence of the profile functions, calculating the corresponding matrix elements and taking the Jacobi coordinates $\mathbf{R} = 1/2\left(\mathbf{r}_1 + \mathbf{r}_2\right)$, $\mathbf{r} = \mathbf{r}_1 - \mathbf{r}_2$, we obtain a spatial profile function as the sum of the Coulomb and nuclear-Coulomb profile functions:

$$\Omega\left(\mathbf{B},\mathbf{r}\right) = \Omega_c\left(\mathbf{B},\mathbf{r}\right) + \Omega_{Nc}\left(\mathbf{B},\mathbf{r}\right), \tag{6}$$

$$\Omega_c\left(\mathbf{B},\mathbf{r}\right) = [1 - e^{2i\sigma\left(\mathbf{B}+\frac{\mathbf{b}}{2}\right)}]e^{-\frac{iQ_z z}{2}}, \tag{7}$$

$$\Omega_{Nc}\left(\mathbf{B},\mathbf{r}\right) = e^{2i\sigma\left(\mathbf{B}+\frac{\mathbf{b}}{2}\right)}[\omega(\mathbf{B}+\frac{\mathbf{b}}{2})e^{-\frac{iQ_z z}{2}} + \omega(\mathbf{B}-\frac{\mathbf{b}}{2})\cos(\frac{Q_z z}{2}) - \omega(\mathbf{B}+\frac{\mathbf{b}}{2})\omega(\mathbf{B}-\frac{\mathbf{b}}{2})\cos(\frac{Q_z z}{2})] +$$

$$+ i\omega(\mathbf{B}-\frac{\mathbf{b}}{2})\sin(\frac{Q_z z}{2}). \tag{8}$$

Finally, we get the amplitude of (d, np) reaction as a sum of two terms, responsible for the Coulomb and nuclear-Coulomb breakups:

$$F(\mathbf{Q},\mathbf{p}) = \frac{ik_d}{2\pi}\int d^2B \exp\left(i\mathbf{Q}_\perp\mathbf{B}\right)\int d^3r \varphi_{\mathbf{p}}^*\left(\mathbf{r}\right)\Omega\left(\mathbf{B},\mathbf{r}\right)\varphi_0\left(\mathbf{r}\right) = F_c + F_{Nc}. \tag{9}$$

As the wave functions of the neutron-proton system, the following model wave functions that satisfy the orthogonality condition are chosen:

$$\varphi_0\left(\mathbf{r}\right) = N\exp(-\gamma r^2),\ N = \left(\frac{2\gamma}{\pi}\right)^{3/4},$$

$$\varphi_{\mathbf{p}}\left(\mathbf{r}\right) = \exp\left(i\mathbf{pr}\right) - f(p)\exp(-\gamma r^2),\ f(p) = \sqrt{8}\exp\left(-\frac{p^2}{4\gamma}\right). \tag{10}$$

3. Amplitude of the Coulomb breakup

By a simple change of two-dimensional integration variable in (9), we find with the help of (7):

$$F_c(\mathbf{Q},\mathbf{p}) = \frac{ik_d}{2\pi}\int d^2B\, e^{i\mathbf{Q}_\perp\mathbf{B}}(1 - e^{2i\sigma(B)})\int d^3r \varphi_{\mathbf{p}}^*\left(\mathbf{r}\right)e^{-\frac{i\mathbf{Qr}}{2}}\varphi_0\left(\mathbf{r}\right). \tag{11}$$

The first integral in (11) can be regarded as the amplitude of the elastic scattering of a point-like charged particle in the Coulomb field of the nucleus. In what follows, this amplitude is represented as a product of the amplitude of elastic scattering of protons with momentum $k_d/2$ on point-like center in the Born approximation

$$f_c(Q,\frac{k_d}{2}) = -\frac{nk_d}{Q^2}\exp[2i(\sigma_0 - n\ln\frac{Q}{k_d})],\quad n = \frac{Ze^2m}{k_p},\quad k_p = \frac{k_d}{2} \tag{12}$$

(σ_0 is the Coulomb scattering phase, Q is the total transferred momentum) and the charge formfactor, which takes finitness of the nucleus dimensions into account:

$$F(Q)=\frac{4\pi}{Q}\int_0^\infty drr\rho(r)\sin Qr,\quad F(0)=1. \tag{13}$$

Choosing the density of the charge distribution in the nucleus in the form of

$$\rho(r)=\rho_0[1+e^{(r-R)/a}]^{-1},\quad \rho_0=[\frac{4}{3}\pi R^3(1+\frac{\pi^2a^2}{R^2})]^{-1} \tag{14}$$

(R is the charge radius of the nucleus), we get the following expression for the charge formfactor:

$$F(Q)=\frac{1}{1+\frac{\pi^2a^2}{R^2}}\frac{2\pi aQ\exp(-\pi aQ)}{1-\exp(-2\pi aQ)}\frac{3}{(QR)^2}\{\frac{\sin QR}{QR}\pi aQ[1+\frac{2\exp(-2\pi aQ)}{1-\exp(-2\pi aQ)}]-\cos QR\}. \tag{15}$$

The second integral in (11) takes into account the fact that the position of the charge in the deuteron does not coincide with its center of mass, and after calculation leads to the following expression:

$$G(\mathbf{Q},\mathbf{p})=(\frac{2\pi}{\gamma})^{3/4}\exp(-\frac{Q^2+8p^2}{32\gamma})[\exp(-\frac{Q^2+8\mathbf{Qp}}{32\gamma})-1]. \tag{16}$$

Thus, the Coulomb breakup amplitude used in the calculations becomes:

$$F_c(\mathbf{Q},\mathbf{p})=2f_c(Q,\frac{k_d}{2})F(Q)G(\mathbf{Q},\mathbf{p}). \tag{17}$$

Note that since the deuteron breakup reaction has a threshold (the minimal transferred momentum is $Q_{z,\min}=2m\varepsilon/k_d$), the amplitude of the Coulomb breakup has no singularity.

4. Amplitude of the nuclear-Coulomb breakup

The amplitude of nuclear breakup with the Coulomb distortion can be written as:

$$\begin{aligned}F_{Nc}(\mathbf{Q},\mathbf{p})=\frac{ik_d}{2\pi}\int d^2B\,\mathrm{e}^{i\mathbf{Q}_\perp\mathbf{B}}\left\langle\varphi_{\mathbf{p}}\left|e^{-\frac{i\mathbf{Q}_\perp\mathbf{b}}{2}}\{e^{2i\sigma(B)}[\omega(B)e^{-\frac{Q_zz}{2}}+\right.\right.\\ \left.\left.+(1-\omega(B))\,\omega(\mathbf{B}-\mathbf{b})\cos(\frac{Q_zz}{2})]+i\omega(\mathbf{B}-\mathbf{b})\sin(\frac{Q_zz}{2})\right|\varphi_0\right\rangle.\end{aligned} \tag{18}$$

It includes the calculation of five-dimensional integrals of oscillatory functions. Therefore, in order to simplify the calculation of the matrix elements with respect to the deuteron coordinate $\mathbf{r}$, we expand the profile function $\omega(\mathbf{B}-\mathbf{b})$ in a series of variable $\mathbf{b}$, which is valid for sufficiently heavy nuclei, when the nucleus radius is much larger than the radius of the deuteron:

$$\omega(\mathbf{B}-\mathbf{b})\approx[1-(\mathbf{b}\nabla)+1/2(\mathbf{b}\nabla)^2]\omega(B).$$

Later in the calculation of the amplitude of the Coulomb breakup (17), all of the terms of the expansion in the nuclear-Coulomb amplitude for simplicity will be calculated with Gaussian functions (10). This allows one to carry out the calculations analytically. The contributions to the amplitude (18) of the zero, first and second orders of the expansion are denoted as $F^{(0)}, F^{(1)}, F^{(2)}$. After integrating with respect to the variable $\mathbf{r}$ and the azimuth angle of two-dimensional vector $\mathbf{B}$, the amplitude of the nuclear-Coulomb breakup can be represented as:

$$F_{Nc}(\mathbf{Q},\mathbf{p})=\sum_{\lambda=0}^{2}F_{Nc}^{(\lambda)}(\mathbf{Q},\mathbf{p}),$$

$$F_{Nc}^{(0)}=ik_dC\int_0^\infty dBB\left[(c_1-1)e^{2i\sigma}(2-\omega)+c_2(1-e^{2i\sigma})\right]J_0(Q_\perp B)\omega(B),$$

$$F_{Nc}^{(1)}=-\frac{ik_d}{2\gamma}C\int_0^\infty dBB\left\{\left[c_1(\boldsymbol{\kappa}_\perp\widehat{\mathbf{Q}}_\perp)-\frac{Q_\perp}{4}\right]e^{2i\sigma}(1-\omega)+c_2(\boldsymbol{\kappa}_\perp\widehat{\mathbf{Q}}_\perp)\right\}J_1(Q_\perp B)\omega'(B),$$

$$F_{Nc}^{(2)}=\frac{ik_d}{4\gamma}C\int_0^\infty dBB\{\left[\left(c_1e^{2i\sigma}(1-\omega)+c_2\right)\left(1-\frac{\kappa_\perp^2}{4\gamma}\right)-\frac{1}{2}e^{2i\sigma}(1-\omega)\left(1-\frac{Q_\perp^2}{32\gamma}\right)\right]J_0(Q_\perp B)\Delta^{(+)}\omega-$$

$$-\left[\left(c_1e^{2i\sigma}(1-\omega)+c_2\right)\frac{\kappa_\perp^2-2(\boldsymbol{\kappa}_\perp\hat{\mathbf{Q}}_\perp)^2}{4\gamma}+e^{2i\sigma}(1-\omega)\frac{Q_\perp^2}{64\gamma}\right]J_2(Q_\perp B)\Delta^{(-)}\omega\},$$

where $\hat{\mathbf{Q}}=\mathbf{Q}/Q$ is a unit vector, $\Delta^{(\pm)}=\frac{d^2}{dB^2}\pm\frac{1}{B}\frac{d}{dB}$, and the following notations are introduced to make the formulae shorter:

$$C=\left(\frac{2\pi}{\gamma}\right)^{3/4}\exp\left(-\frac{Q^2+8p^2}{32\gamma}\right),\quad c_1=\exp\left(-\frac{Q^2+8\mathbf{Q}_\perp\mathbf{p}_\perp}{32\gamma}\right)ch\left(\frac{Q_zp_z}{4\gamma}\right),$$

$$c_2=\exp\left(-\frac{Q^2+8\mathbf{Q}_\perp\mathbf{p}_\perp}{32\gamma}\right)sh\left(\frac{Q_zp_z}{4\gamma}\right),$$

J is Bessel function. In order to obtain the Coulomb phase $\sigma(B)$, the quasiclassical relation between an angular momentum and an impact parameter $l+1/2=k_dB/2$ as well as the equation $\sigma_l=\arg\Gamma(1+l+in)$ are used. The integration in the amplitudes is carried out numerically with the profile function chosen in the Fermi form with the imaginary surface part:

$$\omega(B)=g_1\left[1+\exp\left(\frac{B-R_1}{a_1}\right)\right]^{-1}+ig_2\frac{d}{dB}\left[1+\exp\left(\frac{B-R_2}{a_2}\right)\right]^{-1},\qquad(19)$$

where the parameters g, R and a characterize the geometric dimensions of components of the nucleon profile function.

Parameters of the profile function (19) for various processes

	g_1	R_1	a_1	g_2	R_2	a_2
(d, pn)	–1,29	2,72	0,53	0,87	2,58	0,55
(p, p)	1,36	2,72	0,53	3,10	2,58	0,55

The Table shows the parameters of the nucleon profile function (19) obtained from the comparison with experiment for the description of both the elastic scattering of protons on ^{12}C at the energy of 20 MeV and the deuteron breakup reaction at 56 MeV.

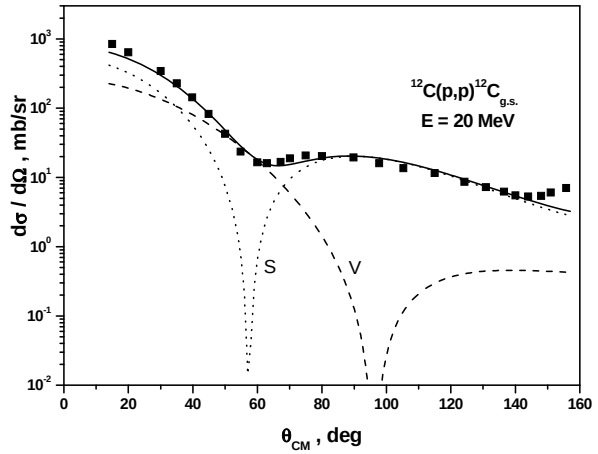

Fig. 1. The cross section of the elastic scattering of deuteron on carbon.

Our calculations show that the cross section of elastic scattering cannot be agreed with the experiment, if only one term is used in the profile function (19). This can be seen from Fig. 1: each term of the profile (V- or S-type) gives a deep minimum in the cross section, which is not observed in the experimental data.

5. Deuteron breakup cross section

The differential cross section of the deuteron breakup is expressed in terms of the amplitude (9) using the relation

$$\frac{d^3\sigma}{d\Omega_pd\Omega_ndE_p}=\frac{1}{(2\pi)^3}\frac{mk_pk_n^3}{K(\mathbf{k}_n\cdot\mathbf{K})}\left|F(\mathbf{Q},\mathbf{p})\right|^2,\quad(20)$$

where the wave vector of the relative motion of the nucleons in the deuteron $\mathbf{p}$ and the wave vector of the center of mass of the deuteron taking into account the recoil $\mathbf{K}$ are expressed in terms of wave vectors of escaping neutron and proton in the laboratory frame as

$$\mathbf{p}=\frac{1}{2}(\mathbf{k}_p-\mathbf{k}_n),\quad\mathbf{K}=\mathbf{k}_p+\mathbf{k}_n-\frac{2\mathbf{k}_d}{A}.$$

The available experimental data on the breakup of the deuteron by nuclei [10], when the products of the deuteron breakup escape at zero angle with respect to the momentum of the deuteron, allow a detailed comparison of our theory

and an experiment. Numerical calculations of the cross section of the deuteron breakup are carried out for carbon nuclei at the energy of 56 MeV. Despite the fact that this energy is higher than the Coulomb barrier, the contribution of the Coulomb breakup is crucial by the magnitude of the cross section as well as by the shape of the energy spectrum of escaping protons.

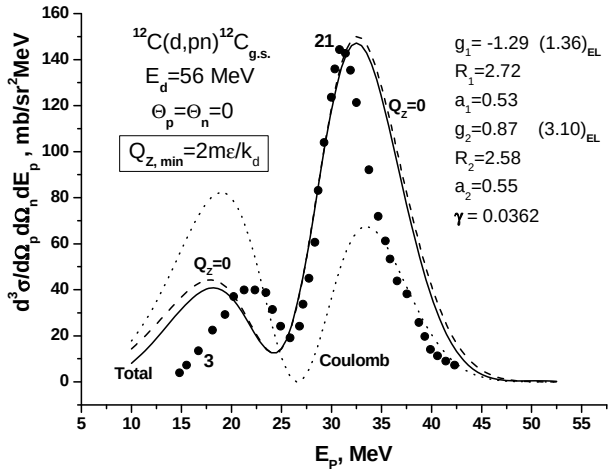

Fig. 2. The cross section of the deuteron diffraction breakup on carbon.

Fig. 2 shows the results of calculations of the energy spectrum of the protons with Gaussian functions in the case of a zero escape angle of the reaction products. Note that at these energies the main peak is dominated by the Coulomb breakup mechanism, which also leads to the appearance of the second maximum of the cross section with a lower magnitude, which corresponds to the experiment.

The effect of longitudinal transferred momentum Q_Z is noticeable, contributes in the "right" way, though not significant. In the spectrum region where the energy of the proton and neutron are close to each other, the curves are practically the same, that is the effect disappears, which is easily explained by the kinematical specifics of this experiment: the nucleons are flying forward with similar energies (almost as a whole) and the momentum transfer is close to its threshold value, which is very little. On the wings of the spectrum, when the energies of the nucleons are very different, the effect of longitudinal transferred momentum is manifested most. Note that at higher energies the role of the effects associated with the transfer of longitudinal momentum, especially in the asymmetric geometry, increases.

REFERENCES

1. *Rybicki F., Austern N.* Distorted-Wave Theory of Deuteron Breakup // Phys. Rev. C. - 1972. - Vol. 6. - P. 1525.
2. *Lang J., Jarczyk L., Muller R.* Deuteron break-up in the field of the nucleus // Nucl. Phys. A. - 1973. - Vol. 204. - P. 97 - 109.
3. *Baur G., Trautmann D., Zoran V.* Sub-Coulomb deuteron break-up and the neutron-nucleus interaction // Nucl. Phys. A. - 1973. - Vol. 208. - P. 261 - 268.
4. *Akhiezer A.I., Sitenko A.G.* Diffractional Scattering of Fast Deuterons by Nuclei // Phys. Rev. - 1957. - Vol. 106. - P. 1236.
5. *Бережной Ю. А., Инопин Е. В.* // ЯФ. - 1967. - Т. 6. - С. 1197.
6. *Бережной Ю. А., Вовенко В. П., Созник А. П.* // УФЖ. - 1976. - Т. 21. - С. 1170.
7. *Faldt G.* Dissociation and Stripping of High-Energy Deuterons // Phys. Rev. D. - 1970. - Vol. 2. - P. 846.
8. *Ситенко А.Г., Полозов А.Д., Евланов М.В.* // УФЖ. - 1974. - Т. 19. - С. 1778.
9. *Левшин Е.В., Фурса А.Д.* Дифракционное расщепление трехнуклонных ядер // ЯФ. - 1976. - Т. 24, № 12. - С. 1115 - 1126.
10. *Okamura H., Hatori S., Matsuoka N. et al.* Strong evidence of the Coulomb breakup of the deuteron at 56 MeV // Phys. Lett. B. - 1994. - Vol. 325. - P. 308 - 312.

YIELD OF BREMSSTRAHLUNG INDUCED REACTIONS AS A PROBE OF NUCLEON-NUCLEON CORRELATIONS IN HEAVY NUCLEI

S. A. Karamian

Flerov Laboratory of Nuclear Reactions, Joint Institute for Nuclear Research, Dubna, Moscow region, Russia

Relative yields of the (γ, α) reactions could serve as a probe to verify the theoretical models which assume total alpha clustering, or multiquark objects in heavy nuclei. A deficit of data on the (γ, α) process probability must be covered in relatively simple activation experiments. Five concrete reactions are distinguished because they provide favorable conditions for detection of the low-probability reaction branch – (γ, α). The following requirements must be satisfied: the target species available in an enriched form, the convenient properties of the product activity, and reasonably soft background restrictions. In the present experiment with bremsstrahlung at E_e = 23 MeV, new results are successfully obtained for (γ, α) reactions in two cases and upper limits are deduced for three others. Much lower probability of (γ, α) compared to (γ, *p*) reactions is proved. Alpha-clustering in heavy nuclei is not supported.

1. Introduction

The status of nucleons within a nuclear matter isn't yet well clarified point despite great interest since the decades. Simplest assumption that nucleons conserve their individual properties, same as in vacuum, was under criticism from different points of view. There is known a spectrum of ideas: on necessity to replace the nucleons by quasi-particles, on interacting bosons inside the nucleus and on complete alpha-clustering in nuclear matter. Over recent decade, an idea of short range nucleon-nucleon correlations with formation of a quark bag attracts an attention, and it is tested in reactions at GeV energies [1]. The mentioned above models also find some application and reach a success in simulation of different processes. The additional tests in experiments are yet relevant. We propose now to use the reactions induced by photons at moderate energy of about (20 - 25) MeV. Electromagnetic radiation perturbs the nucleons in a target nucleus only slightly unlike the influence of strongly interacting projectiles. The product particles are released by the electromagnetic field, and the yield of different reactions may serve as a probe of bonds and correlations between nucleons within the heavy target nucleus.

Recently, there are presented [2] the evidences for regular threshold dependence of the photon-induced reactions. Relative yields were systematized versus the (E_e - E_{th} - B_c) parameter containing an excess of the end-point energy E_e above the sum of reaction threshold E_{th} and the Coulomb barrier B_c for particle emission. The different-reaction yields are normalized to the yield of the most abundant (γ, n) reaction and they show a systematic growth with the increase of the mentioned threshold parameter. A common behavior of the neutron and proton yields confirms the similar mechanism of the release by electromagnetic field including both the compound and direct emission patterns. The multiparticle reactions dominate at $E_e \geq 40$ MeV due to the sequential mechanism and they could not be involved in common systematic together with the elementary processes of nucleon emission. The exclusion is obviously revealed for the (γ, *d*) reaction [2], despite possible contribution from (γ, *pn*) sequential emission.

For light targets, the (γ, α) reaction was since many decades under the scope of the astrophysics relevant studies. However, the literature data is poor for medium-weight and heavy targets. Cross sections of electro and photonuclear reactions were measured in [3, 4] for ^{58}Ni and ^{60}Ni targets. Recently, the abundant yields of the (γ, α) products have been reported in [5, 6] for antimony and mercury targets, respectively. The great specific activity of ^{195m}Pt has been deduced in [6] due to the ^{199}Hg(γ, α) reaction at E_e = 30 MeV. Strictly speaking, this not a confirmation of the great reaction yield, just an indication that the ^{195m}Pt nuclide supplies a significant part of the total Pt production when the mercury target is exposed to photons.

In [5], the yield of ^{121}Sb(γ, α)^{117}In reaction is reported in a value near 0.8% of the (γ, *n*) yield. This looks too high, significantly higher the result of [3]. For Ni target in [3], the yield of alphas was observed at a level by 20 times lower the (γ, *p*) yield, i.e. about 10^{-4} in comparison to the rate of (γ, *n*) reaction. In our measurements [7], the ^{181}Ta(γ, α)^{177}Lu reaction was observed and the yield was appeared to be $\approx 0.7 \cdot 10^{-5}$ in ratio to the (γ, *n*) abundance. Due to such scattering of results over different publications and also due to the general lack of reliable data, one may conclude a necessity to explore relative yields of the bremsstrahlung induced reactions, especially, for (γ, α) reactions in the weakly studied domain of heavy targets. Comparison of the nucleon and alpha emission rates must be productive for conclusions about the nucleon-nucleon correlation status, or at least, to probe an idea of complete alpha clustering in heavy nuclei. Experimental data for (γ, n) and (γ, p) yields were compiled in [2] and the novel regularities were deduced.

2. Results

Inspecting the Nuclide Chart from A =100 to 208 we have tried to find the most promising cases for detection of the (γ, α) reaction by activation method with γ-spectroscopy measurements of the induced activity. The mass numbers of potential targets correspond to the domain of heavy nuclides but out of the alpha radioactive nuclide range. The best five cases are selected for experimental tests in bremsstrahlung irradiations with MT-25 microtron of FLNR, JINR at end-point energy of 23 MeV. The activities listed in Table 1 are chosen because they are characterized by the relatively

intense γ-lines convenient for detection at moderate halflives. The major problem of such experiments would be a presence of the background radiation generated by the isobaric nuclides due to the same transition at the same daughter nuclide but after ε- instead of β^--decay.

Table 1. **Encounter data for the (γ, α) -reaction experiment**

Target	Abundance %	Product	Halflife of β^--decay	Major γ line, keV	Internal background	Origin of the background
^{109}Ag	48.2	^{105}Rh	35.4 h	318.9	^{105}Ag; 41.3 d	^{107}Ag(γ, 2*n*)
^{113}Cd	12.2	^{109}Ag	13.7 h	88.0	^{109}Cd; 463 d	^{110}Cd(γ, *n*)
^{119}Sn	8.6	^{115}Cd	53.4 h	527.9	–	–
^{181}Ta	100	^{177}Lu	6.47 d	208.4	–	–
^{193}Ir	62.7	^{189}Re	24.3 h	245.1	^{189}Ir; 13.3 d	^{191}Ir(γ, 2*n*)

This internal physical background couldn't be excluded by a better shielding of the detector, or so. In two cases at Table 1, the background is absent and they must be considered as the best for reliable detection of the (γ, α) reaction and for the yield estimate. For other targets, the experimental conditions must involve the enriched target isotopes because the background is created typically in reactions with the complementary isotopes present in a target. In our experiment, the targets of natural isotopic composition have been exposed to the bremsstrahlung generated with 23 MeV electron beam in 3mm W converter. The activated target was located downstream the converter, after 15 mm Al radiator to stop the electrons.

The metal target foils of natural isotopic composition were taken typically in a full weight of (0.2 - 0.5) g, and the highly-enriched materials were not used because of relatively high cost. Past irradiation during about 5 hours at the electron beam intensity of 10 μA, the induced activity measurements were continued over one week and in some cases even longer up to one month. The gamma spectra were taken using HP Ge detector with energy resolution better 1.8 keV by the ^{60}Co lines. The set of standard sources was used for energy and efficiency calibration of the detector. Series of spectra measurements were resulted in observation of the γ-lines belonged to the products of (γ, α) reactions in Sn and Ta targets, despite a great activity of other radio-nuclides produced in more abundant reactions. A number of produced ^{115}Cd and ^{177}Lu atoms could be evaluated from the measured γ-line intensities using the standard procedure for gamma spectra processing, the decay schemes from Nuclear Data Sheets, and the mathematics formalism for account of the accumulation and decay factors for the radioactive products. At the same γ-spectra, there were observed the activities produced in (γ, *n*) reactions. Finally, the (γ, α) reaction yield is calibrated to that of the (γ, *n*) reaction, and the ratio is reduced in Table 2.

Table 2. **Experimental results for the yield of (γ, α) reactions**

Target	Product	Threshold parameter $(E_{th} + B_c)$, MeV	Relative yield (γ, α)/(γ, n)	Importance of background
^{nat}Ag	^{105}Rh	13.56	$\leq 3.5 \cdot 10^{-4}$	Yes
^{nat}Cd	^{109}Pd	14.32	$\leq 2.4 \cdot 10^{-4}$	Yes
^{nat}Sn	^{115}Cd	15.31	$(2.9 \pm 0.4) \cdot 10^{-5}$	No
^{nat}Ta	^{177}Lu	14.51	$(0.70 \pm 0.12) \cdot 10^{-5}$	No
^{nat}Ir	^{189}Re	15.84	$\leq 2.8 \cdot 10^{-4}$	Yes

Accurate measurements were carried out also for other targets listed in Table 2, but the (γ, α) yields in Ag, Cd and Ir targets could only be estimated in a form of the upper limit. This is due to the presence of internal background as was explained above. The backgrounds could be eliminated if use the well enriched targets. The additional experiments with purified by orders of magnitude sensitivity might be requested. Nevertheless, one can see in Table 2 that the yields of ^{115}Cd and ^{177}Lu products of the (γ, α) reactions are now successfully measured, and they are as low as $\approx 10^{-5}$ of the (γ, *n*) reaction abundance. For three other cases, the upper limits near 10^{-4} additionally confirm the low value of the order of 10^{-5} for (γ, α)-to-(γ, *n*) ratio. For ^{177}Lu, the present experiment shows well agreement with the earlier results of [7]. It must be mentioned that both ^{115}Cd and ^{177}Lu nuclides may exist in a form of high-spin isomers: $11/2^-$ and $23/2^-$, correspondingly. Their activities couldn't be detected now because of much lower yields due to the spin factor [2]. Isomers contribute an insignificant addition to the total (γ, α) yield, and even the standard deviation must be left without changes in Table 2.

Finally, a conclusive result of the present measurements appears in relatively low probability of the (γ, α) reaction ($\approx 10^{-5}$) and this is established reliably for the group of reactions with medium-weight and heavy (A > 100) targets. Definitely, the experiments could be continued applying the highly-enriched targets to replace the upper limits with the accurate values for three reactions mentioned above. It is clear that other cases also could be experimentally explored to incorporate more data into the phenomenology of the (γ, α) reaction yields. Possible candidates for activation measurements are listed in Table 3. Some of them could be pretty convenient in real experiments, for instance, because of the background absence in 4 cases, and some others not as attractive due to the long halflife of the (γ, α) product and necessity to use the highly-enriched target materials. The perspectives are yet promising.

Table 3. **Additional possibilities for detection of the (γ, α) reaction**

Target	Abundance, %	Product	Halflife	E_γ, keV	Background
^{115}In	95.7	^{111}Ag	7.45 d	342	^{111}In from (γ, 2*n*)
^{137}Ba	11.2	^{133}Xe	5.25 d	81	^{133m}Ba from(γ, *n*)
^{143}Nd	12.2	^{139}Ce	138 d	166	–
^{145}Nd	8.3	^{141}Ce	32.5 d	145	^{141}Ce from (γ, *n*)
^{153}Eu	52.2	^{149}Pm	53.1 h	286	^{149}Eu from(γ, 2*n*)
^{160}Gd	21.9	^{156}Sm	9.4 h	204	–
^{163}Dy	24.9	^{159}Gd	18.5 h	364	^{159}Dy from (γ, *n*)
^{176}Yb	12.8	^{172}Er	49.3 h	610	–
^{176}Lu	2.6	^{172}Tm	63.6 h	1094	^{172}Lu from(γ, 3*n*)
^{187}Re	62.6	^{183}Ta	5.1 d	246	^{183}Re from(γ, 2n)
^{203}Tl	29.5	^{199}Au	75.3 h	158	–
^{207}Pb	22.1	^{203}Hg	46.6 d	279	^{203}Pb from (γ, n)

3. Discussion

A role of (γ, α) reactions in nucleosynthesis at stellar conditions is out of discussion here because such special topics must be developed and described elsewhere. We are interested for the nuclear-physics conclusions. When many reactions are studied, it would be possible to follow the variation of the (γ, α) yields with Z and A of a target nucleus and also to look for the shell-structure manifestations in the observed yields. At the moment, the results are not as developed to establish these regularities. However, in general, the low probability of α emission from excited nucleus must be explained within some realistic interpretation.

There was clear from [2] that nucleon emission (γ, *n*) and (γ, *p*) yields both satisfy a common regularity in account of the Coulomb barrier for proton emission. The yield depends on the "threshold" parameter (E_e - E_{th} - B_c) that was defined above in the Introduction. For α emission the similar approach could be applied, but the regularity is not confirmed. High binding energy of α-particle makes the effective threshold practically the same for alphas and protons. The numerical values of effective threshold (E_{th} + B_c) are given for studied (γ, α) reactions in Table 2. The Coulomb barrier was calculated using well known Bass equation [8]. The scale of (14 - 15) MeV corresponds also to a typical value for (γ, *p*) reactions similarly to (γ, α). But the yields are very different being lower for alphas by two-three orders of magnitude.

The typical (γ, *p*) yields are measured now additionally and the results are given in Table 4. Comparison of the data reduced in Tables 2 and 4 clearly demonstrates that the (γ, α) yields are by orders of magnitude lower than that for (γ, *p*) reactions.

Table 4. **Measured yields of the (γ, *p*) reactions**

Target	Reaction	Product	Halflife	E_γ, keV	(γ, *p*)/(γ, *n*)
^{nat}Cd	^{112}Cd (γ, *p*)	^{111}Ag	7.45 d	342	$(1.15 \pm 0.15)10^{-2}$
	^{113}Cd (γ, *p*)	^{112}Ag	3.12 h	617	$(1.00 \pm 0.15)10^{-2}$
	^{114}Cd (γ, *p*)	^{113}Ag	5.37 h	299	$(0.98 \pm 0.15)10^{-2}$
^{nat}Sn	^{118}Sn (γ, *p*)	^{117g}In	43.2 min	553	$(4.9 \pm 0.5)10^{-3}$
		^{117m}In	116 min	315	
^{nat}Hf	^{178}Hf (γ, *p*)	^{177g}Lu	6.65 d	208	$(1.8 \pm 0.4)10^{-3}$

In the Figure, the alpha-emission and nucleon-emission yields are compared for Sn and Ta/Hf targets exposed to the bremsstrahlung at E_e = 23 MeV. The data of Table 4 and of [2, 7] are in account after averaging of the yields measured with several target isotopes for the (γ, *p*) reaction. Error bars are not greater the size of points. The (γ, *n*) yield is taken equal unity being a reference point for the calibration. The values of effective reaction threshold (E_{th} + B_c) are also shown in the figure by triangles connected with a solid line. Despite practically similar threshold values for (γ, α) and (γ, *p*) reactions, the suppressed probability of (γ, α) is evident for both targets. Higher mass number of alphas compared to protons may influence the probability of penetration through the barrier, but in our case, the processes well above the barrier are detected. Indeed, both for protons and alphas, the parameter (E_e - E_{th} - B_c) exceeds a value of (8 - 10) MeV. Therefore, a subbarrier penetration factor couldn't be used as a real reason for explanation of the much lower α-emission probability.

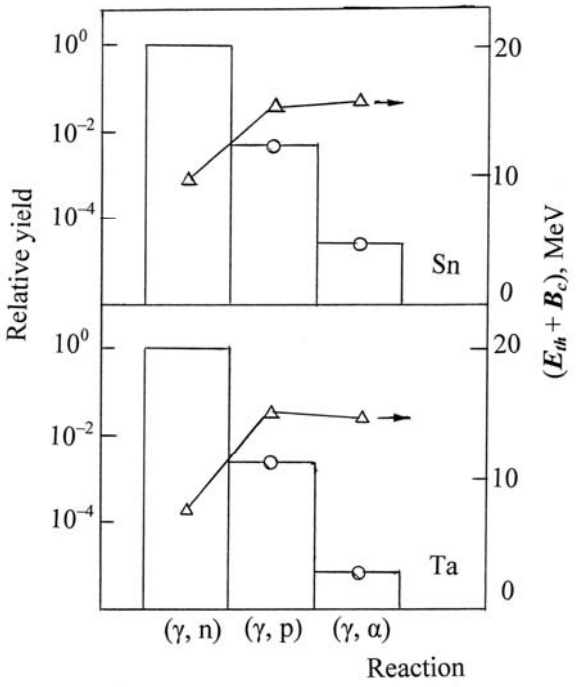

Comparison of measured yields for (γ, *n*), (γ, *p*) and (γ, α) reactions.

After all, one must assume that the pre-formation factor regulates the yield of (γ, α) reaction. Unlike to protons ready for release, the alpha particle might be formed at the first stage of the reaction and, then, emitted if energy is enough. As follows from Figure, the probability of pre-formation should be as low as of about $3 \cdot 10^{-3}$. This conclusion contradicts the ideas of a complete alpha-clustering inside the nuclear matter. Clusters may permanently exist in light nuclei, but not in A > 100 species. Another point is open for additional analysis, namely, the idea of nucleon-nucleon correlations with formation of the quark bags instead of the nucleon gas (liquid) in the bound nuclei. Without theoretical calculations, it would be difficult to make a solid conclusion, whether our results cancel the idea on multiquark objects inside a nucleus or just mean some restricted probability for short-range nucleon-nucleon correlations. The theoretical analysis was performed for reactions at GeV energies [1], but the (γ, α) reaction at low energy was not yet theoretically studied in this look.

4. Summary

Possibilities for detection of (γ, α) reactions in relatively simple activation experiments were analyzed and some favorable cases are distinguished. When the experiment is performed at relatively low photon energy, the measurements could be informative to clarify a status of nucleons in the heavy nucleus. Yields of five (γ, α) reactions are measured with bremsstrahlung beam at the end-point energy of 23 MeV, and pretty low probability of about 10^{-5} is deduced for the (γ, α)-to-(γ, *n*) yield ratio. The conclusion follows that the models describing a nucleus as construction built of α-clusters are not supported. Probably, the pre-formation factor for alphas must be in account. Short-range nucleon-nucleon correlations leading to formation of multiquark objects (quark bags) in nucleus could also influence the (γ, α) probability. This point must be additionally analyzed in theory for conclusive simulation of the experimental data.

ACKNOWLEDGEMENTS

The beam supply with MT-25 accelerator by A.G. Belov is gratefully acknowledged.

REFERENCES

1. *Kukulin V.I.* Di- and multi-baryon clusters in nuclei. Nontraditional look at the nuclear force problem and nuclear structure // Phys. of Atomic Nuclei. - 2011. - Vol. 74. - P. 1594 - 1614.
2. *Karamian S. A.* Threshold and spin factors in the yield of bremsstrahlung-induced reactions. - Dubna. 2012. (Prepr. / JINR; E15-2012-65). (Submitted to Phys. of Atomic Nuclei).
3. *Volkov Y.M., Ignatiev A.I., Kolomenskii G.A. et al.* α-decay of giant resonances in $^{58, 60}$Ni nuclei // Phys. of Atomic Nuclei. - 1980. - Vol. 32 - P. 595 - 602.
4. *Dolbilkin B.S., Kan Sh., Kim T. et al.* ^{58}Ni(e, e'α) reaction at excitation-energy range of 8- 25 MeV // Bull. RAS. Phys. - 1991. - Vol. - 55. - P. 967 - 970.
5. *Dikiy N.P., Dovbnya A.N., Lyashko Y.V. et al.* Method of ^{195m}Pt production on powerful electron accelerator // Book of Abstracts of Int. Conf. NUCLEUS 2007. - Voronezh, 2007. - P. 293.
6. *Vishnevsky I.N., Zheltonozhsky V.A., Kadenko I.N. et al.* Integral cross-sections of the photonuclear reactions on ^{118}Sn and ^{121}Sb nuclei // Ibid. - P. 121.
7. *Karamian S.A., de Boer J., Oganessian Y.T. et al.* Observation of photonuclear reactions on isomeric targets: ^{178m2}Hf(γ, *n*)^{177m2}Hf, ^{180m}Ta(γ, 2*n*)^{178m,g}Ta and ^{180m}Ta(γ, *p*)^{179m2}Hf // Z. Phys. A. - 1996. - Vol. 356. - P. 23 - 29.
8. *Bass R.* Fusion reactions: successes and limitations of a one-dimensional description // Lect. Notes in Phys. - 1980. - Vol. 117. - P. 281 - 293.

TWO-PARTICLE PHOTODISINTEGRATION OF HELIUM-4: $^4He(\gamma,p)T$, $^4He(\gamma,n)\,^3He$, $^4He(\gamma,d)d$

V. F. Klepikov, Yu. A. Kasatkin, P. E. Kuznietsov, O. E. Koshchii*

Institute of Electrophysics and Radiation Technologies, National Academy of Sciences of Ukraine, Kharkiv, Ukraine
** V. N. Karazin Kharkiv National University, Kharkiv, Ukraine*

On the basis of covariant diagram technique and the concept of nucleus - as an elementary particle, observables for the reaction of the two-particle photodisintegration of the ^4He were calculated. The only functional parameter is the vertex structure function which describes the "collapse" of a helium-4 nucleus and the nucleon remnant or two deuterons, which exhausts these reaction channels. The interaction of a real photon is determined by the values of the charges of the particles, since the electromagnetic form factors are calculated in the photon point - $q^2 = 0$.

As the edges of the strong interaction we use the results in which microscopic calculations are based on the expressions for the missing vertices. Inseparability of the electric charge from the particle's mass allows us to coordinate with the conservation laws of energy-momentum and charge in the interaction so that the requirement of gauge symmetry is automatically satisfied. The covariant amplitude of the process is the sum of pole diagrams and regular part required to keep the dynamic EM current.

A close fit of theoretical calculations and experimental measurements on differential and total cross sections for these reactions was obtained.

1. Introduction

At the previous conference in 2010 we proposed an approach [5, 6] that describes the photodisintegration processes of light nuclei into fragments using generalized Feynman rules. At the same time, it is necessary to follow the requirements of general covariance and dynamically take into account the requirement of gauge invariance. The only (unknown) parameter is the vertex that describes the collapse of strongly interacting particles. The dependence of the vertex from the space-like four-momentum of fragments allows us to keep invariance of the approach irrespective of its explicit form. The approach is based on bringing into consideration the theory of fiber spaces, in which a vector-potential of the electromagnetic field provides a connection. Due to the fact that the electric charge cannot be separated from the mass, consequently, it is not an independent quantity, describing the movement of particles in the base space it is necessary to consider additionally the movements in associated charge space. As the result of these operations it was succeed to harmonize the effect of 4-momentum and charge conservation laws in the amplitude of processes.

Several points that are infusion into the theory by new approach, or, to be more precise, by the regular part of the amplitude, should be noted.

Momentum distributions of the components in various non-local fields of matter are individual and contain information about the steady-state interactions in a coupled system. They also reflect coupled spatial and time evolution of a system during the whole energy and structure range. The information for each non-local field is determined by the degree decreasing of the momentum distribution function, its rate of change and the nature of the curve's curvature (its convexity or concavity).

Another established property of the generalized gauge-invariant pole amplitude, which occurs independently of the explicit form of vertex function is related to the degree of its increasing or decreasing. The relative sign between the pole and regular parts in the amplitude is fixed by the conservation of a total electromagnetic current requirement. If the vertex function of the strong interaction is constant, then the regular part in the amplitude turns into a zero and the pole part is determined by Yukawa asymptotic behavior - a constant that is divided by the pole. For decreasing functions its derivative is negative. This fact changes the sign in the amplitude for the regular part, making the sign equal to the sign of the pole part. In this case, the contribution from the regular part to the total cross section is constructive (positive interference).In the case, when the vertex function increases with the argument increase, its derivative is positive and the contribution to the cross section is changed to the destructive.

Conclusion is that the regular component of the generalized pole amplitude *is a dynamic measure of the bound state non-locality and shows how "quickly" the structural formations of the initial level of matter structure lose their identity upon transition to the other scale of spatial and temporal localization.*

The regular component of the amplitude introduces an additional dependence from the vertex function in the form of its derivative. It was established that for the electric dipole splitting contribution from the regular part to the full amplitude at low energies is determined by the derivative of the strong interaction vertex. Contribution regular part to the total amplitude is determined by the second derivative of the strong interaction's vertex, if the electric dipole transition is absent (splitting into two identical fragments).

2. $^4He(\gamma,p)T$, $^4He(\gamma,n)\,^3He$ reactions

So, let's start to explore the two-particle photodisintegration processes of the helium-4 nucleuses using the new approach. Firstly, we consider the following reactions: $^4He(\gamma,p)T$and $^4He(\gamma,n)\,^3He$.

The matrix element of these processes, which are corresponding to the set of diagrams, is shown in Fig. 1.

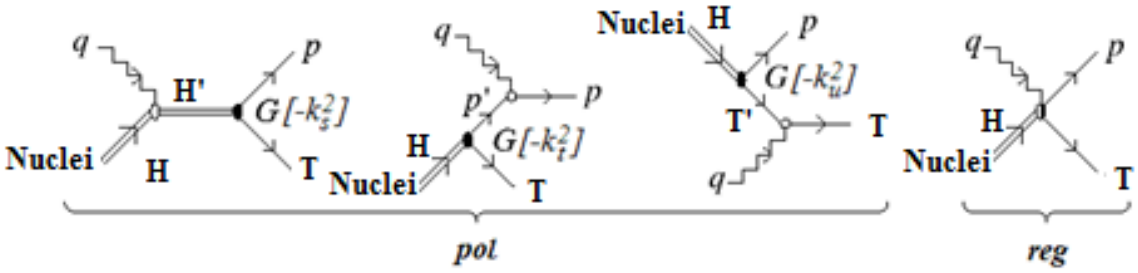

Fig. 1. Set of diagrams.

$$\mathcal{M} = e\varepsilon_\mu \bar{u}(p) \sum_{i=s,t,u,c} M_\mu^{(i)} v(T), \qquad v(t) = C\bar{u}^T(T),$$

where

$$M_\mu^{(s)} = z_H \frac{(H+H')_\mu}{s - m_H^2} G^{(s)} \gamma_5,$$

$$M_\mu^{(t)} = j_\mu^{(t)} \frac{(\hat{p}' + m)}{t - m^2} G^{(t)} \gamma_5,$$

$$M_\mu^{(u)} = G^{(t)} \gamma_5 \frac{(\hat{T}' - m_T)}{u - m_T^2} j_\mu^{(u)},$$

$$M_\mu^{(c)} = \int_0^1 \frac{d\lambda}{\lambda} \frac{\partial}{\partial k_\mu} \{z_N G[-k_{st}^2(\lambda)] + z_T G[-k_{su}^2(\lambda)]\} \gamma_5,$$

*q, H, p, T*are4-momenta of particles. Electromagnetic currents are defined in the standard way: $j_\mu^{(t)} = (z_N + \kappa_N \hat{k})\gamma_\mu$, $j_\mu^{(u)} = (z_T + \kappa_T \hat{k})\gamma_\mu$, where $z_{N(T)}$ and $\kappa_{N(T)}$ are the charge and anomalous magnetic moment of the particle *N(T)*; z_H is thecharge of the ^4He.

Relative 4-momenta that characterize the vertex $^4He \rightarrow NT$in the pole diagrams:

$$k_s = p - \frac{(pH')}{H'^2} H' = \frac{(TH')}{H'^2} H' - T,$$

$$k_t = k_s - \frac{(TH')}{H'^2} k, \qquad k_u = k_s + \frac{(pH')}{H'^2} k.$$

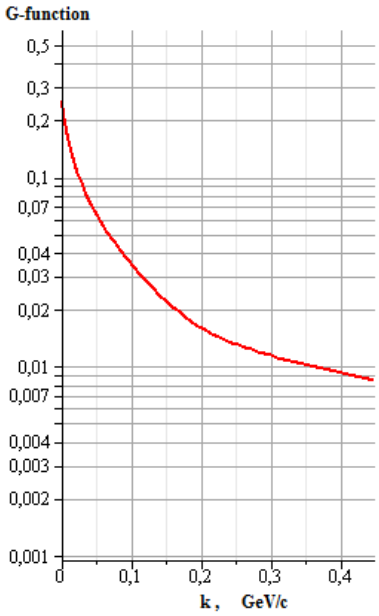

Fig. 2.The energy dependence of G-function [1].

Quantities $k_{st}(\lambda)$ *and* $k_{su}(\lambda)$ are defined as

$$k_{st}(\lambda) = k_s - \lambda \frac{(TH')}{H'^2} k, \qquad k_{su}(\lambda) = k_s + \lambda \frac{(pH')}{H'^2} k.$$

The vertex function *G* describes the virtual collapse $^4He \rightarrow NT$and due to the relativistic invariance depends on the square of the relative four-momentum.

Vertexfunctions $G^{(i)} \equiv G(-k_i^2)$, $(i = s,t,u)$ depend on the appropriate arguments.

We note that in the case $G^{(s)} = G^{(t)} = G^{(u)} = const$ we have: $M_\mu^{(c)} = 0$, and therefore the sum of pole diagrams is gauge-invariant.

We parameterized the vertex function as in [1] for further calculations. And that will finish determination of the problem quantities.

Fig. 2 shows the parametrization of G-function depending on the relative momentum of the fragments.Defining all the quantities in the problem, we calculate the observed and compared with experimental data, without changing any of the previously fixed variables.

Fig. 3 shows the dependence of the differential cross section $^4He(\gamma, N)T$ from the photon energy at angles $\vartheta = 90^\circ$ (E is a photon energy in a laboratory system). The obtained data are in a close fit with experimental ones. It is obvious, according to the results, that the generalized pole amplitude's contri-

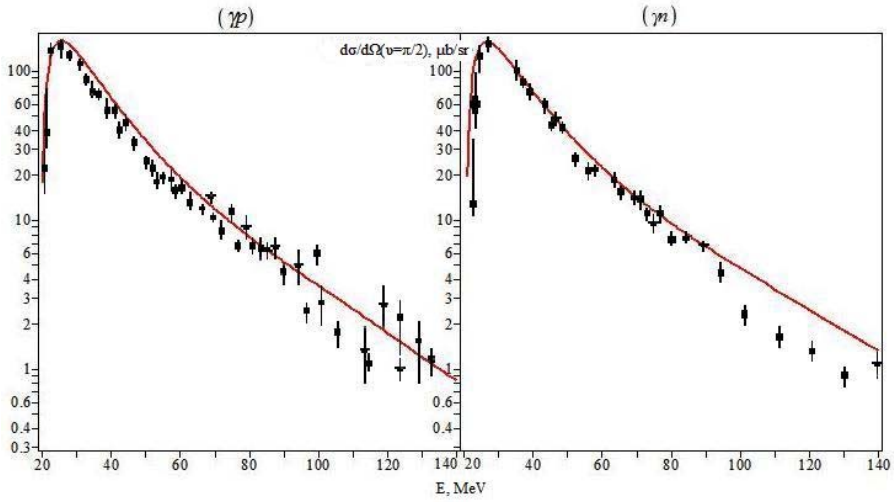

Fig. 3. Dependence of the differential cross section $^4He(\gamma,N)T$ of photon energy at angles $\vartheta = 90^{\circ}$. Experimental data ⋆ - [4], ⊙ - KPTI.

bution does not give a satisfactory description of experimental data.The description is improved by taking into account an additional mechanism – the regular part of the amplitude.We can see the essential role of the regular partconsidering almost all photon energies.

Fig. 4 presents six pairs of the angular spectra at fixed energies. The experimental angular distributions are well described by this model at any considered energy interval.

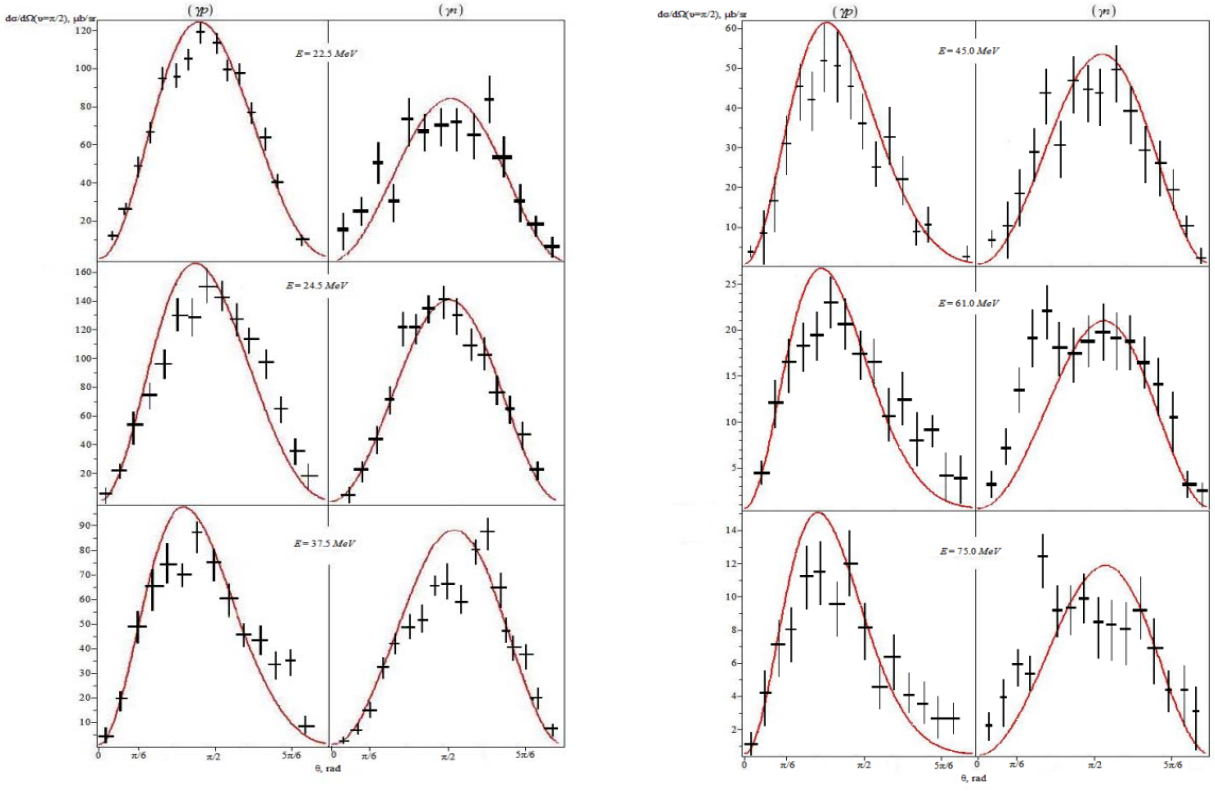

Fig. 4. Angular dependence of differential cross sections for reactions $^4He(\gamma,N)T$ in energy range $E_\gamma = 22.5 \div 75.0$ MeV.† - KPTI data.

In Fig. 5 the red solid line indicates dependence of total cross sections forreactions $^4He(\gamma,N)T$ fromphotonenergy in the range of 20÷44 MeV taking into account all the diagrams. Dash-dotted and dotted lines describe the accounting of pole diagrams and the regular one, respectively.It is evident that the required agreement with experimental data is achieved only when we account both of inputs. Accounting only the pole diagrams does not provide an adequate description of experimental data.

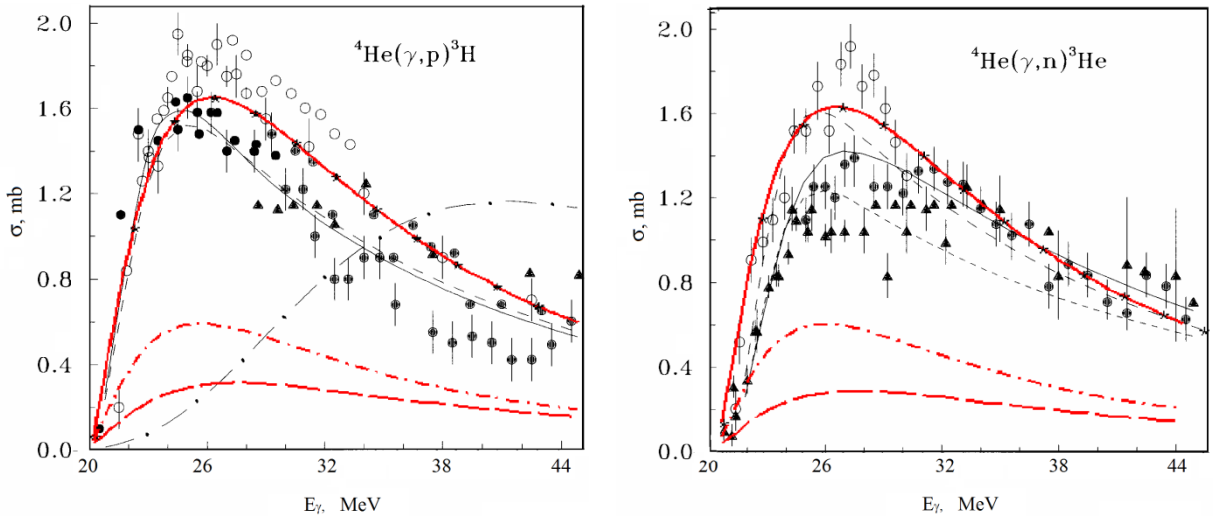

Fig. 5. Dependence of total cross sections for reactions $^4He(\gamma, N)T$ from photon energy in the range 20÷44 MeV. Experimental data [3].

3. $^4He(\gamma, d)d$ reaction

The process $^4He(\gamma, d)d$ is characterized by the factthat, due to isospin selection and particles identity in the final state, the electric dipole moment is suppressed and the process realizes mostly due to quadrupole γ-ray absorption. Therefore, this channel is of considerable interest to study the nature of the quadrupole transition. Most theoretical papers that investigate this reaction have non-relativistic nature. In our paper the problem of ensuring the gradient invariance of amplitude was solved by choosing the next reaction mechanism: to the known field-theoretic row the contact diagram is added. This diagram takes into account multiparticle effects, including the electromagnetic interaction with the "strong interaction carriers".

Rooting from this approach, the amplitude, which satisfies the principles of relativistic and gradient invariance, is determined by the sum of the pole and contact diagrams (Fig. 6).

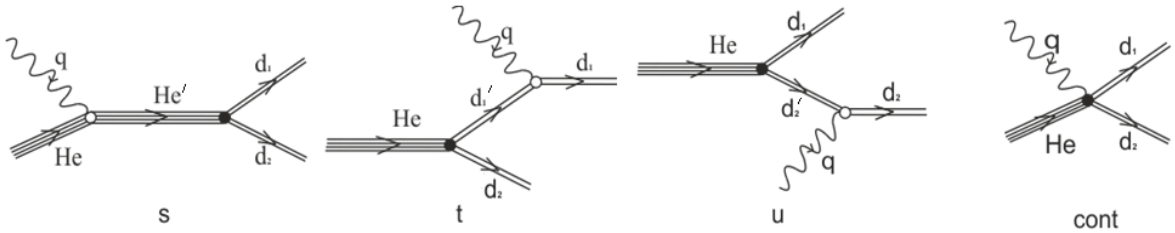

Fig. 6. Set of diagrams for the $^4He(\gamma, d)d$ reaction.

The matrix element pole part of these diagrams is characterized by two electromagnetic vertices $(\gamma\ ^4He \to\ ^4He)$, $(\gamma d \to d)$ and the strong one - $(^4He \to dd)$. It is easy to write down the matrix elements corresponding to the pole s-, t-and u-channel diagrams by defining appropriate vertices that were obtained. It is also easy to obtain the matrix element which corresponds to the contact diagram and is presented in the integral form:

$$M^{(s)} = e\varepsilon_\mu \frac{(2p+q)^\mu}{s - m_{nucl}^2} U_\rho^*(p_1) U_\sigma^*(p_2) G_{\rho\sigma}(p'; p_1, p_2)\,,$$

$$M^{(t)} = e_1 \varepsilon_\mu F_{\beta\rho}^\mu(q, p_1', p_1) \frac{1}{t - m^2} U_\rho^*(p_1) U_\sigma^*(p_2) G_{\beta\sigma}(p; p_1', p_2),$$

$$M^{(u)} = e_2 \varepsilon_\mu F_{\beta\rho}^\mu(q, p_2', p_2) \frac{1}{u - m^2} U_\rho^*(p_1) U_\sigma^*(p_2) G_{\beta\rho}(p; p_1, p_2')\,,$$

$$M^{(c)} = e\varepsilon_\mu U_\rho^*(p_1) U_\sigma^*(p_2) \times \int_0^1 \frac{d\lambda}{\lambda} \frac{\partial}{\partial q^\mu} \left[e_1 G_{\rho\sigma}(p' - q\lambda; p_1 - q\lambda, p_2) + e_2 G_{\rho\sigma}(p' - q\lambda; p_1, p_2 - q\lambda)\right],$$

where $s = (q+p)^2$, $t = (p_1 - q)^2$, $u = (p_2 - q)^2$ are Mandelstam variables, $m\ and m_{nucl}$ are hadrons'(which we consider as equal) and the nucleus target's masses respectively.

The differential cross section of the $^4He(\gamma, d)d$ process in case when γ −ray is polarized in an arbitrary way:

$$\frac{d\sigma}{d\Omega} = \frac{1}{2(8\pi W)^2}\frac{|\boldsymbol{p}|}{|\boldsymbol{q}|} Sp\, R.$$

In the above-mentioned model, the full amplitude of the $^4He(\gamma,d)d$ process is determined by the next sum: $M^{(s)} + M^{(t)} + M^{(u)} + M^{(c)}$. Fig. 7 shows differential cross section angular dependence of the $^4He(\gamma,d)d$ process at photon energies in lab system $E_\gamma = 40$ MeV. A qualitative description of the experimental angular distribution was obtained: the correct location of the cross-section minimum at$\upsilon = 90^\circ$ and maximums at $\upsilon = 45^\circ, 135^\circ$.

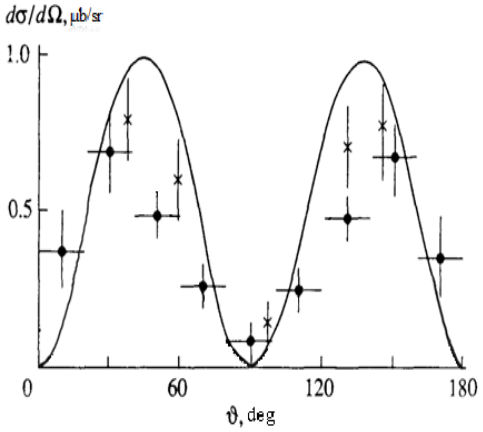

Fig. 7. Angular dependence of the differential cross section of the process $^4He(\gamma,d)d$ at $E_\gamma = 40$ MeV in lab system.Experimental data: ⊙ - KPTI, ×-[2].

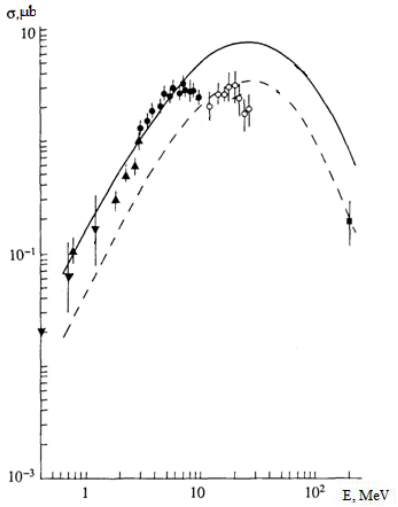

Fig. 8. Dependence of the total cross section for the process $^4He(\gamma,d)d$ from photon energy. Solid line – calculations with the full amplitude of the process; dashed – no contact diagram. Experimental data – [2].

Fig. 8 illustrates dependence of the total cross section for the process $^4He(\gamma,d)d$ from photon energy. In general terms, the description of the total cross section (see Fig. 8) significantly better than non-relativistic calculations. From Fig. 8 also follows that in the whole energy range of γ-ray the role of the contact diagram is significant.

4. Conclusions

Calculations made and comparisons with experimental measurements have shown that a generalization of the Feynman rules for the description of photonuclear processes is working. New look at the theory of electromagnetic processes on compound systems allowed to reproduce the results, which were postulated by the previous model, without any problems. The special role is given to the construction of a regular part of the amplitude, which determines the gauge-closed matrix element. It means that the structure of the matrix element that satisfies the requirements of covariance and the fundamental requirement of gauge symmetry has been adapted to the description of various processes. Issues related to the studying of inter-nuclear dynamics need individual microscopic solution.

REFERENCES

1. *Schiavillaet R. et al.* Momentum distributions in A = 3 and 4 nuclei // Nucl. Phys. - 1986. - Vol. A449. - P. 219 - 242.
2. *Scopic D.M., Shin Y.M., Phenneger M.C. et al.* Photodisintegration of the deuterium determined from electro disintegration process // Phys. Rev. - 1974. - Vol. C9, No. 2. - P. 531 - 536.
3. *Дубовиченко С.Б.* Свойства легких атомных ядер в потенциальной кластерной модели: Изд. второе, исправл. и доп. - Алматы: Изд-во "Денекер", 2004. - 247 с.
4. *Gari M., Hebach H.* Photonuclear reactions at intermediate energies ($40 \leq E_\gamma \leq 400$ MeV) // Phys. Rep. - 1981. - Vol. 72, No. 1. - P. 1 - 55.
5. *Kasatkin Yu.A., Klepikov V.F.* Alternative Construction of QED and Correct Introduction in the Theory of Nonlocal Fields // 3-d Int. Conf. "Current Problems in Nucl. Phys. and Atomic Energy" (Kyiv, 7 - 12 June, 2010). - Kyiv, 2011. - P. 617 - 624.
6. *Kasatkin Yu.A., Klepikov V.F.* Regular Part of the Conserving Structural Current is as Dynamic Measure Non-locality of the Coupled Fields // 3-d Int. Conf. "Current Problems in Nucl. Phys. and Atomic Energy" (Kyiv, 7 - 12 June, 2010). - Kyiv, 2011. - P. 625 - 632.

THE DEVELOPMENT OF NEW PROJECTION METHODS OF RADIATION PROTECTION OF INDUSTRIAL RADIATION INSTALLATIONS

T. V. Kovalinska, I. A. Ostapenko, V. I. Sakhno, A. G. Zelinskyy

Institute for Nuclear Research, National Academy of Sciences of Ukraine, Kyiv, Ukraine

The results of the development experimental researches of problems of radiation protection of powerful industrial techniques are presented.

The projection of new and modernization of existing radiation technique of enterprises always causes conflict situations "cost of the installation – its accordance to standards." The last strictly regulate certain parameters of radiation technique concerning the compliance primarily with ecological requirements and radiation safety. The analysis of the situation shows that these requirements substantially put back wide industrial usage of radiation for the production of goods and services. The situation is very actual in market economy, where the rotation rate of working capital determines the effectiveness of business. Objectively – radiation technologies, because of the excess of formal requirements, can not be spread in the environment of small or medium business due to economic arguments. They are also unacceptable for large business, because of the involvement of controlling social institutions. As the result, real economy doesn't receive huge profits because of technical inability to fulfill modern advanced scientific and energy-efficient production methods, bright representatives of which are radiation technologies.

The main problem of radiation technologies is high cost of biological radiation protection. It is equipped according to standardized methodologies [1, 2] for obtaining standard indicators of influence on the environment near buildings with operating technique. Taking into account the amounts of expenses, the construction of buildings with radiation protection means may exceed in several times the cost of radiation technology itself. These expenses are included into the cost of products, and such production becomes unprofitable and unattractive for the enterprise.

The most prevalent way of reducing the cost of the building is to use natural factors for the absorption of undesirable γ-radiation. The absorption of radiation with air is used mostly – the ceiling of the building protects only against meteorological factors – rain, temperature etc., and only back side walls of buildings have estimated thickness.

This variant was researched for the experimental technological radiation installation of KINR NASU [4] (with 4 MeV electron accelerator and power in the beam of 5 kW), and the industrial technological line of materials irradiation with electron accelerator of the energy of 2 MeV and beam power of 20 - 40 kW [6].

During the creation of the powerful INR installation there were doubts and fears of possible unacceptable high levels of scattered γ - irradiation outside the building. In the calculations simple formula [3] of expected intensity (quantity) of scattered γ-irradiation around the radiation installation was used, for example, of immersed in water or soil (the standard method of protection of isotope radiation technique of previous generation).

$$I_p = 6{,}6 \cdot 10^1 \, Q e^{-0{,}042h} e^{-0{,}001r} \text{ MeV/cm}^2 \cdot \text{s},$$

where h and r are in cm.

In such constructions the effect of quadratic reduction of the value of irradiation flux to the ceiling is used. With this purpose, the walls of the building have a significantly increased height. Then, by means of choosing the thicknesses of overlap, its scattering into the surrounding area outside the building is made.

Pre-estimations, obtained according to recommendations for isotope generators show that in specific correlations of the activity of irradiation source and characteristics of scattering factors, γ-irradiation, diffused in the air, may create rather high levels of radiation at significant distances from radiation technical means.

In order to determine whether it is appropriate to consider these effects for the certification of radiation technique of electrophysical type (here – electron accelerators with small 5 - 25 mm.mrad. beam emittances) special researches of radiation fields of accelerators of different types and at different distances from the outer surface of the walls in the most unfavorable modes of irradiation were conducted. It is worth mentioning, that measurements of indicated parameters near electrophysical pulse technique is a difficult problem, because during the operation, for example, of resonance accelerators, the generation of electrons is simultaneously accompanied with the generation of electromagnetic interferences in the wide range of frequencies. Taking into account extremely high sensitivity of dosimetry devices and peculiarities of their construction, these interferences may significantly distort indicators of devices, and during their processing, the experimenter should carefully estimate the reality of received and interpreted results. These effects are better to be modeled in advance, for example, to make measurements during the minimum intensity of the beam (with "dark" current, and then at different levels of its intensity) to create special measuring devices, which can control the content of any associated effects.

With this purpose on the 4 MeV accelerator of INR radiation installation special system of measurements with the slot device [5], detector of SIF power and control channel of radiation measurements with certified ionization chamber and standard apparatus was created. By means of them it is possible to make the wide range of special measurements in advance, firstly of electromagnetic interferences and to calibrate dosimeter means before beginning the modeling of researched processes.

On the 4 MeV accelerator is was specifically modeled by setting in the reaction chamber different equipment, what

led to the emergence of intensive flows of inhibitory γ- irradiation from electrons' conversion and its subsequent multiple scattering. An additional contribution to the formation of intense radiation fluxes was also made with the special setting of the accelerator for the widest range of generating the beam of electrons (lower threshold of less than 2 MeV – closer to isotopic installations based on Co^{60} for the possibility of binding the results to previous researches).

On the first stage of researches the construction of ceiling was typical and did not provide significant absorption of irradiation. As it was expected (taking into account horizontal direction of the beam movement, its geometry and calculated diagram of the direction of petals of inhibitory irradiation in the reaction chamber of INR installation), the distribution of undesirable γ-irradiation in the space near the corps of the installation had a dramatically uneven character. For measurements the area of the surrounding space with the greatest intensity of γ-rays was chosen. Thus the real picture of the distribution of radiation fluxes (minimal detected energy of γ-rays of 50 keV) near the room of the installation was obtained, which is reflected on the graph 2 (Fig. 1).

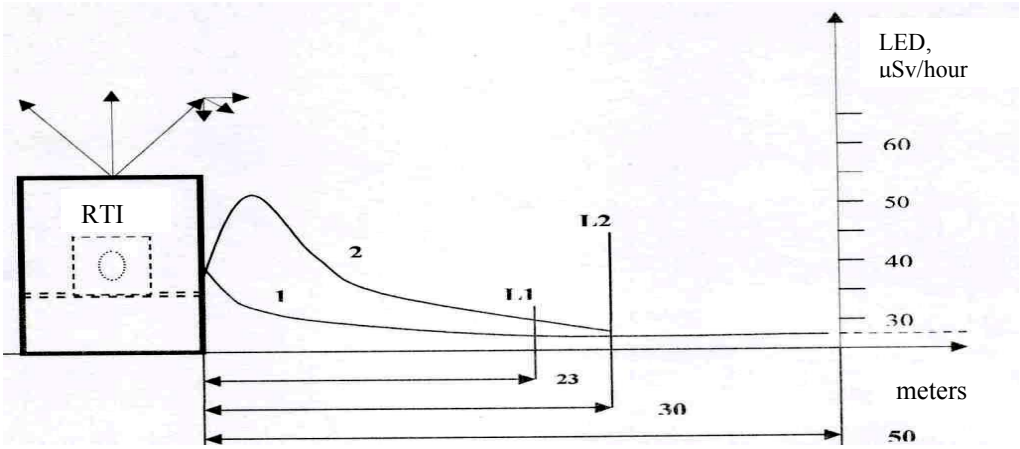

Fig. 1. The distribution of scattered γ-irradiation in the area adjacent to the radiation installation.

There was a deviation of the distribution law from the normal (quadratic) one. Near the corps, the distribution of intensity of γ-irradiation has a peak at the distance of about 2 - 4 m. At longer distances the distribution of the radiation field gradually becomes common and at the distance of 23 m from the corps its distribution corresponds to the quadratic law. Depending on specific conditions (including weather), this distribution changed significantly. But this fact indicated the presence of the perceptible component of ionizing radiation in the received signals of dosimetric devices. Though high level of collateral electromagnetic waves influenced the quality of researches, but preliminary calibration allowed to reduce their impact on the results of dosimetric measurements significantly. The comparison of calculated and actual distribution with theoretical one showed that obtained function is a superposition of the quadratic law and the distribution of γ-quantums, scattered with air.

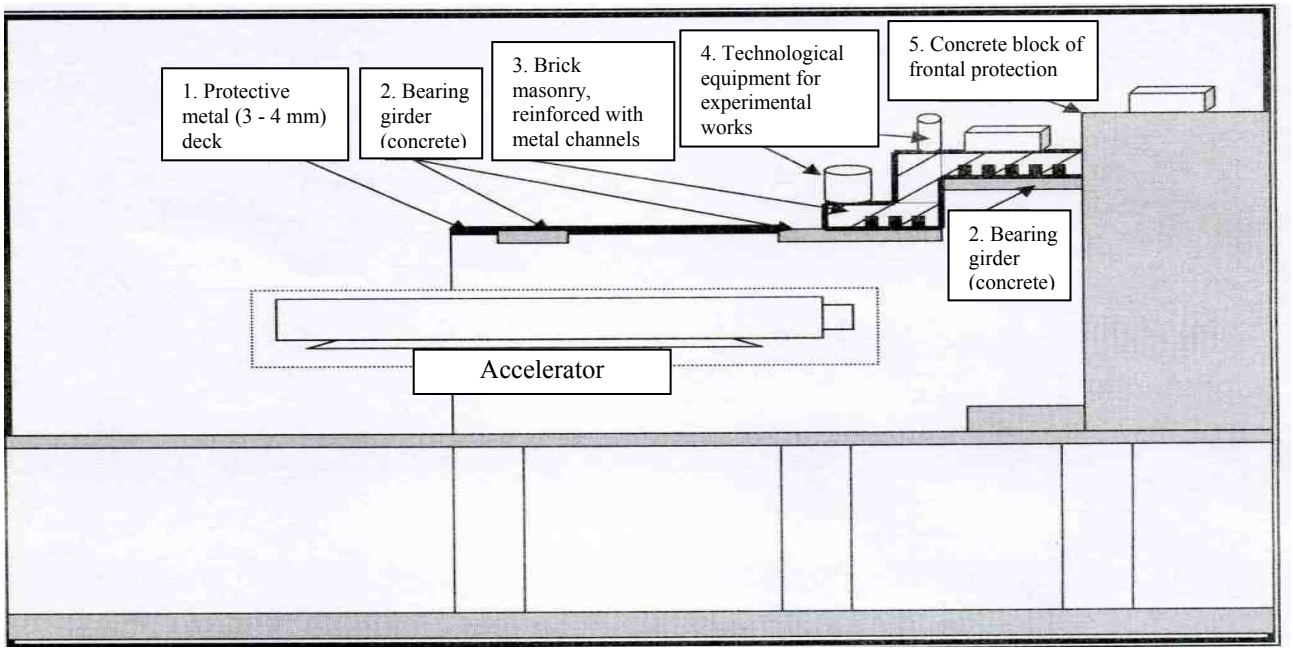

Fig. 2. The scheme of modernization of the overlap of the accelerator's room.

As this installation is located on the INR sanitary protection area, the indicated factor was not an obstacle for its practical use. Already at the distance of 30 m from the outer wall surface the intensity of the additional γ-irradiation from the installation became lower than the natural background on the territory. But taking into account the following practical use of such technique in the real production, the possibility of the improvement of the installation for its location on the territory of an active enterprise was researched, where the availability of a special sanitary protection zone is not provided.

The possibility of setting additional more simplified means for the improvement of radiation protection of the installation on the overlap of the corps was researched, including experimental researches. Their construction took into account the factors of back-scattered inhibitory γ- irradiation and blocked only the surface of the ceiling above the reaction chamber (Fig. 2).

Moreover, the construction of the overlap provided the installation of the additional equipment on it for technological researches of technique and materials for nuclear power plants. This equipment provides an additional radiation protection of structural character due to the absorption of undesirable γ-irradiation with the material, of which it is made (iron, copper, etc.). To improve the effectiveness of the protection, the corners of the overlap construction are made overhung and of the materials with high index of energy albedo. The results of the following (after the completion of the corps) measurement of the radiation field on the adjacent territory are shown on the curve 1 (see Fig. 1). It turned out that after the modernization of the overlap, actual decrease of the intensity of γ-irradiation on adjacent territories corresponds to the square one, and the power of the dose of γ-irradiation on external walls of the installation coincides with the calculations and meets NRPU and MSRU requirements [2].

Similar researches were carried out for radiation technique with vertical direction of motion of the beam (the beam is directed to the floor of the reaction chamber (Fig. 3).

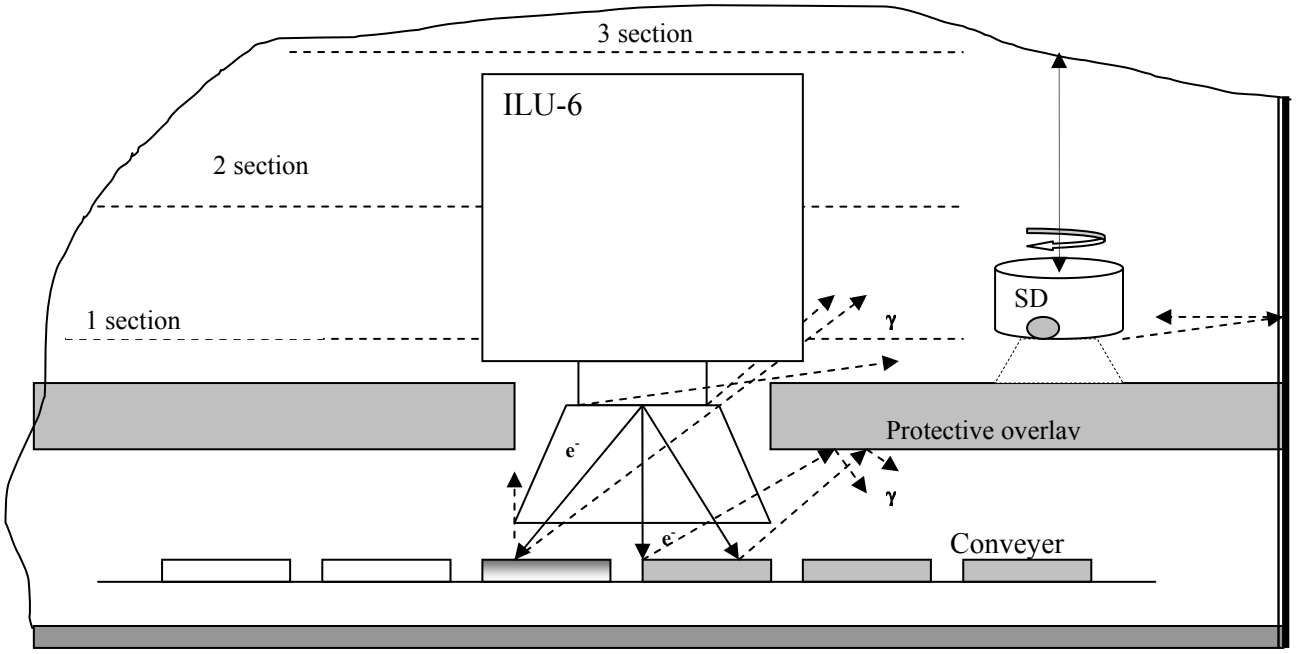

Fig. 3. The scheme of the location of the ILU accelerator in technological rooms of RADMA.

The object of researches was resonant industrial electron accelerator ILU-6 at 2 MeV with the beam power of 20 kW of the State Enterprise RADMA IFC NASU. Like the previous case, this accelerator is a powerful source of megavolt electrons which are accelerated with the energy of high-frequency generator. On the ILU accelerators the power of RF generator reaches 120 kW in the impulse. The efficiency of the unit of acceleration is declared at the level of 25% of the power of RF generator. The difference between ILU-6 and "Electronics" accelerator is in frequency, duration and amplitude of impulses. In both cases, the greater proportion of LF power generators is not used for electrons' acceleration, and is utilized of in special absorbers, and is scattered in the environment. RF irradiation due to the appropriate choice of frequency of the generator on the stage of the projection of this technique (according to current norms) is not the environmental problem.

The problem for current exploitation of the installation were too high indicators of radiation control devices (the task of which was finding and controlling radioactive isotopes) which were perceived as high radiation level on adjacent territories.

The analysis of the results of special researches of the division of these fields, which is carried out taking unto account previous experience in RTU INR, showed that the character of their distribution does not meet parameters of the distribution of ionizing radiation. The formation of high levels at considerable distances from the corps with their

periodic duplication during further increase of the distance indicated that the problem can not be considered the consequence of the influence of ionizing irradiation. Such phenomena are likely to belong to RF oscillations and are known in the radiotechniques as interference pattern near industrial radio stations. The possibility of local contamination was also excluded (industrial accelerators do not lead to the formation of induced radioactivity), and the level of researched fields depended on the work of the installation.

The researches were carried out by measuring the distribution of ionizing radiation fields in technological rooms of the installation, and then, with the connection to previous measurements, irradiation on adjacent territories were researched. For measurements the same slot device was used, as the described one [3]. He was placed in 3 symmetric points of the technological room of the accelerator. In one of them, the device was moved in vertical space, and the distribution of irradiation fields on 3 levels (cross sections) was measured. The family of diagrams of the direction on intense sources of different irradiation near the accelerator was obtained. Fig. 4. provides the general picture of the distribution of irradiation.

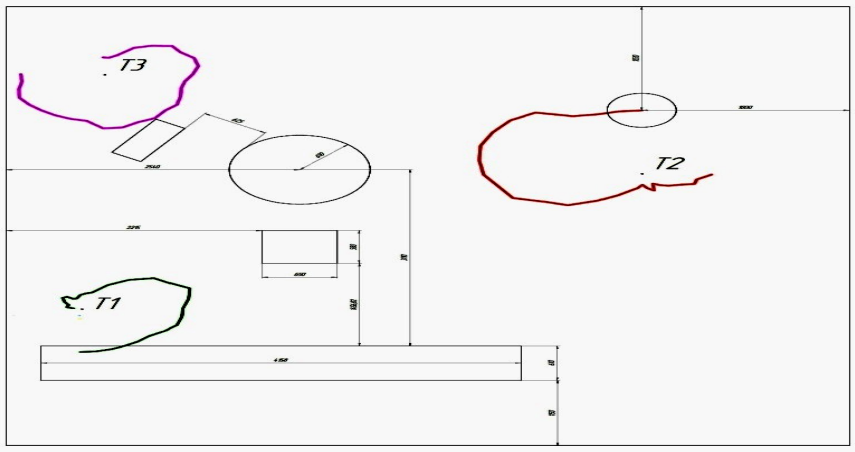

Fig. 4. Topography of the distribution of irradiation of the industrial accelerator ILU-6 of enhanced power in the technological room.

These figures show that the most intense irradiation fluxes are observed from the walls of the room and auxiliary equipment of the accelerator. Using traditional methods of experimental physics for the analysis of this picture, we can state that the actual contribution of ionizing irradiation (pikowave range of electromagnetic irradiation) is insignificant here, and rather lower than the intensity of irradiation of low-frequency range from the equipment of the accelerator. This is also confirmed by the fact that the most intense sources of irradiation (from the real geometry of measurements) are the matching device of RF generator ("megaphone") and the apparatus of the injector (powerful impulse source of high voltage). The vivid evidence of this is the high level of signal from dosimetry devices even when the injector of the accelerator was disconnected, and actual level of possible flow of electrons (the beam) decreased to the value of "dark current" as a result of cold electrons' emission (less than 0,01 - 0,1 % of the average beam current). The same was observed during measurements of intensity of irradiation on the adjacent territory of the installation – the intensity of measured fields remained practically unchanged at any beam current regulations. From theoretical considerations, any change in beam current should be fixed as the change in radiation background, and could not remain unnoticed even in scattered fields of inhibitory irradiation. But the fact, that such decrease in measurements, which were made, is not observed, indicates that the choice of vertical position of the accelerator and the output of the beam into deep floor is the most profitable way to reduce the effects of the influence of secondary irradiation of working industrial radiation technique on the environment. With the appropriate choice of the room construction (considering that secondary inhibitory irradiation forms in the reaction chamber the radiation field of cardioid form with noticeable petals of intensive reverse irradiation (120 - 145^0), inhibitory irradiation practically doesn't penetrate into the technological room of the accelerator and does not create significant problems in terms of radiation safety of the personnel and the environment.

If it is necessary (for example, for the improvement of metrology process and the reliability of functioning of the devices of technological installation management), low frequency oscillations can be reduced with any known methods of the absorption or reflecting them directly to the accelerator's room, and are not the subject of researches because there are numerous instructional materials on these issues. But if there exists the necessity to improve systems of radiation protection (on the installations of increased power, or structurally created as super powerful sources of inhibitory gamma irradiation) it is necessary to modernize the construction of walls of technological rooms in order to flatten intensities within the technological room of their absorption and to reduce the reflectivity of constructions and walls. Such measures are the simplest to be made with methods of facing the room with absorbent materials which are effective for pikowave range of irradiation.

Such possibility was proved experimentally on the radiation installation with electron accelerator of 4 MeV. The peculiarities of scattering of inhibitory irradiation of wide energetic spectrum on various materials were researched –

organic glass (plex - 1.1 g/cm^3), marble (1.8 g/cm^3), iron (7 g/cm^3), lead (11 g/cm^3), concrete (2.2 g/cm^3). The results of these measurements are presented as the family of curves in Fig. 5.

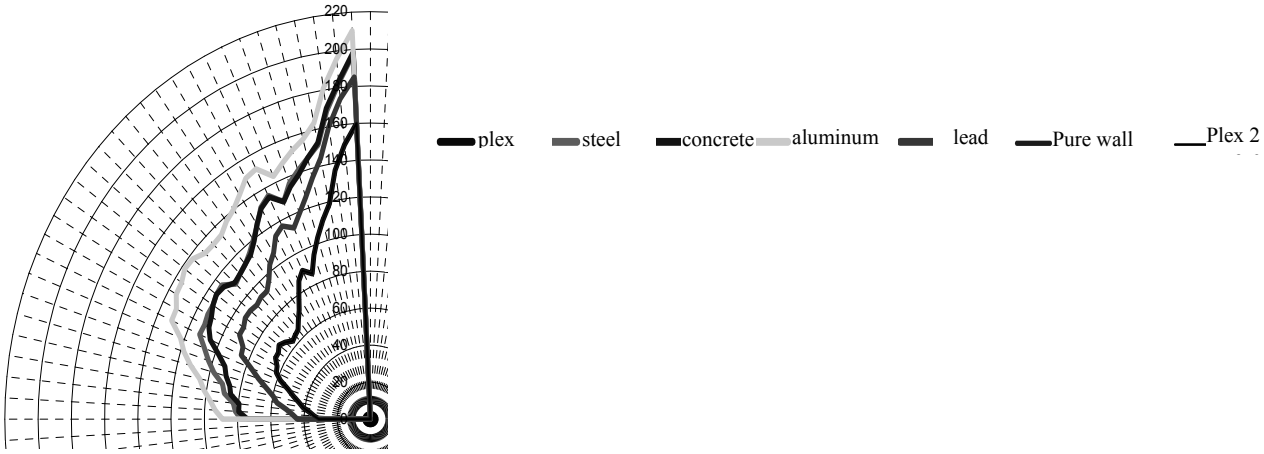

Fig. 5. Space-angular distribution of intensity of reflected and scattered inhibitory γ-radiation of wide energetic spectrum of the linear accelerator of 4 MeV from the constructive of various materials.

The obtained results enable to optimize the choice of structural materials for the construction of the elements of radiation protection of new technique. For example, these data show the unreasonableness of facing angles in labyrinths with steel angles or marble tiles. The reflections of γ-rays from them have almost identical patterns. Therefore in the projection of these units it is unreasonable to be guided solely with structural considerations. However, it is clear that it is also unreasonable to use aluminum in constructions which are inside radiation-loaded rooms. This leads to the formation of intense flows of reverse scattered irradiation. The material with high hydrogen content is promising for the elements of radiation protection – fro example, organic plastics (organic glass, PVC, PPL, etc.) or water. These materials provide minimum indexes of reverse scattering of γ-quanta and will be useful for facing reaction chambers and sharp corners of transport labyrinths. And lead, common protective material which has high index of multiplicity of weakening of γ-irradiation, simultaneously provides insignificant level of reverse scattering.

In general it was found out that in the construction of radiation protection it is possible to use various materials and thus to receive necessary parameters of elements and systems of biological radiation protection.

From the measurements we can state the following:

1. Increased indicators of typical industrial radiation monitoring devices on the adjacent to industrial electrophysical installations territories are the radiation problem (for example, as it happens in the case of installations with isotope generators of irradiation).
2. From the technical point of view – horizontal position of the accelerator is technologically more attractive, but is accompanied with more collateral irradiation and requires additional measures of its compensation.
3. Vertical position provides the reduction of the problem of collateral irradiation, though due to complications of the technology of the installation usage.

REFERENCES

1. *Bulatov B.P., Andryushin M.F.* Back-scattered gamma-rays in radiation technology. - M.: Atomizdat, 1971. - P. 239.
2. *Sanitary* rules of placement and operation of electron accelerators with energies up to 100 MeV. No. 1858-78, USSR MOH. - M., 1981. - P. 145.
3. *Sakhno V.I., Vyshnevskyy I.M., Khrin T.V. et al.* The research of the scattered radiation of electrons linear accelerator // Nuclear Physics and Atomic Energy. - 2007. - No. 2(20). - P. 126 - 130.
4. *Sakhno V.I., Vyshnevskyy I.M., Zelinskyy A.G. et al.* KINR radiaton plant with electrons accelerator // Atomic energy. - 2003. - Vol. 94, Issue 2. - P. 163 - 166.
5. *Sakhno V.I.* Problems of optimization of radiation protection of industrial radiation processing plants // XVI Int. Conf. on physics of radiation phenomena and radiation material (Alushta, Crimea, 6 - 11 Sept., 2004). - P. 286.
6. *Sakhno V.I., Shlapatskaya V.* The radiation-technological complex of accelerators "Radmila" IF NAS // Abstracts of the Reports. XV Int. Seminar on linear particle accelerators (Alushta, Crimea, 16 - 21 Sept., 1997). - P. 18.

THE IMPROVEMENT OF KINR NASU EXPERIMENTAL BASE AND METHODS OF NONDESTRUCTIVE CONTROL OF FUNCTIONAL CHARACTERISTICS OF NUCLEAR POWER STATIONS' EQUIPMENT AND MATERIALS

T. V. Kovalinska, I. A. Ostapenko, V. I. Sakhno, A. G. Zelinskyy

Institute for Nuclear Research, National Academy of Sciences of Ukraine, Kyiv, Ukraine

The ways of the improvement of technical base of the INR of NAS of Ukraine for functional researches, and new technologies of control over the state of the equipment on NPPs are discussed. The scientific work is completed in the department of radiation technologies within the national program of the enhancement of the reliability of nuclear energetic and the prolongation of exploitation terms of nuclear power installations.

Jobs on the formation of modern experimental base for radiation researches are being held in the INR of NAS of Ukraine for more than 20 years. During this period the unique radiation technique was created [1 - 3]. Complex researches of degradation processes in materials and equipment were completed on this technique. The substantial list of radiation and chemical, radiophysical and electrophysical processes in materials and structural elements of NPSs' equipment was determined, which are important in control over the degree of equipment's aging and, respectively, its reliability [4 - 5]. The obtained results helped find optimal ways of further development of radiation technique of the INR of NAS of Ukraine and to formulate technical requirements to the additional specialized equipment for further improvement of radiation research methods, primarily for the determination of resource capabilities of NPPs' materials and equipment [6 - 7].

It was found out that of all the variety of the equipment it is possible to identify certain groups according to the characteristics of radiation resistance.

Organic compositions are the most sensitive to radiation. Mainly, they are used in constructions of NPSs' electrical and technical equipment. Their checkouts are appropriate to be made already in the first stage of the realization of the program by means of complex control over functional suitability (qualification). In these checkouts it is necessary to set the reliability of equipment's functioning in stationary, transient and emergency modes, as well as the influence of unfavorable external factors. In the list of the last ones, it is important to study the processes on the surface of products and their influence on the reliability of functioning.

Such are different isolators, cables and electrotechnical equipment. Objectively this group makes the main part of all the equipment on the NPP. Recent results of the exploitation showed that there is the tendency to an increase of incidents on this equipment, and to an increase of their meaning in the exploitation of nuclear power installations [8]. According to exploitation data of Ukrainian NPPs, dysfunctions of electrical equipment already reached 60% of all incidents. That's why an important task is to prevent these dysfunctions and to reveal the possibilities of their occurrence in advance (what is much better). The researches of radiation-induced processes on the surface of electrotechnical equipment play the main role in this problem solving. Accordingly, the creation of radiation technical means for such researches is an actual engineering problem.

The INR is interested in the expansion of actual researches and in the enhancement of the effectiveness of the usage of existing experimental technique [9, 10]. Recently numerous developments of new technical means for fundamental and applied researches in the branch of radiation physics, radiobiology, and radiation technologies were made. Among them there are experimental researches of effects and processes in electrotechnical insulating materials under the influence of various components of radiation field. The researches were carried out for the determination of the coefficients in differential equations which describe the state of the equipment and its components under γ- and β-irradiation. It was found out that unlike the traditional idea of functional identity of the influence of different types of radiation on the organics [11], in fact, the formation of defects substantially depends on ionizing irradiation type [12].

a *b* *c* *d*

Fig. 1. Photos of destroyed samples of electrical equipment after the influence of ionizing irradiation.

Fig. 1, *a* shows the effect of the complete destruction of styrene insulation under γ-irradiation. The process of the formation of local internal defects in the organics under β-irradiation is shown in Fig. 1, *b*. The results of the destructive influence of radiation on PVC insulation of conductors are shown in Fig. 1, *c*. The destruction of rubber sealing elements under irradiation in mixed radiation field is clearly visible in Fig. 1, *d*. This indicates that all the components of radiation field are strong factors of intensive aging of the irradiated equipment and enhance known processes of

"normal" aging, which are traditionally considered during the exploitation of the equipment in ordinary objects. Having the information about the peculiarities of radiation-induced degradation processes, it is possible to formulate reliable models of aging of the equipment on nuclear power installations.

The results, obtained in new radiation researches, significantly expand knowledge of these processes. The researches confirmed that the dysfunction of products which contain organic materials, is a multi-component process, and is determined with the cumulative influence of various factors (radiation, temperature, etc.). It is shown, that the main component of radiation aging are secondary electrons which emerge as the result of the influence of ionizing irradiation.

Table 1 summarizes obtained experimental results. They show that for the formation of reliable expert conclusions about the state of the equipment it is necessary to control more extended list of parameters. In particular, it is clear that radiation factors (unlike ordinary power objects) play a decisive role in the whole complex of unfavorable factors on NPP. They significantly accelerate the degradation of functions of the equipment, and therefore their determination and consideration is a decisive argument of its qualification for the eligibility to work on the NPP.

Table 1.

Factors of influence	Results of the influence on exploitation indexes of the equipment
Ionizing irradiation (up to 10 MeV)	Radiation aging: deepens the occurrence of irreversible processes (suture, destruction, saturation changes); leads to radiolysis of the air and materials of polymers (cable coverings etc.), electrification of the surface of power cables, radiation heating etc.
Secondary irradiation (up to 0.5 MeV)	Electrification of cables' and equipments' surface: electrical characteristics of the equipment deteriorate;
Radiation heating	Increase of the temperature of materials: accelerates the degradation of properties of construction elements; the resource of the equipment decreases;
Electric and magnetic fields	The distribution of absorbed doses in materials is changed: electrical conductivity of dielectrics is increased; the course of radiation-chemical processes is changed;
High temperatures	Accelerate the oxidation reactions: the speed of corrosion increases;
High (low) pressure	The oxidation processes are accelerated: cable coverings rapidly degrade; mechanical loadings increase;
Chemically-active components of the environment	Accelerate the oxidation processes: lead to the destruction of the covering of cable products and electrical equipment under the influence of oxygen, ozone, nitric acid, etc.
Decontamination solutions	Contribute the destruction of materials: mechanical properties of the equipment are reduced; the aging of cable covering is accelerated;
Humidity	Stimulates active oxidation: nitric acid is formed on the surface of the equipment.

The necessity of the consideration of the destruction processes under secondary irradiation, which enhances the influence of direct ionizing irradiation on materials of the constructions and promotes the electrification of the surface of cables and the equipment, was also determined. The analysis of obtained information and special theoretical studies indicate that we should expect a significant contribution of low energy γ- and β-irradiation (less than 0.5 MeV) to the overall destructive processes.

It is problematic to separate the component of the degradation from the radiation of low energies of the previous cycle of studies in the INR of NASU on the radiation installation with electron accelerator on the average energy of 4 MeV. It is also impossible to use the data from other information sources, because the research of the degradation of functions of the equipment under the influence of ionizing irradiation of low energies has not been conducted till nowadays because of the lack of necessary technical base.

Fig. 2 shows a typical spectrum of bremsstrahlung [10], which is possible to be obtained on a typical electrophysical source of electrons. The experiments with different methods and technique of the conversion of electrons on brake targets showed that it is impossible to obtain continuous spectrum of irradiation in the range 0.1 - 5 MeV which is necessary for rapid radiation checkouts. Therefore, the installation technically meets basic requirements of functional checkouts of the equipment of NPPs only in high-energetic sphere of energetic spectrum of ionizing irradiation which is typical for nuclear objects – except for the low-energy sphere (accented in Fig. 2). The most perspective way of solving this problem is the creation of additional means and further modernization of technical base of radiation experiments in the INR.

With this purpose the ways of the development of the structure of the existing experimental installation of the INR NASU were worked out, on the basis of the accelerator with energy of 4 MeV with its technical equipment. One more electrophysical source was included into its structure (electron accelerator up to 0.5 MeV and of beam power no less than 20 kW), which covers all necessary spectrum of ionizing irradiation. In such configuration, radiation complex of the INR will certainly meet the main requirements of rapid checkouts – the reproduction of the conditions of the

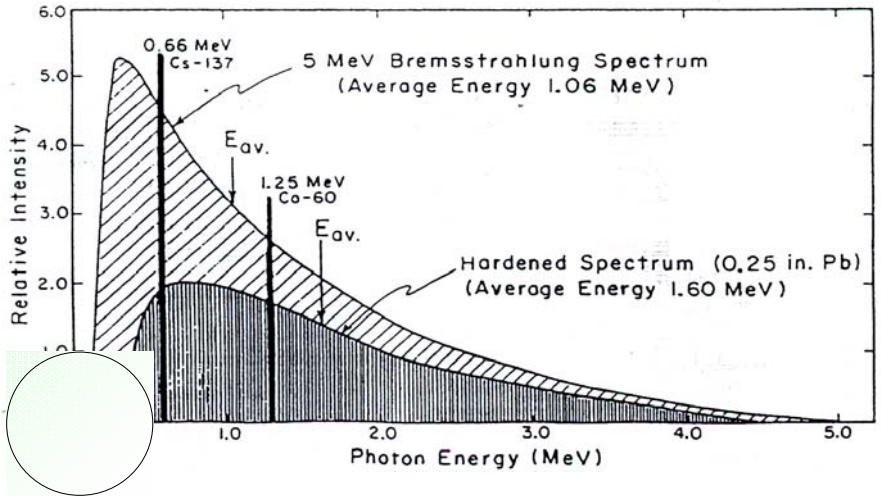

Fig. 2. Typical spectrum of bremsstrahlung of electrons' accelerator of 4 - 5 MeV.

exploitation of NPP's equipment. Accordingly, this will provide opportunities to research radiation-stimulated degradation processes of NPP's equipment in the low energetic range of irradiation and to compensate the lack of information about its behavior on real nuclear energetic objects. To implement this way of modernization, it is necessary to choose an optimal source of irradiation of this energetic sphere, to input it technically into the existing experimental radiation complex (installation) and to create a stand for functional checkouts on its basis.

Researches of the market of such technical means showed that real industry produces a wide range of accelerators on low energies. The results are shown in Tables 2 and 3.

Table 2.

Accelerator or generator type	Energy, MeV	Average power in the beam, kW
Electron-4	0.5	10
Aurora-2	0.5	25
Cascade generator CGE-2.5	2.5	2.5
Three-phase electronic accelerator TPEA-3	0.4	75

Table 3.

Model	Accelerating voltage, kV	Beam current, mA	Length of the outlet, cm	Beam power before the outlet, kW
1. Electrocurtain plants (with extended hot cathod and ribbon beam of electrons)				
CB175/30/5	175	45	30	7.9
CB175/50/5	175	75	50	13
CB225/50/15	225	300	50	67
CB225/100/10	225	400	100	90
CB275/50/5	275	125	50	34
CB275/100/5	275	250	100	69
Pilot 200	200		45	
2. Electrocure plants (with acceleration tube and scanned beam)				
SB300/30/20	300	25	30	7.5
SB300/50/30	300	37.5	50	11
SB300/65/40	300	50	65	15
SB300/80/50	300	62.5	80	19
SB300/95/60	300	75	95	22.5
SB300/110/70	300	87.5	110	26
SB300/125/ 80	300	100	125	30
SB300/140/90	300	112.5	140	34
SB300/155/100	300	125	155	37.5
3. Electropulse plants				
Electropulse-208	200	2.5	15	0.5
Dynametrons (RD, USA)				
Dynametron	400	100	183	40
Dynametron	550	50	91.5	27.5

Table 2 shows the accelerators of Russian producers, and Table 3 – of American companies. Almost all of them provide necessary radiation and technical characteristics as sources of irradiation and are suitable for the modernization of the experimental base of the INR NASU.

Electron accelerators of this range of energies differ with a variety of the construction and the range of the power of beams, and thus promote a selection of the optimal type of the installation for our usage.

Price indexes for such technique are stabilized in the world now [13, 14]. Depending on the configuration of technical means, which are used in the construction of such accelerators, their cost varies from $10 - 20 per 1 kW of the beam. Calculations show that taking into account available technological rooms and engineering communications, the suggested resupply of the experimental complex of the INR with electrophysical source of 0.5 MeV will cost only $200000 - 400000 and won't require additional expenses for radiation protection (Fig. 3).

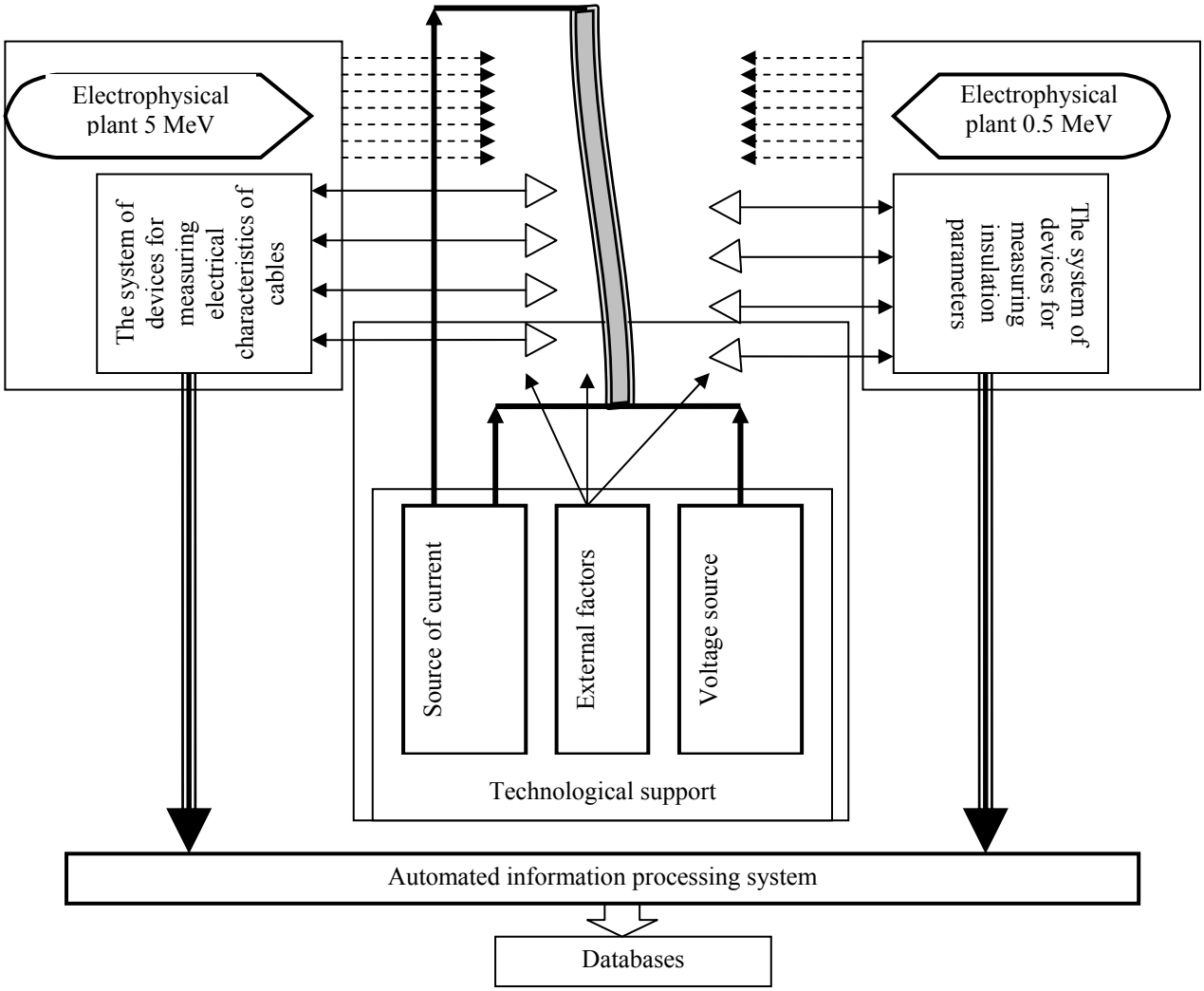

Fig. 3. KINR radiation research complex.

The results of researches and workouts, presented above, lead us to the following conclusions.

1. It is important to ensure maximum reproduction of the equipment operating conditions, especially concerning radiation factors, in order to obtain necessary metrological parameters during the qualification of the equipment of NPPs.

2. In the list of the equipment of NPPs a big group of the equipment is separated for which the most important negative factors of accelerated aging is gamma- and β-irradiation. This equipment is currently the most numerous in the list of the equipment of NPPs. There is permanent tendency of the increase of their contents. Producers of the equipment switch to production technologies with the usage of composite materials with high content of organic materials. Therefore, the emphasis in the organization of the qualification in the early stages should be done on the creation of stands for such equipment.

3. The simplest way of achieving this goal – the organization of functional researches of critical equipment of NPPs – is the creation of a radiation stand on the basis of two electron accelerators on different energies, which provide the possibility to obtain a continuous spectrum of irradiation in the range of energies, typical for industrial nuclear energetic installations.

4. The analysis of the existing and available electrophysical sources reveals technical possibility of completing such a stand with various necessary sources of electrons in the range from 0.1 to 10 MeV, which is not only scientifically substantiated, but also meets the requirements of the general and radiation safety for their implementation.

REFERENCES

1. *Sakhno V.I., Vyshnevskyy I.M., Tomchay S.P.* Radiation-technological installation with linear electron accelerator SC "INR" NAS of Ukraine // Materials of the Annual Scientific Conference of the INR (Kyiv, January 27 - 30, 1998). - P. 111.
2. *Sakhno V.I., Khrin T.V., Vyshnevskyy I.M. et al.* The installation for radiation checkouts of the equipment of NPPs // Int. Conf. "Current Problem in Nuclei Physics and Atomic Energy" (Kyiv, May 29 - June 3, 2006): Book of abstracts. - Kyiv, 2006. - P. 188.
3. *Sakhno V.I., Khrin T.V., Vyshnevskyy I.M. et al.* Problems of the creation of the technical basis for the qualification of cable products of NPPs // The 1st Int. Conf. "The prolongation of exploitation terms of energetic units of NPPs. The estimation of technical conditions and management of aging of the equipment and cable products // CD-ROM Windows 98/2000 NT/XP. - Kyiv, 2007.
4. *Sakhno V.I., Khrin T.V., Vyshnevskyy I.M. et al.* Problems of radiation checkouts of cables of NPP's on the installation of the INR // Questions of atomic science and technique. Ser.: Radiation damages physics and radiation materials science (91). - 2007. - No. 6. - P. 128 - 130.
5. *Sakhno V.I., Sakhno O.V., Tomchay S.P.* The research of radiation-induced factors of the degradation of NPP's equipment // Scientific paper of Institute for Nucl. Res. - 2001. - No. 1(3). - P. 102 - 105.
6. *Sakhno V.I., Vyshnevskyy I.M., Tomchay S.P. et al.* The problems of radiation methods usage of testing the NPP's equipment // The 2nd Int. Conf. "Current Problems in Nuclear Physics and Atomic Energy" (Kyiv, June 9 - 15, 2008): Book of abstracts. - Kyiv, 2008.
7. *Sakhno V.I., Khrin T.V., Vyshnevskyy I.M. et al.* Specialized stand for functional checkouts of cable products of NPPs// Nuclear Physics and Energy. - 2007. - No. 1(19). - P. 140 - 144.
8. *Sakhno O.V.* Research and development of methods and technical means of radiation checkouts of the equipment of NPPs on electrophysical installations: Dissertation synopsis. - Kyiv, 2008.
9. *Sakhno V.I., Khrin T.V., Vyshnevskyy I.M. et al.* Radiation installation with electron accelerator of the INR NASU // Atomic energy. - 2003. - Vol. 94, Issue 2. - P. 163 - 166.
10. *Sakhno V.I.* The creation of electrophysical radiation installations and the research of changes in the properties of the materials in industrial radiation technologies: Dissertation synopsis. - Kyiv, 2009. - 36 p.
11. *Ivanov V.S.* Radiation chemistry of polymers // Manual. - Lviv, 1988. - 320 p.
12. *Kovalinska T.V.* The research of radiation changes of materials and products for NPP's: Dissertation synopsis. - Kyiv, 2011.
13. *Svinin M.P.* Calculation and projection of high-voltage accelerators for radiation technology. - M.: Energoatomizdat, 1989. - 143 p.
14. *Radiation* processing: environmental applications. -Vienna: IAEA. - 2007. - P. 25.

THE DESCRIPTION OF THE Hg ISOTOPES YIELD WITHIN THE TWO STEP REACTION MODEL

V. L. Litnevsky[1], F. A. Ivanyuk[2], G. I. Kosenko[3], V. V. Pashkevich[1]

[1] Bogoliubov Laboratory for Theoretical Physics, Joint Institute for Nuclear Research, Dubna, Moscow region, Russia
[2] Institute for Nuclear Research, National Academy of Sciences of Ukraine, Kyiv, Ukraine
[3] Omsk State University, Omsk, Russia

In the fusion-fission reactions the same compound system can be formed by the different combination of the target and projectile ions. The investigation of the yield of such reactions can give the information about the mechanism of the fusion-fission process. In the present work we have calculated the energy and the mass-energy fission fragment distribution, fusion cross section, evaporation residue formation cross section and the multiplicity of light particles evaporation in the reactions ^{48}Ca + ^{142}Nd and ^{40}Ar + ^{144}Sm in which the compound nucleus Hg is formed. The calculated results are compared with the available experimental data

1. Introduction

The analysis of the potential energy surface of heavy nuclei (A>200) calculated with account of the shell structure [1] shows the presence of the two fission valleys, the one corresponds to the symmetric fission and another to the asymmetric fission fragments. By decreasing the mass number only symmetric valley survive. In [2] it was mentioned that the yield of the asymmetric mode is not observed already by the fission of ^{201}Tl and ^{198}Hg. Nevertheless the old [2] and the recent [3] investigations of the fission of nuclei with A < 200 show the two humped structure of the fission fragments mass distribution. The mass asymmetry of the distribution is rather small, $A_H / A_L \simeq 1.1$ for ^{198}Hg and $A_H / A_L \simeq 1.25$ for ^{180}Hg. This effect is caused by the shell effects at the bottom of the fission valley. The theoretical description of this effect allows to check how accurate are the models used for the fission process.

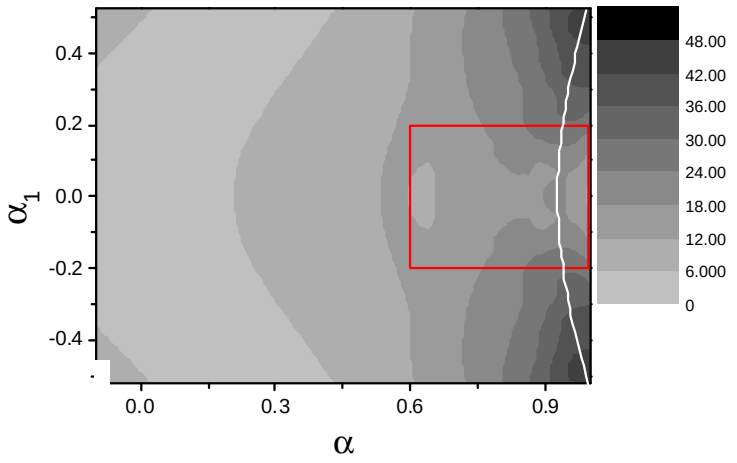

Fig. 1. The map of the liquid drop potential energy ^{188}Hg. The white line is ridge line. The ground state corresponds to α = 0 and α_1 = 0. The scission (zero neck radius) happens at α = 1, for any α_1.

In the work of Alma-Ata group [2] the reactions with alpha-particles ^{194}Pt(α, f) and protons ^{197}Au(p, f) were studied. In the present work we study the reactions with heavy incoming ions $^{48}Ca + ^{142}Nd \Rightarrow {}^{190}Hg$ and $^{40}Ar + ^{144}Sm \Rightarrow {}^{184}Hg$ and will try to clarify whether the asymmetry effect in the mass distribution will be present by the fission of Mercury isotopes. For the relatively light compound nuclei, like Hg isotopes, the saddle-to-scission path is very short. The mass distribution of the fission fragments is formed practically at the ridge between the ground state and the "fission valley". The words fission valley are in inverted commas because in this case the valley is almost absent, instead of valley there is a sharp fall off of the potential energy (Fig. 1). For the actinide nuclei, on the contrary, there is a long descent along the fission valley from the saddle till the scission point. In the reaction with very light projectiles only small angular moments of relative motion contribute to the reaction cross section, thus, the influence of the rotation on deformation energy surface can be neglected.

2. The dynamical model for the approaching stage

In the approaching phase of the projectile and target the distance between their centers of mass is denoted by r. The shape of the surface of both nuclei is described in terms of Cassini ovaloids, which are defined in parametric way as [1]:

$$\rho_s(x) = \frac{1}{\sqrt{2}}\left[(R_0^4 + 2sR_0^2(2x^2-1) + s^2)^{1/2} - R_0^2(2x^2-1) - s\right]^{1/2},$$
$$z(x) = \frac{sign(x)}{\sqrt{2}}\left[(R_0^4 + 2sR_0^2(2x^2-1) + s^2)^{1/2} + R_0^2(2x^2-1) + s\right]^{1/2}. \quad (1)$$

Here ρ_S and z are the cylindrical coordinates of the point on the nuclear surface and x is a parameter given on the interval [-1, 1]. The R_0 is the radius of spherical nuclei with the same volume. The parameters $\alpha \equiv s / R_0^2$ fixes the

deformation of the target (α_t) or projectile (α_p). These are the two additional collective variables which specify the shape of the system. In calculations we assumed that the target and projectile are oriented arbitrary.

The dynamics of the collision is described by the Langevin equations for r, α_t, α_p variables:

$$\frac{dr}{dt} = p/m, \quad \frac{dp}{dt} = -\left[\frac{\partial F(r,\vec{\alpha})}{\partial r} + K_r^r \frac{p}{m} + \sum_j K_r^j \frac{\pi_j}{D_j}\right] + \xi_r(t),$$
$$\frac{d\alpha_i}{dt} = \frac{\pi_i}{D_i}, \quad \frac{d\pi_i}{dt} = -\left[\frac{\partial F(r,\vec{\alpha})}{\partial \alpha_i} + K_i^r \frac{p}{m} + \sum_j K_i^j \frac{\pi_j}{D_j}\right] + \xi_i(t). \tag{2}$$

In (2) i attains the value t (target) or p (projectile), $\vec{\alpha} = \{\alpha_p, \alpha_t\}$. The $\xi_r(t)$ and $\xi_i(t)$ are the normal distributed random forces.The m is the reduced mass, F is the Helmholz free energy of the target and projectile, $F = V_{pot} - aT^2$, a being the level density parameter. The potential energy V_{pot} includes the energies of Coulomb V_C and nuclear V_{GK} interaction [4], the rotational energy V_{rot} and the deformation energy of the target and projectile

$$V_{pot} = V_{Coul} + V_{GK} + V_{rot} + E_{def}, \quad E_{def} = E_{LDM} + E_{shell}. \tag{3}$$

The deformation energy was calculated within macroscopic-microscopic approach [5, 6] as the sum of the liquid drop deformation energy plus the shell correction The dependence of the shell correction on the excitation energy (temperature) was parameterized in the form $E_{shell} = E_{shell}(T=0)e^{-\gamma T^2 a}$. The parameters γ and a were taken the same as in [7, 8]. The friction and mass parameter for the $r-$ motion were defined in the same way as in [9],

$$K_i^r = \frac{1}{2} K_r^r \frac{R_{i0}}{\sqrt{\alpha_i + 1}}, \; K_j^i = \frac{1}{4} K_r^r \frac{R_{i0} R_{j0}}{\sqrt{(\alpha_i + 1)(\alpha_j + 1)}} + \delta_{ij} K_i.$$

The mass parameters D_i and the friction coefficients K_i related to the variation of the shape of the target and projectile were calculated within the linear response theory and locally harmonic approximation [10, 11].

The equations (2) were integrated numerically starting from the initial value $r = r_{in}$ until the ions would touch at the touching point R_{touch} or, after reaching some minimal value (larger than R_{touch}), r would start to increase and reach r_{in} again. As it was shown earlier, due to the random force some ions cannot reach the touching point even if they overcame the fusion barrier (the maximum of the potential energy (3)). The value of R_{touch} is defined by the relation $R_{touch} = R_1 + R_2 + (a_{d,tar} + a_{d,pro})/2$, where R_1 and R_2 are the radii of the target and projectile and $a_{d,tar}$, $a_{d,pro}$ are the diffuseness of their density distribution. We have checked that the increase of r_{in} does not change the results of calculations but increases substantially the computation time. Besides r_{in} at the initial moment the kinetic energy of incoming ions and the angular moment L are fixed.

Due to the action of random forces, we get not the strictly defined quantities at the touching point but the distributions. The calculations have to be repeated many times until the results become stable with respect to the number of trajectories. By trajectory we mean here the dependence of r on time for a given initial conditions.

On each integration step we calculate the dissipated energy by the kinetic energy loss,

$$E_{dis} = E_{CM} - \frac{p_r^2}{2m} - \sum_i \frac{\pi_i^2}{2D_i} - V. \tag{4}$$

The dissipated energy defines the temperature (excitation energy) of the system at the touching point.

The touching probability $T(L)$ is calculated as the ratio of the number of trajectories, that reached the touching point N_{touch}, to the total number N_L of considered trajectories, $T(L) = N_{touch}/N_L$. Besides the touching probability by solving equations (2) we find the potential energy of the system, the excitation energy and the deformation of the target and projectile at the touching point. These data are used as the initial conditions for the description of evolution of the compact system.

3. The results of numerical calculations

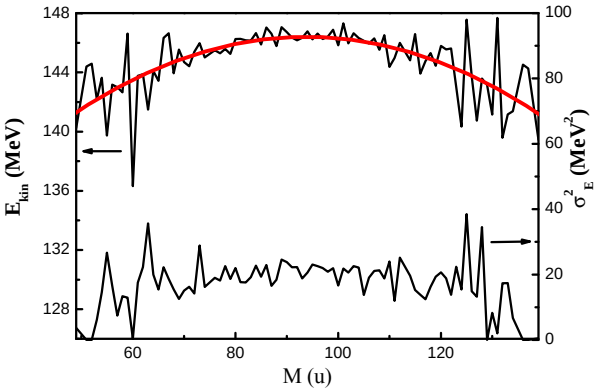

Fig. 2. The kinetic energy distribution of the fission fragments in the reaction ^{40}Ar + ^{144}Sm (*left scale*) and the width of distribution (*right scale*). The excitation energy at the saddle point is equal to 27 MeV.

One of the main characteristics of the fission fragments which specify the type of reaction is the distribution of the fission fragments in kinetic energy. In Fig. 2 we show the calculated kinetic energy distribution of the fission fragment and its width for the reaction $^{40}Ar + ^{144}Sm \Rightarrow ^{184}Hg$. There is nothing unusual about this Figure. The distribution in the kinetic energy is well approximated by the parabola. The large fluctuations at the end of interval are due to the pure statistics. The increase of the mean value of the kinetic energy compared with the data from [2] is probably due to the fact that we consider here lighter isotope of Hg. Besides, in the case considered here the compound nucleus has rather large excitation energy what can lead to the increase of the pre-scission kinetic energy.

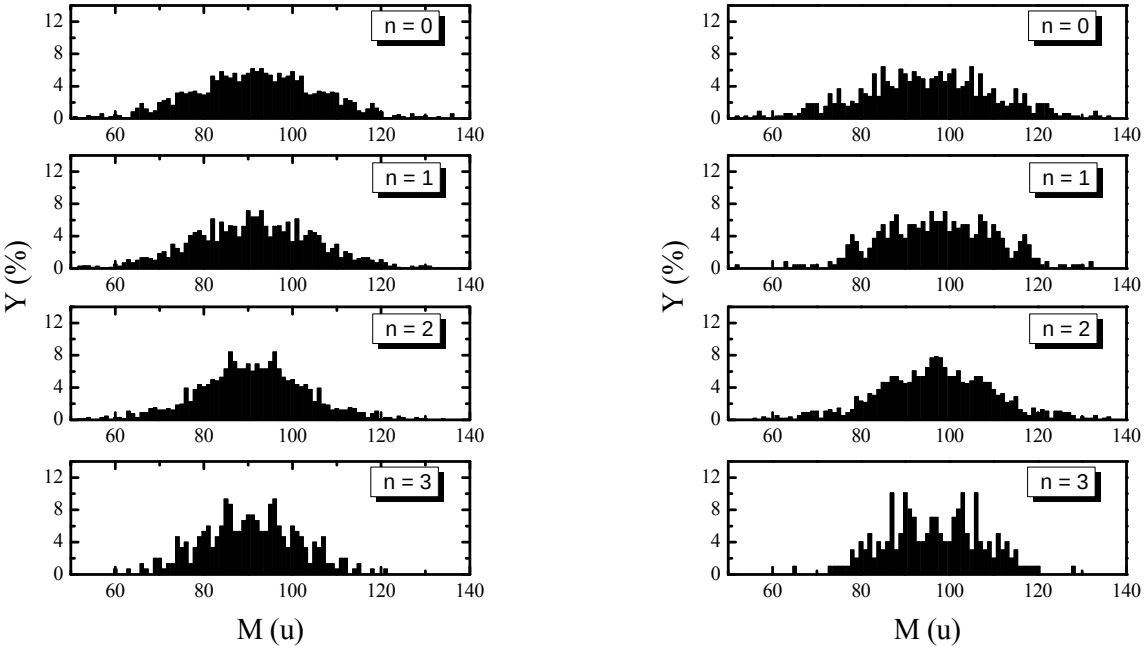

Fig. 3. *Left*: The mass distribution of the fission fragments in the reaction ^{40}Ar + ^{144}Sm. The energy of ions is equal to 27 MeV. *Right*: The same for the reaction ^{48}Ca + ^{142}Nd at the same energy of incoming ions.

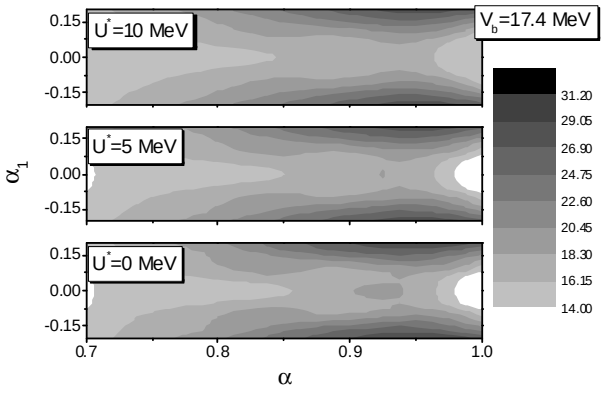

Fig. 4. The deformation energy surface of ^{188}Hg for few values of the excitation energy. The fission barrier height is equal to 17.4 MeV.

In Fig. 3 we show the mass-distributions of the fission fragments at fixed multiplicity of emitted neutrons. By the evaporation of no or one neutron the influence of shell effects is not so large and the potential energy can be well approximated by its liquid-drop part. In this case the mass distribution of the fission fragments is symmetric and rather flat. This corresponds to the presence of only one fission valley. By the evaporation of larger number of neutrons the excitation energy of the composite system is substantially reduced and the role of shell effects is getting larger. In Fig. 4 we show the deformation energy of ^{188}Hg which is formed after the evaporation of two neutrons from ^{190}Hg. Due to the shell effects on the potential energy surface the two minima appear placed symmetrically with respect to $\alpha_1 = 0$. The deformation region

displayed in Fig. 4 corresponds to the area in the square in Fig.1.

The shell structure leads to the asymmetric peaks in the mass distribution. This is seen quite well for the case of three neutrons evaporation; see Fig. 3, when the compound system looses almost all its excitation energy.

Thus, like in the case of reactions with light incoming particles [2], in reactions with heavy ions the mass distribution of the fission fragments contains the mass-asymmetric peaks despite the fact that the deformation energy at the saddle is mass-symmetric. Note, however, that the mass distribution is mass-asymmetric only when the number of emitted neutrons is large.

4. Conclusions

- The two step model for fusion-fission reactions, proposed earlier by the authors, is used for the description of the fission fragments distribution of two Mercury isotopes formed in the reactions $^{48}Ca + ^{142}Nd \Rightarrow ^{190}Hg$ and $^{40}Ar + ^{144}Sm \Rightarrow ^{184}Hg$.
- We have shown that symmetric deformation at the saddle point results in the mass-asymmetric distribution of fission fragment at low excitation energy due to the shell effects in the fission valley.

ACKNOWLEDGEMENTS

One of the authors (G.K.) is grateful to the organizers of the conference for the invitation and warm hospitality during his stay at Kyiv.

REFERENCES

1. *Pashkevich V. V.* On the asymmetric deformation of fissioning nuclei // Nucl. Phys. - 1971. - Vol. A169. - P. 275 - 293.
2. *Itkis M.G. et al.* Mass Asymmetry Of The Symmetric Mode In Fission Of Nuclei With A≈200 (in Russian) // Sov. J. Nucl. Phys. - 1990. - Vol. 52 - P. 944 - 959.
3. *Andreyev A.N. et al*. New Type of Asymmetric Fission in Proton-Rich Nuclei// Phys. Rev. Lett. - 2010. - Vol. 105. - P. 252502/1 - 5.
4. *Gross D.H.E., Kalinowski H.* Friction Model of Heavy Ion Collision // Phys. Rep. - 1978. - Vol. 45. - P. 175 - 210.
5. *Strutinsky V.M.* Shell effects in nuclear masses and deformation energies // Nucl. Phys. - 1967. - Vol. A95. - P. 420 - 442.
6. *Brack M. et al.* Funny Hills: The Shell-Correction Approach to Nuclear Shell Effects and Its Aplications to the Fission Process // Rev. Mod. Phys. - 1972. - Vol. 44. - P. 320 - 405.
7. *Ignatyuk A.V., Smirenkin G.N., Tishin A.S.* The phenomenological description of the energy dependence of the level density parameter (in Russian) // Sov. J. Nucl. Phys. - 1975. - Vol. 21. - P. 485 - 490.
8. *Iljinov A.S. et al.* Phenomenological statistical analysis of level densities, decay widths and life time of excited nuclei. // Nucl. Phys. - 1992. - Vol. A543. - P. 517 - 557.
9. *Fröbrich P.* Fusion and Capture of Heavy Ions above the Barrier: Analysis of Experimental Data with the Surface Friction Model // Phys. Rep. - 1984. - Vol. 116. - P. 337 - 400.
10. *Hofmann H.* A Quantal Transport Theory for Nuclear Collective Motion: The Merits of a Locally Harmonic Approximation // Phys. Rep. - 1997. - Vol. 284. - P. 137 - 380.
11. *Ivanyuk F.A., Hofmann H.* Pairing and shell effects in the transport coefficients of collective motion // Nucl. Phys. - 1999. - Vol. A657. - P. 19 - 58.

TRANSURANIUM ELEMENTS PRODUCTION IN PULSE NEUTRON FLUXES

Yu. S. Lutostansky[1], V. I. Lyashuk[1,2]

[1] *Russian Research Center "Kurchatov Institute", Moscow, Russia*
[2] *Institute of Nuclear Research, Russian Academy of Sciences, Moscow, Russia*

A model of the transuranium isotopes production under conditions of pulse nucleosynthesis in a neutron flux with densities of up to ~10^{25} neutron/cm^2 is considered. The pulse process allows us to divide it in time into two stages: the process of multiple neutron captures ($t < 10^{-6}$ s) and the subsequent β-decay of neutron-rich nuclei. The modeling of the transuranium yields takes into account the adiabatic character of the process, the probability of delayed fission, and the emission of delayed neutrons. A target with a binary composition of ^{238}U and ^{239}Pu, ^{248}Cm, and ^{251}Cf isotopes is used to predict the yields of heavy and superheavy isotopes.

1. Introduction

Transuranium elements production in nature takes place in powerful neutron flux, owing to reactions of multiple neutron capturing (radiation capturing) followed by β-decays. This process of rapid nucleosynthesis (the *r*-process) is realized, e.g., in the explosions of supernova stars, where neutron density exceeds 10^{20} neutron/cm^3 at temperatures of ~10^9 K [1]. Pulsed nature of the process of nucleosynthesis flowing supernovae explosions and lasting a few seconds assumes time-dependent external conditions – neutron flux and temperature. Model that describes the dynamic process of nucleosynthesis was developed earlier [2, 3].

Under artificial conditions, the *r*-process is realized in nuclear explosions, which produce neutron fluences above 10^{24} neutron/cm^2 in a time of ~10^{-6} s. Transuranium isotopes (up to ^{255}Fm) were found for the first time in the "Mike" thermonuclear explosion in 1952 [4]. At that time, studies were performed in the United States to examine the possibility of synthesizing transuranium elements under the conditions of nuclear explosion (the "Plowshare" program). The most complete data on transuranium yields up to $A = 257$ were obtained in the "Par" experiment [5]. In order to increase yields of transuranium isotopes and to search for isotopes with mass numbers $A > 257$, experiments were conducted that produced high fluences of neutrons. In the "Hutch" tests, a maximum fluence of $2.4 \cdot 10^{25}$ neutrons/cm^2 was achieved [6], but no isotopes with $A > 257$ were found. Nuclides created during pulse nucleosynthesis are very neutron-rich and fast decaying. Analysis of the nuclides composition, however, is completed about 2 days after nucleosynthesis; in this time, nuclei with high numbers of neutrons are decayed [6, 7].

In modeling the *r*-process under astrophysical conditions [1, 8], we must consider the (n, γ)-reaction of radiation capture and the inverse (γ, n)-process; induced and spontaneous nuclear fissions; the β-decay of neutron-rich nuclei accompanied by processes of delayed neutron emission (β, n) and delayed fission (β, *f*) [9]; and so on. To perform calculations, we must establish neutron and neutrino fluxes, temperature conditions, and the parameters of more than 3000 nuclei. In the experimental pulse process, the model description of the synthesis of heavy elements allows important simplifications: processes of radiation neutron capture and β-decay are strongly separated in time [(t(n, γ) ≈ ≈ 10^{-6} s)<< t_β], which can significantly limit the range of nuclei involved in the *r*-process.

2. Binary adiabatic model

In modeling the *r*-process under artificial conditions [10, 11], i.e., nuclear (thermonuclear) explosions significant simplification were made because the processes of neutron capture and beta-decay are separated in time. This model of heavy nuclides creation under the condition of pulse nucleosynthesis in intensive neutron flux [11] is used for calculation of transuranium elements production. As starting isotopes in the first stage the binary composition of ^{238}U and ^{239}Pu was used along with the mixture of another uranium and (or) plutonium isotopes or other composition of initial nuclei on the next stages of calculations. Transuranium yields were obtained additively from independent solutions of nucleosynthesis equations. Half-life periods, probability of emission for one and two delayed neutrons (DN), probability of delayed fission (DF) for neutron-rich isotopes were calculated taking into account the β-strength function, which obtained from the finite-Fermi system theory [12].

The production of transuranium elements under the conditions of nuclear (thermonuclear) explosions can be described by the system of equations for concentrations N_z^n:

$$\begin{aligned}
\partial N_z^n \big/ \partial t &= (\lambda_\beta N)_{z-1}^{n+1} + (\lambda_\alpha N)_{z+2}^{n+2} + \\
&+ \int_0^\infty F(E,t)\left\{\left[\sigma_{n,\gamma} N\right]_z^{n-1} + \left[\sigma_{n,2n} N\right]_z^{n+1} + \left[\sigma_{n,3n} N\right]_z^{n+2}\right\} dE - \\
&- (\lambda_\beta N)_z^n - (\lambda_\alpha N)_z^n - (\lambda_f N)_z^n - \\
&- \int_0^\infty F(E,t)\left\{\left[\sigma_{n,\gamma} N\right]_z^n + \left[\sigma_{n,2n} N\right]_z^n + \left[\sigma_{n,3n} N\right]_z^n + \left[\sigma_{n,f} N\right]_z^n\right\} dE,
\end{aligned} \tag{1}$$

where z and n are the charge and the number of neutrons of the nucleus; λ_β, λ_α, and λ_f are the rates of β- and α-decays and spontaneous fission; $\sigma_{n,\gamma}$, $\sigma_{n,\,2n}$, $\sigma_{n,\,3n}$, and $\sigma_{n,\,f}$ are the respective cross-sections of the reactions; and $F(E, t)$ is the neutron flux.

We shall further simplify the model taking into account the features of the process over time and the contribution from reactions. The chain reaction proceeds for ~10^{-7} s [13], and the duration of multiple radiation captures of neutrons does not exceed 10^{-6} s [14]. The contribution from β- and α-decays and spontaneous fission are negligibly small, since the respective rates λ_β, λ_α, and λ_f are much smaller than the rate of n-capture $\lambda_{n,\gamma}$. We can ignore the contribution from reactions (n, f); (n, 2n), which have a higher energy threshold with respect to the (n, γ) reaction. In the simplified scheme (a static model) a neutron flux with a given energy in the range 20 - 30 keV is presumed.

The scheme for transuranium isotope creation in intense (explosive) neutron fluxes (the r- process) is shown in Fig. 1, as compared to the slower (s process) trunsuranium creation that occurs, e.g., in nuclear reactors.

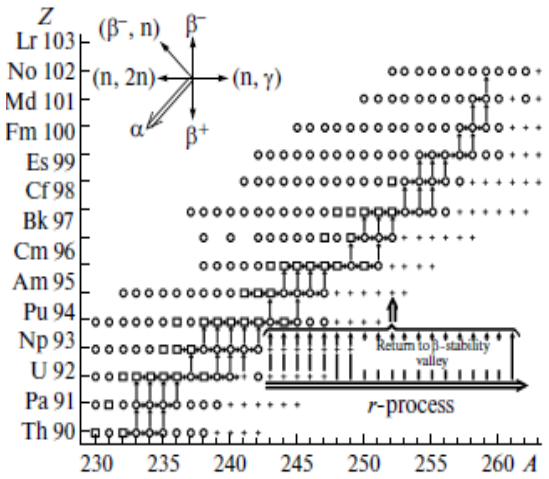

Fig. 1. Scheme of actinide creation in artificial slow (s-process) and rapid (r-process) nucleosynthesis: □ – nuclei with $T_{1/2} \geq 1$ year; – nuclei with $T_{1/2} < 1$ year; + – predicted neutron_rich nuclei from the NDS JAEA data base (Japan); the line denotes the path of the s process at a flux density of neutrons ~ (10^{14} - 10^{16}) neutron/(cm^2 s).

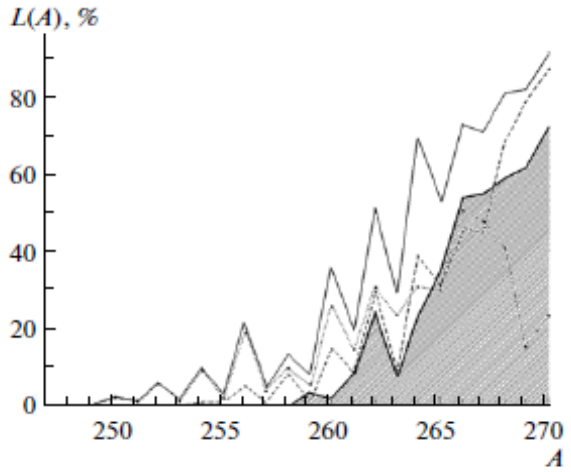

Fig. 2. Losing factor $L(A)$ (%) in isobaric chains for initial isotopes of U and Pu. For uranium, the dotted line is the contribution from delayed fission; the dashed line is the contribution from delayed neutron emission; and the solid line is the summed effect. For plutonium, the bold line (shaded portion) is the summed effect.

Further development involves introducing dynamic elements to this static model, which accounts for the change in radiation capture cross-sections over the time (~10^{-6} s) of multiple neutron capture conduction. After the completion of chain fission (~10^{-7} s), matter scatters quickly [13]; in the range of the r-process we are interested in (~10^{-6} s), the increase in the volume of highly heated plasma leads to fast cooling of the substance involved in the motion. The falling temperature of the target material determines the cross section of neutron capture $\sigma_{n,\gamma}$ relative to current time. The dependence of temperature on time for the time interval [t_A–t_B] is determined by the range (T_1–T_2) of decrease in temperature, and it is assumed that the radial expansion velocity of a heated substance is constant in the interval [t_A–t_B], and the dependence of temperature on volume is adiabatic [10, 15, 16]: $T = (\text{const}/V)^{\gamma-1}$.

In our calculations, it was assumed that the initial volume conformed to a sphere with radius $R_0 = 5$ cm [17] and the adiabatic index γ ranged from 1.5 to 2.0 [18]; a reduction in ($T_1 - T_2$) temperature [16] was fixed in the range from 60 to 1 keV.

3. Losing factor

Following pulse nucleosynthesis, neutron-rich isotopes undergo β-decay, upon which two processes leading to a change in concentration are possible: (β, n)-delayed emission of neutrons, and (β, f)-delayed fission. These processes lose isotopes in isobaric chains with the constant mass number A and, as a result, the distribution of the isotope yield according to the mass number A changes considerably to the end of the r-process. The losing effect summarized by the isobar chain gives a relative reduction in concentrations for a given A and is expressed as the $L(A)$ coefficient (the losing factor, where $L(A) \leq 1$) and the concentration of isotopes with given A, calculated at the moment of the end of multiple captures, must be multiplied by the factor $R(A) = 1 - L(A)$.

Fig. 2 shows the resulting coefficients of the drop in concentrations $L(A)$ and contributions from the (β, n) and (β, f) processes to $L(A)$ coefficients. In calculations with the initial isotope ^{238}U, the losing factor $L_U(A)$ increases at A = 252, 254, 256, 258 (i.e., at even A isotopes. In this case, the main contribution comes from the (β, f) processes on even A neptunium isotopes, which explains the observed abnormality in the yields distribution.

Spontaneous fission was not considered in our calculations of $L(A)$, but it is significant for mass number $A \geq 256$ of isotopes ^{256}Cf, ^{258}Fm, and heavier nuclei [19]. For the initial isotope ^{239}Pu, the $L_{Pu}(A)$ factor is substantial for $A > 260$ and is systematically smaller than the $L_U(A)$ factor, since uranium and neptunium isotopes are excluded from the calculations. Data on the binding energy of neutrons and

fission barriers from [20, 21] were used in our calculations of the $L(A)$ coefficients.

In the case of a plutonium target, the losing factor is very small for neutron-rich isotopes with $A < 260$. The $L_U(A)$ and $L_{Pu}(A)$ factors for the initial irradiated uranium and plutonium isotopes differ strongly, and in Fig. 2 this is explained by the different amounts of nuclides participating in the formation of the losing factor.

4. Even-odd anomaly

The calculations for the yields of transuranium isotopes are shown in Fig. 3, relative to the experimental yields measured in the "Par" test, where all yields up to $A = 257$ were obtained for the first time [5]. The results were normalized using nuclide yield with $A = 245$, as in [5]. The calculated data up to $A = 270$ were obtained in an integral neutron flux of ~ $6 \cdot 10^{24}$ neutron/cm^2 for a uranium-plutonium target with the initial concentration ^{238}U(95%) + ^{239}Pu(5%). In the experimental yields with $A > 250$, the effect of even–odd inversion was observed as a break at $A \approx 250$ in the characteristic saw-toothed yields, and as inversion of the yields at $A > 250$ (see Fig. 3).

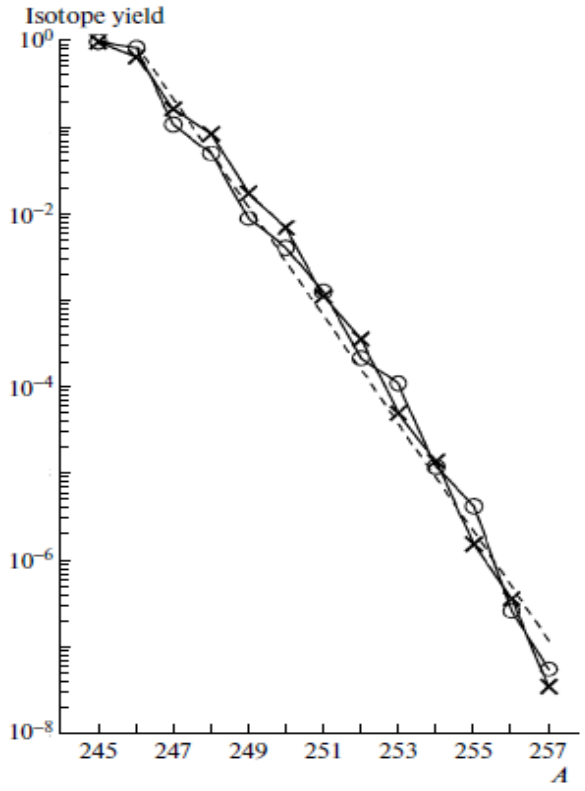

Fig. 3. Isotope yields in the "Par" experiment: ○ – experimental data; **x** – calculation results without consideration of the process dynamics; the dashed line denotes the fitting of the calculated isotope yields by the function: $Y = \exp(-1.442A + 354.56)$.

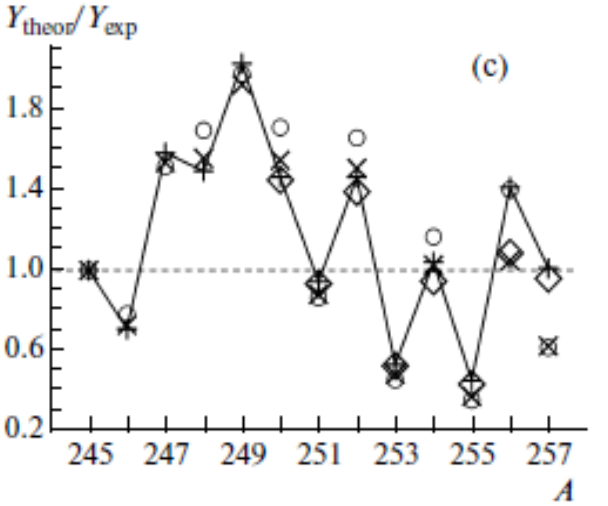

Fig. 4. Ratio of calculated to experimental values of isotope yields in the "Par" test for mass numbers $A = 245$ - - 257: ○- calculated results for the model with ^{238}U as a single isotope in the target; × - calculated results with allowance for the losing factor for the adiabatic model with ^{238}U as a single isotope in the target; + - calculated results (solid line) for the model with the binary target (^{238}U, 95%; ^{239}Pu, 5%) in which losing factor is ignored; ◊ - calculated results for the model with the binary target and with the losing factor.

To explain the even–odd effect in the model, the influence of the delayed processes – DF and DN is considered as a correction due to the $L(A)$ losing factor, which increases for the even A of nuclides as A rises (see Fig. 3) and acts in the right direction, approaching the calculated results for experimental concentrations [11, 22] registered after fissions. The model was further complicated by the simultaneous inclusion of two isotopes, ^{238}U and ^{239}Pu [11], in the composition of the initial target. It should be noted that the dependences of the calculated yields on A for ^{238}U and ^{239}Pu are in opposite phases (as are the respective cross sections of (n,γ)-reactions), which improves agreement with the experimental data in the region of the inversion effect at $A > 250$.

The resulting yields calculations for "Par" experiment are presented in Fig. 4 (the horizontal dashed line at the level of unity corresponds to complete agreement with the experimental data) as relations to the experimental data for the initial target concentration ^{238}U(95 %) + ^{239}Pu(5 %) and losing factors $L_U(A)$ and $L_{Pu}(A)$.

So we can explain the even-odd anomaly mainly by influence of beta-delayed fission and in smaller part, by influence of plutonium impurity in starting isotopes.

5. On the possibility of the formation of super-heavy elements by a pulse of neutrons

Including heavier chemical elements in a target during neutron nucleosynthesis could be a promising way of synthesizing heavy and superheavy elements. Yields of heavy nuclides were therefore evaluated for the inclusion of

small additives of ^{248}Cm and ^{251}Cf isotopes (available during reactor operation) into the initial uranium target. In our calculations, the losing factor $L(A)$ was incorporated without the inclusion of spontaneous fission. It should be noted that the $L(A)$ factor is in this case smaller than for the abovementioned uranium and plutonium, since the number of nuclides taking part in β-decay is smaller.

The inclusion of small masses of curium into the seed mixture with ^{238}U (Fig. 5) enables us to increase the yields of isotopes with mass numbers $A > 250$ by an order of magnitude at a 0.5% concentration of ^{248}Cm, and up to two orders of magnitude at concentrations of ~5 %. Introducing small doses of ^{251}Cf into the ^{238}U mixture strongly increases the yield at $A = 253, 254, 255$.

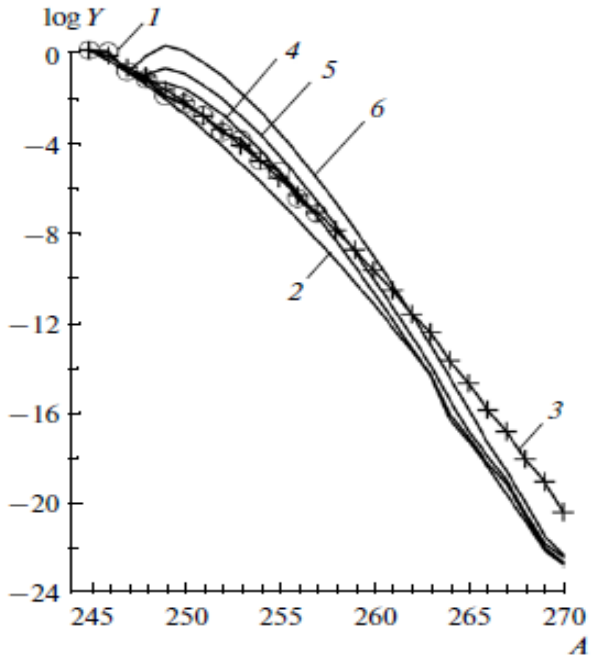

Fig. 5. Comparison of the calculated yields Y for (U + Cm) and (U + Pu) targets at a flux of $6 \cdot 10^{24}$ neutrons/cm^2. Curves: *1* - "Par" exp. data; *2* - *6* – calculations using various targets; *2* - ^{238}U(100 %); *3* - ^{238}U(95 %) + ^{239}Pu(5 %); *4* - ^{238}U + ^{248}Cm(0.1 %); *5* - ^{238}U + ^{248}Cm(0.5 %); *6* - ^{238}U + ^{248}Cm(5.0%).

At a concentration of 0.001 % ^{251}Cf there is thus a fivefold increase in the yield of isotopes with the mass number $A = 253$. As can be seen from Fig. 5 using Cm isotope additives at small concentrations in a target mainly consisting of uranium does not have a great effect on transuranium nuclides as does a U + Pu binary target. The same is for and Cf isotope [23]. In order to enhance the effect, the concentration of additives should be far higher, which does not make much sense in experiments with a destructible target.

6. Conclusion

The binary model of transuranium elements production in pulse neutron fluxes is developed. The calculations of the transuranium isotopes yields up to $A = 280$ in pulsed neutron fluxes of high intensity in the adiabatic binary model were performed with start isotopes: ^{238}U, ^{239}Pu, ^{248}Cm and ^{251}Cf. Comparison of yields calculations up to $A = 257$ for binary targets with experiment data were carried out to "*Par*", "*Barbel*" and "*Mike*" thermonuclear explosions.

Evolution of the nucleosynthesis model from one to two-component model allowed to improve the agreement of calculation results with experimental data of thermonuclear tests "Par", "Barbel" and "Mike" (USA). The calculations were performed for different proportions between initial concentrations of uranium and plutonium isotopes.

Experimental data on the yields of transuranium in nuclear explosions revealed anomalous odd-even effect, which manifests itself in the mass number $A > 250$, which is explained by the delayed fission process, calculations with which leads to better agreement with experiment. The agreement of the calculated isotopes yields with the experimental data is up to 50 %.

The "eating away" effect – the losing effect, which gives the relative decreasing of the concentration of nuclei with fix A and which is due to the emission of delayed neutrons and delayed fission - the processes leading to changes in the concentrations of β-decay of short-lived intermediates formed nuclei with large neutron excess. It is shown that the $L(A)$-effects associated with the observed even-odd inversion in yields for the transuranium nuclides with A > 250.

It is shown that nuclei with $A \approx 270$ can be obtained in the "Par" experiments with the yields ~ 10^{-22} using a uranium target, and – with the yields ~ $10^{-18} \div 10^{-20}$ using binary U + Pu and U + Cm targets. Heavier nuclei with $A \approx 280$ can be obtained with a yields ~ $10^{-29} \div 10^{-31}$ using binary U + Pu and U + Cm target. Such low concentrations can not be detected by modern experimental methods. Moreover, these nuclides decay rapidly.

So the calculations were carried out up to the values of $A = 280$. It was obtained that the isotopic relations of some transuranium elements, for example - curium, depends on the value of the pulse neutron flux. This may be an indicator of the pulse component in cases of extreme accidents at the nuclear power stations.

ACKNOWLEDGMENTS

The authors are grateful to Yu. V. Gaponov, G. V. Domogatsky, I. V. Korneev, I. V. Panov, V. N. Tikhonov, S. V. Tolokonnikov, E. E. Sapershtein for assistance and helpful comments.

The work was supported by the Russian Foundation for Basic Research Grants no. 11-02-00882, 12-02-00955 and 12-02-12114.

REFERENCES

1. *Lutostansky Yu.S., Chechetkin V.M.* Neitronoizbytochnye yadra i obrazovanie elementov v prirode (Neutron Excess Nuclei and Elements Creation in Nature). - M.: MIFI, 1987. - 59 p.
2. *Lyutostansky Yu.S., Panov I.V.* Heavy Element Formation During Explosive Nucleosynthesis // LEWI`90: Proc. Int. School “Low Energy Weak Interaction”. - Dubna, 1991. - P. 148 - 157.
3. *Lyutostansky Yu.S.* The Description of Charge - Exchange Exited States in the Neutron - Rich Nuclei and the Heavy Elements Nucleosynthesis // ISNES`92: Proc. of the Second Int. Symp.on Nuclear Exited States. - Lodz: University Lodz, 1993. - P. 202 - 208.
4. *Ghiorso, A., Thompson, S.G., Higgins, G.H. et al*. New Elements Einsteinium and Fermium, Atomic Numbers 99 and 100 // Phys. Rev. - 1955. - Vol. 99. - P. 1048 - 149.
5. *Bell G.I.* Production of Heavy Nuclei in Par and Barbel Devices // Phys. Rev. B. - 1965. - Vol. 139. - P. 1207 - 1216.
6. *Hoff R.W.* Production of Einsteinium and Fermium in Nuclear Explosions. - Livermore, 1978. - 30 p. - (Prepr. / Lawrence Livermore Laboratory; UCRL-81566).
7. *Krivokhatskii A.S., Romanov, Yu.F*. Poluchenie transuranovykh i aktinoidnykh elementov pri neitronnom obluchenii (Transuranium and Actinoid Elements Creation under Neutron Radiation). - M.: Atomizdat, 1970. - 174 p.
8. *Lutostansky, Yu.S., Ptitsin, D.A., Sinyukova, O.N. et al*. Production of Elements with $A > 80$ in Neutron Flucs ander Astrophysical Conditions // Yad. Fiz. (Phys. At. Nucl.) - 1985. - Vol. 42. - P. 215 -223.
9. *Lutostansky, Yu.S.* Processes accompanying β-decay of nuclei with the large neutron excess // Izv. Akad. Nauk SSSR, Ser. Fiz. - 1986. - Vol. 50. - P. 834 - 846.
10. *Lutostansky, Yu.S., Lyashuk, V.I., Panov, I.V.* Calculation of Transuranium Elements Synthesis in Intensive Neutron Fluxes under Adiabatic Conditions // Bull. Russ. Acad. Sci. Phys. - 2010. - Vol. 74. - P. 504 - 508.
11. *Lutostansky Yu.S., Lyashuk V.I., Panov I.V*. Production of Transuranium Elements in a Binary Model under Conditions of Pulse Nucleosynthesis // Bull. Russ. Acad. Sci. Phys. - 2011. - Vol. 75. - P. 533 - 537.
12. *Gaponov Yu.V., Lutostansky Yu.S*. Giant Gamow-Teller Resonance in Neutron Rich Nuclei // Phys. At. Nucl. - 2010. - Vol. 73. - P. 1360 - 1375.
13. *Yampol’skii P.A.* Neitrony atomnogo vzryva (Atomic Explosion Neutrons). - M.: Gosatomizdat, 1961. - 155 p.
14. *Bell G.I.* Cross Sections for Nucleosynthesis in Stars and Bombs // Rev. Mod. Phys. - 1967. - Vol. 39. - P. 59 - 68.
15. *Korobeinikov V.P*. Zadachi teorii tochechnogo vzryva (Problems of Point Explosion Theory). - M.: Nauka, 1985. - P. 133 - 141.
16. *Lyashuk V.I*. - M., 1997. - (Prepr. / Institute for Theoretical and Experimental Physics; No. 7).
17. *Kukhtevich V.I., Goryachev I.V., Trykov, L.A*. Zashchita ot pronikayushchei radiatsii yadernogo vzryva (Protection against Penetrating Radiation Caused by Atomic Explosion). - M.: Atomizdat, 1970. - P. 17.
18. *Zeldovich Ya.B., Raizer Yu.P*. Fizika udarnykh voln i vysokotemperaturnykh gidrodinamicheskikh yavlenii (Physics of Shock Waves and High-Temperature Hydrodynamic Phenomena). - M.: Nauka, 1966.
19. *Panov I.V., Korneev, I.Yu, Thielemann, F.-K. r*-Process in the Transuranium Region and Input of fission Products in Nucleosynthesis of Nuclei with $A \leq 130$ // Astron. Lett. - 2008. - Vol. 34. - P. 213 - 221.
20. *Moller P., Nix J.R., Myers W.D., Swiatecki W.J.* Nuclear ground-state masses and deformations. // At. Data Nucl. Data Tabl. - 1995. - Vol. 59. - P. 185 - 381.
21. *Moller P. et al*. Heavy-element fission barriers // Phys. Rev. C. - 2009. - Vol. 79. - P. 064304(1 - 38).
22. *Lutostansky Yu.S., Lyashuk V.I., Panov I.V*. Influence of the delayed fission effect on the production of transuranium elements // Izv. Akad. Nauk SSSR. Ser. Fiz. - 1990. - Vol. 54. - P. 2137. - 2141.
23. *Lutostansky Yu.S., Lyashuk V.I.* Evaluating the Yield of Transuranium Nuclides with Masses of up to $A = 270$ via Pulsed Nucleosynthesis // Bull. Russ. Acad. Sci. Phys. - 2012. - Vol. 76. - P. 462 - 466.

MODEL OF BREMSSTRAHLUNG EMISSION ACCOMPANYING INTERACTIONS BETWEEN PROTONS AND NUCLEI FROM LOW UP TO INTERMEDIATE ENERGY

S. P. Maydanyuk

Institute for Nuclear Research, National Academy of Sciences of Ukraine, Kyiv, Ukraine

A new model of the bremsstrahlung emission which accompanies proton decay and collisions of protons off nuclei in the energy region from the lowest up to intermediate has been developed. This model includes spin formalism, potential approach for description of interaction between protons and nuclei, and operator of emission includes component of the magnetic emission. In the problem of the bremsstrahlung during the proton decay in the first time a role of the magnetic emission is studied using such a model. For the ^{146}Tm nucleus it is studied the following: (1) How strongly does the magnetic emission change the full spectrum? (2) At which angle is the magnetic emission the most intensive relatively electric one? (3) How intensive is the magnetic emission in the tunneling region? It is shown that the model is able to describe well experimental data of the bremsstrahlung in collisions of protons off the ^{12}C and ^{64}Cu nuclei at the incident energy T_{lab} = 72 MeV (at the photon energy up to 60 MeV), the ^{9}Be and ^{208}Pb nuclei at the incident energy T_{lab} = 140 MeV (at the photon energy up to 120 MeV).

1. Introduction

According to theory of collisions of protons off nuclei, interactions between two nucleons play a leading role. Two nucleons interaction is based in relativistic models of collisions. But, consideration of nucleus as medium allows including space distribution of nucleons, as non-locality of quantum mechanics. What is more fundamental, interaction between different point-like nucleons of the nuclear medium or quantum effects of non-locality in it?

Models with nucleon-nucleon interaction should be the most accurate, if the collective effects caused by interactions between nucleons are small. But, we know that this is not so at low energies. If to analyze bremsstrahlung emission in collisions of protons off nuclei, then there are indications that two-nucleon interactions give the largest intensity. But, we find that many-nucleons effects arise at increasing of energy of the emitted photons.

Properties of the bremsstrahlung accompanying scattering of protons off nuclei have been studied well (see review [1, 2]). But, as it pointed in [3], properties of the nuclear bremsstrahlung emission in nucleon-nucleus and nucleus-nucleus collisions (especially, in intermediate energy region up to 150 MeV / nucleon) have been studied worst of all. This causes our interest in use of the optical potentials [4]. But, in study of the bremsstrahlung, which accompanies α-decay (see [5] and reference therein), spontaneous fission (see [6] and reference therein), ternary fission [7], collisions of nucleons, ions and nuclei off nuclei [2, 3] at non-relativistic energies, the emission caused by the magnetic moment of the fragment moving relatively the nucleus has not been taken into account. Microscopic models provide a powerful formalism for many-nucleons interactions. But, we see that magnetic emission was not studied in such models [8].

The magnetic emission is connected with magnetic momentum and spin of the fragment, interacting with nucleus. Attempt to take such aspects into account leads to matrix form of equations and many-component wave function (see [9], p. 32 - 35, 48 - 60). However, such aspects are included in relativistic models of collisions of nucleons between themselves and with nuclei at intermediate energies (based on Dirac equation). Note two lines of intensive investigations, Refs. [10] and [11], where main emphasis was made on construction of correct relativistic description of interaction between two nucleons. It could be interesting to obtain the model, combining spin formalism of interacting fragments (with magnetic momentum) and potential description of interactions. The problem of the bremsstrahlung during collisions of protons off nuclei and proton decay covers these lines. In Ref. [12] the bremsstrahlung during proton-decay was studied. However, here the magnetic emission caused by the magnetic moment of proton was not included. In order to clarify its role, a model with such aspect is needed. Main aim of this paper is construction of such a model.

2. Model

We shall start from generalization of Pauli equation for A + 1 nucleons of the proton-nucleus system in laboratory frame (starting from Eq. (1.3.6) in [9], p. 33). In center-of-masses frame hamiltonian is $\hat{H} = \hat{H}_0 + \hat{W}$, where $\hat{W}$ is operator of emission of the bremsstrahlung photon caused by nucleons, $\hat{H}_0$ is rest of hamiltonian without the emission of photons. Neglecting by relative motion of nucleons of nucleus, items at $e^2\mathbf{A}^2c^2$ and A_0, we find:

$$\hat{W} = Z_{\text{eff}} \frac{e}{mc} \sqrt{\frac{2\pi\hbar c^2}{w_{\text{ph}}}} \sum_{\alpha=1,2} e^{-i\mathbf{k}_{ph}\mathbf{r}} \left(i\, \mathbf{e}^{(\alpha)}\nabla - \frac{1}{2}\boldsymbol{\sigma}\cdot[\nabla\times\mathbf{e}^{(\alpha)}] + i\frac{1}{2}\boldsymbol{\sigma}\cdot[\mathbf{k}\times\mathbf{e}^{(\alpha)}] \right). \quad (1)$$

Here, $\mathbf{r}$ is distance between center-of masses of proton and nucleus, Z_{eff} and m are effective charge and reduced mass of the proton-nucleus system, $\boldsymbol{\sigma}$ are Puali matrixes, $\mathbf{e}^{(\alpha)}$ are unit vectors of polarization of photon, $\mathbf{k}_{\text{ph}}$ is wave vector of the photon and $w_{\text{ph}} = k_{\text{ph}}c = |\mathbf{k}_{\text{ph}}|c$. Vectors $\mathbf{e}^{(\alpha)}$ are perpendicular to $\mathbf{k}_{\text{ph}}$ in Coulomb calibration. We define the matrix element in the form:

$$F_{fi} = \left\langle k_f \left| \hat{W} \right| k_i \right\rangle = \int \psi_f^*(\mathbf{r})\, \hat{W}\, \psi_i(\mathbf{r})\, \mathbf{dr} = Z_{\text{eff}}\, \frac{e}{mc} \sqrt{\frac{2\pi\hbar c^2}{w_{\text{ph}}}} \left\{ p_{\text{el}} + p_{\text{mag},1} + p_{\text{mag},2} \right\} \tag{2}$$

$$\begin{aligned} p_{\text{el}} &= i \sum_{\alpha=1,2} \mathbf{e}^{(\alpha)} \left\langle k_f \left| \exp(-i\mathbf{k}_{\text{ph}}\mathbf{r})\, \nabla \right| k_i \right\rangle, \\ p_{\text{mag},1} &= \frac{1}{2} \sum_{\alpha=1,2} \left\langle k_f \left| \exp(-i\mathbf{k}_{\text{ph}}\mathbf{r})\, \boldsymbol{\sigma} \cdot [\mathbf{e}^{(\alpha)} \times \nabla] \right| k_i \right\rangle, \\ p_{\text{mag},2} &= -i \frac{1}{2} \sum_{\alpha=1,2} [\mathbf{k} \times \mathbf{e}^{(\alpha)}] \left\langle k_f \left| \exp(-i\mathbf{k}_{\text{ph}}\mathbf{r})\, \boldsymbol{\sigma} \right| k_i \right\rangle. \end{aligned} \tag{3}$$

Here, $\psi_i(\mathbf{r}) = \left| k_i \right\rangle$ and $\psi_f(\mathbf{r}) = \left| k_f \right\rangle$ are stationary wave functions of the proton-nucleus system in the initial *i*-state (i.e. before emission of photon) and final *f*-state (i.e. after emission) [5 - 7].

We define the wave function of proton in field of the nucleus in form of bilinear combination of eigenfunctions of orbital and spinor subsystems as Eq. (1.4.2) in [9] (see p. 42). Substituting it to (3) and applying multipolar expansion for vector potential **A,** we obtain:

$$\begin{aligned} p_{\text{el}} &= \sqrt{\frac{\pi}{2}} \sum_{l_{\text{ph}}=1} (-1)^{l_{\text{ph}}} \sqrt{2l_{\text{ph}}+1} \sum_{\mu=\pm1} h_\mu \sum_{m_i m_f} \sum_{\mu_i \mu_f = \pm 1/2} C_{l_f m_f 1/2 \mu_f}^{j_f M_f, *} C_{l_i m_i 1/2 \mu_i}^{j_i M_i} \left\{ i\mu\, p_{l_{ph}\mu}^{M m_i m_f} + p_{l_{ph}\mu}^{E m_i m_f} \right\}, \\ p_{\text{mag},1} &= \sqrt{\frac{\pi}{2}} \sum_{l_{\text{ph}}=1} (-1)^{l_{\text{ph}}} \sqrt{2l_{\text{ph}}+1} \sum_{\mu=\pm1} h_\mu \mu \sum_{m_i m_f} \sum_{\mu_i \mu_f = \pm 1/2} C_{l_f m_f 1/2 \mu_f}^{j_f M_f, *} C_{l_i m_i 1/2 \mu_i}^{j_i M_i} \left\{ i\mu\, p_{l_{ph}\mu}^{M m_i m_f} + p_{l_{ph}\mu}^{E m_i m_f} \right\}, \\ p_{\text{mag},2} &= \sqrt{\frac{\pi}{2}} \sum_{l_{\text{ph}}=1} (-1)^{l_{\text{ph}}} \sqrt{2l_{\text{ph}}+1} \sum_{\mu=\pm1} h_\mu \sum_{m_i m_f} \sum_{\mu_i \mu_f = \pm 1/2} C_{l_f m_f 1/2 \mu_f}^{j_f M_f, *} C_{l_i m_i 1/2 \mu_i}^{j_i M_i} \times \\ &\times \left[-1 + i(\delta_{\mu_i, +1/2} - \delta_{\mu_i, -1/2}) \right] \cdot \left\{ i\mu\, \tilde{p}_{l_{ph}}^{M} + \tilde{p}_{l_{ph}}^{E} \right\}, \end{aligned} \tag{4}$$

where

$$\begin{aligned} p_{l_{ph}\mu}^{M} &= \sqrt{\frac{l_i}{2l_i+1}}\, I_M(l_i, l_f, l_{ph}, l_i - 1, \mu) \cdot \left\{ J_1(l_i, l_f, l_{ph}) + (l_i+1) \cdot J_2(l_i, l_f, l_{ph}) \right\} - \\ &- \sqrt{\frac{l_i+1}{2l_i+1}}\, I_M(l_i, l_f, l_{ph}, l_i + 1, \mu) \cdot \left\{ J_1(l_i, l_f, l_{ph}) - l_i \cdot J_2(l_i, l_f, l_{ph}) \right\}, \end{aligned} \tag{5}$$

$$\begin{aligned} p_{l_{ph}\mu}^{E} &= \sqrt{\frac{l_i(l_{ph}+1)}{(2l_i+1)(2l_{ph}+1)}}\, I_E(l_i, l_f, l_{ph}, l_i - 1, l_{ph} - 1, \mu) \cdot \left\{ J_1(l_i, l_f, l_{ph} - 1) + (l_i+1) \cdot J_2(l_i, l_f, l_{ph} - 1) \right\} - \\ &- \sqrt{\frac{l_i l_{ph}}{(2l_i+1)(2l_{ph}+1)}}\, I_E(l_i, l_f, l_{ph}, l_i - 1, l_{ph} + 1, \mu) \cdot \left\{ J_1(l_i, l_f, l_{ph} + 1) + (l_i+1) \cdot J_2(l_i, l_f, l_{ph} + 1) \right\} + \\ &+ \sqrt{\frac{(l_i+1)(l_{ph}+1)}{(2l_i+1)(2l_{ph}+1)}}\, I_E(l_i, l_f, l_{ph}, l_i + 1, l_{ph} - 1, \mu) \cdot \left\{ J_1(l_i, l_f, l_{ph} - 1) - l_i \cdot J_2(l_i, l_f, l_{ph} - 1) \right\} - \\ &- \sqrt{\frac{(l_i+1) l_{ph}}{(2l_i+1)(2l_{ph}+1)}}\, I_E(l_i, l_f, l_{ph}, l_i + 1, l_{ph} + 1, \mu) \cdot \left\{ J_1(l_i, l_f, l_{ph} + 1) - l_i \cdot J_2(l_i, l_f, l_{ph} + 1) \right\}, \end{aligned}$$

$$\begin{aligned} J_1(l_i, l_f, n) &= \int_0^{+\infty} \frac{dR_i(r, l_i)}{dr}\, R_f^*(r, l_f)\; j_n(k_{\text{ph}} r)\, r^2 dr, \\ J_2(l_i, l_f, n) &= \int_0^{+\infty} R_i(r, l_i)\, R_f^*(r, l_f)\; j_n(k_{\text{ph}} r)\, r\, dr, \end{aligned} \tag{6}$$

$$\begin{aligned} I_M(l_i, l_f, l_{\text{ph}}, l_1, n) &= \int Y_{l_f m_f}^*(\mathbf{n}_\mathbf{r})\, \mathbf{T}_{l_i, l_1, m_i}(\mathbf{n}_\mathbf{r})\, \mathbf{T}_{l_{ph}, l_{ph}, \mu_{ph}}^*(\mathbf{n}_\mathbf{r})\, d\Omega, \\ I_E(l_i, l_f, l_{\text{ph}}, l_1, l_2, n) &= \int Y_{l_f m_f}^*(\mathbf{n}_\mathbf{r})\, \mathbf{T}_{l_i, l_1, m_i}(\mathbf{n}_\mathbf{r})\, \mathbf{T}_{l_{ph}, l_2, \mu_{ph}}^*(\mathbf{n}_\mathbf{r})\, d\Omega. \end{aligned} \tag{7}$$

We define the photon emission probability as (see also Refs. [3, 5 - 7]):

$$\frac{dP(\phi_f,\theta_f)}{dw_{\rm ph}}=\frac{dP_{\rm el}(\phi_f,\theta_f)}{dw_{\rm ph}}+\frac{dP_{\rm mag,1}(\phi_f,\theta_f)}{dw_{\rm ph}}+\frac{dP_{\rm mag,2}(\phi_f,\theta_f)}{dw_{\rm ph}}+\frac{dP_{\rm interference}(\phi_f,\theta_f)}{dw_{\rm ph}}, \tag{8}$$

$$\frac{dP_{\rm el}}{dw_{\rm ph}}=g_i\left\{\frac{p_{\rm el}\,dp^*_{\rm el}}{d\cos\theta_f}+c.c.\right\},\quad \frac{dP_{\rm mag,1}}{dw_{\rm ph}}=g_i\left\{\frac{p_{\rm mag,1}\,dp^*_{\rm mag,1}}{d\cos\theta_f}+c.c.\right\},\quad \frac{dP_{\rm mag,2}}{dw_{\rm ph}}=g_i\left\{\frac{p_{\rm mag,2}\,dp^*_{\rm mag,2}}{d\cos\theta_f}+c.c.\right\},$$

where $g_i=Z_{\rm eff}^2e^2w_{\rm ph}E_i\big/(2\pi c^5m^2k_i)$. We call $dP_{\rm el}$ as *electric emission*, $dP_{\rm mag,1}$ as *magnetic emission*, $dP_{\rm mag,2}$ as *correction of magnetic emission*, $dP_{\rm interference}$ as *interference component of emission*. For bremsstrahlung during collisions of protons off nuclei we shall use cross-section as

$$\frac{d^2\sigma}{dw_{\rm ph}d\cos\theta_f}=N_0w_{\rm ph}\left\{p\frac{dp^*}{d\cos\theta_f}+c.c.\right\}, \tag{9}$$

where N_0 is factor of normalization of the calculated full spectrum on experimental data.

3. Results

We calculate the bremsstrahlung probability by Eq. (8). The potential of interaction between the proton and the daughter nucleus is defined in [12]. The wave functions of the decaying system are calculated in the spherically symmetric approximation. The boundary conditions and normalization are used in form of (B.1) - (B.9) in [12]. In [12] the ^{157}Ta, ^{161}Re, ^{167}Ir and ^{185}Bi nuclei decaying from the $2s_{1/2}$ state (at $l_{\rm i}=0$), the ^{109}I, ^{112}Cs nuclei decaying from the $1d_{5/2}$ state and the ^{146}Tm, ^{151}Lu nuclei decaying from the $0h_{11/2}$ state (at $l_i\neq0$) were selected. I shall analyze only one nucleus ^{146}Tm at $l_i\neq0$ (as calculations for this nucleus are essentially more difficult than for nuclei at $l_{\rm i}=0$). For ^{146}Tm we have $l_{\rm i}=5$, $l_{\rm f}=4$, $Q=1.140$ MeV [12].

3.1. Electrical, magnetic emissions and angular distributions

At first, let us see how much the magnetic emission is visible. The result of our calculations of the bremsstrahlung during proton decay of ^{146}Tm are presented in Fig. 1.

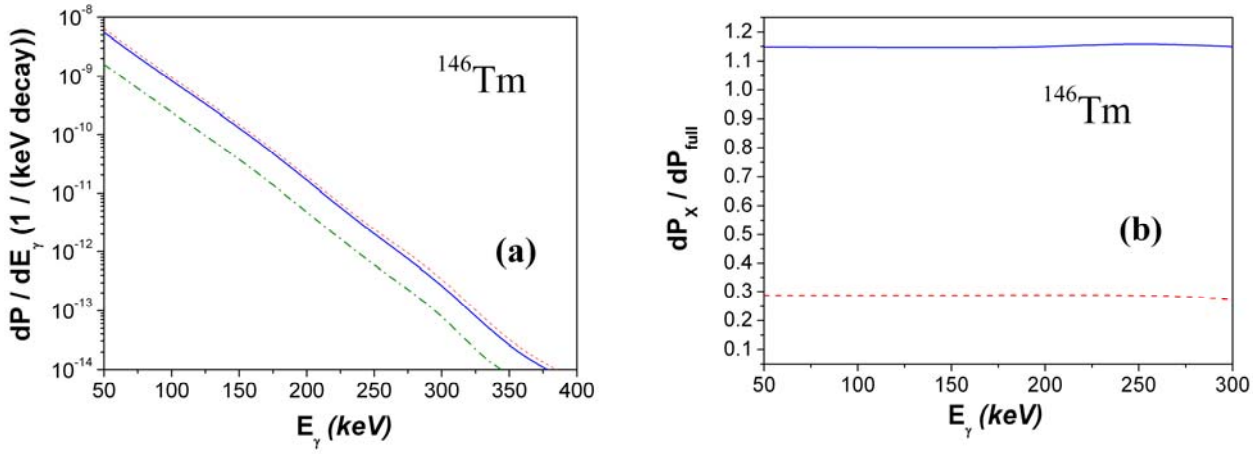

Fig. 1. The full bremsstrahlung spectrum, electric and magnetic components of emission defined by Eqs. (8) (at $\theta=90^{\rm o}$): (*a*) the full spectrum (full blue line), electric component $dP_{\rm el}$ (red dashed line) and magnetic component $dP_{\rm mag,1}$ (green dash-dotted line), (*b*) ratio of the components to the full spectrum (full blue line is for $dP_{\rm el}/dP_{\rm full}$, red dashed line for $dP_{\rm mag,1}/dP_{\rm full}$). One can see that the magnetic emission gives contribution about 28 percents inside energy region 50 - 300 keV.

The electric and magnetic components are included also on these figures. One can see that the magnetic emission is smaller than electric one. But it gives contribution about 28 percents into the full spectrum (see Fig. 1, *b*), i.e. it is not so small to be neglected and it should be taken into account in further calculations of the bremsstrahlung spectra during nuclear decays with emission of charged fragments with non-zero spin. However, the magnetic component suppresses the full emission probability: according to Fig. 1, *b* (see blue solid line), inclusion of the magnetic component into calculations is determined by $P_{\rm el}/P_{\rm full}=1.14$, which is larger unity. This effect of suppressing of the total emission can be explained by a presence of not small destructive interference between the electric and magnetic components inside whole studied energy region. According to Fig. 1, *b*, ratios of the electric and magnetic components to full spectrum are not changed in dependence on the energy of the emitted photon.

In Fig. 2 the angular distributions of the electric and magnetic emissions during the proton decay of ^{146}Tm are shown. One can see that the electric and magnetic components increase proportionally with increasing of the θ angle.

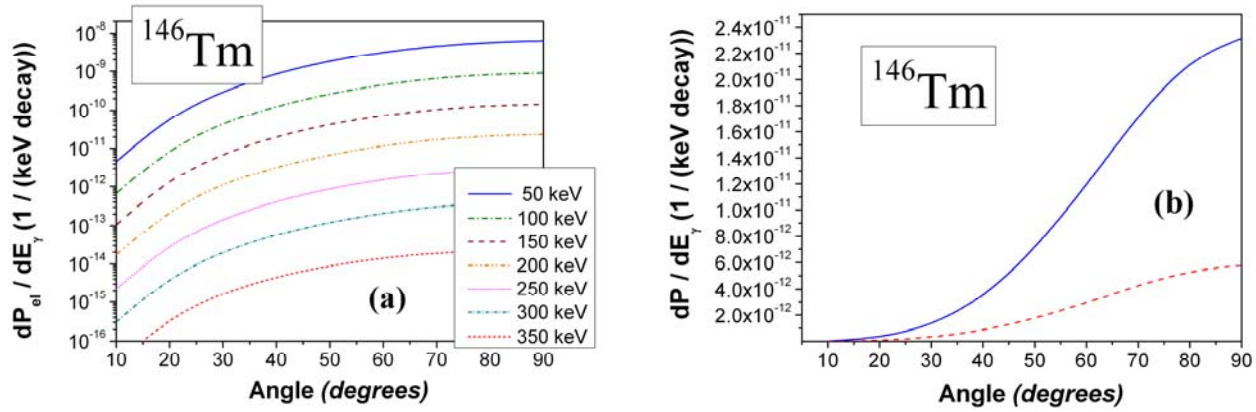

Fig. 2. The angular distributions of the bremsstrahlung during proton decay of ^{146}Tm: *a* – the electric emission, dP_{el}, calculated at different energies of the emitted photons; *b* – the electric component dP_{el} (full blue line) and magnetic component $dP_{mag,1}$ (red dashed line) for the chosen photon energy 200 keV. One can see that both spectra increase proportionally (similarly) with increasing of the angle.

3.2. Spectra in collisions of protons off nuclei at intermediate energies

I shall shortly demonstrate applicability of the model in the problem of the bremsstrahlung during collisions of protons off nuclei at intermediate energies of incident protons. I calculate the normalized cross-sections by Eq. (9), use the same form of the proton-nucleus potential and parameters (defined as for the problem of proton-decay). Results of my calculations are presented in Figs. 3 and 4. In Fig. 3, *a* one can see that my approach describes enough well experimental data for p + ^{9}Be from 20 MeV to 120 MeV in comparison with results obtained by Nakayama and Bertsch in [13] and calculations performed by Nakayama in [10]. In Fig. 3, *b* I compare my calculations for p + ^{208}Pb with experimental data [14] and results of Remington, Blann and Bertsch in [15]. In Fig. 4 I present my calculations of the bremsstrahlung cross-sections for collisions p + ^{9}C and p + ^{64}Cu in comparison with experimental data [16] at the incident proton energy T_{lab} = 72 MeV. I show the full spectrum calculated by Eq. (9) and corrected spectrum obtained by Eq. (9) with division on k_f (according to formula (9) of cross-section defined in [2]). Comparison with quantum calculations of Kopitin, Dolgopolov, Churakova and Kornev in [2] shows more stable calculations in our approach.

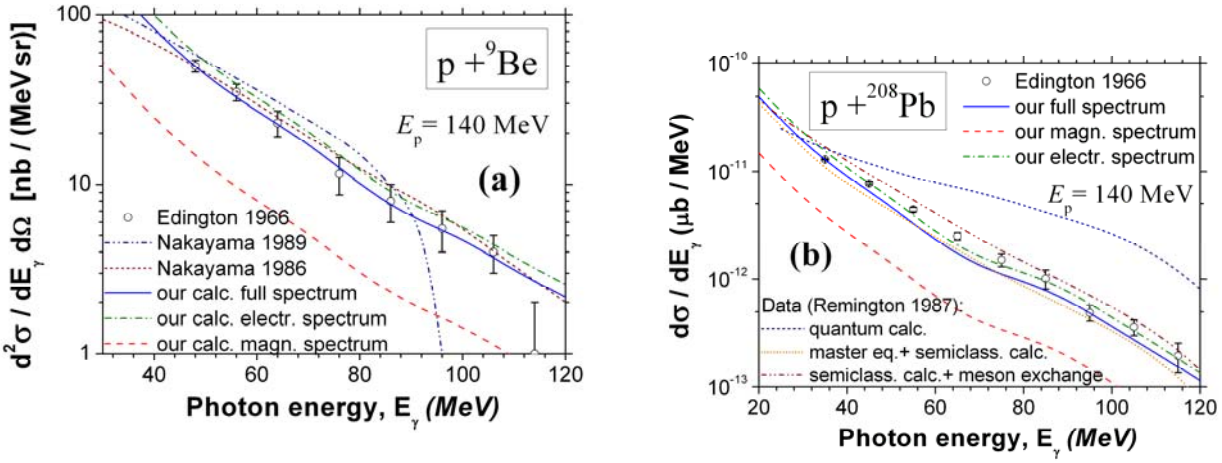

Fig. 3. The proton nucleus bremsstrahlung probability rates in the laboratory system at the incident energy T_{lab} = 140 MeV (in calculations we use photon emission angle $\theta = 90^{o}$): *a* - Comparison for p + ^{9}Be between the calculations by our model (blue solid line is for full spectrum, green dash-dotted line for electric contribution, red dashed line for magnetic contribution), calculations from (Nakayama 1986: [13], wine short-dashed line), calculations from (Nakayama 1989: [10], navy dash double-dotted line) and experimental data (Edington 1966: [14]); *b* – Comparison for p + ^{208}Pb between the calculations by our model (blue solid line is for full spectrum, green dash-dotted line for electric contribution, red dashed line for magnetic contribution), calculations by Remington, Blann and Bertsch in (Remington 1987: [15], wine dash double-dotted line is for calculations by master equation using the semiclassical bremsstrahlung cross sections, orange short dotted line for semiclassical cross sections multiplied by 2 for meson exchange, and navy short dashed line for quantum bremsstrahlung cross sections) and experimental data (Edington 1966: [14]).

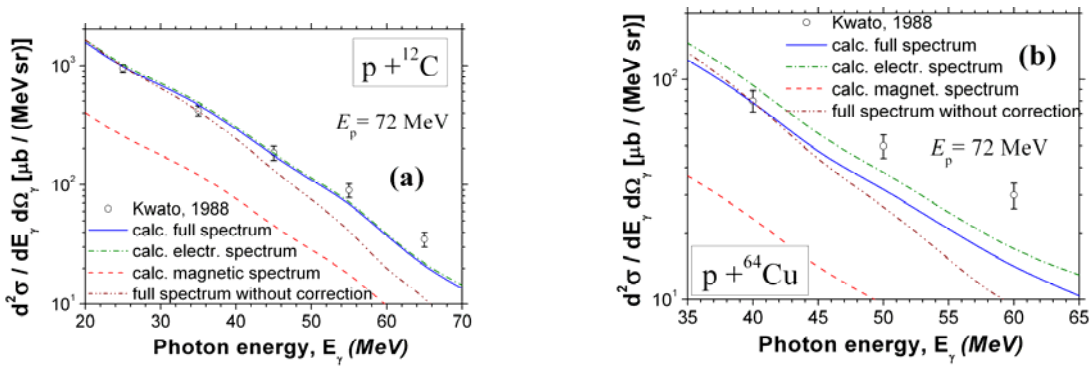

Fig. 4. The proton nucleus bremsstrahlung probability in laboratory system at T_{lab} =72 MeV and θ = 90º: Comparison for p + ^{12}C (*a*) and *p* + ^{64}Cu (*b*) between the full cross-section calculated by Eq. (9) (wine dash double-dotted line), corrected cross-section by Eq. (9) with division on k_f (blue solid line) and experimental data (Kwato 1988: [16]).

4. Conclusions and perspectives

The new model of the bremsstrahlung emission which accompanies proton decay and collisions of protons off nuclei in the energy region from the lowest up to intermediate has been developed. This model includes spin formalism, potential approach for description of interaction between protons and nuclei, and operator of emission includes the component of magnetic emission. For such investigations the ^{146}Tm nucleus is chosen. We obtain the following:

- Inside energy region from 50 up to 300 keV the magnetic emission gives contribution about 28 percents into the full spectrum (see Fig. 1). But, the magnetic component suppresses the full emission probability (P_{el}/P_{full} = 1.14).
- With increasing of angle between directions of the outgoing proton and emitted photon the electric and magnetic components increase proportionally (see Fig. 2).
- The model describes well experimental data of the bremsstrahlung in collisions of protons off ^{12}C, ^{64}Cu at T_{lab} = 72 MeV, and ^{9}Be, ^{208}Pb at T_{lab} = 140 MeV (see Figs. 3 and 4).

REFERENCES

1. *Pluyko V.A., Poyarkov V.A.* // Phys. El. Part. At. Nucl. - 1987. - Vol. 18. - P. 374 - 418.
2. *Kamanin V.V., Kugler A., Penionzhkevich Yu.E. et al.* // Phys. El. Part. At. Nucl. - 1989. - Vol. 20. - P. 743 - 829.
3. *Kopitin I.V., Dolgopolov M.A. et al. //* Yad. Fiz. - 1987. - Vol. 60. - P. 869 - 879.
4. *Becchetti F.D. Jr., Greenlees G.W.* Nucleon-nucleus optical-model parameters, A>40, E<50 MeV // Phys. Rev. - 1969. - Vol. 182. - P. 1190 - 1209.
5. *Maydanyuk S.P.* Multipolar approach for description of bremsstrahlung during α-decay and unified formula of the bremsstrahlung probability // TONPPJ. - 2009. - Vol. 2. - P. 17 - 33.
6. *Maydanyuk S.P., Olkhovsky V.S., Mandaglio G. et al.* Bremsstrahlung emission of high energy accompanying spontaneous of ^{252}Cf // Phys. Rev. C. - 2010. - Vol. 82. - P. 014602.
7. *Maydanyuk S.P., Olkhovsky V.S., Mandaglio G. et al.* Bremsstrahlung emission of photons accompanying ternary fission of ^{252}Cf // J. Phys.: Conf. Ser. - 2011. - Vol. 282. - P. 012016.
8. *Liu Q.K.K., Tang Y.C., Kanada H.* Microscopic study of $p + \alpha$ bremsstrahlung // Phys. Rev. C. - 1990. - Vol. 42. - P. 1895 - 1898.
9. *Ahiezer A.I., Berestetskii V.B.* Kvantovaya Elektrodinamika. - M.: Nauka, 1981. - 432 p.
10. *Nakayama K.* High-energy photons in neutron-proton and proton-nucleus collisions // Phys. Rev. C. - 1989. - Vol. 39. - P. 1475 - 1487.
11. *Li Yi, Liou M.K., Schreiber W.M., Gibson B.F.* Proton-proton bremsstrahlung: consequences of different on-shell-point conditions // Phys. Rev. C. - 2011. - Vol. 84. - P. 034007.
12. *Maydanyuk S.P.* Multipolar model of bremsstrahlung accompanying proton decay of nuclei // Jour. Phys. G. - 2011. - Vol. 38. - P. 085106.
13. *Nakayama K., Bertsch G.* High energy photon production in nuclear collisions // Phys. Rev. C. - 1986. - Vol. 34. - P. 2190 - 2200.
14. *Edington J., Rose B.* Nuclear bremsstrahlung from 140 MeV protons // Nucl. Phys. - 1966. - Vol. 89. - P. 523 - 552.
15. *Remington B.A., Blann M., Bertsch G.F. n-p* bremsstrahlung interpretation of high energy gamma rays from heavy-ion collisions // Phys. Rev. C. - 1987. Vol. 35. - P. 1720 - 1729.
16. *Kwato Njock M., Maurel M., Nifenecker H. et al.* Nuclear bremsstrahlung production in proton-nucleus reactions at 72 MeV // Phys. Lett. B. - 1988. Vol. 207. - P. 269.

MECHANISM OF TELLURIUM ISOMERS EXCITATION IN (γ, n) REACTIONS

V. M. Mazur, D. M. Symochko, Z. M. Bigan, T. V. Poltorzhytska, P. S. Derechkey

Institute of Electron Physics, National Academy of Sciences of Ukraine, Uzhgorod, Ukraine

Isomeric yield ratios for the ^{119}Te, ^{121}Te, ^{123}Te, ^{127}Te, ^{129}Te nuclei were obtained in (γ, n) reactions with bremsstrahlung end point energies ranging 10 - 22 MeV with ΔE = 0.5 MeV step. Experimental isomeric ratios were used to calculate the cross-sections of $(\gamma, n)^m$ reactions, that were further compared with TALYS-1.4 calculations.

1. Introduction

Gamma beams are an accurate tool for investigating different processes in nuclear physics and astrophysics. Photons with energies of tens MeV bring relatively small changes to nuclei and due to the pure electromagnetic character of photonuclear reactions can be used to obtain information on nucleon-nucleon interactions [1], collective motions of the nuclear matter (giant dipole resonance, pygmy dipole resonance etc) [2], mechanism of the particular nuclear states excitation [3, 4], etc. Photonuclear reactions are also important for understanding the processes of elements creation in a stellar environment. Particularly to explain the abundances of p-nuclei which are mainly synthesized through the chain of photonuclear reactions on r- or s-precursors [5]. ^{120}Te is one of these p-process nuclei and the reaction ^{120}Te(γ, n)^{119}Te partly determines the cross-section of its photodisintegration. Moreover, in view of the fact that ^{120}Te is produced by photodisintegration of the s-only nucleus ^{122}Te followed by that of ^{121}Te, cross-sections of ^{122}Te(γ, n)^{121}Te can be treated as part of the production cross-section of the p-nucleus. To determine p-abundances a database that includes exact values for thousands of reaction cross-sections is needed. As the experimental information on reactions involved in the p-process is very scarce, reaction rates based on Hauser - Feshbach calculations [6] are used for modeling of the p-process flow. One of the methods to check the conformity of the statistical model based on compound nucleus assumption is to compare its results with experimental data on isomeric states population

The isomeric ratios and cross-sections of $(\gamma, n)^m$ reactions on Te isotopes in the GDR energy region were not sufficiently studied previously. There are only two published works [7, 8] that contains complex studies of Te isomeric yields ratios, but measured for the particular energies up to $E_{\gamma max}$ = 25 MeV. At the same time, Te isotopes are remarkable because they could allow for the investigation of the evolution of isomeric ratios with the change of neutron subshell population through a wide mass range (A = 119 - 130).

2. Experiment

The activation technique was used in the experiment. Samples were irradiated with a bremsstrahlung beam from electron accelerator Microtron M-30 of the Institute of Electron Physics of NAS of Ukraine [9] within the 10 - 18 MeV endpoint energy range in △E = 0.5 MeV steps. The electron beam extracted from the accelerator was converted into bremsstrahlung with a 0.5 mm thick tantalum radiator. The intensity of the magnetic field was measured by the NMR method and it allowed achieving less than 50 keV uncertainties in the electron beam energy spread determination. The mean current of beam electrons was 5 μA and was controlled by a secondary-emission monitor with the 1.2 s timestep. For the energies 20 - 22 MeV the bremsstrahlung beam from betatron B25/30 of Uzhhorod National University was used. Tellurium targets were placed on the beam axis at a distance of 30 cm from Tantalum radiator. Targets were made from glass-like TeO_2 of natural isotopic composition (99.99 % chemical purity) in the form of disks (25 mm diameter, 2.5 mm thickness).Follow the irradiations and cooling period, the residual activity in the samples was measured in a low-background environment by an ORTEC spectroscopic system consisting of the calibrated 175 cm^3 HPGe-detector and a multichannel analyzer. The detector was screened from background radiation by the combined Pb-Cd-Cu shield. The energy resolution was 2 keV for ^{60}Co gammas.

To extract optimal amount of data from the decay of the residual nuclei the measurement process was organized as following. After the irradiation and 1 - 2 h cooling time (to reduce dead-time of the detector) the decay of the ^{129}Te^g ground state was measured. Gamma-spectra obtained during next 24 h were used to obtain data on the decay of ^{119}Te^m, ^{119}Te^g, ^{127}Te^g, ^{129}Te^m states. Measurements of long-lived reaction products were done during 1 - 3 days after 7-20 days of cooling. We used spectroscopic data for the investigated nuclei from ENSDF data base [10].

In the general case isomeric yields ratios d are determined as [11]:

$$d = Y_m / Y_g = \left[\frac{\lambda_g}{\lambda_m} \cdot \frac{f_m(t)}{f_g(t)} \left(c \cdot \frac{N_g}{N_m} \cdot \frac{\phi_m}{\phi_g} - p \frac{\lambda_g}{\lambda_g - \lambda_m} \right) + p \frac{\lambda_m}{\lambda_g - \lambda_m} \right]^{-1}, \quad (1),$$

where $N_{m,g}$ are the counts in photopeaks associated with isomer and ground sates decay; $\varphi_{m,g}$ – coefficient which includes detector efficiency ε, self-absorption in the targets μ and gamma-lines intensity α; p – branching ratio; c – correction factor for detector "dead-time" and pulse overlapping; $f_{m,g}$ – time functions expressed in following way:

$$f_{m,g} = \left[1 - \exp\left(-\lambda_{m,g} \cdot t_{irr}\right)\right] \cdot \exp\left(-\lambda_{m,g} \cdot t_{cool}\right) \left[1 - \exp\left(-\lambda_{m,g} \cdot t_{meas}\right)\right], \quad (2)$$

where $\lambda_{m,g}$ denote decay constants of isomeric and ground states, t_{irr}, t_{cool}, t_{meas} – intervals of irradiation, cooling and measurements.

Obtained experimental isomeric yields ratios d = f($E_{\gamma max}$) with standard errors are shown as dots in Fig. 1. Essentially, dependences d = f($E_{\gamma max}$) grow from the (γ, n)^{m} reactions thresholds for all presented cases and reach the plateau within 20 - 22 MeV energy range.

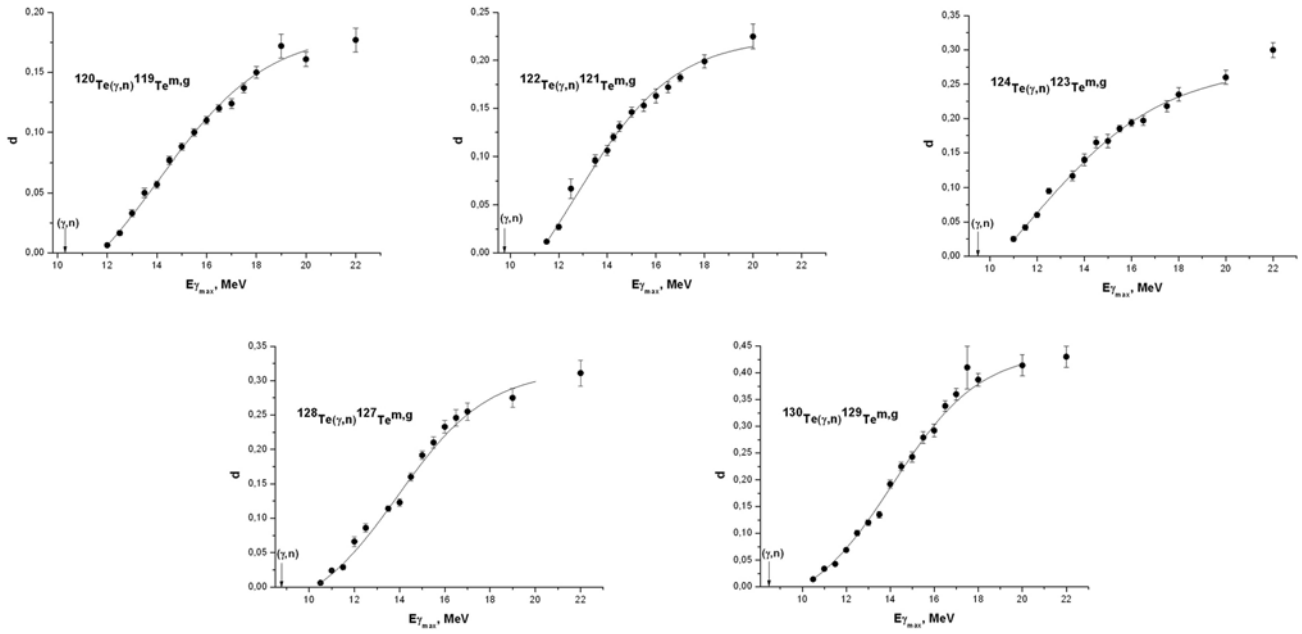

Fig. 1. Experimental isomeric yields ratios for the ^{120}Te(γ, n)^{119}Te^{m,g}, ^{122}Te(γ, n)^{121}Te^{m,g}, ^{124}Te(γ, n) ^{123}Te^{m,g}, ^{128}Te(γ, n)^{127}Te^{m,g}, ^{130}Te (γ, n) ^{129}Te^{m,g} reactions.
Dots – experimental values, solid line – approximation of experimental results.

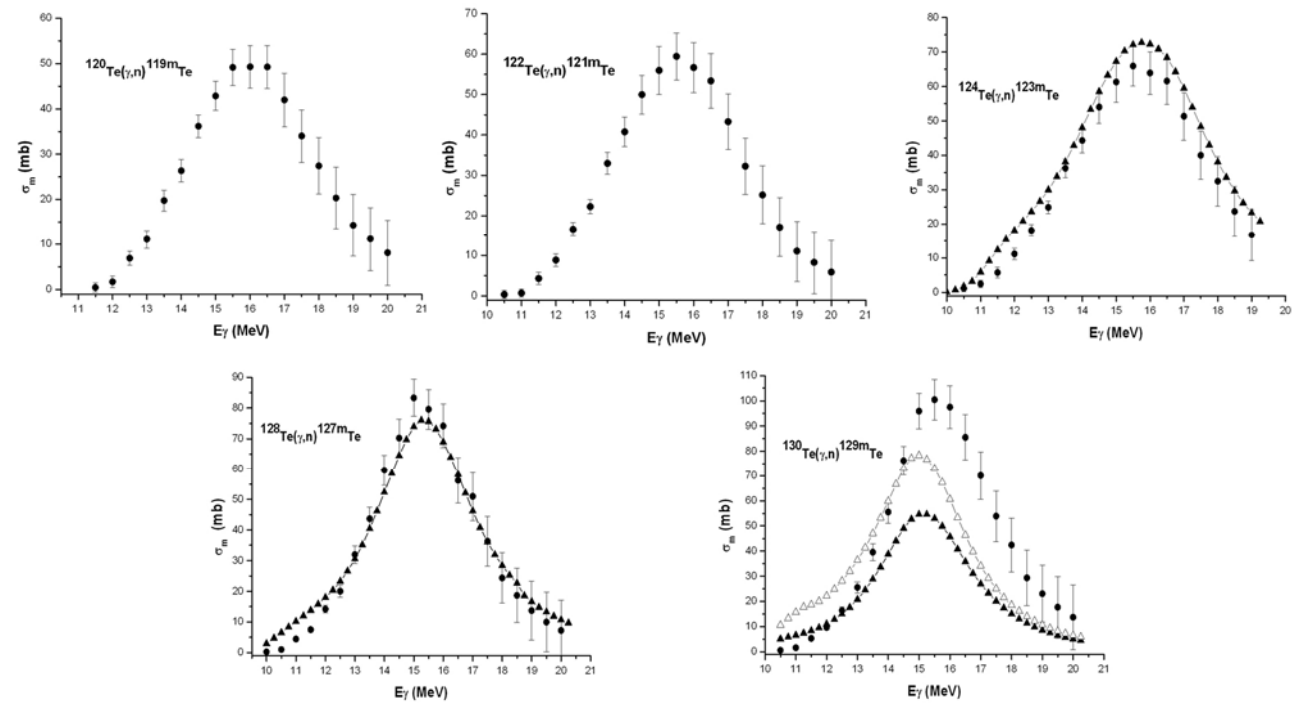

Fig. 2. The cross-sections of the ^{120}Te(γ, n)^{119}Te^{m}, ^{122}Te(γ, n)^{121}Te^{m}, ^{124}Te(γ, n) ^{123}Te^{m}, ^{128}Te(γ, n)^{127}Te^{m}, ^{130}Te (γ, n) ^{129}Te^{m}. Dots – experimental values, filled triangles- TALYS-1.4 calculations with RIPL-3 standard level structure, open triangles - TALYS-1.4 calculations with modified level structure.

The solid lines in Fig. 1 resulted from approximation of experimental isomeric ratios with Boltzmann curves:

$$d = A + (B - A) \Big/ \left[1 + \exp\left(\frac{E - E_0}{\Delta E}\right)\right], \quad (3)$$

where A, B, E0 and ΔE – parameters. Approximation was carried out by a least square method in the range from reactions thresholds up to 20 MeV.

Experimental dependence of the isomeric yields ratios on the bremsstrahlung endpoint energy $d = f(E_{\gamma max})$ allows to calculate the experimental isomeric state population cross-sections σ_m using known total (γ, n) reaction cross-sections [12]. The calculation was carried out by the reverse matrix method [13]. The yield curves were smoothed before used as an input for the calculations. Obtained cross-sections of isomers population are presented via dots in the Fig. 2. Figs. 1 and 2 reveal that isomeric yields ratios and cross-sections are increasing with growth of isotopes mass from A = 119 to A = 129. It correlates with population of outer subshell $1h_{11/2}$, which starts to fill from ^{122}Te and reach 8 neutrons in ^{130}Te.

3. Model calculations

For the purpose of comparing the experimental and theoretical data on isomeric excitation we performed the calculations of the reaction cross-sections with the help of TALYS-1.4 code [14]. The following scheme was used in calculations. Dipole monochromatic gamma with E_γ energy interacts with nuclear target (Z_i, N_i) and the compound state (J_c, π_c) is formed with excitation energy E_c equal to the energy of incident gamma. Total photoabsorption cross-section σ_{tot} is calculated with the use of experimental GR parameters (if available) or from semiempirical systematics. Both statistical and preequlibrium mechanism contribute to the decay process of the residual nuclei. The main contribution in the investigated energy region belongs to Hauser - Feshbach statistical mechanism. But with increasing energy the part of preequilibrium processes simulated with exciton model [15] becomes more significant. After the gamma absorption the particle-hole pair (exciton) is created. The system evolves through the steps and on each of them the number of excitons is increased by one. Particle emission is possible from every stage of the process. After 6 steps the process is no longer treated as preequilibrium and further reaction flow is simulated with statistical model. Calculations show that statistical mechanism dominates for the GR region and its contribution to the total (γ,n) cross-sections even for higher energies is more than 80 %. After the neutron emission the population of the particular residual nucleus levels is calculated using the transmission coefficients T_l obtained from optical model. RIPL-3 database [16] was used to obtain information on first 80 discreet levels. At higher energies excited states spectrum was treated as continuous and described by the level density ρ(E, J, π) divided into 40 equidistant energy bins. For simulation of the continuous spectra we used the Back-shifted Fermi gas model [17].

The calculated cross-sections are plotted in Fig. 2 with black triangles. We are not presenting results of calculations for ^{120}Te(γ, n)^{119}Te^m and ^{122}Te(γ, n)^{121}Te^m reactions as there is no published experimental data on total (γ, n) cross-sections for this isotopes and this can serve as source of errors in calculations on the stage of photoabsorption cross-section determination. Calculated values are significantly consistent with experimental data for ^{124m}Te, ^{127m}Te, but at the same time we can see very poor agreement in case of ^{129m}Te. Notable disagreement (more than 50 % at the maximum) for the reaction ^{130}Te(γ, n)^{129}Te^m motivated us for additional research. We found that information on discreet levels for the ^{129}Te used in RIPL-3 database originated from the ENSDF evaluation [18] which was not updated from 1996. However, the detailed study of ^{129}Te structure was published in 2003 [19]. This paper introduces the 1221 keV level with $J^\pi = 5/2^-$ which can be the key to understanding the strong population of the ^{129}Te^m isomer. This level effectively accumulates the intensity from higher lying $3/2^-$ states, which can be easily excited in (γ, n) reactions. The substantial part of neutrons will be emitted with L = 0 moment after the decay of 1^- state of giant dipole resonance via photoneutron chanel and it leads to the direct excitation of $3/2^-$ levels in the residual nuclei. Similar mechanisms of the isomer population were found in others Te isotopes [19, 20]. We modified the level structure file according to the information published in the paper [19] and performed additional calculations (open triangles in Fig. 2). We can see that calculations with updated data lead to significantly better agreement with experimental cross-section.

In the statistical model, because of averaging by the large number of overlapped states, we can neglect the matrix elements features that describe the decay of particular states. It results in a similarity of transition matrix elements, i.e. the final levels for the decay of a particular state are equal. Thus, the probability of particular transition is proportional to the final density of states and depends on the transitions multipolarity. In TALYS–1.4 calculations of the γ-transitions probabilities are derived from the gamma-ray strength functions. For E1 transitions the generalized Lorentzian form of Kopecky-Uhl was used, while for the transitions of other multipolarities -standard Lorentzian (Brink-Axel form). It should be noted that E1 transitions are dominating in calculated gamma-cascade (~90 %) with little admixture of E2 and M1 radiation

The situation is different in the low energy part of the spectra where the microscopic calculations of level structure can be performed. In paper [19] it was mentioned that all states in ^{129}Te of negative parity lower 1100 keV are only weakly populated in (d, p) which can serve as a sign for their complicated structure. The interacting boson-fermion

model (IBFM) describes states $3/2^-$ and $5/2^-$ of ^{129}Te as a mixture of the $1h_{11/2}$ neutron wavefunction as a main part with a small $3p$ component, coupled to the first 4+ state of the core [20]. The IBFM calculations reproduce well the energy of the states and confirm the enhanced E2 transitions between the levels of negative parity due to the admixed quadrupole phonons. According to the analysis of the γ-transitions between low-energy levels [18] we can see that the part of E1 transitions is extremely low. States of positive parity decay by M1 and E2 transitions and do not populate levels of negative parity. Their decay path leads to final level $J^\pi = 3/2^+$ and practically do not contribute to the population of $J^\pi = 11/2^-$ isomer. As mentioned above, the enhanced E2 transitions are observed between negative parity states. Therefore the transitions probabilities are mainly defined by their microscopic nature. It is highly possible that same is true for the higher energies described in the calculations as continuous spectra.

As it was mentioned before, the main part of Te isomers excitation cross-section belongs to the statistical mechanism. But the growth of isomeric population and cross-section of $(\gamma, n)^m$ reactions with isotopes mass increasing cannot be explained in the framework of the statistical model. It would be natural to suggest that the increasing contribution of preequilibrium processes can be responsible for that, but calculations showed that their share is too low to explain this effect. Experimental data on nuclear structure of Tellurium isotopes [18 - 20] (including ^{129}Te) suggest that growth is rather caused by redistribution of transitions between low-lying nuclear levels connected with their microscopic nature.

4. Conclusions

Isomeric yields ratio dependence on bremsstrahlung end point energy has been measured for the reactions: ^{120}Te(γ, n)^{119}Te^{m,g}, ^{122}Te(γ, n)^{121}Te^{m,g}, ^{124}Te(γ, n)^{123}Te^{m,g}, ^{128}Te(γ, n)^{127}Te^{m,g}, ^{130}Te(γ, n)^{129}Te^{m,g} in the energy region 10 - 22 MeV. The values of isomeric ratios are increasing with the filling of the subshell $1h_{11/2}$ and are highest for the ^{129}Te. The observed effect of correlation between increasing possibility of isomers $J^\pi = 11/2^-$ excitation and growing of the neutrons number on subshell $1h_{11/2}$ cannot be associated with contribution of statistical or preequilibrium mechanisms, but rather is a consequence the non-statistical distribution of gamma transition probabilities resulted from peculiarities in level structure.

The cross-sections of isomers population in all investigated reactions have been calculated with inverse matrix method. Results were compared with TALYS-1.4 calculations. Theoretical calculations revealed the dominating role of the statistical model based on Hauser - Feshbach formalism in the (γ, n) reactions In most cases calculation reproduce the cross-section and this can serve as evidence of statistical theory adequacy. But the case of ^{130}Te(γ, n)^{129}Te^m reaction showed that results of calculations significantly depends on properties of low-energy levels and transitions between them. Thus, without precise knowledge on nuclear structure, calculations of isomers excitation can produce misleading results.

REFERENCES

1. *Skibinski R. et al.* Search for three-nucleon force effects in two-body photodisintegration of ^{3}He (^{3}H) and in the time reversed proton-deuteron radiative capture process // Phys. Rev. C. - 2003. - Vol. 67. - P. 054002 (8 pages).
2. *Varlamov A.V. e.al.* Atlas of Giant Dipole Resonances. - Vienna: IAEA, 1999. - 311 p.
3. *Mazur V.M.* Excitation of Nuclear Isomeric States in Photoneutron Reactions in the Giant E1 Resonance Region // Phys. Part. Nucl. - 2000. - Vol. 31. - P. 188 - 221.
4. *Gangrsky Ju.P., Mazur V.M.* Scattering of γ-Rays from Nuclei and Excitation of Isomeric States // Phys. Part. Nucl. - 2002. - Vol. 33. - P. 158 - 196.
5. *Mohr P. et al.* Photon-induced Nucleosynthesis: Current Problems and Experimental Approaches // Eur. Phys. J. A. - 2007. - Vol. 3. - P. 357 - 269.
6. *Hauser W., Feshbach H.* The Inelastic Scattering of Neutrons // Phys. Rev. - 1952. - Vol. 87. - P. 336 - 373.
7. *Belov A.G.et al.* Excitation of Isomeric $1h_{11/2}$ States in the Reactions (γ, n) // Phys. Atomic Nuclei. - 1996. - Vol. 59**.** - P. 553 - 562.
8. *Thiep T.D. et al.* The isomeric ratios in photonuclear reactions of natural tellurium induced by bremsstrahlungs with endpoint energies in the giant dipole resonance region // J. Radioanal. Nucl. Chem. - 2011. - Vol. 289. - P. 637 - 645.
9. *Kapica S.P., V.N.Melechin.* The Microtron. - London: Harwood Academic, 1978. - 256 p.
10. *ENSDF* - Evaluated Nuclear Structure Data File. http://www.nndc.bnl.gov/ensdf/
11. *Vanska R., Rieppo R.* The Experimental Isomeric Cross-Section Ratio in the Nuclear Activation Technique // Nucl. Instr. And Meth. - 1981. - Vol. 179. - P. 525 - 532.
12. *Lepretre A. et al.* A Study of the Giant Dipole Resonance of Vibrational Nuclei in the $103 < A < 133$ Mass Region // Nucl. Phys. - 1974. - Vol. A219. - P. 39 - 60.
13. *Bogdankevich O.V., Nikolaev F.A.* Methods in Bremsstrahlung Research. - NY: Academic Press, 1996. - 198 p.
14. *Koning A.J. et al*. TALYS-1.0 // Proc. of the Int. Conf. on Nuclear Data for Science and Technology / Ed. by O. Bersillon, F. Gunsing et al. - EDP Science, 2008. - P. 211 - 214.
15. *Gadioli E., Hodgson P.E.* Pre-equilibrium Nuclear Reaction. - Oxford: Oxford University Press, 1992. - 211 p.
16. *Capote P. et al.* RIPL - Reference Input Parameter Library for Calculation of Nuclear Reactions and Nuclear Data Evaluations // Nucl. Data Sheets. - 2009. - Vol. 110. - P. 3107 - 3214.

17. *Dilg W. et al.* Level density parameters for the back-shifted Fermi gas model in the mass range 40<A<250 // Nucl. Phys. - 1973. - Vol. A217. - P. 269 - 298.
18. *Tendow Y.* Nuclear Data Sheets for A = 129 // Nucl. Data Sheets. - 1996. - Vol. 77. - P. 631 - 770.
19. *Wirth H.F. et al.* Nuclear structure of ^{129}Te studied with (n, γ), (d, p) and (d, t) reactions // Nucl. Phys. -2003. - Vol. A726. - P. 3 - 54.
20. *Bondarenko V. et al.* Origin of the anomalous population of long-lived isomers in odd-*A* Te isotopes // Phys. Rev. C. - 1999. - Vol. 60. - P. 027302 (4 pages).

THE POSSIBILITY OF OBSERVING GAMMA RADIATION ASSOCIATED WITH THE FORMATION AND PRE-EQUILIBRIUM EMISSION OF ALPHA PARTICLES IN NUCLEUS-NUCLEUS COLLISIONS

L. V. Mikhailov

Institute for Nuclear Research, National Academy of Sciences of Ukraine, Kyiv, Ukraine

Introduction

Currently, despite the accumulation of extensive experimental and theoretical data, the problem of education and pre-equilibrium emission of light charged particles and γ-rays in the process of formation and decomposition of strongly heated nuclear systems of greatest interest in the study of nuclear reactions with heavy ions. This is due to several reasons. First, the cross section for light charged particles is large (comparable to the total cross section of the reaction), which is a characteristic of the process of nucleus-nucleus collisions, the understanding of which is impossible without an understanding of the mechanism of formation of these particles. Secondly, the properties of energy, mass and angular distributions of charged particles emitted by the light appeared, as shown by experimental studies, largely unexpected, and sometimes difficult to explain. Finally, the experiments revealed that a significant portion of the particles emitted in the initial stage of interaction of the two nuclei, and, therefore, has direct information about the dynamics of this interaction, in contrast to the decay products of the composite system.

It is considered that the pre-equilibrium complex particles are formed before the emission of the heated core (or hot zone) of the quasi-free nucleons or simple clusters (coalescence) having similar momentum distributions in the direction of emission of complex particles. This mechanism of light particles, for example, (d + d = α, p + t = α, etc.) in the zone of interaction of heavy nuclei is presented in [1], in which the model has been successfully applied coalescence of fragments. Coalescence model is typically used to describe the formation of light and medium composite particles at intermediate energies of the colliding nuclei, when multiple production of nucleons and fragments comparable. The information obtained in this model, is optional for the results obtained for two protons, two deuterons, as well as for the Coulomb correlation of the two heavy pieces, such as carbon. This complements correlation measurements of light fragments [2] and as other temperature-dependent nucleon coalescence model, this model provides a source size of fragments of a given mass and velocity. If the nucleons and light fragments are determined by the same radius of the source and the time of life, the present model predicts the same radius of the source, as a nucleon- coalescence model, however, the present model gives a more realistic results radii coalescence fragments. The advantage of this model is that it does not require long high statistics measurements in space relative to small pulses. Therefore, it can be used for data measured by one detector, assuming that the impact parameter is limited, and that the radiation from the source is suppressed. You do not need high resolution in momentum, as in the case of interferometric measurements, which allow to perform the analysis of data of plants with poorer resolution, but with the kinematic range.

Formulation of the problem

Direct experimental evidence of coalescence of strongly heated by the decay of nuclei is not currently available. However, in [3] in the reaction ^{7}Li photodisintegration observed γ-peak at 8.5 MeV, corresponding to the binding energy of tritium. Methodological and experimental results using the technique Registered γ-rays and charged particles in order to study the dynamics of interaction of complex nuclei are presented in [4-6]. Based on the observation of the peak γ-rays and measure its width (150 KeV) concluded that within the nucleus ^{7}Li before emission triton cluster is formed from ^{3}H quasifree nucleons and the duration of this process is 10 - 21 s. In [3] also noted that similar peaks in the spectrum of photons must accompany any reaction in which the particles are formed before its emission from the nucleus. If we assume, for example, α-particle is formed in the hot core before leaving quasifree nucleons or other clusters, and this process is accompanied by the emission of γ-rays in accordance with the channel coalescence, then the following options:

1. p + p + n + n = ^{4}He + γ (28,3 MeV)
2. d + d = ^{4}He + γ (23,85 MeV)
3. n + ^{3}He = ^{4}He + γ (20,6 MeV)
4. p + T = ^{4}He + γ (19,8 MeV)

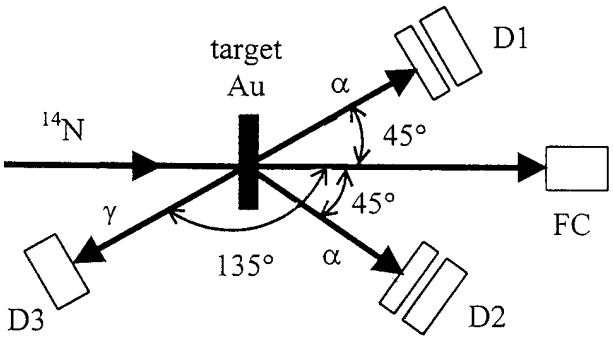

Thus the formation of α-particles of protons and neutrons (1) together with the α-particle emissions be emitted γ-rays with energy E = 28.3 MeV. Coalescer deuteron (2) E = 23.85 MeV neutron and ^{3}He (3) E = 20.6 MeV proton and triton E = 19.8 MeV (4). Potential of an experiment to study the formation of α-particles in the reaction ^{14}N + ^{198}Au at energy E(^{14}N) = 700 MeV is presented in the Figure.

Detectors D1 and D2 are used to measure α-particles and their identification. D3 detector measures the energy γ-spectrum in coincidence with α-particles entering the detector D1 or D2. FC-Faraday cup. Measurement of the two spectra with the detector D3 in coincidence with α-detectors D1 and D2 can suppress γ-background caused by the coincidence of conventional brake γ-rays with α-particles. Spectra measured detector D3, has a peak due to the emission of γ-rays from the α-particles measured by the detector D1, which is 18-20% shifted to lower the amount of energy due to the Doppler effect, compared with that of γ-peak, measured detector D2. Subtract one from the other allows spectra inhibit γ-radiation due to the coincidence of conventional brake γ-rays with α-particles.

Conclusions

1. In this paper the experiment to study the emergence of the γ-quants with energy equal to the binding energy of the composite particles emitted from the interaction region of nucleus-nucleus collisions.

2. If this effect will be detected and recorded above the background of the bremsstrahlung γ-quants, a new method for the experimental study of the γ-emission of brake mechanism of the discharge strongly heated nuclear systems.

REFERENCES

1. *Llope W.J. et al.* The fragment coalescence model // Physical Review. C. - 1995. - Vol. 52. - P. 2004 - 2012.
2. *Jacak B.V. et al.* Coalescence of complex fragments // Physical Review. C. - 1985. - Vol. 31. - P. 704 - 706.
3. *Ishkhanov B.S. et al.* Radiative transitasions accompanying photofission of lithium // Nuclear Physics. - 1981. - Vol. 33. - P. 28 - 32.
4. *Kamanin V.V. et al.* Experimental evidence for the emission of high-energy gamma-rays from the dinuclear system formed at the first stage of the fusion reactions Sn + Ne // Z. Physic A. Atomic Nuclei. - 1990. - No. 337. - P. 111 - 113.
5. *Fomichev A.S. et al.* A note on application of CsI (Tl) counte to light charget particle detection in the spontaneous fission of ^{252}Cf // Nuclear Instruments and Methods. - 1996. - Vol. A368. - P. 852 - 854.
6. *Sobolev Yu.G. et al.* A multimodule (MULTI) spectrometer of light charged particles in the 16-230 MeV/A energe rang // Instruments and Experimental Techniques. - 1997. - Vol. 40, No. 5. - P. 149 - 153.

SPECTRA OF NUCLEI ^{9}Be AND ^{9}B IN A THREE-CLUSTER MICROSCOPIC MODEL

A. V. Nesterov, V. S. Vasilevsky, T. P. Kovalenko

M. M. Bogolyubov Institute for Theoretical Physics, National Academy of Sciences of Ukraine, Kyiv, Ukraine

Within a microscopic three-cluster α + α + n(p) model, which is a three-cluster version of the algebraic approach to the Resonating Group Method (RGM), we consider the spectra of the low-lying states of mirror nuclei ^{9}Be and ^{9}B in the energy range from zero to 5 MeV excitation. The obtained theoretical results are compared with the available experimental data.

Introduction

We will study the spectra of low-lying states of nuclei ^{9}Be and ^{9}B. As is known, nucleus ^{9}Be is bound only in the ground state, whereas nucleus ^{9}B, which is the mirror one relative to ^{9}Be, has no bound states at all. In other words, except for the ground state of nucleus ^{9}Be, we will deal mainly with resonance states, the interest in which is determined by a number of the following factors.

The study of the low-lying states of nucleus ^{9}Be is of interest for astrophysics, in particular for the problem of nuclear synthesis of elements. The resonances lying above the threshold of disintegration of ^{9}Be determine the rate of synthesis of this nucleus under the bursts of supernovas. At sufficiently high concentrations of neutrons and alpha-particles in a star, the radiative capture reaction α(αn, γ)^{9}Be can run with high rate in the resonance mode. This reaction is followed by ^{9}Be(α, n)^{12}C [1, 2]. Along with the three-alpha capture α(αα, γ)^{12}C, the mentioned reactions can play a significant role in overcoming the barrier for the creation of elements with A > 8. This barrier is related to the absence of bound states of the nuclei with A = 5 and A = 8 (^{5}H, ^{5}Li, ^{8}Be), i.e., to the so-called “mass dip”.

Of interest is also the comparison of the spectra of the low-lying states of mirror nuclei ^{9}Be and ^{9}B presenting the example of the influence of the Coulomb interaction of protons on the spectra of light atomic nuclei. Especially, this concerns the states $½^+$, $½^-$, and $5/2^+$. Despite the many-year efforts, there is no complete information about the energies and the widths of these resonances. In particular, the spins are known not for all states. Especially, this is true for ^{9}B. Moreover, its state $½^+$, which is analogous to that with an excitation energy of 1.68 MeV in nucleus ^{9}Be, was not given in the recent compiled work [3] among the detected experimentally states of nucleus ^{9}B.

The interest in the situation concerning these nuclei is manifested in a large number of experimental [4 - 11] and theoretical works [12 - 21] (we have indicated only a part of them) devoted to the consideration of properties of nuclei ^{9}Be and ^{9}B.

The choice of a model for the description of properties of the nuclei under consideration is determined by the domination of the three-cluster channels α + α + n and α + α + p at small energies. The threshold energies of these channels are minimal among all channels. We note that the next-in-energy threshold of the channel ^{7}Li + d in nucleus ^{9}Be (and ^{7}Be + d in ^{9}B), where the α-cluster is broken, is much higher than the threshold of the three-cluster channel (more than 15 MeV). Moreover, the α-clusters themselves have no excited states below approximately the same energy. Therefore, it is possible to assume surely that the low-energy spectrum of these nuclei is formed by the three-cluster channels α + α + n and α + α + p, where the density distribution for nucleons in α-clusters can be considered frozen. This is also indicated by the energy position of the bound state of nucleus ^{9}Be: it is near the threshold of α + α + n, by 1.57 MeV below. It is worth noting that the three-cluster systems under consideration have no bound binary subsystems. In this case, the lifetimes of nuclei ^{8}Be and ^{5}He in the ground state are, respectively, $0.97 \cdot 10^{-16}$ and $1.1 \cdot 10^{-21}$ s ($4.4 \cdot 10^{-22}$ s for ^{5}Li). This indicates that the cluster representation α + α + n (α + α + p) for nucleus ^{9}Be (^{9}B) dominates at comparatively low energies. This circumstance must be taken into account in a model for nuclei ^{9}Be and ^{9}B.

In the present work, we use the microscopic approach as such one, namely the three-cluster algebraic version of the Resonating Group Method (see details in [22, 23]), where the function of relative motion of clusters is expanded in the eigenfunctions of a six-dimensional harmonic oscillator in hyperspherical coordinates.

The main positions of the model in use are briefly presented in Section 2, and the results are given in Section 3.

Method

The many-particle wave function of a three-cluster system consisting of A nucleons ($A = A_1 + A_2 + A_3$)with the full account for the antisymmetrization can be represented as

$$\Psi(\mathbf{q}_1,..,\mathbf{q}_{A-1}) = \hat{\mathcal{A}}\left[\Psi_1(A_1)\,\Psi_2(A_2)\,\Psi_3(A_3)\,\Psi_Q(Q)\right], \quad (1)$$

where $\hat{\mathcal{A}}$ is the operator of antisymmetrization. In this case, we assume that the center-of-mass coordinate for the A-nucleon system is excluded by the transition to the Jacobi coordinates $\mathbf{q}_i$. This reduces the problem to the consideration of the internal dynamics of the system. The functions $\Psi_i(A_i)$ set the internal structure of the i-th cluster. The function

$$\Psi_Q(Q) = \Psi_Q(\mathbf{q}_1, \mathbf{q}_2) \tag{2}$$

characterizes the relative motion of clusters, depends on the Jacobi coordinates $\mathbf{q}_1$ and $\mathbf{q}_2$, and can be expanded in the approach under consideration in the basis of a six-dimensional harmonic oscillator.

Since the wave functions of clusters are fixed in our case and are constructed only on the ($0s$)-orbitals, the problem of classification of the states of the system after the expansion of the function of relative motion in the basis is completely transferred onto the basis states describing the intercluster motion. In our specific case, such basis states are the eigenfunctions of a six-dimensional harmonic oscillator $|n_\rho, K, l_1, l_2, LM>$. They are characterized by the hypermoment K, the number of quanta of hyperradial excitations n_ρ, partial angular momenta l_1 and l_2 connected with the first and second Jacobi vectors, respectively, the total angular momentum L produced by the coupling of the partial momenta l_1 and l_2, and its projection M. In this case, the relation $N = 2n_\rho + K$ holds for each oscillator shell with the principal quantum number N.

The expansion of the wave function of relative motion

$$\Psi_Q(\mathbf{q}_1, \mathbf{q}_2) = \sum_\nu C_\nu \Psi_\nu(\mathbf{q}_1, \mathbf{q}_2), \tag{3}$$

where $\{\Psi_\nu\} \equiv |n_\rho, K, l_1, l_2, LM>$ ($\nu = \{n_\rho, K, (l_1 l_2) LM\}$), leads to the infinite system of algebraic equations

$$\sum_{\nu'} \left[<\nu|\hat{H}|\nu'> - E <\nu|\nu'> \right] C_{\nu'} = 0 \tag{4}$$

for the coefficients C_ν. Totally, these coefficients determine the wave function in the oscillator representation.

System (4) is a consequence of both the choice of a trial function in the form (1) and expansion (3), while solving the many-particle Schrödinger equation. The quantities $<\nu|\hat{H}|\nu'>$ and $<\nu|\nu'>$ are matrix elements of the Hamiltonian and the identity operator on the antisymmetrized many-particle basis functions $|\nu> = |n_\rho, K, l_1, l_2, LM>$. The presentation of the technique of calculations of these quantities required for the following consideration is omitted here for brevity (see works [22, 23] and references therein). We note only that, like the solution of the problems with a continuous or discrete spectrum, where the asymptotic formulas for the wave functions at large distances in the coordinate representation are used to set the boundary conditions, the solution in the oscillator representation involves a practically equivalent procedure. At large values of the number of radial oscillator quanta for the relative motion of clusters, we use again the asymptotic formulas, but already for the expansion coefficients C_ν.

In view of the results of works [24, 25], the expansion coefficients $C_{n_\rho}^{(\pm)}$ corresponding to incoming and outgoing waves can be presented at large values of the number of quanta of hyperradial excitations n_ρ as follows:

for uncharged clusters,

$$C_{n_\rho}^{(\pm)K} \simeq \sqrt{2} \left\{ \begin{matrix} H_{K+2}^{(1)}\left(k\rho_{n_\rho}\right) \\ H_{K+2}^{(2)}\left(k\rho_{n_\rho}\right) \end{matrix} \right\}, \tag{5}$$

in the presence of the Coulomb interaction,

$$C_{n_\rho}^{(\pm)K} \simeq \sqrt{2} \left\{ \begin{matrix} W_{i\eta, K+2}\left(2ikb\rho_{n_\rho}\right) / \sqrt{\rho_{n_\rho}} \\ W_{-i\eta, K+2}\left(-2ikb\rho_{n_\rho}\right) / \sqrt{\rho_{n_\rho}} \end{matrix} \right\}. \tag{6}$$

In formulas (5) and (6), $k = \sqrt{\dfrac{2mE}{\hbar^2}}$, the letters H and W stand for the Hankel and Whittaker functions, respectively, $\rho_{n_\rho} = b\sqrt{4n_\rho + 2K + 6}$, b is the oscillator radius, and η is the Sommerfeld parameter.

We note that the asymptotic solutions for neutral (uncharged) clusters depend exclusively only on the hypermoment K, rather than on all values of quantum numbers. In this case, the channels with different K are uncoupled. In this sense, it is logical to represent the compound index $\nu = \{n_\rho, K, (l_1 l_2) LM\}$ as $\nu = \{K, \nu_0\}$, by separating K among other quantum numbers. The asymptotic solutions for charged clusters depend on K and the partial angular momenta (see

[29] for details). For short-range forces, the decoupling of channels ar large values of n_ρ poses practically no problems. The case of Coulomb forces requires a somewhat higher attention, but we omit the discussion of related questions analyzed in works [22, 23]. Finally, we deal with the situation where the states with different K and ν_0 are connected by means of nuclear and Coulomb forces only in the internal domain (the interaction domain), i.e., we arrive at the approximation of coupled channels.

For the consideration of the asymptotics, it is convenient to write our system of equations in the form

$$\sum_{K',m_\rho} \left\langle n_\rho, K \left| \hat{H} - E \right| m_\rho, K' \right\rangle C_{m_\rho}^{K'} = 0, \tag{7}$$

where K stands for the collection of all indices except for n_ρ.

Since we will use the S-matrix formalism while solving the scattering problem, we represent the expansion coefficients $C_{n_\rho}^{K}$ at large values of n_ρ as

$$C_{n_\rho}^{K} = C_{n_\rho}^{(0)K} + \delta_{K_i K} C_{n_\rho}^{(-)K} - S_{K_i K} C_{n_\rho}^{(+)K}, \tag{8}$$

where, for each of K-channels, $C_{n_\rho}^{(0)K}$ is the so-called residual coefficient, and $C_{n_\rho}^{(\pm)K}$ are asymptotic coefficients related to convergent and divergent waves. The matrix elements $S_{K_i K}$ describe the coupling between the output channel K and the input channel K_i.

The substitution of (8) in the equations of system (7) gives the system of dynamical equations for the multichannel problem. This system of equations will be solved in order to determine the residual coefficients $C_{n_\rho}^{(0)K}$ and the S-matrix elements $S_{K'K}$.

In order to optimally obtain the most exact approximation in the solution of the system, we will distinguish some internal domain with $n_\rho \le N_\rho$ and the asymptotic domain with $n_\rho > N_\rho$. The choice of N_ρ should be such that the expansion coefficients $\left\{ C_{n_\rho}^{(0)K} \right\}$ be characterized by the essential smallness in the asymptotic domain.

Solving the system of dynamical equations for each of N_{ch} input channels, we obtain the S-matrix $\| S_{\nu,\nu'} \|$, which contains a detailed information about the elastic and inelastic processes in the three-cluster system. It is convenient to analyze the S-matrix, by transforming it to the diagonal form. Such a representatioin of the S-matrix is usually called the representation of eigenchannels and leads to the so-called eigenphases of scattering δ_α:

$$S_\alpha = \exp\{2i\delta_\alpha\}, \qquad \alpha = 1, 2, \ldots N_{ch}, \tag{9}$$

where α enumerates the uncoupled eigenchannels.

The eigenphases of scattering are used to determine the parameters of resonances such as their energies and widths. With the help of the well-known formula for the r-th resonance in the α-eigenchannel, it is easy to find the energy and the width of a resonance:

$$\left. \frac{d^2\delta_\alpha}{dE^2} \right|_{E=E_{\alpha,r}} = 0, \quad \Gamma = 2 \left(\frac{d\delta_\alpha}{dE} \right)^{-1} \Bigg|_{E=E_{\alpha,r}}. \tag{10}$$

Results

The results presented in this section are obtained with the Minnesota potential, whose central part is taken from work [26], and the spin-orbit one from work [27] (version IV). In calculations, the oscillator radius *b* was taken to be 1.285 Fm. This value of *b* minimizes the binding energy of each separate α-particle. The value of exchange parameter *u* in the potential is determined to be such that the binding energy for the ground state of nucleus ^{9}Be relative to the α+α+n threshold is reproduced. To attain the suitable accuracy of calculations, we used all hyperharmonics with hypermoments $K \le 13$ and $K \le 14$ for the states with negative and positive parities, respectively, and took the values of n_ρ from zero to 70 for each of the channels. The total number of basis functions used in calculations exceeded 3000. The solution of the problem is somewhat simplified by the fact that the binary α-α subsystem has only even momenta of the relative motion of clusters due to the symmetry.

The choice of the Minnesota potential as a nucleon-nucleon one is not accident. This potential was most frequently used in microscopic calculations of the properties of light atomic nuclei and, in particular, ^{9}Be and ^{9}B [12, 15, 17]. This circumstance facilitates the comparison of our results with those obtained in the other theoretical works. We note that the exchange parameter u of the potential in the mentioned works was chosen to be 0.94 in order to reproduce the properties of the binary subsystems α+α and α+nucleon most properly. However, such a choice of the parameter u implies that nucleus ^{9}Be becomes overbound, and a bound state appears in nucleus ^{9}B.

Prior to the calculation of the three-cluster systems, we studied how strongly the choice of the parameter u of the Minnesota potential affects the characteristics of the resonance states of two-cluster subsystems. In Table 1, we show the energies and the widths of resonances of nuclei ^{8}Be, ^{5}He, and ^{5}Li calculated with $u = 0.928$ and $u = 0.94$.

Table 1. **Comparison of the parameters of the resonance states of two-cluster subsystems calculated with $u = 0.928$ and $u = 0.940$ with experiments. The energies and the widths of the resonance states are given in MeV**

		Algebraic version of RGM				Experiment	
		$u = 0.928$		$u = 0.94$			
Nucleus	J^{π}	E	Γ	E	Γ	E	Γ
^{8}Be	0^{+}	0.17	$7.15 \cdot 10^{-4}$	0.02	$1.03 \cdot 10^{-7}$	0.09	$5.6 \cdot 10^{-6}$
	2^{+}	3.09	1.81	2.93	0.51	3.13	0.51
	4^{+}	12.91	5.63	12.57	5.02	11.5	~ 3.50
^{5}He	$3/2^{-}$	1.06	1.17	1.00	1.04	0.80	0.65
	$1/2^{-}$	2.26	8.63	2.24	8.38	2.07	5.57
^{5}Li	$3/2^{-}$	1.93	2.00	1.86	1.80	1.69	1.23
	$1/2^{-}$	3.11	10.24	3.10	9.96	3.18	6.60

The results of calculations of the spectra of nuclei ^{8}Be, ^{5}He, and ^{5}Li performed by us with u=0.94 are in good agreement with experimental data. Naturally, the decrease of u to 0.928 somewhat increases the energies of the resonances and their widths, since the odd components of the nucleon-nucleon potential grow, but their values remain reasonable.

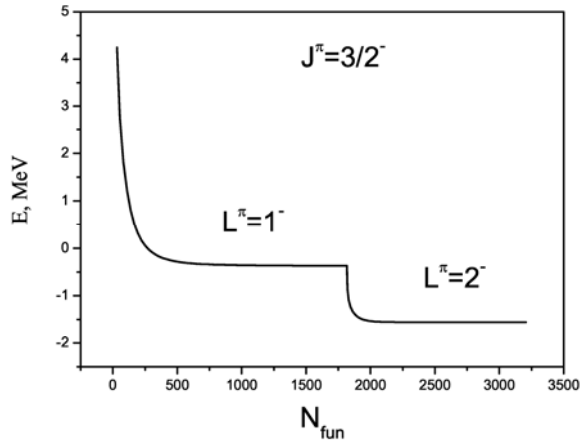

Fig. 1. Binding energy of the ground state of nucleus ^{9}Be versus the number of basis functions used in calculations.

In brief, we consider the results obtained for the ground state of nucleus ^{9}Be. It is a bound state, and we can trace easily the convergence of its energy with the use of Fig. 1, as the basis is extended. In this Figure, we present the binding energy E versus the total number of basis states N_{fun} used in the calculation. The breaking point on the curve is located at the point, where the basis functions with $L^{\pi} = 2^{-}$ are added to the states with $L^{\pi} = 1^{-}$. At this point, the energy becomes negative (becomes less than the three-particle threshold), which indicates the importance of the consideration of spin-orbit forces. We recall that this calculation was performed with the maximum value of hypermoment ($K = 13$).

For the analysis of the size of nucleus ^{9}Be, we present the proton, neutron, and mass rms radii calculated by us: $R_{\text{p}} = 2.27$ Fm, $R_{\text{n}} = 2.46$ Fm, and $R_{\text{m}} = 2.38$ Fm. As would be expected, the radius of the neutron cloud is larger than that of the proton one. We can compare the proton radius with the experimental values. For example, the recent work [28] gives $R_{\text{p}} = 2.519(12)$ Fm, which is close to the result in [17] and can indicate the higher clusterization of the nucleus than that in our model. On the whole, the experimental data deviate to the larger side from ours not so strongly (see, e.g., [3], where $R_{\text{p}} = 2.39(17)$ Fm).

To give a more complete information about the structure of the ground-state wave function of nucleus ^{9}Be, we present Fig. 2 showing the weight W_{sh} of the contribution of each oscillator shell to the wave function, which is normalized to 1. The shells are successfully enumerated so that the shell number N_{sh} corresponds to the principal quantum number $N = 2 \cdot N_{\text{sh}} + 3$. The plot is cut on the right side at $N_{\text{sh}} = 22$, though the calculation involved all functions of 70 oscillator shells. The plot indicates that the wave function is distributed over a rather large number of shells, which is a manifestation of the strong clusterization of the nucleus.

Before the consideration of the resonance states of nuclei ^{9}Be and ^{9}B, we recall that our main tool for the determination of parameters of the resonance states are the eigenphases of scattering. Their behavior is shown by Fig. 3 presenting the dependence of the eigenphases of scattering on the energy for the state $J^{\pi} = 3/2^{-}$ of nucleus ^{9}Be. From three curves, only one reveals the resonance behavior, which allows us to obtain, with the use of (10), the resonance parameters. To complete the pattern, we note that the resonance can manifest itself in some cases in at least two eigenphases.

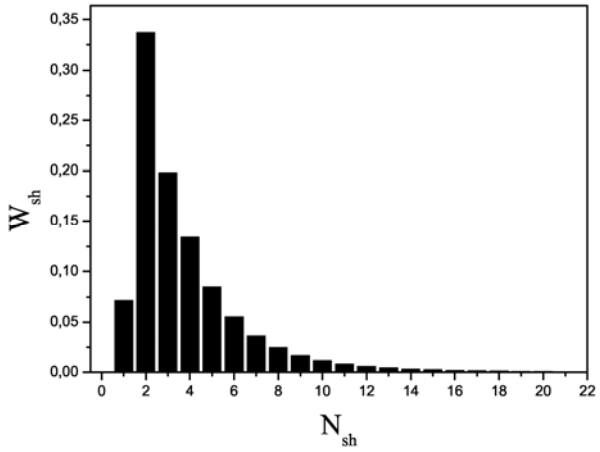

Fig. 2. Contributions of various oscillator shells to the ground state of nucleus ^{9}Be.

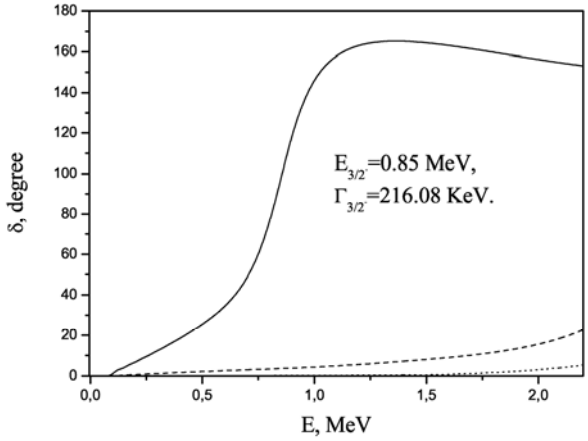

Fig. 3. Eigenphases of scattering for the state $J^{\pi}=3/2^{-}$ of nucleus ^{9}Be.

The basic quantitative characteristics of the bound and resonance states of nuclei ^{9}Be and ^{9}B, obtained in our calculations, are presented in Tables 2 and 3 together with relevant experimental data. In these calculations, we limited ourselves by the excitation energies at most 5 MeV. From the viewpoint of the shell model, these are the energies, at which the states of valent neutron (proton) dominate.

Table 2. **Parameters of the lowest states of nucleus ^{9}Be. The energy is mesured from the α + α + n threshold**

		Algebraic version of RGM				Experiment [3]	
		First state		Second state			
Nucleus	J^{π}	*E,* MeV	Γ, keV	*E*, MeV	Γ, keV	*E,* MeV ± keV	Γ, keV
^{9}Be	$3/2^{-}$	-1.56	-	0.85	261.08	-1.57	-
	$1/2^{+}$	0.25	14.63	-	-	0.11 ± 7	217 ± 10
	$5/2^{-}$	0.99	0.54	2.11	448.24	0.85 ± 1.3	0.78 ± 13
	$1/2^{-}$	0.79	142.77	1.68	458.23	1.23 ± 120	1080 ± 110
	$5/2^{+}$	1.48	315.92	2.60	264.30	1.48 ± 9	282 ± 11

Table 3. **Parameters of the lowest he states of nucleus ^{9}B. The energy is mesured from the α + α + p threshold**

		Algebraic version of RGM				Experiment [3]	
		First state		Second state			
Nucleus	J^{π}	*E,* MeV	Γ, keV	*E,* MeV	Γ, keV	*E*, MeV ± keV	Γ, keV
^{9}B	$3/2^{-}$	0.29	0.39	1.30	460.99	0.28	0.54 ± 21
	$1/2^{+}$	0.59	121.65	-	-	-	-
	$5/2^{-}$	2.60	692.67	2.77	31.48	2.64 ± 5	81 ± 21
	$1/2^{-}$	1.44	185.13	2.83	587.33	3.03 ± 300	3.130 ± 20
	$5/2^{+}$	1.90	459.19	3.77	851.76	3.07 ± 30	550 ± 40

It is seen at once that the region of energies under study includes two resonance states, whereas only one state is observed in experiments. It is worth noting that we have already met a similar situation, for example, in the calculation of parameters of the 0^{+} and 2^{+} resonances of nuclei ^{6}He and ^{6}Be. At the reasonable agreement with experiments, we obtained also some resonances with higher energies and large widths [29].

First, such a situation was perceived by us as some drawback of our approach caused by a too high kinematic barrier in the three-particle exit channels. However, the calculations performed with the Complex Scaling Method [30, 31], which is not related to the hyperspherical basis and the form of boundary conditions, indicate also the possibility of the existence of similar resonances.

The spectra of nuclei ^{9}Be and ^{9}B are much richer than those of ^{6}He and ^{6}Be; therefore, the situation turns out, naturally, more complicated. We obtained an underestimated width of the $1/2^{+}$- state of nucleus ^{9}Be. But, on the whole, our results concerning the "first states" describe sufficiently well the experiment in all cases except for the state $1/2^{-}$. Possibly, we must compare the second higher-energy resonance with experimental data for nucleus ^{9}B (e.g., $5/2^{-}$-state) rather than the first one with the hope for that the low-energy states have not yet observed experimentally. This is quite possible, since the spectra of these nuclei, especially ^{9}B, are difficult to be studied due to the large number of overlapping states. Moreover, these nuclei are not the very convenient objects for experimental studies.

Among the states of nucleus ^{9}B, the $1/2^{+}$-state is of special interest. As was mentioned above, this state was not

included in the spectra in the recent work [3], though its existence was discussed many times in experimental works (see, e.g., [4, 32 - 35] and references therein), where its excitation energy varied from 0.8 to 1.8 MeV, and the width did from 400 to 1300 keV. For this state, we predict a very low excitation energy of about 0.3 MeV and a width of 122 keV, which are less than those in available theoretical works. For example, $E_x = 1.0$ MeV, $\Gamma = 1.8$ MeV [36]; $E_x = 0.94$ MeV, $\Gamma = 1.64$ MeV [16]; $E_x = 1.3$ MeV, $\Gamma = 2.0$ MeV [37]; and $E_x = 1.2$ MeV, $\Gamma = 1.3$ MeV [12]. In this case, we recall that the analogous state $½^+$ in nucleus ^{9}Be obtained by us has a reasonable value of excitation energy, but the width is less than the experimental one.

As was indicated above, the problem under consideration is many-channel one. It includes the specific channels, which can be classified with the help of the hypermoment K and the partial momenta l_1 and l_2. In this case, we associate the partial momentum l_2 to the binary subsystem α-α. The technique of determination of the partial decay widths for such channels was proposed in [38]. Our experience of the calculation of partial widths indicates that the total width is usually composed by a small number of channels with the minimum values of hypermoment K and with the relevant values of partial angular momenta. Probably, this is caused by the fast increase in the height and the width of the kinematic barrier with K for three-particle-decay channels. For the comparatively narrow resonances, with which we deal in the present work, the width is determined by only a single channel. Indeed, 99 % of the total width of the state of nucleus ^{9}Be with $E_{3/2^-} = 0.85$ MeV, $\Gamma_{3/2^-} = 261.08$ keV are determined by the channel with $K = 1$, $l_1 = 1$, $l_2 = 0$, and the total width of the state of the same nucleus with $E_{1/2^+} = 0.25$ MeV, $\Gamma_{1/2^+} = 14.63$ keV is completely determined by the channel with $K = 0$, $l_1 = 0$, $l_2 = 0$.

Conclusions

Within the three-cluster microscopic model, we have studied the spectrum of the low-lying states of nuclei ^{9}Be and ^{9}B. To classify the channels of the three-cluster continuum, we used the basis of hyperspherical functions. In the numerical calculations of the bound and resonance states of these nuclei, we involve a large number of hyperspherical and hyperradial states to achive the convergence of results with suitable accuracy. It is shown that the theory reproduces satisfactorily the experimental structure of excited states of nuclei ^{9}Be and ^{9}B. It turns out that our theoretical spectrum contains more states, than the available experimental one. The dominating channels of decay of three-cluster resonances are revealed.

REFERENCES

1. *Woosley S.E.R., Hoffman R.I.* The alpha-process and the r-process // Astrophys. J. Part 1. - 1992. - Vol. 395, No. 1. - P. 202 - 239.
2. *Meyer B.S., Mathews G.J., Howard W. M. et al.* R-process nucleosynthesis in the high-entropy supernova bubble // Astrophys. J. Part 1. - 1992. - Vol. 399, No. 2. - P. 656 - 664.
3. *Tilley D.R., Kelley J.H., Godwin J.L. et al.* Energy levels of light nuclei A = 8, 9, 10 // Nucl. Phys. A. - 2004. - Vol. 745, Issue 3 - 4. - P. 155 - 362.
4. *Tiede M. A., Robson N. R., Caussyn D. et al.* Measurement of low-lying states in ^{9}B Phys. Rev. C - 1995. - Vol. 52. - Issue 3 - P.1315 - 1325.
5. *Shoda K., Tanaka T.* Clusters in the photodisintegration of ^{9}Be // Phys. Rev. C. - 1999. - Vol. 59, No. 1. - P. 239 - 251.
6. *Akimune H., Fujimura M., Fujiwara M. et al.* Evidence for a 3.8 MeV state in ^{9}B // Phys. Rev. C. - 2001. - Vol. 64. - Issue 4. - P. 041305(R).
7. *Utsunomiya H., Yonezawa Y., Akimune H. et al.* Photodisintegration of ^{9}Be with laser-induced Compton backscattered γ-rays // Phys. Rev. C. - 2001. - Vol. 63, Issue 1. - P. 018801.
8. *Fulton B.R., Cowin R.L., Woolliscroft R.J. et al.* Exclusive breakup measurements for ^{9}Be // Phys. Rev. C. - 2004. - Vol. 70, Issue 4. - P. 047602.
9. *Prezado Y., Borge M.J.G., Diget Aa. et al.* Low-lying resonance states in the ^{9}Be continuum // Phys. Lett. B. - 2005. - Vol. 618, Issue 1 - 4. - P. 43 - 50.
10. *Papka P., Brown T.A.D., Fulton B.R. et al.* Decay path measurements for the 2.429 MeV state in 9Be: Implications for the astrophysical $\alpha + \alpha + n$ reaction // Phys. Rev. C. - 2007. - Vol. 75, Issue 4. - P. 045803.
11. *Burda O., Von Neumann-Cosel P., Richter A. et al.* Resonance parameters of the first 1/2+ state in ^{9}Be and astrophysical implications // Phys. Rev. C. - 2010. - Vol. 82, Issue 1. - P. 015808.
12. *Descouvemont P.* ^{9}Be and ^{9}B nuclei in a microscopic three-cluster model // Phys. Rev. C. - 1989. - Vol. 39, No. 4. - P. 1557 - 1562.
13. *Voronchev V.T., Kukulin V.I., Pomerantsev V.N., Ryzhikh G.G.* Three-Body Calculations of A = 9 Nuclei with Supersymmetric α-α Potentials // Few-Body Systems. - 1995. - Vol. 18, Issue 2 - 4. - P. 191 - 202.
14. *Barker F.C.* Energy of the first excited state of ^{9}B // Phys. Rev. C. - 1996. - Vol. 53, No. 5. - P. 2539 - 2541.
15. *Arai K., Ogawa Y., Suzuki Y., Varga K.* Structure of the mirror nuclei ^{9}Be and ^{9}B in a microscopic cluster model // Phys. Rev. C. - 1996. - Vol. 54, No. 1. - P.132 - 146.
16. *Efros V.D, Bang J.M.* The first excited states of ^{9}Be and ^{9}B // Eur. Phys. J. A. - 1999. - Vol. 4, Issue 1. - P. 33 - 39.
17. *Arai K., Descouvemont P., Baye D., Catford W.N.* Resonance structure of ^{9}Be and ^{9}B in a microscopic cluster model

// Phys. Rev. C. - 2003. - Vol. 68, Issue 1. - P. 014310.
18. *Arai K.* Resonance structure of ^{9}Be and ^{10}Be in a microscopic cluster model // Nucl. Phys. A. - 2004. - Vol. 738. - P. 342 - 346.
19. *Grigorenko L.V., Zhukov M.V.* Three-body resonant radiative capture reactions in astrophysics // Phys. Rev. C. - 2005. - Vol. 72, Issue 1. - P. 015803.
20. *Theeten M., Baye D., Descouvemont P.* Comparison of local, semi-microscopic, and microscopic three-cluster models // Phys. Rev. C. - 2006. - Vol. 74, Issue 4. - P. 044304.
21. *Filikhin I., Suslov V.M., Vlahovic B.* ^{9}Be Low-Lying Spectrum Within a Three-Cluster Model // Few-Body Syst. - 2010. - Vol. 50, Issue 1 - 4. - P. 255 - 257.
22. *Vasilevsky V.S., Nesterov A.V., Arickx F., Broeckhove J.* Algebraic model for scattering in three-s-cluster systems. I. Theoretical background // Phys. Rev. C. - 2001. - Vol. 61. No. 3. - P. 034606.
23. *Nesterov A.V., Arickx F., Broeckhove J., Vasilevsky V.S.* Three-cluster description of properties of light neutron- and proton-rich nuclei in the framework of the Algebraic Version of the Resonating Group Method // Phys. Part. Nucl. - 2010. - Vol. 41, No. 5. - P. 716 - 765.
24. *Филиппов Г.Ф. ,Охрименко И.П.* О возможности использования осцилляторного базиса для решения задач непрерывного спектра // ЯФ - 1980. - Т. 32, вып. 4(10). - С. 932 - 939.
25. *Vasilevsky V.S., Arickx F.* Algebraic model for quantum scattering: reformulation, analysis and numerical strategies // Phys. Rev. A. - 1997. - Vol. 55, Issue 4. - P. 265 - 286.
26. *Thompson D.R., Lemere M., Tang Y.C.* Systematic investigation of scattering problems with the resonating-group method // Nucl. Phys. A. - 1977. - Vol. 286, Issue 1. - P. 53 - 66.
27. *Reichstein I., Tang Y.C.* Study of N + α system with the resonating-group method // Nucl. Phys. A. - 1970. - Vol. 158, Issue 2. - P. 529 - 545.
28. *Nörtershäuser W., Tiedemann D., Žáková M. et al.* Nuclear Charge Radii of Be 7,9,10 and the One-Neutron Halo Nucleus Be11 // Phys. Rev. Lett. - 2009. - Vol. 102, Issue 6. - P. 062503.
29. *Vasilevsky V.S., Nesterov A.V., Arickx F., Broeckhove J.* II. Resonances in three-cluster continuum of ^{6}He and ^{6}Be // Phys. Rev. C. - 2001. - Vol. 63. - P. 034607 - 1 - 7.
30. *Aoyama S., Mukai S., Kato K. et al.* Binding Mechanism of a Neutron-Rich Nucleus ^{6}He and Its Excited States // Prog. Theor. Phys. - 1995. - Vol. 93, No. 1. - P. 99 - 114.
31. *Aoyama S., Mukai S., Kato K. et al.* Theoretical Predictions of Low-Lying Three-Body Resonance States in ^{6}He // Prog. Theor. Phys. - 1995. - Vol. 94, No. 3. - P. 343 - 352.
32. *Burlein M., Fortune H.T., Kutt P.H. et al.* Energies and widths of states in ^{9}B // Phys. Rev. C. - 1988. - Vol. 38, Issue 5. - P. 2078 - 2080.
33. *Arena N., Cavallaro Seb., Fazio G. et al.* Energy and width measurement of the ^{9}B first excited state observed by the ^{10}B(^{3}He, α)^{9}B(p)^{8}Be and ^{10}B(^{3}He, α)^{9}B(α)^{5}Li reactions // EPL. - 1988. - Vol. 5. - P. 517.
34. *Tiede M.A., Kemper K.W., Fletcher N.R. et al.* Measurement of low-lying states in ^{9}B // Phys. Rev. C. - 1995. - Vol. 52, Issue 3. - P.1315 - 1325.
35. *Buchmann. L., Gete E., Chow J.C. et al.* β-delayed particle decay of ^{9}C and the A = 9, T = 1/2 nuclear system: R-matrix fits, the A = 9 nuclear system, and the stellar reaction rate of ^{4}He(αn, γ)^{9}Be // Phys. Rev. C. - 2001. - Vol. 63, Issue 3. - P. 034303.
36. *Sherr R., Fortune H.T.* Low-lying levels of ^{9}B // Phys. Rev. C. - 2004. - Vol. 70. - P. 054312.
37. *Tanaka N., Suzuki Y., Varga K., Lovas R.G.* Unbound states by analytic continuation in the coupling constant // Phys. Rev. C. - 1999. - Vol. 59. - P. 1391.
38. *Vasilevsky V.S., Arickx F., Broeckhove J. et al.* The ^{5}H resonance structure studied with a three-cluster J-matrix model // J. Phys. G. - 2007. - Vol. 34. - P. 1955 - 1970.

INFLUENCE OF PAULI PRINCIPLE AND POLARIZATION ON $^{16}O + ^{16}O$ INTERACTION POTENTIAL

V. A. Nesterov

Institute for Nuclear Research, National Academy of Sciences of Ukraine, Kyiv, Ukraine

In the work have studied the dependence of the interaction potential on taking into account the Pauli principle as well as monopole and quadrupole polarization within approaches based on the energy-density formalism and two-center shell model wave functions for $^{16}O + ^{16}O$ system. In the adiabatic approximation it is shown that the contribution of the Paui principle and polarization in colliding nuclei radically changes the behavior of interaction potential.

1. Introduction

Atomic nuclei interaction is one of the most important problems in nuclear physics. During all time a large number of different approaches were created, including microscopic approaches. Resonating group method [1] (RGM) at present is one of the most successive approximations. In the framework of the RGM the Pauli principle is taken into account exactly and interaction potential of the nuclei is calculated not only in frozen density approximation but also with taking into account cluster polarization, in particular - monopole polarization [2 - 8] and quadrupole polarization in the algebraic version of the method [9 - 17]. Calculations were carried out at relatively low energies of the colliding nuclei and they indicated a significant effect of polarization on the nuclei interaction. But due to the extreme complexity of the above approaches such calculations have been performed only for the s-shell nuclei interaction.

If we want to consider the interaction of nuclei heavier than the s-shell nuclei we must choose more simple approach. Our aim is to calculate the real part of nucleus-nucleus interaction potential taking into account Pauli principle, monopole and quadrupole polarization of the interacting nuclei. It is obviously that the polarization of the interacting nuclei should manifest itself most clearly when they approach is sufficiently slow. Therefore, we use adiabatic approximation that is relative motion of the interacting nuclei is slow and reconstruction of the nuclei is full at any given distance between their centers of mass.

In the work to calculate ρ and τ we use two-center shell model [18 - 23]. As in [18], we represent the total wave function of a system in the form of Slatter determinant constructed on the three-dimensional harmonic oscillator functions with two oscillator wells whose centers are separated by a distance *R*. The coordinate axis *z* along which the nuclear motion occurs is directed along the straight line connecting the centers of masses of the nuclei. Our wave function contain two oscillator lengths (*b* – for *x* and *y* axis, *c* - for *z*) as the parameters. Thus we have one preferred direction - *z* axis, and the potential interaction of the nuclei is presented as a function of *R*. In addition minimizing the energy for each *R* we define current values of the oscillator lengths *b* and *c*.

We use that approach to calculate the real part of the interaction potential of two ^{16}O nuclei. In our calculations we take into account the Pauli principle as well as the polarization of the nuclei, i.e. deformation of nucleon orbitals in the interacting nuclei. In the next section we will present the formalism of the used model and in third section we discuss obtained results.

2. The formalism of the model

In the energy density approach potential energy of interaction between two nuclei is determined as the difference of whole system energy at a finite distance *E(R)* and the sum of binding energies of the separate nuclei $E_1 + E_2 = E(\infty)$ at infinite distance:

$$V(R) = E(R) - E_1 - E_2 . \tag{1}$$

Here

$$E_{1(2)} = \int h\left[\rho_{1(2)n}(\bar{r}), \rho_{1(2)p}(\bar{r}), \tau_{1(2)n}(\bar{r}), \tau_{1(2)p}(\bar{r})\right] d\bar{r} \tag{2}$$

$$E = \int h\left[\rho_n(\bar{r}),\ \rho_p(\bar{r}),\ \tau_n(\bar{r}),\ \tau_p(\bar{r})\right] d\bar{r} , \tag{3}$$

where $\tau_{1(2)n}(\bar{r})$ and $\tau_{1(2)p}(\bar{r})$ - kinetic energy densities for neutrons and protons of a single first (second) nucleus, $\rho_{1(2)n}(\bar{r})$ and $\rho_{1(2)p}(\bar{r})$ - neutrons and protons density distributions in the nuclei, expression for the energy density h, written for the Skyrme forces, which depends on the density we have taken from [24]. We use Skyrme forces due to the fact that their using in calculations in Hartree - Fock method leads to good results in describing binding energies of nuclei as well gives us good results in the framework of semiclassical approach with sufficiently heavy nuclei.

Next, to simplify the solution of the problem we neglect the spin-orbit and Coulomb interactions. Considering nuclei with $N = Z$, we assume that the neutron density is the same as the proton one and each of them is equal to half the total nucleon density. The same relates to the kinetic energy density.

To describe the state of ^{16}O - ^{16}O system we use two-center shell model, so in each of two oscillator wells whose centers have coordinates $-R/2$ and $R/2$ on the axis z are 8 neutrons and 8 protons which completely filling the s- and p-state. Oscillatory length for x and y axes are the same but they differs from the z axis oscillator length. Our system is cylindrically symmetric and, respectively, in cylindrical coordinates τ and ρ depends only on two variables r and z.

3. Results

The purpose of our calculations is to study the effect of antisymmetrization, as well as monopole and quadrupole polarization on the ^{16}O - ^{16}O interaction potential with using different Skyrme forces dependent on the density. Since using different Skyrme forces parameterization does not lead to any qualitative changes we will show the results only for the SkP parametrization [23], a well established to describe the binding energies of nuclei in a wide range of mass numbers.

We investigate first the effect of Pauli principle on the nucleus-nucleus interaction potential. As a result of the Pauli principle accurate accounting potential well depth is reduced drastically, and at small distances between the nuclei we can see significant repulsion. Similarly, it seems necessary to take into account the fact that during the interaction process nuclei change their size and shape that is polarized. Most evidently we can see this at low energies of their relative motion. Note that results previously were cited in [25], similar results were obtained in [18].

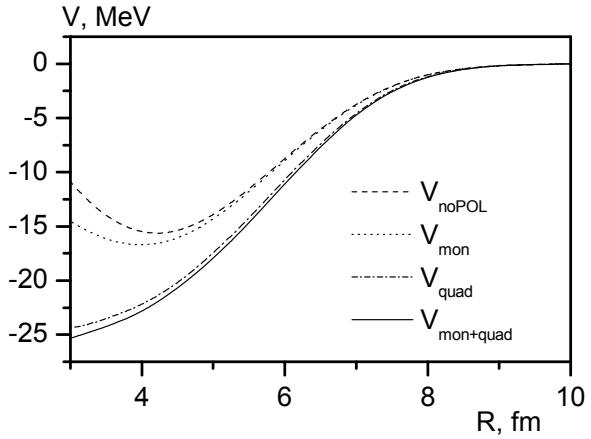

Fig. 1. ^{16}O - ^{16}O interaction potential. There V_{noPOL} - potential without polarization; V_{mon} - potential with monopole polarization; V_{quad} - potential with quadrupole polarization; $V_{mon+quad}$ potential with monopole and quadrupole polarizations. In all cases the Pauli principle is taken into account exactly.

Effect of polarization for two ^{16}O nuclei interaction potential is shown in Fig. 1. The upper curve in this figure was obtained in "frozen density" approximation (here and below we refer to results obtained with exact accounting of the Pauli principle). Below we can see the curve with possibility of a monopole nuclear polarization that is nuclei can change their size without changing shape. Single monopole polarization don't give us significant impact on the capture well width and depth, it leads only for a few potential depth increasing and decreasing repulsion at small distances. Comparison of these curves indicates that quadrupole mode of motion makes the dominant contribution to these changes in the potential.

Fig. 2 gives an oscillator radii behavior depending on the distance between the nuclei. Figure 2a shows the oscillator radius b depending on the distance between the nuclei for monopole polarization only. The curve indicates that at that approach nuclei swell more, increasing their size but remains spherically. Recall that in the spherically symmetric oscillator model mean square radii of nuclei is proportional to the oscillator radii. Fig. 2, b shows the behavior of oscillator radius associated with z axis along which the nuclei is moving at a fixed value of the oscillator radius $b = b_\infty$ (x-axis and y). Compared to the previous case the changes of the radius are more significant. They makes up to tens of percents of the initial value $c_\infty = b_\infty$ that tell us that quadrupole mode of motion manifests itself as a much gentler than a monopole one.

The behavior of b and c for the case of both monopole and quadrupole polarization is shown in Fig. 2, c. While c is increasing similar to the previous case b firstly even slightly decreasing. That is, in general, where the nucleus overlaps slightly and our approximation can be considered quite reasonable, the nuclei are trying to maximize an elongated shape due to the attraction that arises between their nucleons.

The behavior of the total nucleon density for two ^{16}O nuclei (its cross-section by zx (zy) plane) is shown in Fig. 3. We begin our consideration from center mass distance 9 fm where their density is already beginning to overlap by their tails. You can see that the greatest impact on nucleon density make quadrupole polarization leading to a significant spreading of the density along z axis as the nuclei approaching.

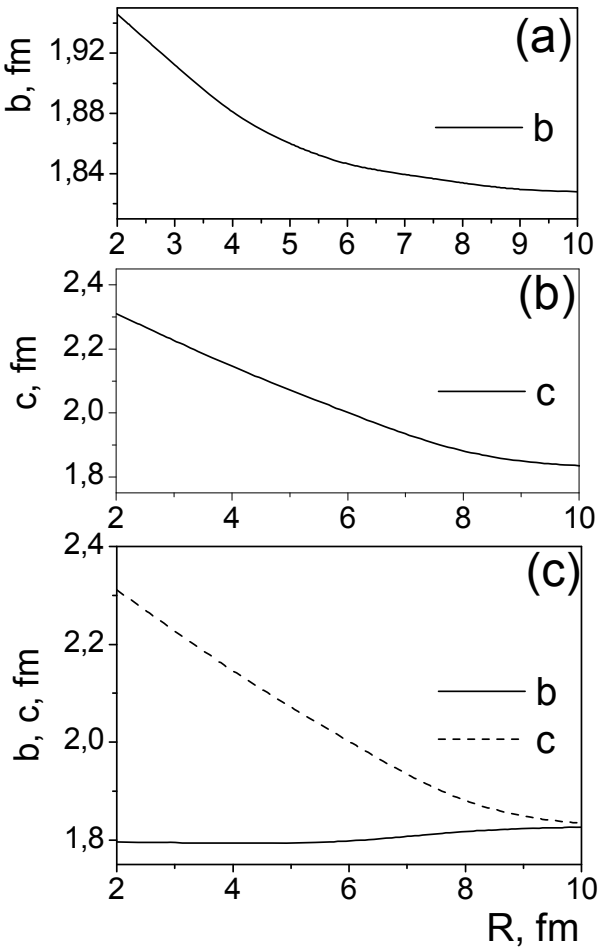

Fig. 2. Oscillator radii dependent from the distance between centers of mass of the nuclei in the case of monopole (*a*), quadrupole (*b*), the monopole and quadrupole polarizations (*c*).

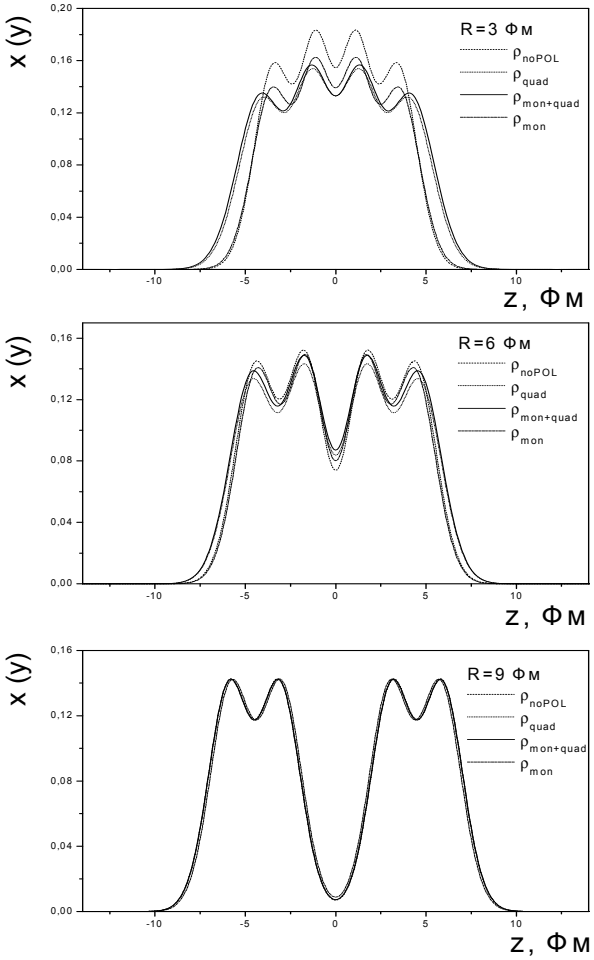

Fig. 3. Cross sections of nucleon densities by *zx* (*zy*) plane without polarization (ρ_{noPOL}), with monopole polarization only (ρ_{mon}), with quadrupole polarization only (ρ_{quad}), with both monopole and quadrupole polarizations ($\rho_{mon+quad}$).

4. Conclusions

Consideration of the nuclear-nuclear interaction potential for $^{16}O+^{16}O$ system in the adiabatic approximation with an exact accounting of the Pauli principle and the polarization of the interacting nuclei indicates that the inclusion of both factors has a very significant impact on the results. At the same time, those factors act in different directions. Pauli principle leads to very large changes in the potential which reduces attraction between the nuclei while polarization, especially a quadrupole, increases the attraction markedly. At the same time the polarization itself, due to an earlier and stronger overlapping of nucleon densities, increases the effect of the Pauli principle, but generated by the polarization attraction overpowers the repulsion generated by the Pauli principle intensification.

REFERENCES

1. *Вильдермут К., Тан Я.* Единая теория ядра. - М.: Мир, 1980. - 504 с.
2. *Stubeda D.J., Fujiwara Y., Tang Y.C. N* + ^{6}Li system with flexible cluster wave function // Phys. Rev. C. - 1982. - Vol. 26. - P. 2410 - 2416.
3. *Kanada H., Kaneko T., Tang Y.C.* Convergence features in the pseudostate theory of the d + α system // Phys. Rev. C. - 1988. -Vol. 38. - P. 2013 - 2018.
4. *Kanada H., Kaneko T., Tang Y.C.* Specific distortion effects in ^{3}H + α and ^{3}He + α systems // Nucl. Phys. A. - 1982. - Vol. 380. - P. 87 - 110.
5. *Kanada H., Kaneko T., Tang Y.C.* Specific distortion effects in the d + α system and charge form factor of ^{6}Li // Nucl. Phys. A. - 1982. - Vol. 389. - P. 285 - 300.
6. *Kanada H., Kaneko T., Nomoto M., Tang Y.C.* // Prog. Theor. Phys. - 1984. - Vol. 72. - P. 369.
7. *Kanada H., Kaneko T., Shen P.N., Tang Y.C.* Characteristic features of specific distortion in light nuclear systems // Nucl. Phys. A. - 1986. - Vol. 457. - P. 93 - 108.
8. *Kajino T., Matsuse T., Arima A.* Effects of breathing excitations of the triton nucleus on the alpha + triton cluster in

7Li // Nucl. Phys. A. - 1984. - Vol. 414. - P.185 - 205.
9. *Филиппов Г.Ф., Василевский В.С., Нестеров А.В.* О структуре монопольных резонансов легких атомных ядер // ЯФ - 1984. - Т. 40. - С. 1418 - 1429.
10. *Филиппов Г.Ф., Василевский В.С., Нестеров А.В.* Высоколежащие монопольные резонансы ядра ^{8}Be // Изв. АН СССР. Сер. физ. - 1984. - Т. 48. - С. 91 - 96.
11. *Filippov G.F., Vasilevsky V.S., Chopovsky L.L.* Solution of problems in the microscopic theory of the nucleus using the technique of generalized coherent states // Sov. J. Part. Nucl. - 1985. - Vol. 16. - P. 153 - 177.
12. *Филиппов Г.Ф., Василевский В.С., Бруно М. и др.* Коллективные возбуждения ^{4}He в d + d, n + ^{3}He и p + ^{3}H рассеянии // ЯФ - 1990. - Т. 51, № 6. - С. 1551 - 1560.
13. *Filippov G.F., Vasilevsky V.S., Nesterov A.V.* Excitation of ^{8}Be monopole resonances under αα scattering // Nucl. Phys. A. - 1984. - Vol. 426. - P. 327 - 352.
14. *Filippov G.F., Vasilevsky V.S., Kruchinin S.P., Chopovsky L.L.* On the nature of the resonances observed in photonuclear reactions // Sov. J. Nucl. Phys. - 1986. - Vol. 43. - P. 536 - 542.
15. *Deumens E.* Analysis of resonances in ^{8}Be using polarized α-particles // Nucl. Phys. A. - 1984. - Vol. 423. - P. 52 - 76.
16. *Sytcheva A., Arickx F., Broeckhove J., Vasilevsky V.S.* Monopole and quadrupole polarization effects on the α-particle description of ^{8}Be // Phys. Rev. C. - 2005. - Vol. 71. - P. 044322.
17. *Sytcheva A., Broeckhove J., Arickx F., Vasilevsky V.S.* Influence of monopole and quadrupole channels on the cluster continuum of the lightest p-shell nuclei // J. Phys. G. - 2006. - Vol. 32. - P. 2137.
18. *Brink D., Stancu F.* Interaction potential between two ^{16}O nuclei derived from the Skyrme interaction // Nucl. Phys. A. - 1975. - Vol. 243. - P. 175 - 188.
19. *Gupta R.K., Greiner W.* Heavy Elements and Related New Phenomena. Vol. 1. - Singapore, 1999. - P. 536.
20. *Mirea M.* Energy partition in low energy fission // Phys. Rev. C. - 2011. - Vol. 83, No. 5. - P. 054608.
21. *Gupta R., Malik S.S.* Spontaneous fission in actinides and heavy elements: A semiclassical view // Euro. Phys. J. A. - 2010. - Vol. 45, No. 2. - P. 239 - 250.
22. *Malik S.S.* Semiclassics for superheavy elements // Nucl. Phys. A. - 2008. - Vol. 813, No. 3 - 4. - P. 262 - 278.
23. *Skyrme T.H.R.* The effective nuclear potential // Nucl. Phys. - 1959. - Vol. 9. - P. 615 - 634.
24. *Vatherin D., Brink D.* Hartree - Fock Calculations with Skyrme's Interaction. I. Spherical Nuclei // Phys. Rev. C. - 1972. - Vol. 5. - P. 626 - 638.
25. *Денисов В.Ю., Нестеров В.А.* Принцип Паули и потенциал ядерно-ядерного взаимодействия // ЯФ. - 2010. - Т. 73, № 7. - С. 1181 - 1190.

ON THE CROSS SECTION AND DURATION OF THE NEUTRON-NUCLEUS SCATTERING WITH TWO OVERLAPPED RESONANCES IN THE CENTER-OF-MASS SYSTEM AND LABORATORY SYSTEM

V. S. Olkhovsky[1], N. L. Doroshko[1], T. I. Lokotko[2]

[1] *Institute for Nuclear Research, National Academy of Sciences of Ukraine, Kyiv, Ukraine*
[2] *Taras Shevchenko National University, Kyiv, Ukraine*

Here we study the cross section and the duration of the neutron-nucleus scattering with two overlapped resonances in the laboratory (*L*-) system. We show that in the *L*-system the delay-advance phenomenon does not occur and only the trivial time delay is observed. At the same time the transformations from *C*-system into the *L*-system appeared to be different from the standard kinematical transformations because the motion of a compound nucleus is absent in the *C*-system but is present in the *L*-system. The results of the calculated cross-sections for the neutron elastic scattering by some nuclei at the range of two overlapped compound resonances are presented in the *L*-system and also in the *C*-system. The calculated results are confronted with two experimental data.

1. Introduction

Firstly we remind the delay-advance phenomenon in nucleon elastic scattering by nuclei near a resonance, distorted by the non-resonant background (in the C-system). Usually (see, for instance, [1 - 3]) the amplitude $F_C(E, \theta)$ for the elastic scattering of nucleons by spherical nuclei near an isolated resonance in the C-system can be written as

$$F^C(E, \theta) = [A(E^* - E^*_{res}) + iB\Gamma/2]\,(E^* - E^*_{res} + i\Gamma/2)^{-1}, \tag{1}$$

where

$$A = f(E, \theta) + (k)^{-1}(2l+1)P_l(\cos\theta)\exp(i\delta_l^b)\sin\delta_l^b,$$

$$B = f(E, \theta) + (ik)^{-1}(2l+1)P_l(\cos\theta)\exp(i\delta_l^b)\cos\delta_l^b,$$

Here E, E_{res} and Γ are the excitation energy, the resonance energy and the width of the compound nucleus, respectively; we neglect the spin-orbital interaction and consider a comparatively heavy nucleus.
For the total scattering *duration* $\tau^C(E,\theta)$ we have

$$\tau^C(E, \theta) = 2R/v + \hbar\partial\arg F/\partial E \equiv 2R/v + \Delta\tau^C(E, \theta). \tag{2}$$

In formula (2), $v = \hbar k/\mu$ is the projectile velocity, R is the interaction radius, and $\Delta\tau^C$ is

$$\Delta\tau^C(E, \theta) = -(\hbar\mathrm{Re}\alpha/2)[(E^* - E^*_{res} - \mathrm{Im}\alpha/2)^2 + (\mathrm{Re}\alpha)^2/4]^{-1} + \Delta\tau_{res}, \tag{3}$$

with $\Delta\tau_{res} = (\hbar\Gamma/2)[(E^* - E^*_{res})^2 + \Gamma^2/4]^{-1}$, $\alpha = \Gamma B/A$.

From (3) one can see that, if $0 < \mathrm{Re}\alpha < \Gamma$, the quantity $\Delta\tau(E, \theta)$ appears to be *negative* in the energy interval ~Reα around the center at the energy $E^*_{res} + \mathrm{Im}\alpha/2$.
In [4] for two overlapped resonances the scattering amplitude for an elastic reaction can be written in center-of-mass system in form (1):

$$F^C(E, \theta) = f(E, \theta) + f_{l,res}(E, \theta)$$

where

$$f(E,\theta) = f_{coul}(E,\theta) + (2ik)^{-1}\sum_{\lambda=0}^{\lambda_{max}}(2\lambda+1)P_\lambda(\cos\theta)\left[\exp(2i\delta_\lambda^b) - 1\right] \tag{4a}$$

and

$$f_{l,res}(E,\theta) = (2ik)^{-1}(2l+1)P_l(\cos\theta)\exp(2i\delta_l^b)\cdot \tag{4b}$$

$$\cdot\left[\left(\frac{E - E_{res,1} - i\Gamma/2}{E - E_{res,1} + i\Gamma/2}\right)\left(\frac{E - E_{res,2} - i\Gamma/2}{E - E_{res,2} + i\Gamma/2}\right) - 1\right]$$

we obtain the following expression for the total scattering *duration* $\tau^C(E, \theta)$

$$\tau^C(E, \theta) = 2R/v + \hbar\partial\arg F/\partial E \equiv 2R/v + \Delta\tau^C(E, \theta)$$

for the quasi-monochromatic particles which have very small energy spreads $\Delta E << \Gamma$, when one can use *the method of*

stationary phase for approaching the group velocity of the wave packet (see, for instance, [4]).
We can find value of λ_{max} from the following expression: $\lambda_{max} = k \cdot R$, where R – radius of the nucleus, and k – wave number. We have used six phases $\delta_\lambda = 1, 2, 3, 4, 5, 6$.
In Figs. 1 and 2 we can see the energy dependence of $\Delta t^C(E,\theta)$ for two couples of overlapped resonances:

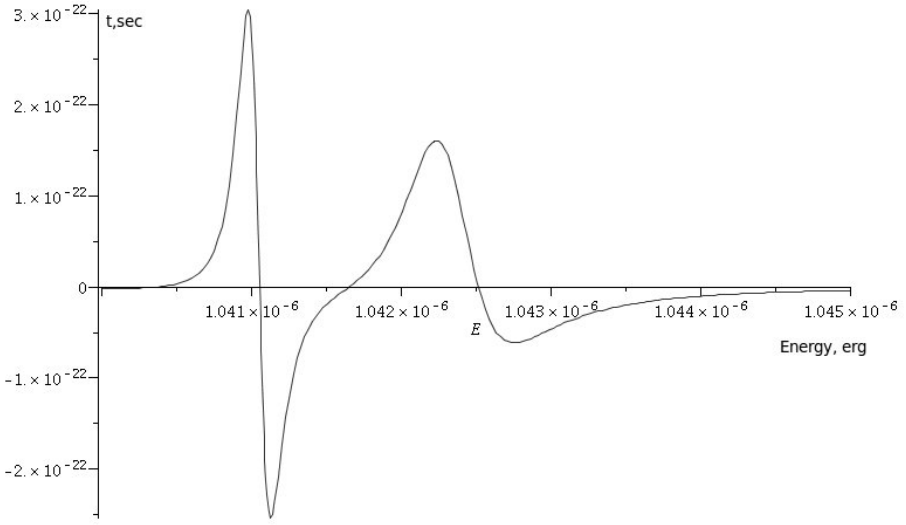

Fig. 1. Energy dependence of $\Delta t^C(E,\theta)$ near two overlapped resonances ^{58}Ni
$E_1 = 649.8$ keV; $\Gamma_1 = 0.168$ keV and $E_2 = 650.6$ keV; $\Gamma_2 = 0.521$ keV.

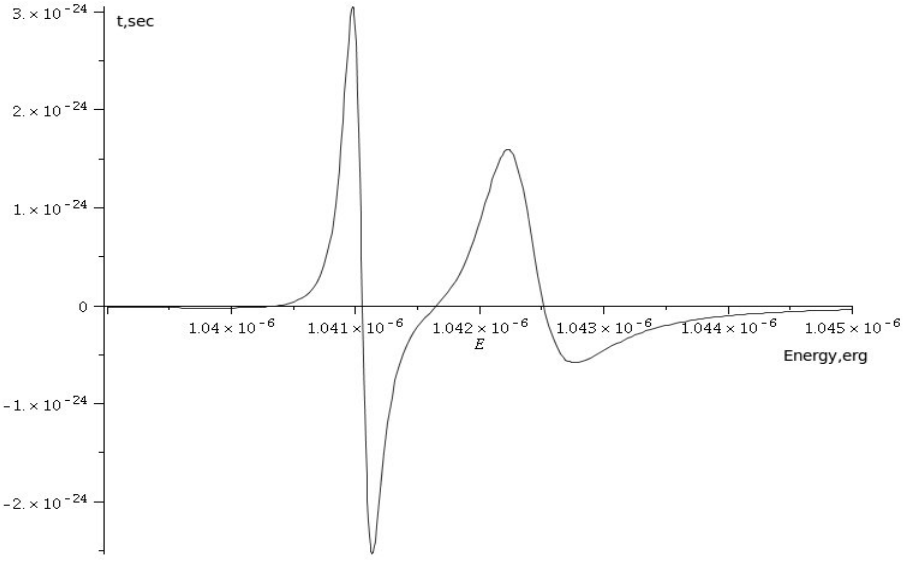

Fig. 2. Energy dependence of $\Delta t^C(E,\theta)$ near two overlapped resonances ^{58}Ni
$E_3 = 745.6$ keV; $\Gamma_3 = 0.7$ keV and $E_4 = 746{,}5$ keV; $\Gamma_4 = 0{,}8$ keV.

2. Time analysis of the neutron-nucleus scattering in the *L*-system in the case of the resonance presence

In Fig. 3, *a* and *b* these two processes in the ***L***-system are pictorially presented. They represent a prompt (direct) and a delayed compound-resonance mechanism of the emitting ***y*** particle and ***Y*** nucleus, respectively. The both mechanisms are *macroscopically* schematically indistinguishable but they are *microscopically* different processes:
Fig. 3, *a* represents the direct process of a prompt emission of the final products from the collision point C_0 with a very small time duration τ_{dir}, while Fig. 3, *b* represents the motion of a compound-resonance nucleus Z^* from point C_0 to point C_1, where it decays by the final products ***y*** + ***Y*** after traveling a distance between C_0 and C_1 which is equal to ~V_C $\Delta\tau_{res}$ before its decay. Here V_C is the compound-nucleus velocity, equal to the center-of-mass velocity.

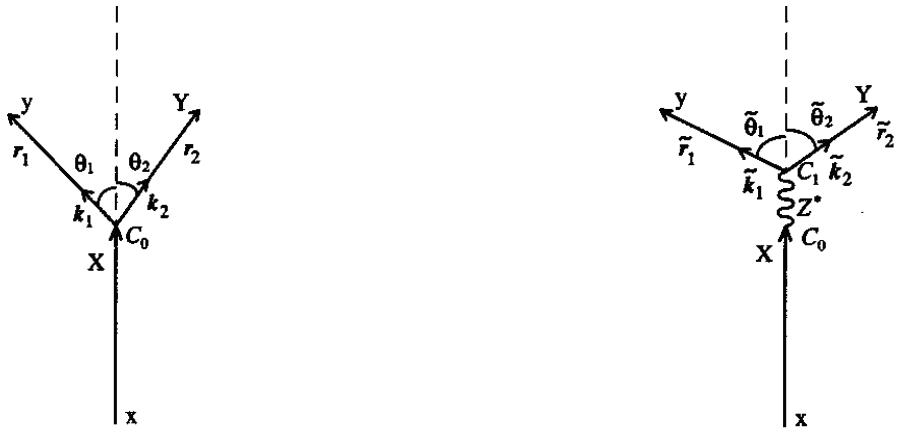

a *b*

Fig. 3.

For the case of two overlapped resonances we have to calculate the wave function quite similarly to the case of one resonance before:

$$\Psi_{r_1\to\infty} \approx 0, \qquad \text{when} \qquad t < t_i + \frac{r_1}{V_1^0}, t < t_i + \tau + \frac{\tilde{r}_1}{V_1^0},$$

$$\Psi_{r_1\to\infty} \approx \text{const}\cdot$$

$$+\frac{J_{C\to L}^{1/2}\gamma_Z}{\left(E_Z - E_{res,Z1} + i\Gamma_{Z1}/2\right)\left(E_Z - E_{res,Z2} + i\Gamma_{Z2}/2\right)}*$$

$$\exp\left[-\Delta E\left[\left(t - t_i - \tau - \frac{\tilde{r}_1}{V_1^0}\right) + \left(t - t_i - \tau - \frac{\tilde{r}_2}{V_2^0}\right)\right]/\hbar\right] +$$

$$+\exp\left[ik_1^0\Delta r_1 + ik_2^0\Delta r_2\right]), \quad \text{when} \quad t > t_i + \frac{r_1}{V_1^0}, t > t_i + \tau + \frac{\tilde{r}_1}{V_1^0}.$$

Here $V_{1,2}^0 = \hbar k_{1,2}^0 / m_{1,2}$, $\Delta r_{1,2} = V_{1,2}\,\Delta\tau_{res}$, where $V_{1,2}$ – projection of the speed of nucleus Z^* on the vectors $\vec{k}_{1,2}$, t_i – initial moment of time.

To calculate the time of delay in the L-system we have to use this formula:

$$\left\langle \tau_{general} \right\rangle = \frac{\int_{t_{min}}^{\infty} tj_i dt}{\int_{t_{min}}^{\infty} j_i dt} - t_{initial} \approx \frac{\hbar}{4\Delta E},$$

where $j_i = \text{Re}\left[\psi^+ \frac{\hbar}{im}\frac{\partial\psi}{\partial x}\right]$ is an initial current.

So, if we will take into account the movement of the compound-nucleus *the advanced time vanishes* also here because also here we neglect the real compound-nucleus motion .

3. Analysis the cross section of the neutron-nucleus scattering with two overlapped resonances

In this case we can't calculate the cross section in the usual form: $\sigma = \left|f\left(E,\theta\right)\right|^2$. That's so because of the compound nucleus moves during the reaction. This effect is not taken into account in the formula $\sigma = \left|f\left(E,\theta\right)\right|^2$. If we want to take into consideration the moving of the compound nucleus, we have to use another formula for cross section:

$$\sigma(\theta) = \int dt \int dr_2 \psi^+_{r_1\to\infty} \hat{j}_1 \psi_{r_1\to\infty} \approx \int dt \int dr_2 \left|\psi_{r_1\to\infty}\right|^2 = \sigma_{0(incoh)} + \sigma_{1(interf)}, \tag{5}$$

where

$$\sigma_0 = \left|f_{dir}^{(L)}\right|^2 + \frac{J_{C\to L}\left|\gamma_{Z^+}^{(C)}\right|^2}{\left(\left(E_Z^+ - E_{res,Z1}\right)^2 + \Gamma_{Z1}^2/4\right)\left(\left(E_Z^+ - E_{res,Z2}\right)^2 + \Gamma_{Z2}^2/4\right)}, \tag{6}$$

$$\sigma_1 = 2\left|f_{dir}^{(L)}\frac{J_{C\to L}^{1/2}\gamma_{Z^+}^{(C)}}{\left(E_Z^+ - E_{res,Z1} + i\Gamma_{Z1}/2\right)\left(E_Z^+ - E_{res,Z2} + i\Gamma_{Z2}/2\right)}\right|\cos\Phi. \tag{7}$$

We can calculate phase Φ the same way, as in the case with the one resonance.
Other values can be found this way:

$$f_{dir}^{(L)} = \sqrt{J_{C\to L}}\,f_{dir}^{(C)} = \sqrt{J_{C\to L}}\,f_b\left(E_1^C, \theta_1^C\right), \tag{8}$$

$$\frac{\gamma_{Z^+}^{(C)}\left(E_1, E_2\right)}{\left(E_Z^+ - E_{res,Z1} + i\Gamma_{Z1}/2\right)\left(E_Z^+ - E_{res,Z1} + i\Gamma_{Z1}/2\right)} = f_{l,res}\left(E_1^C, \theta_1^C\right). \tag{9}$$

In Figs. 4 - 7 we can see theoretical functions, calculated by the formulas (13 - 16) and experimental data. The method of least squares was used to fit the function and experimental data. Experimental data where taken from [5].

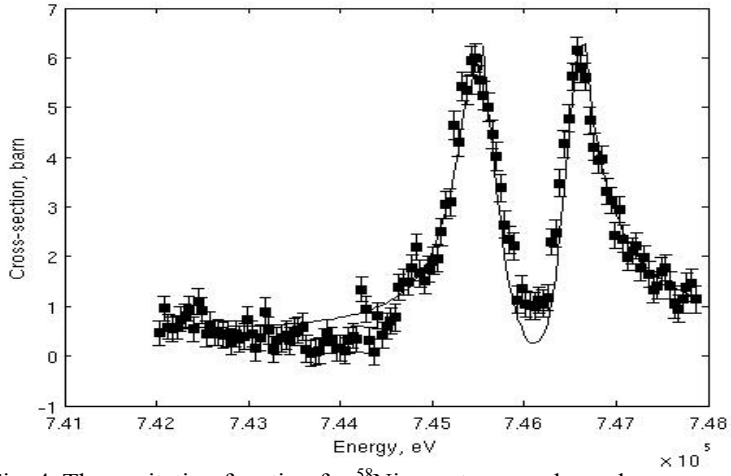

Fig. 4. The excitation function for ^{58}Ni near two overlapped resonances.
E_1 = 649.8 keV; Γ_1 = 0.168 keV and E_2 = 650.6 keV; Γ_2 = 0.521 keV .

After approximation we had such values of the parameters:

$\delta_i : \delta_0 = 4.39$, $\delta_1 = 5.28$, $\delta_2 = 3.01$, $\delta_3 = 4.83$, $\delta_4 = 0.37$, $\delta_5 = 5.55$, $\delta_6 = 3.13$.

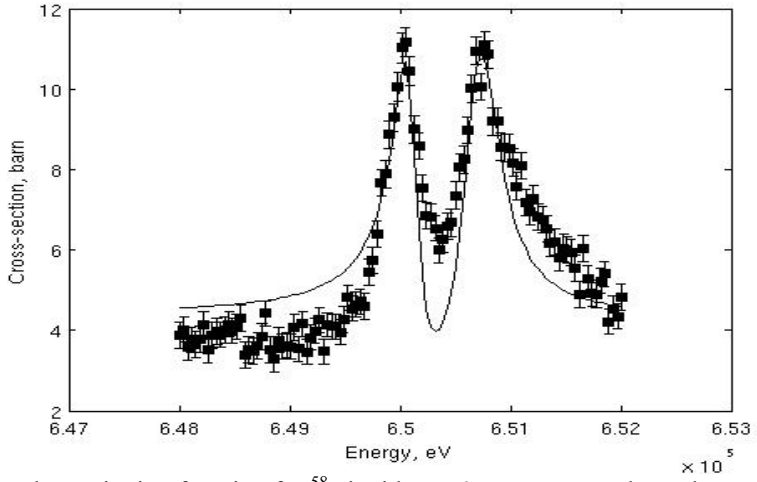

Fig. 5. The excitation function for ^{58}Ni with $\varphi = 0$ near two overlapped resonances.
E_1 = 649.8 keV; Γ_1 = 0.168 keV and E_2 = 650.6 keV; Γ_2 = 0.521 keV .

After approximation we had such values of the parameters:

$$\delta_i : \delta_0 = 4.39\,,\ \delta_1 = 5.28\,,\ \delta_2 = 3.01\,,\ \delta_3 = 4.83\,,\ \delta_4 = 0.37\,,\ \delta_5 = 5.55\,,\ \delta_6 = 3.13\,.$$

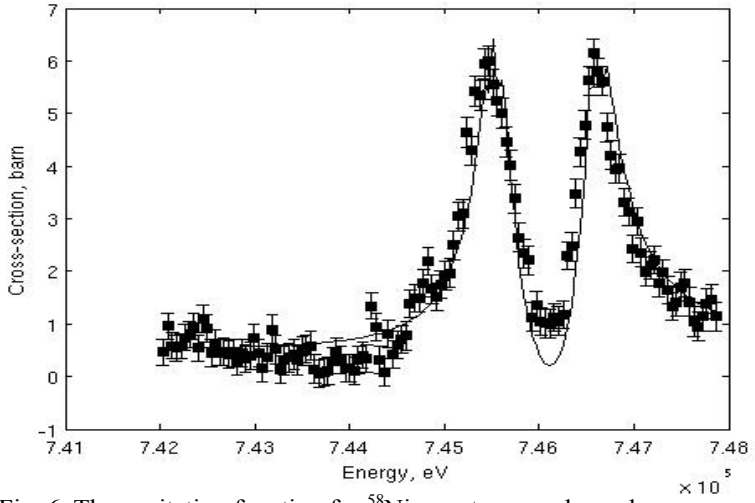

Fig. 6. The excitation function for ^{58}Ni near two overlapped resonances.
$E_3 = 745.6$ keV; $\Gamma_3 = 0.7$ keV and $E_4 = 746{,}5$ keV; $\Gamma_4 = 0{,}8$ keV .

After approximation we had such values of the parameters:

$$\delta_i : \delta_0 = 3.14\,,\ \delta_1 = 6.27\,,\ \delta_2 = 3.04\,,\ \delta_3 = 3.12\,,\ \delta_4 = 6.27\,,\ \delta_5 = 2.98\,,\ \delta_6 = 3.59\,.$$

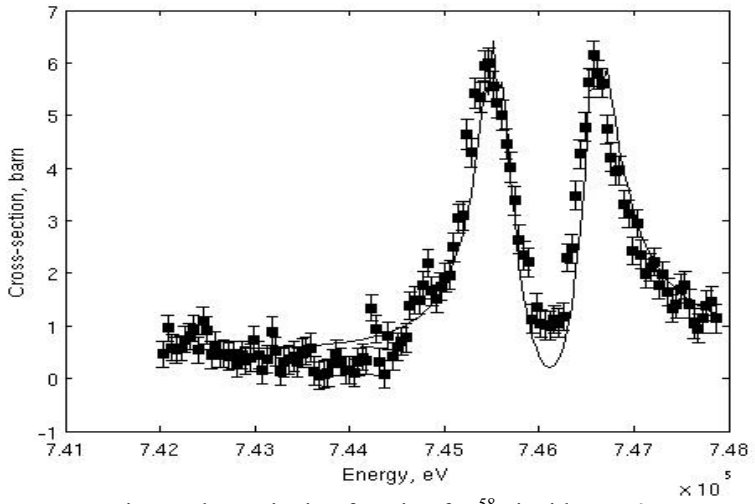

Fig. 7. The excitation function for ^{58}Ni with $\varphi = 0$.
$E_3 = 745.6$ keV; $\Gamma_3 = 0.7$ keV and $E_4 = 746{,}5$ keV; $\Gamma_4 = 0{,}8$ keV .

After approximation we had such values of the parameters:

$$\delta_i : \delta_0 = 3.14\,,\ \delta_1 = 6.27\,,\ \delta_2 = 3.04\,,\ \delta_3 = 3.12\,,\ \delta_4 = 6.27\,,\ \delta_5 = 2.98\,,\ \delta_6 = 3.59\,.$$

4. Conclusions and perspectives

Presented here time analysis of the experimental data on low-energy neutron-nuclear scattering in the region of two overlapped resonances lets formulate the following conclusions and perspectives.

1. A simple application of time analysis for quasi-monochromatic neutron-nucleus scattering near two overlapped resonances in the ***C***-system brings to the paradoxical virtual effect of time advance near a resonance in any two-particle channel. Here **such paradox is *eliminated* by the space-time analysis *in the L*-system.**

2. Moreover, **the *known standard formulas of transformations between the L-system and C–system are not valid in the presence of two collision mechanisms – rapid (direct or potential) process, when the center-of-mass does not practically shifted during collision, and delayed process, when the long-living compound nucleus is moving in the L*-system.** The obtained by us new analytical transformations of the cross sections ***between the C-system and L–system*** are illustrated by the energy behavior of cross sections by nuclei ^{58}Ni near couples of overlapped resonances in the ***L*** – system.

3. New formulas (5) - (9) can be easily generalized for improving the known methods of analysis in the case of more general nucleon-nucleus and even more complex collisions in ***L***-system.

REFERENCES

1. *Olkhovsky V.S., Doroshko N.L.* // Europhys. Lett. - 1992. - Vol. 18. - P. 483 - 486.
2. *D'Arrigo A., Doroshko N.L., Eremin N.V. et al.* // Nucl. Phys. - 1992. - Vol. A549. - P. 375 - 386.
3. *D'Arrigo A., Doroshko N.L., Eremin N.V. et al.* // Nucl. Phys. - 1993. - Vol. A564. - P. 217 - 226.
4. *Prokopets G.A.* // Nucl. Phys. - 2011. - Vol. 74. - P. 740 - 746.
5. *Brusegan A., Rohr G., Shelley R. et al.* Very high resolution transmission measurements and resonance parameters of Ni^{58} and Ni^{60} // Proc. of the Conf. on Nucl. Data for Sci. and Techn. - Gatlinburg, USA, 1994. - P. 224.

ON THE CROSS SECTION AND DURATION OF THE NEUTRON-NUCLEUS SCATTERING WITH ONE OR TWO OVERLAPPED RESONANCES, DISTORTED BY A NON-RESONANT BACKGROUND, IN THE CENTER-OF-MASS SYSTEM AND LABORATORY SYSTEM

V. S. Olkhovsky, M. E. Dolinska, S. A. Omelchenko

Institute for Nuclear Research, National Academy of Sciences of Ukraine, Kyiv, Ukraine

Here we study the cross section and the duration of the neutron-nucleus scattering in the laboratory (*L*-) system. We show that in the *L*-system the delay-advance phenomenon does not occur and only the trivial time delay is observed. At the same time the transformations from *C*-system into the *L*-system appeared to be different from the standard kinematical transformations because the motion of a compound nucleus is absent in the *C*-system but is present in the *L*-system. The results of the calculated cross-sections for the neutron elastic scattering by some nuclei at the range of one or two overlapped compound resonances, distorted by a non-resonant background, are presented in the *L*-system and also in the *C*-system. The calculated results are confronted with the experimental data.

1. Introduction and the pre-history of the problem

It is found in [4] (see also [5]) that the standard formulas of the cross-section transformations from the L-system to the C-system are not valid in the cases of two collision mechanisms. And there is practically no motion of the C-system for a prompt process and there is the motion of the long-living decaying compound nucleus in the L-system. This motion of the compound nucleus coincides with the motion of the center-of-mass in the L-system. The existing standard pure cinematic transformations from the L-system into the C-system and vice versa are valid only for one collision mechanism.

Now we remind the delay-advance phenomenon in nucleon elastic scattering by nuclei near a resonance, distorted by the non-resonant background (in the C-system). Usually (see, for instance, [1 - 3]) the amplitude $F_C(E, \theta)$ for the elastic scattering of nucleons by spherical nuclei near an isolated resonance in the C-system can be written as

$$F_C(E, \theta) = f(E, \theta) + f_{l, res}(E, \theta), \tag{1}$$

where

$$f_{l,res}(E,\theta) = (2ik)^{-1}(2l+1)\,P_l(\cos\theta)\,[\exp(2i\,\delta_l^b)\frac{E - E_{res} - i\Gamma/2}{E - E_{res} + i\Gamma/2} - 1]$$

$$f(E,\theta) = (2ik)^{-1}\sum_{\lambda \neq l}(2\lambda+1)\,P_\lambda(\cos\theta)[\exp(2i\,\delta_\lambda^b) - 1].$$

Here E, E_{res} and Γ are the excitation energy, the resonance energy and the width of the compound nucleus, respectively; we neglect the spin-orbital interaction and consider a comparatively heavy nucleus.

Rewriting (1) in the form

$$F^C(E, \theta) = [A(E^* - E^*_{res}) + iB\Gamma/2]\,(E^* - E^*_{res} + i\Gamma/2)^{-1}, \tag{1a}$$

where

$$A = f(E, \theta) + (k)^{-1}(2l + 1)P_l(\cos\theta)\exp(i\delta_l^b)\sin\delta_l^b,$$

$$B = f(E, \theta) + (ik)^{-1}(2l + 1)P_l(\cos\theta)\exp(i\delta_l^b)\cos\delta_l^b,$$

we obtain the following expression for the total scattering *duration* $\tau^C(E, \theta)$

$$\tau^C(E, \theta) = 2R/v + \hbar\partial\arg F/\partial E \equiv 2R/v + \Delta\tau^C(E, \theta) \tag{2}$$

for the quasi-monochromatic particles which have very small energy spreads $\Delta E << \Gamma$, when one can use *the method of stationary phase* for approaching the group velocity of the wave packet (see, for instance, [1]). Formula (2) was obtained in [1]. In formula (2), $v = \hbar k/\mu$ is the projectile velocity, R is the interaction radius, and $\Delta\tau^C$ is

$$\Delta\tau^C(E, \theta) = -(\hbar\mathrm{Re}\alpha/2)[(E^* - E^*_{res} - \mathrm{Im}\alpha/2)^2 + (\mathrm{Re}\alpha)^2/4]^{-1} + \Delta\tau_{res} \tag{3}$$

with $\Delta\tau_{res} = (\hbar\Gamma/2)[(E^* - E^*_{res})^2 + \Gamma^2/4]^{-1}$, $\alpha = \Gamma B/A$.

From (3) one can see that, if $0 < \mathrm{Re}\alpha < \Gamma$, the quantity $\Delta\tau(E, \theta)$ appears to be *negative* in the energy interval ~$\mathrm{Re}\alpha$ around the center at the energy $E^*_{res} + \mathrm{Im}\alpha/2$. When $0 < \mathrm{Re}\alpha/\Gamma << 1$ the minimal delay time can obtain the value $-2\hbar\,\mathrm{Re}\alpha < 0$. Thus, when $\mathrm{Re}\alpha \to 0^+$, the interference of the resonance and the background scattering can bring to *as much as desired large of the advance* instead of the delay! Such situation is mathematically described by the zero $E^*_{res} + i\alpha/2$, besides the pole $E^*_{res} - i\Gamma/2$, of the amplitude $F^C(E, \theta)$ (or the correspondent *T*-matrix) in the lower

unphysical half-plane of the complex values for energy E. We should notice that a very large advance can bring to the problem of causality violation (see, for instance the note in [2]). The *delay-advance phenomenon* in the C-system was studied in [1 - 3] for the nucleon-nucleus elastic scattering.

2. Time analysis of the neutron-nucleus scattering in the *L*-system in the case of one resonance

In Fig. 1, *a* and *b* these two processes in the ***L***-system are pictorially presented. They represent a prompt (direct) and a delayed compound-resonance mechanism of the emitting ***y*** particle and ***Y*** nucleus, respectively. The both mechanisms are *macroscopically* schematically indistinguishable but they are *microscopically* different processes:

a *b*

Fig. 1. *a* - diagram of direct process; *b* - diagram of process with the formation of the compound nucleus.

Fig. 1, *a* represents the direct process of a prompt emission of the final products from the collision point C_0 with a very small time duration τ_{dir}, while Fig. 1, *b* represents the motion of a compound-resonance nucleus Z^* from point C_0 to point C_1, where it decays by the final products ***y*** + ***Y*** after traveling a distance between C_0 and C_1 which is equal to $\sim V_C\, \Delta\tau_{res}$ before its decay. Here V_C is the compound-nucleus velocity, equal to the center-of-mass velocity, and $\Delta\tau_{res} = (\hbar\Gamma/2)/[(E_Z - E_{res,Z})^2 + \Gamma^2/4]$ is the mean time of the nucleus Z^* motion before its decay [8] for the case of one compound resonance, the energy spread ΔE of the incident particle ***x*** being very small in comparison with the resonance width Γ, $E_Z = E^*$, $E_{res,Z} = E^*_{res}$. For the clarity of the difference between both processes in time, we impose the evident practical condition

$$\tau_{dir} << \Delta\tau_{res}(E_Z) \quad \text{for} \quad (E_Z - E_{res,Z})^2 \approx \Gamma^2. \tag{4}$$

For the *macroscopically* defined cross sections, in the case of very large macroscopic distances r_1 (near the detector of the final particle ***y***) with very small angular and energy resolution ($\Delta\theta_1 << \theta_1$ and $\Delta k_1 << k_1$), the angles θ_1 and θ'_1, as well as momentums k_1 and k'_1, can be considered as practically coincident. Really, $\theta_1 - \theta'_1 \sim \Delta r_1 / r_1$ and $k_1 - k'_1 \sim \Delta r_1 / r_1$ with $|\Delta r_1| = |r_1 - r'_1|$. Using the *usual macroscopic definition of the cross section* with the help of some transformations for the exit asymptotic wave packet of the system ***y*** + ***Y***, in [4] it was obtained the following expression for the cross section σ of reaction (4) in the ***L***-system:

$$\sigma = \sigma_0^{(\text{incoh})} + \sigma_1^{(\text{interf})}, \tag{5}$$

where

$$\sigma_{0(\text{incoh})} = \left|f_{dir}^{(L)}\right|^2 + \frac{J_{C\to L}\left|\gamma_Z^{(C)}\right|^2}{(E_Z - E_{res,Z})^2 + \Gamma^2/4}, \tag{6}$$

$$f_{dir}^{(L)} = \sqrt{J_{C\to L}}\, f_{dir}^{(C)}(E_1^C, \theta_l^C), \qquad f_{dir}^{(C)} = \frac{1}{2ik_l^C}\sum_{l'\neq l}(2l'+1)P_{l'}(\cos\theta_1^C)(e^{2i\delta_{l'}} - 1), \tag{7}$$

$$\sigma_1^{(\text{interf})} = 2f_{dir(L)} \cdot \frac{J_{C\to L}^{1/2}\gamma_Z^{(C)}}{E_Z - E_{res,Z} + i\Gamma/2}\cos\Phi \tag{8}$$

$$\frac{\gamma_Z^{(L)}(E_1, E_2)}{E_Z - E_{res,Z} + i\Gamma/2} = f_{l,res}(E_1^C, \theta_l^C) = \frac{\lambda_Z^{(L)}}{2ik_l^C}(2l+1)P_l(\cos\theta_1^C)\left\{e^{2i\delta_l}\frac{E^C - E_{res}^C - i\Gamma/2}{E^C - E_{res}^C + i\Gamma/2} - 1\right\}, \tag{9}$$

$$\Phi = \chi + \beta + \varphi, \quad \chi = \arg(J^{1/2}_{C\to L}\gamma^{(L)}_{Z}) - \arg(f^{(L)}_{dir}), \quad \beta = \arg(E_Z - E_{res.Z} + i\Gamma/2)^{-1}, \tag{10}$$

$$\varphi = k_1\Delta r_1 + k_2\Delta r_2, \quad \Delta r_{1,2} = V_{1,2}\,\Delta\tau_{res}.$$

$V_{1,2}$ is the projection of the Z^*-nucleus velocity to the direction of $\vec{k}_{1,2}$, δ_l is the l-wave scattering background phase shift. Formulas (5) - (10) were obtained for a quasi-monochromatic incident beam ($\Delta E << E$) and a very small angular and energy resolution ($\Delta\theta_1 << \theta_1$, $\Delta E << \Gamma$) of the final-particle detector.

For the simplicity we neglect here the spin-orbital coupling and we suppose also that the absolute values of all differences $r_n/v_n - r_p/v_p$ ($n \neq p = 1,2$) are much less than the time resolutions. Here $J_{C\to L}$ is the standard Jacobian of pure cinematic transformations from the ***C***-system to the ***L***-system.

We underline that formulas (5) - (10) for the cross section σ, obtained in [4] and defined by the usual *macroscopic* way, take into account a real *microscopic* motion of the compound nucleus. So, the formulas (5) - (10) differ from the standard cinematic transformation of $\sigma^C(E,\theta) = |F^C(E,\theta)|^2$ from the C-system into the L-system, considering only the cinematic transformations of the energies and angles from the C-system (with $\varphi = 0$) to the L-system. Such difference arises because the formal expression for $\sigma^C(E,\theta)$ was taken *without consideration* of the microscopic difference between the processes in Fig. 1, *a* and *b*, and thus *without consideration* of the parameter $\varphi = k_1\Delta r_1 + k_2\Delta r_2$, $\Delta r_{1,2} = V_{proj1,2}\,\Delta\tau_{res.}$

3. The absence of time advance near compound-resonances in the *L*-system

Earlier (see, for instance, [1 - 3]) usually the analysis of the amplitudes, cross sections and durations of the elastic scattering had been made on the base of formulas (1) → (1a) in the ***C***–system where the compound- nucleus motion in the ***L***-system had not been taken into account. But if one considers the motion of the decaying compound nucleus in the ***L***-system, then the roles of the ***C***-system in a prompt (direct and potential) process and in a delayed compound-nucleus process appear to be different in principle: The expression for the amplitude of the resonance compound-nucleus process in the ***C***- and ***L***-system differ not only by the standard cinematic transformations $\{E^C, \theta^C\} \leftrightarrow \{E^L, \theta^L\}$ but also by the motion of the decaying compound nucleus along the distance $V_C\,\Delta\tau_{res}$, as it is shown in figs.1a,b, taken from [8]. Applying the general approach from [4] for the mean collision duration

$$< \tau_{general} > = \frac{\int_{t_{\min}}^{\infty} t\Psi_{r_1\to\infty}\hat{j}_1\Psi_{r_1\to\infty}dt}{\int_{t_{\min}}^{\infty} \Psi_{r_1\to\infty}\hat{j}_1\Psi_{r_1\to\infty}dt} - t_i \approx \hbar/2\Delta E$$

we obtain after some simplifications, mentioned in [4], the general time delay which is compatible with time-energy uncertainty relation $\tau_{general}\Delta E \sim \hbar$ for quasi-monochromatic particles (for which $\Delta E << \Gamma$, $\Delta\tau_{res}\,\Delta E << 1$). So, we obtain the trivial mean time delay in the approximation (5) *without any advance caused by the "virtually unmoving" compound nucleus in the C-system***.**

Formulas (5) - (10) present the self-consistent approach to the realistic analysis of the experimental data on the cross sections for the nucleon-nucleus scattering in the ***L***-system. The reason is namely that in this case we neglect the real compound-nucleus motion.

4. Calculations of the energy behavior of the cross section for neutron-nucleus scattering near a distorted resonance with the help of realistic description of the experimental data on the base of the formulas (6) - (10)

The excitation functions $\sigma(E)$ for low-energy elastic scattering of neutrons by nuclei ^{52}Cr, ^{56}Fe and ^{64}Ni near distorted resonances $E_{res} = 50{,}5444$ keV and $\Gamma = 1{,}81$ keV, $E_{res} = 27.9179$ keV and $\Gamma = 0.71$ keV, $E_{res} = 24.7402$ keV and $\Gamma = 0.695$ keV, respectively. The values of parameters for the amplitudes of direct and resonance scattering *separately* in the ***C***-system for $l = 0$ in formulas (5) - (10) were chosen with the help of the standard procedure. Fitting parameter χ was chosen to be equal $0.948\,\pi$ or $0.956\,\pi$ or π, respectively.

The results of calculations performed by formulas (5) - (10) in comparison with the experimental data, taken from [5] for ***n* + ^{52}*Cr*, *n* + ^{56}*Fe*, *n* + ^{64}*Ni***, represented in Figs. 4 - 6, respectively. And the results of calculations, performed by standard cynematic formulas of transformations from the ***C***- into the ***L***-system, using formulas (5) - (10) with $\varphi \equiv 0$ (i.e. without the consideration of the diagram, depicted in Fig. 3, *b*), are presented in Figs. 4, *a* - 6, *a*. One can see that for $\varphi \equiv 0$ minima do not totally filled.

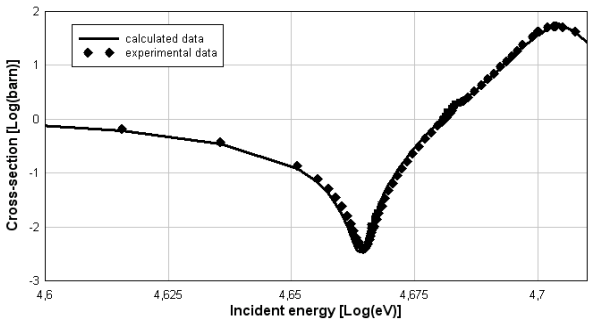

Fig. 4. The excitation function for $^{52}Cr(n, n)$.

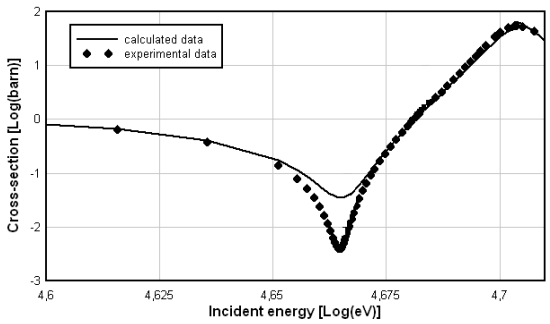

Fig. 4, *a*. The excitation function for $^{52}Cr(n, n)$ with $\varphi \equiv 0$.

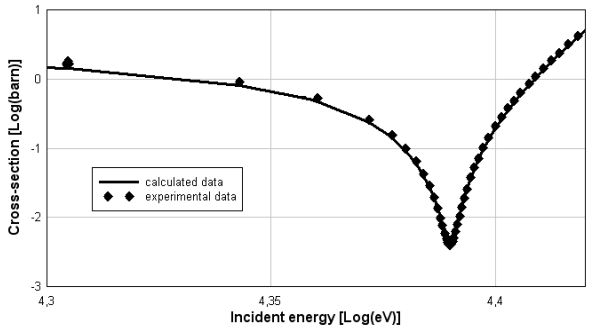

Fig. 5. The excitation function for $^{56}Fe(n, n)$.

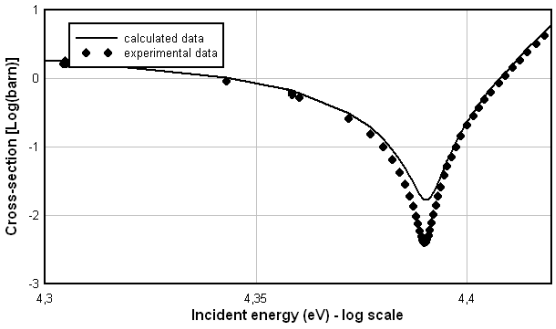

Fig. 5, *a*. The excitation for $^{56}Fe(n, n)$ with $\varphi \equiv 0$.

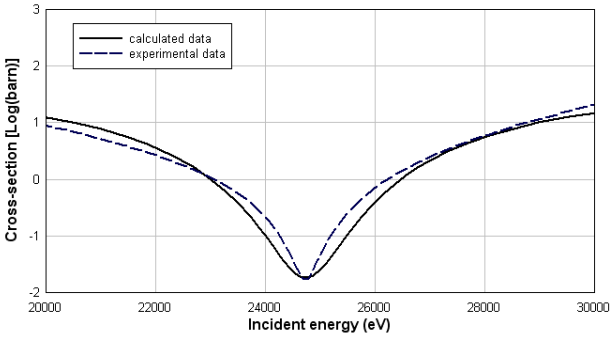

Fig. 6. The excitation function for $^{64}Ni(n, n)$.

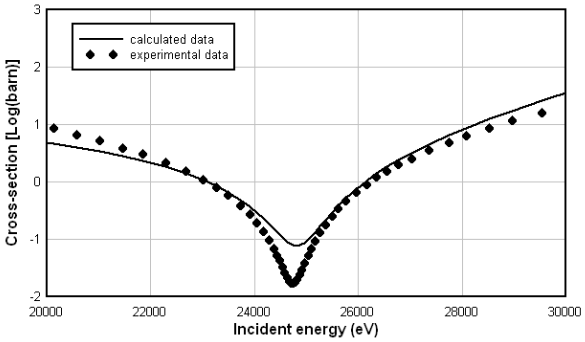

Fig. 6, *a*. The excitation function for $^{64}Ni(n, n)$ with $\varphi \equiv 0$.

5. Conclusions and perspectives

1. A simple application of time analysis for quasi-monochromatic neutron-nucleus scattering near isolated resonances, by the non-resonant background in the ***C***-system brings to the paradoxical virtual effect of time advance near a resonance in any two-particle channel. Her**e such paradox is *eliminated* by the space-time analysis *in the L*-system.**

2. Moreover, **the *standard formulas of transformations between the L-system and C–system are not valid in the presence of two collision mechanisms – rapid (direct or potential) process, when the center-of-mass does not practically shifted during collision, and delayed process, when the long-living compound nucleus is moving in the L*-system.** The obtained analytical transformations of the cross sections ***between the C-system and L–system*** are illustrated by the energy behavior of cross sections by some examples of elastic neutron-nucleus by nuclei ^{28}Si, ^{52}Cr, ^{56}Fe and ^{64}Ni near isolated distorted resonances.

REFERENCES

1. *Olkhovsky V.S., Doroshko N.L.* // Europhys. Lett. - 1992. - Vol. 18. - P. 483 - 486.
2. *D'Arrigo A, Doroshko N.L., Eremin N.V. et al.* // Nucl. Phys. - 1992. - Vol. A549. - P. 375 - 386.
3. *D'Arrigo A., Doroshko N.L., Eremin N.V. et al.* // Nucl. Phys. - 1993. - Vol. A564. - P. 217 - 226.
4. *Eremin N.V., Giardina G., Olkhovsky V.S., Omelchenko S.A.* // Mod. Phys. Lett. - 1994. - Vol. 9. - P.2849 - 2456.
5. *Harvey J.A., Larson D.C.*, ORNL. The JEFF - 3.1.1.Nuclear Data Library, OECD NEA/NEA2009; EXFOR 13759.002. - 1974.

DEUTERON AND TRITON DECAY OF ^{5}He RESONANCES IN THE REACTION ^{7}Li(d, α)^{5}He

Yu. N. Pavlenko[1], V. L. Shablov[2], V. O. Kyva[1], O. K. Gorpinich[1], N. L. Doroshko[1], A. V. Stepanyuk[1], O. I. Rundel[1], L. L. Dulger[3], D. V. Kasperovych[3]

[1] *Institute for Nuclear Research, National Academy of Sciences of Ukraine, Kyiv, Ukraine*
[2] *Obninsk Institute for Nuclear Power Engineering, Obninsk, Russia*
[3] *Taras Shevchenko National University, Kyiv, Ukraine*

The processes of excitation and decay of high excited ^{5}He resonances into the d + t channel have been studied in the three-particle channels of reaction ^{7}Li(d, α)^{5}He at the cyclotron U-240 of the Institute for Nuclear Research using the deuteron beam with energy E_d = 37 MeV. In the inclusive spectra of α-particles on a significant background caused by the accompanying three-particle reaction channels, in addition to the contributions of well known ^{5}He resonances the high excited states with $E_x \sim 19$ MeV and $E_x > 20$ MeV were observed. Cluster decay of these resonances was also identified in αd- and αt-coincidence spectra. For the first time the decay into the d + t channel was observed for ^{5}He resonances with $E_x \geq 22$ MeV. The determined resonance energy and width are partially agreed with the R-matrix analysis of data obtained in the study of binary reactions d + ^{3}H and n + ^{4}He. The possible Coulomb effects in three-particle channels of reaction ^{7}Li(d, α)^{5}He are also analyzed for different conditions of observation of high excited ^{5}He resonances.

1. Inroduction

The properties of light nuclei may essentially differ depending on the number of neutrons. It is striking illustrated by the chain of helium isotopes where the increasing the neutron number leads to the transformation of stable ^{4}He nucleus in unbound ^{5}He. Then we have weakly bound ^{6}He, unbound ^{7}He, weakly bound ^{8}He and unbound ^{9}He nucleus[1]. The properties of resonances of light nuclei and their cluster structure attend considerably to research, that is promoted by modern possibilities of correlation measurements [2, 3]. But this time, cluster decay and structure of high excited states of light nuclei, including the ^{5}He nucleus, are insufficiently studied.

In this work the processes of excitation and decay of ^{5}He resonances into the d + t channel have been investigated in the reaction ^{7}Li(d, α)^{5}He at the energy of deuteron beam of 37 MeV. A high Q-value for this reaction allows to study the excitation spectrum of ^{5}He up to $E_x \sim 40$ MeV.

Besides well known ^{5}He resonances [4] the high excited states with excitation energies $E_x \sim 19$ MeV and $E_x > 20$ MeV were observed in the inclusive spectra of α-particles from reaction ^{7}Li(d, α)^{5}He (see also [5]). Analysis of α-particle inclusive spectra for this reaction is rather complicated because of very large background caused by different accompanying three- and four-particle reaction channels [5]. The most reliable data can be obtained by correlation measurements that provide the full determination of kinematics of three-particle reactions. In this work cluster decay of a number of ^{5}He resonances was observed in αd- and αt-coincidence spectra.

2. Experiment

The differential cross sections of reaction ^{7}Li(d, α)^{5}He have been measured at the cyclotron U-240 of the Institute for Nuclear Research at deuteron beam energy of 37 MeV. The target with the thickness of 1,5 mg/cm^2 has been produced by rolling of lithium film with natural content of ^{7}Li. The reaction products have been detected by *ΔE-E*-method using four *ΔE-E*-telescopes of silicon detectors with the thickness of ~ 50 μm for *ΔE*- and 550 μm for E-detectors. The thickness of *ΔE*-detectors have been specified in a way to have a low energy threshold of registration preserving appropriate mass resolution. Solid angles of detector telescopes were $\Omega_1 = 0.92 \cdot 10^{-3}$ sr and $\Omega_2 = 1.82 \times \times 10^{-2}$ sr. Total energy resolution of reaction products registration was mainly determined by the dispersion of the beam energy, solid angles of detectors and energy losses of particles in the target and approximately consists of 1,5 % of the beam energy. The signals from the detectors were processed for multi-parameter measurements of inclusive and coincidence spectra of reaction products in the same manner as described in details in [6]. Data analysis has been performed using different procedure with two- and one-dimensional histograms for particle identification, determination of their energies and selection of reaction channels [6].

Fig. 1, *a* shows typical *E-ΔE*-spectrum measured by one telescope in coincidences with the reaction products registered by the second telescope which was placed at the opposite side from the beam. As it is shown the range of energy measurements for protons and deuterons was restricted by the thickness of *E*-detectors, which was insufficient to stop these high energy particles.

Two-dimensional spectrum of alpha-particle coincidences with tritons is shown in the Fig. 1, *b*. The events located in the upper part of this spectrum correspond to the three-particle reaction channel d + ^{7}Li → α + t + d. The events in the below region of spectrum are caused by four-particle reaction d + ^{7}Li → α + t + p + n.

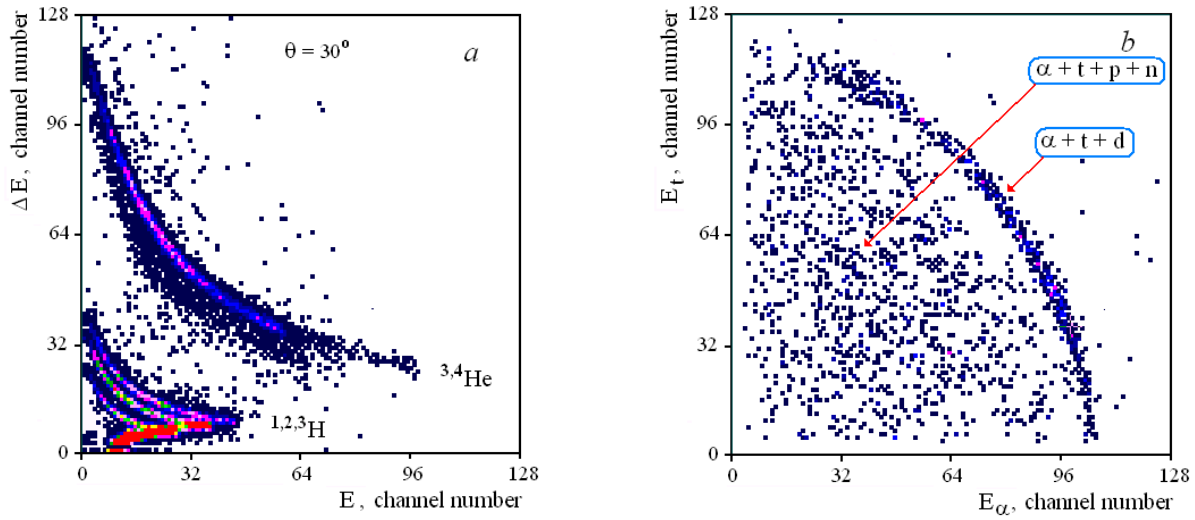

Fig. 1. *ΔE-E*-spectrum measured at the angles $\theta_1 = 30°$, $\varphi_1 = 180°$ in coincidences with all products of reaction d + ^{7}Li which were registered at the angles $\theta_2 = 79°$, $\varphi_2 = 0°$ (*a*). Two-dimensional plot of energy spectrum of αt–coincidences in the exit reaction channels d + ^{7}Li → α + t + d and d + ^{7}Li → α + t + p + n, which were measured at the angles $\theta_\alpha = 30°$, $\theta_t = 79°$, $\varphi_1 - \varphi_2 = 180°$ (*b*). Arrows indicate the location of three- and four-particle reaction channels.

The measurements of time coincidence spectra have been also used for evaluation of background which was caused by the registration of random coincidence events (Fig. 2). Peaks marked by number 1 correspond to the registration of two reaction products induced by deuteron interaction from one bunch of deuteron beam and contain real coincidence events and random time coincidences. Peaks marked by number 2 correspond to the registration of two reaction products from two different bunches of beam and contain only random coincidence events. As it is shown, the contributions of random coincidences in time spectra, which correspond to the registration of all reaction products (see Fig. 2, *a*), as well as in the spectra of coincidences of α-particles with tritons (see Fig. 2, *b*) are rather small. The ratio of random to real coincidence events is equal 0.25 and 0.05 for the spectra in Fig. 2, *a* and *b*, respectively. This ratio for events corresponding the three-particle exit channels α + t + d (see Fig. 1, *b*) and α + d + t is equal ~ 0.01. Thus, the background contribution of random coincidences can be neglected for reaction channels ^{7}Li(d, αt)d and ^{7}Li(d, αd)t.

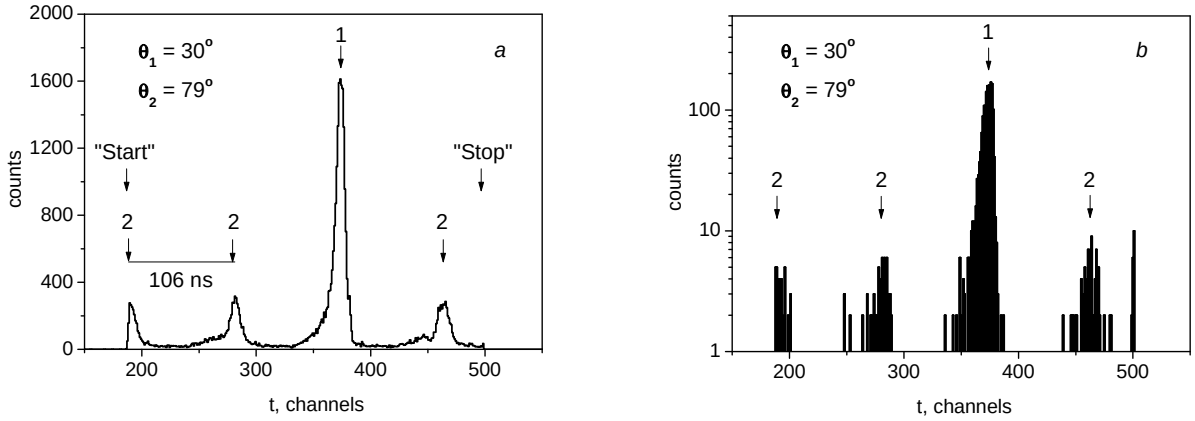

Fig. 2. Total time coincidence spectrum measured by two telescopes at the registration of all products of reaction d + ^{7}Li at the angles $\theta_1 = 30°$, $\theta_2 = 79°$, $\varphi_1 - \varphi_2 = 180°$ (*a*). Time spectrum of αt-coincidences measured at the same angles (*b*). Peaks in the spectra marked as 1 and 2 correspond to the events from neighboring bunch of deuteron beam.

3. Analysis and results

Alpha-particle energy spectra measured in coincidences with deuterons and tritons are shown in the Fig. 3. These spectra (triple differential cross section) were obtained from two-dimensional spectra of αt- (see Fig. 1, *b*) and αd-coincidences using usual procedures [6]. Correlation spectra have been decomposed in some Breit - Wigner curves which correspond to the contributions of ^{5}He resonances:

$$\frac{d^3\sigma}{d\Omega_\alpha d\Omega_{d(t)} dE_\alpha} = \frac{C_i}{(E_{d-t} - E_R)^2 + \Gamma^2/4}\rho(E_\alpha), \qquad (1)$$

where $E_R = E_x - E_{b(dt)}$ and Γ are resonance energy and width, $E_{b(dt)}$ is bound energy of deuteron and triton in ^{5}He nucleus, $E_{d\text{-}t} = f(E_\alpha)$ is relative energy in (d-t)-subsystem depending on the alpha-particle energy E_α, $\rho(E_\alpha)$ is the phase space factor [7] for three-particle reaction ^{7}Li(d, αd)t or ^{7}Li(d, αt)d, C_i is the coefficient which determines the intensity of resonance with number i.

Besides ^{5}He resonances the excitation and decay of ^{6}Li and ^{7}Li resonances can be also observed in coincidence spectra from reactions ^{7}Li(d, αd)t and ^{7}Li(d, αt)d. These resonances are formed in accompanying reaction channels ^{7}Li(d, d)^{7}Li* and ^{7}Li(d, t) ^{6}Li*. The position of possible contributions of ^{6}Li and ^{7}Li resonances can be calculated using the kinematical dependencies of relative energies in (α–d)- and (α–t)-subsystems on the alpha-particle energy E_α. The dependencies of excitation energy of ^{5}He, ^{6}Li and ^{7}Li resonances on the energy of one of the reaction products can be obtained using simple equation: $E_x = E_{rel} + E_b$, where E_{rel}, E_b are the relative energy and bound energy of one of the cluster in corresponding subsystem, respectively. As it shown in Fig. 4, the known resonances of ^{6}Li and ^{7}Li [4] do not contribute to the high energy part of measured coincidence spectra ($E_\alpha > 19$ MeV). The well known "thermonuclear" resonance of ^{5}He with excitation energy $E_x = 16.75$ MeV cannot be also observed in the analyzed spectra.

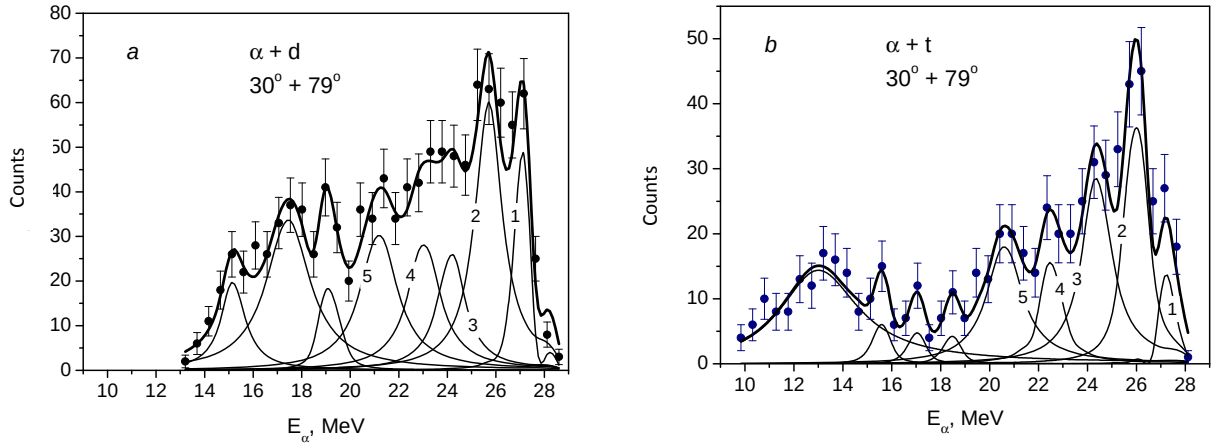

Fig. 3. Energy spectra of alpha-particle measured in coincidences with deuterons (*a*) and tritons (*b*) for reactions ^{7}Li(d, αd)t and ^{7}Li(d, αt)d at $E_d = 37$ MeV, $\theta_\alpha = 30°$, $\theta_{d(t)} = 79°$, $\varphi_\alpha - \varphi_{d(t)} = 180°$. Solid lines represent the results of the fit by equation (1) for each resonance (see Table). Thick line corresponds to the sum of all resonance contributions.

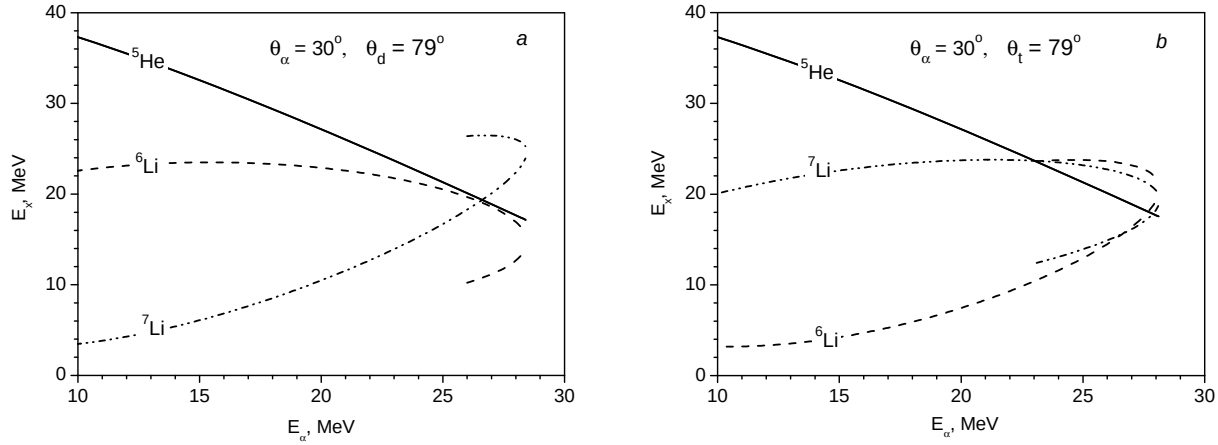

Fig. 4. The dependencies of excitation energy of ^{5}He, ^{6}Li and ^{7}Li resonances, which can be observed in the reactions ^{7}Li(d, αd)t (*a*) and ^{7}Li(d, αt)d (*b*), on the alpha-particle energy E_α. Calculations were performed under kinematical conditions specified in the capture of Fig. 3.

Extracted values of ^{5}He resonance parameters are given in the Table. Some resonances which contributions can be overlapped with accompanying resonances of ^{6}Li and ^{7}Li have been excluded from consideration. Resonances with $E_x \sim 19$ MeV have been previously identified at the study of reactions ^{2}H(α, pd)^{3}H [8] and ^{3}H(α, dd)^{3}H [9] in kinematically complete experiments. The results of many inclusive experiments indicate the presence only one broad level with $E_x \sim 20$ MeV [4]. Existence of three resonances with $E_x = 19.14$, 19.26, 19.31 MeV, approximately equal width $\Gamma = 3.56$, 3.96, 3.02 MeV and different spin follows from multichannel R-matrix analysis of experimental data for binary reactions d + ^{3}H and n + ^{4}He [10].

The parameters obtained for the second resonance with $E_x \sim 20$ MeV are agreed well with R-matrix analysis of binary reactions ($E_x = 19.96$ MeV, $\Gamma = 1.92$ MeV [10]) and reaction ^{2}H(^{6}He, dt)^{3}H ($E_x = 19.7 \pm 0.3$ MeV [11]). Third resonance with $E_x = 22$ MeV and $\Gamma = 1.7$ MeV have not been observed at the study of binary reaction [10]. R-matrix analysis [10] has suggested the presence of two broad ($\Gamma \sim 5$ MeV) resonances with approximately equal excitation

energy E_x = 23.97 and 24.06 MeV and different spins. We identified more narrow resonance with excitation energy E_x ~ 24 MeV (Γ ~ 1.2 – 1.9 MeV) and E_x ~ 26 MeV (Γ ~ 2 MeV) which has not been previously observed.

^{5}He resonance parameters obtained for reactions ^{7}Li(d, αd)t and ^{7}Li(d, αt)d.

Numbers in the first column correspond to the numbers of lines in Fig. 3.

Resonance number	Reaction ^{7}Li(d, αd)t		Reaction ^{7}Li(d, αt)d	
	E_x, MeV	Γ, MeV	E_x, MeV	Γ, MeV
1	18.7 ± 0.1	0.5 ± 0.2	18.5 ± 0.2	0.7 ± 0.2
2	20.4 ± 0.2	1.7 ± 0.6	20.3 ± 0.2	1.8 ± 0.5
3	22.2 ± 0.4	1.7 ± 0.5	22.0 ± 0.2	1.7 ± 0.5
4	23.6 ± 0.4	1.9 ± 0.5	24.2 ± 0.2	1.2 ± 0.5
5	25.7 ± 0.3	2.1 ± 0.8	26.4 ± 0.3	2.0 ± 0.8

All the products of studied reactions are charged. In this case under certain conditions we can expect the Coulomb effects which can modify the observable resonance parameters [12]. Calculations show that for decay of ^{5}He resonances with E_x = 18 - 26 MeV and Γ ~ 1 - 2 MeV into (d + t)-channel the maximal shift and width change of resonance curves caused by the Coulomb field of accompanying alpha-particles exceed the value of 200 keV. This can explain the widening resonance curves which have been observed in the inclusive spectra, for example at E_x ~ 20 MeV.

4. Conclusions

The decay of high excited ^{5}He resonances with E_x > 17 MeV into the d + t channel have been studied in the three-particle reactions ^{7}Li(d, αd)t and ^{7}Li(d, αt)d at deuteron beam energy E_d = 37 MeV. In kinematically complete experiments a new data for ^{5}He resonance energies and widths have been obtained. The data within experimental errors are consistent partly with those obtained by other authors (see [4, 8 - 11]), but the decay of resonances with E_x ~ 24 and 26 MeV into the d + t channel was observed for the first time. Determined parameters for some resonances are also agreed with the extended R-matrix analysis of data for binary reactions d + ^{3}H and n + ^{4}He [10]. Performed calculations show that three-particle Coulomb effects are quite observable in the studied reactions at E_d = 37 MeV for ^{5}He resonances with E_x ~ 18 – 26 MeV.

Obtained results will be useful to clarify the causes of inconsistency between an existing data as well as to test the various theoretical models.

REFERENCES

1. *Golovkov M. S., Grigorenko L. V., Fomichev A. S. et al.* New insight into the low-energy ^{9}He spectrum // Phys. Rev. C. - 2007. - Vol. 76, No. 2. - P. 021605 (1 - 5).
2. *Grenier F., Chbihi A., Roy R. et al.* Multi-particle correlation function to study short-lived nuclei // Nucl. Phys. A. - 2008. - Vol. 811, No. 3 - 4. - P. 233 - 243.
3. *Caamano M., Cortina-Gil D., Mittig W. et al*. Experimental study of resonance states in ^{7}H and ^{6}H // Phys. Rev. C. - 2008. - Vol. 78, No. 4. - P. 044001 (1 - 8).
4. *Ajzenberg-Selove F.* Energy levels of light nuclei A = 5 - 10 // Nucl. Phys. A. - 1988. - Vol. 490, No. 1. - P. 1 - 225.
5. *Pavlenko Yu.N., Gorpynych O.K., Dobrikov V.N. et al.* Experimental study of the excited states of helium isotopes in the reactions ^{7}Li(d,^{3,4,6}He) at deuteron energy of 37 MeV // Nucl. Phys. At. Energy. - 2006. - No. 2(18). - P. 16 - 27.
6. *Pavlenko Yu.N., Kiva V.O., Kolomiets I.N. et al.* The methods of multiparameter correlation measurements for the study of nuclear reactions // Sci. Papers of the Inst. for Nucl. Res. - 2005. - No. 2(15). - P. 151 - 161.
7. *Ohlsen G.G.* Kinematic relations in reactions of the form A + B→C + D + E // Nucl. Instr. and Meth. - 1965. - Vol. 37. - P. 240 - 248.
8. *Treado P.A., Lambert J.M., Kane R.J. et al.* Excited States of ^{4}He and ^{5}He from Sequential α + d Reactions at $E_α$ = 70 MeV // Phys. Rev. C. - 1973. - Vol. 7, No. 5. - P. 1742 - 1750.
9. *Gorpinich O.K., Povoroznyk O.M., Yachmeniov A.A.* The structure of high excited states of ^{5}He nucleus // Izv. RAN. Ser. Phys. - 2005. - Vol. 69. - P. 745.
10. *Tilley D.R., Cheves C.M., Godwin J.L. et al.* Energy levels of light nuclei A = 5, 6, 7 // Nucl. Phys. A. - 2002. - Vol. 708, No. 1. - P. 3 - 163.
11. *Ter-Akopian G.M., Fomichev A.S., Golovkov M.S. et al.* New insights into the resonance states of ^{5}H and ^{5}He // Eur. Phys. J. - 2005. - Vol. A25. - P. 315.
12. *Pavlenko Yu.N., Dobrikov V.N., Doroshko N.L. et al*. Decay properties of short lived resonances of light nuclei in many-particle nuclear reactions // Int. Journal of Modern Physics E. - 2010. Vol. 19, Issue 5 - 6. - P. 1220 - 1226.

SUB-BARRIER INTERACTION OF DEUTERONS WITH ^{58,62}Ni, ^{124}Sn AND ^{208}Pb NUCLEI

Yu. N. Pavlenko, O. I. Rundel, K. O. Terenetsky, V. P. Verbytsky, I. P. Dryapachenko, V. V. Ostashko, O. K. Gorpinich, L. I. Slusarenko, Yu. Ya. Karlyshev, A. V. Stepanyuk, E. M. Mozhzhukhin

Institute for Nuclear Research, National Academy of Sciences of Ukraine, Kyiv, Ukraine

The elastic scattering and (d, p) reaction on nuclei ^{58,62}Ni, ^{124}Sn and ^{208}Pb have been studied in order to determine the features of sub-barrier interaction of deuterons with nuclei of different masses. Experimental data were obtained at electrostatic tandem accelerator EGP-10K of the Institute for Nuclear Research (Kyiv) using the deuteron beam with energy in the range E_d = 3.5 - 7.3 MeV. The calculations of differential and integral (over the neutron emission angles) cross sections of reactions A(d, p)nA were performed. Analysis of the calculations and the measured inclusive spectra of protons and their integrated over the energy yields showed that the differences of experimental and theoretical cross sections of deuteron elastic scattering on the ^{58,62}Ni, ^{124}Sn and ^{208}Pb nuclei are mainly caused by the process of neutron transfer to the target nuclei (reaction A(d, p)A + 1), which was not included in the calculations, but not by deuteron break-up reaction A(d, p)nA.

1. Introduction

Study of weakly bound nuclei interaction is important because of significant influence of dynamic effects caused by nuclei spatial patterns. Deuteron Coulomb breakup at sub-barrier energies is one of the simplest cases when such effects can take place. Some theoretical models [1, 2] consider "deuteron-like" cluster structure of neutron rich nuclei, for example ^{6}He with dineutron configuration and strongly bound α-cluster as a "proton".

This experiment was performed with the aim to test the capability of this model to describe the feature of sub-barrier interaction of deuteron with ^{124}Sn nuclei and to compare the measured angular distributions of differential cross sections of ^{124}Sn(d, d) elastic scattering and ^{124}Sn(d, p) reaction with similar data obtained for ^{58,62}Ni [3] and ^{208}Pb [4] nuclei. The role of deuteron break-up and neutron transfer processes at sub-barrier energies are also analysed for all nuclei mentioned above.

It should be noted that there is no experimental data for deuteron elastic scattering and (d, p) reaction measured simultaneously in the wide angular range for ^{124}Sn nuclei as well as for other nuclei with middle value of mass number A. Existing data in the energy region around the Coulomb barrier are limited by the values of the cross sections for several points of the angular distribution (for example, see [5] for d + ^{124}Sn interaction).

2. Experiment

The measurements were carried out with the deuteron beam accelerated to the energy E_d = 4 - 5.5 MeV at the Tandem Electrostatic Generator ESG-10K (Institute for Nuclear Research, Kyiv). Thick self-support ^{124}Sn (5 mg/cm^2) target was used in the experiment. The differential cross sections of (d, d) and (d, p) reactions were measured in the angular range of $\theta = 30^o$ - 160^o. Deuterons and protons were registered by two ΔE-E telescopes of semiconductor detectors with the thicknesses ~ 20 and ~ 500 μm. The low energy threshold of registration was reached owing to the utilization of thin ΔE-detectors. Deuteron beam intensity was controlled with Faraday cup and two monitor detectors, which were installed in the reaction chamber at the fixed angles $\theta = 27^o$ and 150^o.

The utilized data acquisition system is described in [3, 4, 6]. Data analysis was done by software that is designated for execution of procedures which are necessary for identification of registered reaction products and reconstruction of their energy spectra.

3. Results and analysis

As it is customary, the differential cross sections of elastic scattering were determined by integrating of energy spectra over the observed scattering peak and by normalizing the cross section values, measured at forward angles, to the cross sections of Rutherford scattering. Angular distributions of differential cross sections for ^{124}Sn(d, d) elastic scattering measured at the energies of 4.0, 5.0 and 5.5 MeV are shown in Fig. 1. Considerable deviation between measured differential cross sections and Rutherford ones is observed at the middle and backward scattering angles at E_d = 5.0 and 5.5 MeV. This deviation is essentially larger than those predicted by theoretical calculations [1, 2], that take into account the process of Coulomb break-up using adiabatic approximation. Besides, measured angular distribution has unexpected non-monotonic behaviour.

Similar results were obtained at the study of sub-barrier elastic scattering ^{58,62}Ni(d, d) [3] and ^{208}Pb(d, d) [4]. The cross sections of deuterons elastic scattering on ^{208}Pb nuclei, measured at the energy of 7.3 MeV, also differ from Rutherford cross sections greater than was predicted by calculations with taking into account the Coulomb break-up of deuterons (Fig. 2). Though experimental data agree with values of differential cross sections obtained in [5] at the close energies E_d = 7.0 and 8.0 MeV. The same behaviour of the differential cross sections was observed for elastic scattering

on ^{58}Ni at the energies of 3.5, 4.5 and 5.16 MeV and ^{62}Ni at the energy of 5.16 MeV [3] (Fig. 3). It is necessary to mention that the cross sections for these nickel isotopes are very close at the energy of 5.16 MeV.

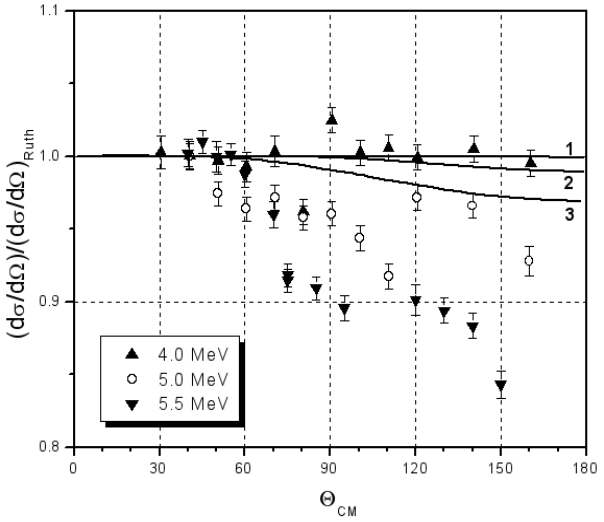

Fig. 1. The differential cross sections of ^{124}Sn(d, d) elastic scattering measured at the energies E_d = 4.0, 5.0 and 5.5 MeV. Points show the experimental values and lines show the theoretical calculations with consideration of Coulomb break-up: *1* – E_d = 4.0 MeV; *2* – 5.0 MeV; *3* – 5.5 MeV.

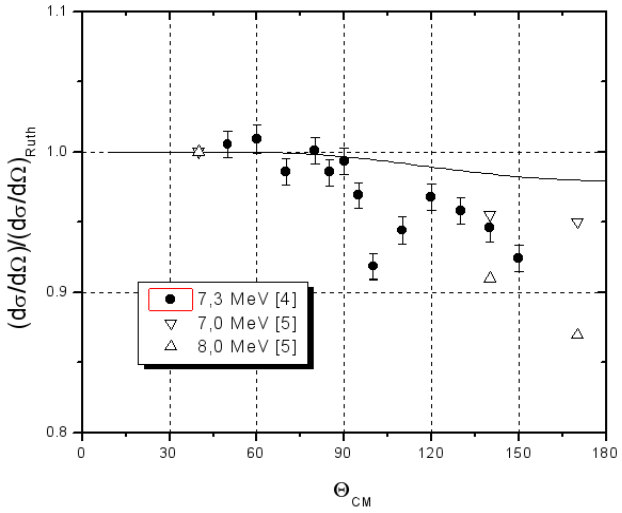

Fig. 2. The differential cross sections of ^{208}Pb(d, d) elastic scattering measured at the energies E_d = 7.3 MeV [4] and E_d = 7.0 and 8.0 MeV [5]. Line shows the results theoretical calculation with taking into account the Coulomb break-up at E_d = 7.3 MeV.

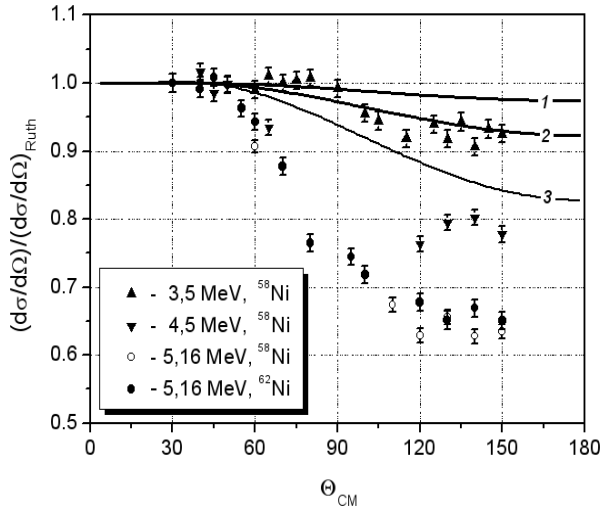

Fig. 3. The differential cross sections of ^{58,62}Ni(d, d) elastic scattering measured at the energies E_d = 3.5, 4.5 and 5.16 MeV [3]. Line shows the results of theoretical calculations with taking into account the Coulomb break-up at different deuteron energies: *1* – E_d = 3.5 MeV; *2* – 4.5 MeV; *3* – 5.16 MeV.

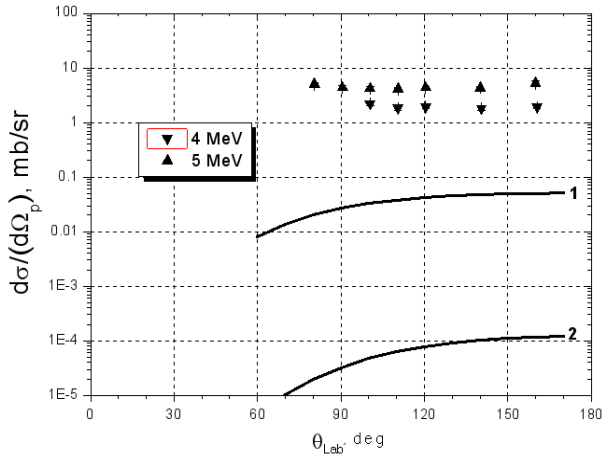

Fig. 4. The differential cross sections of ^{124}Sn(d, p) reaction measured at E_d = 4.0 and 5.0 MeV. Lines show the calculated Coulomb break-up cross sections [7] integrated over neutron emission angle and proton energy: *1* – E_d = 5.0 MeV; *2* – 4.0 MeV.

The differential cross sections of the ^{124}Sn(d, p) reaction were also measured. The proton spectra were integrated over full range of proton energy (E_p > 1.8 MeV). The triple differential cross sections of deuteron break-up calculated according to [7] were integrated over the neutron emission angle and the proton energy for the estimation of possible break-up contribution to the proton yield in the ^{124}Sn(d, p) reaction. It can be seen that this contribution cannot explain such large (d, p) cross section (Fig. 4).

It was shown earlier that the process of neutron transfer is also more intensive than the Coulomb break-up for ^{58,62}Ni(d, p) [3] and ^{208}Pb(d, p) reactions [4] at sub-barrier energies. The experimental data for differential cross sections

of these (d, p) reactions, which were obtained by integrating the measured spectra over the proton energy, and the calculated contributions of deuteron break-up are shown in Fig. 5 and Fig. 6.

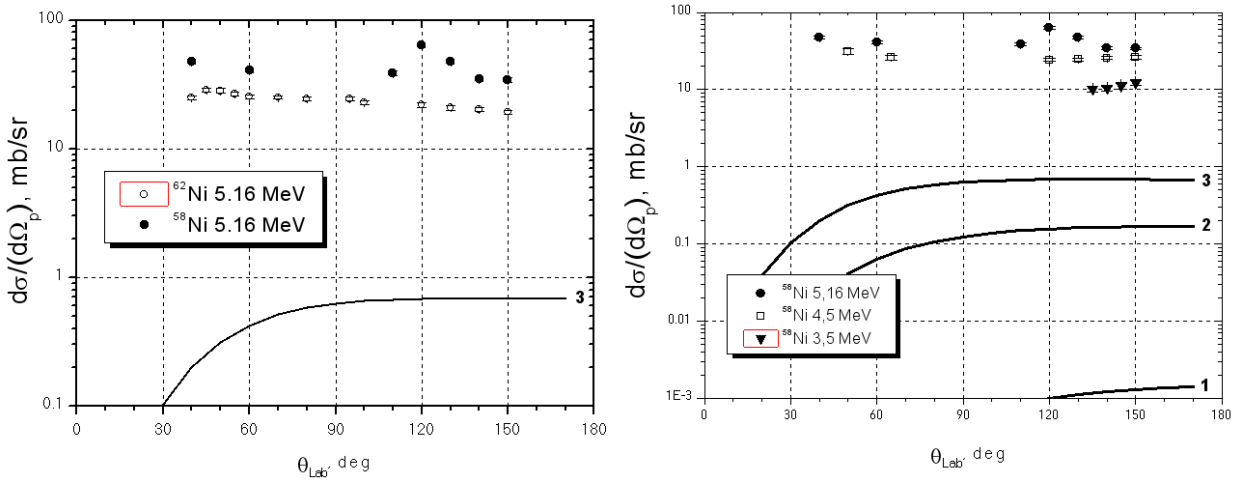

Fig. 5. The differential cross section of the ^{58,62}Ni(d, p) reaction at E_d = 5.16 MeV (left panel) and ^{58}Ni(d, p) reaction at E_d = 3.5, 4.5 and 5.16 MeV (right panel). Points show the experimental data integrated over the proton energy [3]. Lines show the calculated Coulomb break-up cross sections integrated over neutron emission angle and proton energy: *1* – E_d = 3.5 MeV; *2* – 4.5 MeV; *3* – 5.16 MeV.

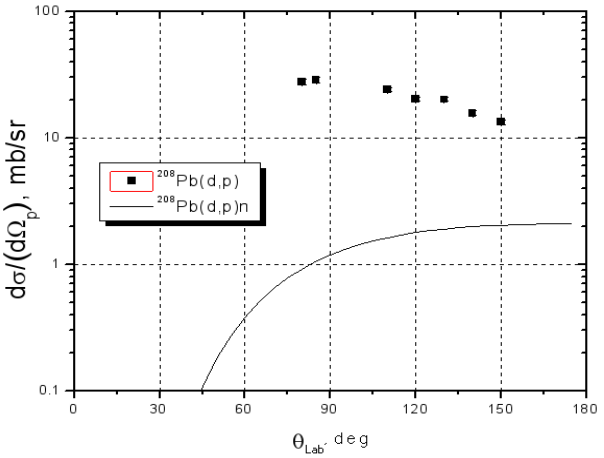

Fig. 6. The differential cross section of the ^{208}Pb(d, p) reaction at E_d = 7.3 MeV. Line shows the calculation of possible contribution of the deuteron Coulomb break-up to the measured cross sections.

4. Conclusions

The sub-barrier interaction of deuterons with ^{124}Sn nuclei has been experimentally studied at E_d= 4.0, 5.0 and 5.5 MeV. Measured differential cross sections of elastic scattering at the middle and backward angles differ from the values of Rutherford scattering. The theoretical calculations with consideration of deuteron polarizability and Coulomb break-up according to the model proposed in [1, 2] predict considerably lesser cross section decrease with the growth of scattering angle. Non-monotonic change of experimental cross sections at the middle angles is also not reproduced by this model. Similar behaviour of angular dependence of cross section was also observed for the ^{58,62}Ni(d, d) [3] and ^{208}Pb(d, d) [4] elastic scattering.

According to the calculations the main yield of protons must be observed at the backward angles. However, the measured differential cross sections of the ^{124}Sn(d, p) reaction are larger by the order of magnitude and do not depend on the scattering angle in such way as it is predicted by the model [1, 2]. Therefore, we can assume that at sub-barrier energies of deuterons the neutron transfer is a dominant mechanism for ^{124}Sn(d, p) reaction as well as for ^{58,62}Ni(d, p) and ^{208}Pb(d, p) reactions [3, 4].

The obtained results show necessity of detailed complex study of (d, d), (d, p) and (d, pn) reactions on the middle and heavy nuclei at sub-barrier energies.

REFERENCES

1. *Terenetsky K.O.* Description of elastic scattering of deuterons by nuclei in the adiabatic approximation. // Sov. J. Nucl. Phys. - 1983. - Vol. 37, No. 5. - P. 698 - 701.
2. *Verbytsky V.P., Terenetsky K.O.* Sub-barrier scattering of weakly bound neutron excess light nuclei // Sov. J. Nucl. Phys. - 1992. - Vol. 55, No. 2. - P. 198 - 201.
3. *Pavlenko Yu.N., Terenetskii K.O., Verbitskii V.P. et al.* Sub Barrier Interaction between Deuterons and $^{58, 62}$Ni Nuclei // Bull. of the Russian Academy of Sciences. Physics. - 2012 - Vol. 76, No. 8. - P. 888 - 891.
4. *Pavlenko Yu.N, Terenetsky K.O., Verbitsky V.P. et al.* Deuterons Interaction with Nuclei ^{208}Pb at Sub-Barrier Energies

// Nucl. Phys. At. Energy. - 2010. - Vol. 11, No. 4. - P. 400 - 404.
5. *Stromich A., Steinmetz B., Bangert R.* (d, p) reaction on ^{124}Sn, ^{130}Te, ^{138}Ba, ^{140}Ce, ^{142}Nd and ^{208}Pb below and near Coulomb barrier // Phys. Rev. C. - 1977. - Vol. 16, No. 6. - P. 2193 - 2207.
6. *Pavlenko Yu.N., Kyva V.O., Kolomiets I.N. et al.* The methods of multiparameter correlation measurements for the study of nuclear reactions // Sci. Papers of the Inst. for Nucl. Res. - 2005. - No. 2(15). - P. 151 - 161.
7. *Terenetsky K.O., Verbytsky V.P*. Energy spectra of deuteron Coulomb breakup at subbarrier energies // Nucl. Phys. At. Energy. - 2006. - Vol. 1(17). - P. 45 -50.

VVER-1000 FUEL REARRANGEMENT OPTIMIZATION TAKING INTO ACCOUNT BOTH FUEL CLADDING DURABILITY AND BURNUP

S. N. Pelykh, M. V. Maksimov

Odesa National Polytechnic University, Odesa, Ukraine

A VVER-1000 fuel element (FE) cladding failure estimation method based on creep energy theory (CET-method) is physically grounded. Using CET-method, the VVER-1000 regime and fuel design parameters that determine cladding failure conditions are found. The VVER-1000 average cladding failure parameter after 500 day cycles, for the most strained axial segment, at power maneuvering with constant average coolant temperature is 8.7 % greater than the same with constant coolant inlet temperature. It is proved that it is possible for four years at least, to stay at the steady creep stage, on condition that the corrosion rate is sufficiently small. Practically FE cladding rupture life at normal variable loading operation conditions can be controlled by an optimal assignment of coolant temperature regime and fuel assembly (FA) rearrangement algorithm. The probabilistic FA rearrangement efficiency criterion based on Monte Carlo Sampling takes into account robust operation conditions and gives results corresponding to the deterministic ones in principle, though the robust efficiency estimation is more conservative. It is shown that CET-method allows us to create an automized program-technical complex making control of FE cladding durability and optimization of fuel rearrangements in VVER-1000.

1. Introduction

Recently the problem of fuel cladding life control at nuclear power plants (NPP) with VVER-1000 reactors has become actual in Ukraine. The VVER-1000 fuel element (FE) cladding total damage parameter is usually estimated by the relative service life of cladding, when steady-state operation and varying duty are considered separately. This approach has the following principal disadvantages: disagreement between experimental conditions and real operating environment; the physical mechanism (creep) of cladding damage accumulation and the real stress history are not taken into account; uncertainty of this cladding life estimate forces us into assumption of an unreasonably high safety factor; the cladding failure criterion components depend on VVER-1000 loading conditions, power maneuvering methods, dispositions of regulating units, fuel assembly (FA) rearrangement algorithms, etc.; there is no public data on cladding failure criterion components for all possible VVER-1000 loading conditions, power maneuvering methods, dispositions of regulating units, FA rearrangement algorithms, etc. [1].

The problem of VVER-1000 fuel cladding life control under variable loading consists of several subproblems: creating a physically based method of VVER-1000 fuel cladding failure estimation; determination of main factors influencing VVER-1000 fuel cladding life; working out methods to optimize main factors influencing VVER-1000 fuel cladding life.

The light water reactor (LWR) fuel analysis finite element code FEMAXI [2] was used for determination of the evolution of VVER-1000 cladding creep stresses and strains under variable loading in a given power history and coolant conditions. Sintered uranium dioxide was assumed to be the pellet material, while stress-relieved zircaloy-4 was assumed to be the cladding material. The amplitude of relative linear heat rate (LHR) jumps at FE axial segments (ASs) occurring when the reactor thermal capacity N increases at power maneuvering, was estimated using the "Reactor Simulator" (RS) code [3]. To predict likelihood of VVER-1000 fuel cladding failure accurately, it is necessary to use a relevant physical model of the fuel cladding failure process during cyclic pressurization. When loading frequency is below 1 Hz, creep governs the entire deformation process in zircaloy-4 cladding [4]. According to creep energy theory (CET), energy spent for FE cladding material destruction is called as specific dispersion energy (SDE) [5].

For the first time, a method of analysis of VVER-1000 FE cladding running time at variable loading based on CET (CET-method) was proposed in [6]. The main features of CET-method are: creep is the main mechanism of cladding deformation when VVER-1000 is operated at variable loading; creep and destruction processes proceed in common and influence against each other; at any moment intensity of failure is estimated by SDE accumulated during creep process by this moment; cladding failure criterion components do not depend on VVER-1000 loading conditions, power maneuvering method, disposition of regulating units, FA rearrangement algorithm, etc.

Having found the VVER-1000 regime and fuel design parameters that determine cladding failure conditions, the problem of cladding life control is split into optimization of FE constructional parameters (cladding diameter and thickness; pellet and pellet centre hole diameters; pellet effective density; initial He pressure and grid spacing; etc.) and reactor regime parameters (FE maximum LHR; coolant inlet temperature, pressure and velocity; etc.).

The VVER-1000 FE cladding failure estimation method based on CET is physically grounded because it takes into account influence of real reactor operating environment, stress history as well as the physical mechanism (creep) of cladding damage accumulation. CET-method is universal because it is fit for different types of LWR, fuels, fuel claddings, and the cladding failure criterion components do not depend on loading conditions, power maneuvering methods, dispositions of regulating units, FA rearrangement algorithms, etc.

Considering real FA transposition algorithms, as well as a real disposition of control rods, it has been obtained that the AS located between z = 2.19 and 2.63 m is most strained and limits fuel cladding operation time at VVER-1000 day

cycle power maneuvering. The fuel pellets corresponding to this limiting AS could be made with holes to increase cladding durability.

Taking into account that coolant inlet temperature T_{in} during reactor power maneuvering influences greatly on axial offset (AO) stability, the problem of cladding durability is closely connected to the problem of thermal neutron flux axial distribution stability. The VVER-1000 thermal neutron flux axial distribution can be significantly stabilized at power maneuvering by means of a proper coolant temperature regime assignment. Assuming the maximum divergence between the instant and equilibrium AOs equal to 2 %, the regulating unit movement amplitude at constant coolant average temperature $< T >$ is 6 %, while the same at constant T_{in} is 4 %. Therefore, when using the method with $< T >$ = const, a greater regulating unit movement amplitude is needed to guarantee LHR axial stability, than when using the method with T_{in} = const, on the assumption that all other conditions for both the methods are identical. The VVER-1000 average cladding failure parameter after 500 day cycles, for the most strained AS, at power maneuvering with $< T >$ = const is 8.7 % greater than the same with T_{in} = const, on the assumption that AO stability is identical for both the methods [7]. For the VVER-1000 conditions, the rapid creep stage is degenerated when using the zircaloy-4 cladding corrosion models MATPRO-A and EPRI [8], at the correcting factor COR = - 0.43. This phenomenon proves that it is possible for four years at least, to stay at the steady creep stage, where cladding equivalent creep and radial total strains do not exceed 1 - 2 %, on condition that the corrosion rate is sufficiently small. The VVER-1000 cladding corrosion rate is determined by design constraints for cladding and coolant, and depends slightly on a regime of variable loading. At the same time, practically FE maximum LHR is determined not only by current reactor capacity level, which is a value given to a NPP by the integrated power system, but also by FA rearrangement algorithm. Therefore, the FE cladding rupture life at normal variable loading operation conditions can be controlled by an optimal assignment of coolant temperature regime and FA rearrangement algorithm.

2. Optimization of VVER-1000 FA rearrangement algorithm

Optimization of FA rearrangements is undertaken for a core segment containing 1/6 of all the FAs, as well as 1/6 of all the regulating units used for power maneuvering. Disposition of the 10th regulating group in case of A-algorithm and the analyzed core segment are shown in Fig. 1.

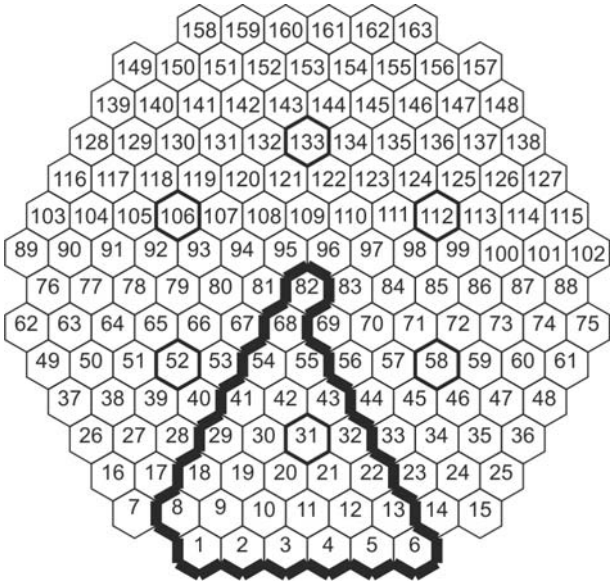

Fig. 1. Disposition of the 10th group: (figure) FA cell number (360 symmetry). The 10-th group cells and the analysed core segment (1/6) borders are in bold.

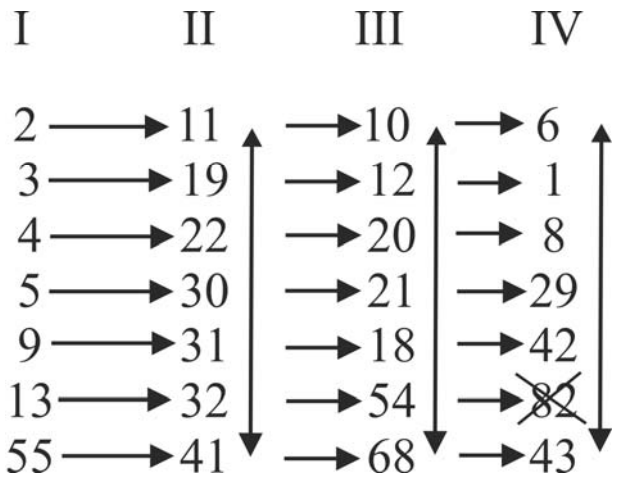

Fig. 2. Transpositions of FAs during rearrangements: (number) FA cell number; (roman numerals I, II, III and IV) 1st, 2nd, 3rd and 4th campaign year, respectively (6 cells for the 4th year FAs).

According to the distribution of long-lived and stable fission products specified for the start of the 5th four-year campaign of KhNPP Unit 2, distribution of FAs in the core segment by campaign year is given in the input data file for the RS code. Having used RS, to establish conditions at the start of the 5th campaign, it was found that there are 7 FAs of each campaign year in the specified core segment. Hence, it can be assumed that at the beginning of each campaign year FAs are placed according to the distribution shown in Fig. 2.

Nowadays two main approaches are used at NPP with VVER-1000 [9]: 1) a 4th year FA is placed in the central core cell 82, and 7 core cells are appointed for FAs of each year; 2) a 1st or a 2nd year FA is placed in cell 82, and 7 core cells are appointed for FAs of each year, with the exception of 4th year FAs which can be placed in 6 core cells only. In this case cell 82 is not considered when making optimization of FA rearrangements. The last approach is used in

practice mainly, because it gives an optimal fuel utilization to ensure the necessary campaign duration, so this approach with 6 cells appointed for 4th year FAs will be considered when making optimization of rearrangements (see Fig. 2).

2.1. Calculation of damage in the FE cladding

Cladding durability is estimated for the most strained AS (No. 6), taking into account the disposition of regulating units in the A-algorithm case, as well as considering the amplitude of regulating unit movement necessary to stabilize AO at daily power maneuvering with T_{in} = const. Changes in SDE during the 4-year campaign (1460 calendar days) were calculated using the MATPRO-A corrosion model by the following procedure: 1) Using RS, for the cells shown in Fig. 2, calculation of relative power coefficients $k_{6,j}$ in AS 6 at N = 80 and 100 %; 2) Using FEMAXI, calculation of stress-strain development in FE cladding and fuel burnup; 3) Using CET-method and A_0 = 30 MJ/m^3 (SDE at the moment of cladding material failure beginning), calculation of $\omega(1460\,\text{d})$ and burnup $B(1460$ d) for selected rearrangement algorithms.

Because of a great number of possible variants, when considering a new FA rearrangement algorithm, a random choice of core cells using the MATLAB function "rand" was adopted. To illustrate the method, it was adopted that $N_{alg} = 18$, that is 18 rearrangement algorithms containing 126 different rearrangements were analyzed, where 16 algorithms containing 112 rearrangements were randomly chosen, while two algorithms were practically used at Zaporizhzhya NPP, Unit 5 [9]. These two practical algorithms which were used during campaigns 22 and 23 (algorithms 17 and 18, respectively) are shown in Table 1.

Table 1. **Cladding failure parameter and burnup for algorithms 17 and 18**

Algorithm number (j)	Rearrangement	A, MJ/m^3	$\omega(\tau) = \frac{A}{A_0}$, %	B, MW·d/kg
17	2-22-12-6	1.463	4.877	54.35
	3-41-29	1.184	3.947	48.8
	4-11-68-43	1.078	3.593	60.63
	5-19-10-8	1.498	4.993	57.18
	9-30-20-1	2.058	6.86	59.39
	13-32-21-42	2.667	8.89	68.23
	55-31-54-18 $B_j^{\min}$	2.437	8.123	67.45
18	2-22-21-6	1.55	5.167	54.86
	3-41-68	1.18	3.933	48.83
	4-11-29-18	1.159	3.863	60.84
	5-19-20-1 $B_j^{\min}$	1.449	4.83	54.55
	9-32-12-42	2.586	8.62	67.86
	13-30-10-43	2.551	8.503	67.73
	55-31-54-8	1.982	6.607	61.37

2.2.The criterion of FA rearrangement efficiency

Considering all the FAs used in a rearrangement algorithm j, let's suppose that $\omega_j^{\max}$ is the maximum value of cladding failure parameter, $<\omega>_j$ is the average value of cladding failure parameter; $B_j^{\min}$ is the minimum value of fuel burnup. Let's introduce

$$\omega^{\text{opt}} = \min\left\{\omega_j^{\max}\right\};\ <\omega>^{\text{opt}} = \min\left\{<\omega>_j\right\};\ B^{\text{opt}} = \max\left\{B_j^{\min}\right\} \tag{1}$$

Let's accept that $\omega^{\lim}$, $<\omega>^{\lim}$ and $B^{\lim}$ are specified permissible limits for $\omega_j^{\max}$, $<\omega>_j$ and $B_j^{\min}$, respectively. Hence, the permissible values of $\omega_j^{\max}$, $<\omega>_j$ and $B_j^{\min}$ lie in the following ranges:

$$\omega^{\text{opt}} \le \omega_j^{\max} \le \omega^{\lim};\ <\omega>^{\text{opt}} \le <\omega>_j \le <\omega>^{\lim};\ B^{\lim} \le B_j^{\min} \le B^{\text{opt}}. \tag{2}$$

Then we obtain

$$\omega^{\lim,*} \le \omega_j^{\max,*} \le 1;\ <\omega>^{\lim,*} \le <\omega>_j^{*} \le 1;\ B^{\lim,*} \le B_j^{\min,*} \le 1, \tag{3}$$

where

$$\omega^{\lim,*} \equiv (1-\omega^{\lim})/(1-\omega^{\text{opt}});\ \omega_j^{\max,*} \equiv (1-\omega_j^{\max})/(1-\omega^{\text{opt}});\ <\omega>^{\lim,*} \equiv (1-<\omega>^{\lim})/(1-<\omega>^{\text{opt}});$$

$$<\omega>_j^{*} \equiv (1-<\omega>_j)/(1-<\omega>^{\text{opt}})\ ;\ B^{\lim,*} \equiv B^{\lim}/B^{\text{opt}};\ B_j^{\min,*} \equiv B_j^{\min}/B^{\text{opt}}. \tag{4}$$

As $\left|B^{\lim,*};\ 1\right|$ can be >> $\left|\omega^{\lim,*};1\right|$, from the condition of equal importance of nuclear safety and economy requirements:

$$\omega^{\lim,*} = <\omega>^{\lim,*} = B^{\lim,*}. \tag{5}$$

Hence having some value of $\omega^{\lim}$, the corresponding values of $<\omega>^{\lim}$ and $B^{\lim}$ are defined from the following equations

$$<\omega>^{\lim} = 1-(1-\omega^{\lim})(1-<\omega>^{\text{opt}})/(1-\omega^{\text{opt}});\ B^{\lim} = (1-\omega^{\lim})B^{\text{opt}}/(1-\omega^{\text{opt}}). \tag{6}$$

To compare efficiency *Eff* of different FA rearrangement algorithms, the FA rearrangement algorithm efficiency criterion is proposed:

$$Eff_j = 1 - L_j / L^{\lim}, \tag{7}$$

where

$$L_j = \sqrt{\left(1-\omega_j^{\max,*}\right)^2 + \left(1-<\omega>_j^{*}\right)^2 + \left(1-B_j^{\min,*}\right)^2}, \tag{8}$$

$$L^{\lim} = \sqrt{\left(1-\omega^{\lim,*}\right)^2 + \left(1-<\omega>^{\lim,*}\right)^2 + \left(1-B^{\lim,*}\right)^2}. \tag{9}$$

Using Eqs. (4), (5) and (9)

$$L^{\lim} = \sqrt{3}\left|1-\omega^{\lim,*}\right| = \sqrt{3}\left|\omega^{\lim}-\omega^{\text{opt}}\right|/(1-\omega^{\text{opt}}). \tag{10}$$

The physical meaning of criterion (7) is: 1) if any of the dimensionless components ($\omega_j^{\max,*}$, $<\omega>_j^{*}$ or $B_j^{\min,*}$) lies out of the permissible range $[\omega^{\lim,*};1]$, then this component gives a negative contribution to the total efficiency defined by Eq. (7); 2) advantage of some algorithm over another is determined on the basis of summation of advantages given by the dimensionless components; 3) weight factors can be used in Eq. (5) to give priority to some component.

Using criterion (7) and setting $\omega^{\lim} = 13\,\%$, *Eff* was calculated for 18 algorithms. Algorithm 2 having the worst *Eff*, the first five algorithms (3, 4, 6, 8, 14) having the greatest values of *Eff*, as well as the practical algorithms (17 and 18) are shown in Table 2.

Table 2. **Algorithm efficiency**

j	$\omega_j^{\max}$, %	$<\omega>_j$, %	$B_j^{\min}$, MWd/kg	$\omega_j^{\max,*}$	$<\omega>_j^{*}$	$B_j^{\min,*}$	Eff_j, $\omega^{\lim}=13\,\%$
2	8.84	5.861	47.61	0.9786	0.999	0.8709	-0.1442
3	7.51	5.865	54.67	0.9929	0.999	1	0.9372
4	6.87	5.796	54.05	0.9998	0.9997	0.9887	0.9008
6	6.847	5.787	53.05	1	0.9998	0.9704	0.741
8	7.017	5.771	54.27	0.9982	1	0.9927	0.9341
14	8.247	5.864	54.07	0.985	0.999	0.989	0.8371
17	8.89	5.898	48.8	0.9781	0.999	0.8926	0.0420
18	8.62	5.932	48.83	0.981	0.9983	0.8932	0.0515

It can be seen: 1) algorithms 3 and 8 are characterizied by both high cladding durability and high burnup, hence all the corresponding dimensionless criterion components are high, so Eff_3 and Eff_8 are highest; 2) algorithms 17 and 18 have both cladding durability and burnup worse than the ones of algorithms 3 and 8, so Eff_{17} and Eff_{18} are close to 0; 3) algorithm 2 is characterizied by cladding durability close to the same for algorithms 17 and 18, but burnup is considerably lower than the same for these algorithms, and as a result $Eff_2 < 0$.

2.3. The robust model

Let us suppose that the calculated maximum LHR in FA j $q_{l,j,\max}$ is the mean of some random variable $q^{\text{rand}}_{l,j,\max}$, i.e.:

$$q_{l,j,\max} \equiv \left\langle q^{\text{rand}}_{l,j,\max} \right\rangle. \tag{11}$$

To take into account VVER-1000 robust operating conditions when making the probabilistic analysis, cladding damage parameter and burnup in the most strained AS are calculated for rearrangements of the best algorithms 3, 4, 6, 8 and 14 at $\left\langle q^{\text{rand}}_{l,cn,\max} \right\rangle - 10\%$ and $\left\langle q^{\text{rand}}_{l,cn,\max} \right\rangle + 10\%$, where *cn* is core cell number for the corresponding campaign year, e.g., for algorithm 3 and rearrangement 9-19-21-8: *cn* = 9, 19, 21 and 8 for 1st, 2nd, 3rd and 4th year, respectively. Hence, use of deterministic criterion (7) allows us to reduce N_{alg} from $N_{alg} = 18$ to $N_{alg} = 5$.

The efficiency of rearrangement algorithm j is calculated using Eqs. (4) and (7), and 1) there are 2 random variables ($\omega^{\text{rand}}_{j,k}$ and $B^{\text{rand}}_{j,k}$) for each pair of algorithm j and rearrangement k; 2) $\omega^{\max}_j = \max\{\omega^{\text{rand}}_{j,k}\}$, $<\omega>_j = <\{\omega^{\text{rand}}_{j,k}\}>$, $B^{\min}_j = \min\{B^{\text{rand}}_{j,k}\}$, where $j = 1,...,N_{alg}$; $k = 1,...,7$. Hence, we have the total number of input random variables $2 \cdot N_{alg} \cdot 7 = 70$, that is 35 rearrangements are described by 70 random variables.

For $k = 1,...,7$ and j = 3, 4, 6, 8, 14, using three sigma rule (assuming normal distribution), the corresponding means $<\omega^{\text{rand}}_{j,k}>$, $<B^{\text{rand}}_{j,k}>$ and standard deviations $\sigma(\omega^{\text{rand}}_{j,k})$, $\sigma(B^{\text{rand}}_{j,k})$ of random variables $\omega^{\text{rand}}_{j,k}$, $B^{\text{rand}}_{j,k}$ are calculated. For instance, algorithm 3 − (9-19-21-8 + 5-41-68-43 + 55-22-10 + 13-11-20-6 + 3-30-54-1+ 4-32-18-42 + 2-31-12-29) − is described by the following random values $\tau_{j,p,k}$, where p = 1 denotes $\omega^{\text{rand}}_{j,k}$ and p = 2 denotes $B^{\text{rand}}_{j,k}$:

$$\tau_{3,1,1} \equiv \omega^{\text{rand}}_{9\text{-}19\text{-}21\text{-}8};\ ...\tau_{3,1,7} \equiv \omega^{\text{rand}}_{2\text{-}31\text{-}12\text{-}29};\ \tau_{3,2,1} \equiv B^{\text{rand}}_{9\text{-}19\text{-}21\text{-}8};\quad ...\tau_{3,2,7} \equiv B^{\text{rand}}_{2\text{-}31\text{-}12\text{-}29}.$$

Hence, for rearrangement 9-19-21-8 of algorithm 3, $\tau_{3,1,1}$ and $\tau_{3,2,1}$ are random values described by $\{<\omega^{\text{rand}}_{3,1}>$, $\sigma(\omega^{\text{rand}}_{3,1})\}$ and $\{<B^{\text{rand}}_{3,1}>$, $\sigma(B^{\text{rand}}_{3,1})\}$, respectively.

As we have 70 random variables, non-intrusive polynomial chaos (NIPC) methods [10] are not computationally attractive in comparison with Monte Carlo Sampling (MCS) methods. To use the MCS method, a set of normally distributed random variables $\tau_{j,p,k}$ is obtained substituting the means and standard deviations of $\omega^{\text{rand}}_{j,k}$ and $B^{\text{rand}}_{j,k}$ into the MATLAB function "normrnd", and the efficiency of algorithm j is found using Eq. (7) in the form:

$$Eff_j = f\left(\theta_{j,1,1}, \theta_{j,1,2}, \theta_{j,2,1}\right), \tag{12}$$

where $j = 1,...,N_{alg}$; $\theta_{j,1,1} = \max\left\{\tau_{j,1,1},...,\tau_{j,1,7}\right\}$; $\theta_{j,1,2} = <\left\{\tau_{j,1,1},...,\tau_{j,1,7}\right\}>$; $\theta_{j,2,1} = \min\left\{\tau_{j,2,1},...,\tau_{j,2,7}\right\}$.

2.4. Optimization of rearrangements

Thus, the efficiency of algorithm j is calculated using Eq. (12). For the case of uncertain conditions, ω^{opt}, $<\omega>^{\text{opt}}$, B^{opt} and L^{lim} can not be set as for the deterministic case (Table 3).

Table 3. **Difference between the deterministic and robust cases**

Deterministic case			Robust case			
$\omega^{\text{lim}} = 13\,\%$						
ω^{opt}	$<\omega>^{\text{opt}}$	B^{opt}	MCS	ω^{opt}	$<\omega>^{\text{opt}}$	B^{opt}
6.847	5.771	54.67	1	8.1212	6.79261	55.2311
$<\omega>^{\text{lim}} = 1-(1-\omega^{\text{lim}})(1-<\omega>^{\text{opt}})/(1-\omega^{\text{opt}}) = 0.12;$			10	10.6683	7.93351	55.6857
$B^{\text{lim}} = (1-\omega^{\text{lim}})B^{\text{opt}}/(1-\omega^{\text{opt}}) = 51.06;$			100	9.9501	7.44926	53.8346
$L^{\text{lim}} = \sqrt{3}\left\|\omega^{\text{lim}} - \omega^{\text{opt}}\right\|/(1-\omega^{\text{opt}}) = 0.1144;$			$<\omega>^{\text{lim}}, B^{\text{lim}}, L^{\text{lim}}, \omega^{\text{lim},*}$ are variable on MCS.			
$\omega^{\text{lim},*} \equiv (1-\omega^{\text{lim}})/(1-\omega^{\text{opt}}) = 0.9339.$						

It should be noted that if N_{alg} increases, then ω^{opt} decreases. On the contrary, when the number of core cells used for optimization increases, ω^{opt} increases also. The trade-off between the mean value of Eff_j and its standard deviation, as estimated using MCS, for the best five FA transposition algorithms, as well as for the simplest robust optimization of FA rearrangements taking into account only two core cells appointed for each year, is shown in Fig. 3.

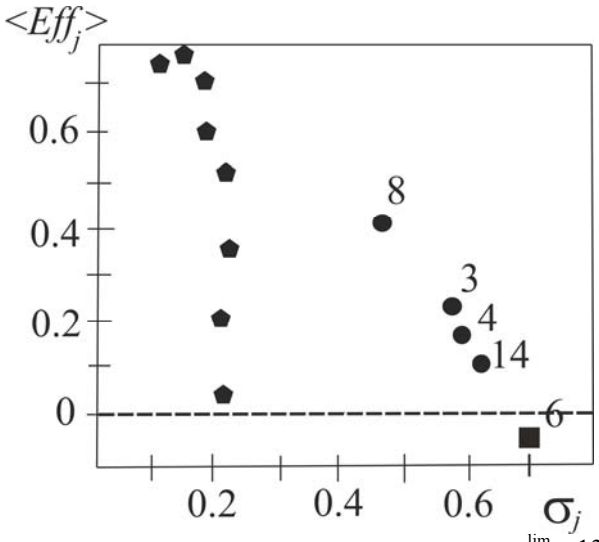

Fig. 3. Mean efficiency and standard deviation for $\omega^{\lim} = 13$ % in the robust case: (number) algorithm number for optimization with 7 cells per year (excluding year 4), $A_0 = 30$ MJ/m^3; (pentagon) random algorithm for optimization with 2 cells per year, $A_0 = 40$ MJ/m^3.

Algorithm 3 had the largest efficiency in the deterministic case, while in the robust case algorithm 8 is most efficient (see Fig. 3). This can be explained by the fact that $\omega_3^{\max} \approx 7.5\%$, while $\omega_8^{\max} \approx 7\%$. As dependence of SDE on LHR is nonlinear and SDE depends greatly on FA rearrangement history, in the robust case this difference $\omega_3^{\max} - \omega_8^{\max} = 0.5\%$ turned to be sufficient to obtain a greater mean efficiency for algorithm 8 in comparison with algorithm 3. In addition, algorithm 3 has a greater standard deviation than algorithm 8, and thus there is no trade-off between these two options. Both algorithms dominate all the other options, having both higher mean efficiencies and smaller standard deviations.

3. Conclusions

1. The deterministic FA rearrangement efficiency criterion taking into account both safety (cladding durability) and economic (burnup) factors allows us to improve existing methods of fuel rearrangement optimization which take into account only economic efficiency estimated in terms of fuel burnup, power form factor, etc., as well as pin failure probability for a hypothetical severe depressurization accident [11].

2. The probabilistic FA rearrangement efficiency criterion based on Monte Carlo Sampling takes into account robust operation conditions and gives results corresponding to the determinisic ones in principle, though the robust efficiency estimation is more conservative. Hence deterministic FA rearrangement optimization can be used as a preliminary procedure to decrease the number of analysed rearrangement algorithms.

3. CET-method allows us to improve existing control and protection equipment by creating an automized program-technical complex making control of FE cladding durability and optimization of fuel rearrangements in VVER-1000.

REFERENCES

1. *Pelykh S. N., Maksimov M. V.* Cladding rupture life control methods for a power-cycling WWER-1000 nuclear unit // Nucl. Eng. and Des. - 2011. - Vol. 241, No. 8. - P. 2956 - 2963.
2. *Suzuki M.* Light water reactor fuel analysis code FEMAXI-V (Ver.1). - Tokai: Japan atomic energy research institute, 2000. - 285 p.
3. *Philimonov P.E.*, *Mamichev V.V., Averyanova S.P.* The “Reactor Simulator” program modelling WWER-1000 load following regimes // Atomic Energy. - 1998. - Vol. 84, No. 6. - P. 560 - 563 (in Russian).
4. *Kim J.H., Lee M.H., Choi B.K., Jeong Y.H.* Deformation behavior of Zircaloy-4 cladding under cyclic pressurization // Journ. of Nucl. Sci. and Tech. - 2007. - No. 44. - P. 1275 - 1280.
5. *Sosnin O.V., Gorev B.V., Nikitenko A.F.* Energy variant of the theory of creep. - Novosibirsk: The Siberian branch of the Russian Academy of Sciences, 1986. - 94 p. (in Russian).
6. *Pelykh S.N., Maksimov M.V., Baskakov V.E.* Model of cladding failure estimation under multiple cyclic reactor power changes // Proc. of the 2-nd Int. Conf. “Current Problems of Nuclear Physics and Atomic Energy” (Kyiv, June 09 - 15, 2008). - Kyiv, 2009. - P. 638 - 641.
7. *Pelykh S.N., Maksimov M.V.* Theory of fuel life control methods at Nuclear Power Plants (NPP) with Water-Water Energetic Reactor (WWER) // Nuclear reactors / Ed. by A. Z. Mesquita. - Rijeka: InTech, 2012. - P. 197 - 230.
8. *Suzuki M.* Modelling of light-water reactor fuel element behaviour in different loading regimes. - Odessa: Astroprint, 2010. - 248 p. (in Russian).
9. *Vorobyev R.Y.* Albums of neutron-physical characteristics of the reactor core, Unit 5, Zaporizhzhya NPP. Campaigns 20 − 23. - Energodar: Zaporizhzhya NPP, 2008 − 2011. - 323 p. (in Russian).
10. *Ghisu T., Parks G.T., Jarrett J.P., Clarkson P.J.* Adaptive polynomial chaos for gas turbine compression systems performance analysis // AIAA Journ. - 2010. - No. 6. - P. 1156 - 1170.
11. *Parks G.T.* An intelligent stochastic optimization routine for nuclear fuel cycle design // Nucl. Technol. - 1990. - No. 2. - P. 233 - 246.

CAPTURE CROSS SECTIONS FOR HEAVY-ION REACTIONS PRODUCING COMPOUND SYSTEM WITH Z = 120

N. A. Pilipenko, V. Yu. Denisov

Institute for Nuclear Research, National Academy of Sciences of Ukraine, Kyiv, Ukraine

The fusion cross sections for reactions ^{50}Ti + ^{249}Cf, ^{54}Cr + ^{248}Cm, ^{58}Fe + ^{244}Pu and ^{64}Ni + ^{238}U are evaluated in the framework of simple barrier-penetration model, which takes into account quadrupole and hexadecapole surface deformations of nuclei.

1. Introduction

Super-heavy elements with Z = 112 - 118 have been synthesized in Dubna and Darmstadt by using hot fusion reactions ^{48}Ca + X, where X is the heavy transuranium element. The heaviest element with proton number 118 has been synthesized in reaction ^{48}Ca + ^{249}Cf. However, it is impossible to use ^{48}Ca beam for the synthesis of more heavy elements, because the elements with Z > 98 are not available for experiments. Therefore it is necessary to search other reactions for the synthesis of elements with proton number more than 118.

Taking into account the long time and complexity of experiment on the synthesis of super-heavy elements it is very useful to estimate the capture cross sections for various collision systems leading to superheavy elements with Z > 118. We have proposed a relatively simple and accurate method of calculating the potential interaction between deformed nuclei and their capture cross sections in previous papers [1, 2].

Note that the range of barrier height variation induced by mutual orientation of heavy well-deformed heavy nuclei is approximately 15÷20 MeV. The range of barrier distance changing is around 2.5 fm. [1]. Due to this deformation of nuclei and their mutual orientation during approaching are extremely important for subbarrier and near barrier heavy-ion fusion studies.

2. Fusion of deformed nuclei

The interaction potential $V(R,l,\Theta_1,\Theta_2,\Phi)$ of two deformed nuclei at distance R between mass centers and mutual orientation described by angles Θ_1,Θ_2 and Φ (Fig. 1) consists of

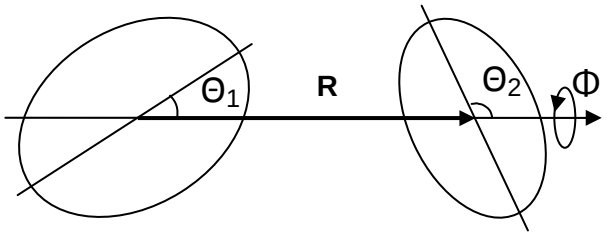

Fig. 1. The angles Θ_1,Θ_2 and Φ , and distance between of mass-centers R describing the arbitrary orientation of colliding nuclei.

Coulomb $V_C(R,\Theta_1,\Theta_2,\Phi)$, nuclear $V_N(R,\Theta_1,\Theta_2,\Phi)$ and rotational $V_l(R)=\hbar^2 l(l+1)/(2\mu R^2)$ parts

$$V(R,l,\Theta_1,\Theta_2,\Phi)=V_C(R,\Theta_1,\Theta_2,\Phi)+\eta V_N(R,\Theta_1,\Theta_2,\Phi)+V_l(R). \quad (1)$$

Here η is an adjustable coefficient that determines the contribution of the nuclear potential component $V_N(R,\Theta_1,\Theta_2,\Phi)$ to the total potential. This parameter is used for adjusting the potential at energies higher than barrier height.

The Coulomb interaction of two deformed nuclei is approximated as [1]

$$V_C(R,\Theta_1,\Theta_2,\Phi)=\frac{Z_1Z_2e^2}{R}\{1+\sum_{l\geq 2}[f_{1l}(R,\Theta_1,R_{10})\beta_{1l}+f_{1l}(R,\Theta_2,R_{20})\beta_{2l}]+$$
$$+f_2(R,\Theta_1,R_{10})\beta_{12}^2+f_2(R,\Theta_2,R_{20})\beta_{22}^2+f_3(R,\Theta_1,\Theta_2,R_{10},R_{20})\beta_{12}\beta_{22}+$$
$$+f_4(R,\Theta_1,\Theta_2,\Phi,R_{10},R_{20})\beta_{12}\beta_{22}\}, \quad (2)$$

where Z_1 and Z_2 are the number of protons in corresponding nuclei, β_{il} is the parameter of l-pole deformation of nucleus i (i = 1,2), $f_{1l}(R,\Theta_i,R_{i0})$, $f_2(R,\Theta_i,R_{i0})$, $f_3(R,\Theta_1,\Theta_2,R_{10},R_{20})$ and $f_4(R,\Theta_1,\Theta_2,\Phi,R_{10},R_{20})$ are simple functions [1]. Here R_{i0} is the radius of nucleus i in the case of spherical form.

Applying the proximity theorem [3] we can obtain a simple parametrization of the nuclear part of interaction potential between two deformed nuclei [1]

$$V_N(R,\Theta_1,\Theta_2,\Phi) \approx \frac{C_{10}+C_{20}}{[(C_1^{\text{II}}+C_2^{\text{II}})(C_1^{\perp}+C_2^{\perp})]^{1/2}} \times V_N^0(d(R,\Theta_1,\Theta_2,\Phi)), \tag{3}$$

where C_i^{II} and $C_i^{\perp}$ are the main curvatures of deformed surface of nucleus i at the point closest to the surface of another nucleus, $C_{10}=1/R_{10}$ and $C_{20}=1/R_{20}$ the curvatures of spherical nuclei, $d(R,\Theta_1,\Theta_2,\Phi)$ is the closest distance between surfaces of interacting nuclei, $V_N^0(d)$ is the nuclear part of the interaction potential between spherical nuclei at $d=R-R_{10}-R_{20}$. The nuclear part of potential depends strongly on the value of the closest distance between surfaces of interacting nuclei, therefore we evaluate $d(R,\Theta_1,\Theta_2,\Phi)$ numerically.

The nuclear part of the interaction potential between spherical nuclei $V_N^0(d)$ is described by expression in Ref. [4]. This expression for nuclear part of potential is obtained using the semi-microscopic energy density approach for evaluation of nucleus-nucleus interaction energy [4,5]. The barrier height and barrier radius of the potential between spherical nuclei evaluated with the help of this expression well agree with corresponding empirical values [4].

The surface curvatures $C_2^{\text{II}\perp}$ depend on corresponding orientation angle(s) and deformation parameters. Useful expressions for surface curvatures are given in [1].

Note that effects of surface deformations on the nuclear part of the interaction between nuclei are considered with the same accuracy as the one for the Coulomb part.

Various orientations of deformed nuclei occur during collisions; therefore the fusion reaction cross section induced by two deformed nuclei should be averaged over all possible mutual orientations of colliding nuclei

$$\sigma(E)=\frac{\pi\hbar^2}{2\mu E}\sum_l (2l+1)<T_l(E,\Theta_1,\Theta_2,\Phi)>. \tag{4}$$

Here μ is the reduced mass of colliding nuclei, E is the collision energy, $<T_l(E,\Theta_1,\Theta_2,\Phi)>$ is the transmission coefficient evaluated at orientation of colliding nuclei specified by angles Θ_1,Θ_2,Φ see Fig. 1.

We use the WKB approximation for evaluation of the transmission coefficient for subbarrier energies

$$T_l(E,\Theta_1,\Theta_2,\Phi)=\{1+\exp[\frac{2}{\hbar}\int_a^b \sqrt{2\mu(V(R,l,\Theta_1,\Theta_2,\Phi)-E)}\,dR]\}^{-1} \tag{5}$$

and the Hill-Wheeler approach [6] for over-barrier collision energies.

The inner a$(E,l,\Theta_1,\Theta_2,\Phi)$ and outer b$(E,l,\Theta_1,\Theta_2,\Phi)$ turning points in Eq. (5) are determined from corresponding equations

$$V(\text{a}(E,l,\Theta_1,\Theta_2,\Phi),l,\Theta_1,\Theta_2,\Phi)=E$$

$$V(\text{b}(E,l,\Theta_1,\Theta_2,\Phi),l,\Theta_1,\Theta_2,\Phi)=E.$$

3. Discussion and conclusion

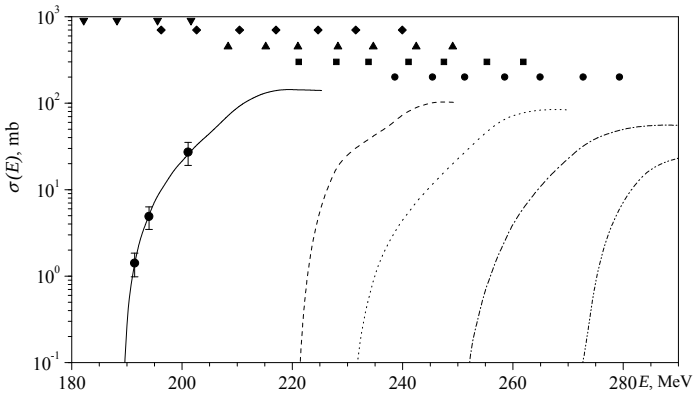

Fig. 2. Fusion cross-section(lines), Q reaction (the most left sign) and thresholds for evaporation of 1, 2, 3, 4, 5, 6 neutrons(dots) for reactions: ^{48}Ca+^{244}Pu, ^{50}Ti+^{249}Cf, ^{54}Cr+^{248}Cm, ^{58}Fe+^{244}Pu, ^{64}Ni+^{238}U.

Using Eqs. (1) - (5) we evaluate the fusion cross section $\sigma(E)$ values for reaction ^{50}Ti + ^{249}Cf, ^{54}Cr + ^{248}Cm, ^{58}Fe + ^{244}Pu and ^{64}Ni + ^{238}U. These reactions are considered as potential candidates for the synthesis of element Z = 120 of the periodic table.

We used reaction ^{48}Ca + ^{244}Pu determine of adjustable coefficient η. The experimental data for this reaction take from Ref. [7]. The cross sections calculated with allowance for the second-order terms in the quadrupole and hexadecapole deformations of the ^{244}Pu and η = 0.896 agree well with experimental data, see solid line in Fig. 2.

Value of deformations parameters of nuclei

X	β_{i2}	β_{i4}
^{48}Ca	0	0
^{50}Ti	0	0
^{54}Cr	0.25	0.045
^{58}Fe	0.2587	-0.019
^{64}Ni	0.179	-0.005
^{238}U	0.2863	0.093
^{244}Pu	0.2931	0.062
^{248}Cm	0.2972	0.04
^{249}Cf	0.55	0

The capture cross section for heavy systems is strongly depends from hexadecapole deformation at sub-barrier energies [2]. Deformations of nuclei presented in the Table, and were taken from [8] for quadrupole and [9] for hexadecapole deformations.

During formation the superheavy nuclei the neutrons are evaporated from formed excited compound-nucleus in competition to the fission of the compound nucleus. If the capture cross-section values are reasonably high for the small excitation energies of the compound nucleus, or corresponding collision energies, than the formation of the superheavy nuclei is probable. Therefore the value of capture cross-section should be relatively high around the thresholds of 3 - 5 neutrons for expectable formation of superheavy elements.

Comparing the values of capture cross-section around thresholds of 3 - 5 neutrons in Fig. 2 we concludethat the most promising reactions for synthesis element with Z = 120 are ^{50}Ti + ^{249}Cf and ^{54}Cr + ^{248}Cm. These reactions are similar to reaction ^{48}Ca + ^{244}Pu and they have reasonably high capture cross section at energies close to emissions 3 - 5 neutrons from the compound nucleus, see Fig. 2.

REFERENCES

1. *Denisov V.Yu., Pilipenko N.A.* // Phys. Rev. C. - 2007.- Vol. 76. - P. 014602.
2. *Denisov V.Yu., Pilipenko N.A.* // Phys. of At. Nucl. - 2010. - 73. - P. 1152.
3. *Blocki J., Randrup J., Swiatecki W.J., Tsang C.F.* // Ann. Phys. - 1977. - 105. - P 427.
4. *Denisov V.Yu.* // Phys. Lett. B. - 2002. - Vol. 526. - P. 315; APS Conf. Proc. - 2004. - Vol. 704. - P. 92.
5. *Denisov V.Yu., Norenberg W.* // Eur. Phys. J. A. - 2002. - Vol. 15. - P. 355.
6. *Hill D.L., Wheeler J.A.* // Phys. Rev. - 1953. - Vol. 89. - P. 1102.
7. *Itkis M.G. et al.* // Proc. Int. Workshop on Fusion Dynamics at the Extremes. - Dubna, 2000.
8. http://cdfe.sinp.msu.ru/services/radchart/radmain.html
9. *Moller P., Nix J.R.* Atomic data and Nuclear data tables. - 1995. - Vol. 59. - P. 185.

ENERGY DEPENDENT OPTICAL POTENTIAL FROM $^{16}O + ^{12}C$ ELASTIC SCATTERING

O. A. Ponkratenko, Yu. O. Shyrma

Institute for Nuclear Research, National Academy of Sciences of Ukraine, Kyiv, Ukraine

The $^{16}O + ^{12}C$ elastic and inelastic scattering was studied in the energy range between 1 and 100 MeV per nucleon. The elastic and inelastic scattering calculations were performed within optical model (OM) and coupled channels method (CC). The energy dependence analysis of $^{16}O + ^{12}C$ optical potential are presented.

1. Introduction

In spite of numerous experimental data of $^{16}O + ^{12}C$ scattering [1 - 16], there are only several works [17, 18] on investigations of the energy dependence of OM potential parameters. Moreover, it has not been found the energy dependence good enough to describe this scattering over the wide energy range in these works. While such dependences were obtained successfully [19] for light incident particles (p, n, α), the problem of finding the dependence for heavy ions is actual. At the same time it is important to build energy dependence of potential parameters in wide energy range. It allows us to minimize the ambiguity in the parameters determination for each energy value and helps to find the energy dependence of OM potential parameters for the interaction of unstable nuclei in output reactions channels.

The choice of $^{16}O + ^{12}C$ system is determined by circumstance that there are rich variety of experimental data from elastic and inelastic scattering for this system in comparison with other pairs of nuclei. The all available scattering data in the energy range extending to 100 MeV per nucleon were combined in OM and CC analyses to obtain the effective energy dependence for the parameters of the $^{16}O + ^{12}C$ potential.

2. Optical model potentials

The phenomenological OM potential used to describe the elastic angular distributions at each energy had the following form

$$U(r) = V(r) + iW(r) + V_C(r)\,, \tag{1}$$

where the real term $V(r)$ was taken as either the square of the Woods - Saxon form factor (*WS2*)

$$V(r) = \frac{V_0}{(1+\exp[(r-R_V)/a_V])^2} \tag{2}$$

or double-folding potential (*DF*) $V(r) = N_R V_{DF}(r)$. The term $V_{DF}(r)$ consists of direct and exchange parts [20, 21]:

$$V_{DF}(r) = V_D(r,E) + V_{EX}(r,E)\,, \tag{3}$$

$$V_D(r,E) = \int \rho_P(\mathbf{r}_P)\rho_T(\mathbf{r}_T)\upsilon_D(\rho,E,\mathbf{s})d^3r_P d^3r_T\,, \tag{4}$$

$$V_{EX}(r,E) = \int \rho_P(\mathbf{r}_P,\mathbf{r}_P+\mathbf{s})\rho_T(\mathbf{r}_T,\mathbf{r}_T-\mathbf{s})\upsilon_{EX}(\rho,E,\mathbf{s})\exp\left(\frac{i\mathbf{k}(\mathbf{r})\mathbf{s}}{\mu}\right)d^3r_P d^3r_T\,, \tag{5}$$

$$\mathbf{s} = \mathbf{r}_P - \mathbf{r}_T + \mathbf{r}\,, \tag{6}$$

where $\rho_P(\mathbf{r})$ and $\rho_T(\mathbf{r})$ are the density distributions of the projectile (*P*) and target (*T*) nuclei. These distributions are described by two-parameter Woods - Saxon forms with radii 2.6 fm (^{16}O) and 2.115 fm (^{12}C), and a surface diffuseness is 0.45 fm for both. We used density dependence effective nucleon-nucleon interaction, called *DDM3Y1*, which is based upon Reid nucleon-nucleon force with exchange terms [21]. Corresponding calculation was performed by code DFMSPH [22].

The imaginary part of OM potential is the sum of volume (*WS*) and surface terms (*WSD*)

$$W(r) = W_S(r) + W_D(r)\,, \tag{7}$$

$$W_S(r) = \frac{W_S}{1+\exp[(r-R_{WS})/a_{WS}]}\,, \tag{8}$$

$$W_D(r) = \frac{4W_D\exp[(r-R_{WD})/a_{WD}]}{(1+\exp[(r-R_{WD})/a_{WD}])^2}\,, \tag{9}$$

where $R_i = r_i(A_P^{1/3} + A_T^{1/3}),\ i = \{V, W_S, W_D\}$.

The Coulomb potential $V_C(r)$ was generated by folding of the projectile $\rho_P^{ch}(\mathbf{r}_P)$ and target $\rho_T^{ch}(\mathbf{r}_T)$ charge distributions

$$V_C(r) = \int \rho_P^{ch}(\mathbf{r}_P)\rho_T^{ch}(\mathbf{r}_T)\upsilon_C(\mathbf{s})d^3r_P d^3r_T\ . \tag{10}$$

In the calculations of elastic and inelastic scattering for inelastic λ-multipole transition within CC method we used the collective model coupled potential

$$V_\lambda(r) = -\delta_\lambda \frac{dU(r)}{dr}\ . \tag{11}$$

One assumed the real and imaginary deformation lengths to be equal $\delta_\lambda^V = \delta_\lambda^W$. The Coulomb deformation length δ_λ^C determined by the electromagnetic transition rate $B(E\lambda)$ as [23]

$$\delta_\lambda^C = \frac{4\pi\sqrt{B(E\lambda)}}{(\lambda+2)Z\left\langle r^{\lambda-1}\right\rangle}, \tag{12}$$

was used to account the Coulomb excitation. The radial part of the coupling potential for mutual simultaneous excitation had the collective model form

$$V_{\lambda\lambda_1\lambda_2}(r) = -\delta_{\lambda_1}\delta_{\lambda_2}\frac{d^2U(r)}{dr^2}, \tag{13}$$

where λ_1 and λ_2 – projectile and target transition multipolarity.

The parameters energy dependence of the OM potential imaginary part $p_i = W_S,\ R_{WS}, a_{WS}, W_D, R_{WD}, a_{WD}$ was approximated by parameterized functions [23, 24]

$$p_i(E) = \begin{cases} p_i(+\infty)(1-\exp[(E_i - E)/\Delta_i]), & E > E_i \quad p_i = W_S, W_D \\ 0, & E < E_i \quad p_i = W_S, W_D \\ p_i(+\infty) + [p_i(0) - p_i(+\infty)]\exp[E/\Delta_i], & p_i = R_{WS}, a_{WS}, R_{WD}, a_{WD} \end{cases} \tag{14}$$

with fitting parameters $p_i(+\infty), E_i, p_i(0), \Delta_i$. The real part energy dependence of OM potential was determined by the dispersion relation between real and imaginary parts [25]

$$V(r,E) = V(r) + \Delta V(r,E)\ , \tag{15}$$

$$\Delta V(r,E) = \frac{1}{\pi} P\int \frac{W(r,E')}{E'-E}dE'\ , \tag{16}$$

$$\Delta V(r,E) = \Delta V(r,E_s) + \frac{1}{\pi}(E-E_s)P\int \frac{W(r,E')}{(E'-E_s)(E'-E)}dE'\ . \tag{17}$$

Here *P* denotes the principal value of the integral. Integral was calculated using *W*(*r, E*) represented by a series of linear segments over the energy [23].

The usual χ^2 criterion was used for searching of the OM potential parameters

$$\chi^2_{E_j} = \frac{1}{n_j}\sum_{i=1}^{n_j}\left(\frac{\sigma_{th}(E_j,\theta_i) - \sigma_{\exp}(E_j,\theta_i)}{\Delta\sigma_{\exp}(E_j,\theta_i)}\right)^2, \tag{18}$$

where $\sigma_{th}(E_j, \theta_i)$, $\sigma_{exp}(E_j, \theta_i)$, and $\Delta\sigma_{exp}(E_j, \theta_i)$ are the theoretical (OM or CC) cross sections, the experimental cross sections and the uncertainties in the experimental cross sections, respectively. θ_i is the center mass scattering angle, n_j is the number of angles and E_j is the projectile energy. Energy-dependent OM potential parameters were determined by summation over the all E_j

$$\chi^2 = \frac{1}{\sum_j n_j}\sum_j n_j\chi^2_{E_j}\ , \tag{19}$$

where *j* is the projectile energy order number.

3. Results and discussion

The $^{16}O + ^{12}C$ elastic and inelastic scattering data were analyzed within the OM and CC method using codes GENOA [26] and FRESCO [27], respectively.

The OM analysis was carried out for 42 projectile energies ($E_{lab}(^{18}O) = 20 \div 1500$ MeV) at which differential cross sections of the $^{12}C + ^{16}O$ scattering were measured [1 - 14]. The imaginary part of the potential was taken in the *WS+WSD* form (7). The two choices were used for the real potential: the square of the Woods-Saxon form *WS2* (2) in the one case and the double-folding potential *DF* (3) in another. The minimization of χ^2 (18) was performed by variation of the nine parameters ($V_0, R_V, a_V, W_S, R_{WS}, a_{WS}, W_D, R_{WD}, a_{WD}$) for the first choice and seven parameters ($N_R, W_S, R_{WS}, a_{WS}, W_D, R_{WD}, a_{WD}$) for second. These parameters were adjusted to reproduce the angular distributions at the forward angles ($< 80^\circ \div 120^\circ$) where the contribution of alpha-transfer is small [2, 17].

We considered a fixed uniform uncertainty in 10 % of the experimental cross section for all the projectile energies and measured angles. This decision was accepted because compared with forward angles the experimental cross section uncertainties may be relatively large at the intermediate and backward angles owing to the smaller cross section [28]. Thus, using a uniform percentage can give a better fits at intermediate and backward angles.

For the purpose of searching smallest χ^2 and demonstration the fact that the found from fitting the sets of potentials parameters are similar in the experimental data describing (potential ambiguity), we performed numerous fits (~1000) with different initial parameters values. The latter values were sampled by Monte-Carlo method. It was used only those extracted from fitting parameters sets which had smallest χ^2. For example, Fig. 1 shows the real (*WS2*) and imaginary (*WS+WSD*) parts of potentials sets at the energy $E_{lab}(^{16}O) = 115.9$ MeV, which are obtained from fitting procedure described above (grey lines). Heavy black curve represents the $E_{lab}(^{16}O) = 115.9$ MeV potential prescribed by the energy dependent parameters obtained from searching of 42 angular distributions at different energies.

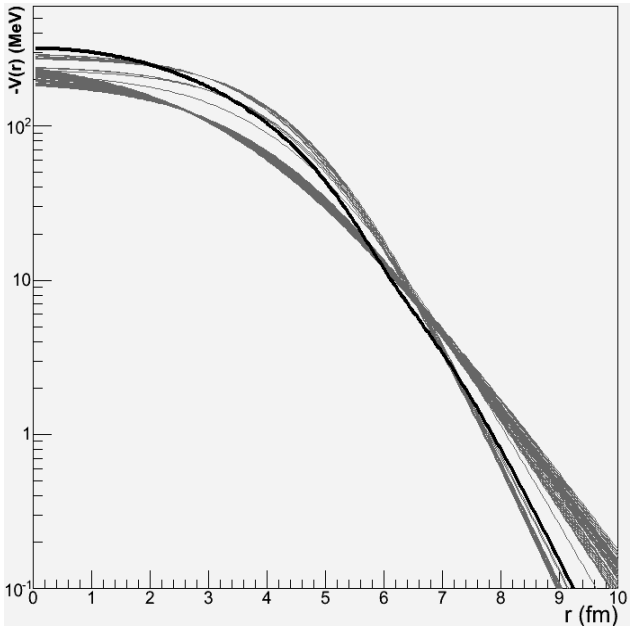

Fig. 1, *a*. Radial dependences of the real part of potentials. See detailed description in text.

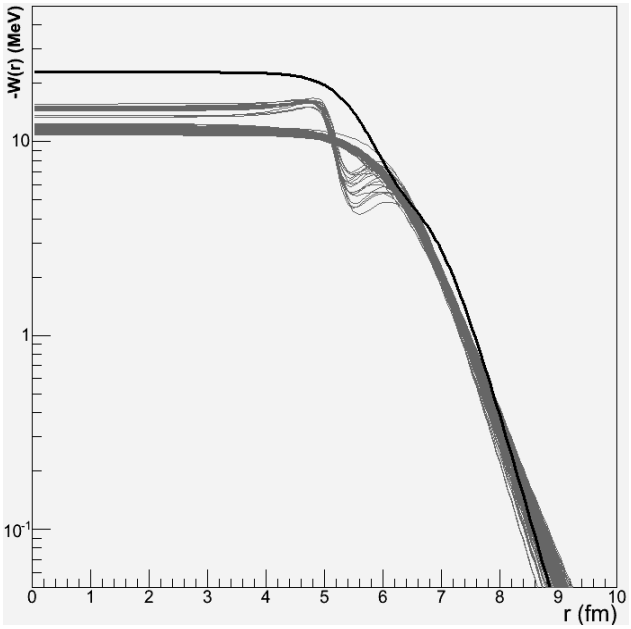

Fig. 1, *b*. Radial dependences of the imaginary part of potentials. See detailed description in text.

We have investigated the dependence of the volume integral of the imaginary potential on the incident particle energy

$$J_W(E) = -\frac{4\pi}{A_P A_T}\int W(r,E) r^2 dr\,. \qquad (20)$$

This dependence is plotted in Fig. 2, *a*. Here the averaged over the large number of fits (~100) values of the volume integral (with mean square deviation) are represented by dots. Heavy curve shows the energy dependence of the volume integral of the imaginary part for the energy dependent potential (14), (15). The same dependences for the reaction cross section obtained by OM are presented in Fig. 2, *b*. For comparison, the experimental values of fusion cross sections for $^{16}O+^{12}C$ collision represented by open circles are also shown at different energies of the incident ion. These experimental data of fusion were taken from the work of [18]. One can observes, the fusion cross sections have peaks in positions, where the reaction cross sections calculated for each energy by OM have peaks too (open circles). The values of these peaks are about: ~ 33, 40 and 49 MeV.

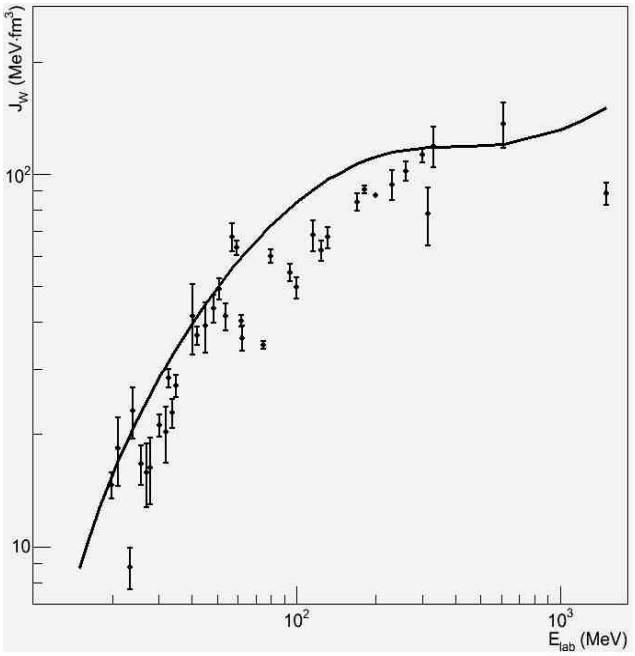

Fig. 2, *a*. The dependence of the volume integral of the imaginary potential on the incident ion energy. See detailed description in text.

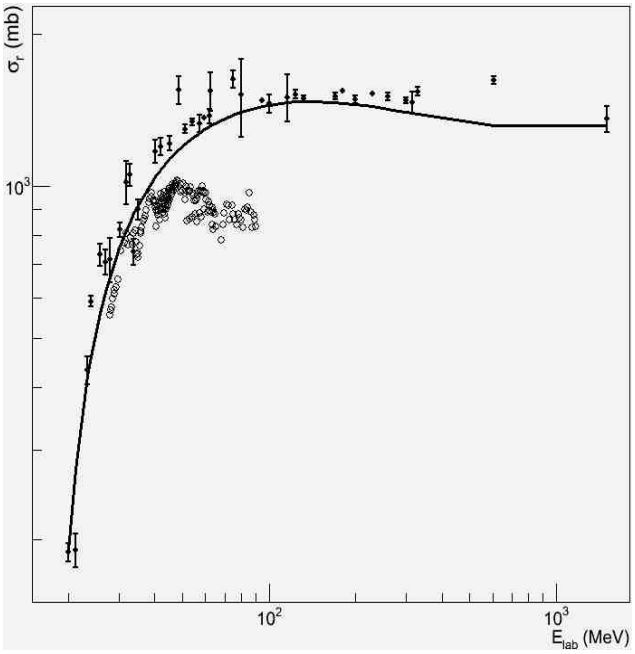

Fig. 2, *b*. The dependence of the reaction cross section on the incident ion energy. See detailed description in text.

Fig. 3б *a* shows the $^{16}O + ^{12}C$ scattering data at the $E_{lab}(^{16}O)$ = 25.8, 75, 124, 181 and 300 MeV in the comparison with OM fits using the Woods-Saxon (*WS2*) and double-folding (*DF*) forms of real potential. One can see that calculations with folding-potential describe the experimental data worse than the ones with Woods-Saxon potential. Because there was only variation of the potential deep in the *DF* case but no variation of potential shape, as in *WS2* case. The relation $\chi^2(DF) / \chi^2(WS2)$ is about 1.5. In Fig. 3, *b* a comparison is provided for the same energies between double-folding potential calculations and the energy dependent potential obtained using (14), (15). It is obvious that energy dependent potential describes the data worse than potential individually calculated for each energy ($\chi^2_E(DF) / \chi^2(DF)$ is about 4). However, one must take into account that the energy dependent potential is specified by only 15 parameters over the whole energy range (1÷100 MeV/nucleon). At the same time one uses 7 parameters for the approximation of the cross sections found at each energy, that is about 300 parameters overall (for 42 measured distributions).

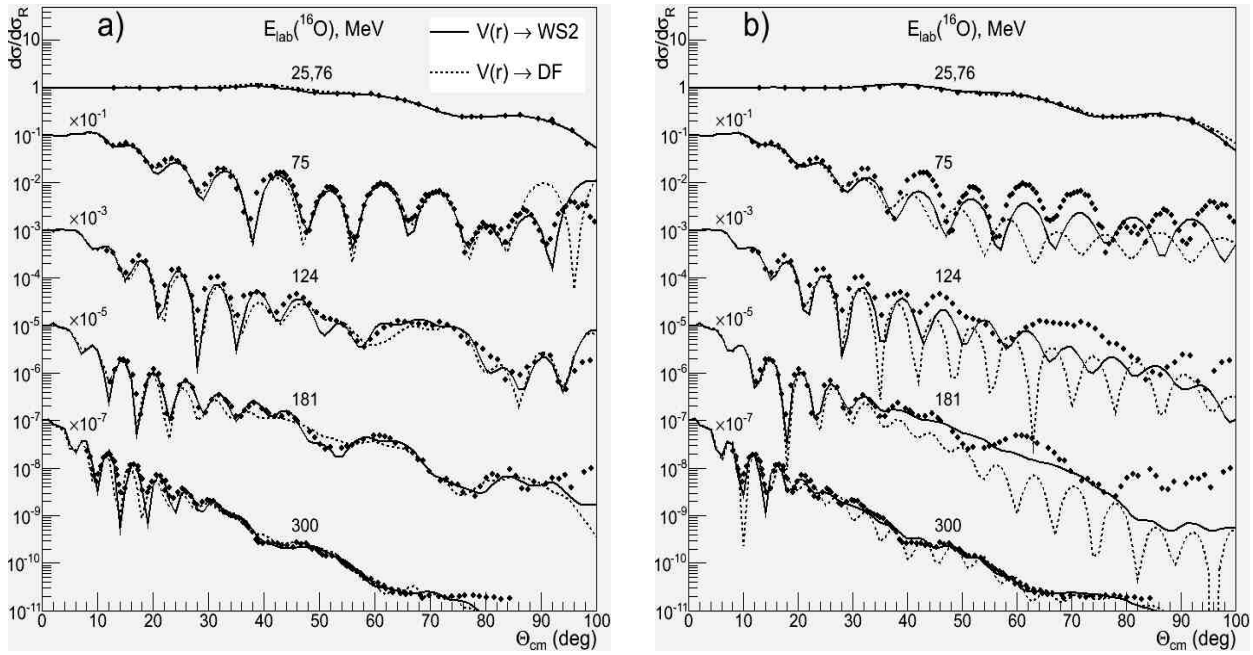

Fig. 3. The comparison of the measured cross sections (in ratio to the Rutherford cross section) of the elastic $^{16}O + ^{12}C$ scattering with the theoretical cross section: a) obtained from the real part of potential *WS2* (solid line) and *DF* (dotted line); b) obtained from the energy dependent potential subject to the analysis of the angular distributions for 42 projectile energies (dotted line) and for these 5 energies (solid line).

In order to demonstrate the influence of the inelastic channels on the $^{16}O + ^{12}C$ interaction potential and showing potential energy dependence for 8 values of the incident ion energy in the 62÷132 MeV range [15], the elastic and inelastic scattering computations within CC method were performed. Coupled potential was calculated according to the collective model (11), (13). The OM potential parameters were fitted as well as the deformation lengths of ^{16}O and ^{12}C excited states. The inelastic excitations of ^{12}C target state ($J^{\pi}=2^{+}$, $E^{*}=4.44$ MeV) and ^{16}O projectile states ($J^{\pi}=3^{-}$, $E^{*}=6.13$ MeV; $J^{\pi}=2^{+}$, $E^{*}=6.9$ MeV) were taken into consideration.

In Fig. 4, the experimental angular distributions of the elastic and inelastic $^{16}O+^{12}C$ scattering at the energy $E_{lab}(^{16}O) = 100$ MeV are compared with that obtained in CC analysis.

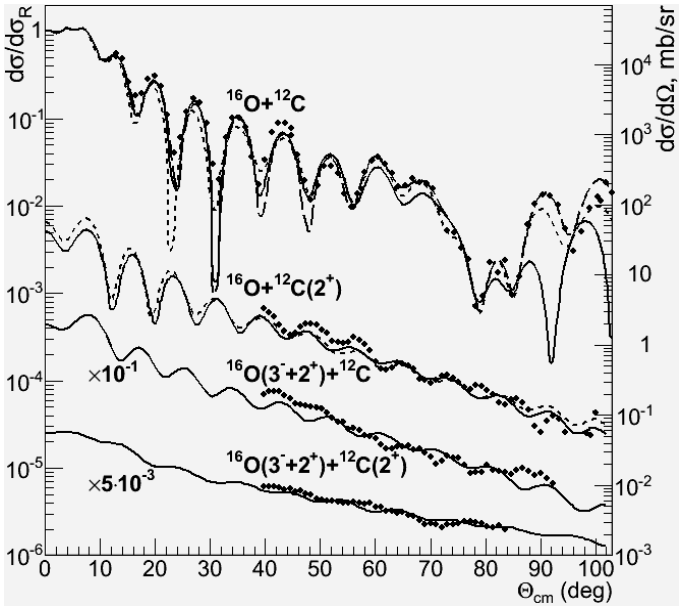

Fig. 4. The comparison of the experimental angular distributions of the elastic and inelastic $^{16}O+^{12}C$ scattering at the energy $E_{lab}(^{16}O) = 100$ MeV with that obtained in CC analysis. See detailed description in text.

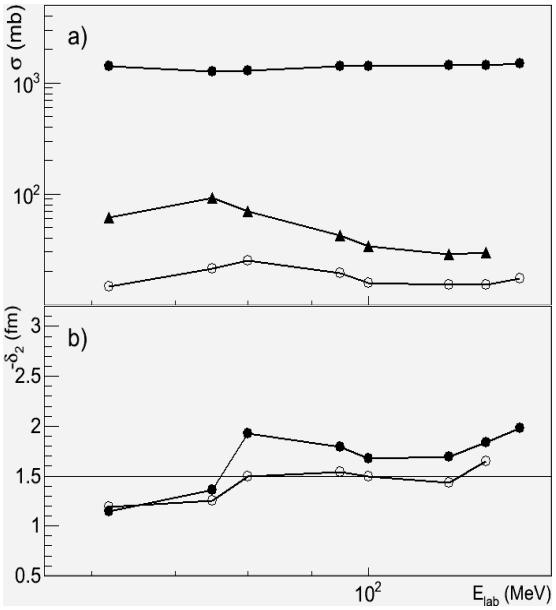

Fig. 5. *a* - the energy dependences of the cross sections calculated within CC (6-channels approximation). See detailed description in text; *b* - the energy dependences of $\delta_2(^{12}C, 2^{+})$ deformation lengths: 2-channels approxi-mation – solid circles, 6-channels – open circles.

The long dashed line shows the angular distributions of the elastic scattering calculated within OM (1-channel approximation). The elastic and inelastic scattering with excitation of ^{12}C ($J^{\pi} = 2^{+}$) state calculated subject to the coupling only between these two channels are represented by short dashed line (2-channels approximation). The solid line illustrates calculations with couplings between 6 channels of $^{16}O + ^{12}C$ scattering (6-channels approximation). It should be noted that mutual excitations of the target and projectile nuclei are simulated by means of two mechanisms: sequential two-step excitation via the intermediate excitation of *P* or *T* nuclei and simultaneous excitations of *P* and *T* nuclei (13). The calculated within CC (6-channels approximation) energy dependences (over the range $E_{lab}(^{16}O) =$ = 62÷132 MeV) of:

- total reaction cross section σ_r (solid circles),
- total inelastic scattering cross section $\sigma(^{12}C, 2^{+})$ with ^{12}C ($J^{\pi}=2^{+}$) state excitation (open circles),
- the sum of inelastic scattering cross sections $\sigma(^{12}C, 2^{+}) + \sigma(^{16}O, 3^{-}) + \sigma(^{16}O, 2^{+}) +$ $+ \sigma(^{12}C, 2^{+} + ^{16}O, 3^{-}) + \sigma(^{12}C, 2^{+} + ^{16}O, 2^{+})$ with *P* and(or) *T* corresponding excitations (solid triangles) are shown in Fig. 5, *a*.

Using the same calculations, we also obtained the energy dependences of $\delta_3(^{16}O, 3^{-})$ and $\delta_2(^{12}C, 2^{+})$ deformation lengths, which were the fitting parameters (it was assumed that $\delta_\lambda = \delta_\lambda^V = \delta_\lambda^W$). These dependences are illustrated in Fig. 5, *b*. Because the data of the inelastic scattering angular distribution for the transitions to the ^{16}O (3^{-}, 2^{+}) states taken from [15] was in the sum of these transitions cross sections, the $\delta_2(^{16}O, 2^{+})$ deformation length was fixed and one supposed that $\delta_2(^{16}O, 2^{+}) = \delta^{C}{}_2(^{16}O, 2^{+})$, where $\delta^{C}{}_2(^{16}O, 2^{+})$ is the deformation length of the Coulomb excitation (12). From fig. 5b one can see, that $\delta_2(^{12}C, 2^{+})$ parameter has the weak energy dependence and are roughly equal to the corresponding deformation lengths of the Coulomb excitation $\delta^{C}{}_2(^{12}C, 2^{+})$ (thin horizontal line in fig. 5b).

Evidently, the potential $U_1(r)$ describing the elastic and inelastic scattering in the 1-channel approximation differs from the diagonal potentials (CC) of 2-channel approximation $U_2(r)$ and 6-channel approximation $U_6(r)$. The differences between OM and CC potentials are demonstrated in Fig. 6.

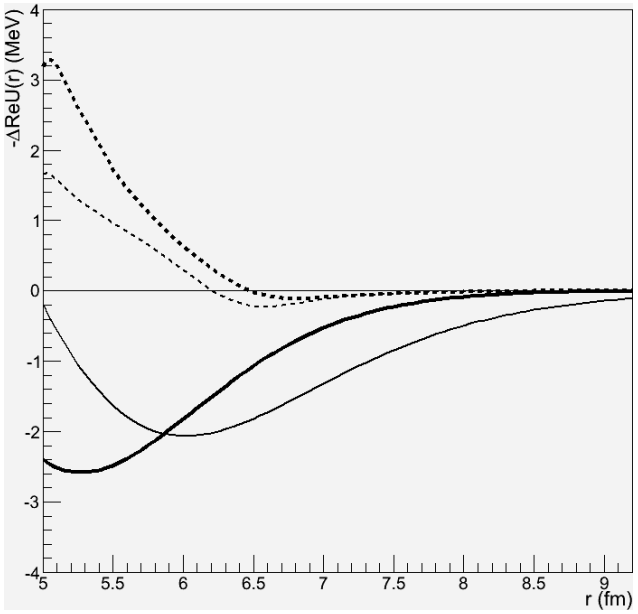

Fig. 6, *a*. The differences between OM and CC real part of potentials. See detailed description in text.

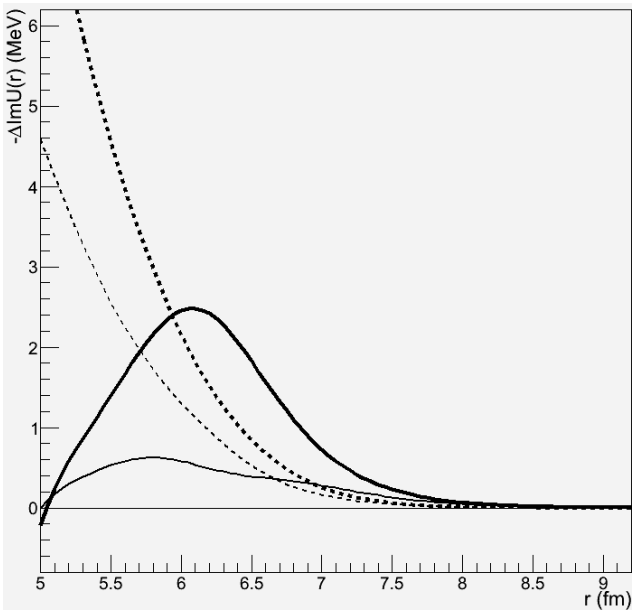

Fig. 6, *b*. The differences between OM and CC imaginary part of potentials. See detailed description in text.

Here the thin solid line denotes the $U_1(r$ - $U_2(r)$ and the thick solid line – the $U_1(r)$ - $U_6(r)$. These differences are the L-independent approximation of the dynamic polarization potential (DPP), where L is the orbital angular momentum of the relative motion. DPP is an additional term to the OM potential induced by the coupling of the elastic channel to the inelastic ones. So called "trivially equivalent local potential" (TELP) [23] is another approximation of DPP. TELP is obtained by averaging the sum of the coupling potentials between the elastic channel and the inelastic ones over the L. The thin dashed line represents TELP for 2-channels approximation and the thick dashed line – for 6-channels approximation.

4. Summary

A systematic analysis of 42 ^{16}O + ^{12}C elastic scattering angular distributions was performed within OM and CC. It has been found the sets of OM potential for each of the 42 incident ion energies. Also, by fitting the angular distributions for 42 energies in the range from 1 to 100 MeV/nucleon, one obtained the energy dependence of the parameters for the imaginary part of potential, which was used for the determination of the energy dependence of the real part via the dispersion relation. The diagonal OM potentials and deformation lengths of the concerned excited states of ^{16}O and ^{12}C nuclei were deduced from analysis of the elastic and inelastic scattering data by the collective model of the coupling channel potential.

REFERENCES

1. *Voos U.C., Von Oertzen W., Bock R.* Optical-model analysis of the elastic scattering of complex nuclei at low energies // Nucl. Phys. A. - 1969. - Vol. 135. - P. 207 - 224.
2. *Morais M.C., Lichtenthaler R.* α-Spectroscopic factor of $^{16}O_{gs}$ from the $^{12}C(^{16}O,^{12}C)^{16}O$ reaction // Nucl. Phys. - 2011. - Vol. 857. - P. 1 - 8.
3. *Kuehner J.A., Almovits E., Bromley D.A.* Elastic scattering of oxygen ions by carbon, magnesium and aluminium // Phys. Rev. - 1963. - Vol. 131. - P. 1254 - 1259.
4. *Schimizu J., Wada R. et al.* A Study of the Anomaly at $E_{c.m.}$= 13.7 MeV in the ^{12}C + ^{16}O System // J. Phys. Soc. Jpn. - 1978. - Vol. 44. - P. 7 - 15.
5. *Charles P., Auger F., Badawy I. et al.* Resonant behaviour of the ^{16}O - ^{12}C elastic scattering cross section // Phys. Lett. B. - 1976. - Vol. 62. - P. 289 - 292.
6. *Nicoli M.P., Haas F., Freeman R.M. et al.* Detailed study and mean field interpretation of ^{16}O + ^{12}C elastic scattering at seven medium energies // Phys. Rev. C. - 2000. - Vol. 61. - P. 034609.
7. *Ikezoe H., Shikazono N. et al.* Measurements of evaporation residues to investigate lower limiting angular momenta in fusion reactions // Nucl. Phys. A. - 1986. - Vol. 456. - P. 298 - 316.
8. *Ogloblin A.A., Glukhov Yu.A., Trzaska W.H. et al.* New measurement of the refractive, elastic ^{16}O + ^{12}C scattering at 132, 170, 200, 230, and 260 MeV incident energies // Phys. Rev. C. - 2000. - Vol. 62. - P. 044601.
9. *Ogloblin A.A., Khoa Dao T. et al.* Pronounced Airy structure in elastic ^{16}O + ^{12}C scattering at E_{lab} = 132MeV // Phys. Rev. C. - 1998. - Vol. 57. - P. 1797 - 1802.
10. *Глухов Ю.А., Гончаров С.А. и др.* Исследование Эйри-структуры в упругом рассеянии ^{16}O + ^{12}C при энергиях

ионов ^{16}O 8-18 МэВ/нуклон // Известия РАН, сер. физ. - 2001. - Т. 65, № 5. - С. 647 - 650.
11. *Гончаров С.А., Изадпанах А.* Дисперсионный полумикроскопический анализ ядро-ядерных столкновений на основе скорректированного потенциала свертки // Ядерная физика. - 2007. - Т. 70, № 9. - С. 1538 - 1546.
12. *Brandan M.E., Menchaca-Rocha A.* Total reaction cross section for ^{16}O - ^{12}C at $E_{c.m.}$ = 60, 93, and 135 MeV // Phys. Rev. C. - 1981. - Vol. 23. - P. 1272 - 1273.
13. *Brandan M.E., Menchaca-Rocha A.* Elastic and inelastic ^{16}O+^{12}C scattering at 38 MeV/nucleon // Phys. Rev. C. - 1986. - Vol. 34. - P. 1484 - 1486.
14. *Roussel P., Alamanos N. et al.* Nucleus-Nucleus Potential inside the Strong-Absorption Radius from ^{16}O + ^{12}C Elastic Scattering at 94 MeV/*u* // Phys. Rev. Lett. - 1985. - Vol. 54. - P. 1779 - 1782.
15. *Szilner S., Haas F., Basrak Z. et al.* Competition between direct and dissipative processes in the binary channels of the ^{16}O + ^{12}C and ^{18}O + ^{12}C reactions // Nucl. Phys. - 2006. - Vol. A779. - P. 21 - 46.
16. *Williams D.J., Steigert F.E.* Inelastic scattering of heavy ions // Nucl. Phys. - 1962. - Vol. 30. - P. 373 - 388.
17. *Rudchik A.T., Shyrma Yu.O., Kemper K.W. et al.* Isotopic effects in elastic and inelastic ^{12}C + $^{16, 18}$O scattering // Eur. Phys. J. A. - 2010. - Vol. 44. - P. 221 - 231.
18. *Gao C., Kondo Y.* A deep optical potential and gross resonant structures in low energy ^{16}O + ^{12}C scattering // Phys. Lett. B. - 1997. - Vol. 408. - P. 7 - 11.
19. *Becchetti F.D., Jr., Greenleesd G. W.* Nucleon-Nucleus Optical-Model Parameters, A>40, E<50 MeV // Phys. Rev. - 1969. - Vol. 182. - P. 1190 - 1209.
20. *Khoa Dao T., Satchler G.R.* Generalized folding model for elastic and inelastic nucleus-nucleus scattering using realistic density dependent nucleon-nucleon interaction // Nucl. Phys. - 2000. - Vol. A668. - P. 3 - 41.
21. *Gontchar I.I., Hinde D.J.* Double folding nucleus-nucleus potential applied to heavy-ion fusion reactions // Phys. Rev. C. - 2004. - Vol. 69. - P. 024610.
22. *Gontchar I.I., Chushnyakova M.V.* A C-code for the double folding interaction potential of two spherical nuclei // Comput. Phys. Commun. - 2010. - Vol. 181. - P. 168 - 182.
23. *Satchler G.R.* Heavy-ion scattering and reactions near the Coulomb barrier and “threshold anomalies” // Phys. Rep. - 1991. - Vol. 199, No. 3. - P. 147 - 190.
24. *Carstoiu F., Trache L. et al.* Refractive effects in the scattering of loosely bound nuclei // Phys. Rev. C. - 2004. - Vol. 70. - P. 054610.
25. *Mahaux C., Hgo H., Satchler G.R.* Causality and the threshold anomaly of the nucleus- nucleus potential // Nucl. Phys. - 1985. - Vol. A449. - P. 354 - 395.
26. *Nilsson B.S.* SPI-GENOA: an Optical Model Search Code. - 1976. - (Report / The Niels Bohr Institute).
27. *Thompson I.J.* Coupled reaction channels calculations in nuclear physics // Comp. Phys. Rep. - 1988. - Vol. 7. - P. 167 - 212.
28. *Szilner S., Nicoli M.P. et al*. Refractive elastic scattering of carbon and oxygen nuclei: The mean field analysis and Airy structures // Phys. Rev. C. - 2001. - Vol. 64. - P. 064614.

DIFFERENT APPROACHES TO ESTIMATION OF RPV MATERIAL EMBRITTLEMENT

V. Revka, L. Chyrko, Yu. Chaikovskiy, O. Trygubenko

Institute for Nuclear Research, National Academy of Sciences of Ukraine, Kyiv, Ukraine

The surveillance test data for the nuclear power plant which is under operation in Ukraine have been used to estimate WWER-1000 RPV material embrittlement. The beltline materials (base and weld metal) were characterized using Charpy impact and fracture toughness test methods. The fracture toughness test data were analyzed according to the standard ASTM 1921-05. The pre-cracked Charpy specimens were tested to estimate a shift of reference temperature T_0 due to neutron irradiation. The maximum shift of reference temperature T_0 is 84°C. A radiation embrittlement rate A_F for the RPV material was estimated using fracture toughness test data. In addition the A_F factor based on the Charpy curve shift (ΔT_F) has been evaluated. A comparison of the A_F values estimated according to different approaches has shown there is a good agreement between the radiation shift of Charpy impact and fracture toughness curves. Therefore Charpy impact test data can be successfully applied to estimate the fracture toughness curve shift and therefore embrittlement rate. Furthermore it was revealed that radiation embrittlement rate for weld metal is higher than predicted by a design relationship. The enhanced embrittlement is most probably related to simultaneously high nickel and high manganese content in weld metal.

1. Introduction

In the frame of surveillance program for WWER-1000 type reactor in Ukraine the Charpy V-notch impact testing is used as simple and inexpensive method to estimate the fracture toughness curve shift due to irradiation and therefore embrittlement rate for the reactor pressure vessel (RPV) steels. However, the evidence is needed that Charpy impact test data is valid to estimate the changes in material fracture toughness due to irradiation considering that RPV is subjected to the static loading during the operation. So according to requirements of surveillance program the pre-cracked Charpy V-notch (PCVN) specimens for a direct determination of static fracture toughness are also used to evaluate an embrittlement rate of RPV materials.

It is known from the test reactor irradiation experiment that Charpy impact test data describes well the changes of material fracture toughness because of radiation damages [1]. This observation is valid only if the ductile to brittle transition temperature does not exceed 100°C. However there is experimental evidence [2] that Charpy impact test data can underestimate a shift of the fracture toughness curve due to irradiation. In this study a comparison of the radiation shift of the Charpy impact and fracture toughness curves has been made from a view point of material embrittlement estimation.

2. Materials and test methods

The studied materials are 15Ch2NMFAA steels (Cr-Ni-Mo-V steel) and its welds (Sv-12ChGNMAA, welding compound ФЦ-16) which are used for WWER-1000 reactor pressure vessel fabrication. The chemical composition of RPV belt line materials is shown in the Table. Materials are low carbon and low alloyed ferritic steels with ferrite and bainite metallographic structure. The typical heat treatment is quenching with high tempering. The materials are extremely pure with regard to impurities of copper and phosphorus. At the same time welds have a high nickel (1,88 % wt.) and manganese (0,97 % wt.) content that increases their susceptibility to neutron irradiation in spite of the low Cu and P content [3, 4]. For base and weld metal in unirradiated condition the yield strength is about 560 MPa and 480 MPa respectively.

Chemical composition for base and weld metal (% wt)

Material	Element									
	C	Si	Mn	Cr	Ni	Mo	Cu	S	P	V
Base metal	0,15	0,33	0,48	2,07	1,12	0,53	0,06	0,009	0,007	0,1
Weld	0,06	0,26	0,97	1,80	1,88	0,65	0,02	0,007	0,006	-

Specimens were irradiated in the standard surveillance capsules within the neutron ($E > 0{,}5$ MeV) fluence range of $(12{,}9 \div 46{,}5)\cdot 10^{22}$ m^{-2}. Irradiation temperature was about 300°C. Surveillance specimens were being irradiated during 16 fuel cycles (~ 4128 days) by neutron flux of about 10^{15} m^{-2}/sec that is usual for WWER-1000 type reactor irradiation condition. For the analysis fracture toughness and Charpy impact test data have been used. The RPV material have been tested at scientific center "Kurchatov Institute" (Russia) in the frame of a standard surveillance program for one NPP unit which is under operation in Ukraine.

The standard Charpy specimens (10 x 10 x 55 mm) were used for the estimation of impact energy in the specified temperature range. For this purpose an impact pendulum machine with 300 Joules capacity and the environment chamber were applied to get the Charpy curves for unirradiated and irradiated materials. A shift of Charpy curves due to

irradiation (ΔT_F) is defined according to PNAE G-7-002-86 approach (an index temperature for the Charpy curve depends on the material yield strength).

A three point bend method was applied to test pre-cracked Charpy specimens and determine the fracture toughness parameters (in this case K_{Jc} value, i.e. elastic-plastic equivalent of a critical stress intensity factor). Specimens without side grooves were L-T and L-S oriented for base and weld metal respectively. For test at low temperatures, liquid nitrogen is used to cool the specimens. A fracture toughness analysis has been performed according to the ASTM 1921-05 standard as well as an estimation of the radiation shift of Master curve (ΔT_0).

A radiation embrittlement rate for base and weld metal was estimated using the fluence dependencies of Charpy impact (ΔT_F) and fracture toughness (ΔT_0) curve shift. The PNAE embrittlement model $\Delta T_F = A_F \cdot F^n$ (where F is neutron fluence in the terms of 10^{22} m^{-2} and a power exponent n = 1/3) was applied to define a chemistry factor A_F using a statistical analysis.

3. Experimental results and discussion

The neutron fluence dependencies of transition T_K and reference temperature T_0 shift based on Charpy impact and fracture toughness test data are shown in Figs. 1 and 2 for base and weld metal respectively. For base metal the ΔT_F value obtained from Charpy impact test is consistent with a T_0 reference temperature shift at low neutron fluence. However some discrepancy between two approaches is observed at high neutron fluence. This is most probably related to the relatively high uncertainty in T_0 determination. For this set three of six PCVN specimens have been tested near lower-shelf toughness range that increases the uncertainty in T_0 determination.

For weld metal the Charpy impact curve shift is consistent with a T_0 reference temperature shift within studied neutron fluence range. The maximum radiation shift of Charpy impact and fracture toughness curves is 82°C and 84°C respectively for irradiated materials. The results indicate that Charpy impact test data is adequate to describe the changes in material fracture toughness due to the radiation damages and, therefore, to estimate reliably the embrittlement rate for this material irradiated up to neutron fluence ~ $45 \cdot 10^{22}$ m^{-2}.

For comparison a PNAE G-7-002-86 design curves for studied materials (a chemistry factor A_F = 23°C for base metal and A_F = 20°C for weld metal) are shown next to the test data points. The chemistry factor A_F estimated from a regression analysis is equal to 11°C for base metal and do not exceed the PNAE design value (see Fig. 1). For weld metal the statistical analysis gives A_F = 24°C (see Fig. 2). This results means that weld metal is more susceptible to radiation damages in comparison to base metal.

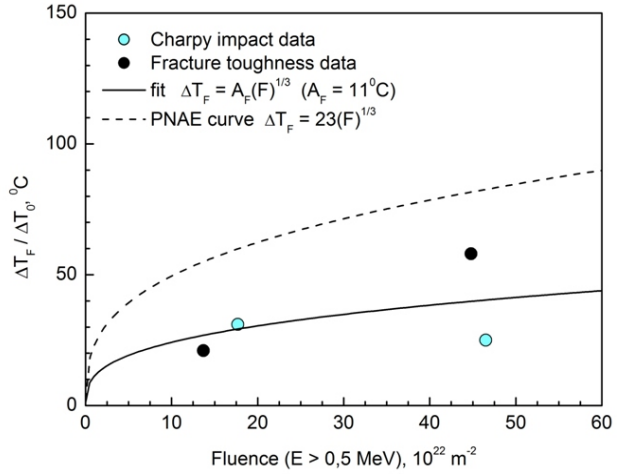

Fig. 1. Neutron fluence dependence of T_K and T_0 shift for base metal.
(Charpy impact and fracture toughness test data).

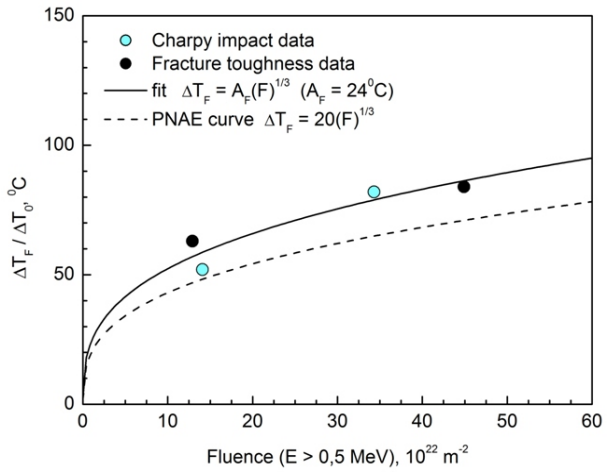

Fig. 2. Neutron fluence dependence of T_K and T_0 shift for weld metal.
(Charpy impact and fracture toughness test data).

Furthermore the radiation embrittlement rate for weld metal is higher then predicted by PNAE G-7-002-86 approach. One of the reason for enhanced embrittlement can be the simultaneously high nickel (1,88 % wt.) and manganese (0,97 % wt.) content in weld metal since it is known these alloying element play a crucial role in the radiation embrittlement phenomena in the case of RPV materials [3, 4]. It should be noted the design A_F value does not takes into account a chemical composition of RPV steels that is one of the shortcoming for PNAE G-7-002-86 approach.

4. Conclusions

In this study the WWER-1000 RPV material embrittlement rate has been evaluated using the surveillance test data for the nuclear power plant which is under operation in Ukraine. A comparison of the radiation shift of the Charpy impact and fracture toughness curves has been made from a view point of material embrittlement estimation.

The following conclusions can be drawn:

for weld metal the Charpy impact curve shift is consistent with a T_0 reference temperature shift up to 84°C;

Charpy impact test data is adequate to describe the changes in material fracture toughness due to the radiation damages and, therefore, to estimate reliably the embrittlement rate for this material irradiated up to neutron fluence $\sim 45 \cdot 10^{22}$ m^{-2};

radiation embrittlement rate for weld metal is higher then PNAE G-7-002-86 design approach prediction. One of the reasons for enhanced embrittlement can be the simultaneously high nickel and manganese content in weld metal.

REFERENCES

1. *Alekseenko N.N, Amaev A.D., Gorynin I.V., Nikolaev V.A.* Radiation Damage of Vessel Steels of Water-Water Type Reactors. - M.: Energoizdat, 1981. - 192 p.
2. *Wallin K., Valo M., Rintamaa R. et al.* Descriptive characteristics of different types of test for irradiation embrittlement // Nucl. Eng. & Design. - 1995. - Vol. 159. - P. 69 - 80.
3. *Miller M.K., Sokolov M.A., Nanstad R.K., Russell K.F.* APT characterization of high nickel RPV steels // Journal of Nuclear Materials. - 2006. - Vol. 351. - P. 187 - 196.
4. *Lambrecht M., Almazouzi A.* Positron annihilation study of neutron irradiated model alloys and a reactor pressure vessel steel // Journal of Nuclear Materials. - 2009. - Vol. 385. - P. 334 - 338.

TIME-DEPENDENT QUANTUM DESCRIPTION OF FEW NUCLEONS TRANSFERS AT NUCLEAR REACTIONS

K. V. Samarin

Chuvash State University, Cheboksary, Russia

Time-dependent Schrödinger equations is numerically solved by difference method for external nucleons of spherical and deformed nuclei at their grazing collisions for energies near to a Coulomb barrier. The spin-orbital interaction and Pauli's exclusion principle were taken into consideration during the solution. The probabilities of transfer of neutrons and protons are determined as function on minimum internuclear distances and quantum numbers of initial nucleons states.

1. Introduction

Neutron transfers in the low energy nuclear reactions allow us to obtain new isotopes of atomic nuclei with increased neutron content [1]. The probability of neutron transfer is highest during so called grazing nuclear collisions [2]. In this case, the distances between the surfaces of the atomic nuclei do not exceed the range of the action of nuclear forces (1 - 2 fm). The most probable transition is the one between the nuclei of the external, most weakly bound neutrons. These processes have been studied in reactions with the participation of both light (e.g., ^{6}He [1]) and heavy neutron rich nuclei. The basis of the microscopic models of nucleon transfer during grazing collisions of atomic nuclei is the so called form factors [2], for which simple empirical approximations are generally used. A new possibility for specifying the form factors for definite pairs of colliding nuclei is provided by studying the evolution of the states of external neutrons by means of a numerical solution for the non stationary Schrödinger equation with allowance for spin–orbital interaction using the approach proposed and developed in [3-5]. In this work we examine a basic questions of non stationary quantum approach and it applications to some examples of nucleons transfer at low-energy nuclear reactions.

2. Theory

The equations of classical mechanics for colliding heavy atomic nuclei

$$m_1\ddot{\vec{r}}_1 = -\nabla_{\vec{r}_1} V_{12}(|\vec{r}_1 - \vec{r}_2|),\ m_2\ddot{\vec{r}}_2 = -\nabla_{\vec{r}_2} V_{12}(|\vec{r}_2 - \vec{r}_1|)\,, \tag{1}$$

where $\vec{r}_1(t)$, $\vec{r}_2(t)$ are nuclei centers with masses m_1, m_2 and $V_{12}(r)$ is the potential energy of nuclei interaction, make it possible to easily obtain numerical solutions by the Runge - Kutta method (usually the fourth order method). The evolution of the components of the spinor wave function of a neutron during collisions nuclei, the centers of which can be considered moving along the classical trajectories $\vec{r}_1(t)$, $\vec{r}_2(t)$ is determined by the system of equations [6]

$$\begin{aligned} i\hbar\frac{\partial}{\partial t}\Psi_1 = &\left(-\frac{\hbar^2}{2m}\Delta + V(\vec{r},t)\right)\Psi_1 + i\frac{b}{2}\left(\frac{\partial V}{\partial x}\frac{\partial \Psi_1}{\partial y} - \frac{\partial V}{\partial y}\frac{\partial \Psi_1}{\partial x}\right) + \\ &+ i\frac{b}{2}\left(\frac{\partial V}{\partial y}\frac{\partial \Psi_2}{\partial z} - \frac{\partial V}{\partial z}\frac{\partial \Psi_2}{\partial y}\right) - \frac{b}{2}\left(\frac{\partial V}{\partial x}\frac{\partial \Psi_2}{\partial z} - \frac{\partial V}{\partial z}\frac{\partial \Psi_2}{\partial x}\right), \end{aligned} \tag{2}$$

$$\begin{aligned} i\hbar\frac{\partial}{\partial t}\Psi_2 = &\left(-\frac{\hbar^2}{2m}\Delta + V(\vec{r},t)\right)\Psi_2 - i\frac{b}{2}\left(\frac{\partial V}{\partial x}\frac{\partial \Psi_2}{\partial y} - \frac{\partial V}{\partial y}\frac{\partial \Psi_2}{\partial x}\right) + \\ &+ i\frac{b}{2}\left(\frac{\partial V}{\partial y}\frac{\partial \Psi_1}{\partial z} - \frac{\partial V}{\partial z}\frac{\partial \Psi_1}{\partial y}\right) + \frac{b}{2}\left(\frac{\partial V}{\partial x}\frac{\partial \Psi_1}{\partial z} - \frac{\partial V}{\partial z}\frac{\partial \Psi_1}{\partial x}\right). \end{aligned} \tag{3}$$

The constant of the spin–orbital interaction b, having the dimensionality of a square of length, can be presented in the form containing a dimensionless constant κ:

$$b = R_0^2\kappa\frac{\hbar^2}{2m^2R_0^2c^2} = 0,022R_0^2\kappa\,, \tag{4}$$

where $R_0 = 1$ fm, m is the neutron mass, and c is the speed of light. The potential energy of a neutron with vector radius $\vec{r}$ up to the contact of colliding nuclei surfaces is the sum of the energies of its interaction with each nucleus. Before contact between the surfaces of spherical nuclei with radii R_1, R_2 at $R = |\vec{r}_2 - \vec{r}_1| > R_1 + R_2$ we may consider that

$$V(\vec{r},t) = V_n^{(1)}(\vec{r} - \vec{r}_1(t)) + V_n^{(1)}(\vec{r} - \vec{r}_2(t))\,. \tag{5}$$

For differential equations (2), (3) on a uniform grid by coordinates with time step Δt the splitting method [7, 8] yields a difference scheme of the second order accuracy. The fast complex Fourier transform [8] and iteration method for intermediate time step [3] were used for determination of spinor wave function components Ψ_1, Ψ_2. The initial conditions for the components Ψ_1 and Ψ_2 of spinor wave functions were chosen as the wave functions with definite values Ω = 1/2, 3/2, … of the module for projecting the total moment on the axis coinciding with the direction of the velocity of the outgoing nucleus projectiles. The radial parts of the wave functions were determined from the numerical solution for the Schrödinger equation in the shell model of spherical nuclei. The total probability densities of neutron clouds of the ^{6}He nucleus and of the ^{18}O nucleus are determined, respectively, by formulas

$$\rho_t(\vec{r},t) = \frac{2}{2j+1}\sum_{\Omega=1/2}^{j}\rho_\Omega\,, \quad \rho_\Omega(\vec{r},t) = \left|\Psi_{1\Omega}(\vec{r},t)\right|^2 + \left|\Psi_{2\Omega}(\vec{r},t)\right|^2\,. \tag{6}$$

3. Results and discussion

The results for the evolution of the probability density of external neutrons for reactions with spherical nuclei ^{40}Ca + ^{96}Zr, ^{18}O + ^{58}Ni and ^{6}He + ^{197}Au are shown correspondently in work [3 - 5]. Similar pictures for probability density of external protons at collision ^{40}Ca + ^{96}Zr are shown in Fig. 1.

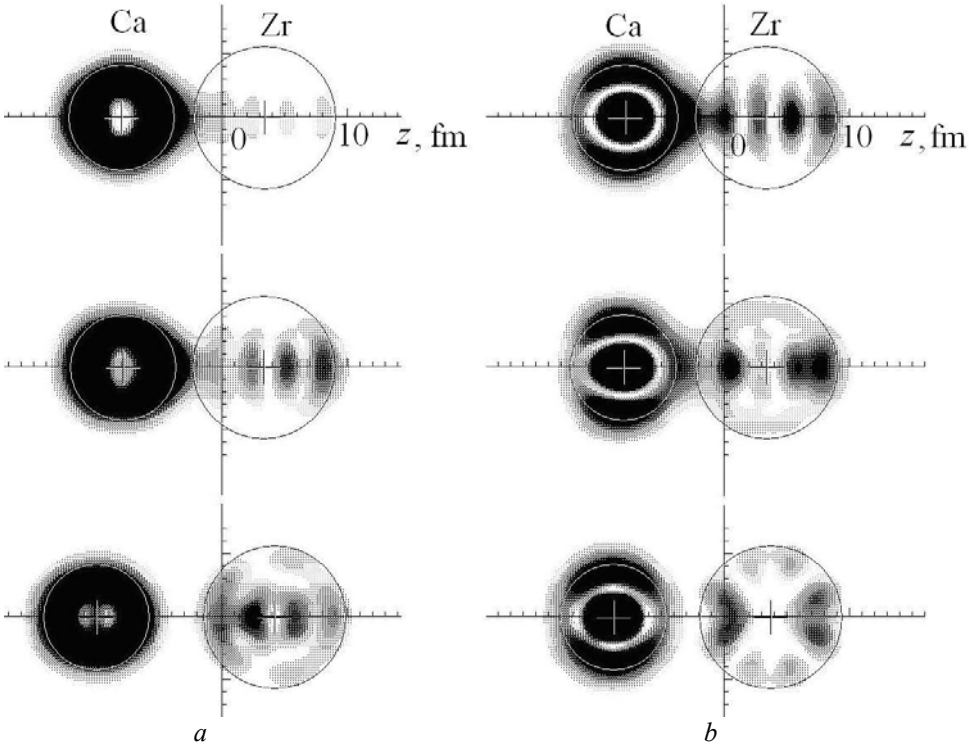

Fig. 1. Change in the probability density $\rho_t(x, y=0, z, t)$ of the external protons of an ^{40}Ca nucleus with the initial state $1d^4_{3/2}$ (*a*) and $2s^2_{1/2}$ (*b*) during a frontal collision with the ^{96}Zr nucleus at energy in the center of mass system E = 98 MeV, radii of the circumferences equal radii of the nuclei, the course of time corresponds to the panels' locations from top to bottom.

Similar pictures for probability density of external neutrons at collision spherical nucleus ^{48}Ca with deformed nucleus ^{238}U are shown in Fig. 2.

The initial conditions for the components Ψ_1 and Ψ_2 of neutron spinor wave functions on axial deformed nucleus were calculated by two methods: offered in work [9] and by decomposing on a system of wave functions of a spherical nucleus.

It has been shown that in pairs of slowly moving atomic nuclei with the distance between their surfaces not exceeding 3 fm, the external neutrons are collectivized and form the two center (molecular) states, while the main neutron transfers from one nucleus to another occur along the position of the internuclear axis. The neutron flux of the probability density crosses a three dimensional, slowly changing potential barrier between the potential wells of colliding nuclei. As the nuclei approach one another, the barrier height falls and a single two center potential well is formed. When the nuclei move away from one another, the potential energy of neutrons varies in the opposite manner.

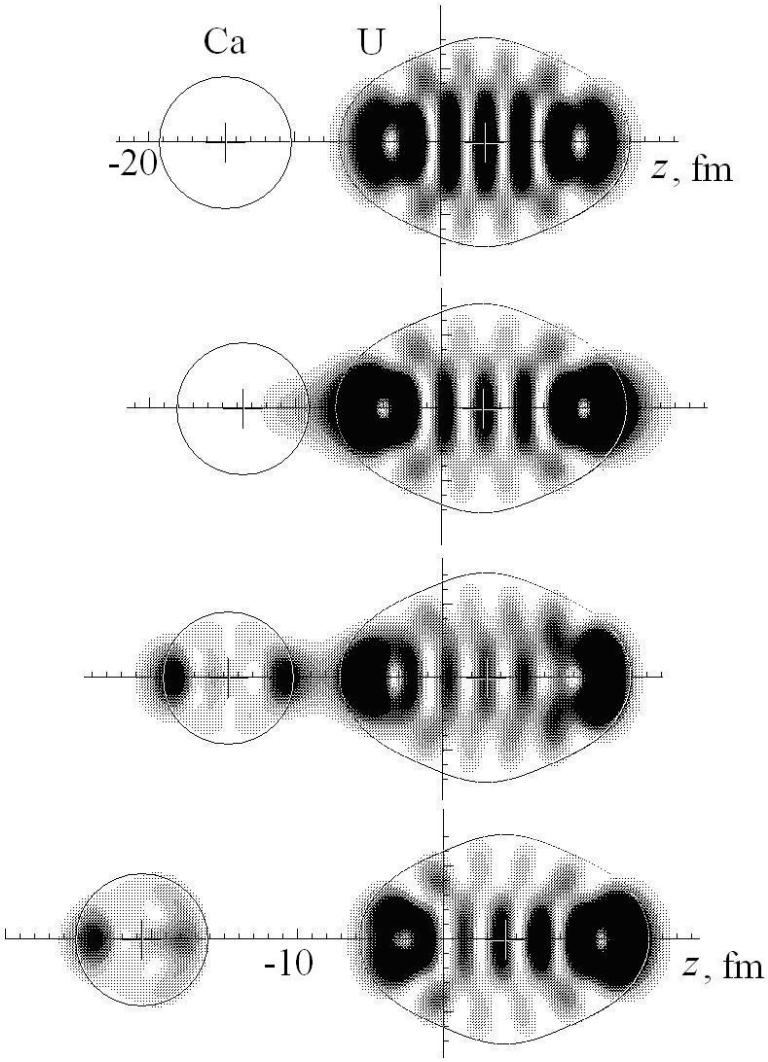

Fig. 2. Change in the probability density $\rho_t(x, y=0, z, t)$ of the external neutrons of an ^{238}U nucleus with the initial state $1d^4_{3/2}$ (*a*) and $2s^2_{1/2}$ (*b*) during a frontal collision with the ^{48}Ca nucleus at energy in the center of mass system *E*=194 MeV, the course of time corresponds to the panels' locations from top to bottom.

The formation of the stable structure of maxima of the probability density in Figs. 1 and 2 indicates that the nucleons preferably occupy first one two center state, and then (after the nuclear separation) one state of the nucleus target. The probability of neutron transfer during the collisions of nuclei without contact between their surfaces was determined by integrating the probability density over the vicinity of the nucleus target:

$$p = \lim_{t\to\infty} p_t(t)\,,\; p_t(t) = \int_{\omega} \rho_t(\vec{r}, t)d\vec{r}\,, \tag{7}$$

with the integration region $\omega \equiv \left\{z - z_1 < \left(R + R_1 - R_2\right)/2, \left|\vec{r} - \vec{r}_1\right| < R_1 + \Delta r\right\}$, and the internuclear axis Oz directed from nucleus projectile 1 to nucleus target 2 and Δr ≈ 2 fm. The results from calculating the probabilities of neutron transfer as a function of on minimum internuclear distance r_m for reactions ^{40}Ca + ^{96}Zr and ^{48}Ca + ^{238}U are shown in Fig. 3. At reaction ^{48}Ca + ^{238}U the states of few external neutrons may strongly changed. Pauli's exclusion principle were taken into consideration by used time dependent many body wave function

$$\Phi_M\left(\vec{r}_1, \ldots \vec{r}_n, t\right) = \frac{1}{M!}\det\begin{bmatrix} \psi_1\left(\vec{r}_1, t\right) & \ldots & \psi_1\left(\vec{r}_N, t\right) \\ \ldots & \ldots & \ldots \\ \psi_M\left(\vec{r}_1, t\right) & \ldots & \psi_M\left(\vec{r}_N, t\right) \end{bmatrix}, \tag{8}$$

and equation for probability of neutron transfers

$$P = \int \bar{\Phi}_M\left(\vec{r}_1, \ldots \vec{r}_M, t\right)\Phi_M\left(\vec{r}_1, \ldots \vec{r}_M, t\right)dV_1 \ldots dV_M\,. \tag{9}$$

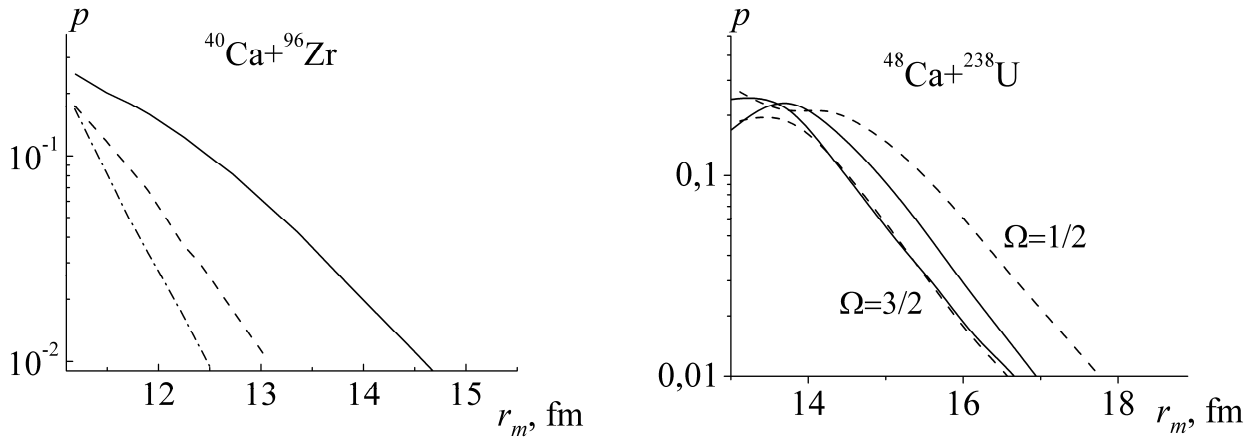

a *б*

Fig. 3. *a* - Probabilities of neutrons pick-up by a nucleus ^{40}Ca from external shell $2d_{5/2}$ of ^{96}Zr and protons stripping from shells ^{40}Ca: $2s^2_{1/2}$ (solid line) and $1d^4_{3/2}$ (dashed lines); *b* - Probabilities of neutrons pick-up (solid lines) by a nucleus ^{48}Ca and neutrons stripping (dashed lines) from shell $1f^8_{7/2}$ of ^{48}Ca in reaction ^{48}Ca + ^{238}U as function on minimum internuclear distance r_m for projections $\Omega = 1/2, 3/2$ of the moment to an internuclear axis.

As can seen in Fig. 3, the probability of neutron transfer with the dynamic tunnel effect during grazing collisions allows simple analytical approximations of the type

$$p \approx A\left[1+\exp(Bs)\right]^{-1}, \tag{10}$$

Here s is the minimum distance between the surfaces of nuclei, $B \approx 1$ fm^{-1}, $A(E)$ is a decreasing function of the energy E, depending also on the initial energy of the neutron ε and the properties of the empty neutron levels of the nucleus target with energies close to ε.

At reaction ^{40}Ca + ^{96}Zr (Fig. 3*a*) neutrons are predominantly transferred from ^{96}Zr to ^{40}Ca and protons are transferred from ^{40}Ca to ^{96}Zr. At reaction ^{48}Ca + ^{238}U (see Fig. 3, *b*) probabilities of neutrons stripping and pick-up are commensurable.

The total cross section of the transfer of some external neutrons from shells containing is

$$\sigma = 2\pi \int_{b_0}^{\infty} w(b) b db\,, \tag{11}$$

where b_0 is the minimum collision impact parameter corresponding to the grazing collision when the surfaces of the nuclei approach the distance a = 0.7 fm, equal to the characteristic size (diffusivity) of the surface region of nuclei. A comparison of the experimental data on the cross section of neutron transfer during the ^{6}He + ^{197}Au, ^{90}Zr + ^{208}Pb, ^{40}Ca + ^{208}Pb, ^{40}Ca + ^{96}Zr reactions in Fig. 4 and the calculation results demonstrates satisfactory quantitative (Fig. 4, *a*) and qualitative (Fig. 4, *b*) agreement between them at energies near the Coulomb barrier. The ^{198}Au isotope can also be formed as a result of the transfer of two neutrons with the subsequent evaporation of one of them. After the transfer of two neutrons to the high lying levels of the Au nucleus, one can fall to a lower level, transferring a part of the energy to the other neutron, which abandons the Au nucleus as a result.

In our calculations, we used an approximation of the conservation of the spherical shape of the nuclei during the collision. The difference between the experimental data and calculation results could be due to possible deformations of the nuclei under the action of the nuclear. It is known that similar deformations lead to an increase in the nuclear forces and lower the Coulomb barrier of the capture of the nucleus projectile by the nucleus target. The difference between the experimental data and the calculation results at the subbarrier energies of $E > V_B$ could be due to the substantial changes in the states of the rest nucleons of colliding nuclei (except for the considered external neutrons of the nucleus projectile) in inelastic and deeply inelastic processes.

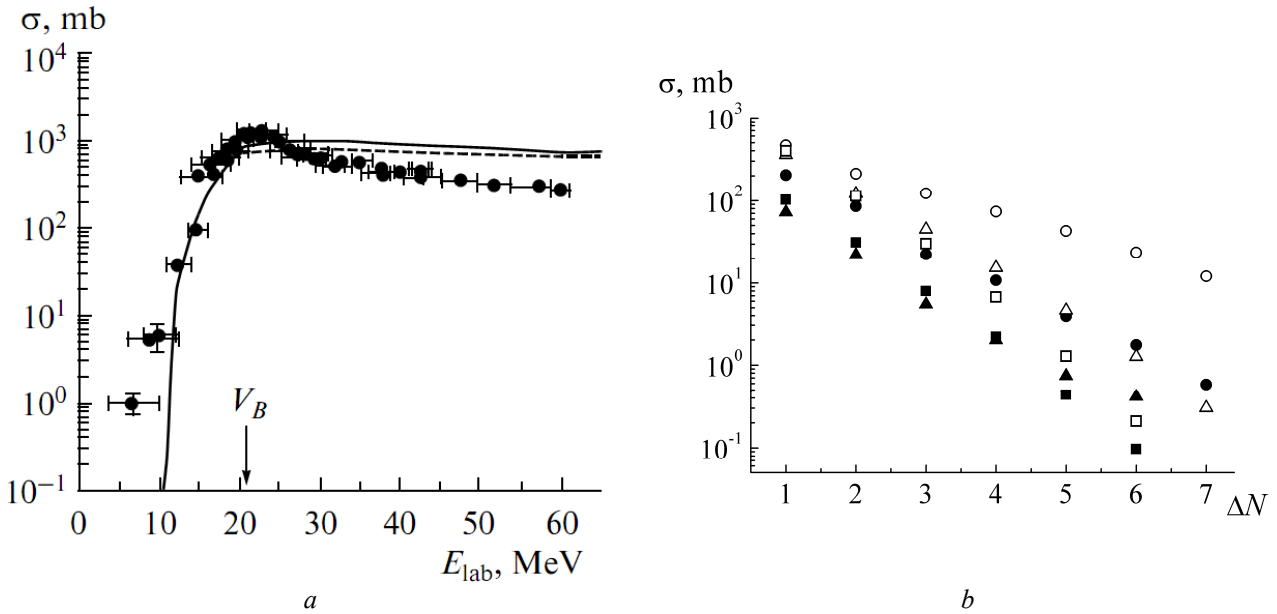

a *b*

Fig. 4. *a* - Energy dependence of the cross section for the formation of the ^{198}Au isotope in the ^{6}He+^{197}Au reaction. Dots represent the experimental data from [1]; the dashed line, calculations for the transfer of one neutron; the solid line, calculations for the transfer of one or two neutrons. V_B is the Coulomb barrier. *b* - Cross-sections for clean neutron pick-up in reactions: ^{90}Zr + ^{208}Pb with $E_{c.m.} = 391$ MeV [10] (circles) , ^{40}Ca+ ^{208}Pb with $E_{c.m.} = 209$ MeV (triangles) [11], ^{40}Ca + ^{96}Zr with $E_{c.m.} = 107$ MeV, (squares) [10]: experimental data − black marks, calculations on the basis of Poisson distribution − white marks.

4. Conclusions

Simple analytical dependences for the probability of the transfers of external neutrons of neutron rich nuclei found by numerical simulation can be used to calculate the cross sections of nucleon transfers and to substantiate theoretical models of the grazing collisions of nuclei. Variations in the states of both external and internal nucleons of colliding nuclei must be considered in the nonstationary quantum approach applied in this work.

REFERENCES

1. *Kulko A.A. et al.* Isomeric ratios for ^{196,198}Tl and ^{196,198}Au from fusion and transfer in the interaction of ^{6}He with ^{197}Au // J. Phys. - 2007. - Vol. G34. - P. 2297 - 2306.
2. *Winther A.* Grazing reactions in collisions between heavy nuclei // Nucl. Phys. - 1994. - Vol. A572. - P. 191 - 235.
3. *Samarin V., Samarin K.* Consideration of the Spin-orbit Interaction in the Description of Nucleon Transfers upon Heavy Ionic Nuclei Collisions // Bull. Russ. Acad. Sci. Phys. - 2010. - Vol. 74. - P. 567 - 571.
4. *Samarin V., Samarin K.* Mechanisms of Transfer Reactions in Low Energy Collisions with Neutron Enriched Nuclei // Bull. Russ. Acad. Sci. Phys. - 2011. - Vol. 75. - P. 964 - 969.
5. *Samarin V., Samarin K.* Dynamic Tunnel Effect at Low Energy Nuclear Reactions with Neutron Rich Nuclei // Bull. Russ. Acad. Sci. Phys. - 2012. - Vol. 76. - P. 450 - 453.
6. *Davydov A.S.* Kvantovaya mekhanika (Quantum Mechanics). - M.: Nauka, 1973. − 703 p.
7. *Riley, M.E., Ritchie B.* Numerical time-dependent Schrödinger description of charge-exchange collisions. // Phys. Rev. - 1999. - Vol. A59. - P. 3544 − 3547.
8. *Marchuk G.I.* Metody vychislitel'noi matematiki (Methods of Computational Mathematics). - M.: Nauka, 1980. − 534 p.
9. *Samarin V.* Nucleon States of Strongly Deformed Nuclei and Dinuclear Systems in the Nonoscillator Two-Center Model. // Phys. of Atom. Nucl. − 2010. − Vol. 73. − P. 1416 - 1428.
10. *Szilner S. et al.* Multinucleon transfer reactions in closed-shell nuclei // Phys Rev. − 2007. - Vol. C76. - P. 024604 (1 - 9).
11. *Szilner S. et al.* Multinucleon transfer processes in ^{40}Ca + ^{208}Pb // Phys. Rev. − 2005. - Vol. C71. - P. 044610 (1 - 8).

DESCRIPTION OF NUCLEON TRANSFERS PROCESSES BY A COUPLED CHANNEL METHOD WITH TWO-CENTER STATES

V. V. Samarin

Joint Institute for Nuclear Research, Dubna, Moscow region, Russia

The problem of quantum description of near-barrier fusion of heavy nuclei taking place under strong coupling of relative motion with external nucleons transfers is studied. The method of perturbed stationary states, founded on decomposing of a full wave function of a system of two nuclei and nucleon by a system of two-center nucleon wave functions, is applied for the description of nucleons transfers at low-energy nuclear reactions. The two-center nucleon energy levels – additions to nucleus-nucleus potential in a channels, and wave functions are calculated by a numerical solution of a Schrödinger equation for an arbitrary axial-symmetrical field with spin-orbit interactions, based on decomposing on Bessel functions and difference scheme along internuclear axis.

1. Introduction

The reactions with neutron-rich nuclei have recently received increased interest as well experimentally as theoretically. The possibility to perform experiments with neutron-rich radioactive fission fragments opens new doors for the production and study of new isotopes and, probably, for synthesis of new superheavy elements [1, 2]. Also great efforts have been devoted to studying near-barrier fusion of light weakly bound nuclei [2, 3]. Unusual effects are expected here both from the halo structure of these nuclei and from the specific tunneling mechanism of the composed weekly bound system that is of general interest for quantum theory. Neutron transfer cross sections are known to be rather large at near-barrier energies of heavy-ion collisions – the result of significant extension of the wave functions of neutrons from the outer nuclear shells. A significant increase in fusion cross sections is observed in a series of reactions if nuclei with excessive neutrons participate in them. Such behavior has established in particular for two low energy fusion reactions, ^{18}O + ^{58}Ni and ^{16}O + ^{60}Ni [4], with similar compound nuclei (Fig. 1). In [2], the transition of external neutrons from the level of the ^{18}O nucleus to underlying levels of the ^{58}Ni nucleus was referred to as the fundamental source of additional energy in the translational motion of nuclei, raising the possibility of overcoming the Coulomb barrier. The interrelated processes of the generation of molecular states in the two nucleus ^{18}O + ^{58}Ni system, the transitions between such levels in the process of nuclei collision, and the transfer of neutrons between nuclei. were investigate on time-dependent quantum description [5].

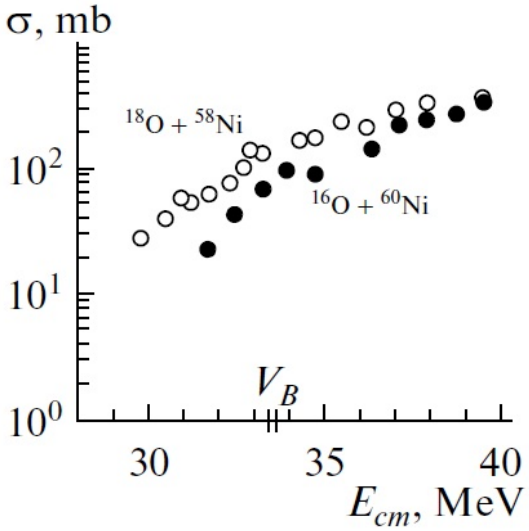

Fig. 1. Experimental dependence of nucleus fusion cross section σ in reactions ^{18}O + ^{58}Ni (white dots) and ^{16}O + ^{60}Ni (black dots) on the energy in the system at the center of mass E_{cm}, according to [4]; V_B is the Coulomb barrier height.

As a consequence there is a prevailing view that coupling with the transfer channels should play an important role in sub-barrier fusion of heavy nuclei [3]. However, if an influence of collective excitations (rotation of deformed nuclei and surface vibrations) on near-barrier fusion of heavy nuclei is well studied experimentally and well understood theoretically, the role of neutron transfer is not so clear. It is very difficult, for many reasons, to take into account explicitly the transfer channels within a consistent channel coupling (CC) approach used successfully for the description of collective excitations in the near-barrier fusion processes [6]. Fundamental coupled channel equations for reactions with particles redistribution were formulated in [7]. In the present study, the calculations for solving these equations for reaction ^{18}O + ^{58}Ni are started.

2. Theory

The microscopic description of capture of nuclei (with masses m_1, m_2) and external nucleon (with mass m_3) transfers guesses the solution of a multidimensional stationary Schrödinger equation with Hamiltonian

$$H = -\frac{\hbar^2}{2m_1}\Delta_{\vec{r}_1} - \frac{\hbar^2}{2m_2}\Delta_{\vec{r}_2} + V_{12}(R) + \sum_i \left[-\frac{\hbar^2}{2m_3}\Delta_{\vec{r}_i} + v_{13}(\rho_{1i}) + v_{23}(\rho_{2i}) \right], \quad (1)$$

$$\vec{R} = \vec{r}_2 - \vec{r}_1\,,\ \vec{\rho}_1 = \vec{r}_3 - \vec{r}_1\,,\ \vec{\rho}_2 = \vec{r}_3 - \vec{r}_2\,. \quad (2)$$

Application of the two-center Jacobi coordinates

$$\vec{r} = \vec{r}_3 - \frac{m_1\vec{r}_1 + m_2\vec{r}_2}{m_1 + m_2}, \tag{3}$$

result in the following Hamiltonian at center of mass system

$$H = -\frac{\hbar^2}{2M}\Delta_{\vec{R}} - \frac{\hbar^2}{2\mu}\Delta_{\vec{r}} + V_{12}(R) + v_{13}(\rho_1) + v_{23}(\rho_2), \tag{4}$$

$$1/M = 1/m_1 + 1/m_2,\ 1/\mu = 1/m_3 + 1/(m_1 + m_2). \tag{5}$$

The coupled channel method based on wave function eigenfunctions expansion for internal degrees of freedom. For neutrons from the outer nuclear shells this eigenfunctions may be calculated in two center shell model with stationary Schrödinger equation

$$\left[-\frac{\hbar^2}{2\mu}\Delta_{\vec{r}} + V(\vec{r}) + V_{LS}(\vec{r})\right]\Phi_\alpha(\vec{r};R) = \varepsilon_\alpha(R)\Phi_\alpha(\vec{r};R). \tag{6}$$

with spin-orbit interaction operator

$$\hat{V}_{LS} = -\frac{b}{2\hbar}\vec{\sigma}[(\nabla V)\vec{p}], \tag{7}$$

inclusive Pauli matrices $\vec{\sigma} = \{\sigma_x, \sigma_y, \sigma_z\}$, momentum operator $\vec{p}$, neutron potential energy $V = V(\vec{r}) = V_{13}(\rho_1) + V_{23}(\rho_2)$ and Wood's-Sakson's potentials $V_{13}(\rho_1),\ V_{23}(\rho_2)$. Wave functions

$$\Phi_\alpha(R,\vec{r}) = \begin{pmatrix}\psi_{\alpha1}(\vec{r})\\ \psi_{\alpha2}(\vec{r})\end{pmatrix}, \tag{8}$$

and energy levels $\varepsilon_\alpha(R)$ for internuclear distance R are calculated by a numerical solution of a Schrödinger's equations at cylindrical coordinates (ρ,φ,z) [8]

$$\left[-\frac{\hbar^2}{2m}\Delta + V(\rho,z) + i\frac{b}{2}\frac{1}{\rho}V_\rho\frac{\partial}{\partial\varphi}\right]\psi_{\alpha1} + i\frac{b}{2}e^{-i\varphi}\left[i\left(V_\rho\frac{\partial}{\partial z} - V_z\frac{\partial}{\partial\rho}\right) - \frac{1}{\rho}V_z\frac{\partial}{\partial\varphi}\right]\psi_{\alpha2} = \varepsilon_\alpha\psi_1, \tag{9}$$

$$\left[-\frac{\hbar^2}{2m}\Delta + V(\rho,z) - i\frac{b}{2}\frac{1}{\rho}V_\rho\frac{\partial}{\partial\varphi}\right]\psi_{\alpha2} - i\frac{b}{2}e^{i\varphi}\left[i\left(V_\rho\frac{\partial}{\partial z} - \tilde{V}_z\frac{\partial}{\partial\rho}\right) + \frac{1}{\rho}V_z\frac{\partial}{\partial\varphi}\right]\psi_{\alpha1} = \varepsilon_\alpha\psi_{\alpha2}, \tag{10}$$

with designation $V_\rho = \frac{\partial}{\partial\rho}V$, $V_z = \frac{\partial}{\partial z}V$.

For wave function of all system

$$\Psi(\vec{r};\vec{R}) = \sum_\alpha F_\alpha(\vec{R})\Phi_\alpha(\vec{r};\vec{R}), \tag{11}$$

we will use simple two states approximation [7]

$$\Psi(\vec{r};\vec{R}) = F_1(\vec{R})\Phi_1(\vec{r};\vec{R}) + F_2(\vec{R})\Phi_2(\vec{r};\vec{R}), \tag{12}$$

with state 1 on projectile nucleus 1 and state 2 on target nucleus 2 The coupled channel equations for function F_α are

$$\left[-\frac{\hbar^2}{2M}\Delta_{\vec{R}} + V_{12}(R) + \varepsilon_\alpha(R) - E\right]F_\alpha(\vec{R}) = \sum_{\alpha'}\Lambda_{\alpha\alpha'}(\vec{R})F_\alpha(\vec{R}). \tag{13}$$

The two-center nucleon energy levels $\varepsilon_\alpha(R)$ are additions to nucleus-nucleus potential $V_{12}(R)$ in a channel α, and coupled channel matrix $\Lambda_{\alpha\alpha'}(\vec{R})$ includes differential operators

$$\Lambda_{\alpha\alpha'}\left(\vec{R}\right)=-\frac{\hbar^2}{M}\vec{Q}_{\alpha\alpha'}\left(\vec{R}\right)\nabla_{\vec{R}}-\frac{\hbar^2}{2M}K_{\alpha\alpha'}\left(\vec{R}\right), \tag{14}$$

$$\vec{Q}_{\alpha\alpha'}\left(\vec{R}\right)=-\langle\Phi_\alpha\left(\vec{R},\vec{r}\right)|\nabla_{\vec{R}}|\Phi_{\alpha'}\left(\vec{R},\vec{r}\right)\rangle, \tag{15}$$

$$K_{\alpha\alpha'}\left(\vec{R}\right)=-\langle\Phi_\alpha\left(\vec{R},\vec{r}\right)|\Delta_{\vec{R}}|\Phi_{\alpha'}\left(\vec{R},\vec{r}\right)\rangle. \tag{16}$$

For spherically symmetric matrix $\Lambda_{ij}(R)$ formulas are simplified

$$\Lambda_{\alpha\alpha'}\left(R\right)=-\frac{\hbar^2}{M}Q_{\alpha\alpha'}\left(R\right)\frac{\partial}{\partial R}-\frac{\hbar^2}{2M}K_{\alpha\alpha'}\left(R\right), \tag{17}$$

$$Q_{\alpha\alpha'}\left(R\right)=-\langle\Phi_\alpha\left(R,\vec{r}\right)|\frac{\partial}{\partial R}|\Phi_{\alpha'}\left(R,\vec{r}\right)\rangle, \tag{18}$$

$$K_{\alpha\alpha'}\left(R\right)=-\frac{2}{R}\langle\Phi_\alpha\left(R,\vec{r}\right)|\frac{\partial}{\partial R}|\Phi_{\alpha'}\left(R,\vec{r}\right)\rangle-\langle\Phi_\alpha\left(R,\vec{r}\right)|\frac{\partial^2}{\partial R^2}|\Phi_{\alpha'}\left(R,\vec{r}\right)\rangle. \tag{19}$$

Partial waves method application result in ordinary differential equation for radial functions $F_\alpha(R)$

$$\left[-\frac{\hbar^2}{2M}\frac{d^2}{dR^2}+\frac{\hbar^2L\left(L+1\right)}{2MR^2}+\varepsilon_\alpha(R)-E+v_{12}(R)\right]F_\alpha(R)+$$

$$+\sum_{\alpha'}\left\{\frac{\hbar^2}{M}Q_{\alpha\alpha'}(R)\frac{dF_{\alpha'}}{dR}+\frac{\hbar^2}{2M}K_{\alpha\alpha'}(R)F_{\alpha'}(R)\right\}=0. \tag{20}$$

For calculation coupled channel matrices $Q_{\alpha\alpha'}(R)$ and $K_{\alpha\alpha'}(R)$ we introduce supporting matrices

$$J_{\alpha\alpha'}\left(R_1,R\right)=\int\Phi^*_\alpha\left(R_1,\vec{r}\right)\Phi_{\alpha'}\left(R,\vec{r}\right)d\vec{r}, \tag{21}$$

with the following properties

$$J_{\alpha\alpha'}\left(R_1,R_1\right)=\int\Phi^*_\alpha\left(R_1,\vec{r}\right)\Phi_{\alpha'}\left(R_1,\vec{r}\right)d\vec{r}=\delta_{\alpha\alpha'}, \tag{22}$$

$$J_{\alpha\alpha'}\left(R_1,R\right)=\delta_{\alpha\alpha'}+\int\left[\Phi^*_\alpha\left(R_1,\vec{r}\right)-\Phi^*_\alpha\left(R,\vec{r}\right)\right]\Phi_{\alpha'}\left(R,\vec{r}\right)d\vec{r}, \tag{23}$$

$$Q_{\alpha\alpha'}\left(R\right)=-\frac{\partial}{\partial R}J_{\alpha\alpha'}\left(R_1,R\right)\Big|_{R_1=R}=\frac{\partial}{\partial R}J_{\alpha'\alpha}\left(R_1,R\right)\Big|_{R_1=R}, \tag{24}$$

$$Q_{\alpha\alpha'}\left(R\right)=-\frac{\partial}{\partial R}J_{\alpha\alpha'}\left(R_1,R\right)\Big|_{R_1=R}\approx-\frac{1}{2\Delta R}\left[J_{\alpha\alpha'}\left(R,R+\Delta R\right)-J_{\alpha\alpha'}\left(R,R-\Delta R\right)\right], \tag{25}$$

$$-\frac{\partial^2}{\partial R^2}J_{\alpha\alpha'}\left(R_1,R\right)\Big|_{R_1=R}\approx-\frac{1}{2\left(\Delta R\right)^2}\left[J_{\alpha\alpha'}\left(R,R+\Delta R\right)+J_{\alpha\alpha'}\left(R,R-\Delta R\right)\right], \tag{26}$$

at $\Delta R\to 0$.

At $R\to\infty$ boundary conditions for full wave function

$$\Psi(\vec{R},\vec{r})\Big|_{R\to\infty}=\sum_\alpha F_\alpha(\vec{R})\Big|_{R\to\infty}\Phi_\alpha(\vec{R},\vec{r})\Big|_{R\to\infty}=\Psi_1(\vec{r}_1)\Psi_{23}\left(\vec{R}_{23}\right)\Psi_\beta\left(\vec{\rho}_{23}\right), \tag{27}$$

$$\Psi(\vec{R},\vec{r})\Big|_{R\to\infty}=\sum_\alpha F_\alpha(\vec{R})\Big|_{R\to\infty}\Phi_\alpha(\vec{R},\vec{r})\Big|_{R\to\infty}=\Psi_2(\vec{r}_2)\Psi_{13}\left(\vec{R}_{13}\right)\Psi_\gamma\left(\vec{\rho}_{13}\right). \tag{28}$$

correspond to neutron location on one-center state β of nucleus 2 and on one-center state γ of nucleus 1. For channel wave functions we have formulas

$$F_\alpha(\vec{R})\Big|_{R\to\infty} \approx \int\left[\Phi^*_\alpha(\vec{R},\vec{r})\Psi_1(\vec{r}_1)\Psi_{23}\left(\vec{R}_{23}\right)\Psi_\beta\left(\vec{\rho}_{23}\right)\Big|_{R\to\infty}\right]d\vec{r}\,, \tag{29}$$

$$F_\alpha(\vec{R})\Big|_{R\to\infty} \approx \int\left[\Phi^*_\alpha(\vec{R},\vec{r})\Psi_2(\vec{r}_2)\Psi_{13}\left(\vec{R}_{13}\right)\Psi_\gamma\left(\vec{\rho}_{13}\right)\Big|_{R\to\infty}\right]d\vec{r}\,. \tag{30}$$

Below we will considerate only two-states approximation (12). If for the first time nucleon stays at state 1 of projectile nucleus, after collisions it may stays at state 1 of projectile nucleus or occupies state 2 of target nucleus. The boundary conditions for channel wave function may be produce in approximate form, which contain determined in quadratures constants $C_{\alpha\alpha'}, D_{\alpha\alpha'}$ and unknown constants A_1 and A_2

$$F_1(\vec{R})\Big|_{R\to\infty} = \exp\left[-ik_1\frac{m_1R}{m_1+m_3}\right]C_{11}(k_1)+\exp\left[ik_1\frac{m_1R}{m_1+m_3}\right]D_{11}(k_1)A_1+\exp\left[ik_2\frac{m_1R}{m_1+m_3}\right]D_{12}(k_2)A_2,$$

$$F_2(\vec{R})\Big|_{R\to\infty} = \exp\left[-ik_1\frac{m_1R}{m_1+m_3}\right]C_{21}(k_1)+\exp\left[ik_1\frac{m_1R}{m_1+m_3}\right]D_{21}(k_1)A_1+\exp\left[ik_2\frac{m_1R}{m_1+m_3}\right]D_{22}(k_2)A_2,$$

$$\frac{d}{dR}F_1(R)\Big|_{R\to\infty} = -ik_1\frac{m_1}{m_1+m_3}\exp\left[-ik_\beta\frac{m_1R}{m_1+m_3}\right]C_{11}(k_1)+$$

$$+ik_1\frac{m_1}{m_1+m_3}\exp\left[ik_1\frac{m_1R}{m_1+m_3}\right]D_{11}(k_1)A_1+ik_2\frac{m_1}{m_1+m_3}\exp\left[ik_2\frac{m_1R}{m_1+m_3}\right]D_{12}(k_2)A_2,$$

$$\frac{d}{dR}F_2(R)\Big|_{R\to\infty} = -ik_1\frac{m_1}{m_1+m_3}\exp\left[-ik_\beta\frac{m_1R}{m_1+m_3}\right]C_{21}(k_1)+$$

$$+ik_1\frac{m_1}{m_1+m_3}\exp\left[ik_1\frac{m_1R}{m_1+m_3}\right]D_{21}(k_1)A_1+ik_2\frac{m_1}{m_1+m_3}\exp\left[ik_2\frac{m_1R}{m_1+m_3}\right]D_{22}(k_2)A_2.$$

After exception unknown constants A_1 and A_2 we shall receive two differential boundary conditions for channel wave function. After transformation set of differential equations and boundary conditions into difference equations and boundary conditions we receive the linear equation set and can solve it by famous numerical methods [9], for example, as for collective degrees of freedom [6]. For far range Coulomb interaction similar formulas may be received.

3. Results and discussion

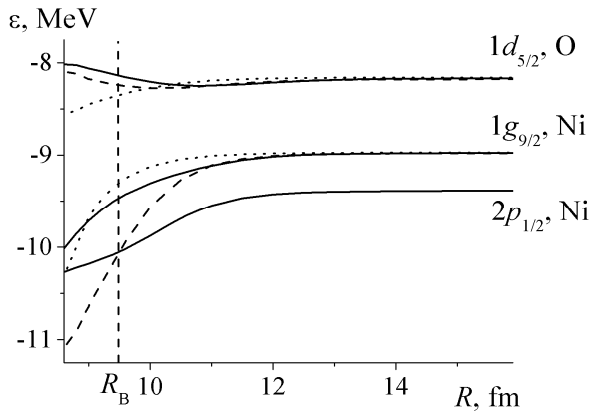

Fig. 2. Some two-center neutron energy levels for a system ^{18}O + ^{58}Ni as a function of internuclear distance R for moment projection on internuclear axis $\Omega = 1/2$ (solid lines), $\Omega = 3/2$ (dashed lines), $\Omega = 5/2$ (dotted lines), R_B corresponds to top of a Coulomb barrier.

The results of calculation energy levels $\varepsilon_\alpha(R)$ for spherical nuclei ^{18}O+^{58}Ni system are shown in Fig. 2 and matrices derivates (25), (26) are shown in Fig. 3 for state $1-1g_{9/2}$ of ^{58}Ni and state $1-1d_{5/2}$ of ^{18}O.

During internuclear distance R reducing, potential barrier between the potential wells of colliding nuclei is changing slowly reduce. As the nuclei approach one another, the barrier height falls and large values of non-diagonal coupled matrices derivates (25), (26) result in neutron transfer from upper level $1d_{5/2}$ of ^{18}O to $1g_{9/2}$ of ^{58}Ni with increasing of probability Coulomb barrier for nuclear fusion. Some probability densities

$$p(\rho,z) = \left|\psi_{\alpha1}(\vec{r})\right|^2 + \left|\psi_{\alpha2}(\vec{r})\right|^2, \tag{31}$$

for spherical nuclei ^{18}O + ^{58}Ni system are shown in Figs. 4 - 6.

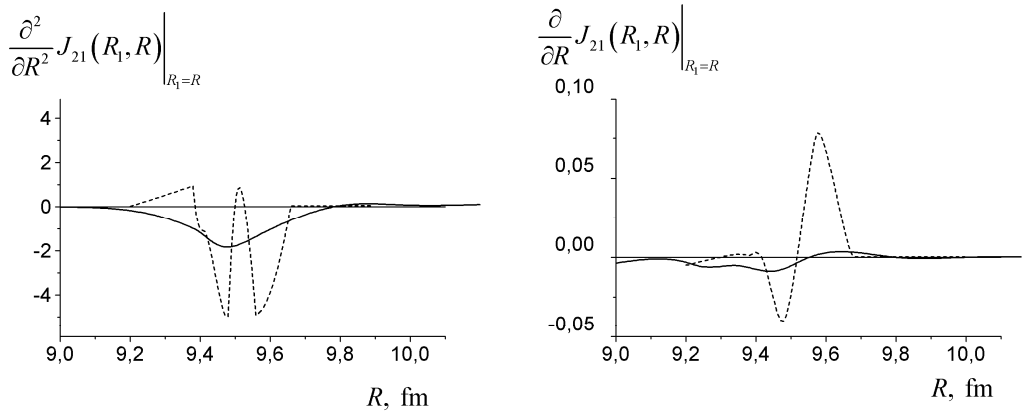

Fig. 3. Matrices derivates (25), (26) for state $1-1g_{9/2}$ of ^{58}Ni and state $1-1d_{5/2}$ of ^{18}O for moment projection on internuclear axis $\Omega = 1/2$ (dashed lines) and $\Omega = 3/2$ (solid lines).

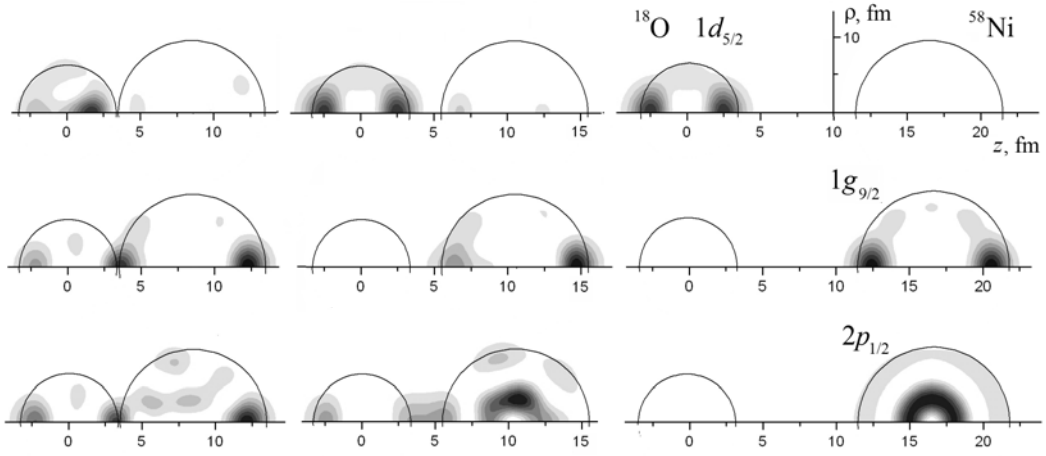

Fig. 4. Some two-center wave functions for a system ^{18}O + ^{58}Ni at three values of internuclear distance R for moment projection on internuclear axis $\Omega = 1/2$.

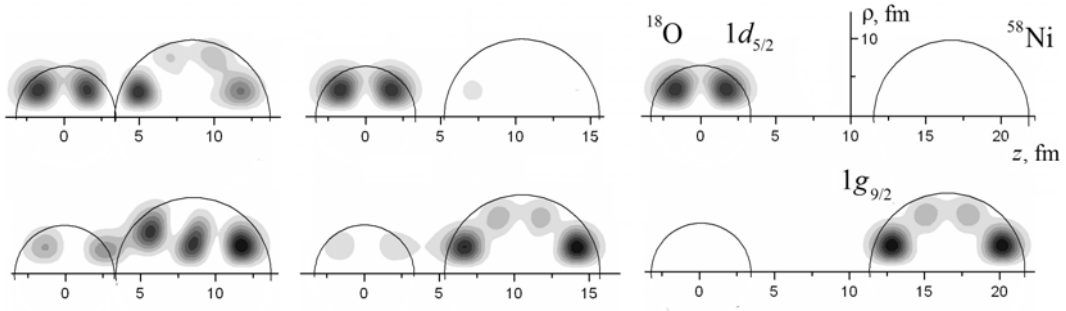

Fig. 5. Some two-center wave functions for a system ^{18}O+^{58}Ni at three values of internuclear distance R for moment projection on internuclear axis $\Omega = 3/2$.

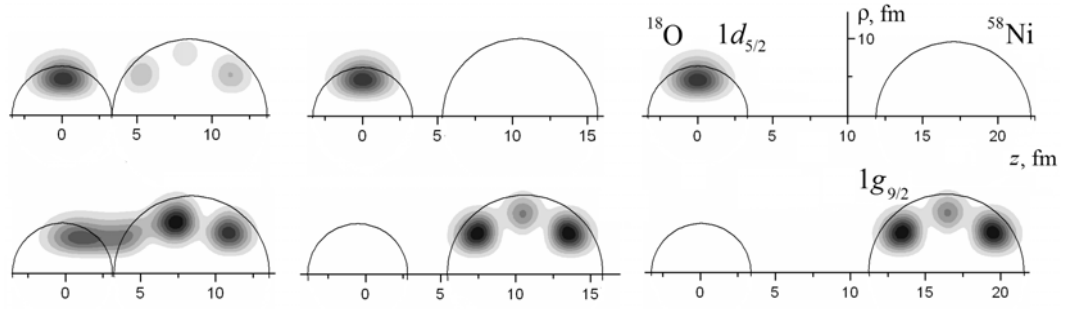

Fig. 6. Some two-center wave functions for a system ^{18}O+^{58}Ni at three values of internuclear distance R for moment projection on internuclear axis $\Omega = 5/2$.

4. Conclusion

The proposed model for calculating nucleon states in asymmetric nuclear systems has made it possible to explain qualitatively experimental data on the excess of the cross section for fusion in the $^{18}O+^{58}Ni$ reaction above the cross section for fusion in the $^{16}O + ^{60}Ni$ reaction. The model can also be useful in analyzing experimental data – in particular, data on exotic and superheavy nuclei and in planning new experiments.

This work was supported in part by the Russian Foundation for Basic Research (RFBR) through Grant No. 12-02-01325-a.

REFERENCES

1. *Zagrebaev V.I.* Synthesis of superheavy nuclei: Nucleon collectivization as a mechanism for compound nucleus formation // Phys. Rev. - 2001. Vol. C64. – P. 034606 (1 - 13).
2. *Zagrebaev V.I.* Sub-barrier fusion enhancement due to neutron transfer // Phys. Rev. - 2003. - Vol. C67. – P. 061601 (1 - 5).
3. *Samarin V.V., Zagrebaev V.I., Greiner W.* Sub-barrier fusion of neutron-rich nuclei and its astrophysical consequences // Phys. Rev. - 2007. - Vol. C75. - P. 035809 (1 - 11).
4. *Borges A.M. et al.* Pair transfer and subbarrier fusion of $^{18}O + ^{58}Ni$ // Phys. Rev. - 1992. - Vol. C46. - P. 2360 - 2363.
5. *Samarin V., Samarin K.* Mechanisms of Transfer Reactions in Low Energy Collisions with Neutron Enriched Nuclei // Bull. Russ. Acad. Sci. Phys. - 2011. - Vol. 75. - P. 964 - 969.
6. *Samarin V.V., Zagrebaev V.I.* Channel coupling analysis of initial reaction stage in synthesis of super-heavy nuclei // Nucl. Phys. - 2004. - Vol. A734. - P. 044610. (E9 - E12).
7. *Zhigunov V.P., Zakhar'ev B.N.* Metod silnoj svyazi kanalov v kvantovoi teorii rassejanija (Coupled-Channel Method in Quantum Scattering Theory). - M.: Atomizdat, 1974. - 216 p.
8. *Samarin V.* Nucleon States of Strongly Deformed Nuclei and Dinuclear Systems in the Nonoscillator Two-Center Model // Phys. of Atom. Nucl. - 2010. - Vol. 73. - P. 1416 - 1428.
9. *Marchuk G.I.* Metody vychislitel'noi matematiki (Methods of Computational Mathematics). - M.: Nauka. 1980. - 534 p.

FEATURES OF NUCLEAR REACTIONS WITH LIGHT WEAKLY BOUND NUCLEI AT ENERGY NEAR THE COULOMB BARRIER

N. K. Skobelev[1], Y. E. Penionzhkevich[1], V. Kroha[2], V. Burjan[2], Z. Hons[2], J. Mrázek[2], Š. Piskoř[2], E. Šimečkova[2], E. I. Voskoboynik[1]

[1] Joint Institute for Nuclear Research, Dubna, Moscow region, Russia
[2] Nuclear Physics Institute, Czech Academy of Sciences, Řež, Czech Republic

In the experiments carried out by ion beam ^{6}He of the cyclotron complex DRIBs (JINR) and ^{3}He beam cyclotron U-120M of the NPI, Czech Academy of Sciences have been investigated reaction ^{45}Sc + ^{3}He,^{6}He and ^{197}Au + ^{3}He,^{6}He in the energy range near the Coulomb barrier. It were obtained the experimental values of the cross sections for complete fusion reactions and direct reactions for formation of the isotopes ^{43}Sc, ^{44}Sc and ^{46}Sc also ^{196}Au and ^{198}Au as a function of the bombarding ^{3}He and ^{6}He energy. Despite the low binding energy of ^{3}He and the positive Q- values leading to the formation of isotopes ^{44}Sc and ^{46}Sc, the behavior of the excitation functions with the formation of these isotopes is different from the excitation functions for d, ^{6}He and ^{6}Li The contribution of different reaction mechanisms in the cross sections of formation isotopes: ^{43}Sc, ^{44}Sc and ^{46}Sc and gold isotopes: ^{194}Au and ^{196}Au are discussed.

1. Introduction

Understanding of the mechanisms of the fusion and transfer reactions with beams of radioactive and weakly bound stable nuclei is essential for the synthesis of superheavy elements and astrophysics. A small binding energy of the valence nucleons in halo nuclei and nuclear clusters in loosely bound nuclei should influence the processes of interacting nuclei at energies near the Coulomb barrier. In addition to on the possibility of reaction affects Q-value, which in these cases is usually positive.

Reactions caused halo nuclei such as ^{6}He, has been actively studied by many research centers. It was found several interesting phenomena: the sub-barrier enhancement for fusion, a high probability of direct processes (breakup of the incident particle, the transfer reactions of one or more nucleons) which have different reaction mechanisms [1 - 3].

Like the halo radioactive nuclei, weakly bound nuclei such as ^{6,7}Li and others have a low threshold for breakup on clusters, and therefore they have a high probability for clustering in the excited state. For the ^{6}Li threshold excitation energy for the formation of clusters, α + d is equal to 1.47 MeV, for ^{7}Li decay into α + t cluster is observed in the excitation energy more than 2.47 MeV. These threshold values are of the same order as the separation energy of two neutrons from ^{6}He, which is equal to 0.975 MeV. The transfer reactions may dominate at energy of the bombarding ions below the Coulomb barrier as from the cluster structure of nuclei well as from the large positive Q-value. Can one expect any-peculiarities in reactions with stable nuclei projectiles as ^{3}He, which has a small binding energy of 7.718 MeV (2.57 MeV/A)? Due to the smaller separation energy of the proton in ^{3}He (S_p = 5.49 MeV), low-energy separation of 2 protons S_{2p} = 7.71 MeV, reactions due to ^{3}He should lead to an increase in the contribution of direct reactions: pickup and stripping of nucleons.

The purpose of this report is the comparison of the reaction mechanisms in the bombardment of targets of ^{45}Sc, ^{197}Au and Pt by ions ^{6}He, ^{3}He and ^{6}Li at energies in the vicinity of Coulomb barrier reactions. This was done by analyzing the excitation functions of reactions for formation of different nuclides as products of the complete fusion and for formation of the same radioactive nuclei in direct reactions, including those with a positive Q-value of the reaction.

2. Experimental procedure

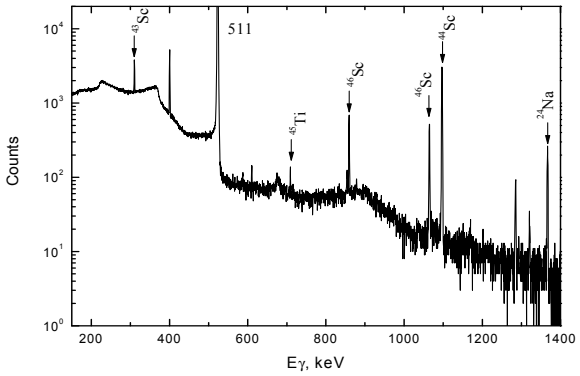

Fig. 1. Gamma-spectrum obtained in the measurement within 30 min, the irradiated foils of 3 μm ^{45}Sc ^{3}He beam with an energy of 22.7 MeV, 5 h after the end of irradiation.

The experiments were performed at the accelerator complex DRIBs [3], the cyclotron U-400M JINR with ACCULINNA separator [4] and the U-120M cyclotron of the Institute of Nuclear Physics of the Czech Republic in Rez [5] using the activation technique. After irradiation by a beam of accelerated ions of ^{3}He, ^{6}He and ^{6}Li of thin foils from ^{45}Sc, ^{197}Au and Pt in there are been measured the induced activities. All measurements were performed on HPGe detectors from 20 to 50% efficiency with respect to NaJ and HWHM of 1.3 to 1.8 keV for the γ-ray energy of 1.3 MeV. Identification of nuclei formed in the reaction was carried out taking into account the γ-decay energies and lifetimes of these nuclei using the nuclear data collected in [ ]. In Fig. 1 shows the characteristic γ-spectra obtained in the measurement of induced activity in Sc target induced by ^{3}He beam. The calculations of cross sections for nuclides produced in nuclear reactions based on the work [3].

3. Experimental results

3.1. Fusion reactions

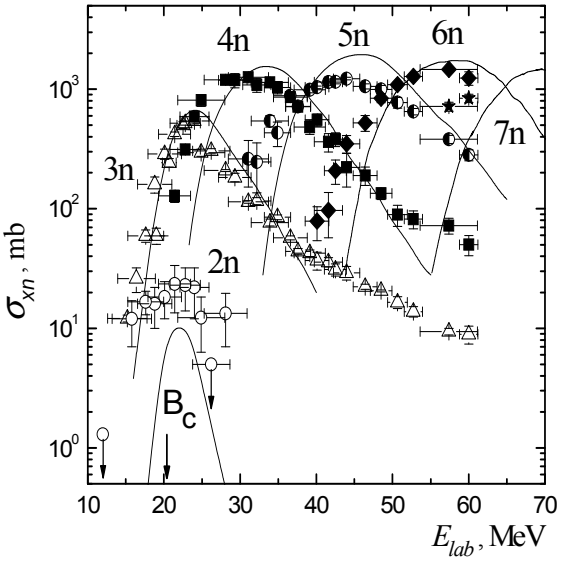

Fig. 2. Experimental excitation functions for the ^{197}Au + + ^{6}He $\rightarrow$ $^{203\text{-xn}}$Tl reaction, where x = 2 - 7. The symbols denote: 2n - 7n evaporation channels; the curves – calculations with the "ALICE-MP" code using the following parameters for the interaction potential: r_0 = 1.29 fm, V = -67 MeV and d = 0.4 fm [3]. B_c - the Coulomb barrier.

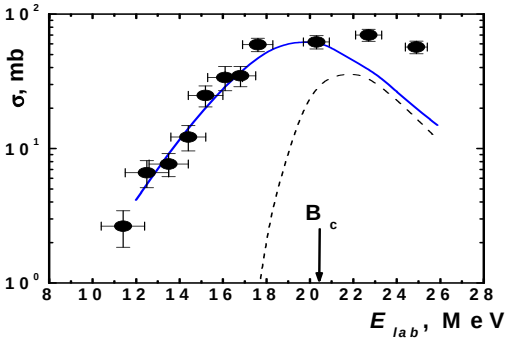

Fig. 3. Excitation function measured for the ^{206}Pb(^{6}He, 2n)^{210}Po reaction. The experimental cross sections for the formation of ^{210}Po (●), dashed line – calculations within the framework of the statistical model, solid line – calculations using the two-step fusion model [5, 6], B_c – the Coulomb barrier.

On the basis of the measured yields of the isotopes, formed after the evaporation from the compound nucleus ^{203}Tl of x- neutrons, taking into account the ^{6}He beam intensity and the target thickness, we could determine the cross sections for the formation of the different isotopes and their dependence on the bombarding energy (the excitation functions). Contrary to the excitation functions for x = 3 - 7 (Fig. 2), the cross sections for the 2n-exit channel (the nucleus ^{201}Tl is formed) are significantly higher than the values, calculated using the one-dimensional barrier between the interacting nuclei. This may be connected with the fact that the reaction with total absorption of ^{6}He by the ^{197}Au target nucleus has a large positive Q-value, equal to +12.2 MeV.

We have observed quite a similar situation in the case of the interaction of ^{6}He with ^{206}Pb [3, 5]. The difference between the two reactions lies in the fact that in the ^{6}He + + ^{206}Pb case, the Q-value is equal to +4.2 MeV. The difference between experiment and calculations is particularly well seen in Fig. 3, where the excitation function for the ^{206}Pb(^{6}He, 2n)^{210}Po reaction is shown. The cross section for this reaction at the maximum, according to the statistical model calculations (the dashed line), should be small, because the maximum is situated at energies below the Coulomb barrier. The agreement between the experimental reaction cross sections for the ^{206}Pb(^{6}He, 2n)^{210}Po reaction with the calculated for the two-step fusion process can be considered as evidence that the sequential fusion process for weakly bound nuclei seems to be the main process, which influences the fusion probability of ^{6}He with ^{206}Pb and leads to the increase in the reaction cross section at energies far below the barrier.

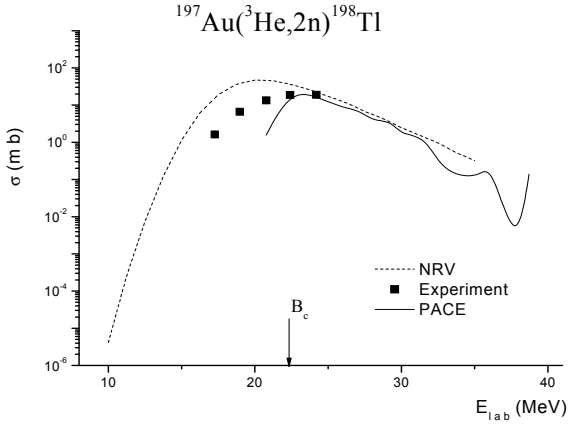

Fig. 4 Excitation functions of reactions of formation of ^{197}Au (^{3}He, 2n) ^{198}Tl. B_c = 22,4 MeV.

The data on fusion reactions, followed by the evaporation of two neutrons (^{206}Pb + ^{6}He and ^{197}Au + ^{6}He) at energies close to the Coulomb barrier differ from predictions within the framework of the statistical model for compound nuclei decay. For these exit channels a strong enhancement is observed and this is in agreement with the model of "sequential fusion".

In the case of a study of reaction ^{197}Au + ^{3}He the Q-value for the compound nucleus reaction 10.8 MeV and it is possible to observe appreciable cross sections for fusion products in the sub-barrier energy region. The excitation

function for the reaction ^{197}Au (^{3}He, 2n) ^{198}Tl are shown in Fig. 4. The results of calculations of cross sections for the same reaction on ^{197}Au using the codes NRV [7] and PACE 4 are shown also. The code NRV is used to the calculation reaction cross sections the couple- channel interaction and included Woods-Saxon potential. They give the closest cross section values to experimental results for some energy range. While we can not insist that the fusion enhancement or suppression occurs in this reaction at energies below the Coulomb barrier.

In the experiments [8] was been shown the absence to fusion hindrance in reaction ^{198}Pt + ^{6}Li in comparison with results of couple- channels calculation using Woods - Saxon potential.

3.2 Direct reactions

First we were observed a large cross section for neutron transfer with the ^{6}He to nucleus of the target in the reactions ^{6}He + ^{197}Au at sub-barrier energies [3]. The excitation functions for the formation of the gold isotopes ^{194}Au, ^{196}Au and ^{198}Au for this reaction are shown in Fig. 5. The contribution of transfer of charged particles and complete fusion for the formation of these isotopes is negligibly small. Thus, the simplest ways in which target-like isotopes might be formed in the given reaction are: the isotopes ^{196}Au and ^{194}Au result after the removal of one and three neutrons from ^{197}Au, respectively, whereas ^{198}Au is formed after the pick-up by ^{197}Au of one neutron from ^{6}He. The transfer reactions of one neutron to the ^{197}Au nucleus from ^{6}He take place with relatively high probability at deep sub-barrier energies. This may be connected with the interaction of quasi-free neutrons.

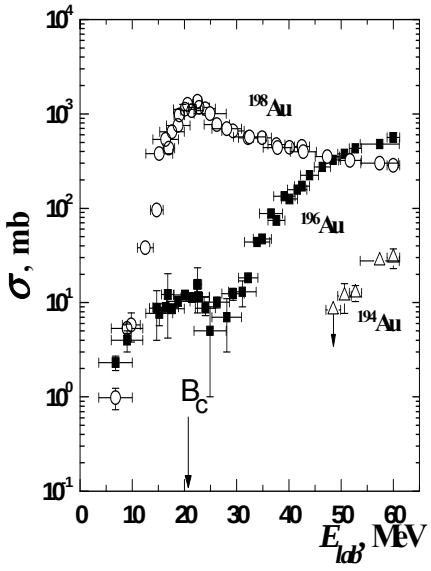

Fig. 5. Experimental excitation functions for the formation of the isotopes Δ - ^{194}Au; ■ - ^{196}Au; ○ - ^{198}Au in the ^{197}Au + ^{6}He reactions [3].

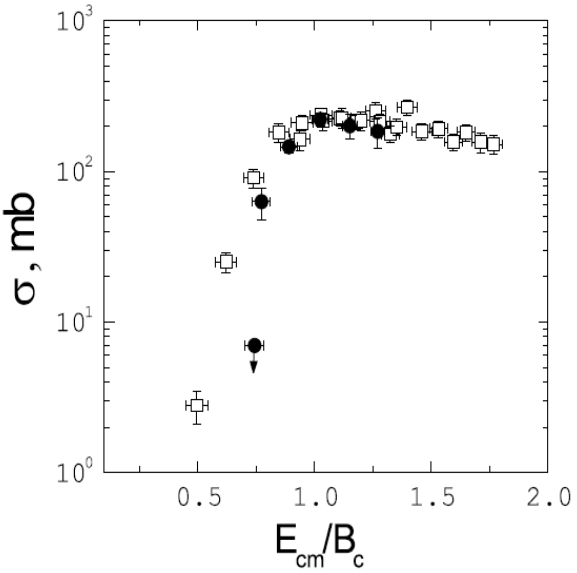

Fig. 6. Excitation function for the isotope ^{199}Au, produced in the interaction of ^{6}Li with ^{198}Pt. [8] ● - our data, for the d + ^{198}Pt reaction presented by □, are shown for comparison.

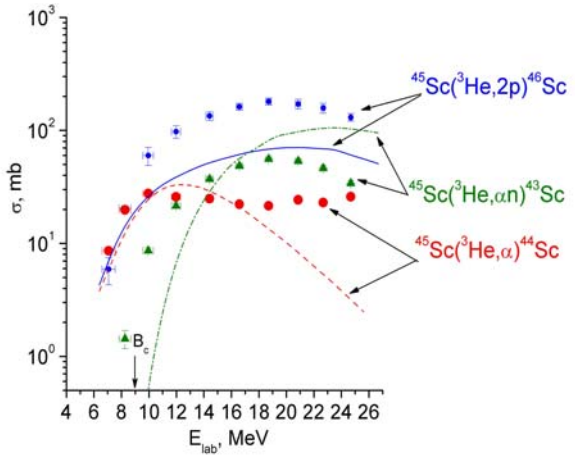

Fig. 7. The excitation functions of the reaction products ^{45}Sc + ^{3}He. Reaction cross sections are presented with symbols: square-cross section of the ^{45}Sc (^{3}He, 2p) ^{46}Sc, triangles-^{45}Sc (^{3}He, αn) ^{43}Sc and mugs-^{45}Sc (^{3}He, α) ^{44}Sc. Curves are calculation of cross sections for these reactions is the code ALICE-MP.

In the study of the reactions with ^{6}Li beam have been measured yields of isotopes with the transfer of nucleons to the target nucleus [9]. In Fig. 6 is shown the excitation function with for formation of isotope ^{199}Au in the reaction ^{198}Pt (^{6}Li, ^{5}He) ^{199}Au, which has a positive Q-value. Comparison of formation cross section for ^{199}Au in the reactions of deuterons and ^{6}Li indicate that, apparently, mainly in the bombardment of Pt nuclei by ^{6}Li, the reaction is the so- called inelastic sequential breakup of ^{6}Li, leading to the target capture from ^{6}Li only deuteron. These data were confirmed in articles [8].

In Fig. 7 are shown the cross sections for formation isotopes of ^{44}Sc and ^{46}Sc Sc via the energy of bombarding particles of ^{3}He at ^{45}Sc+^{3}He for one nucleon transfer reaction as stripping (^{46}Sc) and pickup (^{44}Sc) product. [10].Both of these reactions due to positive Q-values well manifested at energy ^{3}He below the Coulomb barrier. In the case of transfer to the target nucleus ^{45}Sc one neutron from^{3}He excitation function (^{46}Sc) has a characteristic behavior for a single neutron transfer reactions. Some unusual behavior of excitation function

is observed, when ^{44}Sc is formed. Despite on the large positive value of Q (+9,254 MeV) for the reaction (^{3}He, α) there is a clear maximum of the excitation function near the Coulomb barrier. Competing with the channel reaction (^{3}He, αn) appears at energies above the Coulomb barrier, but a neutron pickup channel ^{3}He continues to occur with appreciable cross section.

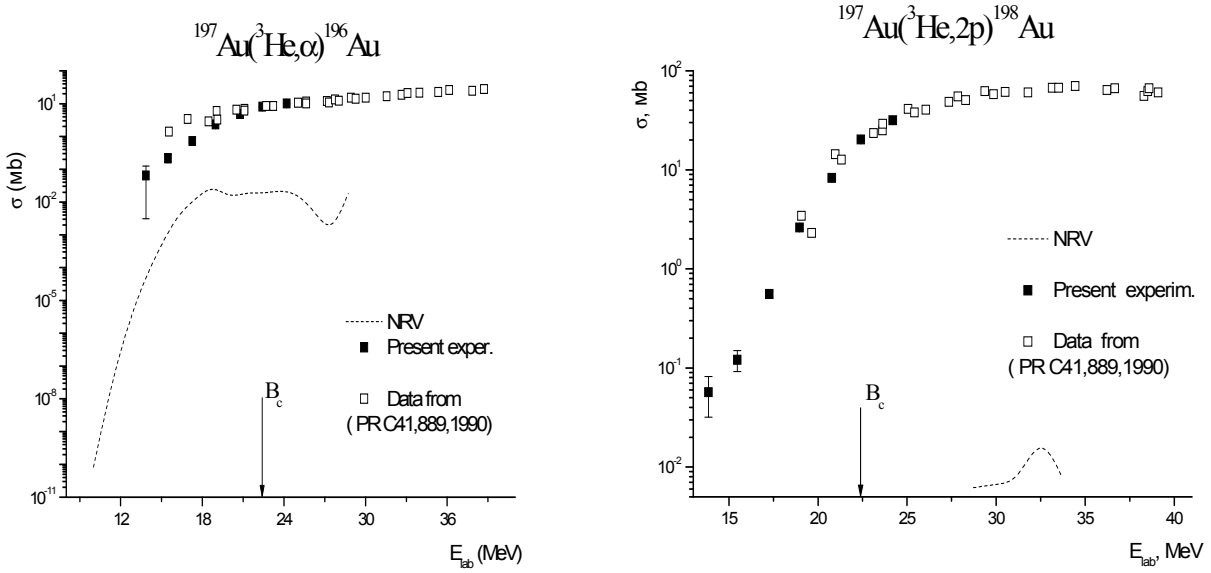

a *b*

Fig. 8. The excitation functions for formation of:
a - ^{196}Au; *b* - ^{198}Au- in the interaction of ^{197}Au with ^{3}He (B_c = 22,4 MeV).

In reactions ^{197}Au + ^{3}He were measured cross-sections of nuclei ^{196} Au and ^{198}Au (Fig. 8). It is noted that in this case, both the reaction ^{197}Au (^{3}He, 2p) ^{198}Au and ^{197}Au (^{3}He, α) ^{196}Au take place at the sub-barrier energy. The excitation function for ^{196}Au, it is formed the α-particle, as in the case of reactions with ^{45}Sc (see Fig. 7), reaches its maximum at the Coulomb barrier of this reaction.

3.3. Fusion reactions up to 20 MeV/A

We have extended the experiments [11] to study the fusion and transfer reactions at higher energy of the accelerated ions of ^{6}He about 20 MeV/A. The results of measurements of excitation functions for complete fusion reactions with the formation of the compound nucleus ^{203}Tl and subsequent evaporation of neutrons are shown in Fig. 9.

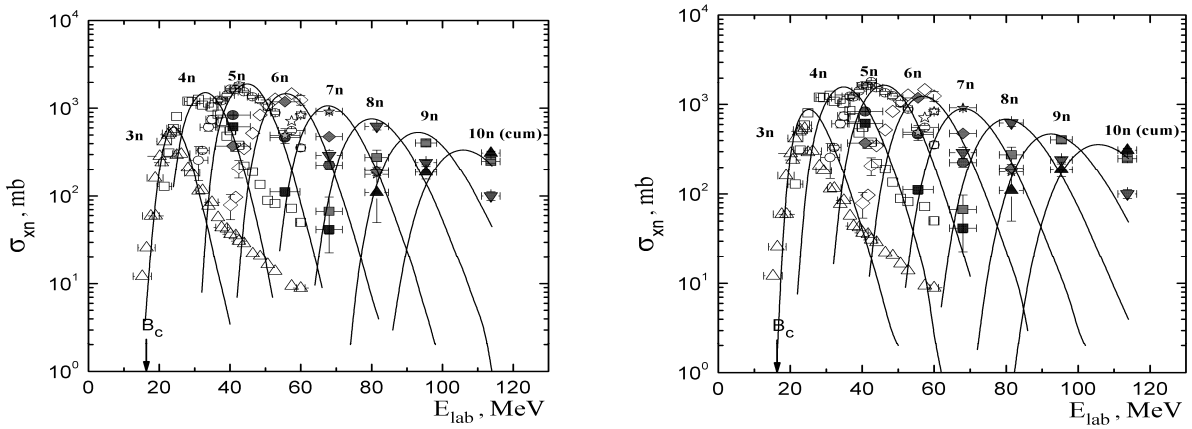

Fig. 9. The excitation functions of reactions ^{197}Au (^{6}He, xn) $^{203\text{-xn}}$Tl. Open symbols-data of [3], the dark symbols-data of the work. [9] Solid curves-calculation program ALICE [3, 9] (*left*) and NRV [7] (*right*).

Calculations were performed using the code ALICE-MP [3] and the NRV [7]. We used the standard parameter values for both codes. Systematic delays in high-energy branches of the experimental excitation functions in comparison with the results of calculations related to the pre-equilibrium process of decay of excited nuclei. A comparison of calculations with experimental data shows that significant suppression for complete fusion is not observed.

Conclusions

On the basis of experimental data on the interaction of the halo nuclei ^{6}He with ^{197}Au and ^{206}Pb can draw the following conclusions:

- The data on two neutrons evaporation channel infusion reactions at energies close to the Coulomb barrier are different from predictions within the framework of the statistical model for compound nuclei decay. The strong enhancement was observed and that is in agreement with the model of "sequential fusion".

- Above the Coulomb barrier, the process of fusion with halo nuclei is well described by the evaporation models, and the suppression in the fusion was not observed at the energy of 20 MeV/A.

- The data on cross sections of reactions and comparison with experiments at lower energies suggest that the features of the nuclear structure of ^{6}He more pronounced at energies near the Coulomb barrier reactions. With increasing energy ^{6}He nature of the interaction in a similar reaction channels is not different from the interaction with other light particles (α and d).

In the case of positive Q-value for reactions with weakly bound nuclei, the neutron transfer could take place both for target and projectile nuclei at sub-barrier energies.

Neutron transfer reaction cross sections or cluster capture cross sections reach its maximum value at the Coulomb barrier in the case of the formation of α-particles as reaction product.

REFERENCES

1. *Canto L.A. et al.* Fusion and breakup of weakly bound nuclei // Phys. Rep. - 2006. - Vol. 424, No. 1. - P. 1 - 112.
2. *Liang J.F., Signorini C.* Fusion Induced by Radioactive Ion Beams Inter // J. Mod. Phys. E. - 2005. - Vol. 14, No. 8. P. 1121 - 1150.
3. *Penionzhkevich Yu.E., Astabatyan R.A., Demekhina N.A. et al.* Excitation functions of Fusion reactions and neutron transfer in the interaction of ^{6}He with ^{197}Au and ^{206}Pb // Eur. Phys. J. A. - 2007. - Vol. 31, No. 2. - P. 185 - 194.
4. *Rodin A.M., Stepantsov S.V., Bogdanov D.D. et al.* // NIM Phys. Res. B. - 2003. - Vol. 204. - P. 114.
5. *Penionzhevich Yu. E. et al.* Deep Sub-Barrier Fusion Enhancement in the ^{6}He + ^{206}Pb Reaction // Phys. Rev. Lett. - 2006. - Vol. 96, No. 16. - P. 162701.
6. *Zagrebaev V.I.* Sub-barrier fusion enhancement due to neutron transfer // Phys. Rev. C. - 2003. - Vol. 67. - P. 061601(R).
7. *Nuclear* reaction video project // http://nrv.jinr.ru/nrv.
8. *Shrivastava A., Navin A et al.* Exploring Fusion at Extreme Sub-Barrier Energies with Weakly Bound Nuclei // Phys. Rev. Lett. - 2009. - Vol. 103. - P. 23702.
9. *Penionzhkevich Yu.E. et al.* Complete and incomplete fusion of ^{6}Li ions with Bi and Pt // J. Phys. G: Nucl. Part. Phys. - 2009. - Vol. 3. - P. 025104.
10. *Skobelev N.K., Kulko A.A., Penionzhkevich Y.E. et al.* Cross Sections for Isotopes ^{43}Sc and ^{46}Sc in the ^{45}Sc + ^{3}He reaction // Submitted to Izvestiya RAN. Seriya Fizicheskaya.
11. *Skobelev N.K., Penionzhkevich Yu.E., Kulko A.A.* Study of Fusion and Nucleon Transfer Channels for the Reaction ^{197}Au + ^{6}He at ^{6}He Energies up to 20 MeV/A // Submitted to Izvestiya RAN. Seriya Fizicheskaya.

MICROSCOPIC DESCRIPTION OF RESONANCE STATES OF LIGHT NUCLEI ABOVE THREE-CLUSTER THRESHOLD. ^{12}C

V. S. Vasilevsky

M. M. Bogolyubov Institute for Theoretical Physics, National Academy of Sciences of Ukraine, Kyiv, Ukraine

We investigate both bound and resonance states in ^{12}C embedded in a three-α-cluster continuum using a three-cluster microscopic model. The model relies on the Hyperspherical Harmonics basis to enumerate the channels describing the three-cluster discrete and continuous spectrum states. It yields the most probable distribution of the three α-clusters in space, and the dominant decay modes of the three-cluster resonances.

Introduction

The ^{12}C nucleus is an interesting example of the so-called Borromean nuclei, as it has no bound states in any two-cluster subsystem of its three-cluster configuration. The lowest dissociation threshold (7.276 MeV above the ground state) is that of a three α particles disintegration. This three-cluster configuration is thus responsible to a great extent for the formation of a few bound, and many resonance states. The next threshold is of a two-cluster nature: ^{11}B + p [1]. It opens when the excitation energy of ^{12}C exceeds 15.96 MeV. One therefore expects only a negligible influence of the latter channel on the bound and resonance states of ^{12}C in the vicinity of the α + α + α threshold. The ^{12}C nucleus is unique because of its excited "Hoyle state". This state is important in the context of the nucleosynthesis of carbon in helium-burning red giant stars. It is a 0^+ state with an energy of 7.65 MeV above the ground state, or 0.4 MeV above the three-cluster α + α + α threshold. Its width is only 8.5 eV, indicating a long lifetime. One immediately relates this to the 0^+ state in ^{8}Be described by two α particles, with an energy of 0.092 MeV above the α + α threshold, and a width of 5.57 eV. Many efforts have been made to reproduce the experimentally observed structure of ^{12}C, and to explore and understand the nature of the ground, excited and resonance states. This was, for example, done within so-called semi-microscopic models (considering structureless α-particles) and within fully microscopic models.

A somewhat general feature of the calculations is that, with potentials which adequately reproduce the α-α interaction (this includes the phase shifts for 0^+, 2^+ and 4^+ states, and the position of the corresponding resonance states), one obtains a noticeably overbound ground state for ^{12}C. To determine the energies and widths of the resonance states created by a three-cluster continuum, only a few methods can be used. One popular method for obtaining the resonance properties in many-cluster, many channel systems is the Complex Scaling Method (see reviews [2, 3] and references therein). Other methods start from a calculated form of the S-matrix in a wide energy range, and determine the resonance states as the pole(s) of the S-matrix. The advantage of these methods is that they provide the scattering quantities (such as phase-shifts, cross-sections, etc.) and the resonance properties (energies and widths), as well as the wave functions of scattering and resonance states. The latter then allow one to obtain more information about the nature of the resonance states.

^{12}C is known from theory and experiment (see, e.g., [4] and [5]) to have some very narrow resonances above the three α threshold. One may wonder why a system with several open channels does not decay instantly, but manifests these narrow resonance states. There are two possible answers to this question. First, a resonance state appears in one single channel of the multi-channel system. Such particular channel is usually weakly coupled to a number, or all, of the other open channels. It is well-known that this weak coupling of channels predetermines the existence of long-lived resonance states. Second, a resonance can be more or less uniformly distributed over all open channels, and the compound system needs (some) time for the resonance to be accumulated by one or a few number of open channels to decay into. Such a distribution over many open channels leads to very narrow resonances, as was predicted by A. Baz' [6]. It is referred to as diffusion-like processes in scattering. This type of resonance is attributed to the effect that "the system spends most of its time wandering from one channel to another"' [6].

In this paper we wish to calculate and analyze the bound and continuum structure of ^{12}C, and gain some insight in the nature of these states. Indeed, in some publications (e.g. [7 - 10]) the suggestion for a dominant linear, chain-like, three-cluster structure appears for some of the ^{12}C resonances. We will look for confirmation of this structure. To this end, we determine the most probable configuration of the three α particles both in coordinate and momentum space. We also qualify those channels on which the resonance states of ^{12}C preferentially decay.

The main results of this paper are obtained by applying the "Algebraic Model in a Hyperspherical Harmonics Basis" (AMHHB) [11 - 13] on a configuration of three α-particles. In this model the three clusters are treated equally, and their relative motion described by Hyperspherical Harmonics. The latter enumerate the channels of the three-cluster continuum and allow one to implement the correct boundary conditions for the three-cluster exit channels. The AMHHB was applied successfully to study resonances in nuclei with a large excess of protons or neutrons such as ^{6}He, ^{6}Be, ^{5}H. The method provides the energies and widths of the resonances, and their total and partial widths, as well as the corresponding wave functions. The latter allow one to analyze the nature of the resonance states. The results of this model are compared to those obtained in other, more or less comparable, microscopic descriptions from the literature, and to experiment. In the next section we elaborate on the method used to calculate the spectrum of ^{12}C. Section three focuses on the results obtained using this method. We also present correlation functions and density functions to characterize more precisely the spatial configuration of the three α particles for specific resonance states. We also compare the results to those of other microscopic calculations as well as to experiment.

1. The microscopic cluster model

In this section we describe the microscopic model used to determine the structure of ^{12}C in the present paper. As it has already been introduced and used in several publications, we will limit ourselves to the most important notations and aspects of importance to the current calculations.

The three-cluster "Algebraic Model in a Hyperspherical Harmonics Basis" (AMHHB) [11 - 14] will be applied to a single ^{12}C = α + α + α three-cluster configuration. This model takes a Hyperspherical Harmonics basis (HH) to characterize and enumerate the different three-cluster channels. In each of these channels an oscillator basis describes the radial behaviour, and is used to expand the many-particle wave function. A matrix version of the Schrödinger equation is obtained after substitution of this wave function. It solved by the Algebraic Method (also called the Modified J-Matrix method [13]) for both bound and scattering states using the correct asymptotics. A similar approach, using the Hyperspherical Harmonics, was proposed in [15, 16] in coordinate representation, using the generator coordinate technique to solve the corresponding Schrödinger equation. The AMHHB wave function for ^{12}C is written as

$$\begin{aligned}\Psi &= \hat{A}\left\{\Phi(\alpha_1)\Phi(\alpha_2)\Phi(\alpha_3) f(\mathbf{x},\mathbf{y})\right\} \\ &= \hat{A}\left\{\Phi(\alpha_1)\Phi(\alpha_2)\Phi(\alpha_3) f(\rho,\theta,\hat{\mathbf{x}},\hat{\mathbf{y}})\right\} \\ &= \sum_{n_\rho,K,l_1,l_2} C_{n_\rho,K,l_1,l_2} \left| n_\rho, K, l_1, l_2; LM; (\rho,\theta,\hat{\mathbf{x}},\hat{\mathbf{y}})\right\rangle,\end{aligned} \tag{1}$$

where $\left|n_\rho, K, l_1, l_2; LM\right\rangle$ is a cluster oscillator function [11]:

$$\left|n_\rho, K, l_1, l_2; LM; (\rho,\theta,\hat{\mathbf{x}},\hat{\mathbf{y}})\right\rangle = \hat{A}\left\{\Phi(\alpha_1)\Phi(\alpha_2)\Phi(\alpha_3) R_{n_\rho,K}(\rho)\chi_{K,l_1,l_2}(\theta)\left\{Y_{l_1}(\hat{\mathbf{y}})Y_{l_2}(\hat{\mathbf{x}})\right\}_{LM}\right\}. \tag{2}$$

These functions are enumerated by the number of hyperradial excitations n_ρ, hyperspherical momentum K and two partial orbital momenta l_1, l_2. The vectors **x** and **y** form a set of Jacobi coordinates, and ρ and θ are hyperspherical coordinates, related to the Jacobi vectors by:

$$\rho = \sqrt{\mathbf{x}^2 + \mathbf{y}^2}$$

$$|\mathbf{x}| = \rho\cos\theta, \quad |\mathbf{y}| = \rho\sin\theta. \tag{3}$$

The notation $\hat{\mathbf{x}}$ and $\hat{\mathbf{y}}$ refers to unit length vectors. Vector **x** corresponds to the distance between two selected α particles, with an associated partial orbital angular momentum l_2. Vector **y** is the displacement of the third α particle with respect to the center of mass of the other two, with an associated angular momentum l_1. The three quantum numbers c = {K, l_1, l_2} determine the channels of the three-cluster system in the AMHHB. The fact that all three clusters are identical leads to some specific issues. The wave function (1) for ^{12}C is antisymmetric with respect to the permutation of any pair of nucleons. Because the three clusters are identical, this function should be symmetric with respect to the permutation of any pair of alpha particles. This imposes constraints on the allowed quantum numbers of the wave function. Because of this symmetry, for instance, the partial orbital momentum l_2 of a two-cluster subsystem can only have even values. As the parity of ^{12}C states is defined as $\pi = (-1)^{l_1+l_2}$, it is fully determined by the partial orbital angular momentum l_1 of the relative motion of the remaining cluster with respect to the two-cluster subsystem.

After solving the system of linear equation of the AMHHB model, we obtain the wave functions of the continuous spectrum states, and the scattering S-matrix. We consider two different representations of the S-matrix. In the first representation, the elements of the S-matrix are described through the phase shifts δ_{ij} and the inelastic parameters η_{ij}:

$$S_{ij} = \eta_{ij}\exp\left\{2i\delta_{ij}\right\} \tag{4}$$

of which one usually only analyzes the diagonal matrix elements by displaying the δ_{ii} and η_{ii} quantities. In the second representation the S-matrix is reduced to diagonal form, leading to the so-called eigenphases, which now represent the elastic scattering of the many-channel system in independent (uncoupled) eigenchannels:

$$\|\mathbf{S}\| = \|\mathbf{U}\|^{-1} \cdot \|\mathbf{D}\| \cdot \|\mathbf{U}\|. \tag{5}$$

Here $\|\mathbf{U}\|$ is an orthogonal matrix, connecting both representations, and $\|\mathbf{D}\|$ is a diagonal matrix with nonzero elements

$$D_{aa} = \exp\left\{2i\delta_\alpha\right\} \tag{6}$$

defining the eigenphases δ_α. The phases shifts δ_{ii}, inelastic parameters η_{ii} and eigenphases δ_α then provide sufficiently

detailed information about the channels that are involved in the production of resonance states. The eigenphases are used to extract the resonance positions and total widths in the traditional way

$$\left.\frac{d^2\delta_\alpha}{dE^2}\right|_{E=E_r} = 0, \quad \Gamma = 2\left(\left.\frac{d\delta_\alpha}{dE}\right|_{E_r}\right)^{-1} \tag{7}$$

whereas the orthogonal matrix $\|\mathbf{U}\|$ leads to the partial decay widths of the resonance (for details see, e.g., [13]).

As we pointed out, the AMHHB model allows one to calculate the scattering properties, but also to obtain the wave function at any energy, in particular at the resonance positions. The latter is of the utmost importance to analyze the nature of the system at these energies. Within the AMHHB model the solution is fully expressed by the expansion coefficients $\{C_{n_\rho,c}\}$ and the S-matrix. The expansion coefficients $\{C_{n_\rho,c}\}$ determine both the total three-cluster wave function of a compound system Ψ, as well as the wave function of the relative motion of three clusters $f(\vec{x},\vec{y})$ (see Eq. (1)). The latter contains all information on the dynamic behaviour of the three-cluster system for bound as well as continuum states. It is interesting to note that these coefficients are identical in both the representations of the wave function in coordinate and momentum space, because of the Fourier transform properties of the oscillator states. The wave function $f(\mathbf{k}, \mathbf{q})$ in momentum space has arguments that are directly related to the coordinate representation: **k** is the momentum of relative motion of two clusters, whereas **q** is the momentum of the third cluster with respect to the center of mass of the two-cluster subsystem. We obtain the density distribution in coordinate space as

$$D(x,y) = D(\rho,\theta) = \int \left|f(\mathbf{x},\mathbf{y})\right|^2 d\hat{\mathbf{x}}d\hat{\mathbf{y}} \tag{8}$$

and the corresponding correlation function as

$$C(x,y) = C(\rho,\theta) = x^2y^2\int \left|f(\mathbf{x},\mathbf{y})\right|^2 d\hat{\mathbf{x}}d\hat{\mathbf{y}} \tag{9}$$

directly from the wave function of relative motion $f(\mathbf{x}, \mathbf{y})$. Both the density distribution and correlation function in momentum space are obtained in the same way using the wave function of relative motion in momentum space $f(\mathbf{k}, \mathbf{q})$. In a calculation with N_{ch} open channels, one obtains N_{ch} independent wave functions describing the elastic and inelastic processes in the many-channel system. It is quite impossible to analyze all of these wave functions when many channels are open. Some principles have to be set up on how to select the most important wave functions. In [13] we formulated some criteria for selecting the dominant wave function of a resonance. We will use the same criteria in this paper to select the "resonance wave functions".

2. Calculations and results

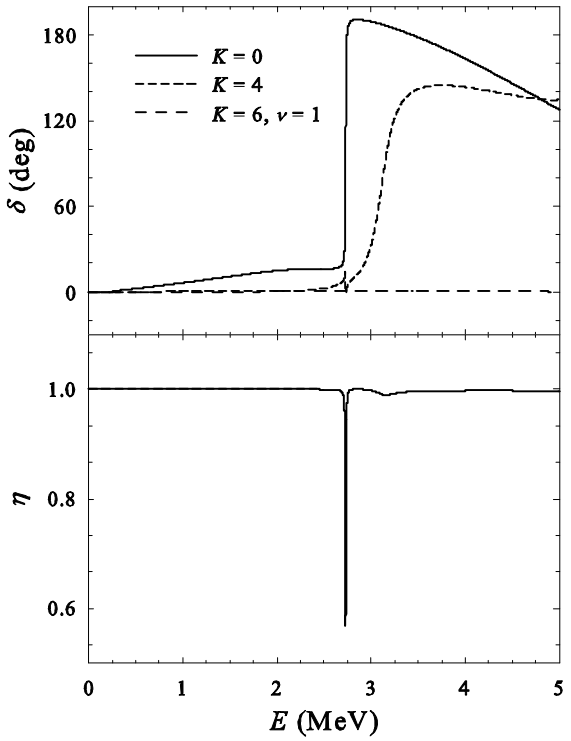

Fig. 1. Diagonal phase shifts and inelastic parameters for the $J^\pi = 2^+$ state.

In the present calculations for ^{12}C we consider for the nucleon-nucleon interaction the Minnesota potential [17]. The oscillator basis is characterized by an oscillator length b = 1.2846 fm, to minimize the ground state energy of the α particle using the above potential. Parameter u of the Minnesota potential is taken to be u = 0.94 to reproduce the phase shifts for α + α scattering, and the 0^+, 2^+ and 4^+ resonances in ^{8}Be. The same parameters were used by Arai [18].

In Fig. 1 we show results of the AMHHB calculations for the 2^+ state in terms of the symmetrical Hyperspherical Harmonic channels through the (diagonal) phase shifts δ_{ii} and the inelastic parameters η_{ii}.

The scattering parameters are obtained from a calculation with maximal Hypermomentum K_{max} = 14. One observes from Fig. 1 that for small energies the channels are totally uncoupled ($\eta_{ii} \approx 1$). A first 2^+ resonance appears at E = 2.731 MeV, and is mainly produced in the first channel with Hypermomentum K = 2, whereas a second resonance at energy E = 3.113 MeV is dominated by Hypermomentum K = 4. The inelastic parameters for the first two channels have a pronounced minimum at the energy of the first resonance, and a shallow minimum at the second resonance energy. Also, the first resonance displays a "shadow resonance" behavior in the second channel. This is a typical behavior

for resonances in a many-channel system (see, for instance, the detailed analysis of two-channel resonances in ^{5}He in [19]). The minimum in the inelastic parameters indicates that the compound system is being reconstructed at this energy, and transits from one channel to another.

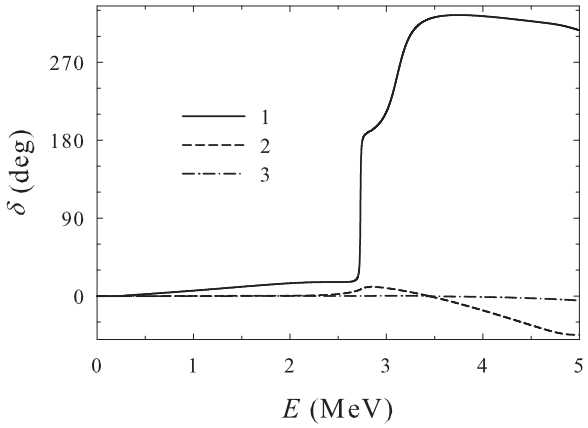

Fig. 2. Eigenphase shifts for $J^\pi = 2^+$ for the first three eigenchannels.

In Fig. 2 we display the corresponding eigenphase shifts δ_α for the first three eigenchannels. One observes now that both resonance states are mainly associated with the first eigenchannel, and that the second eigenchannel only contributes marginally.

A convergence study of the energies (and widths) for bound and resonance states should indicate whether the Hilbert space is sufficiently large for stable and reliable results. The AMHHB model space is characterized by two parameters: the maximal value of Hypermomentum K_{max}, and the maximal value of the Hyperradial excitation n_ρ. Usually the choice is a compromise between the convergence of the results and the computational burden. A set of Hyperspherical Harmonics with K_{max} = 14 for even parity states, and K_{max} = 13 for odd parity states, seems sufficient and remains computationally feasible. This choice accounts for a large number of three-cluster configurations or, in other words, for a sufficient number of inherent (triangular) shapes for the three clusters. We refer to [20] for examples of most probable triangular shapes for the Hyperspherical Harmonics from K = 0 to K = 10. A first convergence test considers the 0^+, 2^+ and 4^+ bound states of ^{12}C, shown in Fig. 3 as a function of K_{max}.

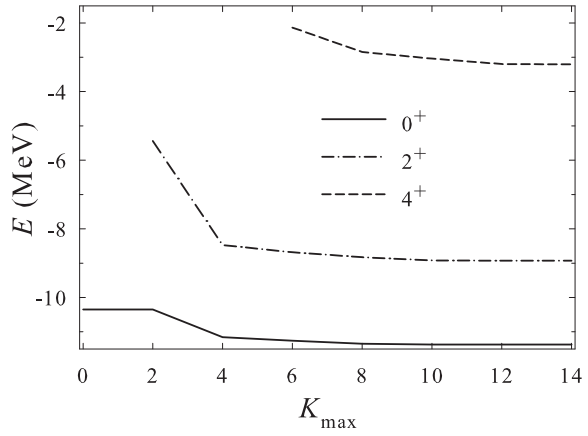

Fig. 3. Convergence of the bound states in AMHHB.

One observes that the deeply bound states ($J^\pi = 0^+, 2^+$) require significantly less Hyperspherical Harmonics for a converged energy than the shallow, or weakly bound, state with $J^\pi = 4^+$. At least all Hyperspherical Harmonics with $K_{max} \geq 6$ are required to bind the latter state, whereas for $J^\pi = J^\pi = 0^+$ one already obtains binding with a single Hyperspherical Harmonic with K = 0. Fig. 3 further demonstrates that the above choice of K_{max} amply leads to sufficient precision for the bound states. In Table 1 we turn to the energies and widths of the 0^+ and 2^+ resonances obtained with increasing number of Hyperspherical Harmonics. One observes that sufficient convergence of the resonances occurs at K_{max} = 12. It is furthermore interesting to note that these resonances already appear with reasonable energy and width values when only the lowest channel (K = 0 for the 0^+, and K = 2 for the 2^+ state) is considered. This is a remarkable result for ^{12}C, as e.g. for ^{6}Be it was impossible to generate a 0^+ resonance with a single K = 0 channel (see [12]).

Table 1. **Low-lying resonances in terms of K_{max}. Energy in MeV, width in keV**

J^π	K_{max}	0	4	6	8	10	12	14
0^+	E	0.40	0.75	0.74	0.72	0.70	0.68	0.68
	Γ	205.08	13.40	11.79	7.10	4.35	2.71	2.78
0^+	E	1.15	7.34	6.09	5.55	5.54	5.16	5.14
	Γ	510.16	897.64	422.50	539.21	586.08	534.33	523.46
2^+	E	-	3.28	2.89	2.83	2.78	2.74	2.73
	Γ	-	30.19	13.07	11.85	9.95	8.84	8.75
2^+	E	-	3.50	3.27	3.22	3.17	3.14	3.11
	Γ	-	274.51	351.57	308.29	280.23	263.80	246.78

In all calculations we have considered states with hyperradial excitation up to n_ρ = 70, which covers a large range of intercluster distances, and reaches well into the asymptotic region.

In Table 2 we display the energy, the total width (Γ) and the partial widths (Γ_i, i = 1, 2, …) in the corresponding decay channels for the even parity resonances, and in Table 3 for the odd parity resonances.

Table 2. **Partial widths of the even parity resonances in ^{12}C. Energy in MeV, widths in keV**

J^π	0^+		2^+		2^+		4^+	
E		0.68		2.78		3.17		5.60
Γ		2.78		9.95		280.24		0.55
Γ_1	$K = 0$	2.78	$K = 2$	6.11	$K = 2$	13.46	$K = 4$	0.23
Γ_2	$K = 4$	0	$K = 4$	3.84	$K = 4$	278.89	$K = 6$	0.15
Γ_3	$K = 6$	0	$K = 6$	$<10^{-5}$	$K = 6$	$<10^{-5}$	$K = 8$	0.16

Table 3. **Partial widths of the odd parity resonances in ^{12}C. Energy in MeV, widths in keV**

J^π	1^-		3^-	
E		3.52		0.67
Γ		0.21		8.34
Γ_1	$K = 3$	0.206	$K = 3$	8.34
Γ_2	$K = 5$	0.002	$K = 5$	0
Γ_3	$K = 7$	$<10^{-5}$	$K = 7$	0

One observes that in most cases only one or two channels are responsible for the decay of the resonance states. The remaining channels contribute negligibly, and the corresponding partial width does not exceed 10^{-5} keV. Only for the 4^+ resonance a significant distribution over multiple channels is apparent.

One should note that, although the resonances are created by only a few channels, the role of the other, very weakly coupled, channels is still important. This can be seen from Table 1 for the first 0^+ resonance: it is indeed generated mainly by the channel with minimal Hypermomentum $K = 0$, but modified substantially with increasing number of Hypermomentum. The same applies to the other resonance states.

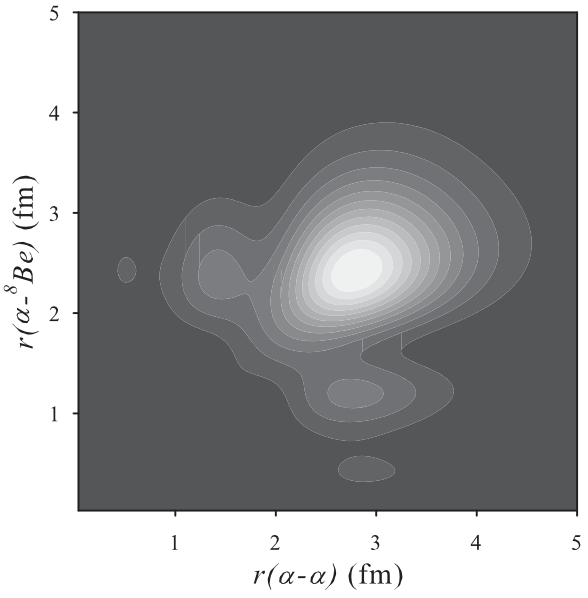

Fig. 4. Correlation function for the ^{12}C ground state in coordinate space.

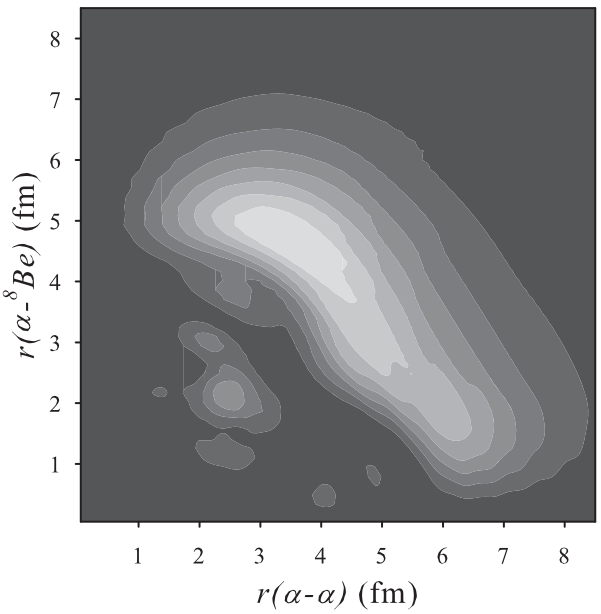

Fig. 5. Correlation function for the first 0^+ resonance state of ^{12}C in coordinate space.

In Fig. 4 we show the correlation function for the ^{12}C ground state, and observe that this state displays a compact spatial configuration, as it is expected for such a deeply bound state. The most probable shape of the three α-cluster system is an almost equilateral triangle with a distance between any two α-particles of approximately 3 fm.

The correlation function for the first 0^+ resonance state on the other hand, shown in Fig. 5, shows a more deformed system with two α particles relatively close to one another (about 3.5 fm) and the third alpha-particle further away (approximately 5 fm). So ^{12}C features a prolate triangle as a dominant configuration for this state. One also observes in Fig. 5 a small maximum for the correlation function corresponding to an almost linear configuration of three α particles, two of them being approximately 4 fm apart, and the third 0.2 fm away from their center of mass. However, the weight of this linear configuration is approximately 6 times less than the weight of the prolate triangular configuration. Our calculations therefore do not agree with other authors advancing a dominant linear structure [7 - 10].

We now compare the AMHHB results to the existing literature. In Table 4 we display the AMHHB results to those of Arai [18] and Pichler et al. [21], both obtained by the Complex Scaling Method (CSM). The latter authors [21] use a somewhat different value for the parameter u in the Minnesota potential, and a different oscillator length b; because of this, different results are obtained for the bound states.

Table 4. **Bound and resonance states of ^{12}C obtained with the AMHHB model, compared to CSM results from the literature**

Method	AMHHB		CSM-Arai		CSM-Pichler et al.	
Reference	Present paper		[18]		[21]	
J^π	E, MeV	Γ, keV	E, MeV	Γ, keV	E, MeV	Γ, keV
0^+	-11.372		-11.37		-10.43	
	0.684	2.78	0.4	<1	0.64	14
	5.156	534.00	4.7	1000	5.43	920
2^+	-8.931		-8.93		-7.63	
	2.775	9.95	2.1	800	6.39	1100
	3.170	280.24	4.9	900		
4^+	-3.208		-3.21			
	5.603	0.55	5.1	2000		
1^-	3.516	0.21	3.4	200	3.71	360
3^-	0.672	8.34	0.6	<50	1.16	25
	4.348	2.89	7.1	5400	11.91	1690
	5.433	334.90	9.6	400		

Comparison with the results of Arai [18] indicates that the AMHHB model leads to resonance states with higher energy and smaller widths than those obtained with the CSM. This can be attributed to the difference in the methods, and to the different Hilbert spaces. Formally the Hilbert space of basis functions used by Arai [18] is quite close to the one considered in the AMHHB. Actually, in the present calculations the partial orbital momenta l_1 and l_2 are restricted by the condition $L \le l_1 + l_2 \le K_{max}$, so that, for instance, for total orbital momentum L = 0, they run from $l_1 = l_2 = 0$ to $l_1 = l_2 = 6$ with $K_{max} = 14$. Arai on the other hand, restricted himself with l_1, $l_2 \ge 4$. In [12 - 14] we observed the tendency that the more Hyperspherical Harmonics (thus the more channels) are involved in the calculation, the smaller the resonance energy and width becomes. This tendency is again confirmed by the present AMHHB calculations. Thus some reduction of the width of the resonances, observed in our calculations with respect to Arai [18], can be attributed to the larger number of channels in our model. Comparing the AMHHB results to the Complex Scaling Model calculations of Pichler et al. [21], one observes that both yield close results for the first and second 0^+ resonance states. On the whole one can conclude that there is consistency in the results for resonance properties in all three microscopic models.

In Table 5 we compare the theoretical AMHHB results for ^{12}C to available experimental data.

Table 5. **Bound and resonance states of ^{12}C obtained with the AMHHB model, compared to experiment**

Method	AMHHB		Experiment	
Reference	Present paper		[1]	
J^π	E, MeV	Γ, keV	E, MeV	Γ, keV
0^+	-11.372		-7.2746	
	0.684	2.78	0.3796±0.0002	$(8.5\pm1.0)\cdot10^{-3}$
	5.156	534.00	3.0±0.3	3000±700
2^+	-8.931		-2.8357±0.0003	
	2.775	9.95	3.89±0.05	430± 80
	3.170	280.24	8.17±0.04	1500 ±200
4^+	-3.208			
	5.603	0.55	6.808±0.015	258 ±15
1^-	3.516	0.21	3.569 ± 0.016	315 ± 25
3^-	0.672	8.34	2.366 ± 0.005	34 ± 5
	4.348	2.89		
	5.433	334.90		

One notices that the first 0^+ resonance state (the Hoyle state) appears in the current calculations as a narrow resonance with an energy of 0.684 MeV and width 2.7 keV, which is considerably wider than the experimental Hoyle state (about $8.5\cdot10^{-3}$ keV). This contrasts with the generally observed feature of the AMHHB calculations that the calculated widths are significantly less than the corresponding experimental widths of the ^{12}C resonances. The discrepancies between the theoretical and experimental data have essentially two origins. The first one relates to the choice of the nucleon-nucleon interaction: it was tuned to reproduce the phase shifts and resonance properties for alpha-alpha scattering. As a result it leads to overbound 0^+ and 2^+ states in ^{12}C, and binds the 4^+ state. The second one relates to the specific choice of three-cluster model and corresponding model space, as well as to the method by which the energy and width of the resonance states are obtained.

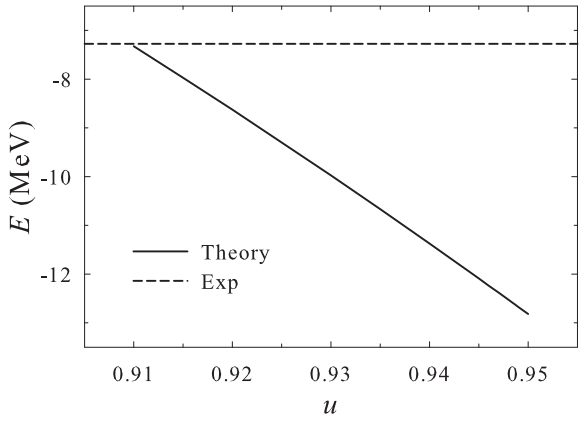

Fig. 6. Energy of the ground state as a function of parameter u of the Minnesota potential.

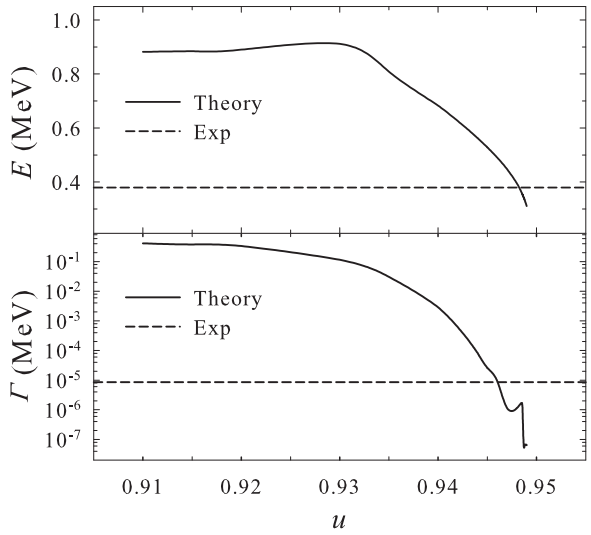

Fig. 7. Position and total width of the first 0^+ resonance state as a function of parameter u.

In this paper we used a Minnesota nucleon-nucleon potential tuned to reproduce the phase shifts for α-α scattering, as well as the ^{8}Be resonances. This however leads to overbound 0^+ and 2^+ states, and a bound 4^+ state. Moreover, the obtained resonance structure for the ^{12}C three-cluster continuum deviates from the experimentally observed one, which can also be attributed to the specific choice of semi-realistic nucleon-nucleon potential. We therefore wish to discuss the dependence of the results to the choice of parameter u on the results. To do so we use different criteria to optimize this parameter. We first determine a value to reproduce the ground state energy of ^{12}C, followed by an attempt to reproduce the energy and width of the 0^+ Hoyle state. In Fig. 6 we display the ground state energy as a function of the parameter u, compared to experiment (dashed line). One observes that the ground state is reproduced with u = 0.910.

One observes a monotonously decreasing linear dependence of the ground state energy on u within the selected range. For the Hoyle state position and width the dependency is less trivial, as is shown in Fig. 7. One however observes that the value u=0.948 reproduces the position of the Hoyle state, and leads to a close match for its width too. The correlation functions for the ground state and Hoyle state obtained with their respective optimal values were very close to the ones obtained with the value u=0.94 and displayed in Figs. 4 and 5, so that the conclusions remain unaltered.

Conclusions

In this paper we described the ^{12}C nucleus with a three-cluster microscopic model. The model correctly handles the three-cluster continuum, i.e. correctly implements the suitable boundary conditions, by using a Hyperspherical Harmonics basis. It leads to the scattering matrix S in many-channel space, and the energy, total and partial widths of the resonance states and their corresponding wave functions can be obtained. It was shown that the obtained resonances of ^{12}C agree well with other methods, and that the lowest resonances are generated by only a few numbers of weakly coupled channels, leading narrow resonance states. The partial widths determine the most probable channels for resonance decay. Correlation functions and density distributions revealed the dominant shape of the three-cluster triangle configuration for the lowest bound and resonance states of ^{12}C. There were no indications of a prominent linear three-cluster structure for the resonance states. It was also shown that it is impossible to fix a unique value for the u parameter of the Minnesota nucleon-nucleon potential to fit all desired physical properties for ^{12}C, and for the disintegrating α particles. However the qualitative conclusions remained unaltered under slight adaptation of u. As a final conclusion we can state that the model is consistent with other microscopic models using the Complex Scaling methodology to determine the energy and total width of three-cluster resonance states.

REFERENCES

1. *Ajzenberg-Selove F.* Energy levels of light nuclei A = 11 - 12 // Nucl. Phys. -1990. - Vol. A506. - P. 1 - 158.
2. *Moiseyev N.* Quantum theory of resonances: calculating energies, widths and cross-sections by complex scaling // Phys. Rep. - 1998. - Vol. 302. - P. 212 - 293.
3. *Ho Y.K.* The method of complex coordinate rotation and its applications to atomic collision processes // Phys. Rep. - 1983. - Vol. 99. - P. 1 - 68.
4. *Muńoz-Britton T., Freer M., Ashwood N.I. et al.* Search for the 2^+ excitation of the Hoyle state in ^{12}C using the ^{12}C (^{12}C, 3α) ^{12}C reaction // J. Phys. G Nucl. Phys. - 2010. - Vol. 37. - P. 105104.
5. *Freer M., Fujita H., Buthelezi Z. et al.* 2^+ excitation of the ^{12}C Hoyle state // Phys. Rev. - 2009. - Vol. C80. - P. 041303.
6. *Baz' A.I.* Diffusion-like processes in the quantum theory of scattering // Soviet J. Exp. Theor. Phys. - 1976. - Vol. 43. - P. 205 - 211.
7. *Anagnostatos G.S.* Alpha-chain states in ^{12}C // Phys. Rev. - 1995. - Vol. C51. - P. 152 - 159.

8. *Merchant A.C., Rae W.D.M*. Systematics of alpha-chain states in 4N-nuclei // Nucl. Phys. - 1992. - Vol. A549. - P. 431 - 438.
9. *Kanada-En'yo Y*. The Structure of Ground and Excited States of ^{12}C // Progr. Theor. Phys. - 2007. - Vol. 117. - P. 655 - 680.
10. *Neff T., Feldmeier H*. Cluster structures within Fermionic Molecular Dynamics // Nucl. Phys. - 2004. - Vol. A738. - P. 357 - 361.
11. *Vasilevsky V., Nesterov A.V., Arickx F., Broeckhove J.* Algebraic model for scattering in three-s-cluster systems. I. Theoretical background // Phys. Rev. - 2001. - Vol. C63. - P. 034606.
12. *Vasilevsky V., Nesterov A.V., Arickx F., Broeckhove J.* Algebraic model for scattering in three-s-cluster systems. II. Resonances in the three-cluster continuum of ^{6}He and ^{6}Be // Phys. Rev. - 2001. - Vol. C63. - P. 034607.
13. *Broeckhove J.*, *Arickx F.*, *Hellinckx P.et al.* // The ^{5}H resonance structure studied with a three-cluster J-matrix model // J. Phys. G Nucl. Phys. - 2007. - Vol. 34. - P. 1955 - 1970.
14. *Vasilevsky V., Arickx F., Broeckhove J.*, *Romanov V.N*. Theoretical analysis of resonance states in ^{4}H, ^{4}He and ^{4}Li above three-cluster threshold // Ukr. J. Phys. - 2004. - Vol. 49. - P. 1053 - 1059.
15. *Korennov S., Descouvemont P.* A microscopic three-cluster model in the hyperspherical formalism // Nucl. Phys. - 2004. - Vol. A740. - P. 249 - 267.
16. *Damman A., Descouvemont P.* Three-body continuum states in a microscopic cluster model // Phys. Rev. - 2009. - Vol. C80. - P. 044310.
17. *Thompson D.R., LeMere M., Tang Y.C.* Systematic investigation of scattering problems with the resonating-group method // Nucl. Phys. - 1977. - Vol. A286. - P. 53 - 66.
18. *Arai K*. Resonance states of ^{12}C in a microscopic cluster model // Phys. Rev. - 2006. - Vol. C74. - P. 064311.
19. *Wildermuth K., Tang Y*. A unified theory of the nucleus. - Braunschweig: Vieweg Verlag, 1977.
20. *Vasilevsky V., Nesterov A.V., Arickx F., Broeckhove J.* S-factor of the ^{3}H(^{3}H, 2n)^{4}He and ^{3}He(^{3}He, 2p)^{4}He reactions using a three-cluster exit channel // Phys. Rev. - 2001. - Vol. C63. - P. 064604.
21. *Pichler R., Oberhummer H., Csótó A., Moszkowski S.A*. Three-alpha structures in ^{12}C // Nucl. Phys. - 1997. - Vol. A618, - P. 55 - 64.

SEMI-EMPIRICAL SYSTEMATICS OF (n, ^{3}He) CROSS SECTIONS FOR 14.6 MeV NEUTRONS

L. Yettou[1], M. Belgaid[2]

[1] *Doctor Yahia Fares University, Faculty of Sciences and Technology, Medea, Algeria*
[2] *Faculty of Physics, University of Science and Technology, Houari Boumediene, Algiers, Algeria*

A new semi-empirical formula for the calculation of the (n, ^{3}He) cross section at 14.6 MeV neutron energy is obtained. It is based on the evaporation model and uses the droplet model of Myers and Swiatecki to express the reaction energy Q (n, ^{3}He). The behavior of the different terms of the droplet model involved in Q (n, ^{3}He) was checked individually before choosing the pertinent terms and setting up the formula. The new formula includes five parameters on 13 nuclei with $31 \leq A \leq 181$. The predictions of this formula are compared with those of the existing formulae and with the experimental data for 13 nuclei. The new formula gives a better fit to the data and shows an improvement in describing the (n, ^{3}He) cross sections data compared with the previous formulae.

1. Introduction

In this paper, we develop a semi empirical formula, which depends only on the mass and charge numbers, in order to calculate the (n, ^{3}He) reaction cross section for 14.6 MeV neutrons. This formula is based on the evaporation statistical model Weisskopf and Ewing [1] and uses the Droplet model mass-formula of Myers and Swiatecki [2] for the reaction energy Q (n, ^{3}He) that is needed.

2. Formalism and model parameters

Let us consider the reaction X (n, b) Y with the symbol definitions given as follow: E_n: the neutron kinetic energy; S_n: neutron separation energy; $E = E_n + S_n$: the excitation energy of the compound nucleus; S_b: emitted particle separation energy; E_b: emitted particle kinetic energy: $U = E - E_b - S_b$: the excitation energy of the residual nucleus. One can write down the (n, b) reaction cross section (Blatt. and Weisskopf [3] and Kikuchi K. and Kawai [4]) as:

$$\sigma_{(n,b)} = \sigma_{CN}^{n} \frac{F_b}{\sum F_{b'}}, \tag{1}$$

where σ_{CN}^{n} is the compound nucleus (CN) formation cross section through the neutron entrance channel. F_b represents a quantity that is proportional to the partial decay width Γ_b of the compound nucleus for the emitted particle through the decay channel (b) calculated via the detailed balance theorem and Σ indicates the sum over all the decay channels b'. One can write F_b as:

$$F_b = \frac{2m_b}{\hbar^2}(2I_b + 1)\int_0^{E-S_b} \sigma_{CN}^{b} E_b \omega(U)\, dE_b, \tag{2}$$

It is related to the nuclear temperature T through the thermodynamical relation:

$$\frac{1}{T} = \frac{d \ln \omega(U)}{dE_b}. \tag{3}$$

In the vicinity of E, one can write

$$\omega(U) \approx \omega_0(E) \exp\left(-\frac{E_b + S_b}{T}\right) \tag{4}$$

σ_{CN}^{b} is the compound nucleus formation cross section through the inverse channel (b), it can be written for charged particle as:

$$\sigma_{CN}^{b} = \begin{cases} 0 & if \quad E_b \leq V_b \\ \pi R^2 \left(1 - \dfrac{V_b}{E_b}\right) & if \quad E_b \rangle V_b \end{cases}, \tag{5}$$

where V_b is the Coulomb barrier for the channel decay b. Using Eq. (5), the quantity F_b of Eq. (2) can be put for helium-3 emission and neutron emission as:

$$F_{3He} = 4\frac{m_{3He}}{\hbar^2}\omega_0(E)\pi R^2 T^2 \exp\left(-\frac{S_{3He}+V_{3He}}{T}\right), \tag{6}$$

$$F_n = 4\frac{m_n}{\hbar^2}\omega_0(E)\pi R^2 T^2 \exp\left(-\frac{S_n}{T}\right), \tag{7}$$

$$\sum F_{b'} = F_n + F_p + F_\alpha + F_{^3He} + \ldots \approx F_n\,. \tag{8}$$

Now with Eqs. (1), (6) and (7), one can write:

$$\sigma_{n,^3He} = \sigma_{CN}^n \frac{m_n}{m_{^3He}} \exp\left(\frac{S_n - S_{^3He}}{T} - \frac{V_{^3He}}{T}\right) = \frac{m_n}{m_{^3He}}\sigma_{CN}^n \exp\left(\frac{Q_{(n,^3He)} - V_{^3He}}{T}\right). \tag{9}$$

On the basis of the mass formula of Myers and Swiatecki, [2], Kalbach [5] gives the separation energy for compound nucleus C into b particle and nucleus Y as:

$$S_b = \alpha_1(A_C - A_Y) + \alpha_2\left(\frac{(N_C - Z_C)^2}{A_C} - \frac{(N_Y - Z_Y)^2}{A_Y}\right) + \alpha_3(A_C^{2/3} - A_Y^{2/3}) +$$

$$\alpha_4\left(\frac{(N_C - Z_C)^2}{A_C^{4/3}} - \frac{(N_Y - Z_Y)^2}{A_Y^{4/3}}\right) + \alpha_5\left(\frac{Z_C^2}{A_C^{1/3}} - \frac{Z_Y^2}{A_Y^{1/3}}\right) + \alpha_6\left(\frac{Z_C^2}{A_C} - \frac{Z_Y^2}{A_Y}\right) - w_b \tag{10}$$

With this, the expression of $Q_{(n,^3He)}$ becomes:

$$Q_{(n,^3He)} = \alpha_1\frac{N-Z+1}{A} + \alpha_2\frac{N-Z+1}{A^{4/3}} + \alpha_3\frac{Z-1}{A^{1/3}} + \alpha_4\frac{Z-1}{A}, \tag{11}$$

where α_i are the constants of the mass formula. Here the different terms are: (N - Z + 1)/A the asymmetry term; $(N - Z + 1)/A^{4/3}$ the surface asymmetry term; $(Z - 1)/A^{1/3}$ the Coulomb term; (Z-1)/A the Coulomb diffuseness term. Eqs. (9) and (11) allow to write $\sigma_{(n,^3He)}$ as:

$$\sigma_{(n,^3He)} = \pi r_0^2 (1 + A^{1/3})^2 \exp\left(\frac{\alpha_1}{T}\frac{N-Z+1}{A} + \frac{\alpha_2}{T}\frac{N-Z+1}{A^{4/3}} + \frac{\alpha_3}{T}\frac{Z-1}{A^{1/3}} + \frac{\alpha_4}{T}\frac{Z-1}{A} - \frac{V_{^3He}}{T}\right) \tag{12}$$

σ_{CN}^n can be approximated at 14 MeV neutron energy to the total reaction cross section σ_R,

$$\sigma_{CN}^n \approx \sigma_R = \pi(R + \lambda\!\!\!^{-})^2 \quad (13)$$

With the dependence of $\sigma_{(n,^3He)}$ on $V_{^3He}/T$ neglected, Eq. (13) can be written as:

$$\sigma_{(n,^3He)} = \sigma_{CN}^n \exp\left(\frac{\alpha_1}{T}\frac{N-Z+1}{A} + \frac{\alpha_2}{T}\frac{N-Z+1}{A^{4/3}} + \frac{\alpha_3}{T}\frac{Z-1}{A^{1/3}} + \frac{\alpha_4}{T}\frac{Z-1}{A}\right). \tag{14}$$

This work helped us to select terms from Eq. (14), which showed a good analytical behaviour against the ratio $\sigma_{(n,^3He)}/\sigma_R$. A good description of the ratio $\sigma_{(n,^3He)}/\sigma_R$ on the $((N - Z + 1)/A)^{1/2}$, $((N - Z + 1)/A^{4/3})^2$, $((Z - 1)/A^{1/3})^{1/2}$ and $((Z-1)/A)^{1/2}$ terms is obtained (Figs. 1 - 4), respectively with the correlation coefficient values R = 0.78, 0.70, 0.80 and 0.69. The systematics resulting from Eqs. (13) and (14) are derived:

$$\sigma_{(n,^3He)} = (1 + A^{1/3})^2 \exp\left(\alpha_1 + \alpha_2\left(\frac{N-Z+1}{A}\right)^{1/2} + \alpha_3\left(\frac{N-Z+1}{A^{4/3}}\right) + \alpha_4\left(\frac{Z-1}{A^{1/3}}\right)^{1/2} + \alpha_5\left(\frac{Z-1}{A}\right)^{1/2}\right). \tag{15}$$

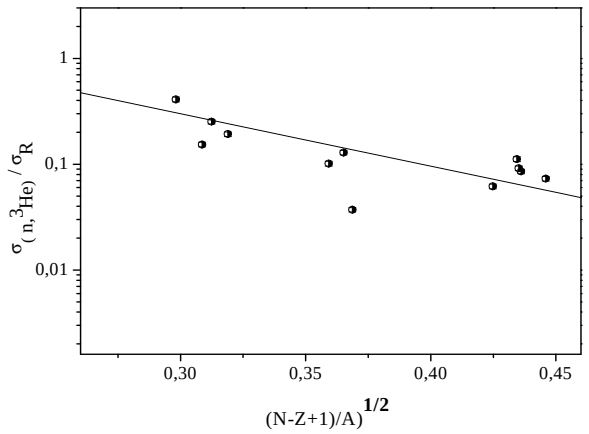

Fig. 1. Values of the ratio $\sigma_{(n,^3He)}/\sigma_R$ for 14.6 MeV neutrons showing a linear dependence of $\ln\sigma_{(n,^3He)}/\sigma_R$ on $((N - Z + 1)/A)^{1/2}$ obtained from Table 2 and Eq. (13).

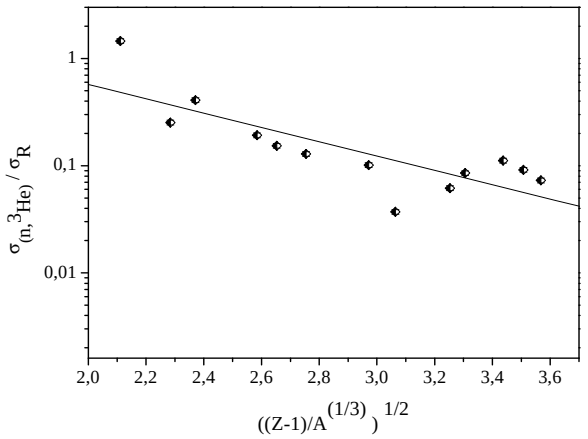

Fig. 2. Values of the ratio $\sigma_{(n,^3He)}/\sigma_R$ for 14.6 MeV neutrons showing a linear dependence of $\ln\sigma_{(n,^3He)}/\sigma_R$ on $((N - Z + 1)/A^{4/3})^2$ obtained from Table 2 and Eq. (13).

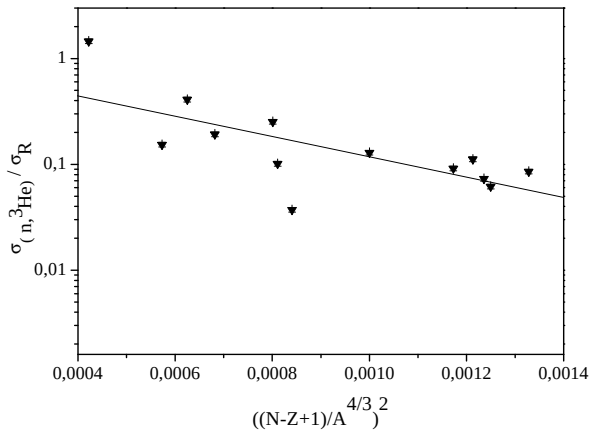

Fig. 3. Values of the ratio $\sigma_{(n,^3He)}/\sigma_R$ for 14.6 MeV neutrons showing a linear dependence of $\ln\sigma_{(n,^3He)}/\sigma_R$ on $((Z - 1)/A^{1/3})^{1/2}$ obtained from Table 2 and Eq. (13).

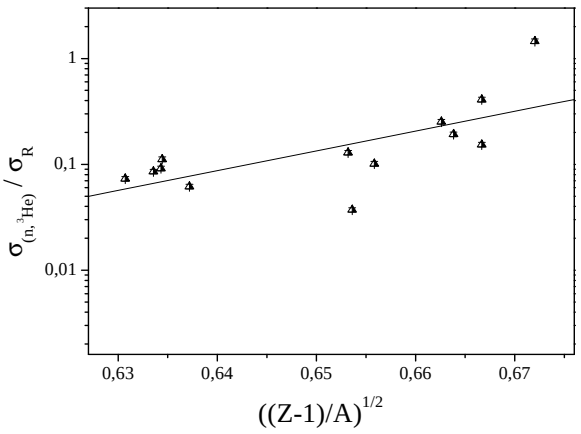

Fig. 4. Values of the ratio $\sigma_{(n,^3He)}/\sigma_R$ for 14.6 MeV neutrons showing a linear dependence of $\ln\sigma_{(n,^3He)}/\sigma_R$ on $((Z - 1)/A)^{1/2}$ obtained from Table 2 and Eq. (13).

3. Fitting of the Systematics parameters

The best fit is obtained with five free parameters α_1, α_2, α_3, α_4 and α_5 of Eq. (15):

$$\Sigma = \sum_{i=1}^{N} \left(\frac{\sigma_i^{\exp} - \sigma_i^{cal}}{\Delta\sigma_i^{\exp}} \right)^2 , \tag{16}$$

where the $\sigma_{(n,^3He)}$ experimental values and their errors taken from Sublet et al. [6], Qaim [7], Qaim [8] and Csikai [9], and σ_i^{cal} is the cross section calculated through Eq. (15). The minimum value, corresponding to the best fit, of χ^2 was deduced through:

$$\chi^2 = \Sigma/(N - M) , \tag{17}$$

where N is the number of experimental points and M the number of free parameters that need to be fitted. Table 1 gives the fit-values for the different parameters α_i for our relation Eq. (15), for two parameters relation of Broeders et al. [10] and Qaim [7] and three others parameters relation of Broeders et al. [10]. Table 2 presents the experimental data, the calculated cross sections σ_i^{cal} and the values $\left((\sigma_i^{\exp} - \sigma_i^{cal})/\Delta\sigma_i^{\exp}\right)^2$.

Table 1. **The parameters α_i of the different systematics with their $\sum$ and χ^2**

	Eq.	$\sum$	χ^2	α_1	α_2	α_3	α_4	α_5
This work	15	4.66	0.51	169.581	-27.942	-3978.17	-2.71	-230.14
Qaim [7]	20	21.8	1.99	8.475×10^{-2}	-1.6467			
Broeders et al. [10]	18	20.8	1.89	5.8701×10^{-3}	1.738×10^{-2}			
	19	15.1	1.51	1.6534	0.15257	-2.3		

Table 2. **The experimental (n, ^{3}He) reaction cross-sections for 14.6 MeV and 14.7 MeV neutrons energy $\sigma^{exp} \pm \Delta\sigma^{exp}$, the calculated cross-sections σ^{cal} through Eq. (15) with parameters from Table 1 and $(\sigma^{exp}-\sigma^{cal})^2/(\Delta\sigma^{exp})^2$ corresponding to the target nucleus with mass number A and charge number Z**

Z	A	Neutron energy, MeV	$\sigma^{exp} \pm \Delta\sigma^{exp}$, μb	Reference	σ^{cal}, μb	$\sum = ((\sigma^{exp}-\sigma^{cal})/(\Delta\sigma^{exp}))^2$
15	31	14.7	25.0±10.0	Sublet et al. [6]	26.19	0.01
19	41	14.6	5± 2.5	Sublet et al. [6]	7.18	0.76
21	45	14.6	8. 5± 4	Sublet et al. [6]	6.98	0.14
27	59	14.6	4. 6 ± 2.1	Qaim [8]	3.86	0.12
29	63	14.6	3. 8± 1.9	Sublet et al. [6]	3.56	0.02
33	75	14.6	3.5 ± 1.9	Qaim [8]	2.48	0.28
41	93	14.6	3. 1 ± 1.5	Qaim [8]	2.12	0.43
45	103	14.7	1. 2 ± 1.	Csikai [9]	1.99	0.62
55	133	14.7	2. 30± 0.43	Sublet et al. [6]	2.45	0.13
58	142	14.6	3. 3 ± 1.3	Qaim [7]	2.71	0.20
65	159	14.6	4. 6 ± 1.8	Qaim [7]	2.74	1.06
69	169	14.6	3.90± 1.95	Sublet et al. [6]	2.77	0.34
73	181	14.6	3.23± 1.42	Sublet et al. [6]	3.22	0. 00

4. Comparison with others systematics

Our relation Eq. (15) gives a better fit ($\chi^2 = 0.51$) than the Broeders et al. [10] pre-equilibrium exciton model formulae Eq. (18) and Eq. (19) ($\chi^2 = 1.89$ and $\chi^2 = 1.51$), and Qaim [7] simple evaporation model formula Eq. (20) ($\chi^2 = 1.99$).

$$\sigma_{(n,^3He)} = \pi r_0^2 (A^{1/3}+1)^2 A^{-1/3} (\alpha_1 (N-Z+1)/A + \alpha_2)^3, \quad (18)$$

$$\sigma_{(n,^3He)} = \pi r_0^2 (A^{1/3}+1)^2 A^{\alpha_3} (\alpha_1 (N-Z+1)/A + \alpha_2)^3, \quad (19)$$

$$\sigma_{(n,^3He)} = \alpha_1 (A^{1/3}+1)^2 \exp\left(\alpha_2 \frac{N-Z}{A}\right). \quad (20)$$

5. Conclusions

In this work a new semi-empirical formula has been derived to systematise the 14.6 MeV (n, ^{3}He) cross section data. This relation is based on the evaporation model and the Droplet model mass-formula used to express the Q(n, ^{3}He). This formula with five parameters leads to the lowest value of χ^2 = 0.58, when compared with the existing relation.

REFERENCES

1. *Weisskopf V.F.*, and *Ewing D.H.* On the Yield on Nuclear Reactions with Heavy Elements // Phys. Rev. - 1940. - Vol. 57. - P. 472 - 935.
2. *Myers W.D., Swiatecki W.J.* Nuclear Masses and Deformations // Nucl. Phys. - 1966. - Vol. 1. - P. 81.
3. *Blatt J.M., Weisskopf V.* Theoretical Nuclear Physics. - New York: John Wiley and Sons, Inc., 1952.
4. *Kikuchi K., Kawai M.* Nuclear Matter and Nuclear Reactions. - North-Holland: Publishing Company Amsterdam, 1968.
5. *Kalbach C.* Systematics of Continuum Angular Distributions. // Phys. Rev. - 1988. - Vol. C37(6). - P. 2350.
6. *Sublet J.-Ch., Koning, A., Forrest, R.A., Kopecky J.* - 2003. - JEFDOC-982.
7. *Qaim S.M.* // Radiochim. Acta. - 1978. - Vol. 25. -P. 13.
8. *Qaim S.M.* // J. Inorg. Nucl. Chem. - 1974. - Vol. 36. - P. 239.
9. *Csikai J.* // Acta Phys. - 1966. - Vol. 21. - P. 229.
10. *Broeders C.H.M., Konobeyev A.Yu.* // Appl. Radiat. Isot. - 2007. - Vol. 65. - P. 454.

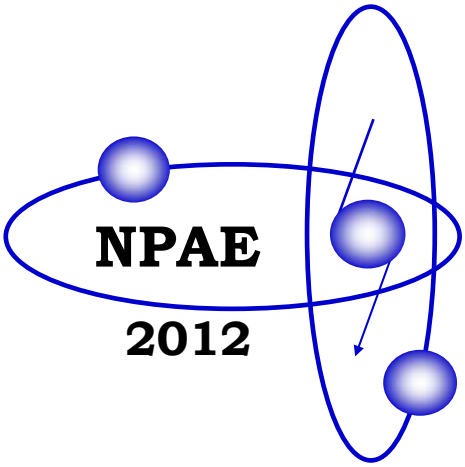

Section 3

Nuclear Structure and Decay Processes

TUNNELING BETWEEN ASYMMETRIC POTENTIAL WELLS AND NO-SEMICLASSICAL CALCULATIONS OF FISSION HALF-LIVES

S. V. Belchikov, S. P. Maydanyuk

Institute for Nuclear Research, National Academy of Sciences of Ukraine, Kyiv, Ukraine

A new fully quantum method of determination of penetrabilities through double-humped spontaneous fission barrier of arbitrary shape is developed. In such approach exact analytical solutions for amplitudes of wave function, penetrability *T* and reflection *R* for the barrier composed from *n* rectangular steps at arbitrary *n* which approximates the studied realistic barrier, are found. Penetrabilities through the barrier and half-lives for variety of actinide nuclides are calculated for spontaneous fission from ground state. In contrast to semiclassical approach, by this method we establish essential dependence of the half-life on starting coordinate ε_{start} in the first internal well (accuracy is $|T+R-1|<10^{-14}$). We impose a new condition: in the beginning of fission the emitted fragment starts to move outside from minimum of the internal well. Such a condition provides minimal calculated half-life and gives stable basis for predictions.

1. Introduction

The most of actinide nuclei exhibit double-humped barrier against fission. Developed procedure of determination of half-lives is based on semiclassical calculations of penetrabilities through such barriers [1]. According to our previous results [2], fully quantum determination of penetrabilities is sensitive to the dynamics and can lead to essentially different results. At the same time semiclassical approach has no such sensitivity.

Initially, the parent nucleus is in ground state, and fission may be considered as a process where the fragment tunnels through potential barrier along the coordinate of deformation. In theory of fission one can find prevailing approach for estimation of half-life based on penetration through the barrier in terms of one-dimensional semiclassical method. Calculation of penetrability of the barrier is keystone in estimation of fission half-lives. Importance of proper choice of boundary condition, reinforces our interest in the fully quantum consideration of unite tunneling process in this task, while the detailed analysis of selection this boundary condition and its real influence on results is practically missed in semiclasical approaches.

A main objective of this paper is to pass from semiclassical description of the process of penetration of fissioning fragment through the barrier used in the semiclasical approach to its fully quantum analogue, to put a fully quantum grounds for determination of the penetrability. In order to provide such a formalism, we have improved method of multiple internal reflections (MIR, see Refs. [2 - 6], and references therein) generalizing it on the fission barriers of arbitrary shapes.

2. Theoretical approach

An approach for description of one-dimensional motion of a non-relativistic particle above a barrier on the basis of multiple internal reflections of stationary waves relatively boundaries has been studied in number of papers and is known (see [7-9] and references therein). Tunneling of the particle under the barrier was described successfully on the basis of multiple internal reflections of the wave packets relatively boundaries (approach was called as *method of multiple internal reflections* or *method MIR*, see Refs. [2 - 6]). In such approach it succeeded in connecting: 1) continuous transition of solutions for packets after each reflection, total packets between the above-barrier motion and the under-barrier tunneling; 2) coincidence of transmitted and reflected amplitudes of stationary wave function in each spatial region obtained by approach MIR with the corresponding amplitudes obtained by standard method of quantum mechanics; 3) all non-stationary fluxes in each step, are non-zero that confirms propagation of packets under the barrier (i. e. their “tunneling”). In frameworks of such a method, non-stationary tunneling obtained own interpretation, allowing to study this process at interesting time moment or space point. In calculation of phase times this method turns out to be enough simple and convenient. It has been adapted for scattering of the particle on nucleus, proton-decay and α-decay in the spherically symmetric approximation with the simplest radial barriers and for tunneling of photons [2 - 6].

However, further realization of the MIR approach meets with three problems (see Ref. [2], for details): (1) problem on effectiveness, (2) problem on correctness and (3) problem on uncertainty in radial problem. The first point indicates on a serious unresolved problem of realization of the approach of multiple reflections in real quantum systems with complicated barriers, and clear algorithms of calculation of amplitudes should be constructed. The second point puts question on whether MIR method gives the same results as standard quantum mechanics or principal difference exists. The third point indicates on influence of potential non-locality on calculations of penetrability in radial tasks (for example, at the same boundary condition we obtain different values of penetrability in dependence on point of start of wave incidenting on the barrier, that connects initial condition and dynamics of decay).

The first attempt to resolve these problems was made in Ref. [2] were we present generalization of MIR approach for calculations of transmission and reflection amplitudes for one-dimensional barrier of arbitrary shape and apply this method for estimation of half-lives of some proton-emitters (at that time, similar estimations were also performed for

alpha-decay problem, and similar results were obtained). The first interesting result was essential influence of conditions of start of wave on penetrability. Practically, by such a way the half-life of proton decay of some emitters can be changed up to 200 times, which essentially differ from existed semiclassical, DWBA and TPA calculations. At the same time (and in contrast to other known approaches), we give standard test of quantum mechanics, perform calculations and demonstations confirmed our results. In this paper, we study spontaneous fission from the ground state in frameworks of tunneling through double-humped barrier using our approach.

2.1. Parameterization of fission barriers

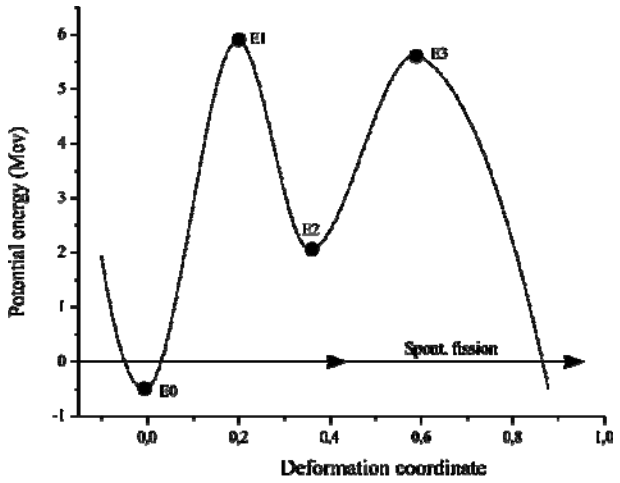

Fig. 1. Asymmetric double-humped fission barrier. The barrier is constructed using smoothly joined parabolic segments, according to Eq. (1).

We shall consider the double-humped barrier of general form used in fission problem. Such barrier consists of primary potential well containing ground state of the spontaneously fissioning nucleus, and the second well flanked by barrier from each side (Fig. 1). In present paper we use parameterization, according to Ref. [1]. The potential barrier has been connected by smoothly joining four parabolas. It is given as a function of dimensional deformation parameter ε by

$$V(\varepsilon) = E_j \pm \frac{1}{2}\mu\, w_j^2(\varepsilon-\varepsilon)^2 . \qquad (1)$$

2.2. Penetrability of barrier composed from arbitrary number of rectangular steps

Let us assume that before fission the nucleus can be considered as system composite from residual nucleus and fragment emitted. Its fission is described by a particle with reduced mass m which moves along deformation coordinate direction through a potential barrier. We shall be interesting in the double-humped barrier of arbitrary shape, which has successfully been approximated by finite number N of rectangular steps:

$$V(\varepsilon) = \begin{cases} V_1, & at\ \varepsilon_{\min} < \varepsilon \le \varepsilon_1 \quad \text{(region 1)}, \\ V_2, & at\ \varepsilon_1 < \varepsilon \le \varepsilon_2 \quad \text{(region 2)}, \\ \ldots & \ldots \quad\quad\quad\quad\quad\ \ldots \\ V_N, & at\ \varepsilon_{N-1} < \varepsilon \le \varepsilon_{\max} \quad \text{(region } N\text{)}, \end{cases} \qquad (2)$$

where V_i are constants (i = 1 … N). We define the first region 1 starting from point $\varepsilon_{\min}$, assuming that the fragment is formed here and then it moves outside. We shall be interesting in solutions for above barrier energies while the solution for tunneling could be obtained after by change $i\chi \to k_i$. A general solution of wave function has the following form:

$$\phi(\varepsilon) = \begin{cases} e^{ik_1\varepsilon} + A_R e^{-ik_1\varepsilon} & \text{at } \varepsilon_{\min} < \varepsilon \le \varepsilon_1 \quad \text{(region 1)}, \\ \alpha_2 e^{ik_2\varepsilon} + \beta_2 e^{-ik_2\varepsilon} & \text{at } \varepsilon_1 < \varepsilon \le \varepsilon_2 \quad \text{(region 2)}, \\ \ldots & \ldots \quad\quad\quad\quad\quad\ \ldots \\ \alpha_{N-1} e^{ik_{N-1}\varepsilon} + \beta_{N-1} e^{-ik_{N-1}\varepsilon} & \text{at } \varepsilon_{N-2} < \varepsilon \le \varepsilon_{N-1} \quad \text{(region } N-1\text{)}, \\ A_T e^{ik_N\varepsilon} & \text{at } \varepsilon_{N-1} < \varepsilon \le \varepsilon_{\max} \quad \text{(region } N\text{)}, \end{cases} \qquad (3)$$

where α_j and β_j are unknown amplitudes, A_T and A_R are unknown amplitudes of transmission and reflection, $k_i = \frac{1}{\hbar}\sqrt{2m(E-V_i)}$ are complex wave numbers. We shall be looking for solution for such problem in approach of multiple internal reflections.

According to this method, scattering of the particle on the barrier is considered on the basis of wave packet consequently by steps of its propagation relatively to each boundary of the barrier (the most clearly idea of such approach can be understood in the problem of tunneling through the simplest rectangular barrier, see Refs. [2–6]). Each step in such consideration of propagation of the packet will be similar to one from the first 2N-1 steps, independent between themselves. From analysis of these steps recurrent relations are found for calculation of unknown amplitudes $A_T^{(n)}$, $A_R^{(n)}$, $\alpha^{(n)}$ and $\beta^{(n)}$ for arbitrary step n, summation of these amplitudes are calculated. We shall be looking for the unknown amplitudes, requiring wave function and its derivative to be continuous at each boundary. We shall consider

the coefficients $T_1^{(\pm)}$, $T_2^{(\pm)}$, $T_3^{(\pm)}$ … and $R_1^{(\pm)}$, $R_2^{(\pm)}$, $R_3^{(\pm)}$ … as additional factors to amplitudes $\exp(\pm ik\varepsilon)$. Here, bottom index denotes number of the boundary, upper (top) signs "+" and "–" denote directions of the wave to the right or to the left, correspondingly. At the first, we calculate $T_1^{(\pm)}$, $T_2^{(\pm)}$ … $T_{N-1}^{(\pm)}$ and $R_1^{(\pm)}$, $R_2^{(\pm)}$ … $R_{N-1}^{(\pm)}$:

$$\begin{aligned} T_j^+ &= \frac{2k_j}{k_j + k_{j+1}} \exp[i(k_j - k_{j+1})\varepsilon_j], \quad T_j^- = \frac{2k_{j+1}}{k_j + k_{j+1}} \exp[i(k_j - k_{j+1})\varepsilon_j], \\ R_j^+ &= \frac{k_j - k_{j+1}}{k_j + k_{j+1}} \exp[2ik_j\varepsilon_j], \qquad\qquad R_j^- = \frac{k_{j+1} - k_j}{k_j + k_{j+1}} \exp[-2ik_{j+1}\varepsilon_j]. \end{aligned} \tag{4}$$

Using recurrent relations:

$$\begin{aligned} \tilde{R}_{j-1}^+ &= R_{j-1}^+ + T_{j-1}^+ \tilde{R}_j^+ T_{j-1}^- \left\{ 1 + \sum_{m=1}^{+\infty} \left[\tilde{R}_j^+ R_{j-1}^- \right]^m \right\} = R_{j-1}^+ + \frac{T_{j-1}^+ \tilde{R}_j^+ T_{j-1}^-}{1 - \tilde{R}_j^+ R_{j-1}^-}, \\ \tilde{R}_{j+1}^- &= R_{j+1}^- + T_{j+1}^- \tilde{R}_j^- T_{j+1}^+ \left\{ 1 + \sum_{m=1}^{+\infty} \left[\tilde{R}_j^- R_{j+1}^+ \right]^m \right\} = R_{j+1}^- + \frac{T_{j+1}^- \tilde{R}_j^- T_{j+1}^+}{1 - \tilde{R}_j^- R_{j+1}^+}, \\ \tilde{T}_{j+1}^+ &= \tilde{T}_j^+ T_{j+1}^+ \left\{ 1 + \sum_{m=1}^{+\infty} \left[\tilde{R}_j^- R_{j+1}^+ \right]^m \right\} = \frac{\tilde{T}_j^+ T_{j+1}^+}{1 - \tilde{R}_j^- R_{j+1}^+}, \end{aligned} \tag{5}$$

and selecting as starting the following values:

$$\tilde{R}_{N-1}^+ = R_{N-1}^+, \quad \tilde{R}_1^- = R_1^-, \quad \tilde{T}_1^+ = T_1^+, \tag{6}$$

we calculate successively coefficients $\tilde{R}_{N-2}^+$ … $\tilde{R}_1^+$, $\tilde{R}_2^-$ … $\tilde{R}_{N-1}^-$ and $\tilde{T}_2^+$ … $\tilde{T}_{N-1}^+$. We determine amplitudes of transmission and reflection, penetrability *T* and reflection *R* as

$$A_T = \tilde{T}_{N-1}^+, \quad A_R = \tilde{R}_1^+, \qquad T_{MIR} = \frac{k_n}{k_1} |A_T|^2, \quad R_{MIR} = |A_R|^2. \tag{7}$$

At finishing, we check the property:

$$\frac{k_n}{k_1} |A_T|^2 + |A_R|^2 = 1 \qquad \text{or} \qquad T_{MIR} + R_{MIR} = 1 \tag{8}$$

which should be test, whether the method MIR gives proper wave function. Now if energy of the particle is located below then height of one step with number *m*, then for description of tunneling it needs to use $k_m \to i\xi_m$. For the potential from two rectangular steps after comparison between the all amplitudes obtained by method of MIR and the corresponding amplitudes obtained by standard approach of quantum mechanics, we obtain coincidence up to first 15 digits. Increasing of number of steps up to some thousands keeps such accuracy and fulfilment of the property (8). This is important test which confirms reliability of the method MIR. So, we have obtained full coincidence between all amplitudes, calculated by method MIR and by standard approach of quantum mechanics.

2.3. Fission half-life calculations

Spontaneous fission decay half-life from the ground state E_g is written as [1]:

$$\tau_{gs} = \hbar \ln 2 \, \frac{2\pi}{w_0} \frac{1}{T(E_g)}, \tag{9}$$

where w_0 is frequency of assault on the barrier which we take to be equal to 1 MeV like [1]. *T* is penetrability through barrier at ground state with energy E_g, which we shall calculate by approach MIR or by approach [1].

3. Results

Results of the fission half-lives calculations are shown in the Table. The interesting result is essential dependence of the half-life on the position where we localize start of the wave incident on the internal barrier (Fig. 2).

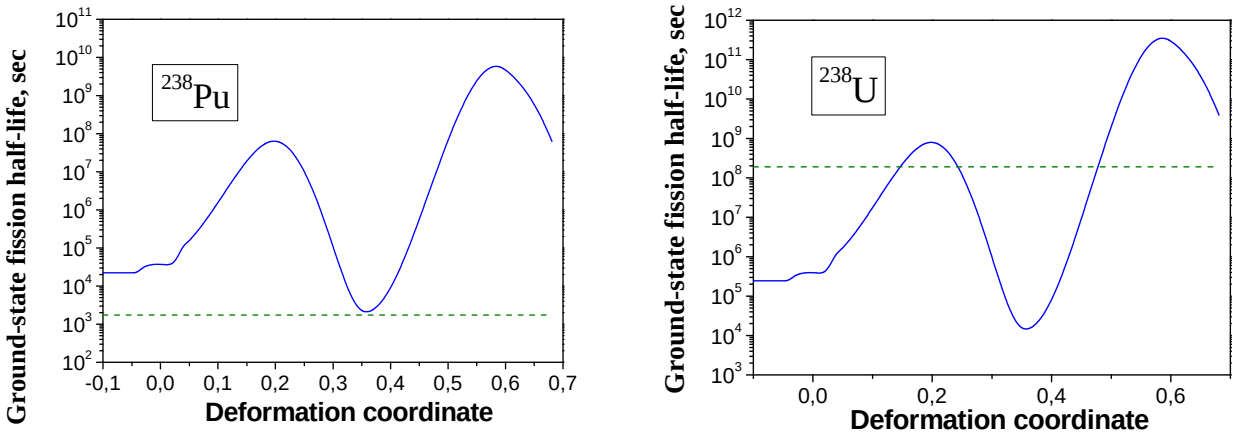

Fig. 2. Dependence of fission half-life on starting coordinate for fission of the ^{238}Pu and ^{238}U nuclei.

Comparison of the ground-state spontaneous fission half-lives calculated using various different parameterisation of double-humped fission barrier versus measured data for half-lives for corresponding nuclei. In calculations by MIR approach for each nucleus we use: number of intervals in region from ε_{min} to maximum of the barrier is 1000, from maximum of the barrier to ε_{max} is 1000

Compound nucleus	Even-odd character of Z - N	Calculated half-lives (s) using the double-humped barrier				Measured values (s), [1]
		Results from Ref. [1] at parameterization			MIR approach	
		Smoothly joined parabolic segments	Third order polynomial	Straight lines		
^{236}U	*e-e*	$3.85 \cdot 10^{9}$	$9.43 \cdot 10^{10}$	$2.15 \cdot 10^{11}$	$5.98 \cdot 10^{8}$	$6.34 \cdot 10^{8}$
^{238}U	*e-e*	$1.10 \cdot 10^{9}$	$2.14 \cdot 10^{10}$	$9.43 \cdot 10^{10}$	$2.049 \cdot 10^{8}$	$1.90 \cdot 10^{8}$
^{237}Np	*o-e*	$4.29 \cdot 10^{10}$	$5.44 \cdot 10^{11}$	$3.51 \cdot 10^{12}$	$9.37 \cdot 10^{10}$	$1.36 \cdot 10^{12}$
^{235}Pu	*e-o*	$9.43 \cdot 10^{10}$	$7.24 \cdot 10^{11}$	$6.52 \cdot 10^{11}$	$1.203 \cdot 10^{10}$	$2.99 \cdot 10^{11}$
^{238}Pu	*e-e (outer region)*	$8.53 \cdot 10^{3}$	$6.21 \cdot 10^{3}$	$3.45 \cdot 10^{3}$	$1.732 \cdot 10^{3}$	$1.744 \cdot 10^{3}$
^{238}Pu	*e-e (2-nd hole)*	$8.53 \cdot 10^{4}$	$7.52 \cdot 10^{3}$	$2.53 \cdot 10^{3}$	$2.044 \cdot 10^{3}$	$1.744 \cdot 10^{3}$
^{242}Cm	*e-e (2-nd hole)*	$8.53 \cdot 10^{-1}$	$2.12 \cdot 10^{-1}$	$3.45 \cdot 10^{-1}$	$3.838 \cdot 10^{-1}$	$2.28 \cdot 10^{-1}$

4. Conclusions

The method of multiple internal reflections (method MIR) is generalized on determination of half-lives for the spontaneous fission of the actinide nuclei. Note the following:

- Exact analytical solutions for amplitudes of wave function, penetrability T and reflection R are found by the method MIR for n-step barrier at arbitrary n, which approximates arbitrary shape of double-humped spontaneous fission barrier. Estimated error is $|T+R-1|<10^{-14}$.
- In contrast to the semiclassical approach [1], the approach MIR gives essential dependence of the penetrability on the starting coordinate ε_{start} inside the internal well which indicates starting condition for further fissioning process. Comparison with the calculations [1] shows that that approach has no such a sensitivity.
- In order to resolve uncertainty in calculations of the half-lives caused by the sensitivity of the penetrability on ε_{start}, we introduce the initial condition: *in the first stage of fission the fragment starts to move outside from state with coordinate in the minimum of the internal well*. Such condition provides minimal calculated half-life and gives stable basis for predictions, and better agreement with experimental data [1].

REFERENCES

1. *Bhandari B. S., Khaliquzzaman M.* Comparison of various parametrizations of the double-humped fission barriers // Phys. Rev. - 1991. - Vol. 44. - P. 292 - 305.
2. *Maydanyuk S.P., Belchikov S.V.* Calculation of penetrability of barriers in the proton-decay problem: fully quantum approach and initial condition of decay // J. Phys. Stud. - 2012. - Vol. 15. - P. 4002 (15 p.)
3. *Olkhovsky V.S., Maydanyuk S.P.* Method of multiple internal reflections in description of tunneling evolution

through barriers // Ukr. Phys. J. - 2000. - Vol. 45. - P. 1262 - 1269.
4. *Maydanyuk S.P., Olkhovsky V.S., Zaichenko A.K.* The method of multiple internal reflections in description of tunneling evolution of nonrelativistic particles and photons // J. Phys. Stud. - 2002. - Vol. 6. - P. 1 - 16.
5. *Maydanyuk S.P.* Time analysis of tunneling processes in nuclear collisions and decays. - Ph. D. dissertation / Supervisor: Prof. Olkhovsky V. S. - Kyiv, 2003. - 147 p. (in Ukrainian).
6. *Cardone F., Maidanyuk S.P., Mignani R., Olkhovsky V.S.* Multiple internal reflections during particle and photon tunneling // Found. Phys. Lett. - 2006. - Vol. 19. - P. 441 - 457.
7. *Fermor J.H.* Quantum-mechanical tunneling // Am. J. Phys. - 1966. - Vol. 34. - P. 1168 - 1170.
8. *McVoy K.W., Heller L., Bolsterli M.* Optical analysis of potential well resonances // Rev. Mod. Phys. - 1067. - Vol. 39. - P. 245 - 258.
9. *Anderson A.* Multiple scattering approach to one-dimensional potential problems // Am. J. Phys. - 1989. - Vol. 57. - P. 230 - 235.

NUCLEAR ASYMMETRY ENERGY, NEUTRON SKIN AND ISOVECTOR STIFFNESS

J. P. Blocki[1], A. G. Magner[2], A. A. Vlasenko[2,3]

[1] *National Centre for Nuclear Research, Otwock, Poland*
[2] *Institute for Nuclear Research, National Academy of Sciences of Ukraine, Kyiv, Ukraine*
[3] *Institute of Physics and Technology, NTUU "KPI", Kyiv, Ukraine*

The isovector particle densities and surface tension coefficients for the average binding energy in the approximation of a sharp edge proton-neutron asymmetric nucleus are used for analytical calculations of its neutron skin and isovector stiffness coefficients. They are significantly different from the well-known ones for the most Skyrme forces. The energies and energy-weighted sum rules of the isovector giant dipole resonances obtained within the Fermi-liquid drop model are in good agreement with the experimental data.

1. Introduction

The neutron skin of the exotic nuclei with a large excess of neutrons against protons is still one of the remarkable subjects of the nuclear and astronomic physics [1 - 6]. The simple and accurate solution for the isovector particle density distributions were obtained within the nuclear effective surface (ES) approximation [7 - 11]. It exploits the property of saturation of the nuclear matter and a narrow diffuse-edge region in finite heavy nuclei. The ES is defined as the location of points of the maximum density gradient. The coordinate system related locally to the ES is specified by a distance ξ from the given point to the surface and tangent coordinate η at the ES. The variational condition of the nuclear energy minimum at some fixed integrals of motion in the local energy-density theory is simplified in the ξ,η coordinates. In particular, in the extended Thomas - Fermi (ETF) approach [12, 13] (with the Skyrme forces [14]) it can be done for any deformations by using expansion in a small parameter $a/R \sim A^{-1/3} \ll 1$ for heavy enough nuclei (a is of the order of the diffuse edge thickness of the nucleus, R is its mean curvature radius, and A the number of nucleons). The accuracy of the ES approximation in the ETF approach without spin-orbit (SO) and asymmetry terms was checked [9] by comparing results of the Hartree - Fock (HF) and ETF theories [12] for some Skyrme forces. The ES approach [7 - 9] was extended by accounting for the SO and asymmetry effects [10]. Solutions for the isoscalar and isovector particle densities and energies in the ES approximation of the ETF approach were applied to analytical calculations of the neutron skin and isovector stiffness coefficients in the leading order of the parameter a/R [11]. Our results are compared with the fundamental researches [1 - 3] in the liquid droplet model (LDM). In the present work, we used the derived energy surface constants for calculations of the Isovector Giant Dipole Resonances (IVGDR) within the Fermi Liquid-Drop model (FLDM**)** [15 - 17].

2. Asymmetry energy and stiffness

We start with the nuclear energy, $E = \int d\mathbf{r}\, \mathcal{E}(\rho_+(\mathbf{r}),\rho_-(\mathbf{r}))$, in the local density approach [7 - 14],

$$\mathcal{E}(\rho_+,\rho_-) \approx -b_V\rho_+ + J\, I^2\rho_+ + \rho_+\left[\varepsilon_+(\rho_+)-\varepsilon_-\right] + \left(\mathcal{C}_+ + \mathcal{D}_+\rho_+\right)\left(\nabla\rho_+\right)^2 + \left(\mathcal{C}_- + \mathcal{D}_-\rho_+\right)\left(\nabla\rho_-\right)^2, \tag{1}$$

where $\rho_\pm = \rho_n \pm \rho_p$ are the isoscalar ρ_+ and isovector ρ_- particle densities; $I = (N-Z)/A$ is the asymmetry parameter; $N = \int d\mathbf{r}\rho_n(\mathbf{r})$ and $Z = \int d\mathbf{r}\rho_p(\mathbf{r})$ are the neutron and proton numbers and $A = N + Z$. As usually, $\mathcal{E}$ (Eq. (1)) contains the volume and surface terms (two first and three last with the gradient-density ones) [7 - 11], $b_V \approx 16$ MeV is the separation energy per particle and $J \approx 30$ MeV is the volume symmetry-energy constant of the nuclear matter. Eq. (1) can be applied approximately for the most of realistic Skyrme forces [14] by neglecting the relatively small semiclassical $\hbar$ corrections of the ETF kinetic energy and Coulomb terms as shown in [9, 10]. They all can be easily taken into account (without small exchange Coulomb terms) [9, 10]. $\mathcal{C}_\pm$ and $\mathcal{D}_\pm$ are constants defined by the Skyrme force parameters ($\mathcal{D}_-$ is relatively small). The isoscalar surface energy-density part, independent explicitly of the density gradient terms, is determined by the function $\varepsilon_+(\rho_+)$ which satisfies the saturation condition: $\varepsilon_+(\bar{\rho}) = 0$, $d\varepsilon_+(\bar{\rho})/d\rho_+ = 0$, where $\bar{\rho} = 3/(4\pi r_0^3) \approx 0.16$ fm^{-3} is the density of the infinite nuclear matter, $r_0 = R/A^{1/3}$ is a radius constant independent of A. The isovector component can be simply evaluated as $\varepsilon_- = J\left(I^2 - \rho_-^2/\rho_+^2\right)$. The isoscalar SO gradient terms in (1) are defined with a constant: $\mathcal{D}_+ = -9mW_0^2/(16\hbar^2)$, where $W_0 \approx 100-130$ MeV$\cdot$fm^5 and m is the nucleon mass (see [12, 14]). From the condition of the minimum energy E under the certain constraints, like the fixed $A = \int d\mathbf{r}\,\rho_+(\mathbf{r})$ and $N - Z = \int d\mathbf{r}\,\rho_-(\mathbf{r})$ one arrives at the Lagrange equations with the isoscalar and isovector multipliers (chemical potentials). To satisfy the condition of the particle number conservation with the required

accuracy we account for relatively small surface corrections ($\propto a/R \sim A^{-1/3}$ at the first order) to the leading terms in the chemical potentials [9, 10].

Using the analytical solutions of the Lagrange equations for the isoscalar and isovector particle densities $\rho_\pm$ one obtains [9 - 11] the nuclear energy, $E = E_V + E_S$, in the ES approximation in terms of the volume, $E_V = -b_V A + JI^2 A$, and the surface, $E_S = E_S^{(+)} + E_S^{(-)}$, components where

$$E_S^{(\pm)} = \sigma_\pm \mathcal{S} = b_S^{(\pm)} \mathcal{S}/(4\pi r_0^2), \qquad b_S^{(\pm)} \approx 8\pi r_0^2 \mathcal{C}_\pm \int_{-\infty}^{\infty} d\xi \left(1 + \mathcal{D}_\pm \rho_+ / \mathcal{C}_\pm\right)\left(\partial\rho_\pm/\partial\xi\right)^2, \tag{2}$$

$\mathcal{S}$ is the area of the ES. For the isovector surface energy constant $b_S^{(-)}$ one obtains

$$b_S^{(-)} = k_S I^2, \quad k_S = 6\bar{\rho}\mathcal{C}_- \mathcal{J}_- / (r_0 a), \quad \mathcal{J}_- = \frac{1}{1+\beta}\int_0^1 dw \sqrt{\frac{w(1+\beta w)}{\varepsilon(w)}}\left[(1-w)(1+\tilde{c}\tilde{w})\right]^2. \tag{3}$$

Here, $a = \sqrt{\mathcal{C}_+ \bar{\rho} K / (30 b_V^2)} \approx 0.5$ fm is the diffuseness parameter, $K \approx 230$ MeV is the incompressibility modulus, $\beta = \mathcal{D}_+ \bar{\rho}/\mathcal{C}_+$ is the dimensionless SO parameter, $\tilde{w} = (1-w)/c_{sym}$, $c_{sym} = a\sqrt{J/(\bar{\rho}\,|\mathcal{C}_-|)}$, $\tilde{c} = (\beta c_{sym}/2 - 1)/(1+\beta)$. With the quadratic approximation $\varepsilon(w) \approx (1-w)^2$ one obtains simple expressions for these constants $b_S^{(\pm)}$ (or k_S, see Eqs. (2) and (3)) in terms of the elementary functions.

According to the theory [1 - 3], one can define the isovector stiffness Q with respect to the neutron skin variable τ (the dimensionless measure of the difference between the neutron and proton radii $R_n - R_p$):

$$E_S^{(-)} = -\frac{\bar{\rho} r_0}{3}\oint d\mathcal{S}\, Q\tau^2 \approx -\frac{Q\tau^2 \mathcal{S}}{4\pi r_0^2}, \qquad \tau = \frac{R_n - R_p}{r_0}. \tag{4}$$

Using also Eq. (2) for the isovector surface energy $E_S^{(-)}$ one may express Q through the isovector surface energy constant k_S as $Q = -b_S^{(-)}/\tau^2 = -k_S I^2/\tau^2$. Defining the neutron and proton ES radii $R_{n,p}$ as the positions of the maxima of the neutron and proton density gradients and expanding in powers of small $R_{n,p} - R$ near the ES up to the first order terms one obtains [11]

$$\tau = \frac{8ag(w_r)}{r_0 c_{sym}^2} I, \quad g(w) = \frac{w^{3/2}(1+\beta w)^{5/2}}{(1+\beta)(3w+1+4\beta w)}\left\{w(1+2\tilde{c}\tilde{w})^2 + 2\tilde{w}(1+\tilde{c}\tilde{w})[\tilde{c}w - c_{sym}(1+2\tilde{c}\tilde{w})]\right\}, \tag{5}$$

where $w_r = w(0)$ is the value of w of the ES, determined by the equation: $\varepsilon(w_r) + w_r(1+\beta w_r)\varepsilon'(w_r) = 0$. Within a good approximation $\varepsilon(w) = (1-w)^2$ [9, 10], one simply has $w_r = (\sqrt{9+8\beta} - 3)/(4\beta)$. In Eq. (5), we used also the expressions for the isovector density ρ_- [9, 10]. The neutron and proton particle-density variations conserve the position of the center of mass in the linear approximation in $\delta R_{n,p}$ and asymmetry parameter I. Using Eqs. (3) - (5) one finally arrives at

$$Q = k_S/\tau^2 = -\nu J^2/k_S, \qquad \nu = k_S^2 I^2/(\tau^2 J^2) = 9\mathcal{J}_-^2/\left[16 g^2(w_r)\right], \tag{6}$$

where $\mathcal{J}_-$ and $g(w_r)$ are given by Eqs. (3) and (5). Note that the first relationship in Eq. (6) between the isovector quantities, the stiffness Q and the volume J and surface k_S energy constants has the same analytical form as predicted in [1 - 3], $Q = -9J^2/(4k_S)$, where $\nu = 9/4$. Its difference from Eq. (6) in terms of J and k_S is in the constant ν which is however proportional to the function $\mathcal{J}_-^2/g^2(w_r)$ in our derivations, instead of 9/4. This function depends significantly on the SO interaction β parameter but not much on the surface asymmetry constant $\mathcal{C}_-$. The constant ν (see Eq. (6)) is weakly sensitive to the specific Skyrme interaction because the most sensitive parameter $\mathcal{C}_-$ was mainly excluded in ν, $\tau \propto 1/c_{sym}^2 \propto \mathcal{C}_-$ and $k_S \propto \mathcal{C}_-$ (see Eqs. (3), (5) and (6)). This constant ν at $\beta = 0$ ($w_r = 1/3$) can be easily evaluated using Eqs. (3), (5) and (6) ($\nu \approx (108/25)[1 - 8/(7c_{sym})]^2[1 - 4/(3c_{sym})]^{-1}$ up to small terms $\propto 1/c_{sym}^2$, $c_{sym} \approx 2 - 6$ for the Skyrme parameters of [14]). Another difference is the expression (3) itself for k_S.

Thus, the isovector stiffness coefficient Q introduced originally by Myers and Swiatecki [1] is not a parameter of our theory but it was found analytically in the explicit closed form (6), (3) through the parameters of Skyrme forces.

3. FLDM and IVGDR

For calculations of the IVGDR we may use the FLDM based on the linearized Landau - Vlasov equations for the dynamical part of distribution functions $\delta f_{\pm}(\mathbf{r},\mathbf{p},t)$ in the phase space [17],

$$\frac{\partial}{\partial t}\delta f_{\pm}(\mathbf{r},\mathbf{p},t)+\frac{\mathbf{p}}{m_{\pm}^{*}}\nabla_{\pm}\left[\delta f_{\pm}(\mathbf{r},\mathbf{p},t)+\delta\left(e-e_{F}\right)\delta e_{\pm}+V_{ext}^{\pm}\right]=\delta St_{\pm}\,, \tag{7}$$

where $m_{\pm}^{*}$ are the isoscalar $(+)$ and isovector $(-)$ effective masses; $e=p^{2}/2m_{\pm}^{*}$, $e_{F}=(p_{F}^{\pm})^{2}/2m_{\pm}^{*}$ is the Fermi energy; $p_{F}^{\pm}=p_{F}(1\mp\Delta)$ is the Fermi momenta; $\Delta=2(1+F_{0}^{\prime})I/3$, $F_{0}^{\prime}=3J/e_{F}-1$ is the isotropic isovector Landau constant of the quasiparticle interaction; $\delta e_{\pm}$ is the quasiparticle interaction energies; $V_{ext}^{\pm}\propto\exp(-i\omega t)$ is the periodic time-dependent external field and $\delta St_{\pm}\approx-\delta f_{\pm}/\mathcal{T}$ is the collision term in the simplest $\mathcal{T}$-relaxation time approximation. Solutions of these equations (7) related to the dynamic dipole particle-density variations, $\delta\rho_{\pm}(\mathbf{r},t)\propto Y_{10}\left(\hat{r}\right)\propto\cos(\theta)$ in the spherical coordinates r, θ, φ can be found in terms of a superposition of the plane waves over angles of the wave vector $\mathbf{q}$ as

$$\delta f_{\pm}=\delta\left(e-e_{F}\right)\int\sin\theta_{\mathbf{q}}d\theta_{\mathbf{q}}d\varphi_{\mathbf{q}}\Phi_{\pm}Y_{10}\left(\hat{q}\right)\exp\left[i\left(\mathbf{qr}-\omega t\right)\right],\qquad\hat{q}=\mathbf{q}/q\,, \tag{8}$$

$\omega=p_{F}^{(\pm)}s^{\pm}q/m_{\pm}^{*}$, $s^{+}=s$, $s^{-}=s\sqrt{NZ/A^{2}}$, $q=|\mathbf{q}|$ (the factor $\sqrt{NZ/A^{2}}$ ensures the conservation of the center-of-mass position, see [18]). $\Phi_{\pm}$ are the amplitudes of the Fermi surface distortions determined from Eq. (7). The dynamical variations of the quasiparticle interaction $\delta e_{\pm}(\mathbf{r},\mathbf{p},t)$ at the first order with respect to the equilibrium energy $p^{2}/2m_{\pm}^{*}$ are defined through the particle and current density variations and Landau interaction constants (the isoscalar (F_{0}) and isovector ($F_{0}^{\prime}$) isotropic interaction constants related to the volume incompressibility modulus K and symmetry energy constant J as well as the anisotropic interaction constants corresponding to the effective masses $m_{\pm}^{*}$). The two dispersion relations (26) in [17] determine the solutions for the two sounds $s=s_{n}$ ($n=1,2$) as functions of $\omega\mathcal{T}$, the main ($n=1$) peak and its satellite ($n=2$) in the nuclear volume due to the nuclear asymmetry.

For the finite Fermi-liquid drop with a sharp ES we may use the macroscopic boundary conditions for the pressures and those for the velocities [10, 11, 17]. For small isovector vibrations near the spherical shape the mean normal velocity u_{ξ} and normal momentum flux-tensor $\delta\Pi_{\xi\xi}$ components (moments of the distribution function δf_{-}, (see Eq. (8)) are reduced to the radial ones, u_{r} and $\delta\Pi_{rr}$, respectively,

$$u_{r}\,|_{r=R}=u_{S}\,.\qquad\delta\Pi_{rr}\,|_{r=R}=\delta P_{S}\quad\text{ with }\quad\delta P_{S}=2\alpha_{S}^{(-)}b_{S}^{(-)}\bar{\rho}A^{1/3}Y_{10}(\hat{r})/3\,. \tag{9}$$

The right hand sides of the boundary conditions are the isovector ES velocity $u_{S}=R\dot{\alpha}_{S}^{(-)}Y_{10}(\hat{r})$ and capillary pressure excess δP_{S}. In Eq. (9), δP_{S} is given through the isovector surface energy constant $b_{S}^{(-)}=4\pi r_{0}^{2}\sigma_{-}$ (Eq. (3)), $\alpha_{S}^{(-)}$ is the dynamical isovector-dipole amplitude of the motion of the neutron drop surface against the proton one ($R(t)=R[1+\alpha_{S}^{(-)}(t)\sqrt{4\pi/5}\,Y_{10}(\hat{r})]$ keeping also the volume and the position of the center of mass conserved).

The energy constant $D=\hbar\omega A^{1/3}$ and energy weighted sum rules (EWSR, $S=-\hbar^{2}\int d\omega\,\omega\,\mathrm{Im}\,\chi(\omega)/\pi$) for the IVGDR can be found from the response function $\chi(\omega)$. Solving the Landau - Vlasov equations (7) in terms of the zero sound plane waves (8) with using the dispersion equations (26) in [17] for s_{n} and macroscopic boundary conditions (9) on the nuclear ES one obtains

$$\chi(\omega)=\sum_{n=1}^{2}\frac{\mathcal{A}_{n}(q)}{\mathcal{R}_{n}(\omega-i\Gamma/2)}\,,\quad\mathcal{R}_{n}(\omega)=j_{1}^{\prime}(qR)+\frac{3e_{F}qR}{2k_{S}A^{1/3}}\left[c_{n}j_{1}^{\prime\prime}(qR)+d_{n}j_{1}(qR)\right]. \tag{10}$$

Here $c_{1}\approx1-3s_{1}^{2}+F_{0}^{\prime}$, $d_{1}\approx1-s_{1}^{2}+F_{0}^{\prime}$ for the main $(n=1)$ IVGDR peak, and more bulky expressions for s_{2} of the satellite ($n=2$) peak of a smaller ($\propto I$) strength (see Eq. (D11) in [17]). $\mathcal{A}_{1}(q)\approx-\bar{\rho}R^{3}j_{1}(qR)/(m\omega^{2})$ and $\mathcal{A}_{2}(q)\propto\Delta$ (Eq. (60) in [17]) are the amplitudes for the $n=1,2$ modes, $j_{1}(z)$ is the standard spherical Bessel function and

$j_1'(z) = dj_1/dz$. The poles of the response function $\chi(\omega)$ Eq. (10) (roots ω_n of the equation $\mathcal{R}_n(\omega - i\Gamma/2) = 0$ or q_n) determine the IVGDR energies $\hbar\omega_n$ as their real part (the IVGDR width Γ is determined by their imaginary part). The residue $\mathcal{A}_n$ is important for the calculations of the IVGDR strength (EWSR) by taking the integral of $\omega \mathrm{Im}\,\chi(\omega)$ (see Eq. (10)) at a small width of the IVGDR Γ. Note that the expression like Eq. (10) for the only one main peak in symmetrical nuclei ($N = Z$) with using phenomenological boundary conditions was obtained earlier in [15]. However, in our derivations of Eq. (10), k_S is related to the surface tension coefficient, $\sigma_- = b_S^{(-)}/(4\pi r_0^2) = k_S I^2/(4\pi r_0^2)$, through the isovector capillary pressure dP_S of Eq. (9) and surface energy $E_S^{(-)}$ (Eq. (2)). Therefore, k_S (with the opposite sign) differs essentially from the isovector stiffness coefficient Q (defined through Eq. (4) in [1 - 3]) by τ^2 (see Eq. (6)), in contrast to another interpretation of the corresponding quantity (denoted by B^-) in Eqs. (3) and (20) of [15].

4. Discussion and summary

The isovector surface energy constants k_S (Eq. (3)), the neutron skin τ (Eq. (5)) and the stiffness coefficients Q (Eq. (6)) in the ES approach using the simplest quadratic approximation for $\varepsilon(w)$ are shown in the Table for several Skyrme forces [14]. The constants k_S (see Eq. (3)) are rather sensitive to the choice of the Skyrme forces. The modulus of k_S for the Lyon Skyrme forces SLy4-7 and SLyb230 [14] is significantly larger than for other forces. Relatively, the stiffness Q is even more sensitive to constants of the Skyrme forces, especially for SGII, than the well-known empiric values $Q \approx 14 - 35$ MeV suggested in [1 - 3]. For T6 [14] one has $\mathcal{C}_- = 0$ and therefore, $k_S = 0$ and $Q = \infty$ (ν is weakly dependent of $\mathcal{C}_-$), in contrast to all other forces shown in the Table. Notice that the isovector gradient terms which are important for the consistent derivations within the ES approach [11] are not also included ($\mathcal{C}_- = 0$) into the energy density in [4, 5]. For RATP [14] the stiffness Q is even negative as $\mathcal{C}_- > 0$ ($k_S > 0$). The reason of significant differences in the Q values might be related to those of the critical isovector Skyrme parameter $\mathcal{C}_-$ in the gradient terms of the energy density (see Eq. (1)). Different experiments used for fitting this parameter were found to be almost insensitive in determining uniquely its value, and hence, k_S (or $b_S^{(-)}$, see Eq. (3)) and Q (Eq. (6)), as compared to the well-known isoscalar $b_S^{(+)}$ surface-energy constant. The isovector surface-energy constant k_S (Eq. (3)) and stiffness Q (Eq. (6)) depend much on the SO β through the constants $\mathcal{J}_-$ in Eq. (3) and $g(w_r)$ of the neutron skin τ (Eq. (5)). In Eq. (6), ν is roughly constant ($\nu \approx 2 - 4$) for all Skyrme forces at $\beta = 0$ but significantly varies as function of β depending on different Skyrme forces. The values of ν are mostly smaller than 9/4 suggested in [1] (besides of SGII where we found much larger values). Swiatecki and his collaborators found [2] the stiffness $Q \approx 14 - 20$ MeV from fitting the nuclear IVGDR energies calculated in the simplest hydrodynamic model (HDM) to the experimental data. Then, larger values $Q \approx 30 - 35$ MeV were suggested in the last two references in [1]. In spite of the several misprints in these derivations [2] (see [11]) the final result for the IVGDR energy constant D is close to that for the asymptotically large values of Q ($3JA^{-1/3}/Q \ll 1$). The IVGDR energy constants D of HDM are roughly in good agreement with the well-known experimental value $D_{\mathrm{exp}} \approx 80$ MeV for heavy nuclei within a precision better or of the order of 10%, as shown in [11] (see also [15 - 17,19 - 21]). More precise $A^{-1/3}$ dependence of D with the finite values of Q seems to be beyond the accuracy of these HDM calculations even accounting more consistently for the ES motion because of several other reasons (structure of the IVGDR, curvature, quantum-shell and Coulomb effects in the low energy region) towards the realistic calculations based on the Skyrme HF approach, see larger $Q \approx 30 - 80$ MeV found in [6, 12]. With larger Q (see the Table) the fundamental parameter of the LDM expansion in [1], $(9J/4Q)A^{-1/3}$, is really small for $A \gtrsim 40$ and therefore, the results obtained by using this expansion are justified.

The Table shows the IVGDR energies $D_n = \hbar\omega_n A^{1/3}$ ($n = 1, 2$) and EWSR S_n (normalized to 100 % for both peaks) obtained within a more precised FLDM [17]. The IVGDRs even for the spherical nuclei have a double-resonance structure, the main peak $n = 1$ which exhausts mainly the EWSR for almost all Skyrme forces and the satellite one $n = 2$ with significantly smaller EWSR contribution proportional to the asymmetry parameter I , especially for heavy nuclei. The last row shows the average $\bar{D}$ weighted by their EWSR distribution in rather good agreement with the experimental data within the same accuracy about 10 %, including SLyb230 ($\bar{D} = 81 - 91$ MeV) and skipped here in Table 1 for the sake of space. Exclusion can be done for the Skyrme forces SIII (see the Table) and SLya230 ($\bar{D} = 101 - 105$ MeV) of [14]. Note that the main characteristics of the IVGDR described by $\bar{D}$ are almost insensitive to the isovector surface energy constant k_S .

The isovector energy, k_S, and stiffness, Q, coefficients for several Skyrme forces [14];
ν is the constant of Eq. (6); τ / I is the neutron skin calculated by Eq. (5); the intervals of functions $D_n(A)$
and $\bar{D}(A) = (D_1 S_1 + D_2 S_2)/(S_1 + S_2)$ are related to $A \approx 60 - 210$

Calculated quantites	Skyrme forces								
	SkM*	SkM	SIII	SGII	RATP	SkP	T6	SLy5	SLy7
$\mathcal{C}_-$ MeV · fm^5	-4.79	-4.69	-5.59	-0.94	13.9	-20.2	0	-22.8	-13.4
β	-0.64	-0.69	-0.57	-0.54	-0.52	-0.37	-0.45	-0.58	-0.65
k_S MeV	-0.77	-1.90	-0.52	-0.21	1.42	-1.93	0	-6.96	-6.32
ν	0.34	0.46	1.42	17.9	0.45	1.76	4.30	0.59	0.67
Q MeV	398	234	2168	60998	-270	823	∞	87	109
τ / I	0.044	0.090	0.40	0.040	0.072	0.035	0	0.0019	0.048
D_1 MeV	75 - 82	75 - 76	49 - 106	76 - 77	87	50 - 122	86 - 88	64 - 91	63 - 92
S_1 %	93 - 98	85 - 96	57 - 92	95 - 99	70 - 90	65 - 98	100	58 - 77	53 - 88
D_2 MeV	50 - 88	51 - 82	118 - 79	51 - 81	55 - 89	75 - 80	60 - 59	92 - 63	92 - 71
S_2 %	7 - 2	5 - 4	43 - 8	5 - 1	30 - 10	35 - 2	0	42 - 29	47 - 12
$\bar{D}$ MeV	73 - 82	71 - 76	79 - 104	74 - 77	77 - 87	70 - 69	86 - 88	76 - 84	77 - 89

As conclusions, simple solutions of the isovector particle density and energies, in the leading ES approximation were used for analytical calculations of the neutron skin and isovector stiffness coefficients. Results for the isovector surface energy constant k_S and stiffness Q are rather sensitive to the choice of the Skyrme force parameters, especially those in the isovector gradient terms ($\mathcal{C}_-$) and SO interaction (β). The mean IVGDR energies and sum rules calculated within the FLDM [17] for the most of constants k_S and Q of the Table are in good agreement with the experimental data. For further perspectives, it would be interesting to compare the found constants with those of [19 - 21] within the macroscopic-microscopic models accounting however for the critical comments mentioned above, especially concerning the structure of the IVGDR. We are going to analyze the k_S dependence of the IVGDR satellite within the FLDM in relation to the well-known pygmy GDR resonances [22, 23] which are expected to be more sensitive to the values of k_S. It would be also worth to apply our results to calculations of the energies and sum rules for the isovector low-lying collective states within the periodic orbit theory [13, 24 - 26].

ACKNOWLEDGEMENT

Authors thank M. Brack, V. Yu. Denisov, V. M. Kolomietz, J. Meyer, M. Pearson, P. Ring, A. I. Sanzhur, and X. Vinas for many useful discussions.

REFERENCES

1. *Myers W.D., Swiatecki W.J.* Average Nuclear Properties // Ann. Phys. - 1969. - Vol. 55. - P. 395-505; *Ibid.* - 1974. - Vol. 84. - P. 186 - 210; Nucl. Phys. - 1980. - Vol. A336. - P. 267 - 278; Phys. Rev. - 1996. - Vol. C601. - P. 141 - 167.
2. *Myers W.D., Swiatecki W.J., Kodama T., El-Jaick L.J., Hilf E.R.* Droplet model of the giant dipole resonances // Phys. Rev. - 1977. - Vol. C15. - P. 2032 - 2043.
3. *Myers W.D., Swiatecki W.J., Wang C.S.* The surface energy of multi-component systems // Nucl. Phys. - 1985. - Vol. A436. - P. 185 - 204.
4. *Danielewicz P.* Surface symmetry energy // Nucl. Phys. - 2003. - Vol. A727. - P. 233 - 268.
5. *Danielewicz P., Lee J.* Symmetry energy in nuclear surface // Int. J. Mod. Phys. - 2009. - Vol. E18. - P. 892 - 899.
6. *Warda M., Vinas X. Roca-Maza X., Centelles M.* Neutron skin thickness in droplet model with surface width dependence: indication of softness of the nuclear symmetry energy // Phys. Rev. - 2009. - Vol. C80. - P. 024316 (13 pages).
7. *Strutinsky V.M., Tyapin A.S.* Quasistatic droplet model of nucleus as the approximation to the statistical model // Soviet Phys. JETP. - 1964. - Vol. 18. - P. 960 - 965.
8. *Strutinsky V.M., Magner A.G., Brack M.* The nuclear surface as a collective variable // Z. Phys. - 1984. - Vol. A319. - P. 205 - 213.
9. *Strutinsky V.M., Magner A.G., Denisov V.Yu.* Density Distributions in Nuclei // Z. Phys. - 1985. - Vol. A322. - P. 149 - 156.
10. *Magner A.G., Sanzhur A.I., Gzhebinsky A.M.* Asymmetry and Spin-Orbit Effects in Binding Energy in the Effective Nuclear Surface Approximation // Int. J. Mod. Phys. - 2009. - Vol. E18. - P. 885 - 893.
11. *Blocki J.P., Magner A.G., Ring P., Vlasenko A.A.* Nuclear asymmetry energy and isovector stiffness within the

effective surface approximation // Phys. Rev. C. - 2012. Submitted to the journal.
12. *Brack M., Guet C., Hakanson H.-B.* Selfconsistent semiclassical description of average nuclear properties - a link between microscopic and macroscopic models // Phys. Rep. - 1985. - Vol. 123. - P. 275 - 364.
13. *Brack M., Bhaduri R.K.* Semiclassical Physics / 2-nd edition. - Boulder: Westview Press, 2003. - 458 p.
14. *Chabanat E., Bonche P., Haensel P. et al.* A Skyrme parametrization from subnuclear to neutron star densities // Nucl. Phys. - 1997. - Vol. A627. - P. 710 - 746; *Ibid.* - 1998. - Vol. A635. - P. 231 - 256.
15. *Denisov V.Yu.* Dipole resonances in the gas-liquid model of the nucleus // Sov. J. Nucl. Phys. - 1986. - Vol. 43. - P. 28 - 35.
16. *Kolomietz V.M., Magner A.G.* Collective excitations in Neutron-Rich Nuclei within the Model of a Fermi Liquid Drop // Phys. Atom. Nucl. - 2000. - Vol. 63. - P. 1732 - 1739.
17. *Kolomietz V.M., Magner A.G., Shlomo S.* Splitting of the isovector giant dipole resonances in neutron-rich spherical nuclei // Phys. Rev. - 2006. - Vol. C73. - P. 024312 (15 pages).
18. *Eisenberg J.M., Greiner W.* Nuclear Theory. Vol. 1. Nuclear Models: Collective and Single-Particle Phenomena. - Amsterdam-London: North-Holland Publishing Company, 1970. - 456 p.
19. *Plujko V.A., Gorbachenko O.M., Capote R., Bondar V.M.* Statistical description of dipole gamma-transitions in atomic nuclei // Proc. of the 3-rd Int. Conf. “Current problems in Nuclear Physics and Atomic Energy (Kyiv, Ukraine, June 7 - 12, 2010). Part I. - Kyiv, 2011. - P. 342 - 346.
20. *Plujko V.A., Gorbachenko O.M., Bondar V.M., Capote R.* Renewed Datebase of GDR Parameters for Atomic Nuclei // J. of the Korean Physical Society. - 2011. - Vol. 59. - No. 2. - P. 1514 - 1517.
21. *Plujko V.A., Capote R., Gorbachenko O.M.* Giant dipole resonance parameters with uncertainties from photonuclear cross sections // Atomic Data and Nuclear Data Tables. - 2011. - Vol. 97. - No 5. - P. 567 - 585.
22. *Ring P.* Theory of dipole-resonances in nuclei close and far from stability // Zakopane Conf. on Nuclear Physics (August 27 - September 2, 2012).
23. *Siem S.* Small resonances on the tail of the giant dipole resonances // The 4-th Int. Conf. “Current Problems in Nuclear Physics and Atomic Energy (Kyiv, Ukraine, September 3 - 7, 2012).
24. *Strutinsky V.M., Magner A.G.* Quasiclassical theory of nuclear shell structure // Sov. J. Part. Nucl . -1976. - Vol. 7. - P. 138 - 418.
25. *Gzhebinsky A.M., Magner A.G., Fedotkin S.N.* Low-lying collective excitations of nuclei as a semiclassical response // Phys. Rev. - 2007. - Vol. C76. - P. 064315 (16 pages).
26. *Blocki J.P., Magner A.G., Yatsyshyn I.S.* Gross-shell effects in the dissipative nuclear dynamics // Int. J. Mod. Phys. - 2012. - Vol. E21. - P. 1250034 (9 pages).

DIFFERENTIAL CROSS-SECTIONS OF PROMPT γ-RAY YIELD PRODUCED IN (n, xγ) REACTIONS BY 14 MeV NEUTRONS ON CADMIUM

B. M. Bondar[1], V. M. Bondar[1,2], O. M. Gorbachenko[1], I. M. Kadenko[1], B. Yu. Leshchenko[1,2], Yu. M. Onishchuk[1], V. A. Plujko[1]

[1] Nuclear Physics Department, Taras Shevchenko National University, Kyiv, Ukraine
[2] National Technical University of Ukraine "Kyiv Polytechnic Institute", Kyiv, Ukraine

Differential cross sections of ^{nat}Cd(n, xγ) reactions measured using time-of-flight method are presented. Pulse neutron generator was used as neutron source of 14 MeV neutrons. Experimental results are compared with theoretical calculations performed within Hauser - Feshbach statistical model. EMPIRE and TALYS codes were used for the calculations. Sensitivity of the calculated cross sections to the characteristics of excited nuclei is analyzed.

Introduction

Nuclear data on (n, xγ) reactions induced by fast neutrons are of considerable interest for the development of the advanced reactor technologies as well as for investigations of the different nuclear reaction mechanisms in the neutron induced reactions, characteristics of excited nuclear states and its decay. The experimental measurements are usually performed with 14.1 MeV neutrons due to the possibility of using neutron generators based on DT-reaction, but the experiments in which γ-spectra was obtained in full energy range (up to the highest possible excitation energy) are practically absent.

In this contribution we present results of the investigation of the γ-spectra within the energy interval from 2 to 18 MeV. Differential cross sections of the (n, xγ) reactions for cadmium were unfolded from amplitude instrumental spectra and cross sections uncertainties were estimated. The experimental cross sections are compared with theoretical calculations performed assuming gamma-emission from compound nucleus as well as emission on preequilibrium processes.

Experimental technique

The measurements of γ-spectra are performed using scintillation γ-spectrometer based on 15×10 cm NaI(Tl) detector. Reaction T(d, n)^{4}He in Ti-T target was used as neutron source. Deuterons were accelerated by low-voltage accelerator with klystron bunching of deuteron beam and finally deuteron energy was 130 KeV. Pulse generation frequency was equal to 7.25 MHz, average neutron intensity ~ 10^7 s^{-1}. Measurements were performed with neutrons of energy 14.0±0.2 MeV which corresponds to the angle 90 ° relatively to the deuteron beam line. The geometry of the experiment is presented in Fig. 1.

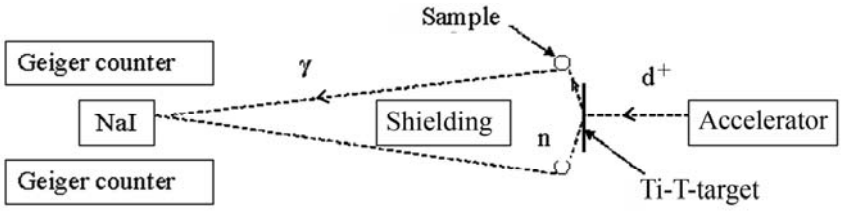

Fig. 1. Geometry of the experiment.

Measurements have been performed in circular geometry. Neutron source was placed in the centre of ring sample of cadmium with radius 16 cm. Time-of-flight method was applied for separation of prompt γ-rays from source neutrons, background and rescattered γ-rays.The flight path between the neutron source and NaI(Tl) detector was equal to 172 cm which provides reliable separation of prompt γ-rays from neutron and γ-ray background. More details concerning experiment can be found in Refs. [1, 2].

Relation between amplitude spectra $A(V, \Delta V, \theta_\gamma)$ and differential cross section $\sigma_\gamma(E_\gamma, \theta_\gamma) \equiv d^2\sigma(E_\gamma, \theta_\gamma) / dE_\gamma d\Omega_\gamma$ is given by the expression

$$A(V, \Delta V, \theta_\gamma) = \int_0^{E_{max}} R(V, E_\gamma) \cdot \sigma_\gamma(E_\gamma, \theta_\gamma) dE_\gamma, \tag{1}$$

$$R(V, E_\gamma) = \int_{V-\Delta V/2}^{V+\Delta V/2} G\alpha_\gamma(E_\gamma)\varepsilon(V, E_\gamma) dV\,, \tag{2}$$

where V is signal amplitude; ΔV - signal amplitude width; θ_γ - scattering angle; E_γ - γ-ray energy; G - geometry

factor; $\alpha(E_\gamma)$ - energy-depended coefficient of the γ-ray self-absorption by sample detector; $\varepsilon(V, E_\gamma)$ - detector response function. Double differential cross section $\sigma_\gamma(E_\gamma, \theta_\gamma)$ have been measured at $\theta_\gamma = 90°$. Weak angle dependence of the cross section allows to estimate energy spectra $\sigma(E_\gamma)$ in the following way

$$\sigma(E_\gamma) \equiv \frac{d\sigma(E_\gamma)}{dE_\gamma} = 4\pi \cdot \sigma_\gamma(E_\gamma, \theta_\gamma) \tag{3}$$

The expression for the detector response function $A(V, E_\gamma)$ was taken from Ref. [3].

Data analysis and results

The Fredholm integral equation of the first kind should be solved to unfold cross section $\sigma(E_\gamma)$ from amplitude spectrum $U(V)$

$$\int_0^{E_{max}} R(V, E_\gamma)\sigma(E_\gamma)dE_\gamma = U(V) \tag{4}$$

There are problems in solving (4) due to instability of unfolded spectra to the experimental data uncertainties (so called ill-posed). To find cross section $\sigma(E_\gamma)$ an algorithm on the compact set of limited variations [4] was used. Uncertainties of the cross sections were estimated in assumption that the amplitude spectrum is distributed with Gauss distributions due to the large number of external factors. More details about estimation of cross section uncertainties can be found in [2].

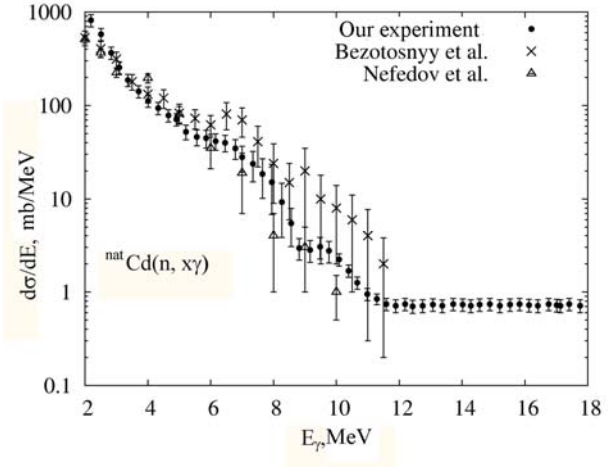

Fig. 2. Differential cross sections of the reactions ^{nat}Cd(n, xγ) obtained using regularization algorithm on the compact set of limited variations: points – results of our experiment, crosses – experimental data from [5], triangles – [6].

Experimental values of the unfolded differential cross sections and their uncertainties are shown in Fig. 2.

As one can see, stable solution is obtained for the cross sections of the ^{nat}Cd(n, xγ) reactions. Set of monotonically decreasing functions were used for the unfolding procedure. Rather good agreement of our experimental results with results from Ref. [5, 6] is obtained.

Calculations and discussions

Experimental results were compared with theoretical calculations performed allowing gamma-emission from compound nucleus (CN) and pre-equilibrium stages [7]. Calculations of inclusive γ-spectrum for (n, xγ) reactions were performed by summarizing of exclusive spectra for all possible $(n, ib_+j\gamma)$ reactions:

$$\frac{d\sigma(n, x\gamma)}{dE_\gamma} = \sum_j \sum_i \frac{d\sigma(n, ib + j\gamma)}{dE_\gamma}, \tag{4}$$

where i – is number of emitted particles b (b =n, p, d, t, α) and j – is number of emitted γ-rays.

Calculations assuming CN emission were performed using the Hauser - Feshbach statistical model. Within the framework of this model for example, cross section of the reaction (*a, bc*) with emission of particles *b* and *c* is given by the following expression

$$\frac{d\sigma(E, J_X, J_z)}{dE_b} = \sum_{J_C, \pi} \sigma_C(J_C, E, J_X, \pi) R_{C,b}(U_Y, J_Y, U_C, J_C, \pi) \cdot \int_0^{E_{max}^{bC} - E_b} RY, c(U_Z, J_Z; U_Y, J_Y), \tag{6}$$

where σ_C – cross section of the compound nucleus (CN) production with excitation energy U_C; spin J_C and parity π, E – energy of initial particle; X – initial nucleus, Y – nucleus residual after emission of particle *b*, Z - nucleus residual after emission of particle *c*, J_X, J_Y and J_Z – spin of X,Y and Z nuclei respectively. Probability $R_{C,b}$ of CN-decay with emission of particle *b* is given by:

$$R_{C,b}(U_Y, J_Y; U_C, J_C) = I_{C,b}(U_Y, J_Y, U_C, J_C) / \left\{ \sum_{b', J_{Y'}} \int_o^{E_{max}^{b'}} I_{C,b'}(U_{Y'}, J_{Y'}; U_C, J_C) \right\}, \tag{7}$$

$$I_{C,b}(U_Y, J_Y; U_C, J_C) = \frac{1}{2\pi\hbar} \times \sum_{j=|J_Y - J_C|}^{J_Y + J_C} \sum_{\pi'} \sum_{l=|j - J_b|}^{j + J_b} T_l^{j,\pi'}(E) \cdot \frac{\rho_{C-b}(U_Y, J_Y, \pi')}{\rho_C(U_C, J_C, \pi)} dE. \tag{8}$$

Here $U_Y = U_C - S_{bC} - E$ is excitation energy of residual nucleus Y; S_{bC} - is separation energy of the particle b from CN; ρ_C is nuclear level density of CN; ρ_{C-b} - nuclear level density of residual nuclei; $T_b^{l,j}$ stands for the transmission coefficient for emitted particle b with energy $E_b = U_C - S_{bC} - U_Y$ and orbital angular momentum l which together with particle spin s couples to the channel angular momentum j. Probability $R_{Y,,c}$ of decay of Y-nucleus with emission of particle c can be defined by Eq. (7) with indexes Y, c and Z instead of C ,b and Y respectively. In case of nucleons - transmission coefficient is calculated using optical model, whether for γ-rays the following expression for transmission coefficient is used:

$$T_l^{lj\pi'} = 2\pi \cdot \sum_{X=E,M} \omega_X(l,\pi') \cdot E_\gamma^{2\lambda+1} \bar{f}_{X\lambda}(E_\gamma), \tag{9}$$

where factor $\omega_X(l,\pi')$ is taking into account law of parity conservation, $\bar{f}_{X\lambda}(E_\gamma)$ - radiation strength function (RSF) of the γ-decay.

Fig. 3 shows experimental differential cross sections of the reactions ^{nat}Cd(n, xγ) in comparison with theoretical calculations performed using EMPIRE [8] and TALYS [9] codes with default set of input parameters. Calculations have been performed with and without taking into account preequiliblirum emission.

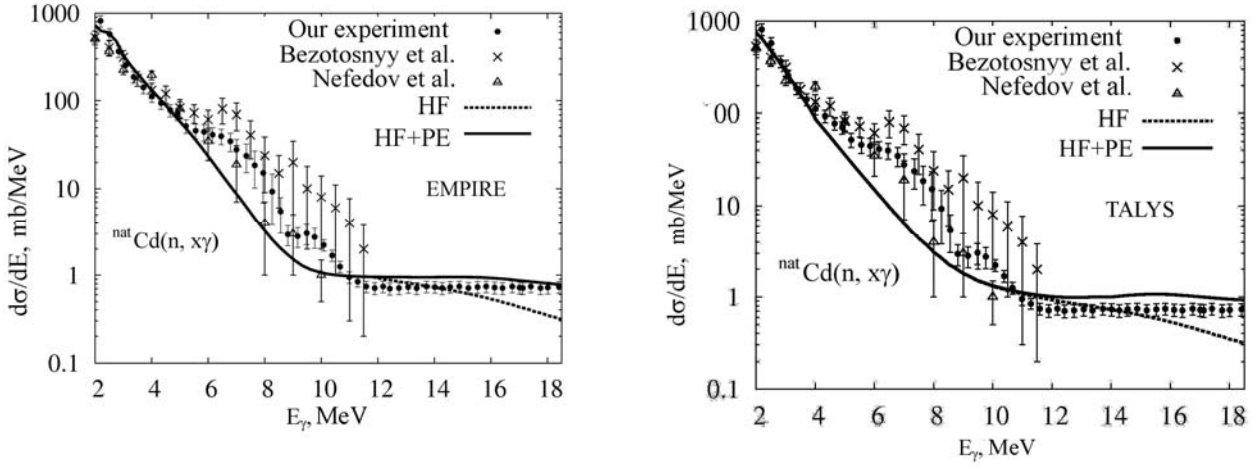

a *b*

Fig. 3. Differential cross sections of the reactions ^{nat}Cd(n, xγ) performed using EMPIRE (*a*) and TALYS (*b*) codes: points – our experimental results, solid curve – calculations within Hauser - Feshbach statistical model, dashed curve – calculations within Hauser - Feshbach statistical model with taking into account preequilibrium emission (PE).

As one can see from Fig. 3, rather satisfactory agreement of the theoretical calculations with experimental data is obtained for the ^{nat}Cd(n, xγ) reactions almost in all energy range accept interval from 6 MeV to 11 MeV, where experimental results exceed theoretical ones. It is also can be concluded that taking into account preequilibrium processes gives the better agreement of experimental data and theoretical calculations for the energy range above 12 MeV. Calculations within EMPIRE and TALYS codes are in rather good agreement.

As it can be seen from Eqs. (6) - (9), the following input parameters are required for cross section calculations: optical potential, nuclear level density and RSF. In this work we analyzed the sensitivity of the calculated cross sections to input parameters mentioned above [10].

To investigate dependence of the cross sections on optical potential we have used different potentials from Refs. [11 - 13]. Potential parameters were obtained from the fitting of the experimental data on the elastic neutron scattering. According to our calculations, cross sections of the ^{nat}Cd(n, xγ) reactions are practically insensitive to the optical potential variation.

To check sensitivity of the cross sections to the different approaches for nuclear level densities the following models were used: Enhanced Generalized Super-Fluid Model (EGSM), Back-Shifted-Fermi-Gas Model (BSFG) and Gilbert-Cameron approach (GC). More detailed description of all the models mentioned above can be found in Ref. [10]. Fig. 4 demonstrates the example of the dependence of ^{nat}Cd(n, xγ) reaction cross sections on nuclear level density. It can be seen from Fig. 4 that theoretical results obtained using both EGSM and BSFG models gives rather same agreement of theoretical calculations with experimental results.

We also checked sensitivity of the calculations to the shape of RSF. Calculations were performed using the following models [10]: Standart Loretzian (SLO), Enchanced Generalized Loretzian (EGLO), modified Loretzian (MLO1), Generalized Fermi liquid (GFL) model. For the nuclear level densities EGSM model was used. Results of the calculations are shown in Fig. 5.

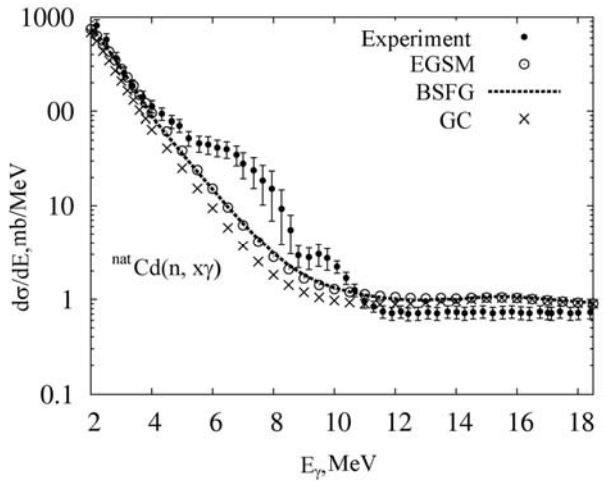

Fig. 4. Differential cross sections of the ^{nat}Cd(n, xγ) reactions calculated with EMPIRE code using different models different models for the nuclear level densities: open circles – EGSM model, dashed curve – BSFG model, crosses – Gilbert-Cameron approach. Experimental results are shown by points.

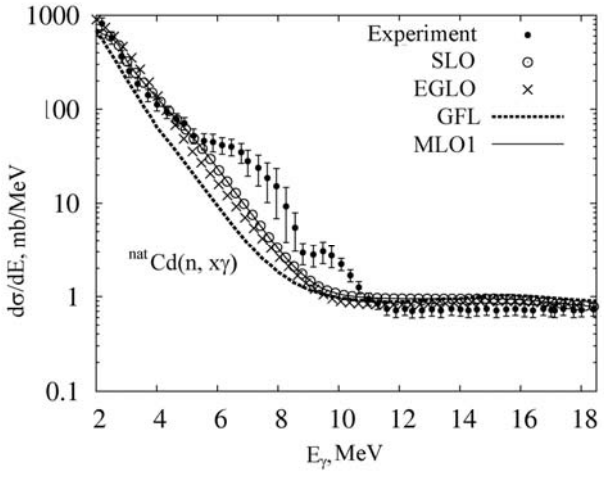

Fig. 5. Differential cross sections of the ^{nat}Cd(n, xγ) reactions calculated with EMPIRE code using different models for the RSF : dashed curve – SLO model, open circles – EGLO, solid line – MLO1. Experimental results are shown by points.

As one can see, the best agreement with the experiment is obtained in case of using SLO and MLO models for radiative strength function.

From the results presented on Figs. 4-6, one can conclude that good agreement of the theoretical calculations with experimental results can be obtained in the case of simultaneous changes of the models both the nuclear level density and radiative strength function .

Conclusions

Differential cross sections of ^{nat}Cd(n, xγ) reactions were measured using time-of-flight technique. The algorithm on the compact set of limited variations was used in order to obtain the cross sections values. Cross section uncertainties are extimated.

Experimental results are compared with theoretical calculations performed in consideration of gamma-emission from equilibrium as well as from preequilibrium stages. Results of the calculations are rather in good agreement with experimental data except energy region from 6 to 11 MeV. Disagreement within mentioned interval can be caused by uncertainties of the input parameters of the calculations. It is also demonstrated that taking into account preequilibrium processes gives the best agreement of experimental data and theoretical calculations.

In order to obtain the best agreement of calculated cross sections with experimental results, the optimal set of models for RSF, nuclear level densities and optical potential should be used. According to our analysis, cross sections of ^{nat}Cd(n, xγ) reactions calculated by the use SLO and MLO models for radiative strength functions with EGSM for the nuclear level densities give the best agreement with experimental results.

REFERENCES

1. *Bondar V.M., Kadenko I.M., Leshchenko B.Yu. et al.* Cross sections of gamma-ray production by fast neutrons on iron and bismuth nuclei // Bull. Russian Acad. Sciences: Physics. - 2009. - Vol. 73. - P. 1511 - 1514.
2. *Bondar V.M., Kadenko I.M., Leshchenko B.Yu. et al.* Differential cross sections of gamma-ray emission in the interactions on fast neutrons with cadmium // Nuclear Physics and Atomic Energy. - 2011. -Vol. 12, No. 2. - P. 129 - 136.
3. *Gurevich G.M., Mazur V.M., Solodukhov G.V.* Apparatus function of scintillation γ-spectrometer based on large NaI(Tl) detector // Instruments and Experimental Techniques. - 1975. - Vol. 2. - P. 59 - 62 (in Russian).
4. *Tikhonov A.N., Goncharsky A.V., Stepanov V.V., Yagola A.G.* Numerical methods for the solution of ill-posed problems. - M., 1990. - 286 p. (in Russian).
5. *Bezotosnyi V.M., Gorbachev V.M., Efimova M.A. et al.* Cross sections of γ-rays in inelastic scattering produced by 14 MeV neurtons on different nuclei // Atomic Energy. - 1980. - Vol. 4. - P. 239 - 242.
6. *Nefedov Yu.Ya, Nagornyy V.I., Semenov V.I. et al.* // Vop. At. Nauki i Tekhn., Ser.Yadernye Konstanty. - 2000. - Vol. 1. - P. 7 - 242.
7. *Gadioli E., Hodson P.E.* Pre-Equilibrum Nuclear Reactions. - Oxford: Clarendon Press, 1992. - 518 p.
8. *Herman M., Capote R., Carlson B. V. et al.* EMPIRE: Nuclear Reaction Model Code System for Data Evaluation // Nucl. Data Sheets. - 2007. - Vol. 108. - P. 2655 - 2719.

9. *Koning A.J., Hilaire S., Duijvestijn M.C.* In TALYS-1.0 // Proc. of the Int. Conf. on Nuclear Data for Science and Technology (ND2007, Nice, France, April 22 - 27, 2007). - P. 211 - 214.
10. *Capote R., Herman M., Oblovzinsky P. et al.* Parameters for calculation of nuclear reactions of relevance for energy and non-energy nuclear applications // Nucl. Data Sheets. - 2009. - Vol. 110. - P. 3107 - 3214; http://www-nds.iaea.org/RIPL-3/.
11. *Koning A.J., Delatoche J.P.* // Nucl. Phys. - 2003. - Vol. A713. - P. 231 - 310.
12. *Wilmore D.*, *Hodgson P.E.* // Nucl. Phys. - 1964. - Vol. 55. - P. 673 - 694.
13. *Becchetti F.D., Greenlees G.W. //* Phys. Rev. - 2000. - Vol. 182. - P. 1190 - 1209.

UNIFIED MODEL FOR ALPHA-DECAY AND ALPHA-CAPTURE

V. Yu. Denisov

Institute for Nuclear Research, National Academy of Sciences of Ukraine, Kyiv, Ukraine

A unified model for alpha-decay and alpha-capture is discussed. Simultaneously the half-lives for alpha-transition between ground states as well as ground and excited states and alpha-capture cross-sections by spherical magic or near-magic nuclei are well described in the framework of this model. Using these data the alpha-nucleus potential is obtained. The simple empirical relations for handy evaluation of the half-lives for alpha-transition, which take into account both the angular momentum and parity of alpha-transition, are presented.

1. Introduction

Alpha-decay is very important and widely known process in nuclear physics [1]. The experimental information on alpha-decay half-lives is extensive and is being continually updated [1]. The theory of alpha-decay was formulated by Georgii Antonovich Gamow in 1927. Various microscopic, macroscopic cluster, fission and simple empirical approaches to the description of alpha-decay have been proposed; see Refs cited in [2 - 6].

The unified model for alpha-decay and alpha-capture (UMADAC) [2 - 5] allows describing two opposite processes the alpha-particle emission from parent nucleus and capture of alpha-particle by daughter nucleus at the same time. The same potential between alpha-particle and daughter nucleus is used for description of the both processes. The ranges of parameters of the model can be reduced and refined by using such set of data. In the framework of the UMADAC we can describe alpha-transitions between ground states as well as ground and excited states for all range of nuclei, which can decay by alpha-emission, and alpha-capture cross-sections near and well-below barrier.

Simple and accurate empirical relationships for handy evaluation the alpha-decay half-lives are still required. Here we discuss the sets of empirical relationships for alpha-decay half-lives [6], which for the first time take into account both the angular momentum and parity of alpha-transition. Due to these effects the accuracy of these empirical relations is drastically improved and very high.

Short description of both the UMADAC and simple empirical relations is presented here.

2. UMADAC

The both data for alpha-decays andsubbarrier fusion for determining the alpha-nucleus potential are used in this model [2 - 5]. The alpha-decay half-lives $T_{1/2}$ in UMADAC depends on the total width Γ of the alpha-emission [2 - 5]

$$T_{1/2} = \hbar \cdot \ln(2)/\Gamma\,. \tag{1}$$

The total width Γ is the averaging on the partial width$\gamma(\theta,\varphi)$, related to alpha-particle emission in direction (θ,φ), therefore

$$\Gamma = \frac{1}{4\pi}\int \gamma(\theta,\varphi)d\Omega. \tag{2}$$

For axial-symmetric nuclei the partial emission width in the direction θ is

$$\gamma(\theta) = \hbar \cdot 10^{\nu} \cdot t(E_\alpha,\theta,\ell), \tag{3}$$

where 10^{ν} is the alpha-particle assault frequency (i.e., the frequency of collisions with the barrier), which takes into account the alpha-particle preformation, $t(E_\alpha,\theta,\ell)$ is the transmission coefficient, which gives the probability of penetration through the barrier, and E_α is the released energy of alpha-decay. The transmission coefficient in the WKB approximation is

$$t(E_\alpha,\theta,\ell) = \frac{1}{1+\exp\left[\frac{2}{\hbar}\int_{a(\theta)}^{b(\theta)} dr\sqrt{2\mu(v(r,E_\alpha,\theta,\ell)-E_\alpha)}\right]}, \tag{4}$$

where $a(\theta)$ and b(θ) are the turning points, where $v(r,E_\alpha,\theta,\ell)|_{r=a(\theta),b(\theta)} = E_\alpha$, μ is the reduced mass. The alpha-nucleus potential $v(r,E_\alpha,\theta,\ell)$ consists of Coulomb $v_C(r,\theta)$, nuclear $v_N(r,E_\alpha,\theta)$ and centrifugal $v_\ell(r,\ell)$ parts

$$v(r,E_\alpha,\theta,\ell) = v_C(r,\theta) + v_N(r,E_\alpha,\theta) + v_\ell(r,\ell), \tag{5}$$

which are

$$v_C(r,\theta) = \frac{2Ze^2}{r}\left[1 + \frac{3R^2}{5r^2}\beta_2 Y_{20}(\theta) + \frac{3R^4}{9r^4}\beta_4 Y_{40}(\theta)\right], \text{for } r \geq r_C,$$

$$v_C(r,\theta) \approx \frac{2Ze^2}{r_C}\left[\frac{3}{2} - \frac{r^2}{2r_C^2} + \frac{3R^2}{5r_C^2}\beta_2 Y_{20}(\theta)\left(2 - \frac{r^3}{r_C^3}\right) + \frac{3R^4}{9r_C^4}\beta_4 Y_{40}(\theta)\left(\frac{7}{2} - \frac{5r^2}{2r_C^2}\right)\right], \text{for } r \leq r_C, \quad (6)$$

$$v_N(r, E_\alpha, \theta) = \frac{V(E_\alpha)}{1 + \exp\left[\left(r - r_C(\theta)\right)/d\right]}, \quad (7)$$

$$v_\ell(r,\ell) = \frac{\hbar^2 \ell(\ell+1)}{2\mu r^2}. \quad (8)$$

Here Z, R, β_2 and β_4 are number of protons, radius, quadrupole and hexadecapole deformations of daughter nucleus, e is the charge of proton, $Y_{20}(\theta)$ and $Y_{40}(\theta)$ are the spherical harmonic functions; $V(E_\alpha)$ and $r_C(\theta)$ are the depth and effective radius of alpha-nucleus potential.

The alpha-particle emission from nuclei obeys the spin-parity selection rule. The minimal value of alpha-particle at alpha-transition is

$$\ell_{\min} = \begin{cases} \Delta_j \text{ for even } \Delta_j \text{ та } \pi_p = \pi_d \\ \Delta_j + 1 \text{ for odd } \Delta_j \text{ та } \pi_p = \pi_d \\ \Delta_j \text{ for odd } \Delta_j \text{ та } \pi_p \neq \pi_d \\ \Delta_j + 1 \text{ for even } \Delta_j \text{ та } \pi_p \neq \pi_d \end{cases}. \quad (9)$$

Here $\Delta_j = |j_p - j_d|, j_p, \pi_p$ and j_d, π_d are the spin and parity values of the parent and daughter nuclei, respectively.

The alpha-capture cross-section is

$$\sigma(E_\alpha) = \frac{\pi\hbar^2}{2\mu E_\alpha}\int_0^{\pi/2}\sum_\ell (2\ell+1)\, t(E_\alpha,\theta,\ell)\sin(\theta)\, d\theta, \quad (10)$$

where transmission coefficient $t(E_\alpha,\theta,\ell)$ is defined by Eq. (4).

To build the alpha-nucleus interaction potential only precise experimental data for alpha-decay half-lives, total probabilities of the alpha-decays and corresponding branch ratios for ground-state to ground-state alpha-transitions are used. The energies of alpha-transitions are evaluated by atomic masses, but the alpha-decay is the pure nuclear process related to emission of alpha-particle from the parent nucleus. Therefore we take into account the contribution of atomic electronic shell energy into the atomic mass at evaluation of the energy of alpha-transition

$$E_\alpha = \Delta M_p - (\Delta M_d + \Delta M_\alpha) + k\left(Z_p^\varepsilon - Z_d^\varepsilon\right), \quad (11)$$

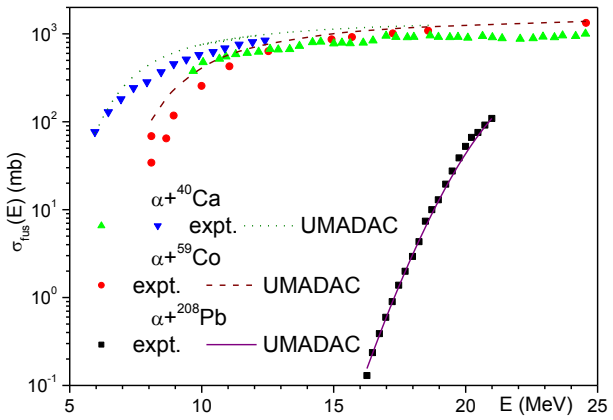

Fig. 1. The comparison of alpha-capture cross-sections near and below barrier for nuclei ^{208}Pb, ^{209}Bi, ^{59}Co and ^{40,44}Ca evaluated in the UMADAC with the experimental data.

where $\Delta M_{p,d,\alpha}$ are the mass defects of parent, daughter and alpha-particle nuclei respectively, kZ_p^ε and kZ_d^ε are electrons binding energy of parent and daughter atoms. The experimental values of the alpha - capture reaction cross sections for spherical and near spherical nuclei ^{208}Pb, ^{209}Bi, ^{59}Co and ^{40,44}Ca are also considered. As the result we find the potential parameters and well describe the data for alpha-decay half-lives in 344 nuclei and alpha-capture cross-section near and below barrier for nuclei ^{208}Pb, ^{209}Bi, ^{59}Co and ^{40,44}Ca. The RMS errors of decimal logarithm of half-lives

$$\delta = \sqrt{\frac{1}{N-1}\sum_{k=1}^{N}\left[\log_{10}\left(T_{1/2}^{theor}\right) - \log_{10}\left(T_{1/2}^{exp}\right)\right]^2}$$

calculated for the total set of nuclei in the framework of the UMADAC is 0.6199 [3]. The RMS errors evaluated

for the even-even, even-odd, odd-even and odd-odd subsets of nuclei in the framework of the UMADAC are 0.2980, 0.7805, 0.7613 and 0.7405 respectively [3].The values of RMS errors are lower than the ones in previous works, see for details [3]. The comparison of alpha-capture cross-section near and below barrier for nuclei ^{208}Pb, ^{209}Bi, ^{59}Co and ^{40,44}Ca evaluated in the UMADAC with the experimental data are given in Fig. 1 (the details for this Figure are discussed in Ref. [2]).

Note that many daughter nuclei formed at alpha-decay are deformed. The deformation of nucleus leads to very important effect on the alpha-nucleus potential (Fig. 2). We see that various direction of the alpha-emission lead to various barrier heights and thicknesses, which are induced the strongly different values of the partial emission width. The emission of alpha-particle from equator of nucleus relates to the higher and thicker barrier, than the ones in the case of emission from the pole of nucleus. However the various direction of alpha-particle emission is equivalent, therefore it is necessary to make averaging on the all possible direction of emission, see eq. (2). The deformations of daughter nuclei are taken into account in the UMADAC. The values of deformation parameters are picked up from the experimental data or theoretical calculations (if there are no experimental data), see detail in [3].

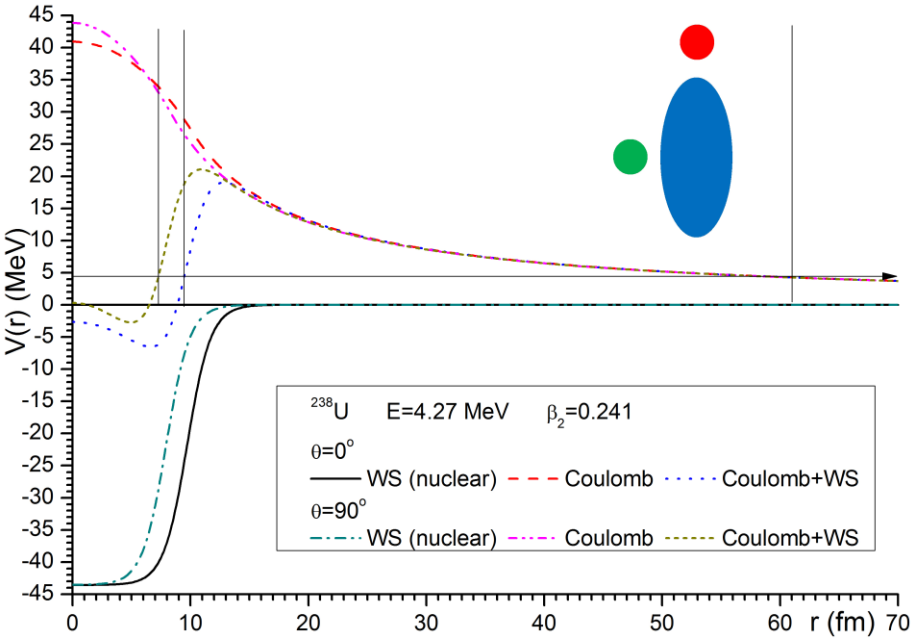

Fig. 2.The Coulomb, nuclear and total potentials between alpha-particle and ^{234}Th, which taken place at the alpha-decay of ^{238}U. E is the energy of alpha-decay transition.

The alpha-decay from the ground state of parent nucleus can go into various final states of daughter nucleus [4]. The experimentalist can observe such various transitions and measure the relative intensity of various transitions [1]. The experimental and theoretical probabilities B and half-lives T of alpha-decay into ground ($0^+ \rightarrow 0^+$transitions with $\ell_{min} = 0$) and first excited ($0^+ \rightarrow 2^+$transitions with $\ell_{min} = 2$) states are presented in the Table 1. Comparing the experimental and theoretical values of probabilities and half-lives we conclude that the UMADAC model describes well the data.

We propose in the framework of UMADAC that the shape of daughter nucleus and structure are the same as in the ground state. Due to this the difference between transitions into the ground and the first excited states is related to the contribution of centrifugal potential, see Eq. (8).However the structure of more excited states became much complex, due to this the structure effects became more important and the nuclear shape of strongly excited states deviate from the ground state the one. As the result, the quality of description of the both probabilities B and half-lives T is reduces with increasing the angular momentum of the transition, see [4] for details. Similar tendencies are also observed in other approximations for alpha-decay [5].

The half-lives of superheavy elements are discussed in the framework UMADAC too [5]. The alpha-decay half-lives of even-even superheavy elements within the range of proton number $104 \leq Z \leq 126$, which can be formed by possible cold and hot fusion reactions,are calculated in the framework of the UMADAC and various other approaches for alpha-decay half-life evaluation and by using the Q-values of alpha-transitions obtained within different approximations for atomic masses. The dependencies of alpha-decay half-lives of superheavy elements on model approaches for both the Q-values and half-lives calculations are discussed in detail [5].

Table 1. **The experimental and theoretical probabilities *B* and half-lives *T* of alpha-decay into ground and first excited states, angular momentum of the transition ℓ_{min} and reaction *Q*-value.**

Parent and daughter nuclei	Transition	Q. MeV	ℓ_{min}	B^{exp}	B^{theor}	$T_{1/2}^{exp}$. s	$T_{1/2}^{theor}$. s
$^{222}_{88}\mathrm{Ra} \rightarrow {}^{218}_{86}\mathrm{Rn}$	$0^+ \rightarrow 0^+$	6.717	0	96.90	96.88	37.33	43.64
$^{222}_{88}\mathrm{Ra} \rightarrow {}^{218}_{86}\mathrm{Rn}$	$0^+ \rightarrow 2^+$	6.393	2	3.05	3.07	$1.19 \cdot 10^3$	$1.38 \cdot 10^3$
$^{224}_{88}\mathrm{Ra} \rightarrow {}^{220}_{86}\mathrm{Rn}$	$0^+ \rightarrow 0^+$	5.827	0	94.92	95.98	$3.33 \cdot 10^5$	$1.10 \cdot 10^6$
$^{224}_{88}\mathrm{Ra} \rightarrow {}^{220}_{86}\mathrm{Rn}$	$0^+ \rightarrow 2^+$	5.586	2	5.06	3.97	$6.25 \cdot 10^6$	$2.67 \cdot 10^7$
$^{228}_{90}\mathrm{Th} \rightarrow {}^{224}_{88}\mathrm{Ra}$	$0^+ \rightarrow 0^+$	5.560	0	72.20	77.39	$8.36 \cdot 10^7$	$1.39 \cdot 10^8$
$^{228}_{90}\mathrm{Th} \rightarrow {}^{224}_{88}\mathrm{Ra}$	$0^+ \rightarrow 2^+$	5.475	2	27.20	21.10	$2.22 \cdot 10^8$	$5.10 \cdot 10^8$
$^{232}_{90}\mathrm{Th} \rightarrow {}^{228}_{88}\mathrm{Ra}$	$0^+ \rightarrow 0^+$	4.121	0	78.20	81.81	$5.67 \cdot 10^{17}$	$1.40 \cdot 10^{18}$
$^{232}_{90}\mathrm{Th} \rightarrow {}^{228}_{88}\mathrm{Ra}$	$0^+ \rightarrow 2^+$	4.057	2	21.70	17.67	$2.04 \cdot 10^{18}$	$6.49 \cdot 10^{18}$
$^{236}_{92}\mathrm{U} \rightarrow {}^{232}_{90}\mathrm{Th}$	$0^+ \rightarrow 0^+$	4.614	0	74.00	72.72	$9.99 \cdot 10^{14}$	$1.16 \cdot 10^{15}$
$^{236}_{92}\mathrm{U} \rightarrow {}^{232}_{90}\mathrm{Th}$	$0^+ \rightarrow 2^+$	4.565	2	26.00	25.15	$2.84 \cdot 10^{15}$	$3.36 \cdot 10^{15}$
$^{238}_{92}\mathrm{U} \rightarrow {}^{234}_{90}\mathrm{Th}$	$0^+ \rightarrow 0^+$	4.311	0	79.00	75.25	$1.78 \cdot 10^{17}$	$4.39 \cdot 10^{17}$
$^{238}_{92}\mathrm{U} \rightarrow {}^{234}_{90}\mathrm{Th}$	$0^+ \rightarrow 2^+$	4.262	2	21.00	23.28	$6.71 \cdot 10^{17}$	$1.42 \cdot 10^{18}$
$^{240}_{94}\mathrm{Pu} \rightarrow {}^{236}_{92}\mathrm{U}$	$0^+ \rightarrow 0^+$	5.298	0	72.80	66.49	$2.84 \cdot 10^{11}$	$2.04 \cdot 10^{11}$
$^{240}_{94}\mathrm{Pu} \rightarrow {}^{236}_{92}\mathrm{U}$	$0^+ \rightarrow 2^+$	5.253	2	27.10	29.15	$7.64 \cdot 10^{11}$	$4.65 \cdot 10^{11}$
$^{242}_{94}\mathrm{Pu} \rightarrow {}^{238}_{92}\mathrm{U}$	$0^+ \rightarrow 0^+$	5.027	0	76.49	68.63	$1.54 \cdot 10^{13}$	$3.02 \cdot 10^{13}$
$^{242}_{94}\mathrm{Pu} \rightarrow {}^{238}_{92}\mathrm{U}$	$0^+ \rightarrow 2^+$	4.982	2	23.48	27.91	$5.02 \cdot 10^{13}$	$7.44 \cdot 10^{13}$

3. Empirical relations

Simple and accurate empirical relationships are very useful for handy evaluation of the alpha-decay half-lives for unknown cases. We found the sets of empirical relationships for alpha-decay half-lives [6], which for the first time take into account both the angular momentum and parity of alpha-transition. For full set of the alpha-transitions between the ground states we found [6] separate relations for even-even, even-odd, odd-even and odd-odd nuclei respectively

$$\log_{10}\left(T_{1/2}^{e-e}\right) = -26.1721 - 1.1549\frac{A^{1/6}Z^{1/2}}{\mu} + \frac{1.6088Z}{\sqrt{Q_\alpha}},$$

$$\log_{10}\left(T_{1/2}^{e-o}\right) = -30.2365 - 1.0726\frac{A^{1/6}Z^{1/2}}{\mu} + \frac{1.6910Z}{\sqrt{Q_\alpha}} + \frac{0.7198\sqrt{\ell(\ell+1)}}{Q_\alpha A^{-1/6}} - 0.6965\left((-1)^\ell - 1\right),$$

$$\log_{10}\left(T_{1/2}^{o-e}\right) = -30.0842 - 1.0853\frac{A^{1/6}Z^{1/2}}{\mu} + \frac{1.6925Z}{\sqrt{Q_\alpha}} + \frac{0.2453\sqrt{\ell(\ell+1)}}{Q_\alpha A^{-1/6}} - 0.6406\left((-1)^\ell - 1\right),$$

$$\log_{10}\left(T_{1/2}^{o-o}\right) = -30.8222 - 0.9874\frac{A^{1/6}Z^{1/2}}{\mu} + \frac{1.6577Z}{\sqrt{Q_\alpha}} + \frac{0.5893\sqrt{\ell(\ell+1)}}{Q_\alpha A^{-1/6}} - 0.2914\left((-1)^\ell - 1\right),$$

where $\mu = [6A/(A-4)]^{1/6}$.

For set of heavy nuclei (with Z > 82 and N > 126) we found [6] corresponding relations for alpha-decay half-lives for the alpha-transitions between the ground states in the forms

$$\log_{10}\left(T_{1/2}^{e-e}\right) = -28.0218 - 1.0790\frac{A^{1/6}Z^{1/2}}{\mu} + \frac{1.5858Z}{\sqrt{Q_\alpha}},$$

$$\log_{10}\left(T_{1/2}^{e-o}\right) = -35.0831 - 0.8378\frac{A^{1/6}Z^{1/2}}{\mu} + \frac{1.6721Z}{\sqrt{Q_\alpha}} + \frac{0.6687\sqrt{\ell(\ell+1)}}{Q_\alpha A^{-1/6}} - 0.6695\left((-1)^\ell - 1\right),$$

$$\log_{10}\left(T_{1/2}^{o-e}\right) = -33.8303 - 0.9461\frac{A^{1/6}Z^{1/2}}{\mu} + \frac{1.7047Z}{\sqrt{Q_\alpha}} + \frac{0.4372\sqrt{\ell(\ell+1)}}{Q_\alpha A^{-1/6}} - 0.5095\left((-1)^\ell - 1\right),$$

$$\log_{10}\left(T_{1/2}^{o-o}\right) = -40.9482 - 0.3717\frac{A^{1/6}Z^{1/2}}{\mu} + \frac{1.5229Z}{\sqrt{Q_\alpha}} + \frac{1.4082\sqrt{\ell(\ell+1)}}{Q_\alpha A^{-1/6}} - 0.0127\left((-1)^\ell - 1\right).$$

For set of light nuclei (rest of nuclei after subtractions the set of heavy nuclei from the full set) we found [6] corresponding relationships for alpha-decay half-lives for the alpha-transitions between the ground states in the forms

$$\log_{10}\left(T_{1/2}^{e-e}\right) = -29.2462 - 1.0372\frac{A^{1/6}Z^{1/2}}{\mu} + \frac{1.6317Z}{\sqrt{Q_\alpha}},$$

$$\log_{10}\left(T_{1/2}^{e-o}\right) = -29.3796 - 1.0807\frac{A^{1/6}Z^{1/2}}{\mu} + \frac{1.6700Z}{\sqrt{Q_\alpha}} + \frac{0.8009\sqrt{\ell(\ell+1)}}{Q_\alpha A^{-1/6}} - 0.7403\left((-1)^\ell - 1\right),$$

$$\log_{10}\left(T_{1/2}^{o-e}\right) = -28.4185 - 1.1143\frac{A^{1/6}Z^{1/2}}{\mu} + \frac{1.6614Z}{\sqrt{Q_\alpha}} + \frac{0.2246\sqrt{\ell(\ell+1)}}{Q_\alpha A^{-1/6}} - 0.7244\left((-1)^\ell - 1\right),$$

$$\log_{10}\left(T_{1/2}^{o-o}\right) = -32.0319 - 1.0415\frac{A^{1/6}Z^{1/2}}{\mu} + \frac{1.7326Z}{\sqrt{Q_\alpha}} + \frac{0.3596\sqrt{\ell(\ell+1)}}{Q_\alpha A^{-1/6}} + 0.0903\left((-1)^\ell - 1\right).$$

The RMS errors of decimal logarithm of half-lives calculated for the total, heavy and light sets of nuclei are presented in Table 2.

Table 2. **The RMS errors of decimal logarithm of half-lives calculated for the total, heavy and light sets of nuclei**

	RMS errors				
	total set	even-even	Even-odd	odd-even	odd-odd
full set of nuclei	0.5488	0.3308	0.6177	0.6772	0.6916
set of heavy nuclei	0.5291	0.1907	0.6610	0.7590	0.5388
set of light nuclei	0.4955	0.2674	0.5767	0.5834	0.6653

In conclusion, we found parameters of UMADAC using both the data for alpha-decay half-lives in 344 nuclei and the data for alpha-capture cross-section near and below barrier for nuclei ^{208}Pb, ^{209}Bi, ^{59}Co and ^{40,44}Ca. We fitted experimental alpha-decay half-lives between ground states for 344 nuclei and find parameters of empirical relations which take into account both the angular momentum and parity of alpha-transitions. We split these relations for full, light and heavy subsets, as well as even-even, even-odd, odd-even and odd-odd subsets additionally. We obtain good description of available data in our approaches.

REFERENCES

1. *http://nndc.bnl.gov*
2. *DenisovV.Yu., Ikezoe H.* α-Nucleus potential for α-decayand sub-barrier fusion // Phys. Rev. C. - 2005. - Vol. 72. - P. 064613.
3. *DenisovV.Yu., Khudenko A.A.* α-Decay half-lives, α-capture, and α-nucleus potential interaction potential // At. Data Nucl. Data Tabl. - 2009. - Vol. 95. - P. 815 - 835; Ibid. - 2011. - Vol. 97. - P. 187.
4. *DenisovV.Yu., Khudenko A.A.* α-Decays to ground and excited states of heavy deformed nuclei // Phys. Rev. C. - 2009. - Vol. 80. - P. 034603 (12 pages); Ibid. - 2010. - Vol. 82. - P. 059902(E) (1 page).
5. *DenisovV.Yu., Khudenko A.A.* α-decay of even-even superheavy elements // Phys. Rev. C. - 2010. - Vol. 81. - P. 034613 (12 pages); Ibid. - 2010. - Vol. 82. - P. 059903(E) (1 page).
6. *DenisovV.Yu., Khudenko A.A.* α-decay half-lives: Empirical relations // Phys. Rev. C. - 2009. - Vol. 79. - P. 054614, (5 pages); Ibid. - 2010. - Vol. 82. - P. 059901(E) (2 pages).

POLARIZED ELECTRIC DIPOLE MOMENT OF WELL-DEFORMED REFLECTION ASYMMETRIC NUCLEI

V. Yu. Denisov

Institute for Nuclear Research, National Academy of Sciences of Ukraine, Kyiv, Ukraine

The expression for polarized electric dipole moment of well-deformed reflection asymmetric nuclei is obtained in the framework of liquid-drop model in the case of geometrically similar proton and neutron surfaces. The expression for polarized electric dipole moment consists of the first and second orders terms. It is shown that the second-order correction terms of the polarized electric dipole moment are important for well-deformed nuclei.

1. Introduction

Reflection asymmetric deformation of nucleus induces the proton-neutron redistribution. As a result, the both proton and neutron density distributions became slightly polarized and reflection asymmetric in the nuclear volume. Due to such density polarization the position of proton center of mass is shifted relatively the nuclear center of mass; therefore reflection asymmetric nuclei have the polarized electric dipole moment (PEDM).

The PEDM of nuclei with quadrupole and octupole surface deformations was firstly obtained by V. M. Strutinsky in 1956 [1] in the framework of liquid-drop model. A short time later A. Bohr and B. R. Mottelson were evaluated the PEDM in the same model [2], but Strutinsky's derivation is the correct [3]. Note the PEDM discussed in Refs. [1 - 3] is only related to the proton-neutron polarization in the volume of nuclei with quadrupole and octupole surface deformations.The proton-neutron density polarization in the nuclear volume induces the variation of proton and neutron radii and, therefore, leads to the corresponding surface contribution into the PEDM [4 - 5].We emphasize that the PEDM obtained in the first non-zero order on multipole deformations of nuclear surface is proportional to $\beta_l\beta_{l+1}$and all expressions for the PEDM presented in Refs. [1 - 5] are derived in this approximation.Numerical study of the PEDM in well-deformed nuclei in Ref. [6] shows that the first approximation for PEDM is strongly underestimated the numerical one. Moreover the difference between the numerical and first-order values of PEDM increases with values of deformation parameters strongly [6].

The nuclei with quadrupole and octupole deformations, *E1* transitions and the PEDM are studied intensively. The PEDM plays important role in various phenomena of well-deformed reflection asymmetric nuclei. Thus Karpeshin has shown that well-deformed fission fragments of such shapes formed during prompt fission give rise to both the anomalous *E1* internal conversion and the prompt gamma radiation related to the PEDM [7 - 9]. The *E1* transitions possibly linked to octupole vibrations around super-deformed shape can be also enhanced by the PEDM [6]. Strong *E1* transitions related to the low-energy shape oscillations of negative parity in the first and second (isomeric) minima in actinides are also connected to the PEDM [10].

However application of expression for the PEDM obtained in the first order for well-deformed nuclei is questionable. Therefore it is desirable to obtain expression for the PEDM in the next order at least, which is the second order approximation for the PEDM contained terms proportional to $\beta_l\beta_{l'}\beta_{l''}$. Such expression should be helpful and practical for description of various nature *E1* transition in well-deformed nuclei. Below we derive such expression for PEDM, see also [11].

2. PEDM

Let us consider the axial nucleus with proton and neutron radii described by

$$\frac{R_p(\vartheta)}{R_{0p}} = \frac{R_n(\vartheta)}{R_{0n}} = 1 + \sum_{l=0}^{n} \beta_l Y_{l0}(\vartheta) = f(\vartheta)\,. \qquad (1)$$

There are no any density polarizations in spherical nuclei, therefore the equilibrium neutron and proton density distributions in deformed nucleus can be presented as $\rho_n = \rho_{0n} + \delta\rho_n$ and $\rho_p = \rho_{0p} + \delta\rho_p$. Here $\rho_{0n} = 3N/(4\pi R_{0n}^3)$ and $\rho_{0n} = 3Z/(4\pi R_{0p}^3)$are the equilibrium neutron and proton densities in spherical nucleus, $\delta\rho_n$ and $\delta\rho_p$ are the variations of neutron and proton densities induced by surface deformation, Z and N are the numbers of protons and neutrons in the nucleus. Due to high value of the nuclear matter incompressibility the total nuclear density $\rho = \rho_n + \rho_p$ in the nuclear volume is constant $\rho = \rho_{0n} + \rho_{0p}$, therefore $\delta\rho_n = -\delta\rho_p$.

We should take into account that the numbers of protons and neutrons in deformed nucleus are, respectively, Z and N; and the center of mass must lie in the plane of mirror symmetry of the nucleus [1, 5, 11, 12], because the reflection asymmetric nuclear shapes are coupled by sub-barrier tunnel transition [5, 11, 12]. These two conditions can be easy fulfilled by introduction of auxiliary monopole β_0 and dipole β_1 deformations. For the sake of simplicity we take into account the most important mutipole deformations of nuclear surface β_2, β_3, β_4, β_5, β_6.

The PEDM is defined as

$$D = e\int r\,\cos\vartheta\,\rho_p(\vartheta)\,d\mathrm{V}. \qquad (2)$$

Due to deviation of the nuclear surface from spherical form there is variation of the proton density into the nuclear volume $\delta\rho_p(r)$. The variation of nucleon density in nuclear volume induces the deviation of the proton radius $\delta R_p(\vartheta)$ from the equilibrium position on the nuclear surface. The proton radius variation induces the proton density variations in the volume $\delta R_p(\vartheta)\Delta S$, where ΔS isthe element of surface square. Therefore the PEDM in reflectionasymmetric nuclei with axial symmetry is relatedto the redistribution of protons relatively neutrons intothe nuclear volume and on the nuclear surface, see also [4, 5, 11],

$$D = D_v + D_s, \tag{3}$$

where

$$D_v \approx \int r\ \cos\vartheta\ [\rho_{0p}+\delta\rho_p(r)]\ dV = 2\pi e\ \int_0^{\pi} d\vartheta\ \sin\vartheta\ \cos\vartheta \int_0^{R_{0p}\,f(\vartheta)} dr\, r^3 \delta\rho_p(r)\,, \tag{4}$$

$$D_s \approx \int R_p(\vartheta)\cos\cos\vartheta\rho_{0p}\delta R_p(\vartheta)\,d\mathrm{S} = \frac{3Ze}{2}\int_0^{\pi} d\vartheta \sin\sin\vartheta\cos\cos\vartheta\left[1+\left(\frac{f'(\vartheta)}{f(\vartheta)}\right)^2\right]^{\frac{1}{2}} f(\vartheta)^3\,\delta R_p(\vartheta). \tag{5}$$

The proton (or neutron) density variation induced by surface deformation produces additional pressure on the free nuclear surface. Due to this pressure the position of corresponding surface is slightly shifted. Both the surface symmetry energy and Coulomb force counteract the surface shift and neutralize the additional pressure on the free nuclear surface induced by density variations, see for details [4, 5]. Normal to the surface variation of the proton radius is defined by the boundary condition [4, 5, 11], which equalizes the normal to surface pressures induced by density fluctuations, neutron-skin stiffness and Coulomb interaction, and equals to

$$\delta R_p(\vartheta) = -\frac{N}{A}\frac{3eR_0}{8QA^{\frac{1}{3}}}\left[\varphi\left(R_p(\vartheta)\right) - \int dS\,\varphi\left(R_p(\vartheta)\right)/\int dS\right], \tag{6}$$

where Q is the neutron-skin stiffness coefficient [4, 5, 11, 12], $\varphi(r)$ is the Coulomb potential related to the protons and A = Z + N. Note that $Z\delta R_p(\vartheta)+N\delta R_n(\vartheta) = 0$ [11].

We can evaluate the PEDM if we know $\delta\rho_p(r)$and $\varphi(r)$. Let us these quantities in the framework of liquid-drop model. The energy density functional, which is described density distribution in the nuclear volume, can be written in the simple form [1, 11]

$$\varepsilon \approx -a_v\,\rho + J\,\frac{(\rho_n-\rho_p)^2}{\rho} + e\,\rho_p\,\varphi = -a_v\,\rho + J\,\frac{(\rho-2\rho_p)^2}{\rho} + e\,\rho_p\,\varphi, \tag{7}$$

where $-a_v$ is the bulk energy per nucleon in symmetric nuclear matter and J is the volume symmetry energy. The energy of nucleus E is related to the energy density functional $E = \int dV\,E$. The equation determined the equilibrium distribution of the charge into the nuclear volume can be obtained by variation of the energy

$$\delta E = \delta\int dV\,[\varepsilon - \lambda\rho_p] = \int dV\,[-4J(\rho - 2\rho_p)/\rho + e\varphi - (a_v+\lambda)]\,\delta\rho_p \tag{8}$$

on $\delta\rho_p$ with the additional condition conserved the number of protons in the nucleus. As the result, we get

$$8J\rho_p = -\rho(e\varphi - 4J - \lambda'), \tag{9}$$

where $\lambda' = a_v + \lambda$ and λ is the Lagrangian coefficient related to the additional condition. The solution of this equation is

$$\rho_{0p} = \rho\left(\frac{1}{2} + \frac{\lambda'}{8J} - \frac{e\varphi}{8J}\right), \tag{10}$$

$$\delta\rho_p = -\frac{3eA(\varphi - <\varphi>)}{32\pi R_0^3 J}, \tag{11}$$

$$<\varphi> = \frac{\int dV\varphi}{\int dV}. \tag{12}$$

Substituting (6), (10) - (12) into (4) - (5) we link volume and surface contributions of PEDM with Coulomb potential, which for deformed nuclei can be presented as

$$\varphi(r) = e\int dV\,\frac{\rho_{0p}+\delta\rho_p(r')}{|r-r'|}. \tag{13}$$

It is possible to find potential $\varphi(r)$ by applying the perturbation theory [11]. We expand the potential and the variation of proton density into the perturbation series

$$\varphi(r) \approx \varphi_0(r) + \varphi_1(r) + \varphi_2(r) + \cdots,$$

$$\delta\rho_p(r) \approx \delta\rho_{p0}(r) + \delta\rho_{p1}(r) + \delta\rho_{p2}(r) + \cdots. \tag{14}$$

As the result, the macroscopic PEDM can be written as [11]

$$D_{macro} = D_{v1} + D_{v20} + D_{v21} + D_{s1} + D_{s20} + D_{s21}, \quad (15)$$

where

$$D_{v1} = \frac{e^3AZ}{\pi J}\left[\frac{9\beta_2\beta_3}{56\sqrt{35}} + \frac{11\beta_3\beta_4}{105\sqrt{7}} + \frac{41\beta_4\beta_5}{246\sqrt{11}} + \frac{441\beta_5\beta_6}{715\sqrt{143}}\right], \quad (16)$$

$$D_{s1} = \frac{15e^3A^{2/3}Z}{8\pi Q}\left[\frac{9\beta_2\beta_3}{56\sqrt{35}} + \frac{11\beta_3\beta_4}{105\sqrt{7}} + \frac{41\beta_4\beta_5}{246\sqrt{11}} + \frac{441\beta_5\beta_6}{715\sqrt{143}}\right], \quad (17)$$

$$D_{v20} = \frac{e^3AZ}{\pi^{3/2}J}\left[\frac{3\beta_2^2\beta_3}{56\sqrt{7}} + \frac{789\beta_2^2\beta_5}{8624\sqrt{11}} + \frac{48721\,\beta_2\beta_3\beta_4}{101640\,\sqrt{35}} + \frac{65685\,\beta_2\beta_3\beta_6}{44044\,\sqrt{455}} + \frac{1658135\,\beta_2\beta_4\beta_5}{2186184\,\sqrt{55}} + \frac{35403\,\beta_2\beta_5\beta_6}{11440\,\sqrt{715}} + \frac{3\beta_3^3}{88\sqrt{7}} + \frac{19557\beta_3^2\beta_5}{1041040\sqrt{11}} + \frac{27147\beta_3\beta_4^2}{220220\sqrt{7}} + \frac{657095\,\beta_3\beta_4\beta_6}{528528\,\sqrt{91}} + \frac{141723\beta_3\beta_5^2}{1041040\sqrt{7}} + \frac{110793\sqrt{7}\beta_3\,\beta_6^2}{5348200} + \frac{245625\beta_4^2\beta_5}{1457456\sqrt{11}} + \frac{46892\,\beta_4\beta_5\beta_6}{36465\,\sqrt{143}} + \frac{327\beta_3^3}{5746\sqrt{11}} + \frac{64461\beta_5\beta_6^2}{369512\sqrt{11}}\right], \quad (18)$$

$$D_{s20} = \frac{e^3A^{2/3}Z}{\pi^{3/2}Q}\left[\frac{297\beta_2^2\beta_3}{2240\sqrt{7}} + \frac{20277\beta_2^2\beta_5}{68992\sqrt{11}} + \frac{80181\,\beta_2\beta_3\beta_4}{54208\,\sqrt{35}} + \frac{204545\,\beta_2\beta_3\beta_6}{352352\,\sqrt{455}} + \frac{16455195\,\beta_2\beta_4\beta_5}{5829824\,\sqrt{55}} + \frac{252207\,\beta_2\beta_5\beta_6}{18304\,\sqrt{715}} + \frac{81\beta_3^3}{704\sqrt{7}} + \frac{56025\beta_3^2\beta_5}{75712\sqrt{11}} + \frac{177669\beta_3\beta_4^2}{352352\sqrt{7}} + \frac{8432595\,\beta_3\beta_4\beta_6}{1409408\,\sqrt{91}} + \frac{1113129\beta_3\beta_5^2}{1665664\sqrt{7}} + \frac{1037259\sqrt{7}\beta_3\,\beta_6^2}{8557120} + \frac{9802305\beta_4^2\beta_5}{11659648\sqrt{11}} + \frac{299061\,\beta_4\beta_5\beta_6}{38896\,\sqrt{143}} + \frac{31455\beta_3^3}{91936\sqrt{11}} + \frac{3679965\beta_5\beta_6^2}{2956096\sqrt{11}}\right], \quad (19)$$

$$D_{v21} = \frac{e^5A^{5/3}Z}{\pi J^2 r_0}\left[\frac{477\beta_2\beta_3}{15680\sqrt{35}} + \frac{3719\beta_3\beta_4}{194040\sqrt{7}} + \frac{176933\beta_4\beta_5}{6342336\sqrt{11}} + \frac{627219\beta_5\beta_6}{5725720\sqrt{143}}\right], \quad (20)$$

$$D_{s21} = \frac{e^5A^{4/3}Z}{\pi JQ r_0}\left[\frac{459\beta_2\beta_3}{7840\sqrt{35}} + \frac{9623\beta_3\beta_4}{258720\sqrt{7}} + \frac{32881\beta_4\beta_5}{604032\sqrt{11}} + \frac{702081\beta_5\beta_6}{3271840\sqrt{143}}\right]. \quad (21)$$

Here D_{v1} and D_{s1} are the volume and surface first-order contributions, which was obtained in [4, 5], $r_0 = R_0A^{-1/3}$. The first term in Eq. (16) is obtained by Strutinsky [1]. D_{v20}, D_{v21}, D_{s20} and D_{s21} are the volume and surface first-order contributions. Terms D_{v20} and D_{s20} are related with direct second-order corrections induced by deformation, while terms D_{v21} and D_{s21} are related to next order perturbation of the Coulomb potential induced by deformation andsequential evaluation of the corresponding integrals in Eqs. (4) and (5).

3. Discussion and results

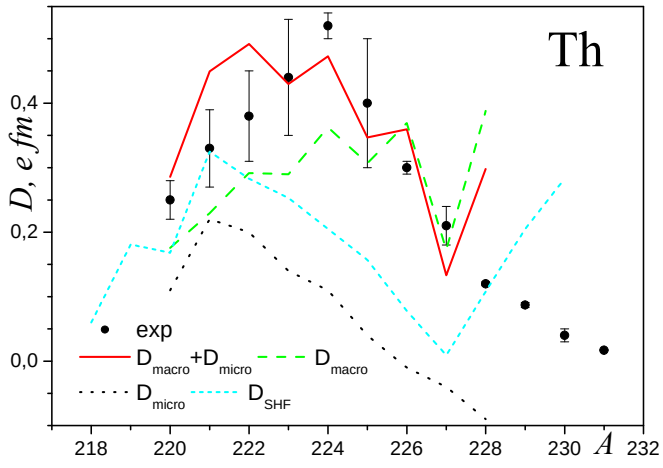

Fig. 1. Experimental (points) and theoretical (lines) values of the PEDM as well as macroscopic and microscopic contributions to the PEDM for Th isotopes. For details on theoretical lines see the text.

The total value of the PEDM, $\boldsymbol{D_{tot}}$, is the sum of the macroscopic, $\boldsymbol{D_{macro}}$, and the microscopic, $\boldsymbol{D_{micro}}$, shell-correction contributions [6, 12, 13] calculated for the same shapes of the proton and neutron surfaces [12], *i.e.*

$$D_{tot} = D_{macro} + D_{micro}. \quad (22)$$

The total values of the PEDM evaluated in the framework of various models are compared with the experimental data for thorium isotopes in Fig. 1. The experimental data are taken from refs. [13, 14, 11]. Our calculation of the macroscopic part D_{macro} is done with the help of Eqs. (15) - (21) using the recent parameter values of the droplet model J = 32.5 MeV, Q = 29.4 MeV, r_0 = 1.16 fm [4]. The values of the multipole deformation parameters β_ℓ and the microscopic part of PEDM, D_{micro}, are taken from ref. [13]. The results obtained in our model well agree with the experimental data for $^{220-228}$Th, see Fig. 1.

The values of the PEDM obtained in the framework of the cranking Skyrme - Hartree - Fock approach D_{SHF} [14] are also presented in Fig. 1. The values of the PEDM evaluated in the cranking Skyrme - Hartree - Fock model underestimatethe experimental data for $^{222-227}$Th and overestimate theones for ^{229,230}Th.

The macroscopic PEDM consists of 6 contributions, see Eqs. (15) - (21). Contributions of all these terms to the PEDM in ^{220}Th as well as the total first- and second-orders macroscopic PEDM values are shown in Figs. 2 - 3. The values of deformation parameters of ^{220}Th are taken from [13].

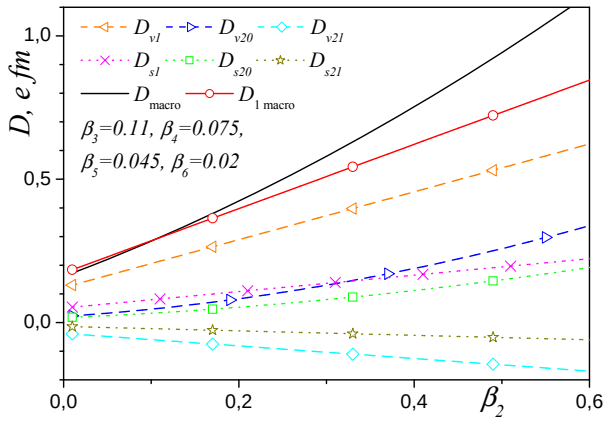

Fig. 2. Dependencies of the total macroscopic PEDM in ^{220}Th evaluatedin the first D_{1macro} and second D_{macro} orders on thequadrupoleβ_2 deformation as well as the same dependenciesof contributions D_{v1}, D_{v20}, D_{v21}, D_{s1}, D_{s20}, and D_{s21} to thePEDM.

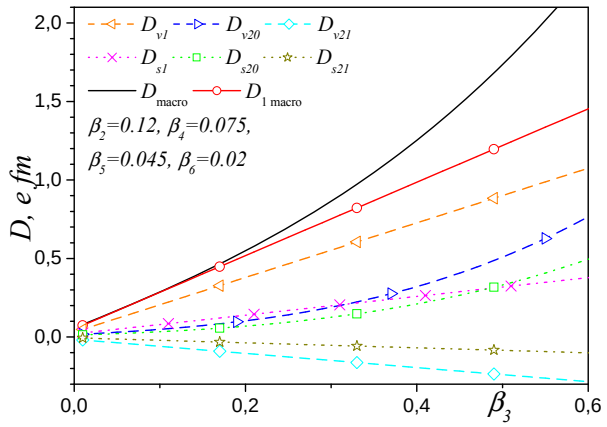

Fig. 3.Dependencies of the total macroscopic PEDM in ^{220}Th evaluatedin the first D_{1macro} and second D_{macro} orders on theoctupoleβ_2 deformation as well as the same dependenciesof contributions D_{v1}, D_{v20}, D_{v21}, D_{s1}, D_{s20}, and D_{s21} to thePEDM.

Comparing the various lines in Figs. 2 and 3 we conclude that:

1. The total first-order contribution of the PEDM is mainly determined by the value of the PEDM at small values of the deformation parameters. The influence of the second-order terms rises with the values of the deformation parameters.
2. The surface contribution of any type is approximately twice as small, than the volume contribution of the same type.
3. The total PEDM evaluated at large octupole and fixed quadrupole deformations is larger than the one for large quadrupole and fixed octupole deformations.

We evaluated the PEDM of the hyperdeformed state of ^{152}Dy. The values of the deformation parameters of^{152}Dy in the hyperdeformed state are $\beta_2 = 0.61$, $\beta_3 = 0.1$,$\beta_4 = 0.11$, $\beta_5 = 0.05$ and $\beta_6 = 0$ [6]. The values of themacroscopic part of the PEDM obtained in the first and second orders using Eqs. (15) - (21) are $D_{macro} = 0.67$ e fm and $D_{1macro} = 0.46$ e fm, respectively. The microscopicshell-correction part of the PEDM (22) evaluated for geometricallysimilar proton and neutron surfaces is $D_{shell} = -0.34$ e fm [6]. As a result the total values of the PEDM (22) found by applying the first- and second-order calculationof the macroscopic part of the PEDM are $D_{macro} + D_{shell} = 0.33$ e fm and $D_{1macro} + D_{shell} =$ $= 0.12$ e fm, respectively. Note that the total value of the PEDM evaluatedusing the exact numerical calculation of the macroscopiccontribution in the framework of the droplet modelis $D_{macroSkalski} + D_{shell} = 0.06$ e fm [6]. Hereby, thePEDM depends strongly on the second-order terms inwell-deformed nuclei as well as on the neutron skin shape.

In conclusion, the expression for macroscopic PEDMtaking into account the first- and second-order terms in the parameters of multipole deformations is obtained inthe case of geometrically similar proton and neutron surfacesof reflection asymmetric nuclei. The second-order terms are important at large valuesof the deformation parameters.

REFERENCES

1. *Strutinsky V.M.* Zamechaniya o zerkalno-asymmetrichukhyadrakh // Atomnaya Energiya. - 1956. - Vol. 4. - P. 150 - 156 (in Russian).
2. *Bohr O., Mottelson B.* Electric dipole moment associated with octupole vibrations of a spheroidal nucleus // Nucl. Phys. - 1957. - Vol. 4. - P. 529 - 531.
3. *Bohr O., Mottelson B.* Electric dipole moment associated with octupole vibrations of a spheroidal nucleus: (Additional remarks) // Nucl. Phys. -1958 - 1959. - Vol. 9. - P. 687 - 688.
4. *Dorso C. O., Myers W.D., Swiatecki W.J.* Droplet-model electric dipole moments // Nucl. Phys. -1986. - Vol. 451. - P. 189-201.
5. *Denisov V.Yu.* Octupole deformation and electric dipole transitions in nuclei // Sov. J. Nucl. Phys. - 1989. - Vol. 49. - P. 399 - 405.
6. *Skalski J.* Octupole-induced dipole moments of very deformed nuclei // Phys. Rev. C. - 1994. - Vol. 49. - P. 2011 - 2017.
7. *Karpeshin F.F.* Prompt gamma radiation from fission fragments due to the Strutinsky - Denisov polarisation // Z.

Phys. A. - 1992. - Vol. 344. - P. 55 - 58.
8. *Karpeshin F.F.* Strutinsky - Denisov polarisation in fission fragments // Proc. of the 3-rd Int. Conf. “Nuclear Physics and Atomic Energy” (Kyiv, Ukraine, 7 - 12 June 2010). - Kyiv, 2011. - P. 441 - 446.
9. *Karpeshin F.F.* Prompt gamma radiation from fission fragments due to the Strutinsky - Denisov polarisation // Eur. Phys. J. A. - 2010. - Vol. 45.- P. 251 - 255.
10. *Kowal M., Skalski J.* Low-energy shape oscillations of negative parity in the main and shape-isomeric minima in // Phys. Rev. C. - 2010. - Vol. 82. - P. 054303 (10 pages).
11. *DenisovV.Yu.* Polarized electric dipole moment of well-deformed reflection asymmetric nuclei // Eur. Phys. J. A. - 2011. - Vol. 47. - P. 80 - 88.
12. *DenisovV.Yu.* Consistent shell correction calculation of polarized electric dipole moment // Sov. J. Nucl. Phys. - 1992. - Vol. 55. - P. 1478 - 1482.
13. *Butler P.A., Nazarewicz W.* Intrinsic dipole moments in reflection-asymmetric nuclei // Nucl. Phys. A. - 1991. - Vol. 533. - P. 249 - 268.
14. *Tsvetkov A., Kvasil J., Nazmitdinov R.G.* Octupole deformations in actinides at high spins within the cranking Skyrme - Hartree - Fock approach // J. Phys. G. - 2002. - Vol. 28. - P. 2187 - 2206.

MEASUREMENT OF ELECTRON MOMENTUM DISTRIBUTIONS IN TUNGSTEN WITH 662 keV GAMMA RADIATION

S. A. Hamouda

Department of Physics, University of Benghazi, Benghazi, Libya

Compton profile measurement of Tungsten polycrystalline sample has been performed with 662 keV γ-radiation from a caesium-137 source scattered at 90^0. The Spectrometer calibration and data corrections for the high energy experiment are discussed. The data are compared with the augmented-plane-wave **(APW)** band theoretical Compton profile of Tungsten. Theoretical predictions show the band theory overestimates the momentum density at low momenta and underestimates it at intermediate momenta**.** The discrepancies between experiment and theory were attributed to some non-local exchange-correlation effects and the spin-orbital interaction effect which were neglected in the theoretical calculation.

1. Introduction

Compton scattering is a technique for obtaining an experimental measure of the momentum distribution of electrons in materials [1, 2]. The scattering from a distribution of moving electrons is Doppler-broadened due to the motion of the target electrons. This broadened line shape, referred to as the Compton profile, $J(p_z)$**,** is defined within the impulse approximation [3] as the projection of the ground state electron momentum density distribution, $\rho(\mathbf{p})$, along the scattering vector (assigned as the z axis) and is given by

$$J(p_z) = \int\int n(p_x, p_y, p_z)\, dp_x dp_y \qquad (1)$$

The impulse approximation implies that the energy transfer is much larger than the one-electron binding energies. However the conditions imposed by the impulse approximation had made Compton profile measurements to be restricted to materials of low atomic number Z when using low gamma-ray energies [4, 5].

To extend the applicability of Compton profile measurements to materials of higher atomic number Z while maintaining the validity of the impulse approximation, together with overcoming the practical limitation imposed by the photoelectric absorption require the use of high gamma-ray energies [6]. For 662 keV gamma ray radiation, the Compton cross section is greater than the photoelectric cross section up to about Z = 90 see DuBard [7]. Since theoretical Compton profile has already been computed for **W**(Z = 74) by Papanicolaou et al. [8] using the wave functions from self-consistent augmented-plane-wave (**APW**) method. It was therefore thought to be of interest to measure the Compton profile of **W** in order to provide a possible check for the new **APW** theoretical calculation.

An outline of this paper is as follows: Sec. II describes briefly the experimental procedure and other experimental aspects of the measurement. Sec. III presents the experiment and data analysis. Sec. IV discusses experimental and theoretical results, followed by some concluding remarks.

II. The experimental procedure

The experimental setup used in this study is introduced elsewhere [9] and can be described as follows: γ-rays from a 10 Ci ^{137}Cs (662 keV) source scatter from a sample through a mean angle of 90^0. The scattered radiation is detected by a **HpGe** detector. A photon entering the detector generates an electrical pulse which was converted to a voltage pulse proportional to the initial photon energy by the detector pre-amplifier. The output pulses are fed to the amplifier at which they are reshaped and transmitted to the Analogue to Digital Converter (ADC). Finally the energy and counts of photons recorded spectrum is stored in a Multi-Channel Analyzer (MCA).

Using the 133-Ba point source lines, the relative efficiency of the HPGe detector was found to be 10 % at the Compton line (288 keV). The energy resolution of the detector was measured using the 133-Ba point source lines in the energy range from 53 keV to 384 keV. At the Compton line the energy resolution of the detector was found to be FWHM = 0.33 a.u. which corresponds to FWHM = 750 eV. The geometrical resolution of the Compton scattered radiation was approximated as FWHM = 0.5 a.u. (1a.u. of momentum is $2.0 \cdot 10^{-24}$ kg m s^{-1}). By combining the detector resolution function and the geometrical resolution function an overall experimental resolution function of FWHM = = 0.6 a.u was obtained.

III. The experiment

The sample used in this experiment was a 20 mm × 40 mm × 1 mm tungsten (Z = 74) polycrystalline sample which has a density of 19.3 gram/cm^3. In this measurement 40,000 counts were collected at the peak channel and 8×10^6 counts under the Compton peak (-10 a.u. to +10 a.u.). The multichannel analyzer channel width was 89 eV which corresponds to 0.04 a.u. The statistical error at the Compton peak was 0.5 and 0.3 % at J(0). The background spectrum was measured (with no sample in position) and time scaled with measurement. The signal-to-background ratio at the Compton peak was 73:1. Before the data can be interpreted, a series of energy dependent corrections have to be applied. Our data reduction procedures were adapted from the software package created by the Compton group at the University

of Warwick [10]. These were applied to the measured data and the corrected data was extracted on a momentum scale (p_z) division of 0.1 a.u. The multiple scattering contributions under the Compton profile from -10 a.u to +10 a.u were 11 %. After correction for multiple scattering the Compton profile was normalized to the free atom profile value of 60.4901 in the momentum range from -10 a.u. to +10 a.u.

IV. Results and Discussion

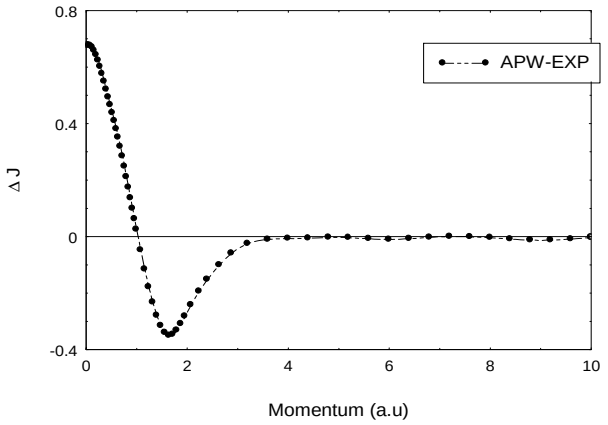

The difference between the APW theory and experimental Compton profile of tungsten measured with 662 KeV radiation

The experimental profile was normalized to the free atom profile value of 30.2475 in the momentum range from 0.0 a.u to 10 a.u. and then compared with the APW calculation of Papanicolaou et al. [8] which was convoluted with 0.60 a.u. to mimic the experimental resolution and normalized to the same area. Figure shows the difference between the APW calculation and the experimental Compton profile of tungsten.

As can be seen from Figure there is a significant difference between the APW calculation and the experimental result. The most obvious feature of this comparison is the excess of electron momentum density for the APW calculation at low momenta (p_z < 1 a.u.). The difference between the APW calculation and the experimental profile amounts to 7.3 % at J(0). On the other hand the APW calculation appears to underestimate the electron momentum density at the intermediate momenta (1.0 a.u. < p_z < 3 a.u.). However, above 3 a.u. the APW calculation is in good agreement with experiment.

Experimental and theoretical Compton profiles of tungsten

P.	EXP.	APW	Free Atom
0.0	8.646 + 0.027	9.322	10.09
0.1	8.618	9.292	9.994
0.2	8.56	9.203	9.727
0.3	8.473	9.062	9.342
0.4	8.355	8.876	8.903
0.5	8.199	8.651	8.464
0.6	8.012	8.393	8.061
0.7	7.803	8.105	7.699
0.8	7.584	7.791	7.375
0.9	7.336	7.454	7.075
1.0	7.077	7.102	6.788
1.2	6.542	6.394	6.231
1.4	6.019	5.74	5.698
1.6	5.534	5.187	5.215
1.8	5.082	4.754	4.802
2.0	4.688	4.419	4.461
2.4	4.118	3.966	3.969
3.0	3.531	3.488	3.495
4.0	2.846 + 0.015	2.853	2.859
5.0	2.236	2.239	2.245
6.0	1.747	1.737	1.728
7.0	1.359	1.358	1.364
8.0	1.102	1.098	1.102
9.0	0.908	0.912	0.914
10.0	0.785 + 0.007	0.782	0.783

The discrepancies between APW calculation and experiment were attributed to some non-local exchange-correlation effects and the spin-orbital interaction effect. All these effects were neglected in the APW calculation of Papanicolaou et al. [8]. The non-local exchange-correlation effects which are not included in the local density approximation may affect the electron momentum distribution since the delocalization of the d electrons was shown to increase from V to Ta see Chang et al. [11]. The spin-orbital interaction has been investigated through the Hamiltonian of $H = \xi l.s.$ by Bacalis et al. [12] and found that the coupling constant ξ to increase with the mass of the element and the average splitting of the d state. This implies that a correction of the spin-orbital interaction for Compton profile may appear larger with an increase of the mass of the element. This may well be applied to the case of tungsten. In a recent work on tungsten, Rozing et al. [13] have suggested that the spin-orbital coupling may affect the Fermi surface and hence the electron momentum distribution. All these effects were neglected in the APW calculation of Papanicolaou et al. [8]. Therefore, the non-local exchange effect and the spin-orbital interaction correction are necessary to correct the band structure theory to bring it closer to experiment. The theoretical and experimental Compton profiles of tungsten are summarized in the Table. The theoretical profile was convoluted with 0.6 a.u. to mimic the experimental resolution. It can be seen from the Table that the experimental profile values smoothly approach the free atom profile values [14].

V. Conclusions

In this paper the performance of the high energy (662 keV) gamma-ray ^{137}Cs 10 Ci Compton spectrometer was tested and its quality was assessed. This was done by measuring the Compton profile of tungsten and compared with the available theoretical models. Despite the reasonable resolution of the present system comparison between experimental data and the theoretical model can be made and the discrepancies can be revealed and distinguished. This has been demonstrated in the measurements made on tungsten discussed above. This allows the use of this system to study a wide range of high Z-materials and their alloys.

ACKNOWLEDGEMENT

I would like to express my gratitude to the Compton group at the University of Warwick for providing the data reduction software package used in this work, and to Dr. E. Zukowski for his fruitful discussions about this work.

REFERENCES

1. *Compton* Scattering / Ed. by B. Williams. - New York: McGraw-Hill, 1977.
2. *Cooper M.J.* Compton Scattering and electron momentum determination // Rep. Prog. Phys. 1985. - Vol. 48. - P. 415.
3. *Eisenberger P., Platzmann P.M.* Compton Scattering of x-ray from Bound Electrons // Phys. Rev. - 1970. - Vol. A2. - P. 415.
4. *Andrejczuk A., Dobrzynski L., Zukowski E. et al.* Compton Scattering Studies of Charge transfer in Fe-Ni-B amorphous alloys // J. Phys.: Condens. Matter. - 1992. - Vol. 4. - P. 2735.
5. *Ahuja B.L., Sharma M.D., Sharma B.K. et al.* Compton Study of the Electronic State in Fe-Ni Alloys // Physica Scripta. - 1998. - Vol. 58**.** - P. 185.
6. *Ahuja B.L., Sharma M.D.* Performance of 20 Ci ^{137}Cs γ-ray Compton spectrometer for the study of momentum densities // Pramana - J. Phys. - 2005. - Vol. 65, No. 1. - P. 137 - 145.
7. *DuBard J.L.* Compton profile measurements of aluminum and iron with 662 KeV γ-radiation // Phil. Mag. - 1978. - Vol. B37. - P. 273 - 283.
8. *Papanicolaou N.I., Bacalis N.C., Papaconstantopoulos D.A.* Handbook of calculated Electron Momentum Distribution, Compton Profiles and X-Ray Form Factors of Elemental Solids. - Florida: CRC Press, 1991.
9. *Hamouda S.A., Cooper M.J.* Compton Profile Measurement of Iron with 662 KeV γ-radiation // Proc. of the Fourth Arab Congress on Materials Science (ACMS-IV) (Al-Fateh University. Faculty of Engineering). - Tripoli, Libya, 2005. - P. 506.
10. *Timms, D.N.* Ph.D. Thesis (unpublished). - University of Warwick, England, 1989.
11. *Chang C.N., Shu Y.M., Liu H.F.* The Compton profiles of tantalum // J. Phys.: Condens. Matter. - 1993. - Vol. 5. - P. 5371.
12. *Bacalis N.C., Blathras K., Thomaides P., Papaconstantopoulos D.A.* Various approximations in augmented-plane-wave calculations // Phys. Rev. - 1985. - Vol. B13. - P. 2292.
13. *Rozing G.J., Mijnarends P.E., Benedek R.* Fully relativistic Calculation of two-photon momentum distribution for positron annihilation in tungsten // Phys. Rev. - 1991. - Vol. B43. - P. 6996.
14. *Biggs F., Mendelsohn L.B., Mann J.B.* // Atomic Data and Nuclear Data Tables. - 1975. - Vol. 16.

NUCLEAR DIFFUSE INTERFACE AND TOLMAN LENGTH

V. M. Kolomietz, S. V. Lukyanov, A. I. Sanzhur

Institute for Nuclear Research, National Academy of Sciences of Ukraine, Kyiv, Ukraine

We redefine the surface tension coefficient for a nuclear Fermi-liquid drop with a finite diffuse layer. Following Gibbs - Tolman concept, we introduce the equimolar radius R_e of droplet surface at which the surface tension is applied and the radius of tension surface R_s which provides the minimum of the surface tension coefficient σ. This procedure allows us to derive both the surface tension and the corresponding curvature correction (Tolman length) correctly for the curved and diffuse interface. We point out that the curvature correction depends significantly on the finite diffuse interface. We show that Tolman's length ξ is negative for a nuclear Fermi-liquid drop. The value of the Tolman length is only slightly sensitive to the Skyrme force parametrization and equals $\xi = -0.36$ fm.

1. Introduction

The curvature correction to the planar tension coefficient and the corresponding Tolman length [1] can be estimated phenomenologically using the polynomial, in powers of $A^{1/3}$, expansion of mass formula [2 - 5]. However the influence of the curved interface on the properties of small quantum systems is still poorly studied because of the finite diffuse layer where particle density drops down to the zero value. The presence of the finite diffuse layer in a small drop creates two, at least, questions: (i) What is the actual radius of a drop? (ii) What is the physical surface where the surface tension is applied? Because of the presence of the diffuse layer, different definitions for the size of the drop are possible [6] which all give the value of drop radius located within the diffuse layer. Note also that though the width of diffuse layer is much less than the range of approximate uniformity of the particle density, one still needs the strict definition of the drop size because of the following reason. In contrast to the planar geometry, the area S for the spherical (curved) surface will depend on the choice of drop radius and this will affect the value of the surface tension σ derived from the surface energy.

Gibbs was the first who addressed the problem of the correct definition ofthe radius and the surface of tension to a small drop with a diffuse interface [7]. After him, Tolman drew attention [1] that two different radii have to be introduced in this case: the equimolar radius R_e which gives the actual size of the corresponding sharp-surface droplet for a given particle number A, and the radius of tension R_s ,which derives, in particular, the capillary pressure, see below in Sec. 2. Following Tolman, see also Ref. [8], the surface tension $\sigma_e \equiv \sigma(R_e)$ approaches the planar limit σ_∞ as

$$\sigma(R_e) = \sigma_\infty \left(1 - \frac{2\xi}{R_e} + O\left(R_e^{-2}\right) \right) , \tag{1}$$

where ξ is the Tolman's length [1]. At the same time the capillary pressure P_{capil}, which is generated by the curvedsurface and provides the equilibrium condition for the well-defined radius R_e, is determined by the radius of tension R_s [7]

$$P_{\text{capil}} = \frac{2\sigma}{R_s} . \tag{2}$$

In general, the presence of the curved interface affects both the bulk and the surface properties. The curvature correction $\Delta\sigma_{\text{curv}} = -2\sigma_\infty \xi / R_e \sim A^{-1/3}$ is usually negligible in heavy nuclei. However, this correction can be important in some nuclear processes. For example the yield of fragments at the nuclear multifragmentation or the probability of clasterization of nuclei from the freeze-out volume in heavy ion collisions are derived by the statistical weight W of the radius fluctuations [9]. In both above mentioned processes, small nuclei necessarily occur and the exponential dependence of the statistical weight W on the surface tension σ [9] should cause a sensitivity of both processes to the curvature correction $\Delta\sigma_{\text{curv}}$.

2. Equimolar surface

We will calculate the dependence of the surface tension coefficient on the position of the dividing surface in a small Fermi-liquid drop with a finite diffuse layer similarly to the procedure described in Ref. [8]. The goal of calculations is to determine the position of the equimolar surface, the dependence of surface tension on the bulk density and the sensitivity of the curvature correction (Tolman length ξ)to the parametrization of the effective nuclear forces.

We consider the uncharged symmetric ($N = Z$) droplet having the number of particles $A = N + Z$, the chemical potential λ and the free energy F . Note that the thermodynamical consideration is most adequate here because of the

finite diffuse interface in a cold nucleus is similar to the vapor environment in a classical liquid drop. In order to formulate proper definition for the drop radius, we will use the concept of dividing surface of radius R, originally introduced by Gibbs [7]. Following Refs. [7, 8], we introduce the formal (arbitrary but close to the interface) dividing surface of radius R, the corresponding volume $V = 4\pi R^3/3$ and the surface area $S = 4\pi R^2$. The droplet free energy F will be then split between the volume, F_V, and surface, F_S, parts

$$F = F_V + F_S\,, \tag{3}$$

where

$$F_V = \left(-P + \lambda\rho_V\right)V\,, \qquad F_S = \left(\sigma + \lambda\rho_S\right)S\,. \tag{4}$$

Here, $P = P(\lambda)$ is the pressure of nuclear matter achieved at some volume particle density $\rho_V = A_V/V$ and $\rho_S = A_S/S$ is the surface particle density, where A_V and A_S are the volume and the surface particle numbers, respectively. Irrespective to the way of calculation of the total free energy F, its volume part F_V stands for the nuclear matter free energy of the uniform density ρ_V within the volume V. The state of the nuclear matter inside the specified volume is chosen to have the chemical potential λ equal to that of the actual (in the presence of the finite diffuse layer) drop. Having the value of λ one can calculate all the intensive quantities like the free energy per particle F_V/A_V, the particle density ρ_V and the pressure $P = -\partial F_V/\partial V\big|_{A_V}$ from the equation of state for the infinite nuclear matter. The surface part of the free energy F_S as well as the surface particle number A_S are considered as the excess quantities responsible for "edge" effects with respect to the corresponding volume quantities. Thus, the chemical potential λ is the key quantity needed to determine both the volume part of the free energy F_V and the surface energy F_S due to Eq. (3).
The actual particle number is given by

$$A = A_V + A_S = \rho_V V + \rho_S S\,. \tag{5}$$

Note also that the surface (superficial) particle number A_S is a formal quantity which is caused by the deviation of the volume part A_V from the actual particle number A through an arbitrary choice of the dividing surface. The value of A_S disappears for the actual size of the sharp-surface droplet given by the equimolarradius R_e, see Refs. [7, 8] and below in Sec. 3.The use of Eqs.(3) - (5) gives the following relation for the surface tension

$$\sigma = \frac{F - \lambda A}{S} + \frac{PV}{S} = \frac{\Omega - \Omega_V}{S}\,, \tag{6}$$

where symbol $\Omega = F - \lambda A$ stands for the grand potential and $\Omega_V = -PV$. To reveal a R-dependence of the surface tension σ, it is convenient to introduce the grand potential per particle $\omega = F/A - \lambda$ for the actual droplet and $\omega_V = F_V/A_V - \lambda = -P\rho_V$ for the volume part. Then the surface tension is written as

$$\sigma[R] = \frac{\omega A}{4\pi R^2} - \frac{1}{3}\omega_V\rho_V R = \frac{\omega A}{4\pi R^2} + \frac{P}{3}R\,. \tag{7}$$

Here, the square brackets denote a dependence of an observable on the dividing surface radius R which is different than the dependence on the physical size of a droplet [8]. Taking the derivative from Eq. (7) with respect to the formal dividing radius R and using the fact that the observable quantities F, λ and P should be R-independent (changing dividing radius R we keep the particle density invariable), one can rewrite Eq. (7) as

$$P = \frac{2\sigma}{R} + \frac{\partial}{\partial R}\sigma[R]\,, \tag{8}$$

which is the generalized Laplace equation.

The choice of the dividing radius R is arbitrary, the only condition is tokeep the same chemical potential λ. So, the formal value of surface density ρ_S can be positive or negative depending on R. From Eq. (5) one finds

$$\rho_S[R] = \frac{A}{4\pi R^2} - \frac{1}{3}\rho_V R\,. \tag{9}$$

The volume part of free energy F_V/A_V is associated with the energy per particle for the nuclear matter, $f(\rho)$, taken at certain value of matter density ρ. Using the evaluated chemical potential λ, we fix the particle density

$\rho_V = \rho_V(\lambda)$ from the condition

$$\left.\frac{\partial F_V}{\partial A_V}\right|_{A_V} = \left.\frac{\partial}{\partial \rho}\left(\rho f(\rho)\right)\right|_{\rho=\rho_V} = \lambda . \tag{10}$$

For an arbitrary dividing radius R we evaluate then the volume particle number $A_V = 4\pi R^3 \rho_V / 3$ and the volume part of free energy F_V / A_V. Finally, evaluating the surface parts $A_S = A - A_V$ and $F_S = F - F_V$, we obtain the surface tension coefficient $\sigma[R]$ and surface density $\rho_S[R]$ for an arbitrary radius R of dividing surface.

Note that, in general, the surface free energy F_S includes both contributions from the surface tension σ itself and from the bulk binding energy of A_S particles within the surface layer. The equimolar surface and the actual physical radius R_e of the droplet are derived by the condition $\rho_S[R_e] = 0$ [1, 8], i.e., the contribution from the bulk binding energy should be excluded from the surface free energy F_S. The equimolar dividing radius R_e defines the physical size of the sharp surface droplet and the surface at which the surface tension is applied. Function $\sigma[R]$ has a minimum at radius $R = R_s$ (radius of the surface of tension [7, 8]) which usually does not coincide with the equimolar radius R_e. The radius R_s denotes the location within the droplet interface. Note that for $R = R_s$ the capillary pressure of Eq. (8) satisfies the classical Laplacerelation

$$P = \left.\frac{2\sigma[R]}{R}\right|_{R=R_s} . \tag{11}$$

3. Surface tension and Tolman length

Considering an arbitrary choice of the dividing surface and following the Gibbs - Tolman concept, we have determined two radii, the equimolar dividing radius R_e which corresponds to zero surface density ρ_S and the radius of tension R_s which corresponds to the minimum value of the surface tension. From Eqs. (7) and (9) the values of these radii are given by

$$R_e = \left(\frac{4\pi\rho_V}{3A}\right)^{-1/3}, \qquad R_s = \left(-\frac{2\pi\rho_V}{3A}\frac{\omega_V}{\omega}\right)^{-1/3} . \tag{12}$$

Following Gibbs and Tolman [1, 7], we will assume that the physical (measurable) value of the surface tension is that taken at the equimolar dividing surface. Taking Eq. (8) for $R = R_s$, using Eqs. (11) and (1) and introducing small value $\eta = R_e - R_s$, we obtain

$$P = \frac{2\sigma_\infty}{R_s}\left(1 - \frac{2\xi}{R_s} + O\left(R_s^{-2}\right)\right). \tag{13}$$

Taking Eq. (8) for $R = R_e$ and Eq. (1) we find

$$P = \frac{2\sigma_\infty}{R_s}\left(1 - \frac{\xi+\eta}{R_s} + O\left(R_s^{-2}\right)\right). \tag{14}$$

Comparing Eqs. (13) and (14) for $R_s \to \infty$, we obtain the Tolman result [1]

$$\xi = \lim_{A\to\infty}\left(R_e - R_s\right). \tag{15}$$

This result leads to the important conclusions. First, one needs to define two different radii: the equimolar radius, R_e, for a proper extraction of the surface energy from the total energy of nucleus and the radius of tension, R_s, to determine the capillary pressure. Second, to obtain the non-zero value of Tolman length, and, consequently, the value of the curvature correction $\Delta\sigma_{curv} \neq 0$ for a curved surface, the droplet must have the diffuse surface layer.

The value of Tolman's length could be positive or negative. Positive value of Tolman's length $\xi > 0$ means $\sigma_e < \sigma_\infty$ (see Eq. (1)) and negative one leads to $\sigma_e > \sigma_\infty$ for curved surface. The Gibbs concept of dividing surface does not imply any specific energy density functional and relies on the value of the binding energy and the chemical potential which are measurable quantities. It is possible to apply this concept to the phenomenological droplet model [2] as well. The result of the Tolman length calculation in terms of the droplet model reads (see [10] for details)

$$\xi = -\frac{a_3}{2a_2} r_0 \ , \tag{16}$$

where $r_0 = \left(4\pi\rho_\infty / 3\right)^{-1/3}$, ρ_∞ is the saturation density for infinite nuclear matter, a_2 and a_3 are, respectively, the surface and the curvature correction coefficients (see [2, 3]).

The value of the Tolman length can be related to nuclear incompressibility, K, with reasonable assumptions [11]. We consider the thermodynamic expansion like (1)around the equilibrium state of the semi-infinite matter also for the density and chemical potential:

$$\rho_V = \rho_\infty + \rho_1 \frac{r_0}{R_e} + \rho_2 \frac{r_0^2}{R_e^2} + \dots \ , \qquad \lambda = \lambda_\infty + \lambda_1 \frac{r_0}{R_e} + \lambda_2 \frac{r_0^2}{R_e^2} + \dots \ . \tag{17}$$

Here λ_∞ is the equilibrium chemical potential for the infinite matter, ρ_i, λ_i are the expansion coefficients. Combining Gibbs - Duhem relation $dP = \rho_V \, d\lambda$ and the generalized Laplace equation (8) with Eqs. (1), (17) one obtains

$$d\left(\frac{2\sigma_\infty}{R_e} - \frac{2\sigma_\infty \xi}{R_e^2} + \dots\right) = \left(\rho_\infty + \rho_1 \frac{r_0}{R_e} + \rho_2 \frac{r_0^2}{R_e^2} + \dots\right) d\left(\lambda_\infty + \lambda_1 \frac{r_0}{R_e} + \lambda_2 \frac{r_0^2}{R_e^2} + \dots\right). \tag{18}$$

Nuclear incompressibility K in terms of expansion (17) reads

$$K = 9 \frac{\partial P}{\partial \rho_V}\bigg|_{\rho_V = \rho_\infty} = 9\rho_V \frac{\partial \lambda}{\partial \rho_V}\bigg|_{\rho_V = \rho_\infty} = 9\rho_\infty \frac{\lambda_1}{\rho_1} \, . \tag{19}$$

Equating in (18) the terms of the same order in curvature R_e^{-1} and taking the advantage of the in compressibility definition (19), one obtains the following relations

$$\rho_1 = 18 \frac{\sigma_\infty}{K r_0} \, , \qquad \lambda_1 = 2 \frac{\sigma_\infty}{\rho_\infty r_0} \, , \tag{20}$$

$$\xi = -\frac{9\sigma_\infty}{\rho_\infty K} - \frac{\lambda_2}{\lambda_1} r_0 \, . \tag{21}$$

Eq. (21) gives an idea how the Tolman length depends on the incompressibility. In particular, if the chemical potential is linear in curvature, namely $\lambda = \lambda_\infty + 2\sigma_\infty \rho_\infty^{-1} R_e^{-1}$ (the second and the higher order terms in (17) are neglected), we can estimate the Tolman length as

$$\xi \approx -\frac{9\sigma_\infty}{\rho_\infty K} \tag{22}$$

It is seen from Eqs. and (21) that such approximation is justified when the inequality $\lambda_2 << \frac{18}{K}\left(\frac{\sigma_\infty}{\rho_\infty r_0}\right)^2$ is fulfilled. In view of Eq. (22), to obtain the nonzero value of ξ the nuclear matter should have finite incompressibility.

4. Numerical results

We have performed the numerical calculations using Skyrme type of the effective nucleon-nucleon interaction. The energy and the chemical potential for actual droplets have been calculated using a direct variational method within the extended Thomas - Fermi approximation [2].The dependence of the surface tension $\sigma[R]$ on the location of the dividing surface for $A = 208$ is shown in Fig. 1. As seen from Fig. 1, function $\sigma[R]$ has a minimum at radius $R = R_s$ (radius of the surface of tension [7]).

Since we consider a non-charged droplet (without Coulomb),the calculation is possible up to very high values of particle number $A \sim 10^6$. Fig. 2 shows the result of calculation for the tension σ_e as a function of doubled droplet curvature $2/R_e$ .The calculation was carried out using the SkM force. Fig. 2 demonstrates the negative value of ξ for this calculation. An extrapolation of curve in Fig. 2 to zero curvature $2/R_e \to 0$ allows one to derive both the surface tension coefficient $\sigma_\infty = \sigma_e\left(R_e \to \infty\right)$ in a planar geometry and the slope of curve which gives the Tolman length ξ .

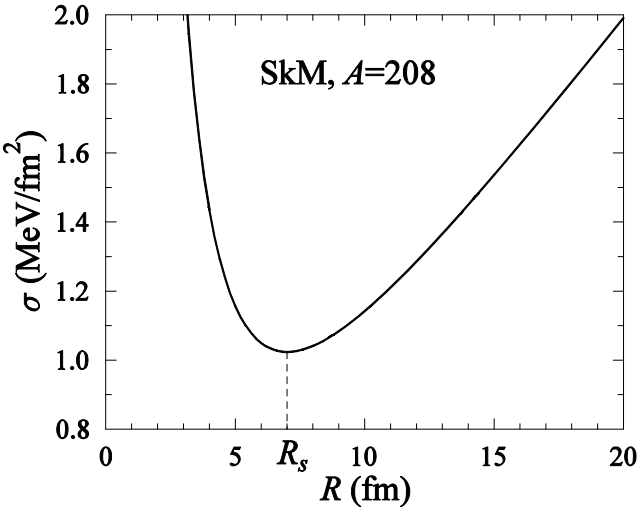

Fig. 1. Surface tension σ as a function of the dividing radius R for $A = 208$. The calculation was performed using the SkM force. R_s denotes the dividing radius where σ approaches the minimum value.

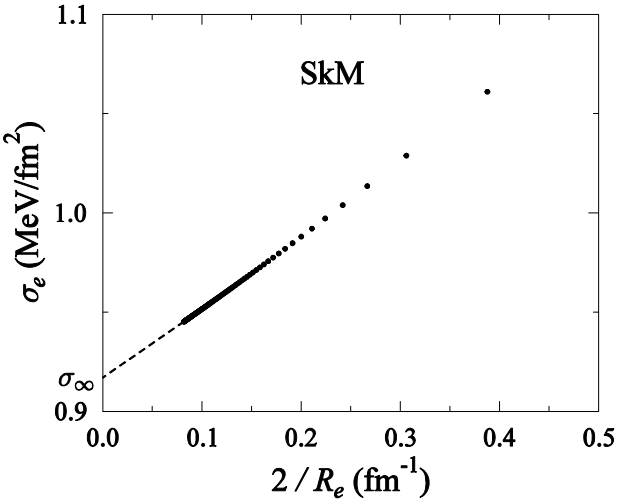

Fig. 2. Surface tension of the droplet versus the surface curvature for the range of particle number $A = 10^2 - 10^4$. The calculation was performed using the SkM force.

The result of such kind of extrapolation of $\sigma_e(R_e)$ is shown in Fig. 2 by dashed line. We have determined the Tolman's length ξ and the planar surface tension σ_∞ for several sets of Skyrme interaction. For this purpose we have performed calculations up to particle number 10^6 and extrapolate them to zero curvature. Results for ξ, σ_∞ (see Eq. (1)) and also expansion coefficients ρ_1, ρ_2, λ_1, λ_2 (see Eq. (17)) are summarized in Table 1.We can see from Table 1 that Tolman's length ξ is negative for a nuclear Fermi-liquid drop. This conclusion is also supported by the results of Ref. [2]. The value of the Tolman length is only slightly sensitive to the Skyrme force parametrization with the exception of old one SIII.

Table 1. **Values of Tolman's length ξ and planar surface tension σ_∞ obtained for different parametrizations of Skyrme forces. Along with values of ξ and σ_∞ the values of expansion coefficients ρ_1, ρ_2, λ_1 and λ_2 are presented**

Force	ξ, fm	σ_∞, MeV/fm^3	ρ_1, fm^{-3}	ρ_2, fm^{-3}	λ_1, MeV	λ_2, MeV
SkM	−0.36	0.92	0.067	−0.025	10.0	1.05
SIII	−0.26	0.93	0.040	−0.013	10.8	0.91
Sly230b	−0.37	1.01	0.069	−0.028	11.0	1.18
T6	−0.36	1.02	0.068	−0.027	11.1	1.16

It is interesting to analyze the applicability of the Gibbs - Tolman approach for the case of small mass numbers. According to Gibbs [7] the the rmodynamical relation (2) remains exact up to the zero value of R_s, provided the pressure is calculated for the matter at the value of chemical potential of the actual drop. The Gibbs - Tolman (GT) procedure described in Sec. 2 defines surface quantities as the excess ones with respect to a certain volume of uniformly distributed matter which conserves the saturation property. This procedure itself does not bring any extra approximation like the leptodermous one, so the question on the applicability of the GT procedure in the case of low masses should be addressed tothe model which is used for the calculation of the free energy and the chemical potential. One can obtain the binding energies for the range of low masses solving numerically the Euler - Lagrange equation within the extended Thomas - Fermi theory [13] avoiding the use of the leptodermous condition. Based on the exact numerical solution of the Euler - Lagrange equation it was shown in Ref. [10] that the use of the leptodermous approximation overestimates the value of the surface tension σ for nuclei with low masses $A \sim 10 - 20$.

The effect of finite size of the drop on the surface tension value can essentially affect the yield of fragments in the nuclear multifragmentation observed for heavy ion collisions. The yield $Y(A)$ of the fragment having a certain mass number A is given by $Y(A) \propto \exp(-w/T)$ [9], where T is the temperature, w is the work which is needed to form the fragment from the nucleon vapor. Leaving apart the temperature dependence of w, let us estimate the effect of the drop size on the value of w. The comparison of w with its value for the semi-infinite matter

Table 2. **The work of the drop formation w in units of the semi-infinite matter estimate w_∞ for mass numbers from 12 to 24. w_{DM} stands for the droplet model result, see [10]**

A	w / w_∞	w_{DM} / w_∞
12	1.17	1.42
16	1.19	1.39
20	1.19	1.36
24	1.20	1.34

$w_\infty = \sigma_\infty (4\pi/3)^{1/3} (A/\rho_\infty)^{2/3}$ should apparently allocate the effect of the finite drop size. We have performed the calculation for the work of drop formation for several small mass numbers using the SkM force. The values of the free energy and the chemical potential were obtained by solving numerically the Euler - Lagrange equation within the extended Thomas - Fermi theory [13]. Then GT procedure was applied to evaluate w, see Ref. [10] for details. The results are presented in the second column of Table 2 and show values of about 20% higher than w_∞ for mass numbers from 12 to 24. This should bring the hindrance of the yield of fragments with those masses due to the effect of the finite fragment size. From the third column of Table 2 one can see a significant overestimation of the work w_∞ if one uses the leptodermous expansion around the value of w_∞ for the semi-infinite matter.

5. Conclusions

Considering a small droplet with a finite diffuse layer, we have introduced a formal dividing surface of radius R which splits the droplet onto volume and surface parts. The corresponding splitting was also done for the free energy. Assuming that the dividing surface is located close to the interface, we are then able to derive the pressure P and the surface free energy F_S. In general, the surface free energy F_S includes the contributions from the surface tension σ and from the binding energy of A_S particles within the surface layer. The equimolar surface and the actual physical size of the droplet was derived by the condition $\rho_S = 0$. In a small nucleus, the diffuse layer and the curved interface affect the surface properties significantly. In agreement with Gibbs - Tolman concept [1, 7], two different radii have to be introduced in this case. The first radius, R_s, is the surface tension radius which provides the minimum of the surface tension coefficient σ and the fulfillment of the Laplace relation (11) for capillary pressure. The another one, R_e, is the equimolar radius which corresponds to the equimolar dividing surface and defines the physical size of the sharp surface droplet, i.e., the surface at which the surface tension is applied. The difference of two radii $R_e - R_s$ derives the Tolman length ξ in an asymptotic limit of large system $A \to \infty$. That means the presence of curved surface is not sufficient for the calculation of the curvature correction to the surface tension. The finite diffuse layer in the particle distribution is also required.

We point out that the Gibbs - Tolman theory allows to treat a liquid drop within thermodynamics with minimum assumptions. Once the binding energy and chemical potential of the nucleus are known its equimolar radius, radius of tension and surface energy can be evaluated using the equation of state for the infinite nuclear matter. In this sense the Gibbs – Tolman approach does not rely on details of the particle density profile. The sign and the magnitude of the Tolman length ξ depend on the interparticle interaction. We have shown that the Tolman length is negative for a nuclear Fermi liquid drop. As a consequence, the curvature correction to the surface tension could lead to the hindrance of the yield of light fragments at the nuclear multifragmentation in heavy ion collisions.

REFERENCES

1. *Tolman R.C.* The Effect of Droplet Size on Surface Tension // J. Chem. Phys. - 1949. - Vol. 17. - P. 333.
2. *Myers W.D., Swiatecky W.J.* Average Nuclear Properties // Ann. Phys. - 1969. - Vol. 55. - P. 395.
3. *Myers W.D., Swiatecky W.J.* Nuclear properties according to the Thomas - Fermi model // Nucl. Phys. - 1996. - Vol. A601. - P. 141.
4. *Stocker W.* Remarks concerning the nuclear surface and curvature energy // Nucl. Phys. - 1973. - Vol. A215. - P. 591.
5. *Tyapin A.S.* A statistical expression for nuclear energy // Sov. J. Nucl. Phys. - 1971. - Vol. 13. - P. 18.
6. *Myers W.D.* Geometric properties of leptodermous distributions with applications to nuclei // Nucl. Phys. - 1973. - Vol. A204. - P. 465.
7. *Gibbs J.W.* Influence of Surfaces of Discontinuity upon the Equilibrium of Heterogeneous Masses. Theory of Capillarity // The Collected Works. Vol. I. - New York: Longmans, Green and Co., 1928. - P. 219.
8. *Rowlinson J.S., Widom B.* Molecular Theory of Cappilarity. Ch. 2. - Oxford: Clarendon Press, 1982.
9. *Landau L.D., Lifshitz E.M.* Statistical Physics. - Oxford: Pergamon Press, 1958.
10. *Kolomietz V.M., Lukyanov S.V., Sanzhur A.I.* Curved and diffuse interface effects on the nuclear surface tension // Phys. Rev. C - 2012. - Vol. 86. - P. 024304.
11. *Blokhius E.M, Kuipers J.* Thermodynamic expressions for the Tolman length // J. Chem. Phys. - 2006. - Vol. 124. - P. 074701.
12. *Kolomietz V.M., Sanzhur A.I.* Equation of state and symmetry energy within the stability valley // Eur. Phys. J. A. - 2008. - Vol. 38. - P. 345.
13. *Brack M., Guet C., Håkansson H.-B.* Selfconsistent semiclassical description of average nuclear properties - a link between microscopic and macroscopic models // Phys. Rep. - 1985. - Vol. 123. - P. 275.

NEUTRON EXCESS EFFECT ON THE NUCLEAR RMS RADII

V. M. Kolomietz, S. V. Lukyanov, A. I. Sanzhur

Institute for Nuclear Research, National Academy of Sciences of Ukraine, Kyiv, Ukraine

The radii of nucleon distribution and bulk density in nuclei beyond the β-stability line are studied within the direct variational method. We evaluate the partial equation of state of finite nuclei and demonstrate that the bulk density decreases beyond the beta stability line. We show that the growth of the neutron skin in unstable nuclei does not obey the saturation condition because of the polarization effect. The calculations of the isovector shift of the nuclear radius show its primarily linear dependence on the asymmetry parameter.

1. Introduction

Our knowledge about the properties of neutron excess in heavy nuclei and its relation to the neutron-rich nuclear matter and the isotopic symmetry energy is still strongly limited. In heavy stable nuclei, the average changes in binding energy and nuclear radius R with nucleon content obey the saturation properties. The volume part E_{vol} of binding energy and the nuclear volume itself are proportional to the particle number A with $E_{vol} = -b_V A$ and $R = r_0 A^{1/3}$, where $b_V > 0$ and r_0 are the constants. Both values of b_V and r_0 depend, however, on the isotopic asymmetry parameter $X = (N - Z)/(N + Z)$. This is because of the difference in saturation bulk density, $\rho_0 \sim r_0^{-3}$, of nuclei with different values of X. The saturation density ρ_0 is smaller beyond the beta-stability line for neutron-rich nuclei where more neutrons are pushed off to form the “neutron coating". One can expect then that the growth of the neutron skin in neutron-rich nuclei violates the saturation property $R \sim A^{1/3}$ for the nuclear radius providing a relative shift of both neutron and proton distributions [1].

In the present paper we study a deviation of nucleon distribution from the saturation behavior in neutron-rich nuclei. We study also the related problems of the nucleon redistribution within the surface region (nuclear periphery), in particular, the neutron coating and the neutron excess for the nuclei far away from the β-stability line.

2. Direct variational approach

We will use the extended Thomas - Fermi approximation. The key point of the ETF is that the total kinetic energy of the many-body fermion system is given by the semiclassical expression [2 - 4] as follows:

$$E_{kin}\{\rho_n, \rho_p\} \equiv E_{kin}\{\rho_q, \nabla\rho_q\} = \int d\mathbf{r}\ \varepsilon_{kin}[\rho_n(\mathbf{r}), \rho_p(\mathbf{r})], \tag{1}$$

where $\varepsilon_{kin}[\rho_n, \rho_p] = \varepsilon_{kin,n}[\rho_n] + \varepsilon_{kin,p}[\rho_p]$, and

$$\varepsilon_{kin,q}[\rho_q] = \frac{\hbar^2}{2m}\left[\frac{3}{5}(3\pi^2)^{2/3}\rho_q^{5/3} + \beta\frac{(\nabla\rho_q)^2}{\rho_q} + \frac{1}{3}\nabla^2\rho_q\right]. \tag{2}$$

Here ρ_q is the nucleon density with $q = n$ for neutron and $q = p$ for proton. The semiclassical consideration gives the value of parameter β in Eq. (2) $\beta = 1/36$ [2, 3]. We point out that in the asymptotic limit $r \to \infty$, the semiclassical particle density ρ_q with $\beta = 1/36$ goes significantly faster to zero than the one from the quantum-mechanical calculation.

We will follow the concept of the effective nucleon-nucleon interaction using the Skyrme-type force. The functional of the total energy of charged nucleus is given by

$$E_{tot}\{\rho_q, \nabla\rho_q\} = E_{kin}\{\rho_q, \nabla\rho_q\} + E_{pot}\{\rho_q, \nabla\rho_q\} + E_C\{\rho_p\}, \tag{3}$$

where $E_{pot}\{\rho_q, \nabla\rho_q\}$ is the potential energy of NN interaction

$$E_{pot}\{\rho_q, \nabla\rho_q\} = \int d\mathbf{r}\ \varepsilon_{pot}[\rho_n(\mathbf{r}), \rho_p(\mathbf{r})], \tag{4}$$

$\varepsilon_{pot}[\rho_n(\mathbf{r}), \rho_p(\mathbf{r})]$ is the density of the potential energy of the nucleon-nucleon interaction and $E_C\{\rho_p\}$ is the Coulomb energy. In our consideration, the potential energy $E_{pot}\{\rho_q, \nabla\rho_q\}$ includes the energy of the spin-orbit interaction also.

Following the direct variational method, we have to choose the trial function for $\rho_q(\mathbf{r})$. We will assume a power of

the Fermi function for $\rho_q(\mathbf{r})$ as

$$\rho_q(\mathbf{r}) = \rho_{0,q}\left[1+\exp\left(\frac{r-R_q}{a_q}\right)\right]^{-\eta}, \tag{5}$$

where $\rho_{0,q}$, R_q, a_q, and η are the unknown variational parameters. Considering the asymmetric nuclei with $X=(N-Z)/A \ll 1$, we will introduce the isotopic particle densities, namely the total density $\rho_+ = \rho_n + \rho_p$ and the neutron excess density $\rho_- = \rho_n - \rho_p$ with $\rho_- \ll \rho_+$. Assuming a small deviation of the isoscalar bulk density $\rho_{0,+} = \rho_{0,n} + \rho_{0,p}$, the radii R_q, and the diffuseness parameters a_q with respect to the corresponding average values of ρ_0, R, and a, we introduce the density profile functions $\rho_+(r)$ and $\rho_-(r)$ to be given by

$$\rho_{+,-}(r) = \rho_{0,1} f(r) - \frac{1}{2}\rho_{1,0}\frac{df(r)}{dr}\left[\Delta_R + \frac{r-R}{a}\Delta_a\right]. \tag{6}$$

Here,

$$f(r) = \left[1+\exp\left(\frac{r-R}{a}\right)\right]^{-\eta}, \tag{7}$$

the values ρ_0 and ρ_1 are related to the bulk density, R is the nuclear radius, a is the diffuseness parameter, and $\Delta_R = R_n - R_p$ and $\Delta_a = a_n - a_p$ are the parameters of the neutron skin. The profile functions $\rho_+(r)$ and $\rho_-(r)$ have to obey the condition that the number of neutrons and protons is conserved. For the ground state of the nucleus, the unknown parameters ρ_0, ρ_1, R, a, Δ_R, Δ_a, and η and the total energy E_{tot} itself can be derived from the variational principle

$$\delta(E - \lambda_n N - \lambda_p Z) = 0, \tag{8}$$

where the variation with respect to all possible small changes of ρ_0, ρ_1, R, a, Δ_R, Δ_a, and η is assumed. The Lagrange multipliers λ_n and λ_p are the chemical potentials of the neutrons and the protons, respectively, and both of them are fixed by the condition that the number of particles is conserved. We will also assume that the leptodermous condition $a/R \ll 1$ is fulfilled.

In general, the change of the radius R of the nucleon distribution with the nucleon number A is caused by two factors. There is a simple geometrical change of R because of $R \propto A^{1/3}$. An additional change can occur due to the polarization effect (the bulk density distortion) with moving away the beta-stability line. In particular, the size of the neutron skin is sensitive to the symmetry and Coulomb energies. To see that we expand the total energy $E_{tot}(\rho_0, X)/A$ around the saturation density $\rho_{0,eq}$ keeping only terms quadratic in $\delta\rho_0 = \rho_0 - \rho_{0,eq}$ [5]

$$E_{tot}(\rho_0, X)/A = E_{tot}(\rho_{0,eq}, X^*)/A + \frac{K_A}{18\rho_{0,eq}^2}\delta\rho_0^2 + \frac{P_{A,sym}}{\rho_{0,eq}^2}(X-X^*)^2\delta\rho_0, \tag{9}$$

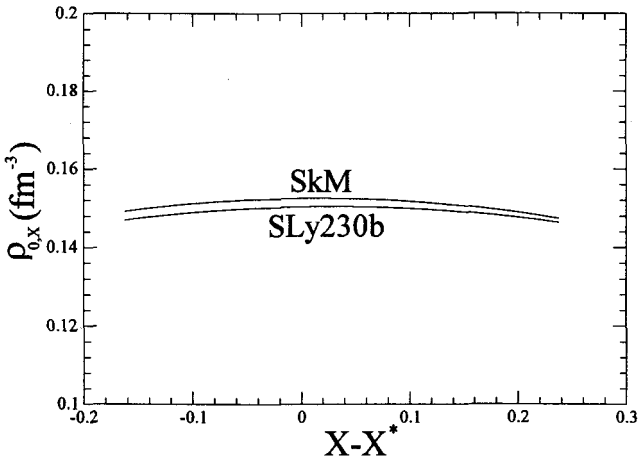

Fig. 1. The equilibrium density $\rho_{0,X}$ as a function of X for $A=120$ calculated for the SkM and SLy230b parametrizations of the Skyrme force. The asymmetry parameter at the beta-stability line $X^* \simeq 0.163$.

where K_A is the incompressibility of finite nucleus and $P_{A,sym}$ is the partial pressure related to the symmetry and Coulomb energies. As seen from Eq. (9), a deviation from the beta-stability line ($X \neq X^*$) implies the change of the bulk density ρ_0. The corresponding change of ρ_0 is dependent on the incompressibility K_A and the partial pressure $P_{A,sym}$. For an arbitrary fixed value of X, the equilibrium density $\rho_{0,X}$ is derived by the condition

$$\frac{\partial}{\partial\rho_0}E_{tot}(\rho_0, X)/A\Big|_{A,\rho_0=\rho_{0,X}} = 0. \tag{10}$$

Using Eqs. (9) and (10), we obtain the expression for the shift of the bulk density (polarization effect) in the neutron rich nuclei

$$\rho_{0,X} = \rho_{0,eq} - 9\frac{P_{A,sym}}{K_A}(X-X^*)^2. \tag{11}$$

In Fig. 1 we have plotted the equilibrium density $\rho_{0,X}$ as a function on the distance $X - X^*$ from the beta-stability line accordingly to (11).

As is seen the equilibrium density has a maximum at the beta-stability line and decreases in directions to the drip lines. That means the partial pressure $P_{A,sym}$ is positive; see also Refs. [6, 7].

3. Radii of nucleon distributions

As above noted, the bulk density $\rho_{0,X}$ is smaller for neutron-rich nuclei; more neutrons should be pushed off to enrich the skin providing a polarization effect. The nuclear rms radius

$$\sqrt{\langle r^2 \rangle} = \sqrt{\int d\mathbf{r}\, r^2 \rho_+(r) / \int d\mathbf{r}\, \rho_+(r)}. \tag{12}$$

does not necessarily obey then the saturation condition having that $\sqrt{\langle r^2 \rangle}$ is nonproportional to $A^{1/3}$. As a consequence, the nuclei with significant excess of neutrons exhibit neutron coating, i.e., are characterized by larger radii for the neutron than for proton distributions.

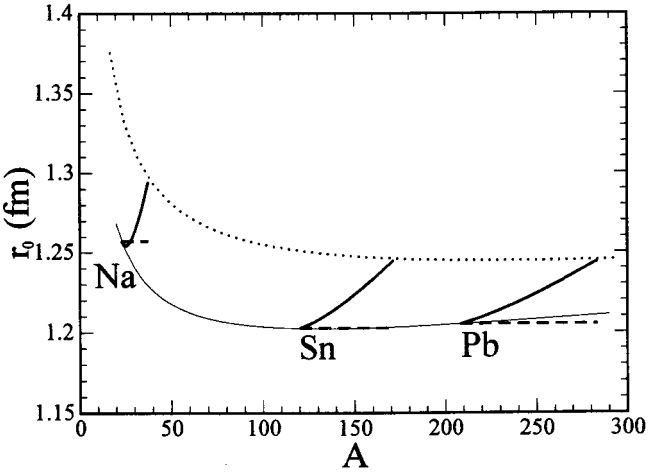

Fig. 2. The value r_0 near the beta-stability line. The thin solid line is for the beta-stability line, the thick solid line is beyond the beta-stability line for three nuclei, and the dotted curve is for the neutron drip line. The dashed lines are the rms radii calculated with the step distribution (13). The calculations have been performed for the SkM parametrization of the Skyrme force.

With the aim to extract the saturation properties we have multiplied the nuclear rms radii $\sqrt{\langle r^2 \rangle}$ by a factor $\sqrt{5/3}$ and divided it on $A^{1/3}$. This is just the value r_0. In Fig. 2 we have plotted it (see the thick solid curves) as obtained from Eq. (12) for three nuclei. The results of Fig. 2 are only slightly sensitive to a small variation of the diffuse layer and we have here assumed that $\Delta_a = 0$. The thin solid line of Fig. 2 represents the rms radius along the beta-stability line $X = X^*(A)$ which is parametrized by $X^*(A) = 0.17A^{2/3}\left(26.5 - 25.6A^{-1/3} + 0.17A^{2/3}\right)$ [8]. The deviation of the rms radii (thick solid lines) from the saturation behavior $\sim A^{1/3}$ (thin solid line) cannot be related directly to the appearance of the giant neutron halo at the approach to the drip line (dotted curve) because we have here assumed $\Delta_a = 0$. As above noted, there are two sources for the change of the radius of nucleon distribution with the nucleon number A. The first one is due to a simple geometrical reason and the second one is because of the polarization effect; see Eq. (11). To extract a simple geometrical change of the rms radius $\sqrt{\langle r^2 \rangle}$ we will perform the calculations of $\sqrt{\langle r^2 \rangle}$ with a step nucleon distribution

$$\rho(r) = \rho_0 \Theta(r - R). \tag{13}$$

Then the geometric rms radius calculated with the step function is given by

$$\sqrt{\langle r^2 \rangle}\Big|_{geom} = \sqrt{\frac{3}{5}} R. \tag{14}$$

We will normalize the “geometrical" rms radius to the one $\sqrt{\langle r^2 \rangle^*}\Big|_{geom} = \sqrt{3/5}R^*$, where R^* is the nuclear radius on the beta-stability line which obeys the saturation behavior $R^* = r_0 A^{1/3}$. Finally we obtain

$$\sqrt{\langle r^2 \rangle}\Big|_{geom} = \sqrt{\frac{3}{5}} R^* \left(\frac{1 - X^*}{1 - X}\right)^{1/3}. \tag{15}$$

The results of calculations by use of Eq. (15) are shown in Fig. 2 with the dashed horizontal lines. As one can see these results for the nuclei ^{23}Na, ^{120}Sn, and ^{208}Pb are very close to the ones on the beta-stability line (thin solid line). The difference between the dashed lines and the thick solid ones represents the magnitude of the polarization effect given by Eq. (11). Thus, we can conclude that the deviation of $\sqrt{\langle r^2 \rangle}$ from the saturation behavior $\sim A^{1/3}$ in the regions of medium and heavy nuclei is caused by the polarization effect which perturbs the distribution of the neutron excess.

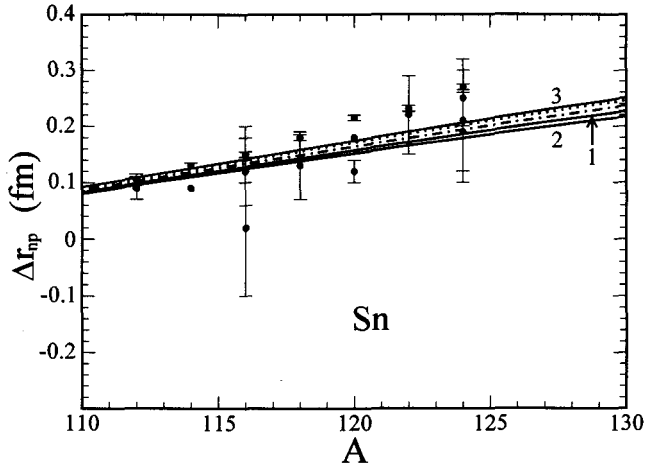

Fig. 3. Isovector shift of nuclear rms radius Δr_{np} in Sn isotopes for the SkM parametrization. Solid line 1 was obtained by use of trial functions Eq. (5), i.e., $\Delta_a \neq 0$, and $\beta = 1/36$. The dotted line is the same but without spin-orbit interaction and the dash-dotted line is without Coulomb interaction. The solid line 2 is for $\Delta_a = 0$ and $\beta = 1/36$; the solid line 3 is for $\Delta_a = 0$ and $\beta = 1/9$.

The A dependence of the size of the neutron coating $\Delta r_{np} = \sqrt{\langle r_n^2 \rangle} - \sqrt{\langle r_p^2 \rangle}$ is illustrated in Fig. 3 for Sn isotopes. The experimental data have been taken from Refs. [9 - 12]. As can be seen from the figure the Coulomb interaction affects the isovector shift of nuclear radii weakly but with growing of A and X this influence slightly increases. The last is because the Coulomb interaction increases the distance between protons, i.e., $\langle r_p^2 \rangle$, and reduces thereby the isovector shift. The spin-orbit interaction produces the same effect as the Coulomb interaction but with stronger magnitude. As was mentioned above, the spin-orbit interaction leads to a deeper potential near the surface region and the nuclear core attracts the external neutrons decreasing the diffuse layer of the neutron distribution. That reduces the isovector shift of nuclear radii. The spin-orbit effect on Δr_{np} increases with X because the increase of X leads to the contribution to the density $\rho_n(r)$ of neutrons with higher angular momentum.

4. Summary

We have applied the direct variational method within the extended Thomas-Fermi approximation with effective Skyrme-like forces to the description of the radii of nucleon distributions. In our consideration, the thin-skinned nucleon densities $\rho_p(\mathbf{r})$ and $\rho_n(\mathbf{r})$ are generated by the profile functions which are eliminated by the requirement that the energy of the nucleus should be stationary with respect to variations of these profiles. An advantage of the used direct variational method is the possibility to derive the equation of state for finite nuclei: dependence of the binding energy per particle or the pressure on the bulk density ρ_0.

We have evaluated the partial equation of state of finite nuclei and demonstrated that the bulk density $\rho_{0,X}$ decreases beyond the beta stability line. That means the partial pressure $P_{A,sym}$ is positive driving off the neutrons in neutron-rich nuclei to the skin.

Using the leptodermous properties of the profile nucleon densities $\rho_p(\mathbf{r})$ and $\rho_n(\mathbf{r})$, we have established the presence of the neutron coating. The size of the neutron coating is growing with moving away from the beta stability line. In Fig. 2 this fact is demonstrated as a deviation of the rms radius of the nucleon distribution from the saturation behavior $\sim A^{1/3}$ in the nuclei beyond the beta-stability line.

We have established the influence of the polarization effect given by Eq. (11) on the rms radius $\sqrt{\langle r^2 \rangle}$ of the nucleon distribution. This effect increases with the asymmetry parameter X and can be responsible for the appearance of the giant neutron halo in the nuclei close to the drip line.

It was also shown that the isovector shift of the nuclear radius Δr_{np} is primarily linear dependent on the asymmetry parameter X. The Coulomb and spin-orbit interactions do not affect significantly the isovector shift of the nuclear radius.

REFERENCES

1. *Meng J., Toki H., Zeng J.Y. et al.* // Phys. Rev. - 2002. - Vol. C65. - P. 041302.
2. *Kirzhnitz D.A.* Field Theoretical Methods in Many Body-Systems. - London: Pergamon, 1967.
3. *Brack M., Guet C., Håkansson H.-B.* // Phys. Rep. - 1985. - Vol. 123. - P. 275.
4. *Kolomietz V.M.* Local Density Approach for Atomic and Nuclear Physics. - K.: Nauk. dumka, 1990. - 164 p.
5. *Kolomietz V.M., Lukyanov S.V., Sanzhur A.I.* // Nucl. Phys. At. Energy - 2010. - Vol. 11. - P. 335.
6. *Oyamatsu K., Tanichata I., Sugahara S. et al.* // Nucl. Phys. - 1998. - Vol. A634. - P. 3.
7. *Oyamatsu K., Iida K.* // Progr. Theor. Phys. - 2003. - Vol. 109. - P. 631.
8. *Kolomietz V.M., Sanzhur A.I.* // Phys. Rev. - 2010. - Vol. C81. - P. 024324.
9. *Ray L.* // Phys. Rev. - 1979. - Vol. C19. - P. 1855.
10. *Starodubsky V.E., Hintz N.M.* // Phys. Rev. - 1994. - Vol. C49. - P. 2118.
11. *Karataglidis S., Amos K., Brown B.A., Deb P.K.* // Phys. Rev. - 2002. - Vol. C65. - P. 044306.
12. *Clark B.C., Kerr L.J., Hama S.* // Phys. Rev. - 2003. - Vol. C67. - P. 054605.

STOCHASTIC RESONANCE AT DIFFUSION OVER A POTENTIAL BARRIER

V. M. Kolomietz, S. V. Radionov

Institute for Nuclear Research, National Academy of Sciences of Ukraine, Kyiv, Ukraine

The general problem of diffusive overcoming of a single-well potential barrier in the presence of a periodic time forcing is studied within the generalized Langevin approach. We found that the thermal diffusion over the barrier can be resonantly accelerated at some frequency of the periodic modulation that is inversely proportional to the mean first-passage time for the motion in the absence of the time-modulation. The resonant activation effect is rather insensitive to the correlation time of the random force term in the Langevin equation of motion.

1. Introduction

Nonlinear systems with a complex dynamics may show significantly different response on an external periodic forcing than the corresponding linear systems. In this respect one can mention stochastic resonance phenomenon [1], when the response of the nonlinear system on the harmonic perturbation is resonantly activated under some optimal level of a noise. The resonant activation of the system occurs when the frequency of the modulation, ω, is close to the Kramers' escape rate, r_{Kr}, $\omega \approx r_{Kr}$, of the transitions from one potential well to another one. One can observe and measure stochastic resonance phenomenon in different physical systems like a ring laser [2], magnetic systems [3], optical bistable systems [4] and others.

In the present paper, our aim is to study thermal non-Markovian diffusion over a one-humped potential barrier in the presence of periodic time modulation.

The paper is organized as follows. In Sect. 2, we set in the basic Langevin equation of motion for diffusive dynamics over the potential barrier in the presence of a sinusoidal time modulation. In Sect. 3, it is considered the unperturbed path of the model system. The periodically perturbed diffusion is discussed in Sect. 4. Finally, the main conclusions are given in Sect. 5.

2. Thermal non-Markovian diffusion over a potential barrier

We start from the generalized Langevin equation of motion for a single dimensionless coordinate $q(t)$ diffusively overcoming the potential barrier in the presence of a periodic force $F_{ext}(t) = \alpha \sin(\omega t)$ [5]:

$$M\,\ddot{q} = -\frac{\partial E_{pot}}{\partial q} - \int_0^t \kappa(t-t')\,\dot{q}(t')dt' + \zeta(t) + \alpha \sin(\omega t)\,, \tag{1}$$

where M is the constant mass parameter, $\kappa(t-t')$ is the memory kernel of the retarded friction force and $\zeta(t)$ is the random force. The potential energy $E_{pot}(q)$ is schematically shown in Fig. 1 and presents a single-well barrier formed by a smooth joining at $q = q'$ of the potential minimum oscillator with the inverted oscillator,

$$E_{pot}(q) = \begin{cases} \dfrac{1}{2} M \omega_0^2 (q-q_0)^2, q < q' \\ E_b - \dfrac{1}{2} M \omega_1^2 (q-q_1)^2, q \geq q' \end{cases}, \tag{2}$$

where E_b is the height of the barrier (Fig. 1).

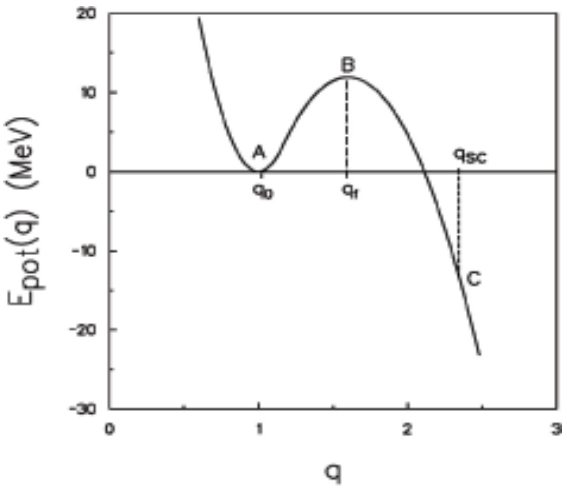

Fig. 1. A potential energy landscape defined by a smooth joining of a ground-state oscillator with an inverted saddle-point oscillator (2) with q_0 being the minimum at the point A, q_1 being the position of the top (point B) of the parabolic barrier.

A noise term $\zeta(t)$ in Eq. (1) is assumed to be Gaussian distributed with zero mean and correlation function related to the memory kernel $\kappa(t-t')$:

$$\langle \zeta(t)\zeta(t') \rangle = T\kappa(t-t'), \tag{3}$$

where T is the temperature of the system. Below we shall assume that the memory kernel is given by

$$\kappa(t-t') = \kappa_0 \exp\left(-\frac{|t-t'|}{\tau}\right), \tag{4}$$

where τ is a correlation time.

3. Unperturbed diffusion over the barrier

At the beginning, we investigated the non-Markovian diffusive dynamics for the infinitely slow ($\omega = 0$) time modulation and calculated a time-dependent escape rate $r(t)$. For that, the Langevin equation (1) was solved numerically by generating a bunch of the trajectories $\{q_i(t)\}, i = 1,...,N_0$ with the following initial conditions:

$$q_i(0) = q_0, \quad \langle \dot{q}_i(0) \rangle = 0, \quad \langle \dot{q}_i^2(0) \rangle = T/M, \tag{5}$$

where N_0 is a total number of the trajectories involved in the calculations.

The escape rate over the barrier was defined by

$$r(t) = -\frac{1}{P(t)}\frac{dP(t)}{dt}, \tag{6}$$

where $P(t)$ is the survival probability, i.e., probability of finding the system on the left from the top of the barrier till the time t:

$$P(t) = \frac{N(t)}{N_0}. \tag{7}$$

Here, $N(t)$ is a number of the trajectories which do not reach the top of the barrier before the time t. In the numerical calculations, all quantities of the dimension of energy is measured in units of the temperature T of the system, quantities of the dimension of time are taken in units of $\sqrt{M/T}$. For the system's parameters we adopted the following values:

$$q_0 = 1, \quad q' = 1.2, \quad q_1 = 1.6, \quad \omega_0 = 6.75, \quad \omega_1 = 9.59, \quad E_b = 5.15, \quad \kappa_0 = 1920, \tag{8}$$

which are typical for diffusion-like studies of fission of highly excited atomic nuclei, see Ref. [6].

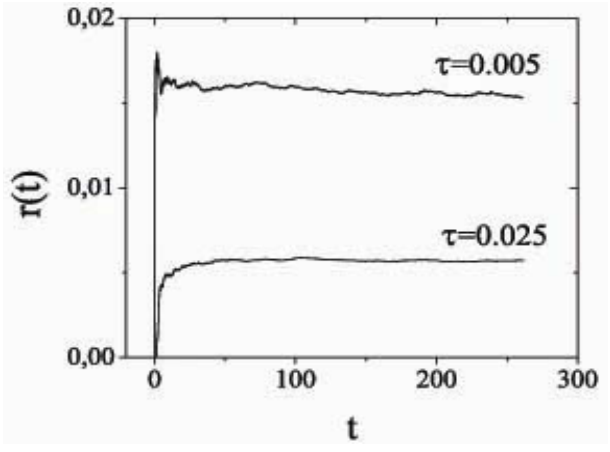

Fig. 2. The time dependence of the escape rate $r(t)$ (see Eq. (6)) for the non-Markovian diffusion dynamics Eqs. (1) - (6) calculated for two values of the correlation time τ: $\tau = 0.005$ (when the memory effects in the diffusive dynamics are quite weak) and $\tau = 0.025$ (when the memory effects are fairly strong), see [6].

In Fig. 2, the typical time behavior of the escape rate $r(t)$ is plotted for two values of the correlation time τ: $\tau = 0.005$ (when the memory effects in the diffusive dynamics Eqs. (1) - (6) are quite weak) and $\tau = 0.025$ (when the memory effects are fairly strong), see [6].

It is seen from Fig. 2 that initially the escape is affected by transient effects, when the survival probability $P(t)$ deviates strongly from the exponential form. With time, the escape process becomes more and more stationary giving rise to the corresponding saturation of the rate $r(t)$ of Eq. (6) establishing of a quasistationary probability flow over the barrier. Qualitatively, one can describe typical time evolution of the escape rate as

$$r(t) = r_0\left(1 - \exp[-t/t_{tran}]\right). \tag{9}$$

In both cases a duration of the transient time, t_{tran}, is almost the same ($t_{tran} \approx 50$) for quite weak and fairly large memory effects in the diffusion process. However,

a saturation value, r_0, of the escape rate is significantly different. It is because of the memory effect for the large values of the correlation time τ.

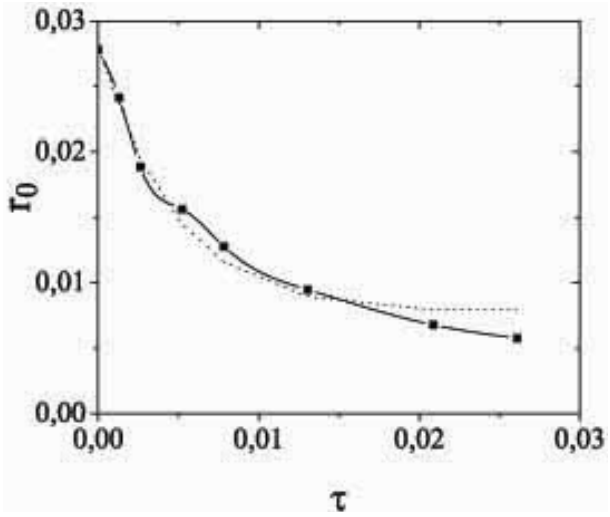

Fig. 3. The saturation value r_0 of the escape rate (see Eq. (9)) vs the correlation time τ, measuring the strength of the memory effects in the non-Markovian diffusion dynamics (see Eqs. (1) - (6)). The dotted line represents the Kramers' result of Eq. (10) for the escape rate calculated with the τ-dependent friction coefficient of Eq. (11).

In Fig. 3, we showed how the value r_0 of Eq. (9) depends on the strength of the memory effects in the diffusive dynamics Eq. (1). Dotted line in Fig. 3 represents the famous Kramers' result for the escape rate [6]

$$r_{Kr} = \frac{\omega_0}{2\pi}\left(\sqrt{\left(\frac{\gamma}{2M\omega_1}\right)^2 + 1} - \frac{\gamma}{2M\omega_1}\right)\exp\left(-\frac{E_b}{T}\right), \quad (10)$$

where the friction coefficient γ is assumed to be τ-dependent [5]

$$\gamma(\tau) = \frac{\kappa_0 \tau}{1 + (\kappa_0 / M)\tau^2}. \quad (11)$$

In paper [5], the friction coefficient of Eq. (11) is used within the Fermi-liquid approach to the nuclear collective motion with τ being the relaxation time of the collective excitations. There, $\gamma(\tau)$ is taken as an interpolation formula for the τ-dependent friction coefficient between the first-sound regime (i. e., the regime of quite frequent collisions between nucleons, $\sqrt{\kappa_0 / M}\,\tau << 1$, when $\gamma(\tau) \propto \tau$) and the zero-sound regime (i. e., the regime of fairly rare collisions between nucleons, $\sqrt{\kappa_0 / M}\,\tau >> 1$, when $\gamma(\tau) \propto 1/\tau$).

We see that the memory effects significantly suppress the value of the escape rate in the saturation regime of probability flow over the potential barrier. Initially (i. e., at relatively small values of the correlation time τ) the suppression is mainly caused by the growing role of the usual friction in the non-Markovian diffusion motion Eqs. (1) - (6). As is followed from Fig. 3, in this case the escape rate at saturation r_0 (9) may be quite well approximated by the Kramers' formula, see Eq. (10). On the other hand, at relatively large correlation times τ, the effect of the friction on the diffusion over the barrier is negligibly weak and the escape rate's suppression appears exclusively due to the additional conservative force, see Ref. [6]. As a result, the stationary value of the escape rate deviates substantially from the Kramers' escape rate Eq. (10) at the fairly strong memory effects in the diffusive motion across the barrier. Note also that, as shown in [8] and [9], the characteristics of the escape process depend much on the shapes of the potential barrier. Thus, for more complicated shapes (than the parabolic one shown in Fig. 1) of the potential energy $E_{pot}(q)$, the Kramers' model [7] cannot be applied.

4. Periodic perturbation effect on the thermal non-Markovian diffusion over the barrier

Now we will study the dynamics over the barrier Eqs. (1) - (6) in the presence of the external harmonic force. We will assume that the amplitude α of the force $\alpha\sin(\omega t)$ in Eq. (1) is so small ($\alpha = 0.05$) that still the reaching the top of the barrier is caused exclusively by diffusive nature of the dynamics. In Fig. 4, we calculated the typical dependencies of the mean first-passage time τ_{mfpt} (as a mean time of the first crossing of the top of the barrier) on the frequency ω of the external harmonic force. The calculations were performed for the weak, $\tau = 0.05$, (lower curve in Fig. 4) and strong, $\tau = 0.025$, (upper curve in Fig. 4) memory effects in the non-Markovian diffusive motion over the barrier.

In both cases the mean first-passage time τ_{mfpt} non-monotonically depends on the frequency of the perturbation that is character for the stochastic resonance phenomenon observed in a number of different physical systems. From Fig. 4 one can conclude that diffusion over the potential barrier in the presence of the harmonic time perturbation is maximally accelerated at some definite so to say resonant frequency ω_{res} of the perturbation,

$$\omega_{res} \approx \frac{1.5}{\tau_{mfpt}(\omega = 0)}. \quad (12)$$

In fact, the quantity $\tau_{mfpt}(\omega = 0)$ presents the characteristic time scale for the diffusion dynamics of Eq. (1). In the case of adiabatically slow time variations of the harmonic force, $\omega << \omega_{res}$, one can approximately use $\alpha\sin(\omega t) \approx \alpha\omega t$ and

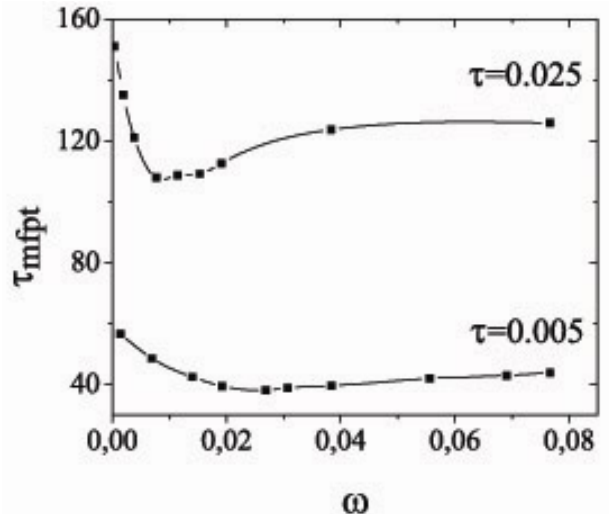

Fig. 4. The mean first-passage time τ_{mfpt} of the non-Markovian diffusion motion of Eqs. (1) - (6) is given as a function of the frequency ω of the harmonic time perturbation at two values of the correlation time $\tau = 0.05$ (*lower curve*) and $\tau = 0.025$ (*upper curve*).

the diffusion over the barrier is slightly accelerated. As a result, the mean first-passage time $\tau_{mfpt}(\omega)$ is smaller than the corresponding unperturbed value $\tau_{mfpt}(\omega = 0)$. The same feature is also observed at the fairly large modulation's frequencies, when $\omega >> \omega_{res}$. In this case the harmonic perturbation $\alpha\sin(\omega t)$ may be treated as a random noise term with the zero mean value and variance α^2. Such a new stochastic term will lead to additional acceleration of the diffusion over the barrier.

5. Conclusions

We have investigated how model dynamics of the non-Markovian diffusion over the single-well parabolic barrier is affected by the external periodic time modulation. We have calculated both the mean first-passage time τ_{mfpt} and the escape rate $r(t)$ over the barrier. These two quantities have been found to be sensitive to the relative strength of memory effects in the diffusive dynamics Eqs. (1) - (6), measured by the correlation time τ. Having calculated the mean first-passage time τ_{mfpt} for different values of the frequency ω of the modulation, we have found that the sinusoidal perturbation accelerates the diffusion over the barrier, see Fig. 4. The maximal (resonant) acceleration is achieved at the $\omega = \omega_{res}$, where ω_{res} is inversely proportional to the mean first-passage time in the absence of the modulation, see Eq. (12). We have seen that a value of the resonant activation over the barrier $\tau_{mfpt}(\omega_{res}) / \tau_{mfpt}(\omega = 0)$ remains practically the same for the quite weak as well as for the fairly strong memory effects in the diffusive dynamics.

REFERENCES

1. *Benzi R., Sutera A., Vulpiani A.* The mechanism of stochastic resonance // J. Phys. A. - 1981. - Vol. 14. - P. L453.
2. *McNamara B., Wiesenfeld K., Roy R.* Observation of stochastic resonance in a ring laser // Phys. Rev. Lett. - 1988. - Vol. 60. - P. 2626.
3. *Grigorenko A., Nikitin P., Slavin A., Zhou P.* Experimental observation of magnetostochastic resonance // J. Appl. Phys. - 1994. - Vol. 76. - P. 6335.
4. *Dykman M.I., Velikovich A.L., Golubev G.P. et al.* Stochastic resonance in an all-optical passive bistable system // JETP Lett. - 1991. - Vol. 53. - P. 193.
5. *Kolomietz V.M., Radionov S.V.* Non-Markovian diffusion over a potential barrier in the presence of periodic time modulation // Phys. Rev. - 2011. - Vol. E84. - P. 051123.
6. *Kolomietz V.M., Radionov S.V., Shlomo S.* Memory effects on descent from the nuclear fission barrier // Phys. Rev. - 2001. - Vol. C64. - P. 054302.
7. *Kramers H.A.* Brownian motion in a field of force and the diffusion model of chemical reactions // Physica. - 1940. - Vol. 7. - P. 284.
8. *Hofmann H., Ivanyuk F.A.* Mean first passage time for nuclear fission and the emission of light particles // Phys. Rev. Lett. - 2003. - Vol. 90. - P. 132701.
9. *Hofmann H., Magner A.G.* Mean first passage time for potentials having structure // Phys. Rev. - 2003. - Vol. C68. - P. 14606.

THE INTERNAL CONVERSION COEFFICIENT FOR THE K-FORBIDDEN E1-TRANSITION WITH THE ENERGY OF 55 keV IN ^{177}Hf

A. P. Lashko, T. N. Lashko

Institute for Nuclear Research, National Academy of Sciences of Ukraine, Kyiv, Ukraine

The precise γ-ray intensities of the transitions following the decay of 160-day isomeric state in ^{177}Lu have been measured by using two different types of HPGe-detectors. The values of the internal conversion coefficient and penetration parameter λ for *E*1-transition with the energy of 55 keV were determined from intensity balance of $21/2^-$ 1260 keV level in ^{177}Hf.

1. Introduction

This article continues the series of works on intranuclear conversion in the *K*-forbidden electric multipole transitions excited by ^{177m}Lu decay. Three of these transitions accompany the decay of the 160-day isomeric state in ^{177}Lu: γ55, γ116, and γ228 keV (Fig. 1). All of them are hindered as compared to single-particle estimates. Some anomalies in γ-ray internal-conversion coefficients (ICC), caused by penetration effect, are possible for such transitions.

In internal conversion theory, by a penetration effect or intranuclear conversion is implied a correction to ICC arising in passing from transition electromagnetic potentials calculated for point-like nucleus to the potentials calculated for finite-size nucleus. Generally, such corrections do not exceed 2 % and have only a slight effect on ICC value. A completely different type of situation occurs in the case of strongly hindered γ-transitions. In such case a contribution from internal conversion may become a crucial factor governing the ICC value. Of course, selection rules, which are responsible for a decrease in probability of γ-radiation, should have essentially smaller effect on the probability of internal conversion.

Appearance of anomalies in ICC of *K*-forbidden transitions is due to admixtures with respect to quantum number *K* in wave functions of initial and final states. There are admixtures that allow conversion transition according to the selection rules with respect to asymptotic quantum numbers, while γ-transition is forbidden. In this case anomalies in ICC caused by the penetration effect are observed. If the selection rules for conversion transition and γ-transition are identical, there are no anomalies. At present, it is very difficult to quantitatively estimate these admixtures. By this reason, it is not feasible to make a prediction of anomalies in ICC for a given *K*-forbidden transition.

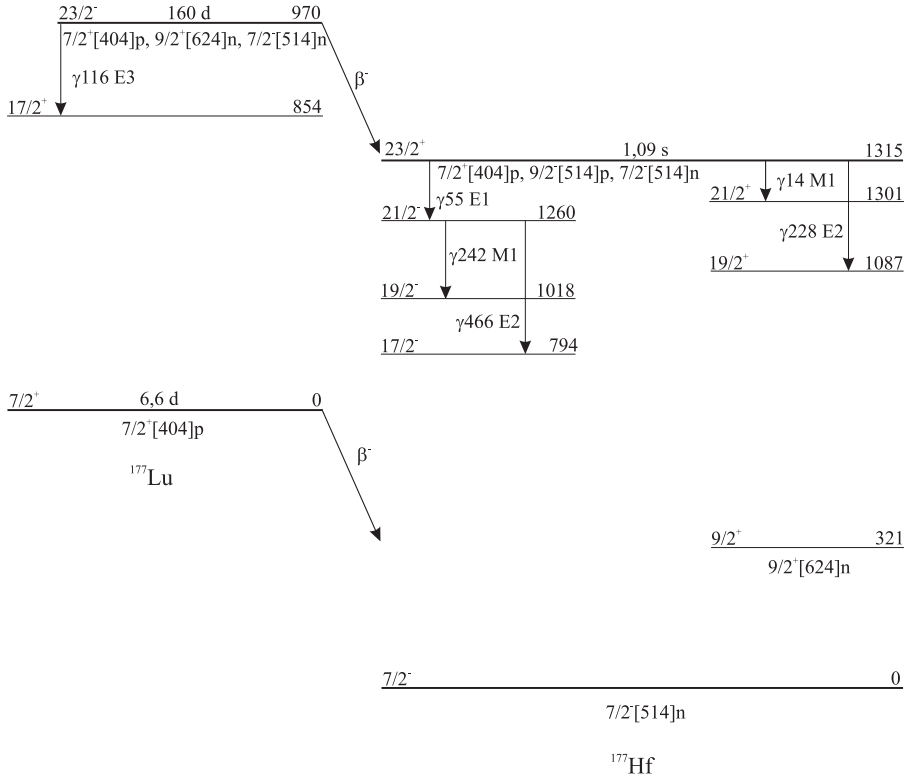

Fig. 1. The partial decay scheme of ^{177m}Lu.

Earlier, in Ref. [1, 2] there was found minor variance between experimental and theoretical values of ICC for γ228 and γ116 keV transitions, which cannot be explained by admixtures of different multipolarities with the same parity. Such deviation can be eliminated by assuming the presence of intranuclear conversion.

The total ICC of the γ55 keV *E*1-transiton can be estimated from the balance of intensities of the 21/2$^-$ 1260 keV level in ^{177}Hf. Following from the ^{177m}Hf decay scheme (see Fig. 1), this level is powered by the γ55 keV transition and deexcited by two intraband γ242 and γ466 keV transitions having the *M*1- and *E*2-multipolarity respectively. The intensities of the strong γ-rays are known with accuracy of (2 ÷ 5) %, but there is disagreement in evaluation of the intensities of some of the weaker lines, such as γ242 keV. Our current research was to clarify all controversial questions in this area and to provide a more accurate estimate of the total ICC of the γ55 keV *E*1-transiton.

2. Experimental technique

The relative intensities of γ-rays following the decay of ^{177m}Lu were measured with a gamma-spectrometer that comprises two horizontal coaxial HPGe-detectors: GMX-30190 and GEM-40195, having the resolution of 1,89 and 1,73 keV for the γ1332-line of ^{60}Co and efficiency of 33 % and 43 % respectively.

The radioactive ^{177m}Lu sources were obtained in the (n, γ) reaction as a result of enriched to 27,1 % in 176 mass number lutetium target irradiation with neutrons at the research nuclear reactor WWR-M. The measurements of gamma-ray spectra started two months after the end of irradiation so that ^{177}Lu ($T_{1/2}$ = 6,6 days), having much larger activation cross-section, must have decayed en masse.

The standard ^{60}Co, ^{133}Ba, ^{137}Cs, ^{152}Eu, ^{228}Th, and ^{241}Am γ-sources were used for accurate calibration of detectors for the energy range of 26 to 1620 keV. The shape of the efficiency curve is well described by the Campbell function [3]:

$$\varepsilon(E) = \sum_{i=1}^{3} p_{2i-1} e^{-p_{2i}E} + p_7 E^{-p_8} . \quad (1)$$

Calibration parameters p_i were found by the least-square method. The uncertainty in the efficiency curve of both detectors does not exceed 2 % throughout the energy range.

To minimize possible systematic errors a series of measurements were performed – using different types of HPGe-detectors, at different geometries, at different gains and channel widths of an amplitude-to-digital converter (8192 and 16384 quantization levels of the input signal) – 20 series of measurements in all.

3. Results and discussion

The γ-ray spectra were analysed using WinSpectrum [4], a computer program which allows determining with high precision the energy and intensity of components that have an asymmetric line shape and the ones that are overlapping. The usage of different types of detectors allowed us to determine the relative intensities of γ-rays for the energy range above 100 keV more precisely. Our data agrees to a great extent with the data of other researchers while having higher precision.

The intensity balance at the 21/2$^-$ 1260 keV level in ^{177}Hf can be written as

$$(1+\alpha(55))I_\gamma(55) = (1+\alpha(242))I_\gamma(242) + (1+\alpha(466))I_\gamma(466) , \quad (2)$$

where α(55), α(242), α(466) and I_γ(55), I_γ(242), I_γ(466) are the total ICCs and transition intensities with the energy of 55, 242, and 466 keV respectively.

Using our data on the intensities of the γ242 and γ466 keV transitions, bringing the experimental value I_γ(55) from Ref. [5] and theoretical values of ICC for γ242 and γ466 keV transitions from Ref. [6], we have calculated the total ICC of the γ55 keV *E*1-transiton to be $\alpha(55)_{exp}$ = 1,08 ± 0,23. The theoretical value of ICC in the hafnium for the γ55 keV *E*1-transiton is much lower, $\alpha(55)_{th}$ = 0,337. To coordinate them the existence of the admixture of *M*2-multipolarity or the existence of the intranuclear conversion should be assumed.

The value of the admixture of *M*2-multipolarity can be calculated using the expression

$$\alpha(55)_{exp} = \alpha(E1)\frac{1}{1+\delta^2(M2/E1)} + \alpha(M2)\frac{\delta^2(M2/E1)}{1+\delta^2(M2/E1)} , \quad (3)$$

where $\delta(M2/E1)$ is *M*2/*E*1 multipole mixing ratio for γ55 keV transition in ^{177}Hf, α(*E*1) and α(*M*2) are the theoretical values of ICC for this transition assuming *E*1- and *M*2-multipolarity respectively.

The obtained value of $\delta^2(M2/E1) = (5{,}2 \pm 1{,}6)\cdot 10^{-3}$ leads to the Weisskopf hindrance factor for the *M*2-component $F_W(\gamma 55\ M2) = (5 \div 9)\cdot 10^6$, while the factors are much higher for other *K*-forbidden transitions in ^{177}Lu and ^{177}Hf (Table 1).

Table 1 shows that the *M*2-component for γ-transition with the energy of 55 keV has a 3,0 to 6,6 times smaller hindrance factor per *K*-forbidenness unit f_ν than other transitions. It means that the *M*2-admixture value is likely to be exaggerated 10^3 to 10^5 times.

Table 1. **Weisskopf hindrance factors for *K*-forbidden transitions in ^{177}Lu and ^{177}Hf**

E_γ, keV	Multipolarity, L	$\Delta K = K_i - K_f$	$\nu = \Delta K - L$	F_w	$f_\nu = (F_w)^{1/\nu}$
14	$M1$	7	6	$7{,}0 \cdot 10^{10}$	64,2
55	$E1$	8	7	$3{,}7 \cdot 10^{13}$	86,8
55	$M2$	8	6	$(5 \div 9) \cdot 10^{6}$	13,1 ÷ 14,4
116	$E3$	8	6	$9{,}1 \cdot 10^{8}$	61,9
228	$E2$	7	5	$1{,}5 \cdot 10^{8}$	43,2

Analyses of the cases of anomalous conversion can be made with the inclusion of penetration corrections developed by Church and Weneser [7]. Using the parameterization of Hager and Seltzer [8] the electric ICC's can be written as

$$ICC = \alpha(EL)(1 + A_1\lambda_1 + A_2\lambda_1^2 + A_3\lambda_2 + A_4\lambda_2^2 + A_5\lambda_1\lambda_2)\,, \quad (4)$$

where $\alpha(EL)$ are the normal (no penetration) ICC's tabulated in Ref. [6], A_i are coefficients calculated in Ref. [8] from electron wave functions for the mulipolarity of interest, and λ_i are the electric penetration parameters. The penetration parameters depend on nuclear structure and are determined from an analysis of the experimental quantities.

If, as it is in our case, independent experimental data are insufficient for finding both penetration parameters λ_1 and λ_2, the calculations are limited to one nuclear current parameter λ_1, which, in general, the anomalies in the *EL*-transitions depend on; the nuclear charge parameter λ_2 is considered to be zero. Because of the fact that in Ref. [8] the penetration coefficients are tabulated only for K-, L-, and M-subshells the following expression was used for the data set analysis

$$\alpha(55)_{exp} = \alpha_L(1 + A_1^L\lambda_1 + A_2^L\lambda_1^2) + \alpha_M(1 + A_1^M\lambda_1 + A_2^M\lambda_1^2) + \alpha_{N+O}\,, \quad (5)$$

where α_L, α_M, α_{N+O} are the theoretical values of ICC, A_i^L, A_i^M are the coefficients for penetration effect analysis in ICC for L-, M-, and N+O-subshells of hafnium respectively.

Theoretical values for the conversion coefficients and penetration coefficients were interpolated from the tables by Hager and Seltzer [6, 8]. The results of calculation are listed in Table 2. Known experimental values of nuclear penetration parameter λ_1 for other *K*-forbidden *E*1-transitions from the Ref. [9] are also given in the Table.

For quantitative estimates of nuclear penetration parameter λ_1 depending on the Weisskopf hindrance factor F_W on the basis of empirical data it is convenient to draw a graph of such relation using the experimental data given in Table 2 (Fig. 2).

Table 2. **Experimental values of the nuclear penetration parameter λ_1 for the *K*-forbidden *E*1-transitions**

Nucleus	E_γ, keV	$\nu = \Delta K - L$	F_w	λ_1	Reference
^{169}Tm	240,3	2	$2{,}9 \cdot 10^{9}$	$4{,}5 \pm 0{,}6$	10
^{171}Tm	295,9	2	$9{,}3 \cdot 10^{8}$	$2{,}7 \pm 0{,}6$ 2,8	11 12
^{171}Tm	308,3	2	$5{,}3 \cdot 10^{8}$	$1{,}2 \pm 0{,}4$ 1,2	11 12
^{171}Yb	19,39	2	$1{,}2 \cdot 10^{9}$	$-(1{,}5 \pm 0{,}5)$	13
^{177}Hf	55,15	6	$3{,}7 \cdot 10^{13}$	12 ± 3 or $-(17 \pm 3)$	present work
^{180}Hf	57,6	7	$3{,}6 \cdot 10^{16}$	$7{,}8 \pm 1{,}0$ 6,9 $7{,}0 \pm 0{,}3$ $6{,}0 \pm 0{,}5$* $6{,}4 \pm 0{,}3$* $7{,}7 \pm 1{,}0$* $7{,}6 \pm 0{,}5$* $7{,}0 \pm 0{,}7$ $6{,}8 \pm 0{,}2$**	14 15 16 17 17 17 17 18

* Using δ^2 from different references.

** Weighted mean.

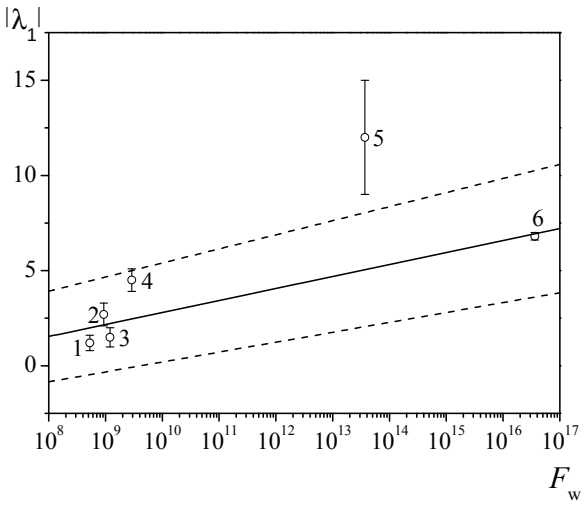

Fig. 2. Relation between the nuclear penetration parameter $|\lambda_1|$ and the Weisskopf hindrance factor F_w for the *K*-forbidden *E*1-transitions. *1* – ^{171}Tm (308,3); *2* – ^{171}Tm (295,9); *3* – ^{171}Yb (19,39); *4* – ^{169}Tm (240,3); *5* – ^{177}Hf (55,15); *6* – ^{180}Hf (57,6); the number in parentheses is the transition energy in keV. Smaller by absolute value, $|\lambda_1| = 12 \pm 3$ is shown for ^{177}Hf.

For Fig. 2 empirical relation (solid line) between the nuclear penetration parameter $|\lambda_1|$ and the Weisskopf hindrance factor F_w for the *K*-forbidden *E*1-transitions was determined without considering the γ55 keV transition in ^{177}Hf. It is described by the equation $\lambda_1 = a + b\log(F_w)$. The following values were found by the least-square method: $a = -(3{,}5 \pm 1{,}5)$; $b = 0{,}63 \pm 0{,}11$. The dashed lines show a 68% confidence interval. As Fig. 2 shows, the obtained experimental value of λ_1 for the γ55 keV transition in ^{177}Hf appear to be higher than expected from the empirical relationship.

Despite that, the explanation of anomalies in the internal conversion coefficients for the *E*1-transition with the energy of 55 keV with occurrence of intranuclear conversion, from our standpoint, is more grounded. As for possible aspects of further research, it would be very interesting to obtain experimental data on the relative intensities of internal-conversion electron lines on L-subshells of ^{177}Hf for this transition, or to attempt to determine more precisely the intensity of the γ55 keV photon in γ-spectrum using high-resolution detectors.

REFERENCES

1. *Bulgakov V.V., Kaznovecky A.B., Kirishchuk V.I. et al.* Revealing of penetration effect in *E*2-transition with energy 228 keV in ^{177}Hf // Izv. Akad. Nauk SSSR. Ser. Fiz. - 1990. - Vol. 54. - P. 1011 - 1013 (in Russian).
2. *Lashko A.P., Lashko T.N.* Anomalies in internal-conversion coefficients of the *K*-forbidden gamma-transitions from the ^{177m}Lu decay // Nucl. Phys. At. Energy. - 2008. - No. 2 (24). - P. 18 - 23 (in Russian).
3. *McNelles L.A., Campbell J.L.* Absolute efficiency calibration of coaxial Ge(Li) detectors for the energy range 160-1330 keV // Nucl. Instrum. Methods. - 1973. - Vol. 109. - P. 241 - 251.
4. *Khomenkov V.P.* Investigation of atomic-nuclear effects in the process of γ-ray internal conversion: Thesis for Ph.D. degree in physics and mathematics. – Kyiv: Institute for Nuclear Research, 2003. - 19 p. (in Russian).
5. *Alexander P., Boehm F., Kankeleit E.* Spin-23/2$^-$ isomer of Lu^{177} // Phys. Rev. - 1964. - Vol. 133. - P. B284 - B290.
6. *Hager R.S., Seltzer E.C.* Internal conversion tables. Part I: K-, L-, M-shell conversion coefficients for Z = 30 to Z = 103 // Nucl. Data Tables. - 1968. - Vol. A4. - P. 1 - 235.
7. *Church E.L., Weneser J.* Effect of the finite nuclear size on internal conversion // Phys. Rev. - 1956. - Vol. 104. - P. 1382 - 1386.
8. *Hager R.S., Seltzer E.C.* Internal conversion tables. Part III: Coefficients for the analysis of penetration effects in internal conversion and *E*0 internal conversion // Nucl. Data Tables. - 1969. - Vol. A6. - P. 1 - 127.
9. *Listengarten M.A.* Anomalous internal conversion in electromagnetic transitions of atomic nuclei // Modern nuclear spectroscopy methods / Ed. by B.S. Dzhelepov. - L.: Nauka, 1986. - P. 142 - 204 (in Russian).
10. *Sergeenkov Yu.V.* Intranuclear conversion for the *K*-forbidden transition with the energy of 240 keV in ^{169}Tm. The 1/2$^-$ [541] band in ^{169}Tm from ^{169}Yb decay // Applications of prism beta-ray spectrometers / Ed. by R.A. Kalinauskas. - Vilnius: Institute of Physics and Mathematics Akad. Nauk LitSSR, 1974. - P. 90 - 96 (in Russian).
11. *Sergeenkov Yu.V., Kharitonov Yu.I.* Penetration matrix elements of the *K*-forbidden ($\Delta K = 3$) *E*1 transitions // Book of abstracts of the XXXII meeting on nuclear spectroscopy and nuclear structure (Kyiv, March 22 - 25, 1982). - L.: Nauka, 1982. - P. 282. (in Russian).
12. *Graham R.L., Geiger J.S., Johns M.W.* Level structure of ^{171}Tm // Can. J. Phys. - 1972. - Vol. 50. - P. 513 - 528.
13. *Artamonova K.P., Grigorev E.P., Zolotavin A.V., Sergeev V.O.* Anomalous conversion of the 19.38-keV *E*1 transition in ^{171}Yb // Izv. Akad. Nauk SSSR. Ser. Fiz. - 1975. - Vol. 39. - P. 1773 - 1777 (in Russian).
14. *Hager R.S., Seltzer E.C.* Concerning the possibility of a parity admixture in the 57.6 keV transition in ^{180}Hf^m // Phys. Lett. - 1966. - Vol. 20. - P. 180 - 182.
15. *Scharff-Goldhaber G., McKeown M.* Anomalous L-subshell conversion coefficients of the highly *K*-forbidden *E*1 transition in Hf^{180m} (5.5 h) // Phys. Rev. - 1967. - Vol. 158. - P. 1105 - 1111.
16. *Dragoun O., Plajner Z., Martin B.* Nuclear structure effect in internal conversion of the 57.54 keV transition in ^{180}Hf // Nucl. Phys. - 1970. - Vol. A150. - P. 291 - 299.
17. *Gvozdev V.S., Grigorev V.N., Sergeenkov Yu.V.* Intranuclear conversion parameters for the 57.54-keV, *K*-forbidden, *E*1 transition in ^{180}Hf // Izv. Akad. Nauk SSSR. Ser. Fiz. - 1970. - Vol. 34. - P. 1680 - 1682 (in Russian).
18. *Fransson K., Becker J., Holmberg L., Stefansson V.* Nuclear-structure effects on the conversion electron particle parameter of the 57.5 keV *E*1 transition in ^{180}Hf // Phys. Scr. - 1981. - Vol. 23. - P. 227 - 230.

THE MASS (CHARGE) SPECTRUM OF SUPERHEAVY NUCLEI FISSION FRAGMENTS: THE NEW PERSPECTIVES FOR THE THEORY OF NUCLEOSYNTHESIS

V. T. Maslyuk

Institute of Electron Physics, National Academy of Sciences of Ukraine, Uzhgorod, Ukraine

A new approach to the problem of nucleosynthesis based on assumption of a nuclear matter or superheavy nuclei series fragmentation up to atomic nuclei is proposed. It is shown that studies of the mass (charge) fragments yields (MCFY) after nuclear matter disintegration is possible within proposed statistical theory. The data of MCFY calculation for exotic superheavy nuclei multifragmentation with A=300, 900 and 1200 and arbitrary Z values are demonstrated.

1. Introduction

It is well known the importance of understanding the chemical elements' origin in the Universe, based on the fundamental processes of interaction and transformation of nuclear matter [1]. At present, the theory of nucleosynthesis is based on the so-called r-, s- [2], or p- [3] processes of nuclei elementary interaction with neutrons or protons that are created under the act of the supernova star disintegration. This trend in the theory of nucleosynthesis based on the so-called "snowball" approximation, when the synthesis of atomic nuclei results from the series of elementary processes' interaction of the initial light nucleus (H, He, Li, B, Be et al) or more heavy nuclei in intense beams of electrons, protons, neutrons or alpha particles accelerated in cosmic strong electromagnetic fields.

However, during the creation, for example, the supernova 2 or neutron stars, when the nuclear matter densities reached up to $r \sim (10^{-2} - 2)\, r_o$, where $r_o \approx 0.15$ fm^{-3} and temperature $T \approx 0.5 - 10$ MeV, the exotic nuclear matter or huge nuclei can be formed [4, 5] and their further disintegration may also cause the formation of nuclei of well-known chemical elements. It should be noted that previously this mechanism of origin of the chemical elements was not been considering. This may be due to a limitation of our knowledge about stability of the nuclear matter at arbitrary values of nucleus mass A and charge Z, and the absence of first principle theories able to explain the nature of its disintegration and nuclear fission fragments formation.

This similar problem exists when one is searching for the islands of stability for superheavy nuclei and their traces in the environmental samples.

It is well-known that new elements with charge only up to Z = 117 (^{293}117 and ^{294}117) were synthesized in the laboratory. Recently was reported about experimental identification of superheavy nuclei with charge within the range from 105 to 130 [6].

In this paper, the results of mass or charge fragments yields calculation obtained under disintegration of the nuclear matter's arbitrary fragments are presented at first time. Current investigation had been conducted by using the proposed statistical method that based on thermodynamic ordering post-fission fragments for arbitrary values and ratios A and Z.

2. Theory

We consider that the scheme of the two-fragment fission should be realized in all possible distribution of initial nucleus' nucleons by two fragments with their different atomic masses and the protons / neutrons ratio [7, 8]. In this case, the *i*-th cluster contains $Z_{j,i}$ protons and $A_{j,i} - Z_{j,i}$ neutrons in the *j*-th fragment, where $j = 1,2$, as well as n_i fission neutrons. In general case, the following conservation conditions for all possible schemes of two-fragment fission hold true

$$A_{1,i} + A_{2,i} + n_i = A_0, \qquad Z_{1,i} + Z_{2,i} = Z_0 - \Delta z_i, \tag{1}$$

where Δz_i is the number of β^+ (at $\Delta z_i < 0$) or β^- ($\Delta z_i > 0$) decays within a single nuclear cluster. Emission of nuclear particles plays an important role in relaxation of heavy-nuclei fission fragments excitation and their approaching the islands of stability.

Each such distribution creates the two-fragment clusters and the set of fragment clusters form a statistical ensemble.

The thermodynamics parameters of two-fragment clusters ensemble are determined by the state of the initial nucleus. The initial nucleus determines the type of created statistical ensemble by considering of the one set fluctuations of the thermodynamics parameters and neglecting the other. In case of nuclear fission we assume that the number of all types' nucleons in two fragment clusters is constant, see (1) and only fluctuation of energy and volume is allowed. It leads to a canonical constant - pressure (P) ensemble.

Within the proposed approach, the problem of the fission fragments yields' study resolves into analysis of the equilibrium conditions for a canonical constant-pressure ensemble.

The fact that emission of fission neutrons decreased the nucleus volume [9] and thus provides the $P\Delta V$ work should be considered as well. The equilibrium parameters of the two-fragment clusters ensemble can be obtained from the condition of the Gibbs' thermodynamic potential minimum [10]:

$$G = U - TS + PV, \tag{2}$$

where T is the nuclei temperature and U is initial or total energy, that determined by binding energy of the two-fragment cluster. Its spectrum $\{\varepsilon_i\}$ is an additive quantity with respect to the binding energy of fission fragments:

$$\varepsilon_i = \sum_{j=1,2} \cdot \sum_{\langle N_p \rangle_i} \cdot \sum_{\langle N_n \rangle_i} U_j(A_{j,i}, Z_{j,i}) , \tag{3}$$

where U_j is the binding energy of the i-th fission fragment, j = 1, 2; the symbol $<...>_i$ means that summation in (3) is taken over the i-th clusters containing two fission fragments with the numbers of protons ($N_{j,i}^{p}$) and neutrons ($N_{j,i}^{n}$) satisfying (1).

The isobaric distribution function, which describe the statistical properties of system in thermodynamic equilibrium and represent the probability of finding a two-fragment nuclear cluster in the i-th state of the ensemble with the energy ε_i, can be expressed in the following way:

$$f_i(V) = \omega_i \exp\{-(\varepsilon_i + PV)/T\}/Z_p , \tag{4}$$

where the statistical sum Z_p is defined as:

$$Z_p = \sum_{k,V} \omega_k \exp\{-(\varepsilon_k + PV)/T\} .$$

The set of equations (2)–(4) is sufficient to study the observable characteristics of nuclear fission

3. Results and discussion

It should be noticed that proposed statistical method contains no adjustable parameters, but only those that can be obtained from experiment. For instance, the temperature T can be defined by analyzing the evaporation spectra of the fission neutrons/protons or fission fragments (see [11] for more detail). The binding energies ei, used in Eq. (3) are tabulated in [12], their extrapolation (mass formula) is given, for example, in [13].

This is the reason of its using to describe the features of the disintegration of nuclear matter. According to (1) we considered the two-fragment fission scheme disintegration of nuclear matter, although the theory allows us to evaluate more complicated cases of nuclear matter multifragmentations. Choice of the evaluation method for the binding energies spectrum ε_i had been determined by the size of nuclear matter fragments. The tabulated values for binding energies obtained [12] only for isotopes with mass numbers up to A = 264 and the proton magic number accounting up to 82, and the same for the neutrons up to 126.

In other words, it can be used in the study of multi fragmentation of the super heavy nuclei with mass numbers up to A = 400 - 500. On the other, mass formulas, see for instance [13], able us to take into account magic numbers for protons up to 164 and same for neutrons up to 184 and is more adequate for the study of the disintegration of nuclear matter with A >> 500.

In Fig. 1 the mass fission fragments yields of heavy nuclei with A = 300 at different ratios of protons/neutrons and nuclear temperature T (excitation energy) are presented as a 3D color fill surface. These figures illustrates us the symmetrization (one hump feature) of fission fragments yields with temperature T rising and their transformation from two to three hump structures with increasing content of protons in the initial nucleus.

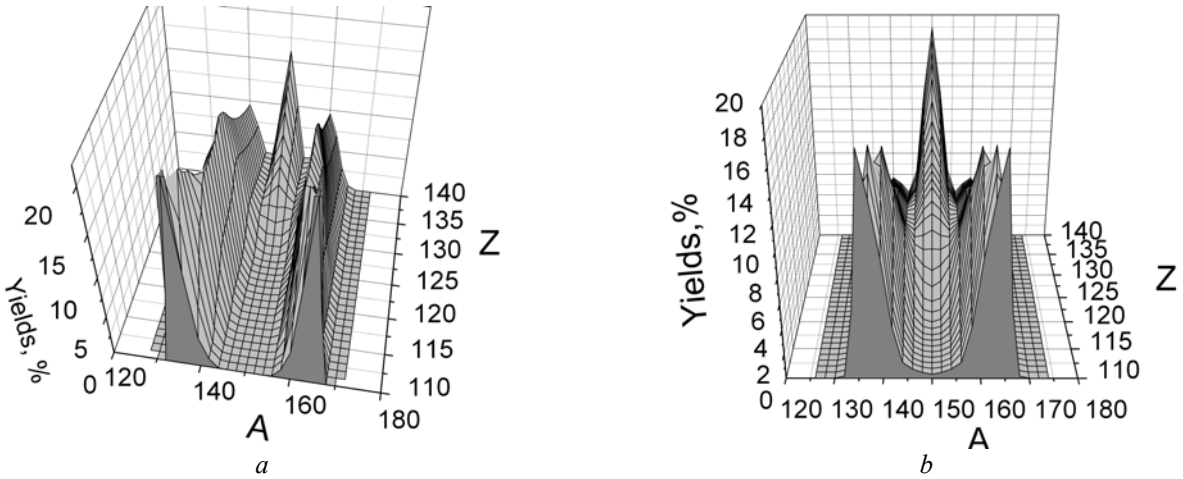

Fig. 1. The fission fragments yields for hypothetical nucleus with A = 300 at different temperatures: *a* - T = 0.5 MeV ; *b* - T = 0.85 MeV.

In Fig. 2 the same mass distributions of fission fragments from the disintegration of nuclear matter with A = 900 (a) and A = 1200 (b) at T = 0.95 MeV is showing. In the first case the 2-fragment clusters with the specific binding energy not less than 5.455 MeV / A were selected and in the last, respectively, - 4.804 MeV / A. It is seen that for large values of A the mass spectra lose the fine structure in a wide range of Z / A ratio and demonstrate symmetrical two-fragment fission.

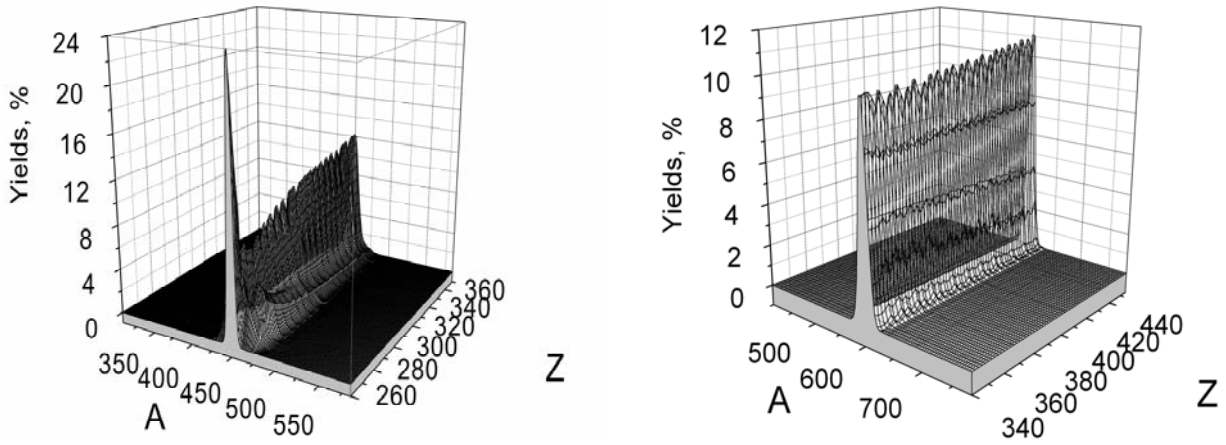

a *b*

Fig. 2. 3D fission fragments yields of the super heavy nuclei with A = 900 (*a*) and A = 1200 (*b*) at different ratios of protons / neutrons. The temperature of the initial nucleus T = 0.85 MeV.

Thus, obtained results demonstrate the possibility of a theoretical study of the nuclear matter fragmentation's effects. This study is very important for the problems of nucleosynthesis. Further development of the proposed theoretical method may be on the way to account the three- or more fragmentation scheme of fission and take into consideration the chains of elementary beta- or neutron emission.

The author is grateful to Prof. E. Skakun for initiation this work and fruitful discussions.

REFERENCES

1. *Fülöp Zs., Elekes Z.* Nuclear processes in nature // EOLSS Enciklopedia - Radiochemistry and Nuclear Chemistry (e-book) / Ed. S. Nagy (http://www.eolss.net/ outlinecomponents/ Radiochemistry-Nuclear-Chemistry.aspx) (2008).
2. *Wallerstein G. et al.* Synthesis of the elements in stars: forty years of progress // Reviews of Modern Physics. - 1997. - Vol. 69. - P. 995 - 1084.
3. *Arnould M., Goriely S.* The p-process of stellar nucleosynthesis: astrophysics and nuclear physics status // Physics Reports. - 2003. - Vol. 384. - P. 1. - 84.
4. *Grebenev S.A., Lutovinov A.A., Tsygankov S.S., Winkler C.* Hard X-ray emission lines from the decay of 44Ti in the remnant of Supernova 1987A // Nature. - 2012. - Vol. 490, No. 7420. - P. 373 - 375.
5. *Botvina A.S., Mishustin I.N.* Stellar matter in supernova explosions and nuclear multifragmentation // Nuclear Physics. - 2008. - Vol. 71, No. 6. - P.1114 - 1120.
6. *The superheavy* elements were found in cosmic rays // http://lenta.ru/news/2011/12/13/ heavy/
7. *Maslyuk V. et al.* Study of Mass Spectra of Light-Actinide Fission Isotopes Kr and Xe in the Framework of a New Statistical Approach // Physics of Particles and Nuclei Letters. - 2007. - Vol. 4, No. 1. - P. 78 - 84.
8. *Maslyuk V.T. et al.* New Statistical Methods for Systematizing the Nuclei Fission Fragments: Post-Scission Approach // http://arxiv.org/abs/1202.0878
9. *Sitenko O.G., Tartakovskii V.K.* Lectures on the theory of the nucleus. - M.: Atomizdat, 1972. - 352 p. [in Russian].
10. *Girifalco L.G.* Statistical Physics of Materials. - N.Y. - Toronto: John Wiley and Sons, 1973. - 382 p.
11. *Goryachev A.M. et al.* Nuclear Temperature Determination from Energy Distribution of Fast Photoneutrons from Medium and Heavy Nuclei // Phys. At. Nucl. - 1994. - Vol. 57. - P. 764 - 768.
12. *Audi G., Wapstra A.H., Thibault C.* The AME2003 atomic mass evaluation (II). Tables, graphs, and references // Nuclear Physics. - 2003. - Vol. A 729. - P. 337 - 676.
13. *Moller P. et al.* // Atomic Data and Nuclear Data Tables. - 1995. - Vol. 59. - P. 185.

CORRELATION RESEARCHES OF THE OUTGOING DIRECTIONS "SHAKE-OFF" ELECTRON AND POSITRON AT β^+-DECAY

N. F. Mitrokhovich, V. T. Kupryashkin, L. P. Sidorenko

Institute for Nuclear Research, National Academy of Sciences of Ukraine, Kyiv, Ukraine

The correlation properties electron "shake-off" at β^+-decay is studied. The measurements were fulfilled in compare with such properties "shake-off" electron at β^--decay for explanation mechanism, accountable for correlation motion "shake-off" electron and main particle (electron at β^--decay and positron at β^+-decay). ^{152}Eu decay was used for it. The measurements were performed on the installation of coincidences of γ-quanta with electrons and low energy electrons, including of e_o-electrons of the secondary electron emission ($\gamma\gamma e e_o$-coincidences). The registration of electrons "shake-off" implemented on e_o-electrons, created by them. On obtained data, the space correlation of electron "shake-off" with positron at β^+-decay in direction forward is much less that those correlating "shake-off"-electron at β^--decay. "Shake-off"-electrons at β^+-decay are predominantly moving in large solid angles relate positron. The mechanism, accountable for it, is proposed.

Introduction

At β-decay nuclear charge sharply changes on 1 that produces strong shakeup of atomic shell and is accompanied by her excitation (SU processes), or ionization (SO processes) [1]. The effects on outer shells are not small: $P_{SO} \sim 0{,}06$, $P_{SU} \sim 0{,}1$ for N-shell ($Z \sim 50$) [2]. Electrons "shake-off" are hardly correlated on direction with primary particle, emitting together to the same hemisphere [3 - 9].

There are many causes for research of "shake-off": for analysis of atomic-nuclear processes (ICC, shape β- spectra), for learn of multielectrons correlations in atoms and correlation motion of particles. These researches performed for study the mechanism, originating the space correlations in motion "shake-off" particle at β-decay [5 - 9]. The investigations of space correlations in emitting an electron of "shake-off" and main (basic) particle (positron at β^+-decay or electron at β^-- decay) are complementing one another and in joint researches are specially relevant. In particular, for the undestanding mechanism, accountable for observation of these correlations [5 - 9]. On our data [7 - 9] correlating of emitting "shake-of" electron along direction motion main particle increases with energy of an electron of "shake-off", qualitatively follows to relation $\sim E^{1/2}$, i.e. is proportional to momentum "shake-off" electron. It point at interaction, responsible for correlative motion of particles, as interaction of currents from moving these charge particles. If it so, the space correlations of electron "shake-off" and main particle at β^-- and β^+- decay should be different.

The study was performed with β^-- and β^+ - components of decay ^{152}Eu.

The experimental methodic for measuring the momentum correlating properties electron "shake-off" - positron at β^+-decay and results

The measurements were performed on the installation of coincidences of γ-quanta with electrons and low energy electrons, including e_o-electrons of secondary electron emission ($\gamma\gamma e e_o$-coincidences) (Fig. 2).

It necessary to note the following. In the given method of measurement, the registration of electrons of "shake-off" on e_o-electrons of a secondary electron emission is carried out. The electrons e_{Sh} of "shake-off", released in some solid angle from source S, originates on aluminum foil Em e_o-electrons. The design of a source and all surrounding forms enough homogeneous electrical field, which one at $U_{Em} = 0$, $U_S > U_L = 190$ V, $U_R = 0$ draws out almost all e_o-electrons from a metal foil Em to the left-hand MCP detector and thus e_o-electrons register only by left-hand MCP detector and only from Em. Thus, at selection quarter $\gamma\gamma_{511} e e_o$-coincidences, an electron of "shake-off" (as e_o) and main particle e (β^+- or β^-- particle) are released in the same solid angle, as (see Fig. 2) the main particle always passes through thin metal foil Em, and the e_o-electrons register only from it. One γ-detector select γ-quanta 511 keV with $\Delta E_{511} = 120$ keV for β^+-decay selection. For β^--decay ΔE_{511} select Compton part registration of transition 779 keV. At $U_S = 0$ V e_o-electrons from "shake-off" electrons are register by left MCP detector from surface of the source ^{152}Eu. At treble $\gamma\gamma_{511} e$-coincidences implements only the selection β^+- or β^--particle by right detector.

In such way in quarter $\gamma\gamma_{511} e e_o$-coincidences the probability of emitting of an electron "shake-off" along a direction of emitting of the main (basic) particle occur, as contrasted to an arbitrary direction its emitting at selection treble $\gamma\gamma_{511} e$-coincidences.

In measurements it is necessary to receive relative (in relation to γ344) intensity of a γ-quantum 511 keV in spectra (Fig. 3 and subsequent) of treble and quarter coincidences. γ-spectrum $\gamma\gamma_{511}\beta^+$-coincidencies (Figs. 4 and 6) corresponds to an arbitrary direction of emitting of an electron of "shake-off" e_{Sh} in relation to positron. The quarter $\gamma\gamma_{511}\beta^+ e_o$-coincidencies (Figs. 5, 7 and 8) corresponds to emitting of electron of "shake-off" e_{Sh} along the direction of mooving of positron.

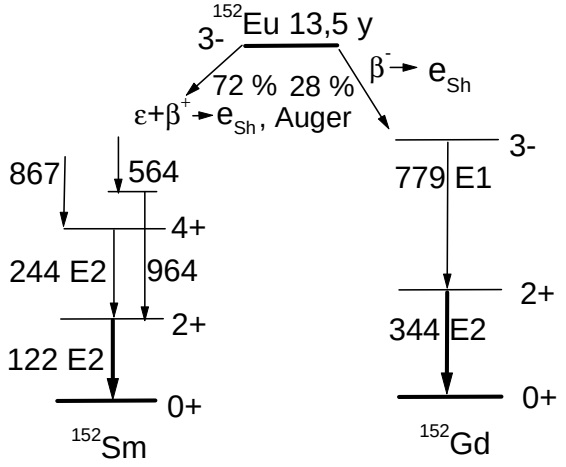

Fig. 1. Branches of the ^{152}Eu decay and main radiations in measuring of γ-spectrum in $\gamma\gamma e e_{sh}$-coincidences for study "shake-off" processes at β^-- and β^+-decay e signed β^-- or β^+-particle, e_{Sh}-"shake-off" electron. Bold arrows indicate the most intensity transition in both branches. E-decay is accompanied by KX-ray and intensive Auger-electrons.

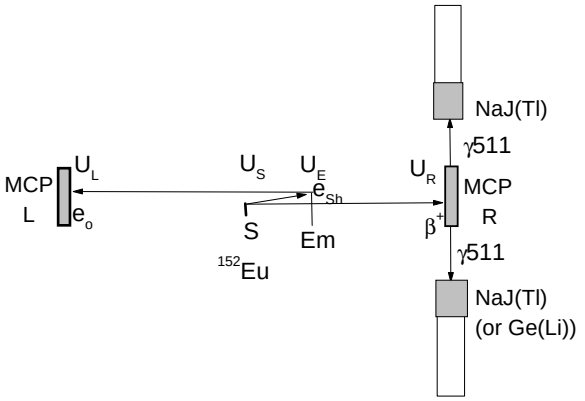

Fig. 2. Technique of definition correlating of motion of e_{Sh}-electron "shake-off" with positron at measurement $\gamma\gamma_{511}\beta^-$- and $\gamma\gamma_{511}\beta^+e_{Sh}$-coincidences from a radioactive source S ^{152}Eu. The source of ^{152}Eu on thin substrate with depth of a radioactive layer 30 mmg/cm^2 was used. Electrons of "shake-off" e_{Sh} are registered on e_o-electrons of the secondary electron emission. MCP- micro-channel-plates detectors of electrons (L and R), NaJ(Tl) or Ge(Li) – axially arranged γ-detectors for registration γ-quanta 511 keV from annigillation of positrons, that occurs in right MCP. Em (Al 0.078 mm)- emitter of e_o-electrons.

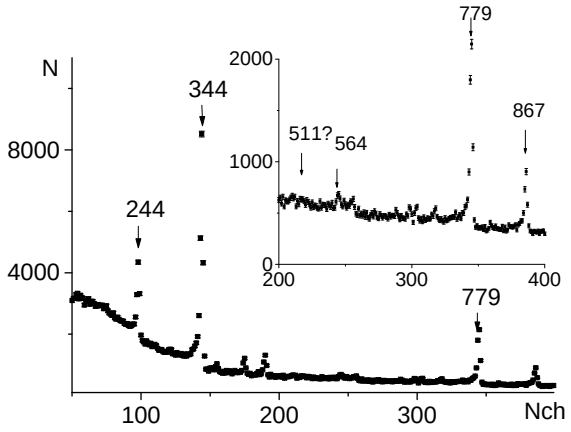

Fig. 3. Part of gamma spectrum in the ^{152}Eu decay. As the intensity β^+-compo-nent is low (estimates at 0.05 % from decay) and gamma quanta 511 keV is not noticeable, arrow indicate only place it in spectrum.

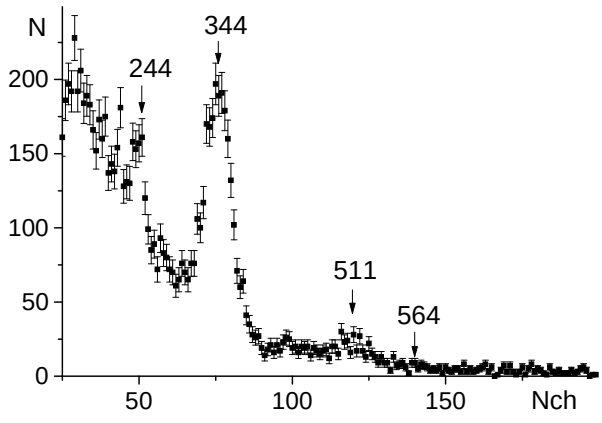

Fig. 4. γ-spectrum in $\gamma\gamma_{511}\beta^+$-coincidences from ^{152}Eu ($\varepsilon+\beta^+$, β^-)-decays. Measured on scintillation detector NaJ(Tl). Direction e_{Sh}-electron relate main particle is arbitrary. Intensity γ511 keV is appreciable (as contrasted those in Fig. 3).

In Figs. 4 - 8 the main results are presented. As intensity β^+-component in ^{152}Eu decay is law (estimates at 0.05 % from decay) it is very much difficult to measure treble and, specially, quarter coincidences with good statistics.

The γ-spectra in Figs. 4 and 5 were measured on scintillation NaJ(Tl) – detector and data, presented on them, show that correlating "shake-off" electron and positron is much less such correlating "shake-off" electron at β^--decay. Really, $(S_{511}/S_{344})_{treble} = 0.100(12) > (S_{511}/S_{344})_{quarter} < 0.05$. This spectra also contain quantum γ244 keV and γ564 keV, that indicate to some registration of KX-ray by the right detector, as conversion electrons IC122 through the emitter Em with depth 0.078 mm cannot pass. It originates coincidences KX-ray with intensive law-energy Auger-electrons (following ε-capture and internal conversion) and with e_o-electrons from it. This circumstance give additional possibility, on relation to β-decay, for analysis of correlating properties "shake-off"-electron and positron at β^+-decay. Additional possibility, as strong correlation KX-ray with Auger-electrons is not expected.

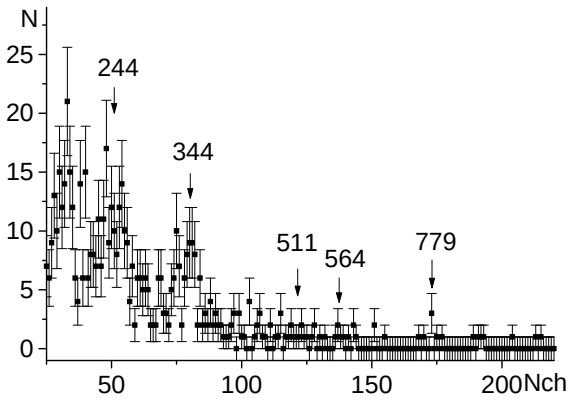

Fig. 5. The γ-spectrum in $\gamma\gamma_{511}\beta^{+}e_{o}$-coincidences from ^{152}Eu ($\varepsilon+\beta^{+}$, β^{-})-decay. Was measured on scintillation detector. e_{Sh} was register on e_0 from Em at U_S = 200 V, U_{Em} = 0 V, U_L = 190 V. Direction is forward for e_{Sh} relate main particle. The intensity γ511, as contrasted those in Fig. 4, is law.

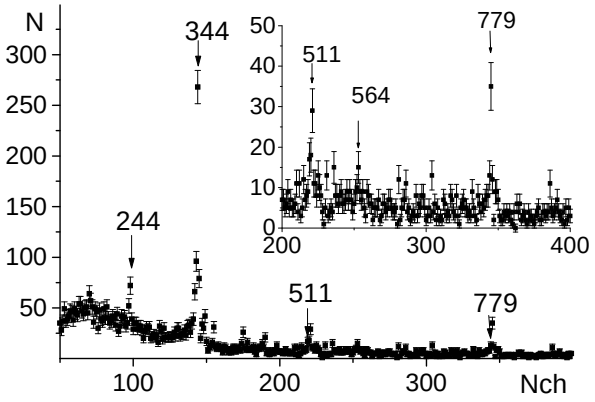

Fig. 6. γ-spectrum from the selection $\gamma\gamma_{511}\beta^{+}$- and $\gamma\gamma_{511}\beta^{-}$-coincidences in ^{152}Eu ($\varepsilon+\beta^{+}$, β^{-})-decays. Measured on Ge(Li) detector. Direction e_{Sh} relate main particle is arbitrary. Intensity γ511 keV is appreciable: S_{511}/S_{344} = 28(7)/239(18) = 0.117(31).

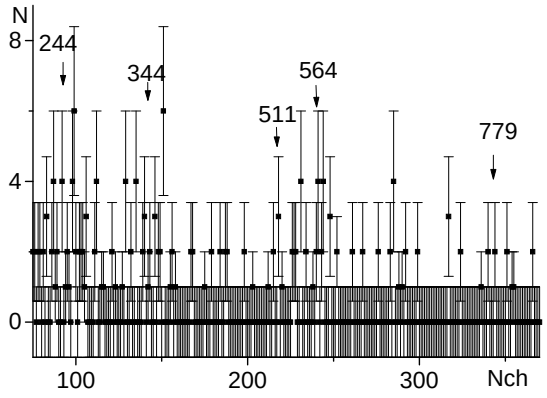

Fig. 7. γ-spectrum of $\gamma\gamma_{511}\beta e_{Sh}$-coincidences in ^{152}Eu ($\varepsilon+\beta^{+}$, β^{-})-decays with registering electron e_{Sh} of "shake-off" on e_o from emitter Em at U_S = 200 V, U_{Em} =0 V, U_L = = 190 V. Intensity of not correlated coincidences γ244 and γ564 keV with KX-ray are large. Intensity γ511 keV is law. Forward direction for e_{Sh}, relate β-particles.

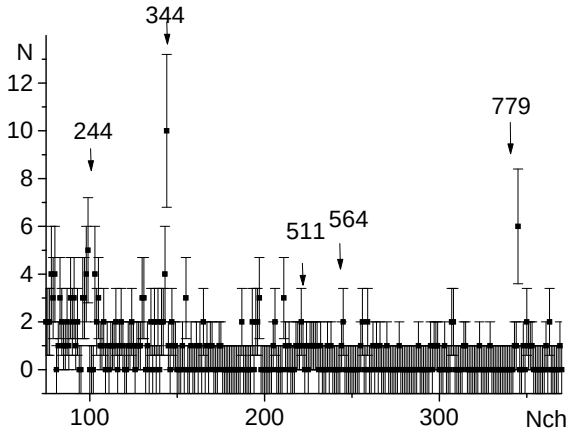

Fig. 8. γ-spectrum of $\gamma\gamma_{511}\beta e_{Sh}$-coincidences in ^{152}Eu ($\varepsilon+\beta^{+}$, β^{-})-decays with registering "shake-off" e_{Sh} on e_o-electrons from surface of source ^{152}Eu at U_S = 0 V, U_{Em} = = 0 V, U_L = 190 V. Relative intensity γ244, γ564 keV is law. Intensity γ511 keV relates γ564 keV is more noticeable, than those in Fig. 7. Large solid angles for e_{Sh} are accessible here. It corresponds to motion "shake-off"-electron in large angles relates β^{+}-particle.

The γ-spectra, presented in Figs. 6 - 8, were measured on Ge(Li)-detector and this information contain. Spectra in Figs. 7 and 8, were measured at different potentials at source, therefore e_o-electrons, using for detecting "shake-off"-electrons and Auger-electrons by left MCP-detector, were registered from different places of their formation: from emitter Em (Fig. 7) or from surface of the source of ^{152}Eu (Fig. 8). In the latest case, at the selection electron of β^{-}-decay, "shake-off"-electrons from it are moving out of source in the same solid angle, as in Fig. 7, owing to strong it correlating with β^{-}-particle.

This circumstances determines the intensity transitions γ244, γ654 keV (both from ε-decay) and transitions γ344, γ779 keV (both from β^{-}-decay) in spectra in Figs. 7 and 8. Though statistics is low, the data on it, nevertheless, demonstrate (table below also), that the intensity γ511 кeV (relative to 564 keV) in spectrum of quarter coincidences at U_S = 200 V (Fig. 7) is much less those at U_S = 0 V (Fig. 8). Thus the solid angles of departure of electrons of "shake-off" to out from the surface of source (therefore and e_o-electrons from it), amounting approximately 2π in Fig. 8, is much greater of solid angles the registration of electrons "shake-off" from outwardly arranged emitter Em in Fig. 7. It is necessary to make a conclusion from it, that electrons of "shake-off" at β^{+}-decay are predominantly moving in relation to positron in much more solid angles, than are moving Auger-electrons in relation to KX-ray. Allowing, that

correlating of an electron of "shake-off" and main (basic) particle at a β^--decay is much above than same correlating of radiations at KX-ray, which one obviously is absent (on the data about intensities of quanta 344 and 244 кеV in spectra in Figs. 7 and 8 and from the Table), it is necessary to draw a conclusion, that correlating of momentums of an electron of "shake-off" and positron at β^+-decay is strong differ from the same correlating of electron of "shake-off" and electron of β^--decay. The predominant motion "shake-off" electron at β^+-decay occurs not in forward direction of main particle, as in case β^--decay, but in 2π or more solid angles relate it.

Number counts under peaks of γ-spectra in treble and quarter coincidences electron "shake-of" (or Auger-electrons), β-particle (positron β^+-decay, electron β^--decay), (or KX-ray) and γ-quanta 511 keV

E γ / measurements	244	344	511	564	γ-detector
$\gamma\gamma_{511}\beta$	223(37)	1551(55)	151(18)	25(9)	NaJ(Tl)
$\gamma\gamma_{511}\beta e_{Sh}$, Em	130(15)	80(11)	1(4)	6(3)	
$\gamma\gamma_{511}\beta$	48(12)	239(18)	28(7)	2(4)	Ge(Li)
$\gamma\gamma_{511}\beta e_{Sh}$, Em	13(3)	6(2)	1(1)	6(2)	
$\gamma\gamma_{511}\beta e_{Sh}$, S	15(4)	17(4)	5(2)	3(2)	

Thus**,** on data two cycles of measuring with different γ-detectors, the space correlating of electron "shake-off" with positron at β^+-decay in direction forward is much less that the same correlating "shake-off"-electron and electron of β^--decay.

Analyses of results and conclusions

The momentum correlating study electron "shake-off"-positron at β^+-decay in relative such properties "shake-off"-electron and electron of β^--decay indicate, that correlating "shake-off"-electron along of direction moving positron at β^+-decay strong differs from correlating at β^--decay and it is much less than those in direction forward. "Shake-off"-electrons at β^+-decay are moving predominantly not in forward direction, as in case β^--decay, but in a direction of large solid angles. These, so different, properties are conditioned apparently by different interactions electron of "shake-off" and main (basic) particle at β^-- and β^+-decay and are stacked in offered in [7 - 9] mechanism, accountable for it. It is apparently the interaction of currents conditioned by motion of charged particles, as charges of main particles (electron – positron) are inverse and interactions currents from it are different: attraction for "shake-off"-electron and β^--particle and pushing away for "shake-off"-electron and β^+-particle at moving in forward direction.

REFERENCES

1. *Матвеев В.И., Парилис Э.С.* Встряска при электронных переходах в атомах // Успехи физических наук. - 1982. - Т. 138, вып. 4. - С. 573 - 602.
2. *Kochur A.G., Popov V.A.* Shake up and shake off probabilities for L-, M-, and N-electrons in atoms with Z = 3 to 60 // Radiation Physics and Chemistry. - 2006. - Vol. 75. - P. 1525 - 1528.
3. *Weber T.H., Giessen H., Weckenbrock M. et al.* Correlated electron emission in multiphoton double ionization // Nature. - 2000. - Vol. 405. - P. 658 - 661.
4. *Moshammer R., Ulrich J., Fisher D.* Strongly directed electron emission in non-sequential double ionization of Ne by intense laser pulses // J. Phys. B.: At. Mol. Opt. Phys. - 2003. - Vol. 36. - P. 113 - 119.
5. *Mitrokhovich N.F.* Correlation β-particle with "shake off" electrons under β-decay ^{152}Eu // Proc. Int. Conf. "Current Problems in Nuclear Physics and Atomic Energy" (Kyiv, May 29 - June 03. 2006). - Kyiv, 2007. - P. 412 - 416.
6. *Mitrokhovich N.F., Kupryashkin V.T.* Correlation electron internal conversion with "shake off" electrons under ε-decay ^{152}Eu // Nuclear Physics and Atomic Energy. - 2007. - No. 1 (19) - P. 61 - 66.
7. *Mitrokhovich N.F.* Energy and correlation properties of "shake-of" electrons at β-decay // Nuclear Physics and Atomic Energy. - 2010. - Vol. 11, No. 2. - P. 136 - 140.
8. *Mitrokhovich N.F.* Energy and correlation properties of electrons "shake-off" at β-decay and internal conversion // Proc. 3-rd Int. Conf. "Current Problems in Nuclear Physics and Atomic Energy" (Kyiv, June 7 - 12, 2010). Part 1. - Kyiv, 2011. - P. 312 - 315.
9. *Mitrokhovich N.F.* The spectra energy of electrons autoionization and their correlation on β-particle emission direction // Nuclear Physics and Atomic Energy. - 2012. - Vol. 13, No. 1. - P. 17 - 21.

DISSIPATIVE STATISTICAL AND DYNAMICAL FISSION RATES: CASE OF THE MICROCANONICAL ENSEMBLE

E. G. Pavlova, I. I. Gontchar

Omsk State Transport University, Omsk, Russia

Accuracy of the approximate analytical formulas for the thermal fission rate is investigated within the framework of the microcanonical ensemble. We compare the analytical rates with the results of the dynamical modeling. Unlike the previous studies we account for the coordinate dependence of both the temperature and the single-particle level density parameter. The shell corrections are included in the potential energy, the entropy and the single-particle level density parameter.

1. Introduction

In modeling of the nuclear fission process it is important to calculate exactly the fission rate R. It can be defined by several methods. Dynamical modeling (the numerical solution of the differential equations) is accurate but computer-time-consuming. The approximate analytical formulas are less precise.

The first analytical formulas for R, which included dynamical (dissipative) effects, were derived by H. A. Kramers in his work [1] about 70 years ago. These formulas allow evaluating R in the case of the Canonical Ensemble (CE). The accuracy of two of those recently has been studied: the approximate Overdamping Kramers Formula (OKF) and the Integral Kramers Formula (IKF). In [2 - 4] it has been shown that the error of the OKF can reach 20 % whereas the IKF provides much better accuracy. In [4] the OKF and the IKF have been derived and investigated for the case of the Microcanonical Ensemble (MCE). In that work the coordinate dependence of the temperature has been accounted for.

Present work continues the study of [2 - 4]. We investigate the accuracy of both the OKF and the IKF in the more realistic case considering the MCE and accounting for the coordinate dependence of the temperature as well as of the single-particle Level Density Parameter (LDP). In addition the shell corrections are included in the potential energy, the entropy and the LDP.

2. The model

Modeling is performed for the case of overdamping. The fission process is described within the framework of both the CE and the MCE. One parameter (dimensionless collective coordinate q) defines the deformation of the nucleus. At the quasistationary state ($q_c = 1$) the nucleus has the spherical shape; $q_a = 2.14$ corresponds to the scission configuration.

Dynamical modeling is based on the Smoluchowski Equation (SE). Its forms for the CE and the MCE are discussed in detail in Refs. [5] and [4] respectively.

According to the method of Shell Corrections (SC) [6], the potential energy consists of a smooth part $U_L(q)$ and the shell correction $\delta E_{Sh}(q)$, $U(q) = U_L(q) + \delta E_{Sh}(q)$.

The smooth part of the potential energy reads:

$$U_L(q) = \begin{cases} 0.5U''_{P3}(q_c)(q-q_c)^2 + 2V_2(q-q_c)^4, & q < q_c; \\ U_{P3}(q), & q > q_c. \end{cases} \quad (1)$$

Eq. (1) corresponds to the F-potential from [4], it is the approximation of the potential energy calculated within the framework of the finite range model (see e. g. Fig. 1 of Ref. [4]), $U_{P3}(q) = \sum_{i=0}^{3} V_i q^i$.

The shell correction $\delta E_{Sh}(q)$ for the potential energy is approximated as:

$$\delta E_{Sh}(q) = -\delta E_{Sh}(q_c)\, ch^{-1}\left[\alpha(q-q_c)\right]. \quad (2)$$

Here $\delta E_{Sh}(q_c)$ is the SC at the quasistationary state, $\alpha = \left[q_b - q_c\right]^{-1} \ln 20$.

The deformation dependence of the smooth part of the LDP is defined as follows [7]: $a_L(q) = a_1 A + a_2 A^{2/3} B_s(q)$. Here A is the mass number, $a_1 = 0.073\ \mathrm{MeV}^{-1}$ and $a_2 = 0.095\ \mathrm{MeV}^{-1}$, $B_s(q)$ is the dimensionless nuclear surface area. To find the dependence $B_s(q)$ we use the approximation of the results from Ref. [9] (see Fig. 2).

With the shell correction the LDP reads [7]:

$$a(q, E_{in}) = a_L(q)\left\{1 + f(E_{in})\,\delta E_{Sh}(q)\, E_{in}^{-1}\right\}, \quad (3)$$

here E_{in} is the intrinsic excitation energy. The function $f(E_{in})$ reaches unity when E_{in} becomes large enough: $f(E_{in}) = 1 - \exp(-kE_{in})$, $k = 0.054\ MeV^{-1}$.

In this work results are presented for $^{204}_{80}Hg$. The height of fission barrier given by Eq. (1) is $B_f = 15.86\ MeV$ and the barrier point is $q_b = 1.90$. The shell correction $\delta E_{Sh}(q_c) = -10.68$ MeV [8].

In all results below the total excitation energy E is used as an argument. The fission rate is calculated for four cases: 1) the CE (the temperature does not depend on the coordinate, $T = T_c$, $E_{in} = E - U_L(q_c)$); 2) the MCE (the temperature depends on the coordinate whereas the LDP does not, $T = T(q)$, $a = a_c$, $E_{in}(q) = E - U_L(q)$); 3) the MCE (both the temperature and the LDP depend on the deformation, $T = T(q)$ and $a = a(q)$, $E_{in}(q) = E - U_L(q)$); 4) the MCE (same as the previous case but with the shell corrections, $\delta E_{Sh}(q)$, $E_{in}(q) = E - U(q)$).

The entropy includes the SC, because it is related to the potential energy via the Fermi gas equation of state. In Fig. 1 the coordinate dependences of the potential energy and of the entropy normalized to be zero at the quasistationary state , $S_n = (S_c - S) \cdot T_c$, are demonstrated. If we compare U_L and U in the panel a) we see $\delta E_{Sh}(q)$. When the total excitation energy E is large enough the approaches based on the CE and the MCE are equivalent: U_L and S_n coincide. As E decreases the normalized entropy becomes different from U_L in the vicinity of the barrier. This fact is caused by the dependence $T(q)$ and discussed in Ref. [4].

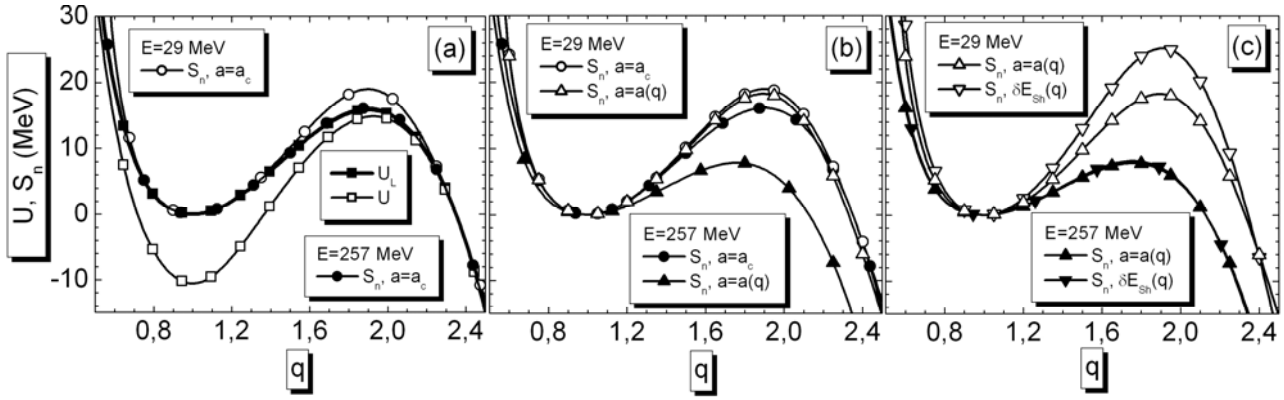

Fig. 1. The coordinate dependence of U and S_n for two values of E: 29 and 257 MeV (open and closed symbols respectively). a – U_L (full squares), U (open squares), S_n for $a = a_c$ (circles); b – S_n for $a = a_c$ and $a = a(q)$ (triangles); c – S_n for $a = a(q)$ and with $\delta E_{Sh}(q)$ (inverse triangles).

In panel *b* we compare the entropies for two cases: $a = a_c$ and $a = a(q)$. This Figure demonstrates how E affects the coordinate dependence of the LDP. When E is large and $a(q)$ is accounted for, the fission barrier decreases and the saddle point shifts towards q_c. If the total excitation energy is small this effect disappears (S_n for both cases coincide).

Panel *c* shows that the SC influence the entropy only at low energies: the values of S_n in the cases of $a(q)$ and $\delta E_{Sh}(q)$ coincide for $E = 257$ MeV. When $E = 29$ MeV the SC result in the increase of the fission barrier height.

The impact of the change of the barrier height and the shift of the saddle point on the value of the fission rate is discussed in the next section.

3. Dynamical and analytical fission rates

Solving the SE allows calculating the fission rate over the saddle point:

$$R_b(t) = \left\{ -D_1(q_b)\, g(q_b, t) + \frac{\partial}{\partial q}\left[D_2(q_b)\, g(q_b, t) \right] \right\} \cdot \left\{ \int_{-\infty}^{b} g(x, t)\, dx \right\}^{-1}. \qquad (4)$$

Here $g(q, t)$ is the probability density; D_1 and D_2 are the drift and diffusion coefficients respectively. Note that the form of these coefficients can be found in Refs. [5] and [4].

For long enough time $R_b(t)$ reaches a quasistationary value (Quasistationary Dynamical Rate of fission, QDR, R_D). Fig. 2 illustrates the dependence of $R_D(E)$ for the low values of E. The rates calculated for the CE and the MCE are distinct when E is small due to the deformation dependence of the temperature, $R_D(E, T_c) > R_D(E, a_c)$. The smaller the total excitation energy the larger is the difference between R_D calculated for $T = T_c$ and for $a = a_c$. For low E accounting for $a(q)$ does not affect the barrier and rates calculated for $a = a_c$ and for $a = a(q)$ reach to each other with the decrease of the total excitation energy. Contrary the SC are essential for low E and decrease R_D in compare to the value of the QDR in the case of $a = a(q)$. The change of the fission rate by the SC can reach 20 %.

In Fig. 3 the E -dependence of R_D for the four cases at the high energies is shown. As E increases the QDR for the CE ($T = T_c$) and the MCE (with $a = a_c$) converge. It is caused by the equivalence of the fission barriers for both cases seen in Fig. 1, *a*).

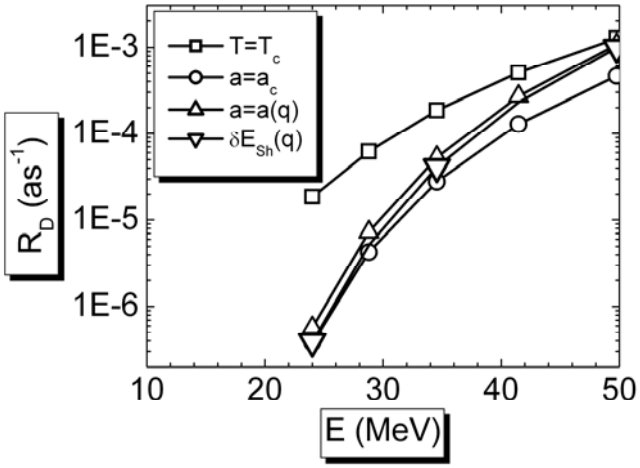

Fig. 2. The energy dependence of R_D for four cases: $T = T_c$, $a = a_c$, $a = a(q)$ and $\delta E_{Sh}(q)$ (squares, circles, triangles and inverse triangles respectively).

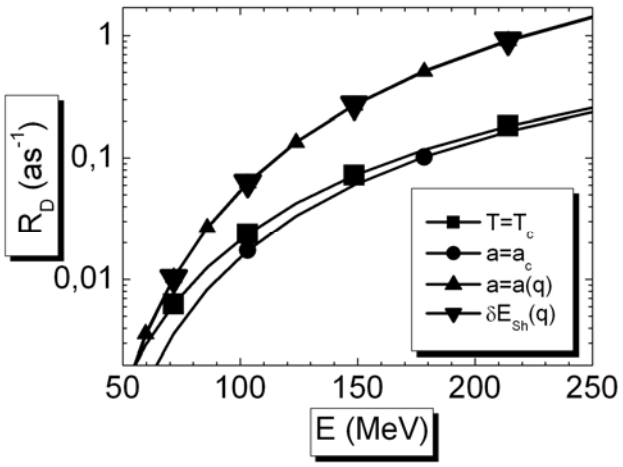

Fig. 3. Same as in Fig. 2, but for large values of the total excitation energy.

The decrease of the barrier results in the growth of the rate when $a(q)$ is accounted for. The values of R_D for $a = a_c$ and $a = a(q)$ differ, and the difference becomes larger as E increases. For high values of E, the SC do not affect the fission barrier and R_D calculated for $a = a(q)$ and $\delta E_{Sh}(q)$ are indistinguishable.

In some cases the dynamical modeling takes much time. For this reason it is used analytical formulas to define the value of R_D. In [4] two such approximate formulas were investigated. The first of them is the conventional Overdamping Kramers Formula (OKF). It was derived by Kramers in [1] for the CE, and in [4] the analogy expression was constructed for the MCE:

$$R_O = \frac{T_b}{2\pi\eta} \cdot \sqrt{\left| \left(\frac{d^2 S}{dq^2}\right)_c \left(\frac{d^2 S}{dq^2}\right)_b \right|} \exp(S_b - S_c). \tag{5}$$

The OKF is obtained from more general expression called the Integral Kramers Formula (IKF):

$$R_I = \left\{ \eta \int_c^a \frac{\exp\left[-S(y)\right]}{T(y)} dy \int_{-\infty}^b \exp\left[S(x)\right] dx \right\}^{-1}. \tag{6}$$

Both the OKF and the IKF were derived for the overdamping.

In the next section we will discuss an applicability of these formulas for the MCE, in which the SC and the deformation dependence of the LDP are taken into account.

4. Results and discussion

In Fig. 4 we present our results. Each panel of this Figure illustrates the ratio of the analytical rate to the dynamical one (R_I / R_D and R_O / R_D). The values of these ratios depend on a parameter B_f / T_c. The values of B_f correspond to the barrier height in case of the CE.

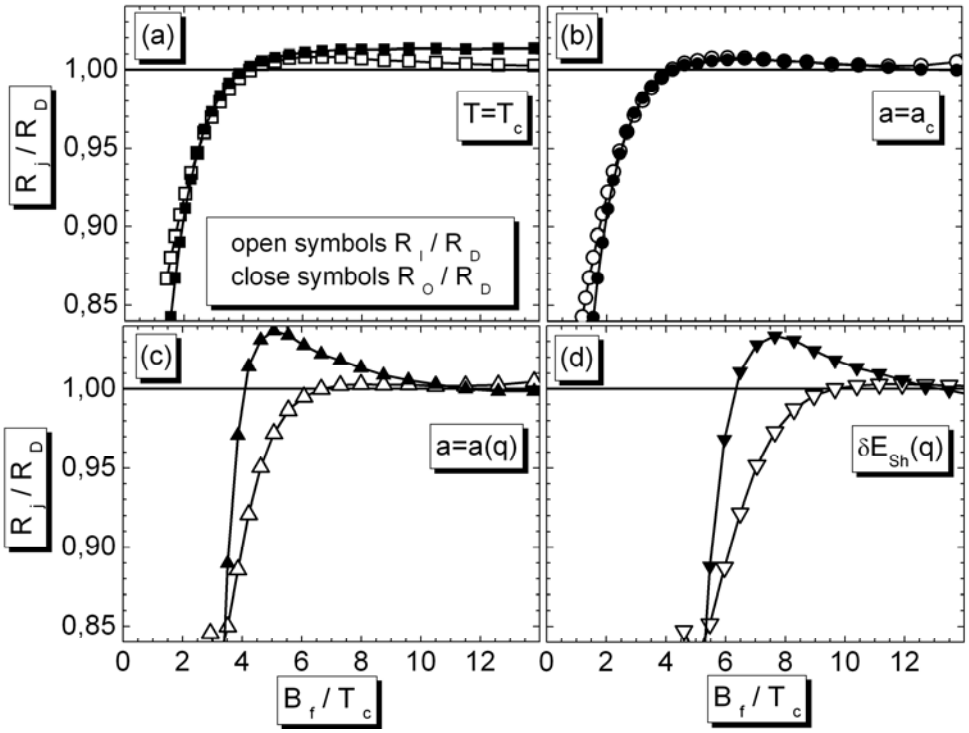

Fig. 4. The ratio of the analytical rates R_I and R_O to the dynamical one R_D (open and full symbols). *a* – the CE; *b* – the MCE with $a = a_c$; *c* – the MCE with $a = a(q)$; *d* – the MCE with $a = a(q)$ and $\delta E_{Sh}(q)$. The horizontal line denotes the ratio of rates equaled unity.

The results demonstrated in panel a) are analogous them that were published in Refs. [2, 3]. As in those works, the ratios between rates reach unity for large values of B_f / T_c. It means that both R_O and R_I agree with R_D within 2 % when B_f / T_c is large enough.

Panel *b* demonstrates the case discussed in [4]: R_I / R_D and R_O / R_D are calculated for the MCE with $a = a_c$. Here and in work [4] it is seen that R_I coincides with R_D and the IKF can be used for the calculation of the QDR. The accuracy of the OKF is not worse than the one for the IKF.

The next two panels illustrate new results. Panel *c* corresponds to cases, when the coordinate dependence of the LDP is accounted for. From Fig. 4, *c* we see that even in this case the IKF allows calculating the fission rate exactly. Contrary the discrepancy between R_O and R_D reaches 4 % when $B_f / T_c \approx 4$. Only for $B_f / T_c > 10$ the value of R_O / R_D becomes close to unity. For range of B_f / T_c up 4 to 10 R_O does not agree with R_D, the OKF overestimates the value of the QDR. Note that R_I / R_D equals to unity for $B_f / T_c > 6$.

The similar situation we observe in panel d) where the SC are accounted for. And in this case the IKF is accurate than the OKF. The behavior of R_O / R_D and R_I / R_D in panel d) are equivalent to the ones in panel *c*. The agreement between R_I and R_D reaches earlier than for R_O and R_D. For medium values of B_f / T_c the error of the OKF equals to 4 % again.

The Fig. 4 proves that the IKF (6) can be used to calculate the fission rate not only in case of the MCE with the coordinate dependence of temperature, but also for the MCE with the deformation dependence LDP $a = a(q)$ and in presence of the SC $\delta E_{Sh}(q)$.

5. Conclusions

In dynamical modeling of the nuclear fission process an actual problem is how to calculate the fission rate. We continue the study of [2 - 4] and investigate the accuracy of two analytical formulas for the fission rate. There are the Overdamping Kramers Formula (OKF, Eq. (5)) and the Integral Kramers Formula (IKF, (6)). In previous works these expressions were studied for the canonical ensemble (CE) and the microcanonical ensemble (MCE) with the deformation dependent temperature. Our work is devoted to more realistic case. We use the MCE, in which the deformation dependence of the temperature and the single-particle Level Density Parameter (LDP) are accounted for. Also we include the shell corrections in calculation of the potential energy, entropy and the LDP.

The results of calculations demonstrate that the IKF is a good alternative to the OKF and can be used for this realistic case. The IKF allows calculating the value of the dynamical fission rate correctly and within the accuracy of the dynamical modeling (2%). This is so for medium and large values of B_f / T_c ($B_f / T_c > 6$). Contrary the error of the OKF reaches 2 - 4 % for medium B_f / T_c and decrease to 1 - 2 % only for large values of B_f / T_c ($B_f / T_c > 11$).

ACKNOWLEDGEMENTS

E.G.P. is grateful to the Dmitry Zimin Foundation “Dynasty” for financial support.

REFERENCES

1. *Kramers H.A.* Brownian motion in a field of force and the diffusion model of chemical reactions // Physica. - 1940. - Vol. 7. - P. 284 - 304.
2. *Gontchar I.I., Chushnyakova M.V., Aktaev N.E. et al.* Disentangling effects of potential shape in the fission rate of heated nuclei // Phys. Rev. C. - 2010. - Vol. 82. - P. 064606.
3. *Gontchar I.I., Pavlova E.G., Litnevsky A.L., Aktaev N.E.* How much accurate is description of nuclear fission rate by means of Kramer’s formula? // Proc. of the 3-rd Int. Conf. “Current Problems in Nuclear Physics and Atomic Energy” (Kyiv, June 7 - 12, 2010). - Kyiv, 2011. - P. 46 - 50.
4. *Gontchar I.I., Kuzyakin R.A.* Integral Kramers formula for the fission rate versus dynamical modeling: The case of deformation-dependent temperature // Phys. Rev. C. - 2011. - Vol. 84. - P. 014617.
5. *Pavlova E.G., Aktaev N.E., Gontchar I.I.* Modified Kramers formulas for the decay rate in agreement with dynamical modeling // Phys. A. – 2012. – Vol. 391, Issue 23. - P. 6084 - 6100. http://dx.doi.org/10.1016 /j.physa.2012.06.064.
6. *Brack M., Damgaard J., Pauli H.C. et al.* // Funny Hills: The shell-correction approach to nuclear shell effects and its application to fission process // Rev. Mod. Phys. – 1972. – P. 320 – 405.
7. *Ignatyuk A.V., Itkis M.G., Okolovich V.N. et al.* Fission of pre-actinide nuclei. Excitation functions for the (α, f) reaction // Yad. Fiz. - 1975. – Vol. 21. – P. 1185 - 1205.
8. http://nrv.jinr.ru/nrv.
9. *Gontchar I.I., Fröbrich P., Pischasov N.I.* Consistent dynamical and statistical description of fission of hot nuclei // Phys. Rev. C. - 1993. - Vol. 47. - P. 2228 - 2235.

FIRST CALCULATION OF THE DEUTERON BINDING ENERGY

B. Schaeffer

7, rue de l'Ambroisie, 75012, Paris, France

No universal constant characterizing the nuclear force has yet been found as for gravity and electromagnetism. The neutron is globally neutral with a zero net charge. The charges contained in a neutron may be separated by the electric field of a nearby proton and therefore being attracted by electrostatic induction in the same way as a rubbed plastic pen attracts small pieces of paper. There is also a magnetic force that may repel the nucleons like magnets in the proper relative orientation. In the deuteron, the heavy hydrogen nucleus, the induced electrostatic attraction is equilibrated by the magnetic repulsion between the opposite and colinear moments of the nucleons. Equilibrium is calculated by minimizing the electromagnetic interaction potential, giving a binding energy of 1.6 MeV, not much lower than the experimental value, 2.2 MeV. No fitting parameter is used: it is a true ab initio calculation.

1. Introduction

The Greeks already knew the electrical properties of amber (elektron) and the magnetic properties of magnetite and iron. Bieler in 1924 wrote "as the angle increases, the ratio of the actual scattering to what would be expected on the inverse-square law diminishes rapidly. This suggests the existence of an attractive force at short distances from the nucleus" [1]. At that time, the neutron was not yet discovered by his colleague, Chadwick, as well as the magnetic moment of the neutron proving that it contains electrical charges. An attractive magnetic force, as imagined by Bieler to interprete his experimental results, can, theoretically, be equilibrated by a repulsive electrostatic Coulomb force but the binding is unstable, the interaction energy being positive. The electromagnetic hypothesis for the nuclear interaction was abandoned when the neutron was discovered.

In this paper it will be shown that an attractive electrostatic induction may equilibrate the magnetic repulsion between the proton and the neutron in the deuteron. The permanent dipole of an isolated neutron is negligible but it may be induced by the electrostatic induction of a nearby proton. Combined with the proton, the neutron becomes the deuteron and the induced dipole the deuteron quadrupole. The nuclear physics literature seems to have neglected the electromagnetic interaction replaced by various hypothetical forces (Wigner, Majorana, Bartlett, Heisenberg, Rosenfeld, Yukawa…) and tensor force [2] combined sometimes with a mysterious repulsive strong core. It will be shown that a simple analytical formula is able to give a reasonable value of the deuteron binding energy, using only universal electromagnetic constants such as the elementary electric charge e, the neutron and proton magnetic moments μ_n, μ_p, the electric permittivity ε_0, the magnetic permeability μ_0, and the light speed c or, equivalently, the fine structure constant α, the neutron and proton Landé factors g_n, g_p, the proton mass mp and the light speed c.

2. Principle of the calculation

2.1. Electrostatic attraction

One proton, positively charged, and one neutron containing electric charges globally neutral, without any dipole when isolated, are the constituents of the deuteron (Fig. 1). The proton, having electric field acting on the neighbouring neutron, may separate the neutron charges by electrostatic induction, creating an electric dipole. The negative charge of the dipole is attracted by the proton and the positive charge repelled. The induced electric dipole, combined with the proton electric charge, becomes the quadrupole of the deuteron $Q = 0.288\ \text{fm}^2 = (0.54\ \text{fm})^2$. This means that the distances between the elementary electric charges are of the order of the nucleon size. "Unfortunately, the multipole expansion is not applicable when the molecules are separated by distances comparable to the molecular dimensions" [3]. This is also true for the atomic nucleus: the far-field approximation is not applicable when the distance between the electric charges is comparable to the nucleon size.

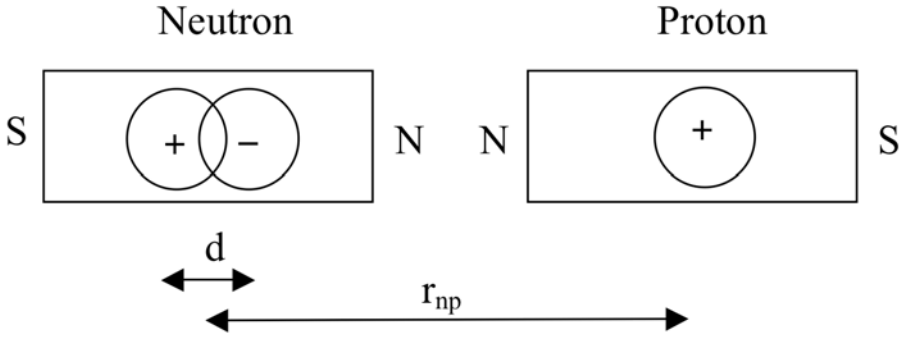

Fig. 1. Deuteron electromagnetic structure.

The positive charge of the neutron, taken away by the positive charge of the proton, may be, in a first approximation, neglected in the calculation of the binding energy. This is justified by the fact that the Coulomb potential law is decreasing in 1/r with the distance r. On the opposite, the negative charge of the neutron is brought closer to the proton. The quark hypothesis needs a multibody calculation, not necessary for a first approach. Nobody having ever seen fractional electric charges, we adopt provisionally the usual elementary charge.

The deuteron is constituted of one proton and one neutron. The neutron contains electric charges with no net charge. The proton contains one elementary charge, the same of that of the deuteron. The proton attracts the negative charge and repulses farther away the positive charge. Both nucleons have magnetic moments whose algebraic sum is the magnetic moment of the deuteron. Their magnetic moments are, in the deuteron, opposite, thus repulsive. There is therefore an electrostatic attraction equilibrated by a magnetic repulsion.

2.2. Magnetostatic repulsion

By reason of symmetry, the neutron and the proton magnetic moments in the deuteron have to be colinear (Fig. 1). The magnetic moment of the deuteron being close to the algebraic sum of the proton and the neutron magnetic moments [2], they repulse themselves like colinear magnets with opposite polarities. Magnetic monopoles having never been observed, the distance between the magnetic charges is unknown. We may thus use the far field approximation for the magnetic interaction between the neutron and proton magnetic dipoles.

2.3. Binding energy

We shall first compute the interacting force and energy between two particles having electrostatic charges and colinear magnetic moments. The spins of the neutron and of the proton being colinear, they have a common axis of rotation and therefore the kinetic energy of the deuteron is already included in the rotation of the nucleons. The purpose of this calculation is to find the potential at equilibrium between electrostatic attraction and magnetic repulsion to obtain the interaction potential between the neutron and the proton and thus the binding energy of the deuteron at the equilibrium of the electrostatic and magnetic forces.

3. Interaction energy equation

Let us consider two particles with electrical charges q_1 and q_2 with magnetic moments $\vec{\mu}_1$ and $\vec{\mu}_2$ and their joining line r_{12}. The interacting electrostatic potential is [4]:

$$U_e = \frac{q_1 q_2}{4\pi\varepsilon_0 r_{12}} \tag{1}$$

The general potential of the tensor force between two magnetic moments is [5]:

$$U_m = \frac{\mu_0}{4\pi r_{12}^3}\left[\vec{\mu}_1 \bullet \vec{\mu}_2 - \frac{3\left(\vec{\mu}_1 \bullet \vec{r}_{12}\right)\left(\vec{\mu}_2 \bullet \vec{r}_{12}\right)}{r_{12}^2}\right] \tag{2}$$

When the moments are colinear, using $\mu_0\varepsilon_0 = 1/c^2$, the formula (2) simplifies into:

$$U_m = -\frac{\mu_0 \mu_1 \mu_2}{2\pi r_{12}^3} = -\frac{\mu_1 \mu_2}{2\pi\varepsilon_0 c^2 r_{12}^3} \tag{3}$$

where μ_1 and μ_2 are now algebraic instead of being vectorial. The electromagnetic interaction potential at a static distance r_{12} is the sum of Eqs. (1) and (3):

$$U = U_e\left(r_{12}\right) + U_m\left(r_{12}\right) = \frac{1}{4\pi\varepsilon_0}\left(\frac{q_1 q_2}{r_{12}} - \frac{2\mu_1 \mu_2}{c^2 r_{12}^3}\right) \tag{4}$$

At equilibrium, the resultant force must be zero:

$$F = -\frac{dU}{dr_{12}} = \frac{1}{4\pi\varepsilon_0}\left(\frac{q_1 q_2}{r_{12}^2} - \frac{6\mu_1 \mu_2}{c^2 r_{12}^4}\right) = 0 \tag{5}$$

We have then

$$r_{12}^2 = \frac{6\mu_1 \mu_2}{q_1 q_2 c^2} \tag{6}$$

A zero force is only possible if the condition $q_1q_2\mu_1\mu_2 > 0$ is satisfied. Replacing r_{12} into the potential energy Eq. (4) gives the basic formula for the binding energy of two particles with electric charges and colinear magnetic moments:

$$B = \frac{q_1 q_2}{6\pi\varepsilon_0}\sqrt{\frac{q_1 q_2}{6\mu_1\mu_2}} \tag{7}$$

With the condition $q_1q_2\mu_1\mu_2 > 0$ there is equilibrium, stable or unstable. If $q_1q_2 < 0$ there is stable equilibrium, that is, binding. We shall write Eq. (7) somewhat differently. The nuclear magneton is

$$\mu_N = \frac{eh}{8\pi m_p} \tag{8}$$

where h is Planck's constant and m_p the proton's mass. The fine structure constant is

$$\alpha = \frac{e^2}{2\varepsilon_0 hc} = \frac{1}{137} \tag{9}$$

Using the Landé factors g, we obtain an interesting formula for the binding energy between two nucleons with colinear magnetic moments

$$B = \left\{\frac{-8\, q_1 q_2}{3\, e^3}\sqrt{\frac{q_1 q_2}{6 g_1 g_2}}\right\}\alpha m_p c^2 \tag{10}$$

In this formula a pure number depending only on the geometry multiplies the mass energy m_pc^2. The parameters in the parentheses depend only on the geometry of the nucleus and on the Landé factors of the neutron and the proton. The fine structure constant α is a fundamental pure number equal to 1/137 characterising the electromagnetic interaction.

4. Binding energy of the deuteron

The deuteron is made of one proton and one neutron. The deuteron magnetic moment is close to the algebraic sum of the colinear magnetic moments of the neutron and the proton. Being colinear and of opposite signs (parallel spins) there is a magnetic repulsion between the proton and the neutron. As stated above, there is, by electrostatic influence of the electric field of the proton on the neutron, separation between the positive, $e_n+ = e$, and negative, $e_n = e$, charges of the neutron. The positive charge e_n+ is pushed away by the proton and the negative charge en is attracted by the proton. The usual far field approximation cannot be used because the separation distance between the dipole charges is comparable to the nucleon size. The repulsion between the proton positive charge e_p+ and the distant positive charge en+ of the neutron may thus be neglected in a first approximation.

When the expression under the radical in the basic formula is positive, interaction energy exists between the electric charges and between the magnetic moments. The expression in the parentheses outside the radical should be negative in order to have a stable equilibrium. Both products $e_ne_p+ = e^2$, and $\mu_p\mu_n$, being negative, binding is possible. Let us apply numerically the basic formula to the neutron-proton interaction. We shall assume that the effective charge in the neutron is – e, the same as the proton charge except for the sign. Eq. (10) becomes:

$$B = \frac{-8}{3\sqrt{6 g_n g_p}}\alpha m_p c^2 = \frac{-8}{3\sqrt{6\square 3.83\square 5{,}58}}\frac{938}{137} = -1.6\ \text{MeV} \tag{11}$$

This calculated binding energy is 30 % lower than the experimental value, –2.2 MeV. A better value of –2 MeV was obtained using a three-body numerical calculation but the purpose of this paper is to find an analytic formula in order to understand the nuclear interaction. The binding energy of the deuteron may thus be predicted electromagnetically. The electromagnetic potential between a neutron and a proton is shown in Fig. 2. According to the usual phenomenological theories the nuclear potential should unrealistically be 10 to 100 times the binding energy due to assumed kinetic energy. This calculation is obtained using only classical electrostatics and magnetostatics and their universal constants. There is no fitting.

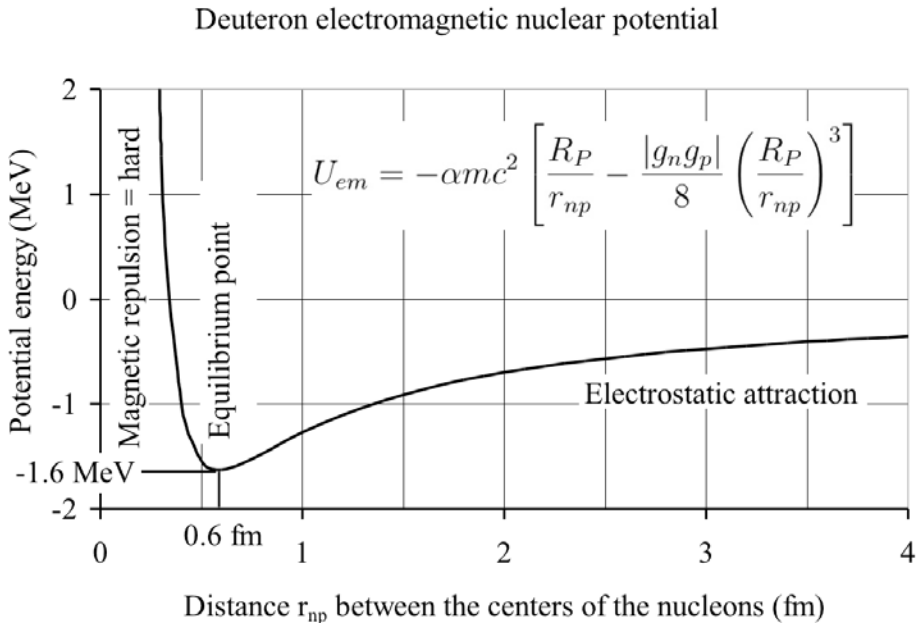

Fig. 2. Electromagnetic potential of the deuteron.

This potential is simplified by the neglect of the positive charge of the deuteron. The electrostatic Coulomb potential in 1/r is predominant at large separation distances and the magnetic Coulomb potential in $1/r^3$ is predominant when the neutron and the proton are intermingled.

5. Nuclear and chemical energies

The typical energy needed to separate an electron from a proton is given by the Rydberg constant

$$R_y = \frac{1}{2} \alpha^2 m_e c^2 = 13.6 \text{ eV} \tag{12}$$

which is the binding energy of a hydrogen atom given by Bohr's formula, very precisely equal to the experimental value of the energy of the ground state of the hydrogen atom. The electronic energy is proportional to the square of the fine structure constant α and the mass m_e of the electron. Formula (10) shows that the nuclear interaction may be characterised by a formula similar to (12) but where α appears to the first power and the proton mass replaces the electron mass:

$$\frac{1}{2} \alpha \, m_p c^2 = 3.4 \text{ MeV} \tag{13}$$

The ratio of these two energies is 250,000. The electromagnetic theory is not as precise for the nucleus as for the atom, the experimental binding energy of a neutron to a proton being 2.2 MeV instead of 3.4 from (13) or 1.6 from (11). The experimental ratio between the formulas (11) and (12) is 160,000 instead of 250,000 between the experimental energy ratios of the nuclear and electronic binding energies, not too bad a result for the electromagnetic interaction.

5. **Conclusion**

Eq. (11) obtained from the electromagnetic hypothesis, electrostatic attraction equilibrated by magnetic repulsion, gives reasonable results for the deuteron binding energy. It seems to be the first time that the binding energy of a nucleus is calculated using universal constants only (ab initio calculation without any fitting parameter). The nuclear interaction is not only an analogue of the electromagnetic interaction: it is electromagnetic and explains why the mean nuclear energy is around 1/137 of the mass energy and around 250,000 times the chemical energy.

REFERENCES

1. *Bieler E. S.* The large-angle scattering of α particles by light nuclei // Proc. R. Soc. Lond. A. - 1924. - Vol. 105. - P. 434 - 450.
2. *Weisskopf V.F., Blatt J.M.* Theoretical Nuclear Physics. - Mineola, New York: Courier Dover Publications, 1991.
3. *Leach A.R.* Molecular modelling: Principles and Applications. - Harlow, Essex: Pearson Education, 2001.
4. *Owen G.E.* Introduction to Electromagnetic Theory. - Mineola, New York: Courier Dover Publications, 2003.
5. *Yosida K.* Theory of Magnetism. - Heidelberg: Springer, 1996.

INVESTIGATION OF ^{138}Ba IN THE (n, n'γ)-REACTION

S. M. Sergiwa[1], A. M. Abuejila[1], S. Y. Arradad[2], G. M. Rateb[2], M. S. Elahrash[3]

[1] *University of Benghazi, Benghazi, Libya*
[2] *Tajoura Research Center, Tripoli, Libya*
[3] *University of Elzawia, Elzawia, Libya*

Excited low energy levels of ^{138}Ba have been investigated in this work by means of the (n, n'γ)-reaction using reactor fast neutrons. Two independent experiments were carried out. One is to measure the angular distribution and the other to measure the linear-polarization of the emitted gammas. Energy levels up to ~ 4 MeV and spins up to 8 $\hbar$ were populated. About 200 γ-transitions have been observed through this study. Due to this work, it was possible to confirm unambiguously the spin of many of the previous assignments. In addition, new spin assignments for some levels have been made.

1. Introduction

This study is part of a systematic study of the barium isotopes with neutron number ranging from 78 to 82. The ^{138}Ba nucleus with 82 neutrons is a closed shell nucleus and can be well described within the frame work of the shell model. Therefore, the low energy single particle excitations of ^{138}Ba can be well understood as being due mostly to exciting protons in the $1g_{7/2}$ and $2d_{5/2}$ configurations. The other barium isotopes show, in addition to the above mentioned excitations, single particle neutron excitations and more of collective excitations. Thus, studying ^{138}Ba is essential to establish the single particle proton excitations at low energies for the barium isotopes.

The low levels of ^{138}Ba have been previously studied by β-decay, thermal neutron capture, Coulomb excitations, inelastic scattering of protons and other reactions. However, owing to the experimentally verified fact that the (n, n'γ)-reaction do not, to a large extent, depend on the angular momentum of excited levels at low energies, it is possible to establish a complete level schemes of nuclei studied by this reaction up to 3 MeV excitation energy.

Excited low energy levels of ^{138}Ba have been studied in this work by means of the (n, n'γ)-reaction using reactor fast neutrons. Two independent experiments were carried out, one to measure the angular distribution and the other to measure the linear-polarization of the emitted gammas. Energy levels up to and spins up to 8 $\hbar$ were populated. About 200 γ-transitions have been observed through this study. Due to this work it was possible to confirm unambiguously the spin of many previous assignments. In addition, new spin assignments for some levels have been made. A 0+ is established for the 2189 keV level, a 2+ for the 2931 keV level, a 4+ for the 3257 keV level and 2+ for the 3601 keV level.

Therefore, from the results of this work, a new decay scheme for ^{138}Ba is presented with level up to ~ 4 MeV excitation energy and J = 8 $\hbar$ spin value.

2. Experimental procedures and data analysis

The experimental measurements were carried out by using the fast neutron beam of the IR8 reactor at I. V. Kurchatov Institute of Atomic Energy, in Moscow. The fast neutron beam was filtered from slow neutrons and γ-rays by using absorbers of 1 mm Cd, 10 mm B_4C, 50 mm metallic uranium and 10 mm ^{10}B. An enriched target of 28.69 g $^{138}BaCO_3$ was used. The relative abundance of the Ba-isotopes in the target were 99.8, 0.16 and 0.04 % of ^{138}Ba, ^{137}Ba and ^{136}Ba respectively. Gamma rays emitted from the target were detected using high purity Ge detectors of 10% relative efficiency and ~ 2 keV resolution at 1.3 MeV. Experimental setups of the two experiments are similar to those of the existing setups in Tajoura Research Center, details of which and data analysis techniques used can be found in Refs. [16 to 18].

3. Results and discussion

The decay scheme was constructed from the results of this work and other workers whose results are compiled NUDAT of the IAEA (20). Table 1, lists the observed γ-rays and the levels which they depopulate including the spin assignments of initial and final levels. Included in the Table the state population obtained from

$$P_s = \sum \left(I_\gamma(out) - I_\gamma(in) \right).$$

In this work we did not attempt to introduce new levels, we only tried to resolve spin ambiguities and establish new spins for states which had no previous assignments. We have also added new γ-transitions to already existing levels. Table 2 lists the results of the angular distribution and linear polarization experiments. It includes, also, δ-values for some transitions and the expected linear polarization values.

Following the procedures of Ref. [19], for spin assignments, and Tables 1 and 2, most of the assignments were straightforward except for few, which we need to say more about:

The level at 2189 keV was previously [20] given the assignments of [1, 2, 3). We have observed only one γ-ray (754 keV) de-exciting the level to the 2+ state with relatively good intensity and no contamination. The experimental angular distribution and linear polarization results indicate that it is an isotropic transition which is characteristic of a $0^+ \rightarrow 2^+$ transition. The absence of any ground state transition from this low energy level makes the 1 or 2+ assignment very remote. The analysis of our results with the help of the CINDY program and the χ^2 criteria shows that all the previous assignments (1, 2, 3) were not possible. On the other hand, a shell model calculation by Larson et a1. [25] predicts a 0^+ state with an energy close to that of this level. Therefore, we suggest a 0^+ assignment for the 2189 keV level.

The level at 2583 keV was observed through the decay of four γ-transitions, one of which was to the ground state. A previous (p, p') experiment [26] claimed that a 4^+ state at the energy of 2584 keV exists. It was also claimed that the 365 and 1147 keV γ-transitions de-excite this level as well as the 2583 keV level. From the measured population of the 2583 keV level (see Table 1) we cannot suggest the existence of a second level at the same energy. On the other hand, the angular distribution of 2583 is clearly indicative of a dipole transition and from Table 2 it is clear that 1^+ is the most probable, therefore, excluding any 4^+ state at this energy.

The 2851.6 keV level was not assigned a unique spin by the NUDAT [20]. However, a previous (n, n' γ) experiment by Dioszegi et al. [27] assigned a 4+ value. From our investigation of the angular distribution of the 953 and 1415 keV gamma transitions (see Table 2) we reconfirm the assignment by Dioszegi et al [27].

The 2931 keV level was observed in (p, p') reaction experiment [26] with weak population and suggesting an unnatural assignment of (I +) we have observed three gamma rays de-exciting this level. Two of which have already been reported and a new 1033 keV we have added. The measured population of the level is as expected for states of (1 - 5) spins at this energy. The angular distribution of the 1495.6 keV is compatible with a 2+ to 2+ transition and therefore a spin of 2+ is assigned to this level.

The level at 3050 keV is observed with very high state population (twice as expected). From our investigation of the gamma rays de-exciting this level, we have concluded that the extra population dose not come from any background contamination of these lines. Furthermore, the observed intensities of 1614 and 1152 keV gamma lines almost identical to those observed by another (n, n'γ) experiment [27]. Therefore, the increase in level population must be a real one which should have a physical reason. The only possible interpretation we can make for this increase is that it is due to the existence of a doublet level at this energy. However, such an assumption requires two different characteristics for the two levels. From our study of the angular correlation of the1614 keV transition, we could not confirm such findings

The 3309 keV level was reported in Ref. [20] with one de-exciting gamma transition (1106 keV) to the 6^+ (2203 keV). We have observed this transition with weak intensity and we could not obtain any angular distribution for this line. However, the very low population of this level indicates that it is more likely to be a high spin state with spin greater than 5.

A level at 3561 keV was reported to have been observed in a (d, p) experiment [26] with spin assignment of $(4)^-$. The compilation of NUDAT did not include this level in their list of adopted levels. In the present work we have observed one gamma line (1163.2 keV) which can de-excite this level to the 1898.5 (4^+) keV state. However, the level population is very low suggesting either unnatural spin assignment, such as 4^-, or a high spin value.

The level at 3601.3 keV was observed previously [20] with only the ground transition. We have, in addition, observed two more gamma transitions to the 2931.4 (2+), and 1898.5(4+) keV levels. Thus making only one choice of spin assignment for this level, that is a 2^+.

The level at 3855.3 keV have been observed with one ground state transition. It was previously reported in a (d, p) experiment [26] that a 3857 keV level exists with possible spin of $(5)^-$. However, from our results it is obvious that this assignment is excluded.

Table 1. **Levels and gamma-transitions scheme of ^{138}Ba**

E_i, keV	J_i^π	E_γ, keV	I_γ, r.u.	P_s, r.u.	J_f^π
1435.85	2^+	1435.85	100.000	43.268	0+
1898.52	4^+	462.67	33.180	12.539	2+
2090.50	6^+	191.87	11.225	3.791	4+
2189.82	0^+ *	753.84	1.975	1.975	2+
2203.02	6^+	112.52	5.463	4.171	6+
2217.89	2^+	782.04	0.266	7.887	2+
		2217.89	9.311		0+
2307.46	4^+	408.84	3.586	6.587	4+
		871.69	3.959		2+

Continuation of the Table 1

E_i, keV	J_i^π	E_γ, keV	I_γ, r.u.	P_s, r.u.	J_f^π
2415.25	5^+	107.75	0.249	4.465	4+
		212.19	1.092		6+
		324.70	1.527		6+
		516.57	2.222		4+
2445.61	3^+	227.59	0.214	4.369	2+
		546.84	1.341		4+
		1009.70	3.723		2+
2582.98	1^+ *	138.08	0.486	2.800	3+
		364.87	0.263		2+
		1147.14	1.799		2+
		2583.05	0.343		0+
2639.53	2^+	421.29	0.192	2.573	2+
		1204.00	0.119		2+
		2639.36	2.640		0+
2779.26	4^+	333.56	0.199	2.950	3+
		363.65	0.469		5+
		880.71	0.215		4+
		1343.53	2.112		2+
2851.55	4+ *	648.91	0.040	2.160	6+
		760.96	0.079		6+
		952.93	0.260		4+
		1415.71	1.881		2+
2880.74	3^-	1444.89	2.658	2.099	2+
2931.41	2+ *	1033.05	0.103	1.596	4+
		1495.58	1.378		2+
		2931.25	0.142		0+
2991.06	3^+	575.31	0.114	1.397	5+
		683.68	0.291		4+
		773.22	0.439		2+
		1555.27	0.629		2+
3050.02	2^+	831.61	0.123	2.538	2+
		1151.53	0.218		4+
		1614.08	1.841		2+
		3049.61	0.356		0+
3154.75	4^+	375.37	0.045	0.789	4+
		709.35	0.111		3+
		739.47	0.122		5+
		1064.27	0.304		6+
		1256.20	0.207		4+

Continuation of the Table 1

E_i, keV	J_i^π	E_γ, keV	I_γ, r.u.	P_s, r.u.	J_f^π
3163.04	3^+	717.65	0.081	0.762	3+
		855.26	0.061		4+
		945.95	0.099		2+
		1264.67	0.323		4+
		1727.05	0.262 <a)		2+
3183.67	8^+	980.88	0.092	0.176	6+
		1093.07	0.193		6+
3242.45	3^+ *	603.22	0.129	0.638	2+
		797.01	0.032		3+
		934.83	0.283		4+
		1806.83	0.194		2+
3257.20	3^+ *	1358.80	0.267	0.659	4+
		1821.57	0.437		2+
3309.00		1105.98	0.068	0.068	6+
3338.83	2^+	1440.28	0.314	0.641	4+
		1902.65	0.028		2+
		3338.85	0.485		0+
3359.58	(7^+)	944.33	0.136	0.136	5+
3366.68	2^+	3366.68	0.539	0.539	0+
3442.49	1^- *	803.04	0.602	0.415	2+
		3442.49	0.166		0+
3504.19	1^+ *	165.93	0.176	0.357	2+
		3504.19	0.181		0+
3561.00		1663.17	0.057	0.057	4+
3601.58	(2^+)**	669.20	0.035	0.175	2+
		1702.54	0.064		4+
		3601.32	0.076		0+
3622.09	10^+	438.42	0.044	0.044	8+
3633.00	(9-)	449.29	0.033	0.033	8+
3643.08	2^+	3643.30	0.243	0.243	0+
3646.59	3^+ *	766.07	0.161	0.237	
		1747.77	0.076		4+
3693.93	$(2^+,3,4^+)$	702.61	0.076	0.219	3+
		812.68	0.068		3-
		841.93	-0.010		4+
		1386.29	0.075		4+
3735.00	$(1^+,2^+)$	571.49	0.064	0.179	3+
		3735.27	0.115		0+
3910.00	(10^+)	726.81	0.032	0.032	8+
3922.50	$(3)^-$	1041.22	- 0.010	0.156	
		2023.81	0.156		4+

Continuation of the Table 1

E_i, keV	J_i^π	E_γ, keV	I_γ, r.u.	P_s, r.u.	J_f^π
3935.19	(2^+)	595.98	- 0.010	0.150	2+
		1054.34	0.109		3-
		2499.63	0.041		2+
4012.30	$(4^+,3,2^+)$	754.95	0.045	0.143	4+
		2112.66	0.054		4+
		577.19	0.044		2+

* New spin assignment due to this work.
** Spin assignment by decay mode.

Table 2. **Experimental and calculated linear-polarization and delta values (δ) for some gamma-transitions from the ^{138}Ba(n, n'γ)-reaction**

E_γ, keV	E_{1ev}, keV	J_i^π → J_f^π	P^{exp}	δ	P^{cal}
324.70	2415.5	5+ → 6+	1.15(46)	-3.82(18)	
363.65	2779.5	4+ → 5+	0.85(39)		
364.87	2583.1	1 → 2+	0.62(35)		
408.84	2307.6	4+ → 4+	2.93(88)	-0.13(2)	3.7
462.67	1898.7	4+ → 2+	1.80(38)		
546.84	2445.7	3+ → 4+	1.26(33)	-.049(15)	0.76
597.77	?		3.82(134)		
753.96	2189.8	0+ → 2+	0.99(30)		
766.07	3646.6	3+ → 3-	2.34(177)	0.14(10,-29)	0.90
773.22	2991.2	3+ → 2+	0.33(19)	-2.0 17(130)	1.5
871.69	2307.6	4+ → 2+	3.11 (127)		
1009.70	2445.7	3+ → 2+	0.62(22)	-.052(5)	0.62
1068.3	?		1.30(113)		
1097.1	?		-9.39(1090)		
1147.14	2583.2	(1,2+) → 2+	1.06(43)	0.09(11)	0.98
1343.53	2779.50	4+ 2+	-8.64(956)		
1415.71	2851.6	(2+) → 2+	5.01(515)		
1435.85	1435.8	2+ → 0+	4.97(461)		
1444.89	2881.0	3- → 2+	1.60(85)	-3.64(8)	1.5
1555.27	2991.2	3+ → 2+	-8.14(1569)	0.249(+19,-45)	-8.1
2217.89	2217.9	2+ → 0+	0.54(45)		

REFERENCES

1. *Achtenberg E., Iglesias F., Jech A. et al.* // Phys. Rev. C. – 1972. – Vol. 5. – P. 1759.
2. *Basinger J., Schick W.C. Jr.,Talbert W.L. Jr.* // Nucl. Inst. Meth. - 1975. – Vol. 124. – P. 381.
3. *Carlson G., Talbert W., McConnell R.* // Phys. Rev. C. – 1974. – Vol. 9. – P. 283.
4. *Carraz L., Monnnand E., Moussa A.* // Nucl. Phys. A. – 1977. – Vol. 171. – P. 209.

5. *Hill C., Fuller D.* // Phys. Rev. C. – 1972. – Vol. 5. – P. 532.
6. *Naghara T., Miyaji N., Kurihara H. et al.* // J. Phys. Soc. Japan. – 1970. – Vol. 28. – P. 283.
7. *Singh B., Johns M.* // Nucl. Phys A. – 1973. – Vol. 212. – P. 382.
8. *Grochev V., Dvoreckij V., Demidov A., Rachimov A.* // Izv. Akad. Nauk SSSR. Ser. Fiz. – 1970. – Vol. 34. – P. 768.
9. *Mariscotti M., Gelletley W., Moraagues J., Kane W.* // Phys. Rev. – 1968. – Vol. 174. – P. 1485.
10. *Kerns J., Saladin J.* // Phys Rev C. – 1972. – Vol. 6. – P. 1016.
11. *Larson D., Austin S.M., Wildenthal B.H.* // Phys. Rev. C. – 1974. – Vol. 9. – P. 1574.
12. Jones W, Borgman L, Hecht K, Bardwick J and Parkinson W 1971 Phys Rev C 4 580.
13. *Kerek A., Kownacki J.* // Nucl. Phys. A. – 1973. – Vol. 206. – P. 245.
14. *Swan C.* // Phys. Rev. C. – 1977. – Vol. 15. – P. 1967.
15. *Demidov A.M., Govor L.I., Cherepantsev Yu.K.* Atlas of Gamma-Ray Spectra from the Inelastic Scattering of Reactor Fast Neutrons. – Moscow: Atomizdat, 1978. - 328 p.
16. *Demidov A., Govor L., Bascova K.* Investigation of excited states of nuclei. Almaata: Nauka, 1986. - 70 p.
17. *Galyamin S., Govor L., Demidov A. et al.* // Yaderna Fizika. – 1984. - Vol. 40. - P. 561.
18. *Araddad S., Rateb G.A., Demidov A. et al.* // Izv. Akad. Nauk SSSR. Ser. Fiz. – 1987. - Vol. 51. – P. 45.
19. *Sergiwa S., Rateb G.A., Zleetni S. et al.* // Proc. of the Second Arab Conference on the Peaceful Uses of Atomic Energy, Cairo, Egypt, 1994.
20. *Compilation* of the Nuclear Data Section. – Vienna: IAEA, 1997.
21. *Klein P., Nishine Y.* // Z. Phys. – 1954. – Vol. 52. – P. 853.
22. *Krane K., Steffen R.* // Phys. Rev. C. – 1970. – Vol. 2. – P. 724.
23. *Sheldon E., Rogers V.C.* // Comput. Phys. Commun. – 1973. – Vol. 6. – P. 99.
24. *Sheldon E., Van Patter D.* // Rev. Mod. Phys. – 1966. – Vol. 38. – P. 143.
25. *Larson D., Austin S., Wildenthal B.* // Phys. Rev. C. – 1975. – Vol. 11. – P. 1638.
26. *Compilation* of the Nuclear Data Sheets for ^{138}Ba. - 1988.
27. *Dioszegi I. et al.* // J. Phys.: Nucl. Phys. – 1984. – Vol. 10. – P. 969.

LOOKING THE COSMOS FROM THE LNGS DEEP UNDERGROUND LABORATORY: THE LUNA EXPERIMENT

D. Trezzi[1] (for the LUNA collaboration)

[1] *Istituto Nazionale di Fisica Nucleare, Sezione di Milano Bicocca, Milano, Italy*

Aim of the LUNA (*Laboratory for Underground Nuclear Astrophysics*) experiment is to measure the cross section of fusion reactions that take place inside the stars and that, in the past, dominated the Big Bang Nucleosynthesis (BBN).

These reactions occur rarely in the laboratory conditions with typical cross sections ranging from pb to fb or even smaller and thus the signal often disappears under the natural background. This circumstance explains why the nuclear astrophysical cross sections are usually extrapolated from higher energy experimental data. Thanks to the low background of the LNGS (*Laboratori Nazionali del Gran Sasso*) underground laboratory in Italy, in the last 20 years, LUNA has been studying fusion reactions in the solar and BBN energy windows with important consequences from the astrophysical point of view.

Recently, the LUNA collaboration has been engaged in the study of the ^{2}H(α, γ)^{6}Li reaction. In this paper the experimental setup and the preliminary data analysis will be outlined.

1. Introduction: Basics on Nuclear Astrophysics

All the stars that we can see during starry nights are (or better were, given the so large distances) nuclear furnaces in the Cosmos able to synthetize, during their lives, all the chemical elements heavier than Beryllium. The lighter elements were instead produced in the past, during the Big Bang Nucleosynthesis era.

Thermonuclear fusion reactions take place at energies lower than the height of the barrier arising from the Coulomb repulsion between nuclei. This is possible thanks to the quantum mechanical tunnel effect that provides a not vanishing probability to overpass the barrier otherwise prohibited from the classical point of view.

The associated cross section σ, i.e. the probability to fuse two nuclei, is given by three factors. The first one, E^{-1}, where E is the energy in the center-of-mass system, represents the quantum nature of the interaction. The second one, P(E), takes into account the probability to have quantum tunneling. The third one, S(E), contains all the information about the nuclear interaction between the involved nuclei. This is named astrophysical S-factor. The energy dependence of P(E) is theoretically known and it is given by:

$$P(E) = \exp\left(-31.29 Z_1 Z_2 \sqrt{\frac{\mu}{E}}\right), \tag{1}$$

where Z_1 and Z_2 are the electrical charges of nuclei, μ is the reduced mass in atomic mass units and E is the energy in the center-of-mass system in keV [1, 2]. The cross section is thus given by:

$$\sigma(E) = \frac{1}{E} S(E) \exp\left(-31.29 Z_1 Z_2 \sqrt{\frac{\mu}{E}}\right). \tag{2}$$

In order to attribute physical sense to the thermonuclear fusion cross section, this must be weighted by the energy distribution of the nuclei in the particular astrophysical environment considered given by a Maxwell-Boltzmann. For non-resonant reactions, the resulting function is peaked in a given energy window known as Gamow peak. This occurs at lower energies the cross section is too small whereas at higher energies the nuclei in the tail of the Maxwell-Boltzmann are too few. A typical Gamow peak energy in astrophysical contexts like stars in the Hydrogen burning phase (main sequence), Novae or BBN reactions, is less than a few hundreds of keV.

At these low energies, the reaction cross section drops to values from picobarn (pb) to femtobarn (fb) and even smaller, preventing a direct measurement on the Earth's surface [3, 4]. Extrapolation from high energy data is thus needed. This could lead to uncertainties, like the possible presence of a resonance in the unmeasured energy region, not accounted for by the extrapolation.

2. The ^{6}Li problem

The astronomical observation of ^{6}Li in metal poor stars provide a quantity of this isotope that is two to three orders of magnitude higher than what was expected from the BBN [5].

In order to solve this puzzle, two different experimental approaches are needed. The first is a new measurement of the ^{6}Li abundance in stars in order to reduce the astronomical uncertainty on the available data (especially systematics). The second is a direct measurement of the ^{2}H(α,γ)^{6}Li nuclear cross section that, without involving non-standard processes, is the only reaction able to produce the ^{6}Li now present in the Cosmos during the BBN era.

In the BBN energy range, the ^{2}H(α, γ)^{6}Li cross section, extrapolated from higher energy data (NACRE compilation [6]), is around 20 pb. As previously reported, this low cross section value prevents any kind of direct measurements on

the Earth's surface laboratories and thus the only experimental data available had been obtained by using Coulomb dissociation of 26 MeV ^{6}Li projectiles at Karlsruhe [7] and recently at GSI [8]. This measurements show too low values of the ^{2}H(α, γ)^{6}Li cross section in order to solve the ^{6}Li puzzle.

3. The ^{2}H(α, γ)^{6}Li reaction at LUNA

A direct measurement of the ^{2}H(α, γ)^{6}Li reaction cross section consists in the detection of the gamma rays coming out from it. However, the main problem is the presence of a natural gamma background due to the natural radioactivity and cosmic rays induced reactions that make the signal practically undetectable also by using active shieldings [4].

The LUNA (Laboratory for Underground Nuclear Astrophysics) experiment consists in a 400 keV accelerator [9] located in the underground Gran Sasso laboratory, Italy (Laboratori Nazionali del Gran Sasso, LNGS). Thanks to the low background of the LNGS (covered by 3800 meters of water equivalent that provide a reduction of a factor of six in the muon flux and three in the neutron one [4]) in the last 20 years LUNA has been studying fusion reactions in the solar and BBN energy windows with important consequences from the astrophysical point of view. LUNA is moreover the only underground facility in the world completely dedicated to direct cross section measurements relevant for nuclear astrophysics.

The LUNA setup consists in a 400 kV electrostatic accelerator that provide H, ^{3}He and ^{4}He ions with a very small beam energy spread (70 eV), a very high beam current even at low energy (maximum value: 500 μA for protons, 250 μA for Helium ions) and a long time stability (5 eV/h). The ions are produced by a radio-frequency source mounted on its high voltage terminal. The terminal voltage is generated by an inline-Cockcroft-Walton power supply. The accelerator is embedded in a tank which is filled with nitrogen, carbon dioxide and SF_6 insulation gas at 20 bar. The accelerated particles are then magnetically switched in two beam lines: one for solid targets and a second one for gas targets.

In the case of the ^{2}H(α, γ)^{6}Li measurement, an alpha beam pass through three different pumping stages and finally goes in the windowless gas target chamber filled with deuterium at a pressure of 0.3 mbar. A steel collimator system is also present in order to reduce the beam spot. A lead castle and an anti-radon box (flushed with nitrogen) is provided for decreasing the gamma background coming from the environmental radioactivity. The gamma rays produced by the reaction are collected by the High Purity Germanium Detector (HPGe).

Another source of background present during the ^{2}H(α, γ)^{6}Li measurement is the beam induced background (BIB). As a matter of fact, the alpha ions coming from the accelerator can make Rutherford scattering onto the deuterons present in the gas target. These become energetic enough to collide with other deuterons producing the parasitic reactions d(d, p)t and d(d, n)^{3}He. Neutrons emitted by the d(d, n)^{3}He reaction could give rise to (n, n'γ) reactions with the surrounding materials (mainly lead, copper, iron and nickel) producing a "beam induced" gamma background. The gamma spectrum for the ^{2}H(α, γ)^{6}Li measurement as seen by the Germanium detector is shown in Fig. 1.

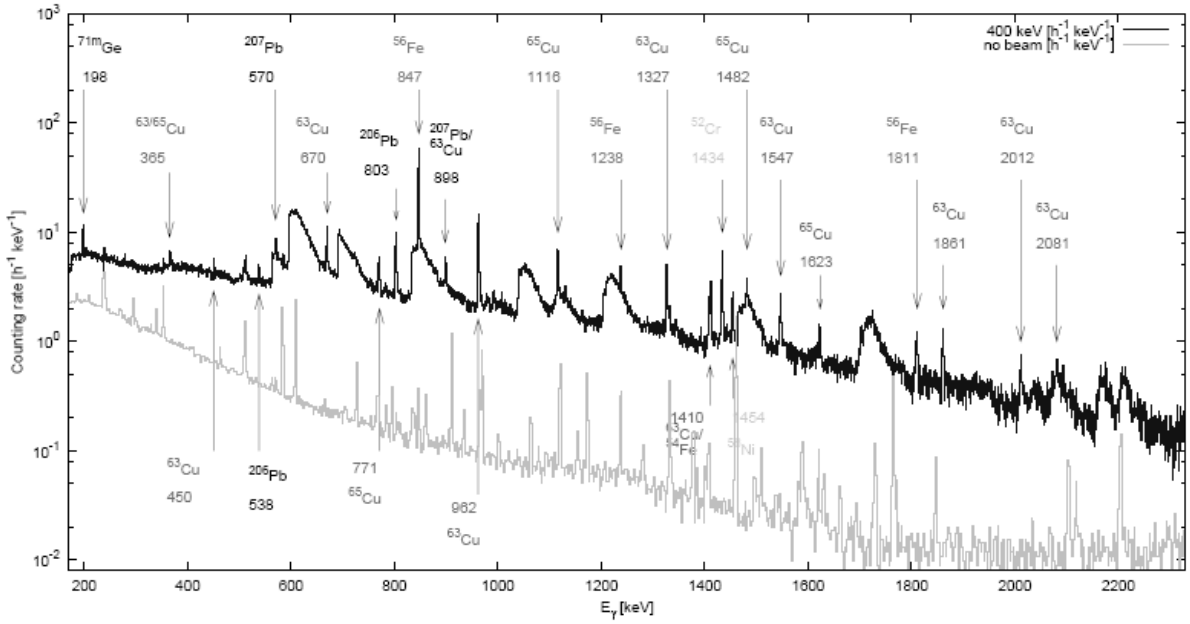

Fig. 1. Spectra taken with the HPGe detector. Black line: in-beam spectrum at beam energy Eα = 400 keV, deuterium pressure 0.3 mbar, laboratory background (grey line) subtracted. The most important lines due to (n, n'γ) and (n, γ) processes on surrounding materials are marked with arrows [11].

A Silicon Detector (SD) mounted close to the interaction area collects the protons coming from the d(d,p)t reaction. This provides important information about the neutron production given that the ratio between the two parasitic reaction rates is theoretically well known. The proton spectrum measured at LUNA is shown in Fig. 2. A broad peak at about 2.0 MeV is present, in good agreement with the Montecarlo GEANT simulations.

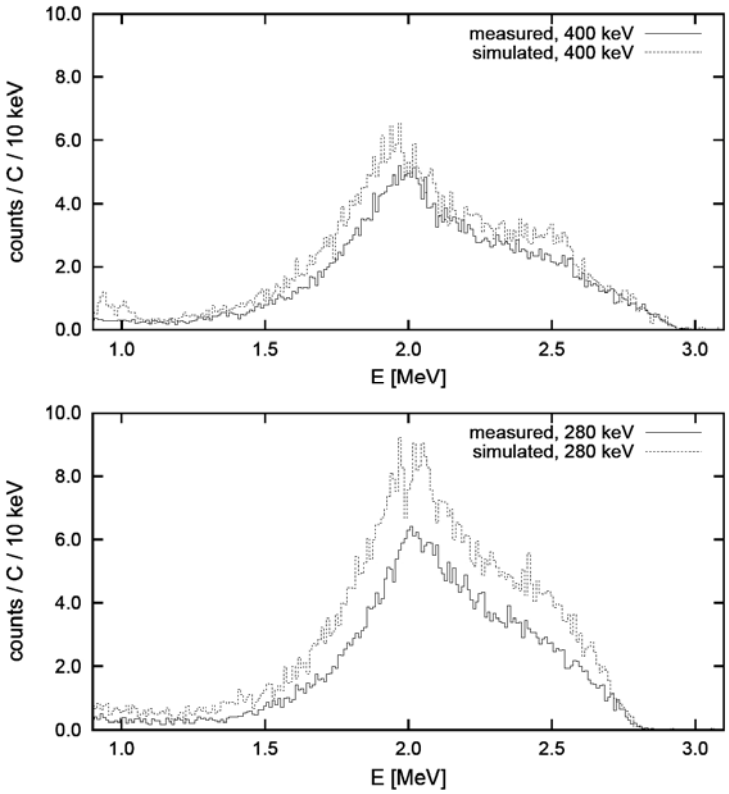

Fig. 2: Experimental (solid line) and GEANT simulated (dashed line) proton spectrum in the silicon detector. Top (bottom) panel, runs at 400 (280) keV. The simulated spectrum is given in arbitrary units.

In order not to increase the low neutron background of the LNGS, a borated High Density Polyethylene HDPE castle is mounted between the lead castle and the anti-radon box.

The alpha beam is finally stopped on the beam calorimeter (made of copper) for measuring the beam current by using a constant temperature gradient [10]. The final setup used for the $^{2}H(\alpha,\gamma)^{6}Li$ reaction at LUNA is summarized in Fig. 3 and described in [11].

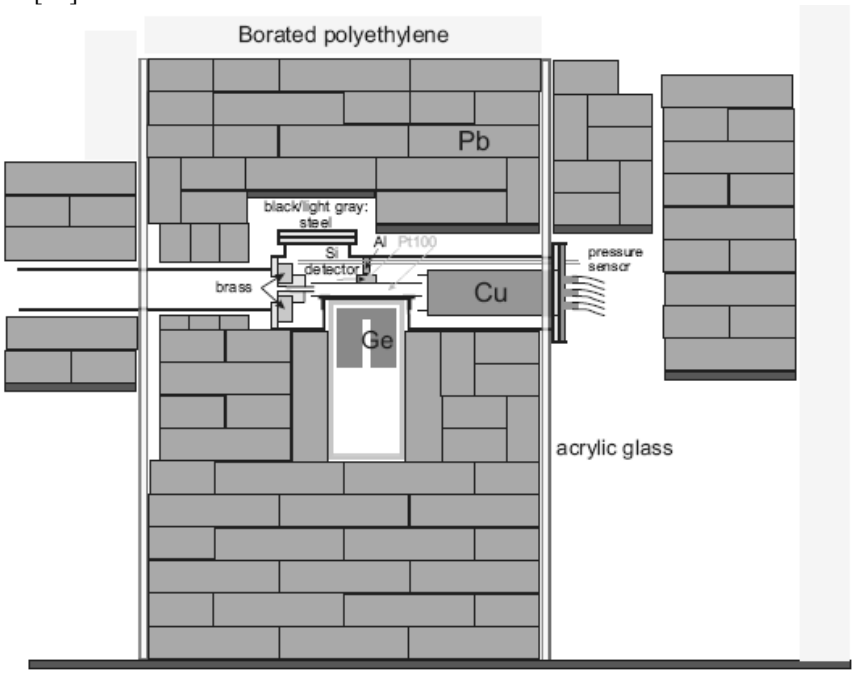

Fig. 3. The experimental setup used for the $^{2}H(\alpha, \gamma)^{6}Li$ reaction at LUNA. The gas target is seen near the center of the plot. The alpha beam enters the target from the left side through the collimator and is stopped at the right side on the beam calorimeter. The HPGe and SD are also shown. The setup is surrounding by a lead castle and walls of borated HDPE. The inner lead castle is surrounded by an anti-radon box made of acrylic glass.

4. Data analysis and first preliminary results

The region of interest (ROI) of the $^2H(\alpha, \gamma)^6Li$ reaction can be theoretically calculated as:

$$ROI = Q + \frac{m_d}{m_\alpha + m_d} E_\alpha - \frac{E_\gamma^2}{2m_{^6Li}c^2} - \frac{v}{c} E_\gamma \cos\theta, \quad (3)$$

where Q is the reaction Q-value, m_α, m_d and m_{6Li} are respectively the alpha, deuteron and ^6Li masses, E_γ is the emitted gamma energy and θ the angle of view measured respect to the alpha direction. In particular the third term represents the ^6Li nucleus recoiling energy and the fourth one the Doppler shift.

Since the BIB is expected to be much higher than the $^2H(\alpha, \gamma)^6Li$ signal, it is not possible to see directly the peak coming from the reaction but a more complex analysis is necessary. Up to now four different analyses are in progress in order to obtain the measured cross section. The common principle is the acquisition of gamma spectra at two different beam energies (with corresponding not overlapping ROIs) and, after a correct normalization, the subtraction of one from the other. The result should be a bipolar signal with peaks in the two respective ROIs.

The LUNA collaboration selected four beam energy values: 240, 280, 360 and 400 keV and performed three different measurement campaigns (namely RUN1 at 280 - 400 keV, RUN2 at 280 - 400 keV and RUN3 at 240 - 360 keV). The respective ROIs are: [1542.0, 1566.0] keV, [1554.5, 1580.0] keV, [1579.5, 1609.0] keV and [1592.0, 1623.0] keV. The first preliminary analysis of RUN1 data is very promising while the analysis of the other two measurement campaigns is still in progress.

Up to now, no resonance in the BBN energy range was measured in order to solve the ^6Li abundance puzzle.

REFERENCES

1. *Clayton DD.*, Principles of Stellar Evolution and Nucleosynthesis. - Chicago: Univ. Chicago Press, 1984.
2. *Rolfs C., Rodney W.,* Cauldrons in the Cosmos. - Chicago: Univ. Chicago Press, 1988.
3. *Constantini H. et al.* LUNA: a laboratory for underground nuclear astrophysics // Rep. Prog. Phys. - 2009. - Vol. 72. - P. 086301.
4. *Broggini C. et al.* LUNA: Nuclear Astrophysics Deep Underground // Annu. Rev. Nucl. Part. Sci. - 2010. - Vol. 60. - P. 53.
5. *Serpico P.D. et al.* Nuclear reaction network for primordial nucleosynthesis: a detailed analysis of rates, uncertainties and light nuclei yields // J. Cosmol. Astropart. Phys. - 2004. - Vol. 2004. - P. 010.
6. *Angulo C. et al.* A compilation of charged-particle induced thermonuclear reaction rates // Nucl. Phys. A. - 1999. - Vol. 656. - P. 3.
7. *Kiener J. et al.* Measurements of the Coulomb dissociation cross section of 156 MeV ^6Li projectiles at extremely low relative fragment energies of astrophysical interest // Phys. Rev. C. - 1991. - Vol. 44. - P. 2195.
8. *Hammache F. et al.* High-energy breakup of ^6Li as a tool to study the Big Bang nucleosynthesis reaction $^2H(\alpha, \gamma)^6Li$ // Phys. Rev. C. - 2010. - Vol. 82. - P. 065803.
9. *Formicola A. et al.* The LUNA II 400 kV accelerator // Nucl. Instrum. Methods. A. - 2003. - Vol. 507. - P. 609.
10. *Casella C. et al.* A new setup for the underground study of capture reactions // Nucl. Instrum. Methods. A. - 2002. - Vol. 489. - P. 160.
11. *Anders M. et al.* Neutron flux induced by an α-beam incident on a deuterium gas target as a background for the study of the $^2H(\alpha, \gamma)^6Li$ reaction at LUNA // Submitted to EPJ.

List of Participants

Valery ABROSIMOV
Institute for Nuclear Research, National Academy
of Sciences of Ukraine, Kyiv, Ukraine
abrosim@kinr.kiev.ua

Dmitry ANCHISHKIN
M. M. Bogolyubov Institute for Theoretical Physics,
National Academy of Sciences of Ukraine,
Kyiv, Ukraine
dima@anchishkin.com

Anatolij ANDREEV
Institute for Nuclear Research, Russian Academy
of Sciences, Moscow, Russia
ava@sci.lebedev.ru

Vladimir ANDRIANOV
V. A. Fock Department of Theoretical Physics
St. Petersburg State University
St. Petersburg, Russia
v.andriano@rambler.ru

Vladimir AUSHEV
Nuclear Physics Department,
Taras Shevchenko National University,
Kyiv, Ukraine
volodymyr.aushev@desy.de

Yegor AUSHEV
National Technical University of Ukraine
"Kyiv Polytechnic Institute",
Kiev, Ukraine
yegora@ukr.net

Oleksandr BABAK
Institute for Nuclear Research, National Academy
of Sciences of Ukraine, Kyiv, Ukraine
a-babak@ukr.ne

Evgeny BALBUTSEV
Bogoliubov Laboratory of Theoretical Physics,
Joint Institute for Nuclear Research,
Dubna, Moscow region, Russia
balbuts@theor.jinr.ru

Alexander BARABASH
Institute of Theoretical and Experimental Physics,
Moscow, Russia
barabash@itep.ru

Sergei BELCHIKOV
Institute for Nuclear Research, National Academy
of Sciences of Ukraine, Kyiv, Ukraine
sergei.sz@yandex.ru

Mohamed BELGAID
Faculté de physique Université des Sciences
et de la Technologie Houari Boumedienne,
Alger, Algeria
belgaidm@yahoo.com

Francesca BELLONI
CEA Saclay, DSM/IRFU/SPhN,
Gif-sur-Yvette, France
francesca.belloni@cea.fr

Vladimir BELOV
Institute of Theoretical and Experimental Physics,
Moscow, Russia
belov@itep.ru

Rita BERNABEI
Dipartimento di Fisica, Università di Roma "Tor Vergata"
and Istituto Nazionale di Fisica Nucleare, Sezione
di Roma "Tor Vergata",
Rome, Italy
rita.bernabei@roma2.infn.it

Emil BĚTÁK
Institute of Physics, Slovak Academy of Sciences,
Bratislava, Slovakia
betak@savba.sk

Boris BONDAR
Taras Shevchenko National University,
Kyiv, Ukraine
miarex@ukr.net

Vira BONDAR
Taras Shevchenko National University,
Kiev, Ukraine
vira_bondar@ukr.net

Maryna BORYSOVA
Institute for Nuclear Research, National Academy
of Sciences of Ukraine, Kyiv, Ukraine
ma@voliacable.com

Leonid BULAVIN
Taras Shevchenko National University,
Kyiv, Ukraine
bulavin@univ.kiev.ua

Dmytro BURDEINYI
National Science Center "Kharkov Institute
of Physics and Technology",
Kharkiv, Ukraine
burdeynyi@kipt.kharkov.ua

Alexander BOTVINA
Institute for Nuclear Research, Russian Academy
of Sciences, Moscow, Russia
a.botvina@gsi.de

Kostyantyn CHERCAS
Institute for Nuclear Research, National Academy
of Sciences of Ukraine, Kyiv, Ukraine
Chercas.Kostya@gmail.com

Kostyantyn CHEREVKO
Taras Shevchenko National University,
Kyiv, Ukraine
Konstantin.cherevko@gmail.com

Dmitry CHERNYAK
Institute for Nuclear Research, National Academy
of Sciences of Ukraine, Kyiv, Ukraine
chernyak@kinr.kiev.ua

Silvio CHERUBINI
University of Catania and INFN-LNS,
Catania, Italy
cherubini@lns.infn.it

Fedor DANEVICH
Institute for Nuclear Research, National Academy
of Sciences of Ukraine, Kyiv, Ukraine
danevich@kinr.kiev.ua

Volodymyr DAVYDOVSKYY
Institute for Nuclear Research, National Academy
of Sciences of Ukraine, Kyiv, Ukraine
odavi.test@gmail.com

Vitali DENISOV
Institute for Nuclear Research, National Academy
of Sciences of Ukraine, Kyiv, Ukraine
denisov@kinr.kiev.ua

Peter DERECHKEY
Institute of Electron Physics, National Academy
of Sciences of Ukraine,
Uzhhorod, Ukraine
derecskei89@gmail.com

Nataliya DOROSHKO
Institute for Nuclear Research, National Academy
of Sciences of Ukraine, Kyiv, Ukraine
kinr@kinr.kiev.ua

Ihor DRYAPACHENKO
Institute for Nuclear Research, National Academy
of Sciences of Ukraine, Kyiv, Ukraine
korohi00@gmail.com

Sergiy DYULDYA
National Science Center "Kharkov Institute
of Physics and Technology",
Kharkiv, Ukraine
sdul@kipt.kharkov.ua

Sergey FEDOTKIN
Institute for Nuclear Research, National Academy
of Sciences of Ukraine, Kyiv, Ukraine
sfedotkin@inbox.ru

Sergii FOMIN
National Science Center "Kharkov Institute
of Physics and Technology",
Kharkiv, Ukraine
sfomin@kipt.kharkov.ua

Karin Guimarães FORNAZIER
Instituto Tecnológico de Aeronáutica,
São José dos Campos, Brazil
karin.fornazier@gmail.com

Azusa GANDO
Research Center for Neutrino Science, Tohoku University,
Sendai, Japan
azusa@awa.tohoku.ac.jp

Huben GANEV
Bogoliubov Laboratory of Theoretical Physics,
Joint Institute for Nuclear Research,
Dubna, Moscow region, Russia
huben@theor.jinr.ru

Volodymyr GANN
National Science Center "Kharkov Institute
of Physics and Technology",
Kharkiv, Ukraine
gann@kipt.kharkov.ua

Oleg GERASHCHENKO
Institute for Nuclear Research, National Academy
of Sciences of Ukraine, Kyiv, Ukraine
geraschenko@kinr.kiev.ua

Andrea GIULIANI
Centre de Spectrometrie Nucleaire
et de Spectrometrie de Masse,
Orsay, France
giuliani@csnsm.in2p3.fr

Larisa GOLINKA-BEZSHYYKO
Taras Shevchenko National University,
Kyiv, Ukraine
lyalkagb@gmail.com

Oleksandr GORBACHENKO
Nuclear Physics Department, Faculty of Physics,
Taras Shevchenko National University,
Kyiv, Ukraine
gorbachenko@univ.kiev.ua

Olga GORPINICH
Institute for Nuclear Research, National Academy
of Sciences of Ukraine, Kyiv, Ukraine
olgagor@kinr.kiev.ua

Konstantin GRIDNEV
St. Petersburg State University,
St. Petersburg, Russia
kgridnev@yahoo.com

Boris GRINJUK
M. M. Bogolyubov Institute for Theoretical Physics,
National Academy of Sciences of Ukraine,
Kyiv, Ukraine
bgrinyuk@meta.ua

Olena GRITZAY
Institute for Nuclear Research, National Academy
of Sciences of Ukraine, Kyiv, Ukraine
ogritzay@kinr.kiev.ua

Anna GRYMALO
Institute for Nuclear Research, National Academy
of Sciences of Ukraine, Kyiv, Ukraine
grimalo.a@gmail.com

Oleksandr GRYTSENKO
Institute for Nuclear Research, National Academy
of Sciences of Ukraine, Kyiv, Ukraine
agrytsen@kinr.kiev.ua

Volodymyr GULIK
Institute for Nuclear Research, National Academy
of Sciences of Ukraine, Kyiv, Ukraine
gulik@kinr.kiev.ua

Samir A. HAMOUDA
University of Benghazi,
Benghazi, Libya
dr_s_hamouda@yahoo.ie

Sophia HEINZ
GSI Helmholtzzentrum für Schwerionenforschung,
Darmstadt, Germany
S.Heinz@gsi.de

Tatsiana HRYHAROVICH
Joint Institute of Power and Nuclear Research - Sosny,
National Academy of Sciences of Belarus,
Minsk, Belarus
sikorin@inbox.ru

Viktor IAKOVENKO
Institute for Nuclear Research, National Academy
of Sciences of Ukraine, Kyiv, Ukraine
vyakovenko@kinr.kiev.ua

Viktor ILKOVYCH
Institute for Nuclear Research, National Academy
of Sciences of Ukraine, Kyiv, Ukraine
vistaldi@kinr.kiev.ua

Alexander ISAYEV
National Science Center “Kharkov Institute
of Physics and Technology”,
Kharkov, Ukraine
isayev@online.kharkov.ua

Fedir IVANYUK
Institute for Nuclear Research, National Academy
of Sciences of Ukraine, Kyiv, Ukraine
ivanyuk@kinr.kiev.ua

Bunryu IMANISHI
Independent
503-2424 Ikeno 125, Ikeda, Ibi
Gifu, Japan
imanishi@m3.dion.ne.jp

Laszlo JENKOVSZKY
M. M. Bogolyubov Institute for Theoretical Physics,
National Academy of Sciences of Ukraine,
Kyiv, Ukraine
jenk@bitp.kiev.ua

Artem KADENKO
Taras Shevchenko National University,
Kyiv, Ukraine
kadenkoartem@gmail.com

Oleksandr KALCHENKO
Institute for Nuclear Research, National Academy
of Sciences of Ukraine, Kyiv, Ukraine
kaltchen@kinr.kiev.ua

Sergii KANDYBEI
National Science Center “Kharkov Institute
of Physics and Technology”,
Kharkiv, Ukraine
kandybei@kipt.kharkov.ua

Sarkis KARAMIAN
Joint Institute for Nuclear Research
Dubna, Moscow region, Russia
karamian@nrmail.jinr.ru

Andrey KARPENKO
Institute for Nuclear Research, National Academy
of Sciences of Ukraine, Kyiv, Ukraine
ayak@kinr.kiev.ua

Yurij KASATKIN
Institute of Electrophysics and Radiation Technologies,
National Academy of Sciences of Ukraine,
Kharkiv, Ukraine
YuKasatkin2007@ya.ru

Nataliya KHAFIZOVA
National Research Nuclear University MEPhI
Sergiev Posad, Russia
nataliya0687@gmail.com

Volodymyr KHOTYAYINTSEV
Taras Shevchenko National University,
Kyiv, Ukraine
vkhot@ukr.net

Olena KHOTYAYINTSEVA
Institute for Nuclear Research, National Academy
of Sciences of Ukraine, Kyiv, Ukraine
elenakhot@gmail.com

Vladimir KIRISCHUK
Institute for Nuclear Research, National Academy
of Sciences of Ukraine, Kyiv, Ukraine
kirisch@mpca.kiev.ua

Vyacheslav KLEPIKOV
Institute of Electrophysics and Radiation Technologies,
National Academy of Sciences of Ukraine,
Kharkiv, Ukraine
ie@iert.kharkov.ua

Alexander KOBYAKIN
Institute for Theoretical and Experimental Physics
Moscow, Russia
Alexander.Kobyakin@itep.ru

Vladislav KOBYCHEV
Institute for Nuclear Research, National Academy of Sciences of Ukraine, Kyiv, Ukraine
kobychev@kinr.kiev.ua

Volodymyr KOLOMIETZ
Institute for Nuclear Research, National Academy of Sciences of Ukraine, Kyiv, Ukraine
vkolom@kinr.kiev.ua

Vladimir KONDRATYEV
Taras Shevchenko National University, Kyiv, Ukraine
vkondrat@i.ua

Grigory KOSENKO
Omsk State University, Omsk, Russia
kosenko@phys.omsu.omskreg.ru

Oleksii KOVALCHUK
Institute for Nuclear Research, National Academy of Sciences of Ukraine, Kyiv, Ukraine
lexxkov@kinr.kiev.ua

Tetiana KOVALINSKA
Institute for Nuclear Research, National Academy of Sciences of Ukraine, Kyiv, Ukraine
sungel@i.ua

Zakhar KOVALYUK
Chernivtsi Department of the Frantsevich Institute for Problems of Materials Science, National Academy of Sciences of Ukraine, Chernivtsi, Ukraine
chimsp@ukrpost.ua

Yaroslav KRIVENKO-EMETOV
Institute for Nuclear Research, National Academy of Sciences of Ukraine, Kyiv, Ukraine
emet@kinr.kiev.ua

Olga KUPRAVA
Institute for Nuclear Research, National Academy of Sciences of Ukraine, Kyiv, Ukraine
kuprava@kinr.kiev.ua

Volodymyr KUPRYASHKIN
Institute for Nuclear Research, National Academy of Sciences of Ukraine, Kyiv, Ukraine
kupryashkinvt@yahoo.com

Anna KURTEVA
Institute for Nuclear Research, National Academy of Sciences of Ukraine, Kyiv, Ukraine
kurteva@ukrpost.ua

Anatoly KYSLYTSKYI
Institute for Nuclear Research, National Academy of Sciences of Ukraine, Kyiv, Ukraine

Valeryi KUZNETSOV
Institute for Nuclear Research, Russian Academy of Sciences, Moscow, Russia
kuvale@gmail.com

Evgenia KUZNETSOVA
Institute for Nuclear Research, Russian Academy of Sciences, Moscow, Russia
evgenia@inr.ru

Volodymyr KYVA
Institute for Nuclear Research, National Academy of Sciences of Ukraine, Kyiv, Ukraine
vkyva@kinr.kiev.ua

Anatolii LASHKO
Institute for Nuclear Research, National Academy of Sciences of Ukraine, Kyiv, Ukraine
lashkoa@yahoo.com

Tamara LASHKO
Institute for Nuclear Research, National Academy of Sciences of Ukraine, Kyiv, Ukraine
lashkoa@yahoo.com

Yuliya LASHKO
M. M. Bogolyubov Institute for Theoretical Physics, National Academy of Sciences of Ukraine, Kyiv, Ukraine
ylashko@gmail.com

Volodymyr LIBMAN
Institute for Nuclear Research, National Academy of Sciences of Ukraine, Kyiv, Ukraine
vlibman@kinr.kiev.ua

Dmitry LITVINOV
Institute for Safety Problems of Nuclear Power Plants, National Academy of Sciences of Ukraine, Kyiv, Ukraine
litvinovda@mail.ru

Zdzisław ŁOJEWSKI
M. Curie-Skłodowska University, Lublin, Poland
zdzislaw.lojewski@poczta.umcs.lublin.pl

Sergiy LUKYANOV
Institute for Nuclear Research, National Academy of Sciences of Ukraine, Kyiv, Ukraine
lukyanov@kinr.kiev.ua

Yuri LUTOSTANSKY
National Research Centre “Kurchatov Institute”, Moscow, Russia
lutostansky@yandex.ru

Petro LYTOVCHENKO
Institute for Nuclear Research, National Academy of Sciences of Ukraine, Kyiv, Ukraine
plitov@kinr.kiev.ua

Vladimir LYASHUK
Institute for Nuclear Research, Russian Academy of Sciences, Moscow, Russia
lyashuk@itep.ru

Alexander MAGNER
Institute for Nuclear Research, National Academy of Sciences of Ukraine, Kyiv, Ukraine
magner@kinr.kiev.ua

Cristina Alice MARGEANU
Institute for Nuclear Research Pitesti, Mioveni, Romania
cristina.margeanu@yahoo.com

Tetyana MARGITYCH
Institute for Nuclear Research, National Academy of Sciences of Ukraine, Kyiv, Ukraine
margtanya@gmail.com

Ludmila MARTCENIUK
Institute for Nuclear Research, National Academy of Sciences of Ukraine, Kyiv, Ukraine
Prolisok77@yandex.ru

Volodymyr MASLYUK
Institute of Electron Physics, National Academy of Sciences of Ukraine,
Uzhhorod, Ukraine
nuclear@email.uz.ua

Sergei MAYDANYUK
Institute for Nuclear Research, National Academy of Sciences of Ukraine, Kyiv, Ukraine
maidan@kinr.kiev.ua

Aleksandr MAZILOV
National Science Center "Kharkov Institute of Physics and Technology",
Kharkov, Ukraine
mazilov@kipt.kharkov.ua

Svitlana MELNIK
Institute of Applied Physics, National Academy of Sciences of Ukraine, Sumy, Ukraine
melnik_s@ipflab.sumy.ua

Kyrylo MERKOTAN
Odesa National Polytechnic University,
Odessa, Ukraine
merkotankir@ukr.net

Ekaterina MIHNEVA
National University of Life and Environmental Sciences of Ukraine,
Kyiv, Ukraine
tkovalinska@kinr.kiev.ua

Leonid MIKHAILOV
Institute for Nuclear Research, National Academy of Sciences of Ukraine, Kyiv, Ukraine
leomix@kinr.kiev.ua

Mykola MIKHAILOV
Institute for Nuclear Research, National Academy of Sciences of Ukraine, Kyiv, Ukraine

Vadim MIKHAILYUK
Institute for Nuclear Research, National Academy of Sciences of Ukraine, Kyiv, Ukraine
mikhailyuk@kinr.kiev.ua

Viktor MILITSIYA
Institute for Nuclear Research, National Academy of Sciences of Ukraine, Kyiv, Ukraine
militsiya@kinr.kiev.ua

Nick MITROKHOVICH
Institute for Nuclear Research, National Academy of Sciences of Ukraine, Kyiv, Ukraine
mitrokhov@kinr.kiev.ua

Valentyna MOKINA
Institute for Nuclear Research, National Academy of Sciences of Ukraine, Kyiv, Ukraine
vmokina@kinr.kiev.ua

Mikhail MORDOVSKOY
Institute for Nuclear Research, Russian Academy of Sciences, Moscow, Russia
mvmordovsk@mail.ru

Volodymyr MOSKALENKO
Institute of Applied Physics, National Academy of Sciences of Ukraine, Sumy, Ukraine
moskalenko@ipflab.sumy.ua

Eduard MOZHZHUKHIN
Institute for Nuclear Research, National Academy of Sciences of Ukraine, Kyiv, Ukraine
tandem@kinr.kiev.ua

Aleksandr NESTEROV
M. M. Bogolyubov Institute for Theoretical Physics, National Academy of Sciences of Ukraine,
Kyiv, Ukraine
nesterov@bitp.kiev.ua

Vasily NESTEROV
Institute for Nuclear Research, National Academy of Sciences of Ukraine, Kyiv, Ukraine
archerix@ukrpost.ua

Claudia NONES
CEA Saclay, DSM/IRFU/SPhN,
Gif-sur-Yvette, France
claudia.nones@cea.fr

Tatiana OBIKHOD
Institute for Nuclear Research, National Academy of Sciences of Ukraine, Kyiv, Ukraine
obikhod@kinr.kiev.ua

Oleksandr OKHRIMENKO
Institute for Nuclear Research, National Academy of Sciences of Ukraine, Kyiv, Ukraine
okhrimenko@kinr.kiev.ua

Vladislav OLKHOVSKY
Institute for Nuclear Research, National Academy of Sciences of Ukraine, Kyiv, Ukraine
olkhovsk@kinr.kiev.ua

Ivan OSTAPENKO
Institute for Nuclear Research, National Academy of Sciences of Ukraine, Kyiv, Ukraine
ostiv@ukr.net

Volodymyr OTSALYUK
Institute for Nuclear Research, National Academy of Sciences of Ukraine, Kyiv, Ukraine
80971538689@mail.ru

Yuliya PALAHINA
Joint Institute of Power and Nuclear Research - Sosny, National Academy of Sciences of Belarus,
Minsk, Belarus
julia_palagina@tut.by

Alexander PANKOV
Gomel State Technical University,
Gomel, Belarus
pankov@ictp.it

Oksana PANTAK
Odesa National Polytechnic University,
Odesa, Ukraine
pantaoksana@yandex.ru

Oleg PARLAG
Institute of Electron Physics, National Academy of Sciences of Ukraine,
Uzhhorod, Ukraine
parlag.oleg@gmail.com

Yuriy PAVLENKO
Institute for Nuclear Research, National Academy of Sciences of Ukraine, Kyiv, Ukraine
ypavlen@kinr.kiev.ua

Elena PAVLOVA
Omsk State Transport University,
Omsk, Russia
lenochka.physics@gmail.com

Volodymyr PAVLOVYCH
Institute for Nuclear Research, National Academy of Sciences of Ukraine, Kyiv, Ukraine
pavlovich@kinr.kiev.ua

Sergey PELYKH
Odesa National Polytechnic University,
Odesa, Ukraine
1@pelykh.net

Volodymyr PEREVERTAILO
SE Institute of Microdevices STC
"Institute for Single Crystals", National Academy of Sciences of Ukraine, Kyiv, Ukraine
detector@carrier.kiev.ua

Ievgenii PETRENKO
Taras Shevchenko National University,
Kiev, Ukrane
ievgeniip@gmail.com

Vitaliy PETRENKO
Institute of Nuclear Physics,
Uzbekistan Academy Sciences,
Ulughbek, Tashkent, Uzbekistan
petrenko@inp.uz

Dmytro PIATNYTSKYI
M. M. Bogolyubov Institute for Theoretical Physics,
National Academy of Sciences of Ukraine,
Kyiv, Ukraine
dvpyat@gmail.com

Nickolay PILIPENKO
Institute for Nuclear Research, National Academy of Sciences of Ukraine, Kyiv, Ukraine
nick.pilipenko@gmail.com

Volodimir PILIPENKO
National Science Center "Kharkov Institute of Physics and Technology",
Kharkiv, Ukraine
vpilipenko@kipt.kharkov.ua

Valerii PIRNAK
Institute for Nuclear Research, National Academy of Sciences of Ukraine, Kyiv, Ukraine
pirnak2000@yahoo.co.uk

Vladimir PLUJKO
Nuclear Physics Department, Faculty of Physics,
Taras Shevchenko National University,
Kyiv, Ukraine
plujko@univ.kiev.ua

Denys PODA
Institute for Nuclear Research, National Academy of Sciences of Ukraine, Kyiv, Ukraine
poda@kinr.kiev.ua

Ruslan PODVIYANUK
Laurentian University, Department of Physics,
Sudbury, ON, Canada
RPodviianiuk@laurentian.ca

Dorin POENARU
Horia Hulubei National Institute for Physics and Nuclear Engineering,
Bucharest-Magurele, Romania
poenaru@theory.nipne.ro

Oksana POLISHCHUK
Institute for Nuclear Research, National Academy of Sciences of Ukraine, Kyiv, Ukraine
polischuk@kinr.kiev.ua

Oleg PONKRATENKO
Institute for Nuclear Research, National Academy of Sciences of Ukraine, Kyiv, Ukraine
oponkrat@yahoo.com

Orest POVOROZNYK
Institute for Nuclear Research, National Academy of Sciences of Ukraine, Kyiv, Ukraine
orestpov@kinr.kiev.ua

Boris PRITYCHENKO
National Nuclear Data Center,
Brookhaven National Laboratory,
Upton, NY, USA
pritychenko@gmail.com

Mykhailo PUGACH
Nuclear Physics Department, Faculty of Physics,
Taras Shevchenko National University,
Kyiv, Ukraine
mvpugach@gmail.com

Valery PUGATCH
Institute for Nuclear Research, National Academy of Sciences of Ukraine, Kyiv, Ukraine
pugatch@kinr.kiev.ua

Sugathan PULLANHIOTAN
Inter University Accelerator Centre,
Aruna Asaf Ali Rd, New Delhi, India
sugathan@gmail.com

Yuriy PYLYPCHENKO
University of Iowa, Iowa City,
Iowa, USA
yuriy.pylypchenko@cern.ch

Zhanna PYSANKO
Institute for Nuclear Research, National Academy of Sciences of Ukraine, Kyiv, Ukraine
pysanko@kinr.kiev.ua

Sergey RADIONOV
Institute for Nuclear Research, National Academy of Sciences of Ukraine, Kyiv, Ukraine
sergey.radionov@mail.ru

Volodymyr RAZBUDEY
Institute for Nuclear Research, National Academy of Sciences of Ukraine, Kyiv, Ukraine
razbudey@kinr.kiev.ua

Oleksii REBROV
Institute of Applied Physics, National Academy of Sciences of Ukraine, Sumy, Ukraine
rebrov88@gmail.com

Volodymyr REVKA
Institute for Nuclear Research, National Academy of Sciences of Ukraine, Kyiv, Ukraine
revkav@kinr.kiev.ua

Peter RING
Physics Department, Technical University of Munich,
Garching, Germany
ring@ph.tum.de

Mariia ROMANIUK
University of Messina,
Messina, Italy;
Institute for Nuclear Research, National Academy of Sciences of Ukraine, Kyiv, Ukraine
romanyukmariya@ukr.net

Guy ROYER
Laboratoire Subatech,
Nantes, France
Guy.Royer@subatech.in2p3.fr

Adam RUDCHIK
Institute for Nuclear Research, National Academy of Sciences of Ukraine, Kyiv, Ukraine
rudchik@kinr.kiev.ua

Andriy RUDCHIK
Institute for Nuclear Research, National Academy of Sciences of Ukraine, Kyiv, Ukraine

Borys RUDENKO
Institute for Nuclear Research, National Academy of Sciences of Ukraine, Kyiv, Ukraine
rudenko@kinr.kiev.ua

Vladimir RUDYCHEV
V. N. Karazin Kharkiv National University,
Kharkiv, Ukraine
rud@pht.univer.kharkov.ua

Nikolay RUKHADZE
Joint Institute for Nuclear Research,
Dubna, Moscow region, Russia
rukhadze@jinr.ru

Oleksandr RUNDEL
Institute for Nuclear Research, National Academy of Sciences of Ukraine, Kyiv, Ukraine
alexrndl@gmail.com

Vasiliy RYAZANOV
Institute for Nuclear Research, National Academy of Sciences of Ukraine, Kyiv, Ukraine
vryazan@yandex.ru

Vyacheslav SAMARIN
Joint Institute for Nuclear Research,
Dubna, Moscow region, Russia
v-samarin@yandex.ru

Dmitry SAMOILENKO
Scientific and Technical Centre, National Nuclear Energy Generating Company “Energoatom”,
Kyiv, Ukraine
samdmitry@gmail.com

Andriy SANZHUR
Institute for Nuclear Research, National Academy of Sciences of Ukraine, Kyiv, Ukraine
sanjour@kinr.kiev.ua

Andriy SAVRASOV
Institute for Nuclear Research, National Academy of Sciences of Ukraine, Kyiv, Ukraine
asavrasov@kinr.kiev.ua

Bernard SCHAEFFER
Independent
7, rue de l’Ambroisie, 75012,
Paris, France
bschaeffer@wanadoo.fr

Nicholas SCIELZO
Lawrence Livermore National Laboratory,
Livermore, CA, USA
scielzo1@llnl.gov

Sergey SEMENOV
National Research Centre “Kurchatov Institute”,
Moscow, Russia
Semenov@imp.kiae.ru

Oleksandr SEMENYUK
Institute for Nuclear Research, National Academy of Sciences of Ukraine, Kyiv, Ukraine
semalex@kinr.kiev.ua

Valentina SEMKOVA
International Atomic Energy Agency,
Vienna, Austria
v.semkova@iaea.org

Sami SERGIWA
University of Benghazi,
Benghazi, Libya
sergiwa@hotmail.com

Viktor SHAKHOV
Institute for Nuclear Research, National Academy of Sciences of Ukraine, Kyiv, Ukraine

Alexander SHKARUPA
Taras Shevchenko National University,
Kyiv, Ukraine
shkarupa@i.kiev.ua

Shalom SHLOMO
Texas A&M University, Cyclotron Institute,
College Station, USA
shlomo@comp.tamu.edu

Nikolai SHUL'GA
National Science Center "Kharkov Institute of Physics and Technology",
Kharkiv, Ukraine
shulga@kipt.kharkov.ua

Yuriy SHYRMA
Institute for Nuclear Research, National Academy of Sciences of Ukraine, Kyiv, Ukraine
shyrma@kinr.kiev.ua

Sunniva SIEM
University of Oslo, Department of Physics,
Oslo, Norway
sunniva.siem@fys.uio.no

Svyatoslav SIKORIN
Joint Institute of Power and Nuclear Research - Sosny,
National Academy of Sciences of Belarus,
Minsk, Belarus
sikorin@sosny.bas-net.by

Ivan SIMENOG
M. M. Bogolyubov Institute for Theoretical Physics,
National Academy of Sciences of Ukraine,
Kyiv, Ukraine
ivsimenog@bitp.kiev.ua

Airat SITDIKOV
Kazan State Power-Engineering University,
Kazan, Russia
airat_vm@rambler.ru

Yevgen SKAKUN
National Science Center “Kharkov Institute of Physics and Technology”,
Institute of High Energy and Nuclear Physics,
Kharkiv, Ukraine
skakun@kipt.kharkov.ua

Nikolay SKOBELEV
Joint Institute for Nuclear Research,
Dubna, Moscow Region, Russia
skobelev@jinr.ru

Vladimir SKORKIN
Institute for Nuclear Research, Russian Academy of Sciences, Moscow, Russia
skorkin@inr.ru

Vasyl SLISENKO
Institute for Nuclear Research, National Academy of Sciences of Ukraine, Kyiv, Ukraine
slisenko@kinr.kiev.ua

Adam SOBICZEWSKI
National Centre for Nuclear Research
Warsaw, Poland
Adam.Sobiczewski@fuw.edu.pl

Alexander SOKOLOV
Institute for Nuclear Research, National Academy of Sciences of Ukraine, Kyiv, Ukraine
sokolov@kinr.kiev.ua

Iurii SOROKIN
Goethe University Frankfurt
Darmstadt, Germany;
Institute for Nuclear Research, National Academy
of Sciences of Ukraine, Kyiv, Ukraine
iurii.sorokin@gmail.com

Yuriy STEPANENKO
Institute for Nuclear Research, National Academy
of Sciences of Ukraine, Kyiv, Ukraine
steprofy@gmail.com

Anatolii STEPANIUK
Institute for Nuclear Research, National Academy
of Sciences of Ukraine, Kyiv, Ukraine
anatolii.stepaniuk@gmail.com

Dmytro STOROZHYK
Institute for Nuclear Research, National Academy
of Sciences of Ukraine, Kyiv, Ukraine
dstorozhyk@kinr.kiev.ua

Leonid SYDORENKO
Institute for Nuclear Research, National Academy
of Sciences of Ukraine, Kyiv, Ukraine
kupryashkinvt@yahoo.com

Rose SUNNIVA
University of Oslo,
Oslo, Norway
sunniva.rose@fys.uio.no

Dmytro SYMOCHKO
Institute of Electron Physics, National Academy
of Sciences of Ukraine,
Uzhhorod, Ukraine
dmytro.simochko@gmail.com

Xiaodong TANG
Department of Physics and Joint Institute
for Nuclear Astrophysics,
University of Notre Dame,
Notre Dame, IN, USA
x.tang@nd.edu

Vyacheslav TARASOV
National Science Center "Kharkov Institute
of Physics and Technology",
Kharkiv, Ukraine
vtarasov@kipt.kharkov.ua

Jan TOKE
University of Rochester, Department of Chemistry,
Rochester, NY, USA
toke@chem.rochester.edu

Domenico TORRESI
Università di Padova & INFN Sezione di Padova,
Padova, Italy
torresi@pd.infn.it

Vladimir TRETYAK
Institute for Nuclear Research, National Academy
of Sciences of Ukraine, Kyiv, Ukraine
tretyak@kinr.kiev.ua

Davide TREZZI
Istituto Nazionale di Fisica Nucleare, Sezione di Milano,
Milano, Italy
davide.trezzi@mi.infn.it

Yury TSYGANOV
Joint Institute for Nuclear Research,
Dubna, Moscow region, Russia
tyura@sungns.jinr.ru

Alexei TUROVSKY
M. M. Bogolyubov Institute for Theoretical Physics,
National Academy of Sciences of Ukraine,
Kyiv, Ukraine
turovsky@bitp.kiev.ua

Andrii TYKHONOV
Department of Experimental Particle Physics,
Jozef Stefan Institute, Ljubljana, Slovenia
andrii.tykhonov@ijs.si

Volodymyr ULESHCHENKO
Institute for Nuclear Research, National Academy
of Sciences of Ukraine, Kyiv, Ukraine
uleshch@kinr.kiev.ua

Tatsiana VASILEUSKAYA
Joint Institute of Power and Nuclear Research - Sosny,
National Academy of Sciences of Belarus,
Minsk, Belarus
hz@npae2012.kiev.ua

Victor VASILEVSKY
M. M. Bogolyubov Institute for Theoretical Physics,
National Academy of Sciences of Ukraine,
Kyiv, Ukraine
VSVasilevsky@gmail.com

Iouri VASSILIEV
GSI Helmholtzzentrum für Schwerionenforschung,
Darmstadt, Germany
i.vassiliev@gsi.de

Vitaly VENEDIKTOV
Institute for Nuclear Research, National Academy
of Sciences of Ukraine, Kyiv, Ukraine
vened@kinr.kiev.ua

Volodymyr VERBYTSKYI
Institute for Nuclear Research, National Academy
of Sciences of Ukraine, Kyiv, Ukraine
vverbit@kinr.kiev.ua

Stepan VOLKOVETSKYI
Institute for Nuclear Research, National Academy
of Sciences of Ukraine, Kyiv, Ukraine
volkovetskyi@gmail.com

Petro VORONA
Institute for Nuclear Research, National Academy
of Sciences of Ukraine, Kyiv, Ukraine
p_vorona@kinr.kiev.ua

Vladimir VYSOTSKII
Radiophysical Department,
Taras Shevchenko National University,
Kyiv, Ukraine
viv@vhome.kiev.ua

Aleksandr ZAKHARCHENKO
National Science Center "Kharkov Institute
of Physics and Technology",
Kharkiv, Ukraine
az@kipt.kharkov.ua

Viktor ZHEMENIK
Joint Institute for Nuclear Research,
Dubna, Moscow region, Russia
laser@jinr.ru

Sergey ZUYEV
Institute for Nuclear Research, Russian Academy
of Sciences, Moscow, Russia
svzuyev@gmail.com

Author Index

For notes

Scientific publication

The 4-th International Conference "Current Problems in Nuclear Physics and Atomic Energy" (NPAE-Kyiv2012)

Proceedings
Part I

Presentations are published in authors' edition

Cover's design *T. O. Margitych*
Computer-aided makeup *O. D. Grygorenko*

Підп. до друку 21.02.2013. Формат 60×84/8. Ум. друк. арк. 40,7
Тираж 200 пр. Зам. № 2

Інститут ядерних досліджень НАН України,
просп. Науки, 47, м. Київ, 03680, тел. 525-14-56
Свідоцтво суб'єкта видавничої справи ДК № 4051 від 18 квітня 2011 р.

Надруковано у ЦСТРІ м. Києва, філія № 7 «КОПІ ЦЕНТР»,
просп. Перемоги, 37, м. Київ, 03056, тел.: 277-88-93, 277-37-49
Свідоцтво суб'єкта видавничої справи ДК № 37096928 від 15 березня 2005 р.